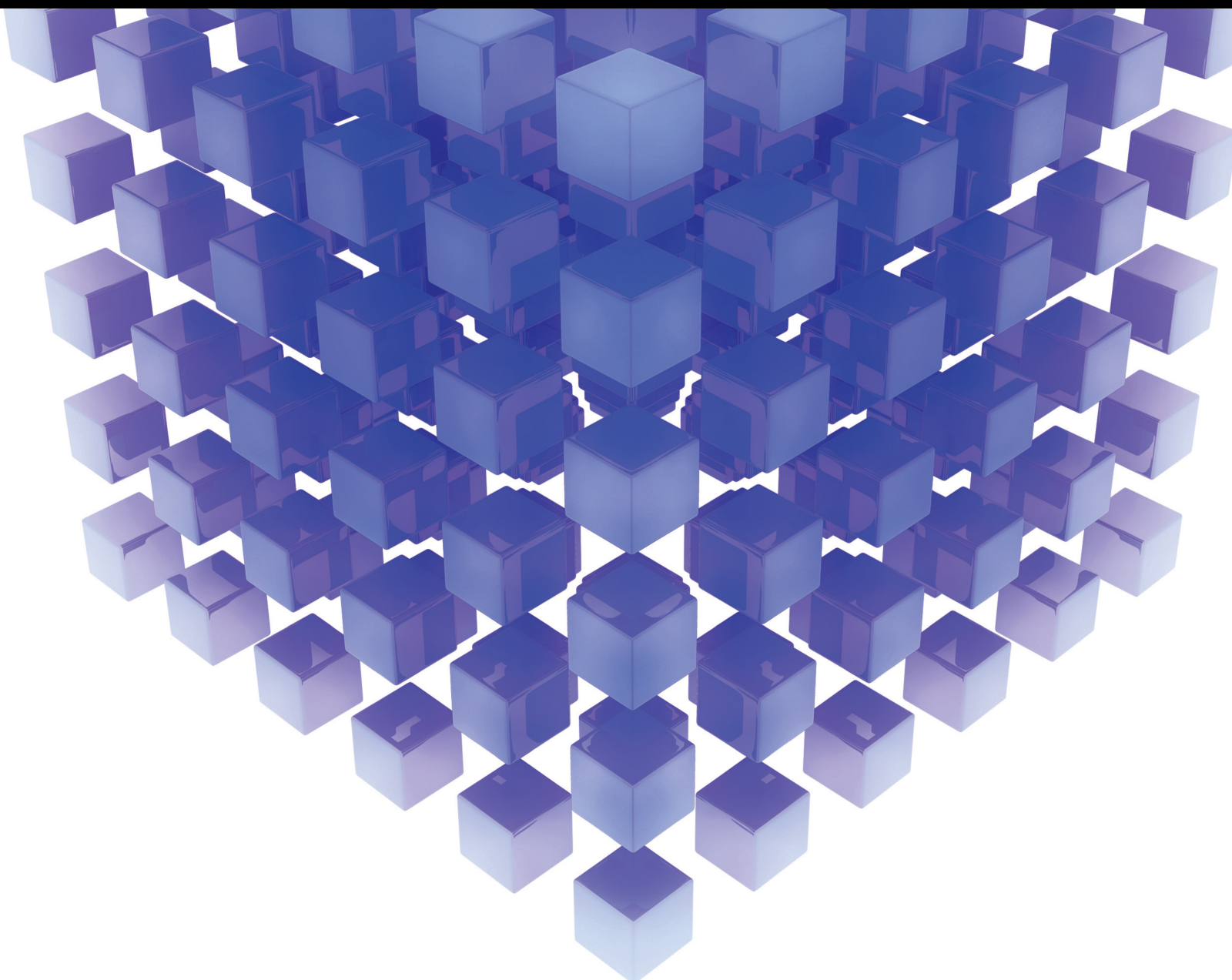


Mathematical Problems in Engineering

# Optimization and Control for Power Grids Integrated with Renewable Energy

Lead Guest Editor: Bo Yang

Guest Editors: Xiaoshun Zhang, Wei Yao, and Ling Jiang





---

# **Optimization and Control for Power Grids Integrated with Renewable Energy**



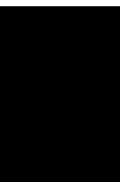
Mathematical Problems in Engineering

---

# **Optimization and Control for Power Grids Integrated with Renewable Energy**

Lead Guest Editor: Bo Yang

Guest Editors: Xiaoshun Zhang, Wei Yao, and Ling  
Jiang




---

Copyright © 2023 Hindawi Limited. All rights reserved.

This is a special issue published in “Mathematical Problems in Engineering.” All articles are open access articles distributed under the Creative Commons Attribution License, which permits unrestricted use, distribution, and reproduction in any medium, provided the original work is properly cited.

# Chief Editor

Guangming Xie , China

## Academic Editors

Kumaravel A , India  
Waqas Abbasi, Pakistan  
Mohamed Abd El Aziz , Egypt  
Mahmoud Abdel-Aty , Egypt  
Mohammed S. Abdo, Yemen  
Mohammad Yaghoub Abdollahzadeh  
Jamalabadi , Republic of Korea  
Rahib Abiyev , Turkey  
Leonardo Acho , Spain  
Daniela Addessi , Italy  
Arooj Adeel , Pakistan  
Waleed Adel , Egypt  
Ramesh Agarwal , USA  
Francesco Aggogeri , Italy  
Ricardo Aguilar-Lopez , Mexico  
Afaq Ahmad , Pakistan  
Naveed Ahmed , Pakistan  
Elias Aifantis , USA  
Akif Akgul , Turkey  
Tareq Al-shami , Yemen  
Guido Ala, Italy  
Andrea Alaimo , Italy  
Reza Alam, USA  
Osamah Albahri , Malaysia  
Nicholas Alexander , United Kingdom  
Salvatore Alfonzetti, Italy  
Ghous Ali , Pakistan  
Nouman Ali , Pakistan  
Mohammad D. Aliyu , Canada  
Juan A. Almendral , Spain  
A.K. Alomari, Jordan  
José Domingo Álvarez , Spain  
Cláudio Alves , Portugal  
Juan P. Amezcua-Sanchez, Mexico  
Mukherjee Amitava, India  
Lionel Amodeo, France  
Sebastian Anita, Romania  
Costanza Arico , Italy  
Sabri Arik, Turkey  
Fausto Arpino , Italy  
Rashad Asharabi , Saudi Arabia  
Farhad Aslani , Australia  
Mohsen Asle Zaem , USA

Andrea Avanzini , Italy  
Richard I. Avery , USA  
Viktor Avrutin , Germany  
Mohammed A. Awadallah , Malaysia  
Francesco Aymerich , Italy  
Sajad Azizi , Belgium  
Michele Bacciocchi , Italy  
Seungik Baek , USA  
Khaled Bahlali, France  
M.V.A Raju Bahubalendruni, India  
Pedro Balaguer , Spain  
P. Balasubramaniam, India  
Stefan Balint , Romania  
Ines Tejado Balsera , Spain  
Alfonso Banos , Spain  
Jerzy Baranowski , Poland  
Tudor Barbu , Romania  
Andrzej Bartoszewicz , Poland  
Sergio Baselga , Spain  
S. Caglar Baslamisli , Turkey  
David Bassir , France  
Chiara Bedon , Italy  
Azeddine Beghdadi, France  
Andriette Bekker , South Africa  
Francisco Beltran-Carbajal , Mexico  
Abdellatif Ben Makhlof , Saudi Arabia  
Denis Benasciutti , Italy  
Ivano Benedetti , Italy  
Rosa M. Benito , Spain  
Elena Benvenuti , Italy  
Giovanni Berselli, Italy  
Michele Betti , Italy  
Pietro Bia , Italy  
Carlo Bianca , France  
Simone Bianco , Italy  
Vincenzo Bianco, Italy  
Vittorio Bianco, Italy  
David Bigaud , France  
Sardar Muhammad Bilal , Pakistan  
Antonio Bilotta , Italy  
Sylvio R. Bistafa, Brazil  
Chiara Boccaletti , Italy  
Rodolfo Bontempo , Italy  
Alberto Borboni , Italy  
Marco Bortolini, Italy

Paolo Boscariol, Italy  
Daniela Boso , Italy  
Guillermo Botella-Juan, Spain  
Abdesselem Boulkroune , Algeria  
Boulaïd Boulkroune, Belgium  
Fabio Bovenga , Italy  
Francesco Braghin , Italy  
Ricardo Branco, Portugal  
Julien Bruchon , France  
Matteo Bruggi , Italy  
Michele Brun , Italy  
Maria Elena Bruni, Italy  
Maria Angela Butturi , Italy  
Bartłomiej Błachowski , Poland  
Dhanamjayulu C , India  
Raquel Caballero-Águila , Spain  
Filippo Cacace , Italy  
Salvatore Caddemi , Italy  
Zuowei Cai , China  
Roberto Caldelli , Italy  
Francesco Cannizzaro , Italy  
Maosen Cao , China  
Ana Carpio, Spain  
Rodrigo Carvajal , Chile  
Caterina Casavola, Italy  
Sara Casciati, Italy  
Federica Caselli , Italy  
Carmen Castillo , Spain  
Inmaculada T. Castro , Spain  
Miguel Castro , Portugal  
Giuseppe Catalanotti , United Kingdom  
Alberto Cavallo , Italy  
Gabriele Cazzulani , Italy  
Fatih Vehbi Celebi, Turkey  
Miguel Cerrolaza , Venezuela  
Gregory Chagnon , France  
Ching-Ter Chang , Taiwan  
Kuei-Lun Chang , Taiwan  
Qing Chang , USA  
Xiaoheng Chang , China  
Prasenjit Chatterjee , Lithuania  
Kacem Chehdi, France  
Peter N. Cheimets, USA  
Chih-Chiang Chen , Taiwan  
He Chen , China

Kebing Chen , China  
Mengxin Chen , China  
Shyi-Ming Chen , Taiwan  
Xizhong Chen , Ireland  
Xue-Bo Chen , China  
Zhiwen Chen , China  
Qiang Cheng, USA  
Zeyang Cheng, China  
Luca Chiapponi , Italy  
Francisco Chicano , Spain  
Tirivanhu Chinyoka , South Africa  
Adrian Chmielewski , Poland  
Seongim Choi , USA  
Gautam Choubey , India  
Hung-Yuan Chung , Taiwan  
Yusheng Ci, China  
Simone Cinquemani , Italy  
Roberto G. Citarella , Italy  
Joaquim Ciurana , Spain  
John D. Clayton , USA  
Piero Colajanni , Italy  
Giuseppina Colicchio, Italy  
Vassilios Constantoudis , Greece  
Enrico Conte, Italy  
Alessandro Contento , USA  
Mario Cools , Belgium  
Gino Cortellessa, Italy  
Carlo Cosentino , Italy  
Paolo Crippa , Italy  
Erik Cuevas , Mexico  
Guozeng Cui , China  
Mehmet Cunkas , Turkey  
Giuseppe D'Aniello , Italy  
Peter Dabnichki, Australia  
Weizhong Dai , USA  
Zhifeng Dai , China  
Purushothaman Damodaran , USA  
Sergey Dashkovskiy, Germany  
Adiel T. De Almeida-Filho , Brazil  
Fabio De Angelis , Italy  
Samuele De Bartolo , Italy  
Stefano De Miranda , Italy  
Filippo De Monte , Italy



































José António Fonseca De Oliveira  
Correia , Portugal  
Jose Renato De Sousa , Brazil  
Michael Defoort, France  
Alessandro Della Corte, Italy  
Laurent Dewasme , Belgium  
Sanku Dey , India  
Gianpaolo Di Bona , Italy  
Roberta Di Pace , Italy  
Francesca Di Puccio , Italy  
Ramón I. Diego , Spain  
Yannis Dimakopoulos , Greece  
Hasan Dinçer , Turkey  
José M. Domínguez , Spain  
Georgios Dounias, Greece  
Bo Du , China  
Emil Dumic, Croatia  
Madalina Dumitriu , United Kingdom  
Premraj Durairaj , India  
Saeed Eftekhar Azam, USA  
Said El Kafhali , Morocco  
Antonio Elipe , Spain  
R. Emre Erkmen, Canada  
John Escobar , Colombia  
Leandro F. F. Miguel , Brazil  
FRANCESCO FOTI , Italy  
Andrea L. Facci , Italy  
Shahla Faisal , Pakistan  
Giovanni Falsone , Italy  
Hua Fan, China  
Jianguang Fang, Australia  
Nicholas Fantuzzi , Italy  
Muhammad Shahid Farid , Pakistan  
Hamed Faruqi, Iran  
Yann Favennec, France  
Fiorenzo A. Fazzolari , United Kingdom  
Giuseppe Fedele , Italy  
Roberto Fedele , Italy  
Baowei Feng , China  
Mohammad Ferdows , Bangladesh  
Arturo J. Fernández , Spain  
Jesus M. Fernandez Oro, Spain  
Francesco Ferrise, Italy  
Eric Feulvarch , France  
Thierry Floquet, France

Eric Florentin , France  
Gerardo Flores, Mexico  
Antonio Forcina , Italy  
Alessandro Formisano, Italy  
Francesco Franco , Italy  
Elisa Francomano , Italy  
Juan Frausto-Solis, Mexico  
Shujun Fu , China  
Juan C. G. Prada , Spain  
HECTOR GOMEZ , Chile  
Matteo Gaeta , Italy  
Mauro Gaggero , Italy  
Zoran Gajic , USA  
Jaime Gallardo-Alvarado , Mexico  
Mosè Gallo , Italy  
Akemi Gálvez , Spain  
Maria L. Gandarias , Spain  
Hao Gao , Hong Kong  
Xingbao Gao , China  
Yan Gao , China  
Zhiwei Gao , United Kingdom  
Giovanni Garcea , Italy  
José García , Chile  
Harish Garg , India  
Alessandro Gasparetto , Italy  
Stylianos Georgantzinou, Greece  
Fotios Georgiades , India  
Parviz Ghadimi , Iran  
Ştefan Cristian Gherghina , Romania  
Georgios I. Giannopoulos , Greece  
Agathoklis Giaralis , United Kingdom  
Anna M. Gil-Lafuente , Spain  
Ivan Giorgio , Italy  
Gaetano Giunta , Luxembourg  
Jefferson L.M.A. Gomes , United Kingdom  
Emilio Gómez-Déniz , Spain  
Antonio M. Gonçalves de Lima , Brazil  
Qunxi Gong , China  
Chris Goodrich, USA  
Rama S. R. Gorla, USA  
Veena Goswami , India  
Xunjie Gou , Spain  
Jakub Grabski , Poland














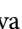
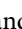
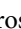









Antoine Grall , France  
George A. Gravvanis , Greece  
Fabrizio Greco , Italy  
David Greiner , Spain  
Jason Gu , Canada  
Federico Guarracino , Italy  
Michele Guida , Italy  
Muhammet Gul , Turkey  
Dong-Sheng Guo , China  
Hu Guo , China  
Zhaoxia Guo, China  
Yusuf Gurefe, Turkey  
Salim HEDDAM , Algeria  
ABID HUSSANAN, China  
Quang Phuc Ha, Australia  
Li Haitao , China  
Petr Hájek , Czech Republic  
Mohamed Hamdy , Egypt  
Muhammad Hamid , United Kingdom  
Renke Han , United Kingdom  
Weimin Han , USA  
Xingsi Han, China  
Zhen-Lai Han , China  
Thomas Hanne , Switzerland  
Xinan Hao , China  
Mohammad A. Hariri-Ardebili , USA  
Khalid Hattaf , Morocco  
Defeng He , China  
Xiao-Qiao He, China  
Yanchao He, China  
Yu-Ling He , China  
Ramdane Hedjar , Saudi Arabia  
Jude Hemanth , India  
Reza Hemmati, Iran  
Nicolae Herisanu , Romania  
Alfredo G. Hernández-Díaz , Spain  
M.I. Herreros , Spain  
Eckhard Hitzer , Japan  
Paul Honeine , France  
Jaromir Horacek , Czech Republic  
Lei Hou , China  
Yingkun Hou , China  
Yu-Chen Hu , Taiwan  
Yunfeng Hu, China  
Can Huang , China  
Gordon Huang , Canada  
Linsheng Huo , China  
Sajid Hussain, Canada  
Asier Ibeas , Spain  
Orest V. Iftime , The Netherlands  
Przemyslaw Ignaciuk , Poland  
Giacomo Innocenti , Italy  
Emilio Insfran Pelozo , Spain  
Azeem Irshad, Pakistan  
Alessio Ishizaka, France  
Benjamin Ivorra , Spain  
Breno Jacob , Brazil  
Reema Jain , India  
Tushar Jain , India  
Amin Jajarmi , Iran  
Chiranjibe Jana , India  
Łukasz Jankowski , Poland  
Samuel N. Jator , USA  
Juan Carlos Jáuregui-Correa , Mexico  
Kandasamy Jayakrishna, India  
Reza Jazar, Australia  
Khalide Jbilou, France  
Isabel S. Jesus , Portugal  
Chao Ji , China  
Qing-Chao Jiang , China  
Peng-fei Jiao , China  
Ricardo Fabricio Escobar Jiménez , Mexico  
Emilio Jiménez Macías , Spain  
Maolin Jin, Republic of Korea  
Zhuo Jin, Australia  
Ramash Kumar K , India  
BHABEN KALITA , USA  
MOHAMMAD REZA KHEDMATI , Iran  
Viacheslav Kalashnikov , Mexico  
Mathiyalagan Kalidass , India  
Tamas Kalmar-Nagy , Hungary  
Rajesh Kaluri , India  
Jyotheeswara Reddy Kalvakurthi, India  
Zhao Kang , China  
Ramani Kannan , Malaysia  
Tomasz Kapitaniak , Poland  
Julius Kaplunov, United Kingdom  
Konstantinos Karamanos, Belgium  
Michal Kawulok, Poland

Irfan Kaymaz , Turkey  
Vahid Kayvanfar , Qatar  
Krzysztof Kecik , Poland  
Mohamed Khader , Egypt  
Chaudry M. Khalique , South Africa  
Mukhtaj Khan , Pakistan  
Shahid Khan , Pakistan  
Nam-Il Kim, Republic of Korea  
Philipp V. Kiryukhantsev-Korneev ,  
Russia  
P.V.V Kishore , India  
Jan Koci , Czech Republic  
Ioannis Kostavelis , Greece  
Sotiris B. Kotsiantis , Greece  
Frederic Kratz , France  
Vamsi Krishna , India  
Edyta Kucharska, Poland  
Krzysztof S. Kulpa , Poland  
Kamal Kumar, India  
Prof. Ashwani Kumar , India  
Michal Kunicki , Poland  
Cedrick A. K. Kwuimy , USA  
Kyandoghere Kyamakya, Austria  
Ivan Kyrchei , Ukraine  
Márcio J. Lacerda , Brazil  
Eduardo Lalla , The Netherlands  
Giovanni Lancioni , Italy  
Jaroslaw Latalski , Poland  
Hervé Laurent , France  
Agostino Lauria , Italy  
Aimé Lay-Ekuakille , Italy  
Nicolas J. Leconte , France  
Kun-Chou Lee , Taiwan  
Dimitri Lefebvre , France  
Eric Lefevre , France  
Marek Lefik, Poland  
Yaguo Lei , China  
Kauko Leiviskä , Finland  
Ervin Lenzi , Brazil  
ChenFeng Li , China  
Jian Li , USA  
Jun Li , China  
Yueyang Li , China  
Zhao Li , China






























Zhen Li , China  
En-Qiang Lin, USA  
Jian Lin , China  
Qibin Lin, China  
Yao-Jin Lin, China  
Zhiyun Lin , China  
Bin Liu , China  
Bo Liu , China  
Heng Liu , China  
Jianxu Liu , Thailand  
Lei Liu , China  
Sixin Liu , China  
Wanquan Liu , China  
Yu Liu , China  
Yuanchang Liu , United Kingdom  
Bonifacio Llamazares , Spain  
Alessandro Lo Schiavo , Italy  
Jean Jacques Loiseau , France  
Francesco Lolli , Italy  
Paolo Lonetti , Italy  
António M. Lopes , Portugal  
Sebastian López, Spain  
Luis M. López-Ochoa , Spain  
Vassilios C. Loukopoulos, Greece  
Gabriele Maria Lozito , Italy  
Zhiguo Luo , China  
Gabriel Luque , Spain  
Valentin Lychagin, Norway  
YUE MEI, China  
Junwei Ma , China  
Xuanlong Ma , China  
Antonio Madeo , Italy  
Alessandro Magnani , Belgium  
Toqeer Mahmood , Pakistan  
Fazal M. Mahomed , South Africa  
Arunava Majumder , India  
Sarfranz Nawaz Malik, Pakistan  
Paolo Manfredi , Italy  
Adnan Maqsood , Pakistan  
Muazzam Maqsood, Pakistan  
Giuseppe Carlo Marano , Italy  
Damijan Markovic, France  
Filipe J. Marques , Portugal  
Luca Martinelli , Italy  
Denizar Cruz Martins, Brazil

Francisco J. Martos , Spain  
Elio Masciari , Italy  
Paolo Massioni , France  
Alessandro Mauro , Italy  
Jonathan Mayo-Maldonado , Mexico  
Pier Luigi Mazzeo , Italy  
Laura Mazzola, Italy  
Driss Mehdi , France  
Zahid Mehmood , Pakistan  
Roderick Melnik , Canada  
Xiangyu Meng , USA  
Jose Merodio , Spain  
Alessio Merola , Italy  
Mahmoud Mesbah , Iran  
Luciano Mescia , Italy  
Laurent Mevel , France  
Constantine Michailides , Cyprus  
Mariusz Michta , Poland  
Prankul Middha, Norway  
Aki Mikkola , Finland  
Giovanni Minafò , Italy  
Edmondo Minisci , United Kingdom  
Hiroyuki Mino , Japan  
Dimitrios Mitsotakis , New Zealand  
Ardashir Mohammadzadeh , Iran  
Francisco J. Montáns , Spain  
Francesco Montefusco , Italy  
Gisele Mophou , France  
Rafael Morales , Spain  
Marco Morandini , Italy  
Javier Moreno-Valenzuela , Mexico  
Simone Morganti , Italy  
Caroline Mota , Brazil  
Aziz Moukrim , France  
Shen Mouquan , China  
Dimitris Mourtzis , Greece  
Emiliano Mucchi , Italy  
Taseer Muhammad, Saudi Arabia  
Ghulam Muhiuddin, Saudi Arabia  
Amitava Mukherjee , India  
Josefa Mula , Spain  
Jose J. Muñoz , Spain  
Giuseppe Muscolino, Italy  
Marco Mussetta , Italy

Hariharan Muthusamy, India  
Alessandro Naddeo , Italy  
Raj Nandkeolyar, India  
Keivan Navaie , United Kingdom  
Soumya Nayak, India  
Adrian Neagu , USA  
Erivelton Geraldo Nepomuceno , Brazil  
AMA Neves, Portugal  
Ha Quang Thinh Ngo , Vietnam  
Nhon Nguyen-Thanh, Singapore  
Papakostas Nikolaos , Ireland  
Jelena Nikolic , Serbia  
Tatsushi Nishi, Japan  
Shanzhou Niu , China  
Ben T. Nohara , Japan  
Mohammed Nouari , France  
Mustapha Nourelfath, Canada  
Kazem Nouri , Iran  
Ciro Núñez-Gutiérrez , Mexico  
Włodzimierz Ogryczak, Poland  
Roger Ohayon, France  
Krzysztof Okarma , Poland  
Mitsuhiro Okayasu, Japan  
Murat Olgun , Turkey  
Diego Oliva, Mexico  
Alberto Olivares , Spain  
Enrique Onieva , Spain  
Calogero Orlando , Italy  
Susana Ortega-Cisneros , Mexico  
Sergio Ortobelli, Italy  
Naohisa Otsuka , Japan  
Sid Ahmed Ould Ahmed Mahmoud , Saudi Arabia  
Taoreed Owolabi , Nigeria  
EUGENIA PETROPOULOU , Greece  
Arturo Pagano, Italy  
Madhumangal Pal, India  
Pasquale Palumbo , Italy  
Dragan Pamučar, Serbia  
Weifeng Pan , China  
Chandan Pandey, India  
Rui Pang, United Kingdom  
Jürgen Pannek , Germany  
Elena Panteley, France  
Achille Paolone, Italy

George A. Papakostas , Greece  
Xosé M. Pardo , Spain  
You-Jin Park, Taiwan  
Manuel Pastor, Spain  
Pubudu N. Pathirana , Australia  
Surajit Kumar Paul , India  
Luis Payá , Spain  
Igor Pažanin , Croatia  
Libor Pekař , Czech Republic  
Francesco Pellicano , Italy  
Marcello Pellicciari , Italy  
Jian Peng , China  
Mingshu Peng, China  
Xiang Peng , China  
Xindong Peng, China  
Yuexing Peng, China  
Marzio Pennisi , Italy  
Maria Patrizia Pera , Italy  
Matjaz Perc , Slovenia  
A. M. Bastos Pereira , Portugal  
Wesley Peres, Brazil  
F. Javier Pérez-Pinal , Mexico  
Michele Perrella, Italy  
Francesco Pesavento , Italy  
Francesco Petrini , Italy  
Hoang Vu Phan, Republic of Korea  
Lukasz Pieczonka , Poland  
Dario Piga , Switzerland  
Marco Pizzarelli , Italy  
Javier Plaza , Spain  
Goutam Pohit , India  
Dragan Poljak , Croatia  
Jorge Pomares , Spain  
Hiram Ponce , Mexico  
Sébastien Poncet , Canada  
Volodymyr Ponomaryov , Mexico  
Jean-Christophe Ponsart , France  
Mauro Pontani , Italy  
Sivakumar Poruran, India  
Francesc Pozo , Spain  
Aditya Rio Prabowo , Indonesia  
Anchasa Pramuanjaroenkij , Thailand  
Leonardo Primavera , Italy  
B Rajanarayan Prusty, India

Krzysztof Puszynski , Poland  
Chuan Qin , China  
Dongdong Qin, China  
Jianlong Qiu , China  
Giuseppe Quaranta , Italy  
DR. RITU RAJ , India  
Vitomir Racic , Italy  
Carlo Rainieri , Italy  
Kumbakonam Ramamani Rajagopal, USA  
Ali Ramazani , USA  
Angel Manuel Ramos , Spain  
Higinio Ramos , Spain  
Muhammad Afzal Rana , Pakistan  
Muhammad Rashid, Saudi Arabia  
Manoj Rastogi, India  
Alessandro Rasulo , Italy  
S.S. Ravindran , USA  
Abdolrahman Razani , Iran  
Alessandro Reali , Italy  
Jose A. Reinoso , Spain  
Oscar Reinoso , Spain  
Haijun Ren , China  
Carlo Renno , Italy  
Fabrizio Renno , Italy  
Shahram Rezapour , Iran  
Ricardo Rianza , Spain  
Francesco Riganti-Fulginei , Italy  
Gerasimos Rigatos , Greece  
Francesco Ripamonti , Italy  
Jorge Rivera , Mexico  
Eugenio Roanes-Lozano , Spain  
Ana Maria A. C. Rocha , Portugal  
Luigi Rodino , Italy  
Francisco Rodríguez , Spain  
Rosana Rodríguez López, Spain  
Francisco Rossomando , Argentina  
Jose de Jesus Rubio , Mexico  
Weiguo Rui , China  
Rubén Ruiz , Spain  
Ivan D. Rukhlenko , Australia  
Dr. Eswaramoorthi S. , India  
Weichao SHI , United Kingdom  
Chaman Lal Sabharwal , USA  
Andrés Sáez , Spain

Bekir Sahin, Turkey  
Laxminarayan Sahoo , India  
John S. Sakellariou , Greece  
Michael Sakellariou , Greece  
Salvatore Salamone, USA  
Jose Vicente Salcedo , Spain  
Alejandro Salcido , Mexico  
Alejandro Salcido, Mexico  
Nunzio Salerno , Italy  
Rohit Salgotra , India  
Miguel A. Salido , Spain  
Sinan Salih , Iraq  
Alessandro Salvini , Italy  
Abdus Samad , India  
Sovan Samanta, India  
Nikolaos Samaras , Greece  
Ramon Sancibrian , Spain  
Giuseppe Sanfilippo , Italy  
Omar-Jacobo Santos, Mexico  
J Santos-Reyes , Mexico  
José A. Sanz-Herrera , Spain  
Musavarah Sarwar, Pakistan  
Shahzad Sarwar, Saudi Arabia  
Marcelo A. Savi , Brazil  
Andrey V. Savkin, Australia  
Tadeusz Sawik , Poland  
Roberta Sburlati, Italy  
Gustavo Scaglia , Argentina  
Thomas Schuster , Germany  
Hamid M. Sedighi , Iran  
Mijanur Rahaman Seikh, India  
Tapan Senapati , China  
Lotfi Senhadji , France  
Junwon Seo, USA  
Michele Serpilli, Italy  
Silvestar Šesnić , Croatia  
Gerardo Severino, Italy  
Ruben Sevilla , United Kingdom  
Stefano Sfarra , Italy  
Dr. Ismail Shah , Pakistan  
Leonid Shaikhet , Israel  
Vimal Shanmuganathan , India  
Prayas Sharma, India  
Bo Shen , Germany  
Hang Shen, China

Xin Pu Shen, China  
Dimitri O. Shepelsky, Ukraine  
Jian Shi , China  
Amin Shokrollahi, Australia  
Suzanne M. Shontz , USA  
Babak Shotorban , USA  
Zhan Shu , Canada  
Angelo Sifaleras , Greece  
Nuno Simões , Portugal  
Mehakpreet Singh , Ireland  
Piyush Pratap Singh , India  
Rajiv Singh, India  
Seralathan Sivamani , India  
S. Sivasankaran , Malaysia  
Christos H. Skiadas, Greece  
Konstantina Skouri , Greece  
Neale R. Smith , Mexico  
Bogdan Smolka, Poland  
Delfim Soares Jr. , Brazil  
Alba Sofi , Italy  
Francesco Soldovieri , Italy  
Raffaele Solimene , Italy  
Yang Song , Norway  
Jussi Sopanen , Finland  
Marco Spadini , Italy  
Paolo Spagnolo , Italy  
Ruben Specogna , Italy  
Vasilios Spitas , Greece  
Ivanka Stamova , USA  
Rafał Stanisławski , Poland  
Miladin Stefanović , Serbia  
Salvatore Strano , Italy  
Yakov Strelniker, Israel  
Kangkang Sun , China  
Qiuqin Sun , China  
Shuaishuai Sun, Australia  
Yanchao Sun , China  
Zong-Yao Sun , China  
Kumarasamy Suresh , India  
Sergey A. Suslov , Australia  
D.L. Suthar, Ethiopia  
D.L. Suthar , Ethiopia  
Andrzej Swierniak, Poland  
Andras Szekrenyes , Hungary  
Kumar K. Tamma, USA




Yong (Aaron) Tan, United Kingdom  
Marco Antonio Taneco-Hernández , Mexico  
Lu Tang , China  
Tianyou Tao, China  
Hafez Tari , USA  
Alessandro Tasora , Italy  
Sergio Teggi , Italy  
Adriana del Carmen Téllez-Anguiano , Mexico  
Ana C. Teodoro , Portugal  
Efstathios E. Theotokoglou , Greece  
Jing-Feng Tian, China  
Alexander Timokha , Norway  
Stefania Tomasiello , Italy  
Gisella Tomasini , Italy  
Isabella Torricollo , Italy  
Francesco Tornabene , Italy  
Mariano Torrisi , Italy  
Thang nguyen Trung, Vietnam  
George Tsiatas , Greece  
Le Anh Tuan , Vietnam  
Nerio Tullini , Italy  
Emilio Turco , Italy  
Ilhan Tuzcu , USA  
Efstratios Tzirtzilakis , Greece  
FRANCISCO UREÑA , Spain  
Filippo Ubertini , Italy  
Mohammad Uddin , Australia  
Mohammad Safi Ullah , Bangladesh  
Serdar Ulubeyli , Turkey  
Mati Ur Rahman , Pakistan  
Panayiotis Vafeas , Greece  
Giuseppe Vairo , Italy  
Jesus Valdez-Resendiz , Mexico  
Eusebio Valero, Spain  
Stefano Valvano , Italy  
Carlos-Renato Vázquez , Mexico  
Martin Velasco Villa , Mexico  
Franck J. Vernerey, USA  
Georgios Veronis , USA  
Vincenzo Vespri , Italy  
Renato Vidoni , Italy  
Venkatesh Vijayaraghavan, Australia


Anna Vila, Spain  
Francisco R. Villatoro , Spain  
Francesca Vipiana , Italy  
Stanislav Vitek , Czech Republic  
Jan Vorel , Czech Republic  
Michael Vynnycky , Sweden  
Mohammad W. Alomari, Jordan  
Roman Wan-Wendner , Austria  
Bingchang Wang, China  
C. H. Wang , Taiwan  
Dagang Wang, China  
Guoqiang Wang , China  
Huaiyu Wang, China  
Hui Wang , China  
J.G. Wang, China  
Ji Wang , China  
Kang-Jia Wang , China  
Lei Wang , China  
Qiang Wang, China  
Qingling Wang , China  
Weiwei Wang , China  
Xinyu Wang , China  
Yong Wang , China  
Yung-Chung Wang , Taiwan  
Zhenbo Wang , USA  
Zhibo Wang, China  
Waldemar T. Wójcik, Poland  
Chi Wu , Australia  
Qihong Wu, China  
Yuqiang Wu, China  
Zhibin Wu , China  
Zhizheng Wu , China  
Michalis Xenos , Greece  
Hao Xiao , China  
Xiao Ping Xie , China  
Qingzheng Xu , China  
Binghan Xue , China  
Yi Xue , China  
Joseph J. Yame , France  
Chuanliang Yan , China  
Xinggang Yan , United Kingdom  
Hongtai Yang , China  
Jixiang Yang , China  
Mijia Yang, USA  
Ray-Yeng Yang, Taiwan



Zaoli Yang , China  
Jun Ye , China  
Min Ye , China  
Luis J. Yebra , Spain  
Peng-Yeng Yin , Taiwan  
Muhammad Haroon Yousaf , Pakistan  
Yuan Yuan, United Kingdom  
Qin Yuming, China  
Elena Zaitseva , Slovakia  
Arkadiusz Zak , Poland  
Mohammad Zakwan , India  
Ernesto Zambrano-Serrano , Mexico  
Francesco Zammori , Italy  
Jessica Zangari , Italy  
Rafal Zdunek , Poland  
Ibrahim Zeid, USA  
Nianyin Zeng , China  
Junyong Zhai , China  
Hao Zhang , China  
Haopeng Zhang , USA  
Jian Zhang , China  
Kai Zhang, China  
Lingfan Zhang , China  
Mingjie Zhang , Norway  
Qian Zhang , China  
Tianwei Zhang , China  
Tongqian Zhang , China  
Wenyu Zhang , China  
Xianming Zhang , Australia  
Xuping Zhang , Denmark  
Yinyan Zhang, China  
Yifan Zhao , United Kingdom  
Debao Zhou, USA  
Heng Zhou , China  
Jian G. Zhou , United Kingdom  
Junyong Zhou , China  
Xueqian Zhou , United Kingdom  
Zhe Zhou , China  
Wu-Le Zhu, China  
Gaetano Zizzo , Italy  
Mingcheng Zuo, China

# Contents


**Retracted: A Stochastic Rolling Horizon-Based Approach for Power Generation Expansion Planning**  
Mathematical Problems in Engineering  
Retraction (1 page), Article ID 9790636, Volume 2023 (2023)







**A Method of Demarcating Critical Failure Impedance Boundary of Multi-Infeed HVDC Systems Based on Minimum Extinction Angle**  
Song Zhang , Guoqing Li, Shuguang Li, and Xintong Liu  
Research Article (14 pages), Article ID 9923737, Volume 2021 (2021)


**Grid Impact Assessment of Centralized and Decentralized Photovoltaic-Based Distribution Generation: A Case Study of Power Distribution Network with High Renewable Energy Penetration**  
Tamer Khatib  and Lama Sabri  
Research Article (16 pages), Article ID 5430089, Volume 2021 (2021)


**Stacked Autoencoder Framework of False Data Injection Attack Detection in Smart Grid**  
Liang Chen , Songlin Gu, Ying Wang, Yang Yang, and Yang Li   
Research Article (8 pages), Article ID 2014345, Volume 2021 (2021)






**[Retracted] A Stochastic Rolling Horizon-Based Approach for Power Generation Expansion Planning**  
Hanyun Wang , Tao Wang , Xinyi Wang , Bing Li , and Congmin Ye   
Review Article (11 pages), Article ID 6635829, Volume 2021 (2021)

**Identification of Permanent Faults and Disturbance Induced by Deicing Based on Permutation Entropy for the Large-Scale Clean Energy Transmission in Winter**  
Yunlong Wang , Tiejun Tang, Xiang Ju, and Dingding Hong  
Research Article (6 pages), Article ID 7037938, Volume 2021 (2021)

**Neutral-Point Potential Balance Control Strategy on Three-Level Active Power Filters**  
Fei Li , Na Geng , Guifeng Wang , Chunjie Li , Zhan Liu , and Zhenglong Xia   
Research Article (9 pages), Article ID 9930767, Volume 2021 (2021)

**Coordinated Planning and Energy Conservation for Distribution Network with Renewable Energy: Standardized Information Model and Software**  
Tianlin Wang, Huazhen Cao, Chong Gao, Zhuohuan Li, Tao Yu , and Ran Cheng  
Research Article (10 pages), Article ID 7688490, Volume 2021 (2021)



**Compulsory Islanding Transition Strategy Based on Fuzzy Logic Control for a Renewable Microgrid System**  
Jiexing Wan , Wei Hua, and Baoan Wang  
Research Article (13 pages), Article ID 9959222, Volume 2021 (2021)

**Machine-Learning-Based Intelligent Mechanical Fault Detection and Diagnosis of Wind Turbines**  
Qiang Gao , Xinhong Wu , Junhui Guo , Hongqing Zhou , and Wei Ruan   
Research Article (11 pages), Article ID 9915084, Volume 2021 (2021)

### **Small-Signal Stability Analysis for Power System Frequency Regulation with Renewable Energy Participation**

Tingyi He, Shengnan Li, Shuijun Wu, and Ke Li   
Research Article (13 pages), Article ID 5556062, Volume 2021 (2021)


### **Robust Kalman Filter-Based Dynamic State Estimation of Natural Gas Pipeline Networks**

Liang Chen , Peng Jin, Jing Yang, Yang Li , and Yi Song  
Research Article (10 pages), Article ID 5590572, Volume 2021 (2021)




### **Biobjective Optimization-Based Frequency Regulation of Power Grids with High-Participated Renewable Energy and Energy Storage Systems**

Tingyi He, Shengnan Li, Shuijun Wu, Chuangzhi Li, and Biao Xu   
Research Article (16 pages), Article ID 5526492, Volume 2021 (2021)







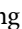

### **Optimal Power Allocation for Cooperative Pattern Division Multiple Access Systems**

Xiurong Zhang, Shaoli Kang, and Xueqian Fu   
Research Article (10 pages), Article ID 5581811, Volume 2021 (2021)



### **Optimization Design of Oil-Immersed Iron Core Reactor Based on the Particle Swarm Algorithm and Thermal Network Model**

Fating Yuan , Kai Lv , Bo Tang, Yue Wang, Wentao Yang, Shihong Qin , and Can Ding  
Research Article (14 pages), Article ID 6642620, Volume 2021 (2021)






### **Multidimensional Intelligent Distribution Network Load Analysis and Forecasting Management System Based on Multidata Fusion Technology**

Weijie Cheng , Renli Cheng , Jinsheng Liu , Weizhe Ma , Jie Li , Weiling Guan , Daolu Zhang , and Tao Yu   
Research Article (24 pages), Article ID 6677842, Volume 2021 (2021)


### **Prediction of Power Outage Quantity of Distribution Network Users under Typhoon Disaster Based on Random Forest and Important Variables**

Min Li, Hui Hou , Jufang Yu , Hao Geng, Ling Zhu, Yong Huang, and Xianqiang Li  
Research Article (14 pages), Article ID 6682242, Volume 2021 (2021)

### **Probabilistic Chronological Production Simulation-Based Coordinated Dispatching for Cascaded Hydro-PV-PSH Combined Power Generation System**

Shuai Zhang , Jingxian Yang , Hongjun Gao , Jichun Liu , and Junyong Liu   
Research Article (14 pages), Article ID 6677301, Volume 2020 (2020)

### **Online Static Voltage Stability Monitoring for Power Systems Using PMU Data**

Jianhong Pan, Aidi Dong, Jiashu Fan, and Yang Li   
Research Article (8 pages), Article ID 6667842, Volume 2020 (2020)

# Contents

---

**Dynamic Neighborhood-Based Particle Swarm Optimization for Multimodal Problems**

Xu-Tao Zhang, Biao Xu , Wei Zhang, Jun Zhang, and Xin-fang Ji

Research Article (13 pages), Article ID 6675996, Volume 2020 (2020)

**Fast Atom Search Algorithm for Reactive Power Optimization of Power Grid with High-Penetration**

**Wind and Solar Energies**

Fang Zeng and Hongchun Shu 

Research Article (15 pages), Article ID 6657181, Volume 2020 (2020)

**Memetic Salp Swarm Algorithm-Based Frequency Regulation for Power System with Renewable Energy Integration**

Fang Zeng and Hongchun Shu 

Research Article (11 pages), Article ID 6661793, Volume 2020 (2020)



## *Retraction*

# **Retracted: A Stochastic Rolling Horizon-Based Approach for Power Generation Expansion Planning**

### **Mathematical Problems in Engineering**

Received 13 April 2023; Accepted 13 April 2023; Published 19 April 2023

Copyright © 2023 Mathematical Problems in Engineering. This is an open access article distributed under the Creative Commons Attribution License, which permits unrestricted use, distribution, and reproduction in any medium, provided the original work is properly cited.

*Mathematical Problems in Engineering* has retracted the article titled “A Stochastic Rolling Horizon-Based Approach for Power Generation Expansion Planning” [1], as substantial overlap has been identified with a manuscript by different authors which had previously been submitted to another journal and has since been published [2].

### **References**

- [1] H. Wang, T. Wang, X. Wang, B. Li, and C. Ye, “A Stochastic Rolling Horizon-Based Approach for Power Generation Expansion Planning,” *Mathematical Problems in Engineering*, vol. 2021, Article ID 6635829, 11 pages, 2021.
- [2] E. F. Bødal, A. Botterud, M. Korpås, “Capacity Expansion Planning with Stochastic Rolling Horizon Dispatch,” *Electric Power Systems Research*, vol. 205, 2022.

## Research Article

# A Method of Demarcating Critical Failure Impedance Boundary of Multi-Infeed HVDC Systems Based on Minimum Extinction Angle

Song Zhang , Guoqing Li, Shuguang Li, and Xintong Liu

*Department of Electrical Engineering, Northeast Electric Power University, Jilin, JL 132012, China*

Correspondence should be addressed to Song Zhang; zhangsongneepu@aliyun.com

Received 7 March 2021; Revised 4 April 2021; Accepted 15 April 2021; Published 1 September 2021

Academic Editor: Bo Yang

Copyright © 2021 Song Zhang et al. This is an open access article distributed under the Creative Commons Attribution License, which permits unrestricted use, distribution, and reproduction in any medium, provided the original work is properly cited.

A method of rapidly demarcating the critical commutation failure (CF) region of a multi-infeed high-voltage direct-current (HVDC) system is proposed. Based on the nodal impedance matrix and nodal voltage interaction factor, for different AC fault conditions—both balanced and unbalanced—a method of calculating the extinction angles of converters in multi-infeed HVDC systems is deduced in detail. First, the extinction angles of convertor stations under single-phase, double-phase, and three-phase ground faults and line-to-line faults occurring at any bus in an AC system are calculated. The minimum extinction angle serves as a CF criterion. If the calculated extinction angle for a certain bus is smaller than the minimum extinction angle, then a fault at that bus will cause CF of the HVDC system and put that bus into a failed bus set. The critical failure impedance boundaries of the topology diagram can therefore be demarcated by examining every bus in the AC system. The validity and accuracy of the proposed index and the method were verified by calculation results based on the three-infeed HVDC system model of the IEEE 39-bus system. Finally, the critical failure impedance boundary was demarcated in the IEEE 118-bus system to demonstrate the application in a wider range of systems.

## 1. Introduction

In multi-infeed high-voltage direct-current (HVDC) systems, an AC system failure may cause commutation failure (CF) at the convertor station near a fault location or even CF of the multi-DC transmission lines at the same time or in succession [1–3]. If the commutation function is not recovered quickly, the secure and stable operation of the power grid will be threatened, and a wide-range power outage might occur as a consequence [4, 5]. However, not all AC system faults can trigger the CF of a DC system [6]. In light of the rapid construction and deployment of DC transmission systems, it is important to establish an accurate, fast scheme for detecting CF and reducing or avoiding simultaneous CFs in multi-DC transmission systems.

A great deal of research and operational experience have proved that when there is a fault in the AC system, a decrease in the extinction angle of the inverter is the primary cause of CF of the converter valve group [5, 7–9]. Based on the minimum extinction criteria, the simulation attempts in [10]

indicate that a weaker AC system in the receiving grid of a multi-infeed HVDC system aggravates the commutation performance of inverters because of the AC system faults cause a larger voltage magnitude reduction at inverter commutating buses. Son and Kim [11] proposed an improved algorithm that mitigates CF by considering the results of previous studies as well as the control characteristics of HVDC systems. Xiao et al. [12] proposed a weak coupling multi-infeed interaction factor to provide insight into how interinverter interactions influence concurrent CF behaviors. However, the study of AC systems is not enough. An analytical method based on critical multi-infeed interaction factors was put forward for detecting concurrent CFs quickly.

This work derives a mathematical equation to calculate the extinction angle of the inverter at the moment of an AC system fault by exploring the relationship between the extinction angle and the nodal impedance matrix. Using the critical extinction angle as a criterion, the critical fault impedance boundary of a multi-infeed DC system could be

identified on the topological graph of a network structure when a three-phase short-circuit ground fault or a single-phase short-circuit ground fault occurs on an AC system. A short-circuit fault at the node lying within the critical fault impedance boundary is more likely to cause CF of a DC system, whereas a fault at the node outside the boundary will not cause CF. The proposed method can quickly identify the critical fault impedance boundary and therefore graphically identify the AC system area where faults can cause CF.

## 2. Commutation Failure Mechanism

The typical six-bridge-arm convertor circuit is an example. When commutation between two bridge arms occurs, if the valve simply stops operating, the conduction fails to restore the interdicting ability during a period. Or, if the commutation process fails to complete during the inverse voltage period, conduction occurs again when the voltage added on the valve is positive. These incidents are called CF. The probability of CF on the inverter side is much larger than on the rectifier side, where CF happens only when a trigger circuit has a fault [13]. Therefore, research efforts on detecting CF usually focus on the inverter.

In a multi-infeed AC/DC system, an AC system disturbance is the main cause of CF [14, 15]. If only AC system faults are considered, a converter bus (CB) voltage drop is the major cause of CF because the extinction angle is smaller than the inherent limit extinction angle of the valve.

The commutation voltage-time area—commutation area for short—is defined as the area surrounded by the line-to-line voltage of the converter bus and timer shaft during the commutation period. Figure 1 is a schematic diagram of the commutation process. The converter needs a certain commutation area  $A$  to complete the commutation process. When an AC system fault occurs, along with a decrease in  $U_L$ ,  $A$  will also increase accordingly. For the actual HVDC power transmission system, even if it is assumed that the DC current is constant and  $A$  remains unchanged under a constant current controller and smoothing reactor, the commutation area inside the original commutation interval will decrease because of the decline of the commutating voltage and the leading phase. Therefore, to meet the commutation demand, it is necessary that  $t_1$ , the zero hours of commutation, be advanced and  $t_2$ , the end moment of commutation, be delayed, which will cause a decrease in the turn-off angle. Hence, at the moment of the AC fault, the inverter extinction angle decreases, along with a decline in the commutation voltage; CF occurs when the extinction angle becomes smaller than the critical extinction angle.

According to the information derived from the literature, the commutation area  $A$  could be calculated as follows [16]:

$$A_{\min} = \int_{\pi-\gamma_{\min}}^{\pi} \sqrt{2}kU_L \sin(\theta) d\theta, \quad (1)$$

where  $k$  is the transformer tap ratio,  $\gamma_{\min}$  is the minimum extinction angle of the converter,  $U_L$  is the RMS value of the line-to-line voltage of the CB, and  $\theta$  is the angle of the CB voltage.

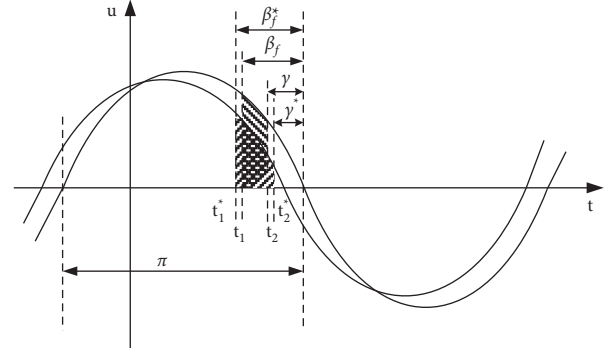


FIGURE 1: Commutation voltage-time area.

From equation (1), it can be concluded that

$$A_{\min} = \sqrt{2}kU_L (1 - \cos \gamma_{\min}). \quad (2)$$

The minimum extinction angle of the converter can be calculated as follows:

$$\gamma_{\min} = \arccos\left(1 - \frac{A_{\min}}{\sqrt{2}kU_L}\right). \quad (3)$$

The deionized response time of the high-power thyristor is around  $400 \mu\text{s}$ . If series element error is considered, the corresponding extinction angle  $\gamma_{\min} = 10^\circ$ . In the following sections, it is used as the reference value.

At the moment of an AC system fault, CB voltage drops, and the adjustment of the transformer ratio and the action of the DC system controller need a certain response time. Therefore, at the moment of the fault, the advance firing angle and ratio remain unchanged; the extinction angle decreases, along with a stepping down of the CB voltage. CF occurs when the extinction angle is smaller than the inherent limit extinction angle of the valve.

To illustrate the CF mechanism, the CIGRE HVDC standard model with a 12-pulse converter was analyzed using the electromagnetic transient analysis software PSCAD. The short-circuit ratios at the rectifier side and the inverter side were both set at 2.5. At  $t = 1 \text{ s}$ , a three-phase short-circuit ground fault occurred in the inverter CB, lasting 50 ms. The results of the simulation are shown in Figure 2.

From Figure 2, it can be concluded that when a three-phase short-circuit fault occurs in an AC system near the CB, the DC voltage drops significantly and DC current increases instantaneously. Similarly, when an unbalanced fault occurs in an AC system, the voltage variation of the CB could lead to CF.

## 3. Commutation Failure Criterion

**3.1. Three-Phase Short-Circuit Fault Commutation Failure Criterion.** Multi-infeed interaction factor (MIIF) is an indicator of the strength of an interaction between converter stations in a multi-infeed HVDC transmission system [17, 18]. The multi-infeed interaction factor  $MIIF_{ij}$  is defined by (4) and is essentially the voltage drop ratio at bus  $i$

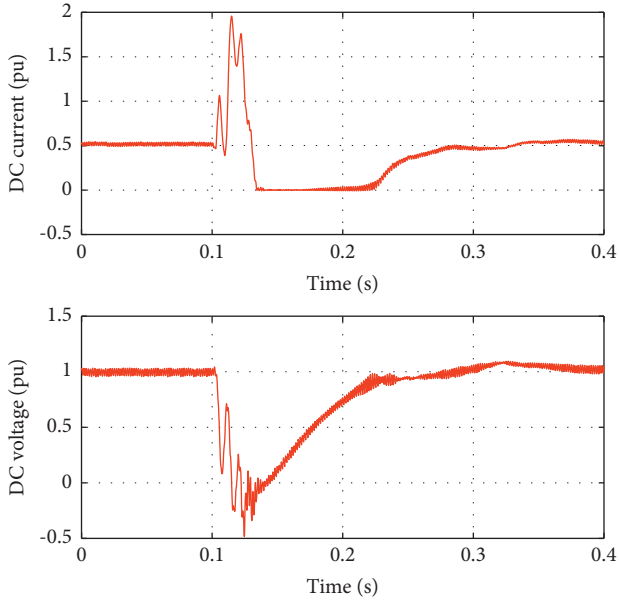


FIGURE 2: Simulation waveform of three-phase short-circuit ground fault.

following a 1% voltage reduction at the ac busbar of converter  $j$  caused by a three-phase balanced inductive fault:

$$\text{MIIF}_{ij} = \frac{\Delta U_i}{1\%U_{j0}} = \left| \frac{Z_{ij}}{Z_{jj}} \right|, \quad (4)$$

where  $U_{j0}$  is the RMS value of the line-to-line voltage of bus  $j$  before the fault and  $\Delta U_j$  is the voltage drop of the line-to-line voltage of bus  $j$ .

Similar to the definition of MIIF, the voltage interaction factor (VIF),  $\text{VIF}_{ij}$ , is defined as the voltage change rate of CB  $i$  following a 1% voltage reduction at the bus  $j$  of the ac system caused by a three-phase balanced inductive fault:

$$\text{VIF}_{ij} = \frac{\Delta U_j}{1\%U_{i0}} = \left| \frac{Z_{ij}}{Z_{ii}} \right|, \quad (5)$$

where  $Z_{ii}$  is the auto-impedance of bus  $i$ ,  $Z_{ij}$  is the mutual impedance between CB  $i$  and bus  $j$ , and  $U_{i0}$  and  $\Delta U_j$  have the same meaning as in (4).

When three-phase to ground metallic short-circuit fault occurs at CB  $i$ , bus voltage  $U_{i0}$  drops to 0, and the voltage drop of CB  $i$  is

$$\Delta U_i = \text{VIF}_{ij} U_{j0} \frac{U_{iN}}{U_{jN}}, \quad (6)$$

where  $U_{iN}$  and  $U_{jN}$  are the rated voltages of CB  $i$  and bus  $j$ , respectively.

Thus, the voltage of CB  $i$  is

$$U_i = U_{i0} - \Delta U_i = U_{i0} - \text{VIF}_{ij} U_{j0} \frac{U_{iN}}{U_{jN}}. \quad (7)$$

When the system is symmetric, the inverter extinction angle can be expressed as follows [19]:

$$\gamma_i = \arccos\left(\frac{\sqrt{2} k_i I_d X_{Li}}{U_L} + \cos \beta\right), \quad (8)$$

where  $I_d$  is the DC current and  $\beta$  is the advance trigger angle.

Substitute (7) into (8), the extinction angle of inverter  $i$  can be expressed as

$$\gamma_i = \arccos\left(\frac{\sqrt{2} k_i I_d X_{Li}}{U_{i0} - (Z_{ij}/Z_{ii})U_{j0}(U_{iN}/U_{jN})} + \cos \beta\right). \quad (9)$$

When three-phase to ground metallic short-circuit fault happens at AC bus  $j$ , CF will happen at the converter which is connected with CB  $i$  when  $\gamma_j \leq \gamma_{\min}$ . This serves as a criterion of CF in detecting the three-phase short-circuit fault.

**3.2. Unbalanced Short-Circuit Fault Commutation Failure Criterion.** When unbalanced faults occur in the AC system, the voltage drop and phase shift of CB are related to the electrical distance of the fault location. To verify the CF criterion of an unbalanced fault, the vector of each phase voltage should be calculated, respectively. Then, the line-to-line voltage which is corresponding to different commutation processes is calculated. Unbalanced short-circuit faults include single line-to-ground fault, double line-to-ground fault, line-to-line fault, etc. In this section, the CF criterion under different kinds of faults' conditions will be introduced in detail.

When unbalanced short-circuit fault happens at bus  $j$ , the voltages of CB  $i$  can be formulated as

$$\begin{cases} \dot{U}_{i(1)} = \dot{U}_{i0} - \dot{I}_{j(1)} Z_{ij(1)}, \\ \dot{U}_{i(2)} = -\dot{I}_{j(2)} Z_{ij(2)}, \\ \dot{U}_{i(0)} = -\dot{I}_{j(0)} Z_{ij(0)}, \end{cases} \quad (10)$$

where  $U_{i0}$  is the initial voltages of CB  $i$ ,  $U_{i(1)}$ ,  $U_{i(2)}$ , and  $U_{i(0)}$  are the positive-sequence, negative-sequence, and zero-sequence voltage components, respectively,  $I_{j(1)}$ ,  $I_{j(2)}$ , and  $I_{j(0)}$  are the three sequences short-circuit currents, and  $Z_{ij(1)}$ ,  $Z_{ij(2)}$ , and  $Z_{ij(0)}$  are the three sequence mutual impedances of converter CB  $i$  and bus  $j$ , respectively.

According to the symmetrical component method, the three-phase voltage of CB  $i$  can be derived as

$$\begin{cases} \dot{U}_{ia} = \dot{U}_{i(1)} + \dot{U}_{i(2)} + \dot{U}_{i(0)}, \\ \dot{U}_{ib} = \alpha^2 \dot{U}_{i(1)} + \alpha \dot{U}_{i(2)} + \dot{U}_{i(0)}, \\ \dot{U}_{ic} = \alpha \dot{U}_{i(1)} + \alpha^2 \dot{U}_{i(2)} + \dot{U}_{i(0)}. \end{cases} \quad (11)$$

**3.2.1. Single Line-to-Ground Fault.** When a single line-to-ground fault occurs on phase A of bus  $j$ , the fault conditions can be written as

$$\dot{I}_{j(1)} = \dot{I}_{j(2)} = \dot{I}_{j(0)} = \frac{U_{j0}}{Z_{jj(1)} + Z_{jj(2)} + Z_{jj(0)}}, \quad (12)$$

where  $Z_{jj(1)}$ ,  $Z_{jj(2)}$ , and  $Z_{jj(0)}$  are the impedances of the three sequences of bus  $j$ , respectively.

Substitute (12) into (10) and (11), the voltage variations of phase A at CB  $i$  is

$$\Delta U_{ia} = \left| \frac{Z_{ij(1)} + Z_{ij(2)} + Z_{ij(0)} \cdot \dot{U}_{j0}}{Z_{jj(1)} + Z_{jj(2)} + Z_{jj(0)}} \right|. \quad (13)$$

As shown in Figure 3, after a single line-to-ground fault happens, the phase voltage of phase B and phase C remains unchanged. According to the triangle relation, the line-to-line voltage between phase A and B and phase A and C is

$$U'_{ab} = U'_{ca} = \sqrt{3 - 3\Delta U_a + \Delta U_a^2}. \quad (14)$$

Therefore, the zero-crossing phase shift of the commutating voltage can be formulated as

$$\phi = \arctan \frac{\Delta U_a}{\sqrt{3}(2 - \Delta U_a)}. \quad (15)$$

At the moment of the fault, the converter transformer ratio remains unchanged; thus, the percentage of

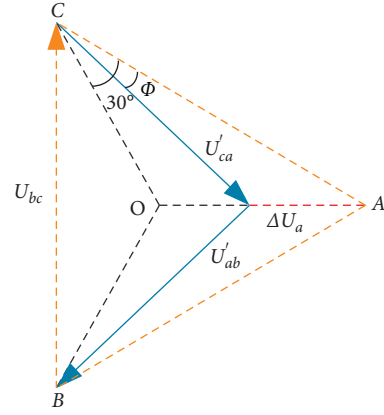


FIGURE 3: AC voltage of converter bus after a single line-to-ground fault.

commutation voltage drop and that of voltage drop at the CB are the same. Therefore, the extinction angle of each converter valve at the moment of phase A to ground short-circuit is

$$\begin{cases} \gamma_{iV1,V4} = \arccos \left( \frac{\sqrt{2} k I_d X_{Li}}{\sqrt{3 - 3\Delta U_a + \Delta U_a^2} U_L / \sqrt{3}} + \cos \beta \right) - \arctan \frac{\Delta U_a}{\sqrt{3}(2 - \Delta U_a)}, \\ \gamma_{iV2,V5} = \arccos \left( \frac{\sqrt{2} k I_d X_{Li}}{\sqrt{3 - 3\Delta U_a + \Delta U_a^2} U_L / \sqrt{3}} + \cos \beta \right) + \arctan \frac{\Delta U_a}{\sqrt{3}(2 - \Delta U_a)}, \\ \gamma_{iV3,V6} = \arccos \left( \frac{\sqrt{2} k I_d X_{Li}}{U_L} + \cos \beta \right). \end{cases} \quad (16)$$

According to (16), when single-phase to ground short-circuit fault happens, the corresponding converter extinction angle  $\gamma_i$  reaches the minimum value. When the corresponding converter extinction angle  $\gamma_i \leq \gamma_{\min}$ , CF will happen at the converter station of DC  $i$ .

**3.2.2. Double Line-to-Ground Fault and Line-to-Line Fault.** The fault conditions for a double line-to-ground fault occurring on phase A and B of bus  $j$  can be written as

$$\begin{cases} \dot{I}_{j(1)} = \frac{\dot{U}_{j|0|}}{Z_{jj(1)} + ((Z_{jj(2)} Z_{jj(0)}) / (Z_{jj(2)} + Z_{jj(0)}))}, \\ \dot{I}_{j(2)} = -\dot{I}_{j(1)} \frac{Z_{jj(0)}}{Z_{jj(2)} + Z_{jj(0)}}, \\ \dot{I}_{j(0)} = -\dot{I}_{j(1)} \frac{Z_{jj(2)}}{Z_{jj(2)} + Z_{jj(0)}}. \end{cases} \quad (17)$$

Equation (17) can be reduced as

$$\begin{cases} \dot{I}_{j(1)} = \frac{Z_{jj(2)} + Z_{jj(0)} \dot{U}_{j|0|}}{k}, \\ \dot{I}_{j(2)} = \frac{Z_{jj(0)} \dot{U}_{j|0|}}{k}, \\ \dot{I}_{j(0)} = \frac{Z_{jj(2)} \dot{U}_{j|0|}}{k}, \end{cases} \quad (18)$$

where  $k = Z_{jj(1)} Z_{jj(2)} + Z_{jj(1)} Z_{jj(0)} + Z_{jj(2)} Z_{jj(0)}$ .

As shown in Figure 4, the phase voltage of phase C remains unchanged after double line-to-ground fault happens; the drop voltages and angle changing of phase A are equal to phase B. Substitute (18) into (10) and (11), the voltage variations of phase A at CB  $i$  are

$$\Delta U_{ia} = \left| \frac{[Z_{jj(0)}(Z_{ij(2)} - Z_{ij(1)}) + Z_{jj(2)}(Z_{ij(0)} - Z_{ij(1)})] \cdot \dot{U}_{j0}}{k} \right|. \quad (19)$$



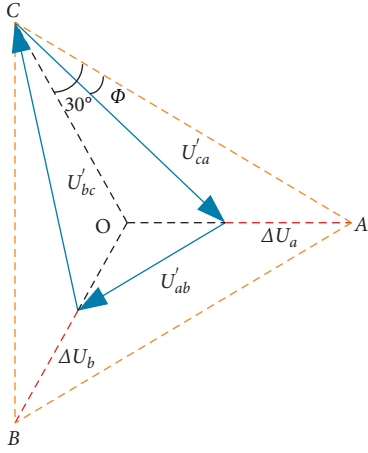


FIGURE 4: AC voltage of CB after double line-to-ground fault.

According to the peculiarity of the parallel triangle, after double line-to-ground fault, the line-to-line voltage between phase A and phase B is

$$U'_{ab} = \sqrt{3}(1 - \Delta U_a). \quad (20)$$

Furthermore, it can be concluded from Figure 4 that the angle of  $U'_{ab}$  is not changed and the relationship of size between each line-to-line voltages is

$$U'_{ca} = U'_{bc} > U'_{ab}. \quad (21)$$

Accordingly, the extinction angle  $\gamma_{V1,V4}$  which is related to  $U'_{ab}$  is smaller than the others. To reduce workload and improve the efficiency of calculation, only the line-to-line voltage between phase A and phase B will be calculated when the double line-to-ground fault happened. Substitute equations (19) and (20) into (6), the extinction angle  $\gamma_{V1,V4}$  after double line-to-ground fault can be formulated as

$$\gamma_{iV1,V4} = \arccos\left(\frac{\sqrt{2}k_i I_d X_{Li}}{\sqrt{3}(1 - \Delta U_a)} + \cos\beta\right). \quad (22)$$

The fault conditions for a line-to-line fault occurring on phase A and B can be represented as

$$\dot{I}_{j(1)} = -\dot{I}_{j(2)} = \frac{\dot{U}_{j|0|}}{Z_{jj(1)} + Z_{jj(2)}}. \quad (23)$$

Like single line-to-ground fault and double line-to-ground fault, substituting equation (17) into (10) and (11), the voltage variations of phase A and phase B of CB  $i$  by line-to-line fault can be formulated as

$$\Delta U_{ia} = \Delta U_{ib} = \left| \frac{Z_{ij(1)} + Z_{ij(2)}}{Z_{jj(1)} + Z_{jj(2)}} \cdot \dot{U}_{j0} \right|. \quad (24)$$

When the line-to-line fault occurs in the AC system, the relationship of voltage phasor of CB is a similarity to the phasor which has occurred after double line-to-ground fault, as shown in Figure 4. Using the same process as in Section 3.2.2, the line-to-line voltage between phase A and phase B can be formulated as equation (20), and the extinction angle can also be formulated by an equation.

When the double line-to-line fault or line-to-line fault occurs at bus  $j$ , the extinction angle  $\gamma_{V1,V4}$  of the corresponding converter at CB  $i$  can be calculated by equations (19), (20), (22), and (24). CF will happen at the converter which is connected with CB  $i$  while  $\gamma_j \leq \gamma_{\min}$ . This serves as a criterion of CF in detecting the line-to-line fault.

#### 4. The Demarcation of the Critical Failure Impedance Boundaries

In a multi-infeed HVDC system which contains  $n$  buses and  $k$  HVDC systems, given static models of generators, transmission lines, transformers, loads, and HVDC systems, the steps of demarcating the critical failure impedance boundaries are as follows:

- (1) Solve AC/DC network load flow and calculate the voltage of each bus.
- (2) Create the impedance matrix of the system.
- (3) Calculate extinction angles  $\gamma$  ( $\gamma_1, \gamma_2, \dots, \gamma_k$ ) of every converter of the multi-infeed HVDC system in different fault conditions. After the three-phase short-circuit fault occurs on bus  $B_i$ , the extinction angles could be calculated by equation 7. To improve the computational efficiency, when the unbalanced fault happened on bus  $B_i$ , only  $\gamma_{V1,V4}$  ( $\gamma_{1V1,V4}, \gamma_{2V1,V4}, \dots, \gamma_{mV1,V4}$ ) which is corresponding to the fault phase should be calculated. When single line-to-ground fault happened,  $\gamma_{mV1,V4}$  could be calculated by equations (14)–(16). When double line-to-ground fault happened,  $\gamma_{mV1,V4}$  could be calculated by equations (19)–(22). When a line-to-line fault happened,  $\gamma_{mV1,V4}$  could be calculated by equations (20), (22), and (24).
- (4) Form the bus sets based on the criterion  $\gamma_{ij} \leq \gamma_{\min}$  which detects the CF. The bus sets are defined in (25) as follows:

$$\begin{aligned} B_{Tfail-i} &= \{B_1, B_2, \dots, B_k\}, & \gamma_i &\leq \gamma_{\min}, \\ B_{Sfail-i} &= \{B_1, B_2, \dots, B_k\}, & \gamma_{iV1,V4} &\leq \gamma_{\min}, \\ B_{Dfail-i} &= \{B_1, B_2, \dots, B_k\}, & \gamma_{iV1,V4} &\leq \gamma_{\min}, \\ B_{Lfail-i} &= \{B_1, B_2, \dots, B_k\}, & \gamma_{iV1,V4} &\leq \gamma_{\min}. \end{aligned} \quad (25)$$

$B_{Tfail-i}$  is the three-phase short-circuit fault bus set; when three-phase short-circuit fault occurs on any bus which is included in this bus set, it may cause the CF fault of DC converter station  $i$ .  $B_{Sfail-i}$  is the single line-to-ground fault bus set when a single line-to-ground fault occurs on any bus which is included in this bus set, it may cause the CF of DC converter station  $i$ .  $B_{Dfail-i}$  is the double line-to-ground fault bus set when a double line-to-ground fault occurs on any bus which is included in this bus set, it may cause the CF of DC converter station  $i$ .  $B_{Lfail-i}$  is the line-to-line fault bus set when a line-to-line fault occurs on any bus which is included in this bus set, it may cause the CF of DC converter station  $i$ .

- (5) Draw the corresponding critical failure impedance boundaries and define the communication failure area according to the bus sets in step (4) on the system topological graph. The area within the critical failure impedance boundary is defined as the corresponding critical failure impedance area. If a three-phase metallic short-circuit fault or single line-to-ground phase to Earth fault occurs in the buses located at the critical failure impedance area, it will lead to the CF of the corresponding DC system. On the contrary, if the fault occurs in the buses located outside the area, it will not lead to the CF of the corresponding DC system.

The detailed process of demarcating the critical failure impedance boundaries is shown in Figure 5.

Figure 6 shows the critical failure impedance boundaries of the three-infeed HVDC system. Short-circuit fault that occurs in the buses in the areas of B1, B2, and B3 will lead to the CF of the DC subsystem 1, 2, and 3, respectively. If the fault occurs in the area of B12, which is the intersection of B1 and B2, CF of the DC subsystem 1 and DC subsystem 2 will happen at the same time. Therefore, this area is defined as the area where two DC systems have CFs. Similarly, B13 is the area where short-circuit fault on buses in that area will lead to CFs of DC subsystem 1 and 3 simultaneously, and B23 is the area where short-circuit fault on buses in that area will lead to CFs of DC subsystem 2 and 3 simultaneously. B123 is the intersection of B1, B2, and B3. Fault happens on buses within that area will lead to CFs of DC subsystem 1, 2, and 3 simultaneously. On the contrary, fault that occurs outside all these above areas will not lead to CF in any DC subsystem.

Compared with the common method which detects the CF utilizing electromagnetic simulation software, the proposed method uses the minimum extinction angle as the criterion and identifies critical impedance area quickly and accurately through a simple calculation. The identified critical impedance area provides a clear and direct perspective to the system operators of the area where faults will be critical to DC CF of the DC system. Moreover, it will provide valuable information for system planning and protection design.

## 5. Case Studies

In this section, the proposed method of detecting CFs' critical impedance boundaries is validated on the IEEE 39-bus and 118-bus test systems. Based on the CIGRE HVDC standard model, the quasi-steady-state model is adopted in the multi-infeed DC system.

*5.1. Study of IEEE 39-Bus Test System.* Three-infeed HVDC systems are established in the IEEE 39-bus test system; parameters of the three HVDC systems are listed in Table 1.

Following the steps in Section 4, the extinction angles of the three-infeed HVDC system in different fault conditions are calculated by substituting the above parameters of the three-infeed HVDC system into formulas (9), (16), and (22).

The detailed calculations of the extinction angle are given in Table 2.

While the calculated extinction angle is less than  $\gamma_{\min}$ , the corresponding bus is highlighted in Table 2. Put these buses into fault bus sets of different fault type. Take HVDC 1 as example, its three-phase short-circuit fault bus set  $B_{Tfail-1}$  contains 33 buses, the single line-to-ground fault bus set  $B_{Sfail-1}$  contains 12 buses, the double line-to-ground fault bus set  $B_{Dfail-1}$  contains 28 buses, and the line-to-line fault bus set  $B_{Lfail-1}$  contains 14 buses. The result is consistent with the severity of bus fault. When three-phase short-circuit fault happens, the voltage drop of CB is largest in four fault conditions. The second largest voltage drop occurs when double line-to-ground fault happens. However, for single line-to-ground fault and line-to-line fault, the number of fault bus set cannot be directly compared and needs to be calculated based on the method proposed in this paper. For example, the number of  $B_{Sfail-1}$  is less than the number of  $B_{Lfail-1}$ , but the number of  $B_{Sfail-3}$  is greater than the number of  $B_{Lfail-3}$ .

Then, demarcate the critical failure impedance boundaries of the three-infeed HVDC system in different fault conditions based on these fault bus sets. The detailed results are shown in Figure 7.

As shown in Figure 7, some buses are included in the overlap region of different critical failure impedance boundaries. When the corresponding fault occurs on these buses, it may cause CF in more than one HVDC system. Some buses are included in the nonoverlap region. When the corresponding fault occurs on these buses, it may cause CF in only one HVDC system. Therefore, the effectiveness of critical failure impedance boundaries can be verified by conducting different types of faults simulation of the buses in the overlap region and some other buses in the nonoverlap region. The three-phase short-circuit fault simulation is conducted on bus 9 and bus 24, the single line-to-ground fault simulation is conducted on bus 5 and bus 15, the double line-to-ground fault simulation is conducted on bus 14 and bus 20, and line-to-line fault simulation is conducted on bus 3 and bus 27.

*Case 1.*  $t = 0.5$  s; a three-phase short-circuit ground fault occurs on bus 24 and lasts 0.1 s. The simulation result is shown in Figure 8.

*Case 2.*  $t = 0.5$  s; a three-phase short-circuit ground fault occurs on bus 9 and lasts 0.1 s. The simulation result is shown in Figure 9.

In Table 2,  $\gamma_{1,24} = 9.14^\circ$ ,  $\gamma_{2,24} = 9.06^\circ$ , and  $\gamma_{3,24} = 9.23^\circ$ , and they are all less than  $\gamma_{\min}$ . According to the calculation results, when three-phase short-circuit fault is applied at bus 24, CF fault will occur on three HVDC systems at the same time, the three inverters will be blocked, and their DC power drops to 0 MW. The calculation results are the same as the simulated waveforms shown in Figure 8. In Table 2,  $\gamma_{1,9} = 11.17^\circ$ ,  $\gamma_{2,9} = 11.24^\circ$ , and  $\gamma_{3,9} = 7.63^\circ$ , and they are all less than  $\gamma_{\min}$ . According to the calculation results, when three-phase short-circuit fault is applied at bus 9, the DC powers of HVDC 1 and HVDC 2 drop slightly and CF only occurs on

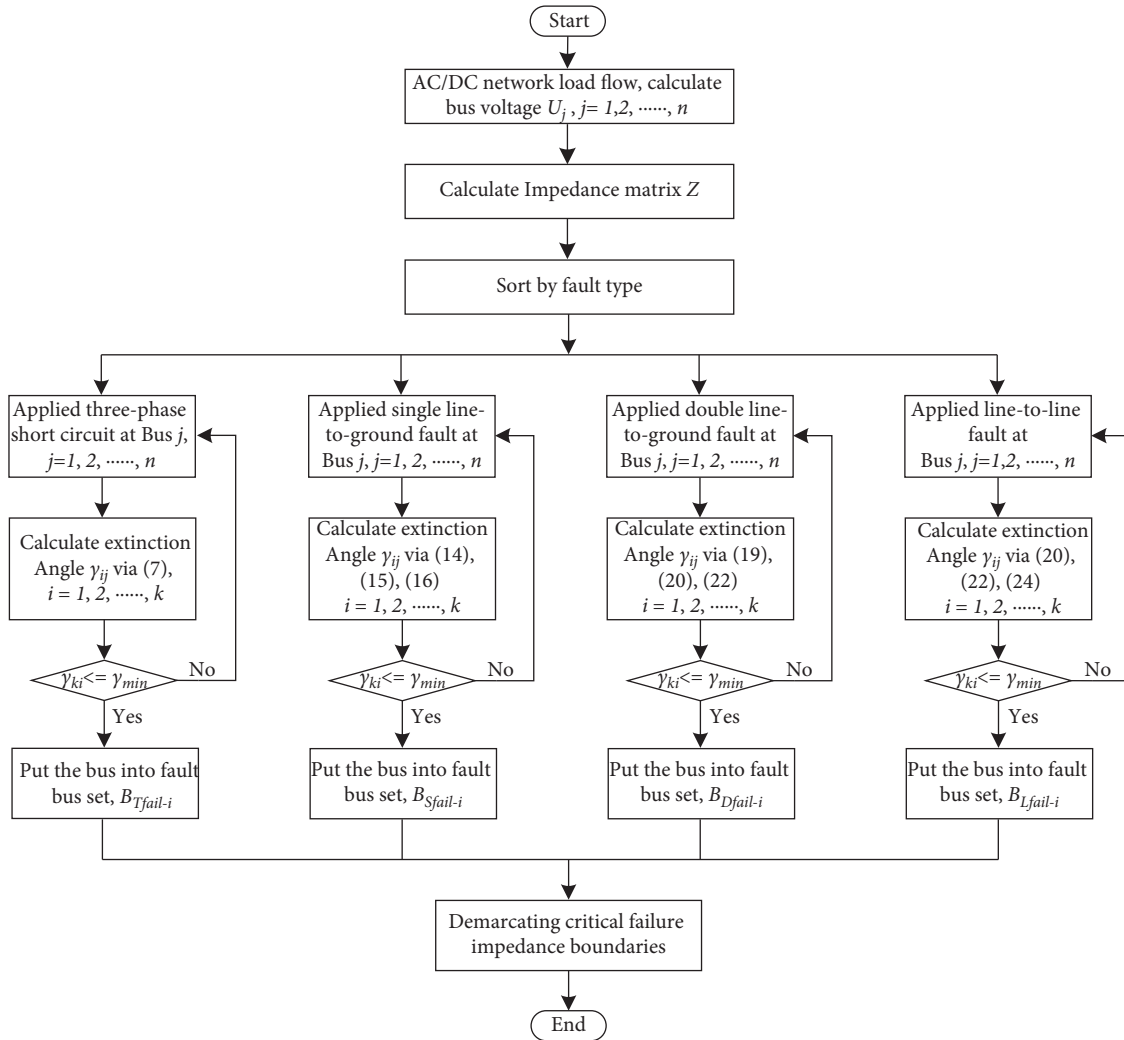


FIGURE 5: Flowchart of delimiting critical failure impedance boundaries of the multi-infeed HVDC system.

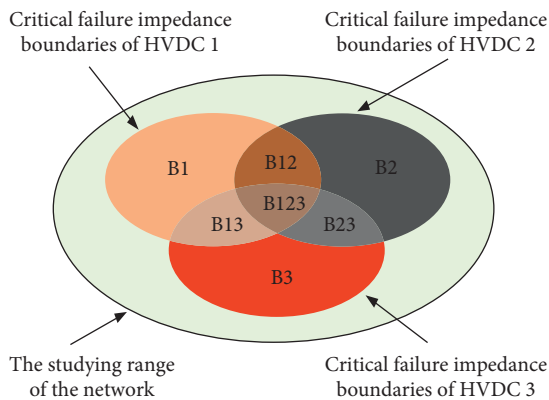


FIGURE 6: Critical failure impedance boundaries of the three-infeed HVDC system.

HVDC 3. The calculation results are the same as the simulated waveforms shown in Figure 9. Thus, the results of the dynamic simulation are consistent with the results of critical impedance boundaries for three-phase short-circuits' ground fault proposed in this paper.

Case 3.  $t = 0.5$  s; a single line-to-ground fault occurs on bus 15 and lasts 0.1 s. The simulation result is shown in Figure 10.

Case 4.  $t = 0.5$  s; a single line-to-ground fault occurs on bus 5 and lasts 0.1 s. The simulation result is shown in Figure 11.

In Table 2,  $\gamma_{1,15} = 9.40^\circ$ ,  $\gamma_{2,15} = 8.61^\circ$ , and  $\gamma_{3,15} = 9.72^\circ$ , and they are all less than  $\gamma_{min}$ . According to the calculation results, when a single line-to-ground fault is applied at bus 15, CF fault will occur on three HVDC systems at the same time, the three inverters will be blocked, and their DC powers drop to 0 MW. The calculation results are the same as the simulation waveforms which are shown in Figure 10. In Table 2,  $\gamma_{1,5} = 12.96^\circ$ ,  $\gamma_{2,5} = 11.45^\circ$ , and  $\gamma_{3,5} = 8.70^\circ$ , and only  $\gamma_{3,5}$  is less than  $\gamma_{min}$ . According to the calculation results, when a single line-to-ground fault is applied at bus 5, the DC powers of HVDC 1 and HVDC 2 drop slightly and CF only occurs on HVDC 3. The calculation results are the same as the simulation waveforms which are shown in Figure 11. Therefore, the results of the dynamic simulation are consistent with the results of critical impedance boundaries for single line-to-ground fault proposed in this paper.

TABLE 1: Parameter of the three-infeed HVDC system.

Subsystem	Rectifier bus	Inverter bus	Control mode	$P_{DC}$ (MW)	$V_{DC}$ (kV)	$R_{DC}$ ( $\Omega$ )	$X_L$ (%)	$\beta$	$K$
HVDC 1	Bus 25	Bus 18	Constant-power	200	500	7.854	15	$38.4^\circ$	1.0
HVDC 2	Bus 29	Bus 17	Constant-power	200	500	7.854	15	$38.4^\circ$	1.0
HVDC 3	Bus 36	Bus 13	Constant-power	200	500	7.854	15	$38.4^\circ$	1.0

TABLE 2: Extinction angles of the three-infeed HVDC system in different faults.

Bus number	Three-phase short-circuit fault			Single line-to-ground fault			Double line-to-ground fault			Line-to-line fault		
	HVDC 1	HVDC 2	HVDC 3	HVDC 1	HVDC 2	HVDC 3	HVDC 1	HVDC 2	HVDC 3	HVDC 1	HVDC 2	HVDC 3
1	12.40	12.46	12.24	15.99	15.93	15.36	18.76	18.65	16.00	16.80	16.74	16.80
2	8.36	8.44	8.48	8.68	8.40	8.55	14.01	12.09	9.17	7.78	7.69	16.91
3	7.92	8.10	8.11	9.06	9.74	9.48	8.84	8.94	8.98	8.04	7.90	9.72
4	8.50	8.56	7.87	9.03	8.43	4.42	8.96	9.03	8.51	7.71	7.65	7.94
5	8.98	9.01	8.28	12.96	11.45	8.70	9.09	9.19	8.17	7.50	17.45	8.13
6	9.05	9.07	8.33	10.77	16.31	8.88	9.10	9.20	8.08	17.47	17.42	8.08
7	9.21	9.23	8.74	12.90	11.28	9.69	9.21	9.32	7.79	17.30	17.25	8.09
8	9.23	9.25	8.82	14.63	12.99	8.48	9.25	9.40	7.93	17.34	17.29	7.86
9	11.17	11.24	7.63	15.98	15.49	11.95	12.79	12.71	12.28	16.69	16.64	9.88
10	9.22	9.23	7.85	16.16	15.07	9.15	8.99	9.08	7.45	17.37	17.33	17.00
11	9.22	9.23	8.22	16.56	15.34	9.29	9.03	9.13	7.59	17.38	17.34	8.22
12	7.34	7.39	5.09	14.53	14.08	16.39	9.12	9.09	9.83	16.34	16.31	8.15
13	9.20	9.21	7.33	17.09	17.16	5.41	8.96	9.03	7.47	17.41	17.38	7.01
14	8.71	8.72	7.77	7.36	6.86	8.43	8.94	8.96	8.28	7.63	7.61	8.35
15	8.72	8.64	8.66	9.40	8.61	9.72	8.73	8.62	8.67	7.69	7.75	8.22
16	8.34	8.16	8.51	5.68	8.71	8.05	8.73	8.61	8.94	7.89	7.99	7.81
17	7.85	7.53	8.31	8.93	5.41	12.68	8.72	8.60	9.06	8.12	8.26	7.82
18	7.52	8.00	8.41	5.41	9.93	7.99	8.52	8.69	9.03	8.27	8.02	7.85
19	7.56	7.35	7.76	15.21	11.11	16.41	9.43	9.60	9.21	16.84	6.92	7.80
20	6.66	6.46	11.77	13.09	13.71	14.29	9.24	9.30	12.14	15.80	15.85	16.78
21	8.53	8.38	8.69	12.06	6.26	16.03	10.00	10.20	9.39	7.32	7.40	15.75
22	17.77	17.56	7.96	17.83	13.77	13.24	9.47	9.69	9.19	16.97	7.05	17.25
23	7.60	7.39	7.80	13.04	18.24	16.98	9.41	9.58	9.17	16.88	16.96	16.91
24	9.14	9.06	9.23	5.73	9.37	9.26	8.42	8.19	8.82	7.61	7.70	16.82
25	8.62	8.66	8.75	6.54	6.90	7.02	9.01	9.08	9.23	7.60	17.54	7.54
26	9.04	9.00	9.17	7.33	7.92	6.98	9.03	8.94	17.56	7.53	7.56	17.52
27	8.83	8.74	9.04	8.60	7.45	9.49	8.79	8.64	10.45	7.68	7.75	12.14
28	17.19	7.12	17.49	13.86	13.27	13.80	17.04	18.07	16.85	16.11	16.13	17.48
29	7.09	7.02	17.38	13.61	13.94	13.92	15.04	11.07	16.86	16.02	16.04	16.00
30	8.14	8.23	18.25	16.03	15.84	15.21	9.22	9.09	16.99	16.68	16.61	15.91
31	7.21	7.28	5.83	13.93	13.70	9.19	13.09	9.06	9.48	15.75	15.72	16.63
32	7.33	7.38	5.08	13.42	13.16	7.35	14.12	9.09	9.75	15.94	15.91	6.15
33	6.69	6.49	16.81	12.12	12.67	12.42	9.23	9.30	13.14	15.73	15.79	6.54
34	6.15	5.99	16.17	12.07	12.61	12.37	9.17	9.21	12.12	14.63	14.66	15.68
35	16.87	6.67	17.01	13.13	13.08	13.91	15.24	12.31	15.13	16.06	16.12	14.60
36	6.38	6.21	16.45	12.96	12.05	12.84	15.18	17.22	15.11	15.33	15.38	16.01
37	7.48	7.55	17.63	14.26	14.56	14.06	14.13	18.10	16.98	16.22	16.18	15.29
38	16.60	6.54	16.83	12.69	12.79	12.17	12.05	17.08	16.93	15.09	15.10	16.16
39	8.03	8.11	17.66	15.64	15.17	16.03	13.80	16.72	18.09	16.61	16.56	15.01
Total	33	36	27	12	13	20	28	28	24	14	14	19

Case 5.  $t = 0.5$  s; a double line-to-ground fault occurs on bus 14 and lasts 0.1 s. The simulation result is shown in Figure 12.

Case 6.  $t = 0.5$  s; a double line-to-ground fault occurs on bus 20 and lasts 0.1 s. The simulation result is shown in Figure 13.

In Table 2,  $\gamma_{1,14} = 8.94^\circ$ ,  $\gamma_{2,14} = 8.96^\circ$ , and  $\gamma_{3,14} = 8.28^\circ$ , and they are all less than  $\gamma_{\min}$ . According to the calculation results, when a double line-to-ground fault is applied at bus

14, CF fault will occur on three HVDC systems at the same time, the three inverters will be blocked, and their DC powers drop to 0 MW. The calculation results are the same as the simulation waveforms which are shown in Figure 12. In Table 2,  $\gamma_{1,20} = 9.24^\circ$ ,  $\gamma_{2,20} = 9.30^\circ$ , and  $\gamma_{3,20} = 12.14^\circ$ , and only  $\gamma_{1,20}$  and  $\gamma_{2,20}$  are less than  $\gamma_{\min}$ . According to the calculation results, when a double line-to-ground fault is applied at bus 20, the DC powers of HVDC 3 drop slightly and CF only

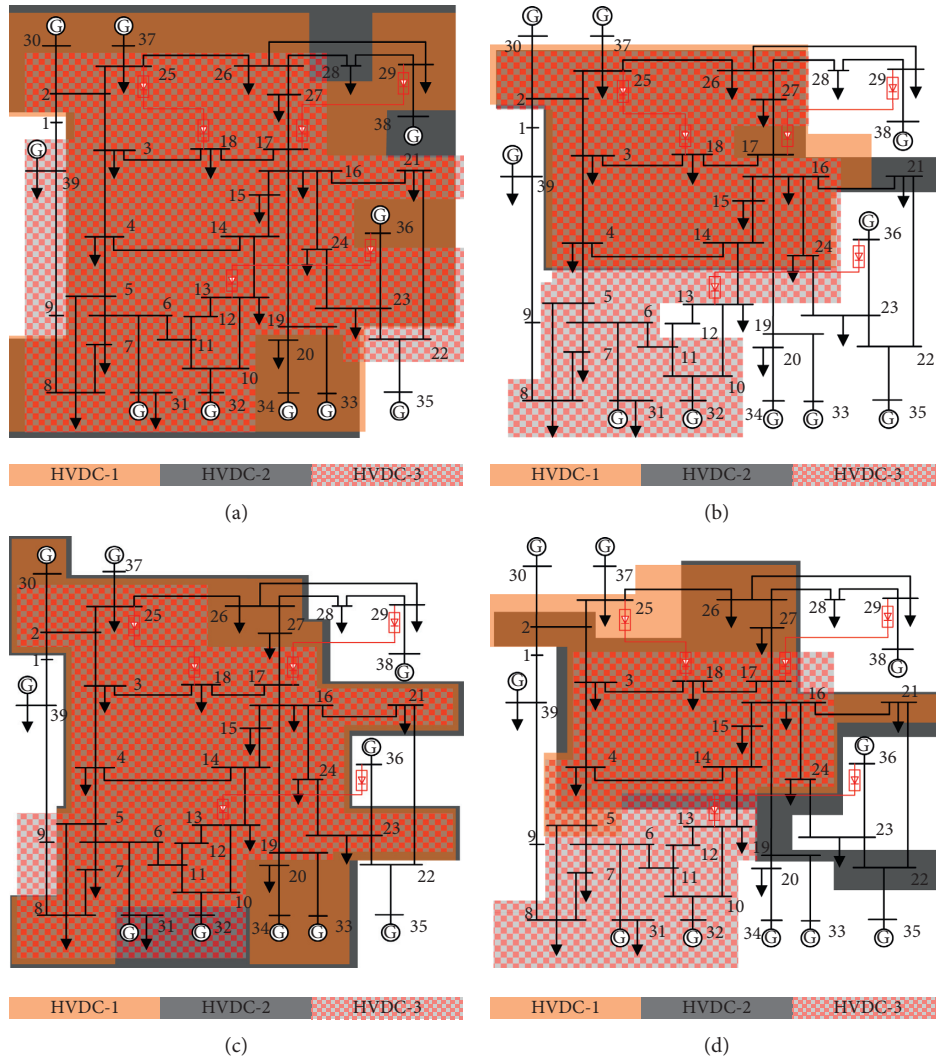


FIGURE 7: Critical failure impedance boundaries of the IEEE 39-bus test system. (a) Three-phase short-circuit fault boundary. (b) Single line-to-ground fault boundary. (c) Double line-to-ground fault boundary. (d) Line-to-line fault boundary.

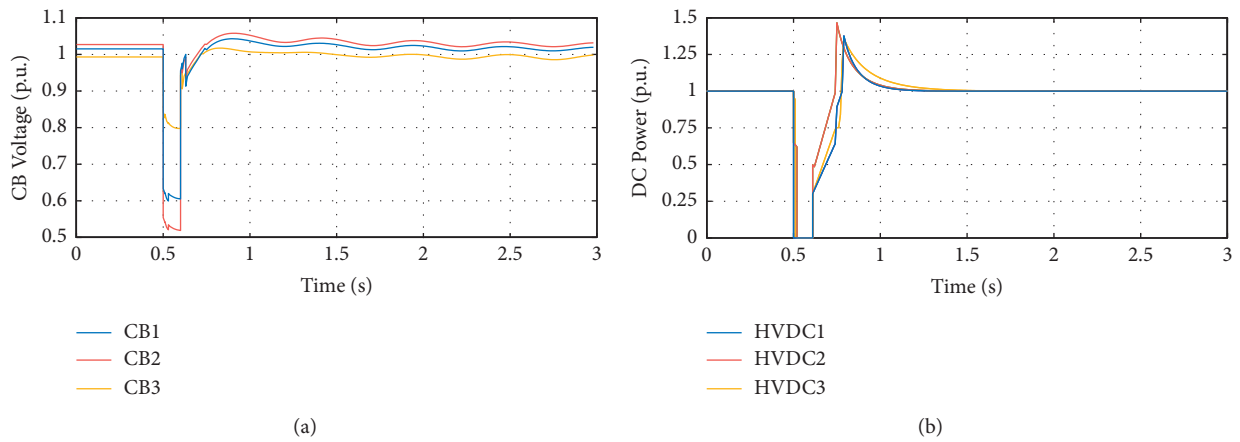


FIGURE 8: Simulation waveform of fault at bus 24. (a) CB voltage. (b) DC power.

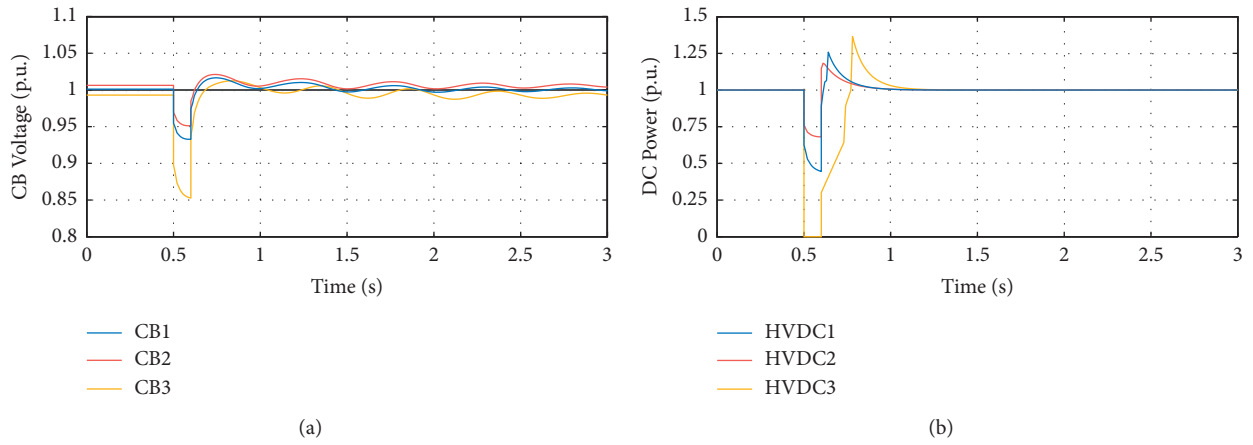


FIGURE 9: Simulation waveform of fault at bus 9. (a) CB voltage. (b) DC power.

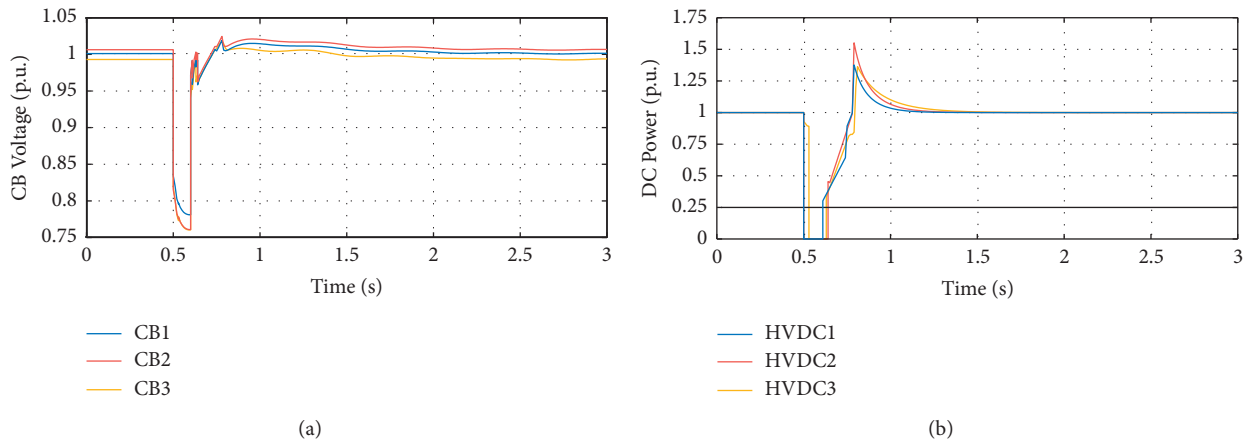


FIGURE 10: Simulation waveform of fault at bus 15. (a) CB voltage. (b) DC power.

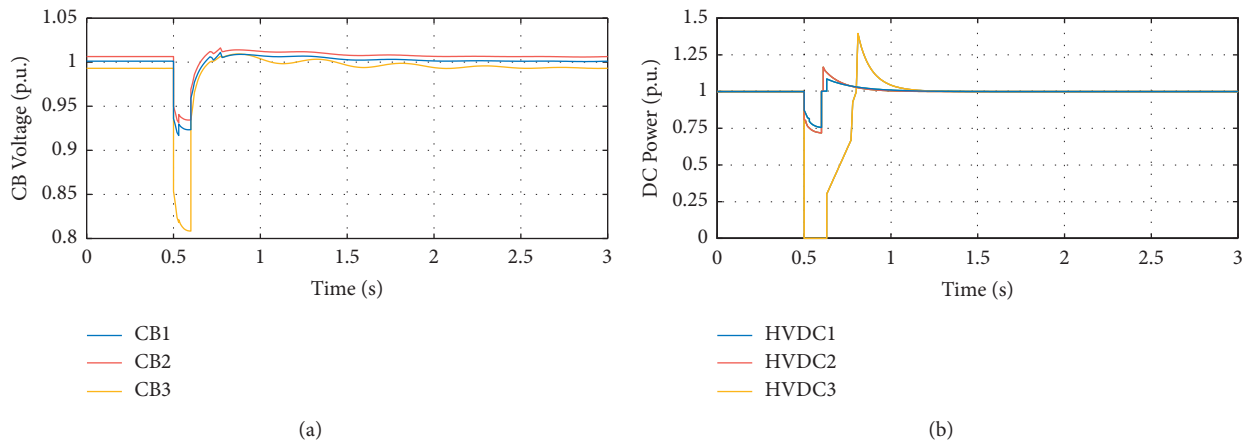


FIGURE 11: Simulation waveform of fault at bus 5. (a) CB voltage; (b) DC power.



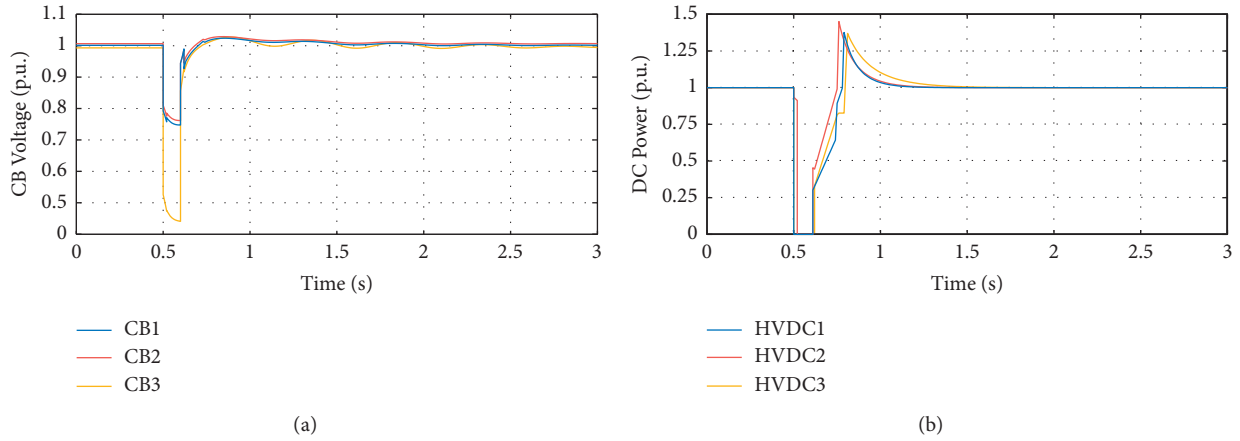


FIGURE 12: Simulation waveform of fault at bus 14. (a) CB voltage; (b) DC power.

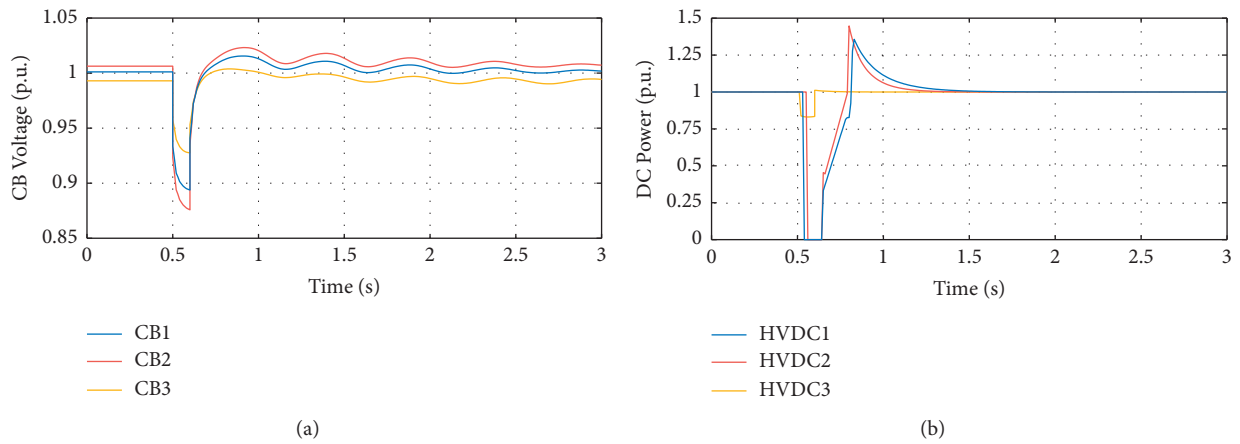


FIGURE 13: Simulation waveform of fault at bus 20. (a) CB voltage. (b) DC power.

occurs on HVDC 1 and HVDC 2. The calculation results are the same as the simulation waveforms which are shown in Figure 13. Therefore, the results of the dynamic simulation are consistent with the results of critical impedance boundaries for double line-to-ground fault proposed in this paper.

*Case 7.*  $t = 0.5$  s; a line-to-line fault occurs on Bus 3 and lasts 0.1 s. The simulation result is shown in Figure 14.

*Case 8.*  $t = 0.5$  s; a line-to-line fault occurs on bus 27 and lasts 0.1 s. The simulation result is shown in Figure 15.

In Table 2,  $\gamma_{1,3} = 8.04^\circ$ ,  $\gamma_{2,3} = 7.90^\circ$ , and  $\gamma_{3,3} = 9.72^\circ$ , and they are all less than  $\gamma_{\min}$ . According to the calculation results, when a line-to-line fault is applied at bus 3, CF fault will occur on three HVDC systems at the same time, the three inverters will be blocked, and their DC powers drop to 0 MW. The calculation results are the same as the simulation waveforms which are shown in Figure 14. In Table 2,  $\gamma_{1,27} = 7.68^\circ$ ,  $\gamma_{2,27} = 7.75^\circ$ , and  $\gamma_{3,27} = 12.14^\circ$ , and they are all less than  $\gamma_{\min}$ . According to the calculation results, when a line-to-line fault is applied at bus 27, the DC powers of

HVDC 1 and HVDC 2 drop slightly and CF only occurs on HVDC 3. The calculation results are the same as the simulation waveforms which are shown in Figure 15. Therefore, the results of the dynamic simulation are consistent with the results of critical impedance boundaries for line-to-line fault proposed in this paper.

From what has been discussed above, the result of PSS/E dynamic simulation is consistent with the result of the proposed method, which verifies the effectiveness and accuracy of the method proposed in this paper. The critical failure impedance boundaries cannot only detect CF of a single HVDC system but also detect simultaneous CFs of multi-infeed HVDC systems. The calculation result is not limited by the location of the converter bus, the scale of the AC system, the capacity of the HVDC system, and the number of the multi-infeed HVDC system.

*5.2. IEEE 118-Bus Test System.* Three-infeed HVDC systems are established in the IEEE 118-bus test system, and parameters of the three HVDC systems are listed in Table 3.

The critical impedance boundaries of the three-infeed HVDC systems in different fault conditions are demarcated

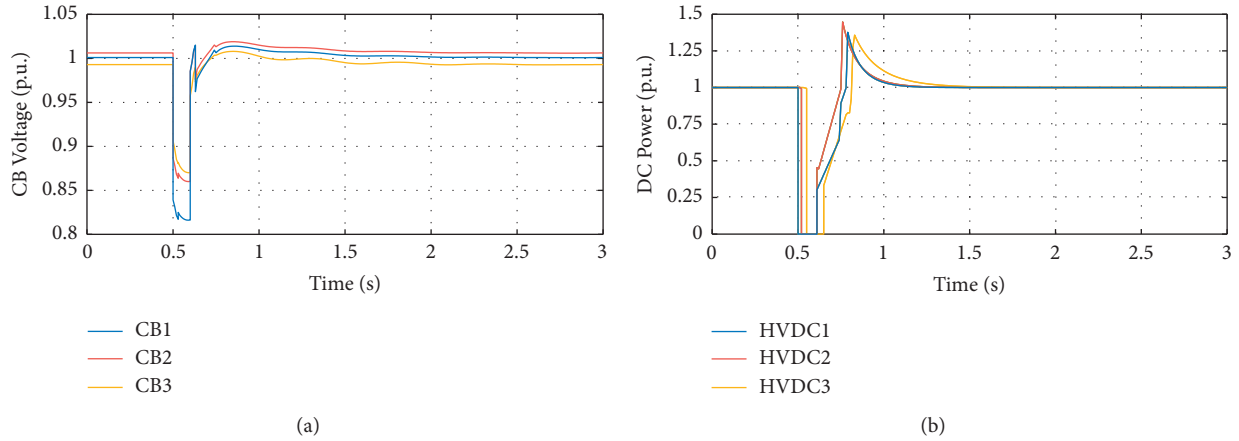


FIGURE 14: Simulation waveform of fault at bus 3. (a) CB voltage. (b) DC power.

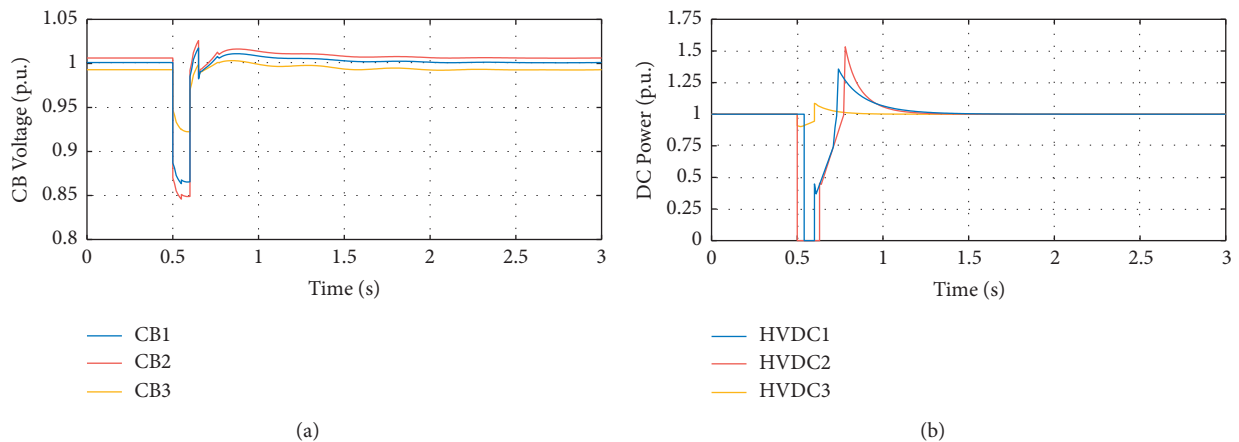


FIGURE 15: Simulation waveform of fault at bus 27. (a) CB voltage. (b) DC power.

TABLE 3: Parameters of the three-infeed HVDC system.

Subsystem	Rectifier bus	Inverter bus	Control mode	PDC (MW)	VDC (kV)	RDC ( $\Omega$ )	XL (%)	$\beta$ ( $^\circ$ )
HVDC 1	Bus 77	Bus 41	Constant-power	800	525	8.20	15	36.8
HVDC 2	Bus 25	Bus 47	Constant-power	800	525	8.20	15	36.8
HVDC 3	Bus 65	Bus 54	Constant-power	800	525	8.20	15	36.8

by the method which is proposed in this paper. The results are shown in Figure 16.

The corresponding critical failure areas which will cause CF in different HVDC systems are clearly shown in Figure 8. The application of the method which is proposed in this paper is demonstrated in a large-scale system. For a large-scale system, a vast workload would be used to set up an electromagnetic transient simulation system by the traditional method and cost a lot of time and much work to simulate them. However, only detailed parameters of the AC/DC system are required, and the method which is

proposed in this paper could demarcate the critical failure impedance boundaries of the large-scale system more efficiently. This method is not limited by the scale of the AC system, and the calculation can cover all the systems.

In a practical power grid, the dispatch department of the power grid can make corresponding security strategy according to critical failure impedance boundaries, and the operation department should strengthen the inspection and detection of buses in critical failure areas. This method can also be applied in the preliminary planning of the power grid.



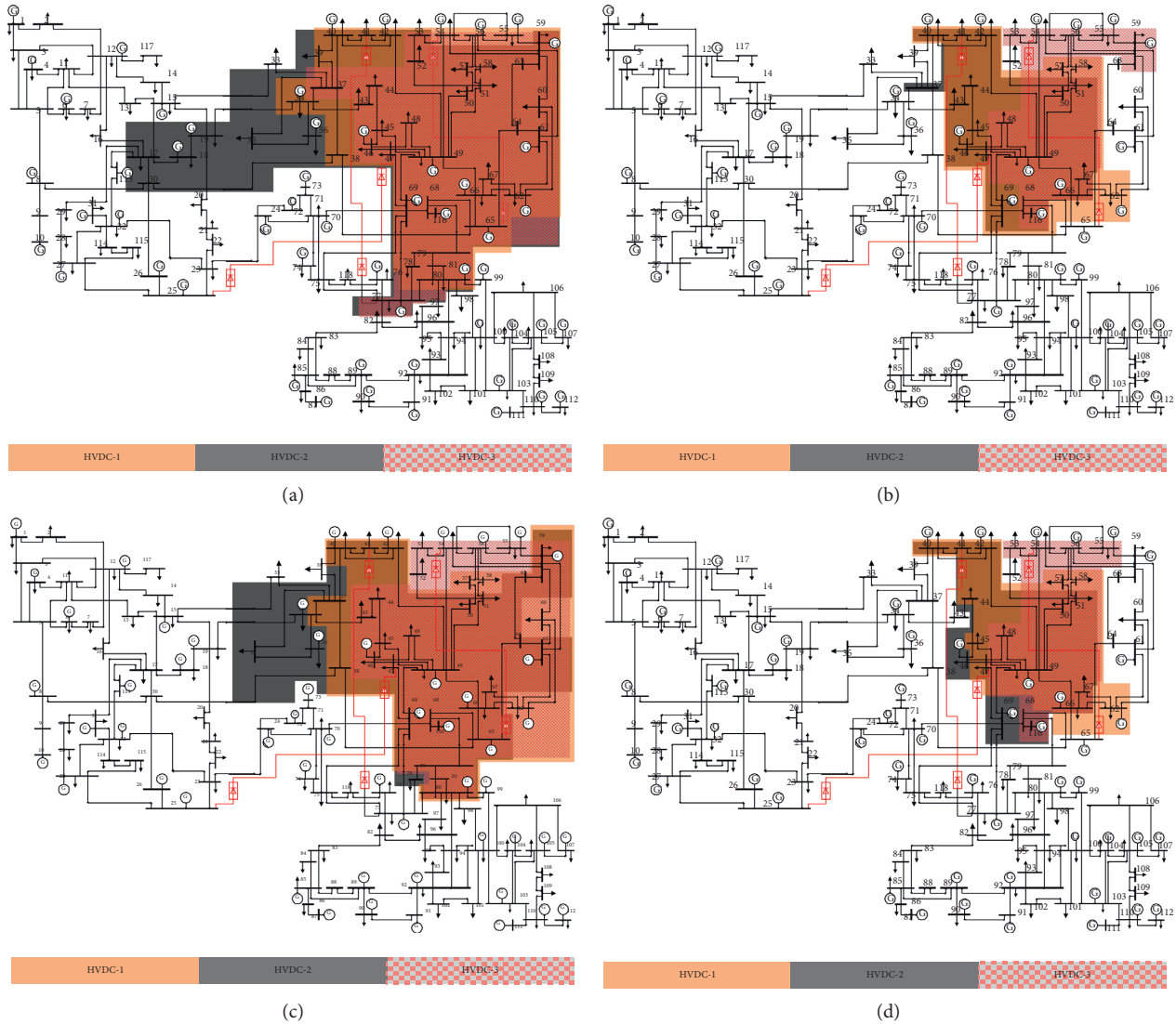


FIGURE 16: Critical failure impedance boundaries of the IEEE 118-bus test system. (a) Three-phase short-circuit fault boundary. (b) Single line-to-ground fault boundary. (c) Double line-to-ground fault boundary. (d) Line-to-line fault boundary.

## 6. Conclusions

This paper proposes a method to detect the CF of multi-infeed HVDC systems based on the critical failure impedance boundary. Using the criterion of the critical extinction angle, the proposed method can identify the critical failure impedance boundary where different kinds of faults are possible to cause the CF of the multi-infeed HVDC system.

Based on theoretical analysis and simulation results, it is concluded that (1) the critical failure impedance boundary increases with the decrease of the intensity of the AC system which is linked to the HVDC system. (2) When the impedance of the interconnected DC system remains constant, the change of system intensity affects the critical fault impedance boundary of the local HVDC subsystem significantly, while it casts little impact on other DC subsystems. (3) Compared with the actual power grid operation, the method presented in this paper is a programmatic

calculation method, and the results are more rigorous. The calculated boundaries of commutation failures will be larger than the actual boundaries.

The proposed method using a critical failure impedance boundary to detect CF of a multi-infeed HVDC system can detect the AC system area where faults could cause the commutating failure of the DC system. It directly reflects the mutual effects between AC and DC systems on the system topology diagram and has the potential of being widely used in power system planning and operation.

## Nomenclature (abbreviations)

- HVDC: High-voltage direct-current
- CF: Commutation failure
- CB: Converter bus
- MIIF: Multi-infeed interaction factor
- VIF: Voltage interaction factor

### Variables

$A$ : Commutation area  
 $k$ : Transformer tap ratio  
 $U_L$ : Voltage magnitude of converter buses  
 $\theta$ : Voltage angle of converter buses  
 $\gamma$ : Extinction angle of the converter  
 $I_d$ : DC current  
 $\beta$ : Advance trigger angle of the converter  
 $Z$ : Impedance  
 $\Delta U$ : Voltage drop of AC buses  
 $\phi$ : Zero-crossing phase shift of the commutating voltage  
 $U'$ : Line-to-line voltage between two phases  
 $\dot{U}$ : Voltage phasor  
 $\dot{I}$ : Current phasor.

### Data Availability

The data used to support the findings of this study are available from the corresponding author upon reasonable request.

### Conflicts of Interest

The authors declare that they have no conflicts of interest.

### Acknowledgments

This paper is an improvement and update of the version of view in Reference [20], further complements the calculation and determination method of the extinction angle under unbalanced short-circuit fault, and carries out simulation verification on a larger scale power grid. The authors would like to thank the previous authors for their efforts and contributions in this field.

### References

- [1] S. Mirsaedi, X. Dong, D. Tzelepis, D. M. Said, A. Dysko, and C. Booth, "A predictive control strategy for mitigation of commutation failure in LCC-based HVDC systems," *IEEE Transactions on Power Electronics*, vol. 34, no. 1, pp. 160–172, 2018.
- [2] A. Zheng, C. Guo, P. Cui, W. Jiang, and C. Zhao, "Comparative study on small-signal stability of LCC-HVDC system with different control strategies at the inverter station," *IEEE Access*, vol. 7, pp. 34946–34953, 2019.
- [3] L. Yang, Y. Li, G. Li, D. Zhao, and C. Chen, "Two-stage multi-objective OPF for AC/DC grids with VSC-HVDC: incorporating decisions analysis into optimization process," *Energy*, vol. 147, pp. 286–296, 2018.
- [4] F. Wang, T. Q. Liu, and X. Y. Li, "Decreasing the frequency of HVDC commutation failures caused by harmonics," *IET Power Electronics*, vol. 10, no. 2, pp. 215–221, 2017.
- [5] Y. Xue, X.-P. Zhang, and C. Yang, "Commutation failure elimination of LCC HVDC systems using thyristor-based controllable capacitors," *IEEE Transactions on Power Delivery*, vol. 33, no. 3, pp. 1448–1458, 2018.
- [6] J. Wu, H. Li, G. Wang, and Y. Liang, "An improved traveling-wave protection scheme for LCC-HVDC transmission lines," *IEEE Transactions on Power Delivery*, vol. 32, no. 1, pp. 106–116, 2017.
- [7] C. H. Li, C. Liu, Z. A. Zhang, W. Yao, J. Y. Wen, and J. B. Wang, "Analysis of commutation failure in HVDC power transmission system considering prediction control of commutation failure and initial fault angle," *Automation of Electric Power Systems*, vol. 42, no. 3, pp. 56–76, 2018.
- [8] E. Rahimi, A. M. Gole, J. B. Davies, I. T. Fernando, and K. L. Kent, "Commutation failure analysis in multi-infeed HVDC systems," *IEEE Transactions on Power Delivery*, vol. 26, no. 1, pp. 378–384, 2011.
- [9] C. Guo, Y. Liu, C. Zhao, X. Wei, and W. Xu, "Power component fault detection method and improved current order limiter control for commutation failure mitigation in HVDC," *IEEE Transactions on Power Delivery*, vol. 30, no. 3, pp. 1585–1593, 2015.
- [10] W. Yao, C. Liu, J. Fang, X. Ai, J. Wen, and S. Cheng, "Probabilistic analysis of commutation failure in LCC-HVDC system considering the CFPREV and the initial fault voltage angle," *IEEE Transactions on Power Delivery*, vol. 35, no. 2, pp. 715–724, 2020.
- [11] H.-I. Son and H.-M. Kim, "An algorithm for effective mitigation of commutation failure in high-voltage direct-current systems," *IEEE Transactions on Power Delivery*, vol. 31, no. 4, pp. 1437–1446, 2016.
- [12] H. Xiao, Y. Li, J. Zhu, and X. Duan, "Efficient approach to quantify commutation failure immunity levels in multi-infeed HVDC systems," *IET Generation, Transmission & Distribution*, vol. 10, no. 4, pp. 1032–1038, 2016.
- [13] Y. Xue, X.-P. Zhang, and C. Yang, "Elimination of commutation failures of LCC HVDC system with controllable capacitors," *IEEE Transactions on Power Systems*, vol. 31, no. 4, pp. 3289–3299, 2016.
- [14] S. F. Huang, H. M. Shen, B. Fei, and O. Li, "Effect of commutation failure on the distance protection and the countermeasures," *IET Generation, Transmission & Distribution*, vol. 9, no. 9, pp. 838–844, 2015.
- [15] X. Ni, C. Zhao, C. Guo, H. Liu, and Y. Liu, "Enhanced line commutated converter with embedded fully controlled sub-modules to mitigate commutation failures in high voltage direct current systems," *IET Power Electronics*, vol. 9, no. 2, pp. 198–206, 2016.
- [16] Y. Shao and Y. Tang, "Fast evaluation of commutation failure risk in multi-infeed HVDC systems," *IEEE Transactions on Power Systems*, vol. 33, no. 1, pp. 646–653, 2018.
- [17] C. Liu, Y. Zhao, C. Wang, H. Li, and G. Li, "Superposition feature of the switching functions for the dynamic phasor model of the converters under commutation failure," *IET Generation, Transmission & Distribution*, vol. 9, no. 12, pp. 1448–1454, 2015.
- [18] J. He, Y. Tang, J. Zhang, Q. Guo, J. Yi, and G. Bu, "Fast calculation of power oscillation peak value on AC tie-line after HVDC commutation failure," *IEEE Transactions on Power Systems*, vol. 30, no. 4, pp. 2194–2195, 2015.
- [19] A. Bagheri-Vandaei and S. Filizadeh, "Generalised extended-frequency dynamic phasor model of LCC-HVDC systems for electromagnetic transient simulations," *IET Generation, Transmission & Distribution*, vol. 12, no. 12, pp. 3061–3069, 2018.
- [20] G. Li, S. Zhang, T. Jiang, H. Chen, and X. Li, "A method of detecting commutation failure in multi-infeed HVDC systems based on critical failure impedance boundary," in *Proceedings of the 2017 IEEE Power & Energy Society General Meeting*, pp. 1–5, Chicago, IL, USA, July 2017.

## Research Article

# Grid Impact Assessment of Centralized and Decentralized Photovoltaic-Based Distribution Generation: A Case Study of Power Distribution Network with High Renewable Energy Penetration

Tamer Khatib  and Lama Sabri

*Department of Energy Engineering and Environment, An-Najah National University, Nablus, State of Palestine*

Correspondence should be addressed to Tamer Khatib; [t.khatib@najah.edu](mailto:t.khatib@najah.edu)

Received 10 April 2021; Revised 3 June 2021; Accepted 28 June 2021; Published 7 July 2021

Academic Editor: Xiao-Shun Zhang

Copyright © 2021 Tamer Khatib and Lama Sabri. This is an open access article distributed under the Creative Commons Attribution License, which permits unrestricted use, distribution, and reproduction in any medium, provided the original work is properly cited.

This paper presents a grid impact assessment of a 5 MWp photovoltaic-based distribution unit on a 33 kV/23 MVA power distribution network with high penetration of renewable energy generation. The adapted network has an average load demand of 23 MVA, with a 3 MWp centralized PV system, and a number of decentralized PV systems of a capacity of 2 MWp. A grid impact assessment is done to an additional 5 MWp of PV generation as a centralized system as well as a number of decentralized systems. Power flow analysis is conducted to the grid considering different generation loading scenarios in order to study grid performance including active and reactive power flow, voltage profiles, distribution power transformers loading, transmission lines ampacity levels, and active and reactive power losses. On the other hand, the distribution of the decentralized systems is done optimally considering power distribution transformer loading and available area using the geographical information system. Finally, an economic analysis is done for both cases. Results showed that grid performance is better considering decentralized PV systems, whereas the active power losses are reduced by 13.43% and the reactive power losses are reduced by 14.48%. Moreover, the voltage of buses improved as compared to the centralized system. However, the decentralized PV systems were found to affect the power quality negatively more than the centralized system. As for the economic analysis, the decentralized PV system option is found slightly less profitable than the centralized system, whereas the simple payback period is 9 and 7 years, respectively. However, decentralized PV systems are recommended considering the technical implications of the centralized PV system.

## 1. Introduction

The technology of distributed generation (DG) is defined as a small-scale generation unit that is installed at the consumer side. There are different types of DGs, whereas they could be from conventional resources such as diesel generators and combustion turbines or renewable energy resources such as solar, wind, and biomass energies [1].

The integration of photovoltaic distributed generation (PVDG) into a distribution system can be a beneficial solution as it is reliable, reduces peak load, reduces grid losses, and supports power quality [2]. Meanwhile, with high

penetration levels, the impact of PVDG would be negative, such as reverse power flow, voltage fluctuations, and system instability [3]. Thus, power flow, power quality, and short-circuit analyses are very essential to assess the impact of PVDG on the grid before its installation.

The main characteristic of solar power is the intermittent nature and unreliable sources of generating power when connected to the grid, due to many reasons such as weather conditions (temperature and irradiance), diurnal variation, and mismatch. As a result, voltage fluctuation can happen and cause problems and consequently reduce voltage quality [4, 5].

Besides that, when PV output power changes rapidly, the area control error of two or more interconnected areas may exceed its prescribed limit. Finally, large uncontrolled PV penetration may change the dispatch of regulating units in the utility causing a violation in dispatch regulating margins [6].

Due to these negative impacts, standards have been imposed to control these impacts, such as IEEE 1547 that provides standards of voltage fluctuation range when interconnection between utility electric power systems and distributed energy resources occurs. In addition to that, many researchers have investigated the impact of high penetration levels of renewable energy on the power grid. In [3], an unacceptable voltage rise is reported and analyzed with 50% of PV penetration, especially at noontime [3]. Meanwhile, according to [7], with high penetration levels of renewable energy, losses can be increased [7]. Similarly in [8], the reverse power problem is discussed, whereas it is claimed that when the out power does not match the demand, it is a serious challenge for the network since all power transformers and protection components are designed for unidirectional power flow [8]. This can make overloading of the distribution feeders and excessive power losses. Finally, in [9], the negative impact of high penetration of renewable energy on harmonics is discussed. Following that, many authors have discussed the methodology and the technical impact of grid impact studies. In [10], procedures of photovoltaic penetration impact on the grid are analyzed and studied. The authors proposed a model that considers the uncertainty of solar power generation and stochastic assessment methods that could accurately estimate the state of the operation of the network with different levels of penetration of solar photovoltaics. In [11], the authors estimate the impact of rapid PV output fluctuations on the power quality in an existing LV grid by performing load flow analyses.

Therefore, a grid impact study should be done on the power network before installing any renewable-energy-based distributed generation. Thus, this study proposes a framework of grid impact study for PVDG by analyzing the following: (i) the power flow analysis of the system is done before and after the installation of the distributed generation unit to evaluate the impact of PVDG on the power system. This process assesses voltage levels, system power flow, and system's power losses. This analysis should be done considering different operational scenarios considering generation and demand. (ii) The short-circuit analysis is done to check the contribution of the newly added renewable energy system to the network of any short circuit considering different voltage contributions to the fault location. (iii) The harmonics analysis of the system should be done to evaluate the impact of the newly added system on the power quality of the system. (iv) The paper discusses impact of centralized and decentralized PVDG in medium-scale distribution networks considering grid health conditions. The contribution of this paper is represented by the technical information and analysis provided for the network in Palestine in specific and distribution network in general with high penetration of renewable energy.

## 2. The Adapted Case Study

Palestinian territories suffer from the scarcity of conventional energy sources, high population growth, and rising prices of energy. Thus, this would lead Palestine to a developing energy crisis [12]. In 2018, Palestine's total energy demand reached around 5,800 GWh, in which Israel Electric Company (IEC) covered around 92.6% of this demand. The rest of the energy supplies are from Jordan (1.5%), Egypt (0.6%), and Gaza Power Plant (4.4%). Meanwhile, renewable energy sources accounting for 0.9% [13]. The high energy imports from the IEC had left the Palestinian Authority (PA) with an estimated debt of 574 million USD [13]. On the other hand, the cost of energy (CoE) is relatively high in Palestine, whereas CoE is approximately 0.19 USD/kWh for the residential sector. On the other hand, the CoE in Israel is approximately 0.14 USD/kWh [13]. It is expected that seasonal power shortages will be emerging in the West Bank following a demand growth of 3.5% per year until 2030.

On the other hand, Palestine has some potential for renewable energy sources that could make a change for the whole situation. For instance, Palestine has an estimated annual average daily solar energy in the range of 5.4 kWh/m<sup>2</sup>–6 kWh/m<sup>2</sup> with sunshine hours over 3,000 hours per year. However, this average daily solar energy goes as low as 2.6 kWh/m<sup>2</sup> in December and reaches up to 8.4 kWh/m<sup>2</sup> in June [14–18]. Based on that, the PA, through the Palestinian Energy and Natural Resources Authority (PENRA), has set several policies for encouraging investment in PV systems. Moreover, Palestine Investment Promotion Fund (PIF), which is a public body connected to the PA, had set PV systems as Palestine's major investment opportunities for local and international investors, with an estimated market size of \$50 million [19]. Following that, many projects have been implemented in Palestinian cities. In summary, there are 39 MW installed PV systems, while 93 MWp of PV systems are still under development. Moreover, there are about 24 MWp PV systems proposed officially for approval, with several MWp (s) of PV system in planning.

In Palestine, there is a governorate called Tubas. This governorate is powered by a 33 kV distribution network. The current penetration level of renewable energy in this network is 21.74%, which is somehow fine. However, recently, there is a new project of 5 MWp to be installed in the network, whereas a lot of disputes are around this project. The installation of this project will increase the penetration level to be 43.47%. This will put the network in a critical situation such as reverse power flow and high-power losses. Thus, it is aimed in this research to determine the impact of such a proposal on the network. Moreover, as such a proposal is assumed to be not suitable as a centralized system, an alternative solution is investigated that is the installation of a group of decentralized systems instead of one centralized system to mitigate the negative impact of the system on the grid.

*2.1. Modeling of the Adapted Power Network.* To produce precise data on network demand, voltage levels, and losses, data collection was conducted including a one-line diagram of Tubas LV and MV power network including loading

profiles, transmission lines characteristics, power transformer characteristics, circuit breaker characteristics, current coupling points, sources of power, grid capacity, and present power factor (PF) levels at LV power transformers.

Tubas power grid is getting electricity supply by 161/33 kV substation called Tayaser power substation with a power capacity of 23 MVA. Other power substations are providing the power grid with power such as AlJalameh power point (8 MVA), Qabatiya power point (2 MVA), Alzawiya power point (5 MVA), and Nassaria power point (5 MVA). These MV connections are with the IEC (Israel Electricity Corporation) grid. There are some local PV power systems in the grid that are 2 MWp distributed systems and a 3 MWp centralized plant. The loads are mostly domestic, and few of them are commercial, agricultural, and industrial.

In this research, all power coupling points with IEC were considered as slack buses with an  $X/R$  value that is equal to 13.2154, while PV power systems were considered as distributed generation units.

The average load demand of the network is 23 MVA, based on daily records of consumption. An average daily load curve is demonstrated in Figure 1. These information are collected from the stakeholder by the authors of this paper. The daily load profile corresponds to a typical load profile for a distribution grid in the region with mostly domestic clients with peak demand at noon (16 MVA) and afternoon (20 MVA) with lower consumption during the night (14–12 MVA) and early morning (10 MVA).

From the load profile, it can be seen that during the solar day and specifically from 10:00 AM to 2:00 PM, the maximum power demanded is about 14–16 MVA, which means that the generating power of any distributed generation source should not exceed these values. Otherwise, reverse power will occur.

In this research, the model was developed based on a one-line diagram. In general, the MV grid is built mainly from overhead line (OHL) 33 kV voltage level and underground cables. The OHLs are usually FEAL-type conductors of 50, 95, and 120 mm<sup>2</sup>. The UGCS is usually TSLE or DKBA type of 3 × 120 mm<sup>2</sup>, 3 × 150 mm<sup>2</sup>, or 3 × 240 mm<sup>2</sup>. Most of them are made of copper and some are of aluminum material.

There is a total number of 78 buses at 33 kV, mostly power consumption nodes (57 nodes), including the concentrated consumption of Qabatiya, Anza, Zawiya, Zababeda, Wadi Douq, Um Al Toot, Tilfit, Tineen, Raba, Private project, Mghayer, Merkeh, Jarba, Jalqumous, Dream Land, Beer Al-Basha, AUU, Al Mtelleh, Wadi Al Faraa, Ras Al Faraa, Keshda, and Faraa Camp. The loads in Tubas, Aqqaba, Atoof, Kufeir, and Tammun were modeled in detail. The load from Qabatiya, Anza, Alzawiya, Zababeda, Wadi Douq, Um Al Toot, Tilfit, Tineen, Raba, Private project, Mghayer, Merkeh, Jarba, Jalqumous, Dream Land, Beer Al-Basha, AUU, and Al Mtelleh were modeled as total load (in node Qabatiya). The loads associated with Wadi Al Faraa, Ras Al Faraa, Keshda, and Faraa Camp were also modeled as cumulated loads.

Based on the information mentioned above, the power flow analysis of the network was performed using Newton–Raphson method in ETAP software.

### 3. Grid Impact Assessment Methodology

When planning for DG size and location, there is no specific rule for that. Some researchers use the role of thumps, while others use optimization techniques. Anyway, in simple words, there is a role of thump for calculating the suitable size of distributed generation assumes that a DG system that covers 30% of the energy consumed during the solar day subject to have a rated power that is lower than the minimum local peak point during the solar day is fine.

By looking at Figure 1, we can say that the local peak value is 14 MVA, the energy consumption during the solar day is about 130 MWh (PF is assumed 0.9). Meanwhile, the yield factor for PV systems in Palestine is about 4.8 kWh/kWp per day. Assume that we need to cover 30% of the load demand. The required size of a PV system is about 8 MWp. Meanwhile, with the proposed system, the capacity of the total PV system is 10 MWp. Thus, there is a dire need for careful grid impact assessment.

In this research, the conducted grid impact assessment has three main assessments that are load flow assessment, short-circuit assessment, and harmonics quality assessment.

**3.1. Load Flow Analysis.** In any power system, the power that is generated from the station is transmitted through transmission lines to the loads. The flow of active and reactive power is known as load flow or power flow. Load flow analysis is an important tool to determine the steady-state operation of a power system. Load flow analysis provides a systematic mathematical approach to determine the bus voltages, phase angles, active, and reactive power flow through different branches, generators, transformer settings, and load under steady-state conditions [20].

The information of load flow is essential for analyzing the effective alternate plan for the system expansion to meet the increasing load demand. The load flow analysis helps identify the over-/underloaded lines and transformers as well as over-/undervoltage buses in the system. It is used to study the optimum location of capacity and their size to improve the unacceptable voltage profile [21].

The resulting equations in terms of power, known as the power flow equations, become nonlinear and must be solved by iterative techniques using numerical methods [22], such as Newton–Raphson method. These equations can be written in the terms of either the bus admittance matrix (YBUS) or the bus impedance matrix. With the availability of fast digital computers, all kinds of power system studies, including load flow, can now be carried out conveniently.

**3.1.1. Newton–Raphson Method.** There are several methods of solving the nonlinear system of equations. The most efficient one is the Newton–Raphson Method. This method begins with initial guesses of all unknown variables such as voltage magnitude and angles at load buses and voltage angles at generator buses. Next, a Taylor series is written, for each of the power balance equations included in the system of equations. The result is a linear system of equations that can be expressed as follows:



$$\begin{bmatrix} \Delta\theta \\ |\Delta V| \end{bmatrix} = -J^{-1} \begin{bmatrix} \Delta P \\ \Delta Q \end{bmatrix},$$

$$\Delta P_i = -P_i + \sum_{k=1}^n |V|_i |V|_k (G_{ik} \cos \theta_{ik} + B_{ik} \sin \theta_{ik}), |V|_i |V|_k (G_{ik} \cos \theta_{ik} - B_{ik} \sin \theta_{ik}),$$

$$\Delta Q_i = -Q_i + \sum_{k=1}^n \quad (1)$$

$$J = \begin{bmatrix} \frac{\partial \Delta P}{\partial \theta} & \frac{\partial \Delta P}{\partial |V|} \\ \frac{\partial \Delta Q}{\partial \theta} & \frac{\partial \Delta Q}{\partial |V|} \end{bmatrix},$$

where  $\Delta P$  and  $\Delta Q$  are called the mismatch equations and  $J$  is a matrix of partial derivatives known as a Jacobian.

The linearized system of equations is solved to determine the next guess ( $m+1$ ) of voltage magnitude and angles based on

$$\begin{aligned} \theta^{m+1} &= \theta^m + \Delta\theta, \\ |V|^{m+1} &= |V|^m + \Delta|V|. \end{aligned} \quad (2)$$

The process continues until a stopping condition is met. A common stopping condition is to terminate if the norm of the mismatch equations is below a specified tolerance. Outline of the solution of the power flow problem is as follows:

- (1) Make an initial guess of all unknown voltage magnitudes and angles. It is common to use a "flat start" in which all voltage angles are set to zero and all voltage magnitudes are set to 1.0 p.u.
- (2) Solve the power balance equations using the most recent voltage angle and magnitude values.
- (3) Linearize the system around the most recent voltage angle and magnitude values.
- (4) Solve for the change in voltage angle and magnitude.
- (5) Update the voltage magnitude and angles.

Check the stopping conditions; if met, then terminate, or else go to step 2.

**3.2. Short-Circuit Analysis.** The key application of short-circuit calculations is in the design of the protection system. Short-circuit analysis is mainly needed to determine the three-phase fault level at one or more nodes (buses) in the system. The three-phase fault level is used to assess the short-circuit current interruption potential of the circuit breakers [23].

A general representation of a balanced three-phase fault is shown in Figure 2, where F is the fault point with

impedances  $Z_f$  and  $Z_g$ . Figure 3 shows the sequences networks interconnection diagram [24].

From Figure 3, it can be noticed that the only one that has an internal voltage source is the positive-sequence network. Therefore, the corresponding currents for each of the sequences can be expressed as follows:

$$\begin{aligned} I_{a0} &= 0, \\ I_{a2} &= 0, \\ I_{a1} &= \frac{1.0 \angle 0^\circ}{Z_1 + Z_f}. \end{aligned} \quad (3)$$

If the fault impedance  $Z_f$  is zero,

$$I_{a1} = \frac{1.0 \angle 0^\circ}{Z_1}. \quad (4)$$

Equation (4) is substituted into the following equation:

$$\begin{bmatrix} I_{af} \\ I_{bf} \\ I_{cf} \end{bmatrix} = \begin{bmatrix} 1 & 1 & 1 \\ 1 & a^2 & a \\ 1 & a & a^2 \end{bmatrix} \begin{bmatrix} 0 \\ I_{a1} \\ 0 \end{bmatrix}. \quad (5)$$

Solving the above equation,

$$\begin{aligned} I_{af} &= I_{a1} = \frac{1.0 \angle 0^\circ}{Z_1 + Z_f}, \\ I_{bf} &= a^2 I_{a1} = \frac{1.0 \angle 240^\circ}{Z_1 + Z_f}, \\ I_{cf} &= a I_{a1} = \frac{1.0 \angle 120^\circ}{Z_1 + Z_f}. \end{aligned} \quad (6)$$

Since the sequence networks are short-circuited over their own fault impedance,

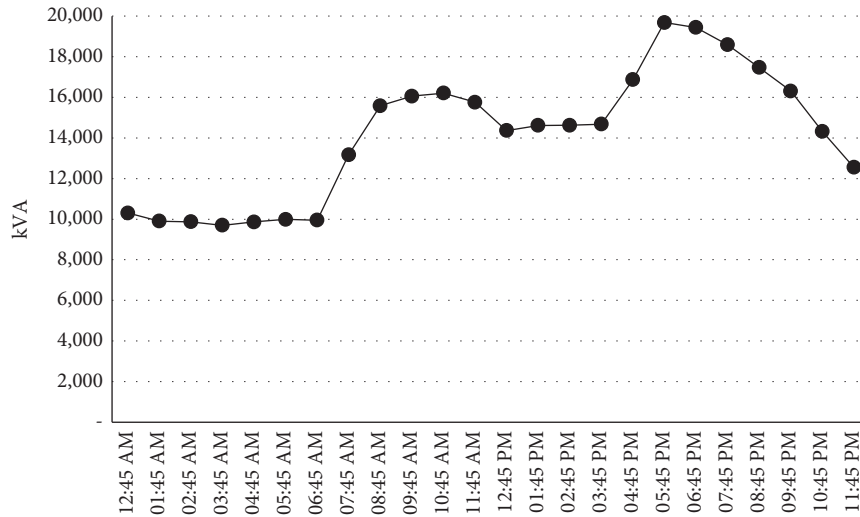


FIGURE 1: Characteristic daily load curve for the network.

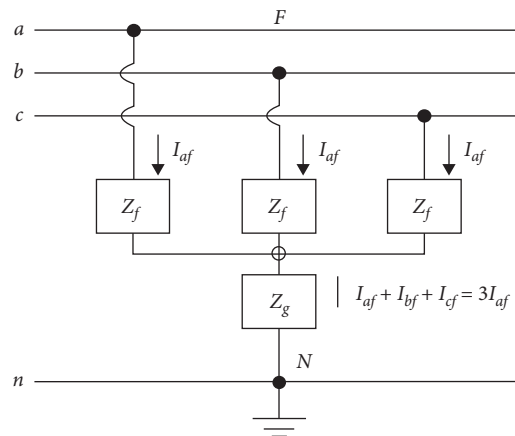


FIGURE 2: General representation of a balanced three-phase fault [20].

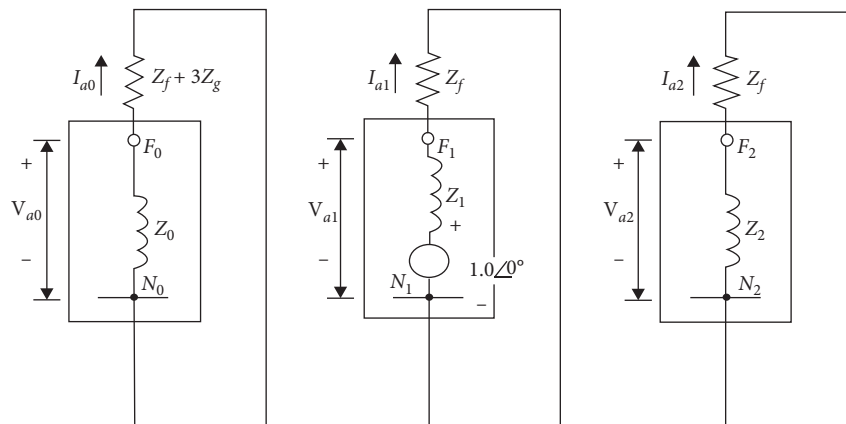


FIGURE 3: Sequence network diagram of a balanced three-phase fault [24].

$$V_{a0} = 0, \quad (7)$$

$$V_{a1} = Z_f I_{a1}, \quad (8)$$

$$V_{a2} = 0. \quad (9)$$

Equations (7)–(9) are substituted into the following equation:

$$\begin{bmatrix} V_{af} \\ V_{bf} \\ V_{cf} \end{bmatrix} = \begin{bmatrix} 1 & 1 & 1 \\ 1 & a^2 & a \\ 1 & a & a^2 \end{bmatrix} \begin{bmatrix} 0 \\ V_{a1} \\ 0 \end{bmatrix}. \quad (10)$$

Therefore,

$$\begin{aligned} V_{af} &= V_{a1} = Z_f I_{a1}, \\ V_{bf} &= a^2 V_{a1} = Z_f I_{a1} \angle 240^\circ, \\ V_{cf} &= a V_{a1} = Z_f I_{a1} \angle 120^\circ. \end{aligned} \quad (11)$$

The line-to-line voltages are

$$\begin{aligned} V_{ab} &= V_{af} - V_{bf} = V_{a1}(1 - a^2) = \sqrt{3} Z_f I_{a1} \angle 30^\circ, \\ V_{bc} &= V_{bf} - V_{cf} = V_{a1}(a^2 - a) = \sqrt{3} Z_f I_{a1} \angle -90^\circ, \\ V_{ca} &= V_{cf} - V_{af} = V_{a1}(a - 1) = \sqrt{3} Z_f I_{a1} \angle 150^\circ. \end{aligned} \quad (12)$$

If  $Z_f$  is equal to zero,

$$\begin{aligned} I_{af} &= \frac{1.0 \angle 0^\circ}{Z_1}, \\ I_{bf} &= \frac{1.0 \angle 240^\circ}{Z_1}, \\ I_{cf} &= \frac{1.0 \angle 120^\circ}{Z_1}. \end{aligned} \quad (13)$$

The phase voltages become

$$V_{af}, V_{bf}, V_{cf} = 0. \quad (14)$$

The line voltages become

$$V_{a0}, V_{a1}, V_{a2} = 0. \quad (15)$$

**3.3. Power Quality Assessment.** The aim of the harmonic analysis is to determine the distribution of harmonic currents, voltages, and harmonic distortion indices in a power system. This analysis is then extended to the study of resonant conditions and harmonic filter designs and also other effects of harmonics on the power system, that is, notching and ringing, neutral currents, saturation of transformers, and overloading of system components [25].

For the first step, a frequency scan is obtained, which plots the variation of the impedance modulus and the phase angle of the selected bus with frequency variation or generates  $R$ – $X$  impedance plots. This allows the determination of the resonant

frequencies. Harmonic current flows in the lines are measured, and the network, which is presumed to be linear at each stage of the calculations with the added constraints, is solved to obtain harmonic voltages [25]. The equations shall contain the harmonic distortion indices.

## 4. Economic Evaluation Criteria

Different indicators were considered in order to compare centralized system and decentralized system for economic analysis as follows; the simple payback period (SPP), the net present value (NPV), and internal rate return (IRR) that are significant economic parameters will be used to evaluate the feasibility for investors to invest into a rooftop PV system.

The simple payback period of investments is defined as the ratio of the initial investment's size to the value of the estimated cash flow as follows:

$$SPP = \frac{IC_0}{CF_1}, \quad (16)$$

where  $IC_0$  is the value of the invested capital and  $CF_1$  is the cash flow. This value is achieved as the result of the implementation of energy-saving measures and savings in operating costs or expected to be achieved at the stage of project development after the end of the calendar year.

Net present value (NPV) is also used in this research. NPV is a method that is used to determine the current value of all future cash flows generated by a project, including the initial capital investment. The formula of NPV is as follows:

$$NPV = \frac{CF}{(1+i)^n} - \text{initial investment}, \quad (17)$$

where  $n$  is the investment period and  $i$  is the discount rate of return that could be earned in alternative investment.

Finally, the discount rate (IRR) is used as well. IRR is the discount rate that makes the NPV of a project zero. In other words, it is the expected compound annual rate of return that will be earned on a project or investment.

The formula for IRR is as follows:

$$0 = NPV = \sum_{n=0}^N \frac{CF_n}{(1+IRR)^n}, \quad (18)$$

where  $N$  is the holding period.

## 5. Results and Discussion

**5.1. Results for Power Flow Analysis of the Adapted Power Distribution Network.** In general, the voltages of the 33 kV distribution points of the Tubas network are facing many under voltages. Figure 4 shows the thermal contouring map of the network.

As indicated in Figure 4, the warmer color indicates lower voltage levels, while the green color means a normal situation. The network situation is critical. In general, renewable energy penetration is about 21.74%, which is very high for such types of networks under similar conditions.

The results of power flow revealed that ten transformers were overloaded as demonstrated in Table 1. Also, an enormous



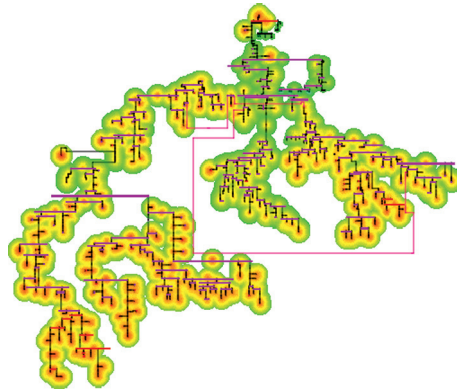


FIGURE 4: Power flow analysis of Tubas power distribution grid.

TABLE 1: Loading levels, conditions, and PV connected to the transformers.

Transformers	Condition	Rating/limit	Unit	Operating	% operating	PV connected
Afaq, Dreamland	Overload	0.400	MVA	0.61	153.6	0
Aqqaba water treatment	Overload	0.100	MVA	0.13	131.3	0
Ashraf Khader	Overload	0.160	MVA	0.27	167.8	0
Hawooz Aqqaba	Overload	0.250	MVA	2.4	959	97 kW
Maslamani F.C.	Overload	0.400	MVA	0.47	116.6	500 kW
Meselya Water East Stn	Overload	0.630	MVA	0.76	120.5	0
Qetaf Co	Overload	0.160	MVA	0.52	326.8	0
School Taysaer	Overload	0.160	MVA	0.2	122.8	0
Tubas Park	Overload	0.100	MVA	0.1	103.7	0
Zoghioul, ZA	Overload	0.160	MVA	0.44	272	15 kW

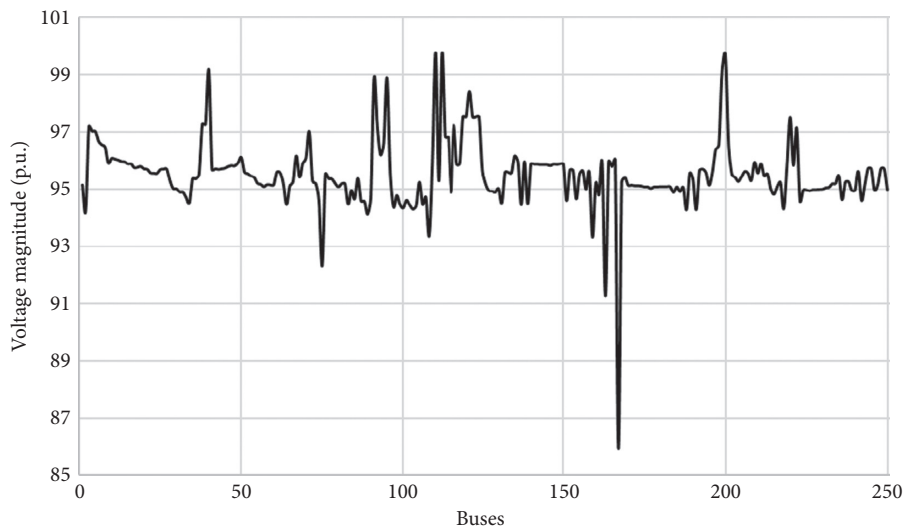


FIGURE 5: Voltage profile of Tubas network.

number of buses were undervoltage. Moreover, there were a lot of buses and PV arrays that are in marginal condition considering voltage level as can be seen in Figure 5.

The total losses in the network are 7.03% of the fully active power generation, while the reactive power losses are 14.34% of the fully reactive power generation.

5.2. Results for Centralized and Decentralized PVDG System Impact on the Grid. In this section, two scenarios are studied: first, installing the proposed 5 MWp system as a centralized system at the proposed location by the operator at 33 kV level and, second, proposing a group of small-scale PV systems to be at the 0.4 kV network.

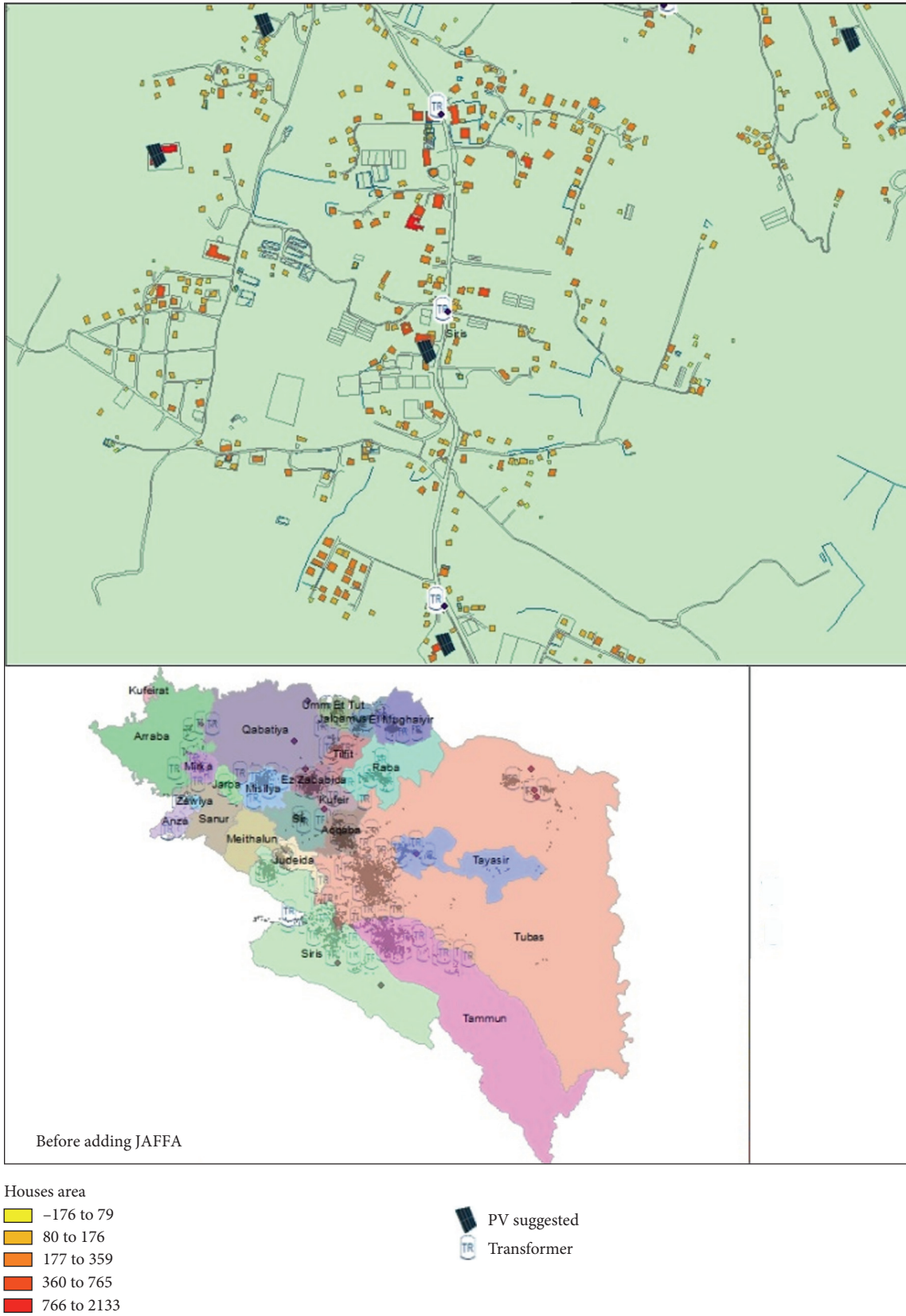


FIGURE 6: Tubas with suggested PVDG on rooftops.

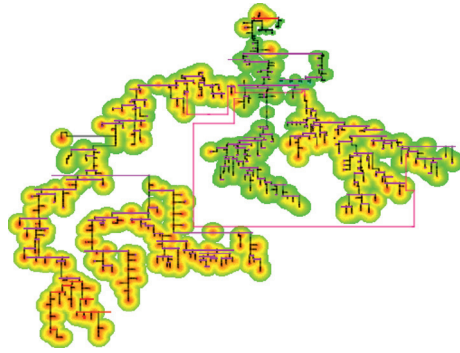


FIGURE 7: Thermal contouring map for the centralized case.

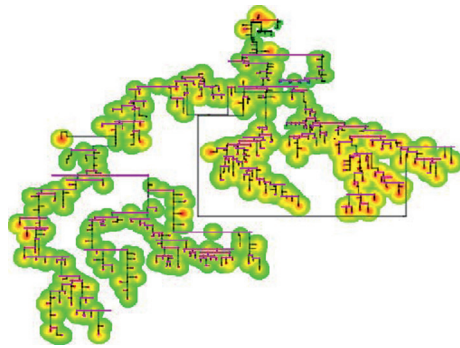


FIGURE 8: Thermal contouring map for the decentralized case.

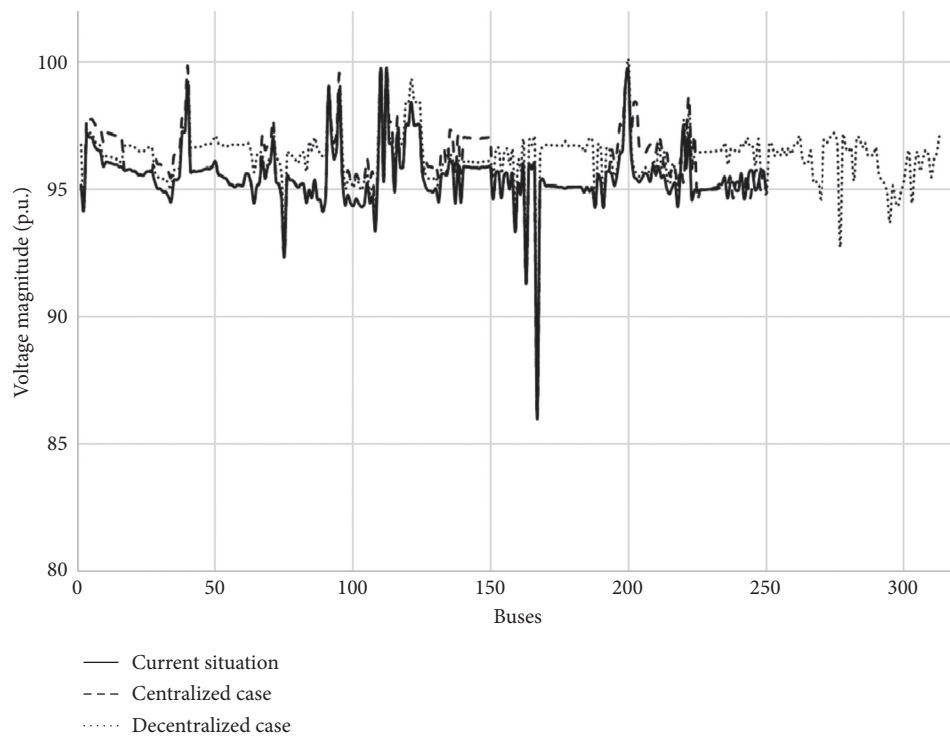


FIGURE 9: Voltage profile of Tubas network in the three cases.

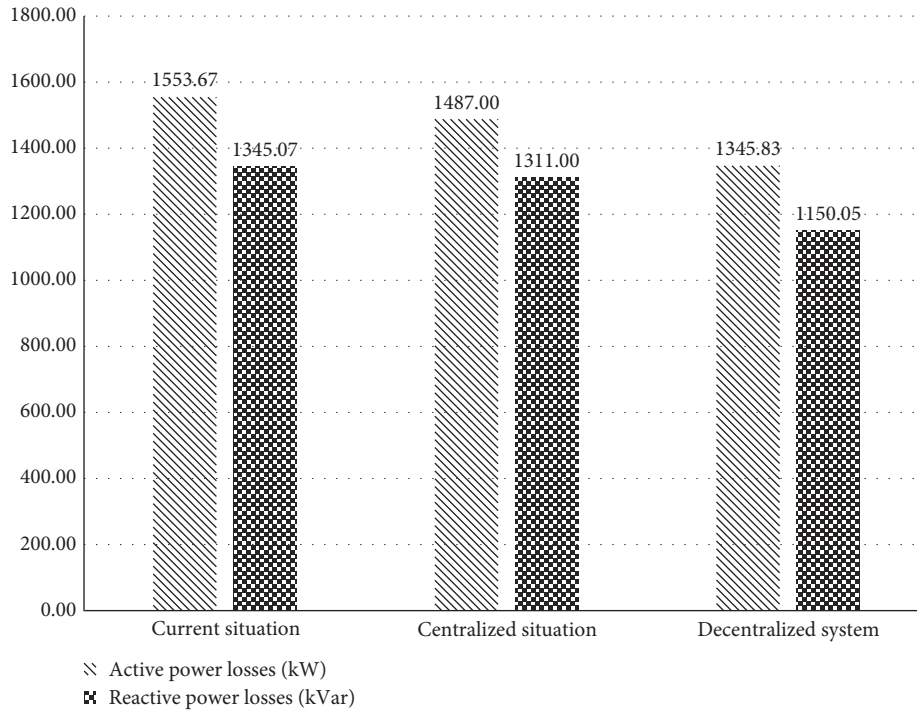


FIGURE 10: Active and reactive power losses.

TABLE 2: Point of common coupling loading.

	P (MW)	Q (MVar)	S (MVA)	% PF	% loading
Current situation	8.57	2.90	9.05	94.72	39.34
Centralized	4.19	2.91	5.10	82.13	22.15
Decentralized	7.73	2.81	8.23	93.98	35.77

TABLE 3: Description of Tubas network in the three cases.

	Current situation	Centralized case	Decentralized case
Critical situation			
Undervoltage buses	176	124	36
Overvoltage buses	0	0	0
Overloaded transformers	10	12	11

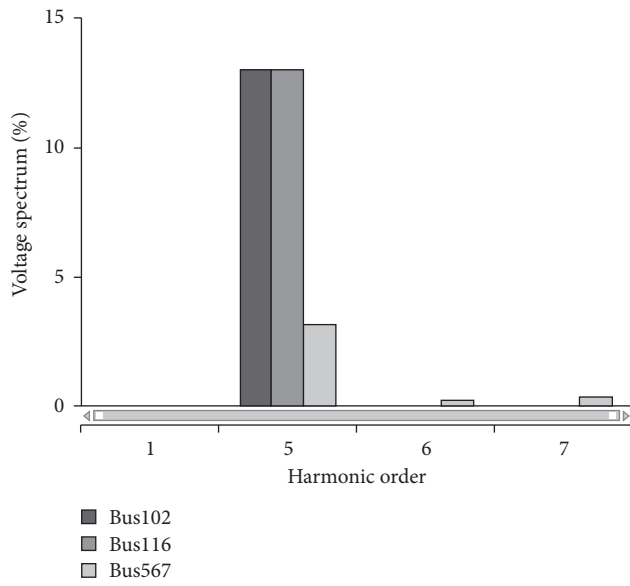
TABLE 4: Highest short-circuit current in the three cases.

	Highest short-circuit current (kA)	% increase in short-circuit current
Current situation	64.85	—
Centralized case	67.51	4.11
Decentralized case	68.93	6.30

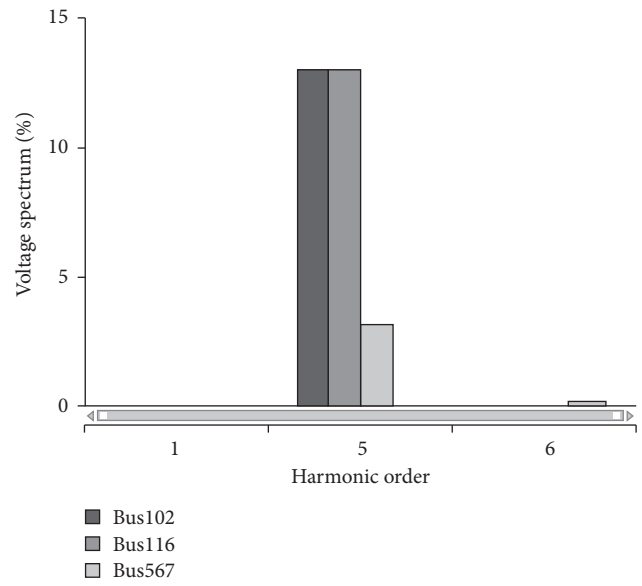
To implement the decentralized approach of the system, the results obtained from power flow are used to have the voltage of transforms as well as its capacity. After that, it is suggested to install PVDG on these transformers by considering 25% of transformer capacity. Here, any other PV system installed previously is considered within the 25% assumption. Available areas around each

transformer are also considered. Here, all the small PV systems are considered rooftop PV systems. However, the area of the suggested PVDG was not enough to mount 5 MWp in the actual houses, so it was reduced to 4.2348 MWp to be compatible with the real situation.

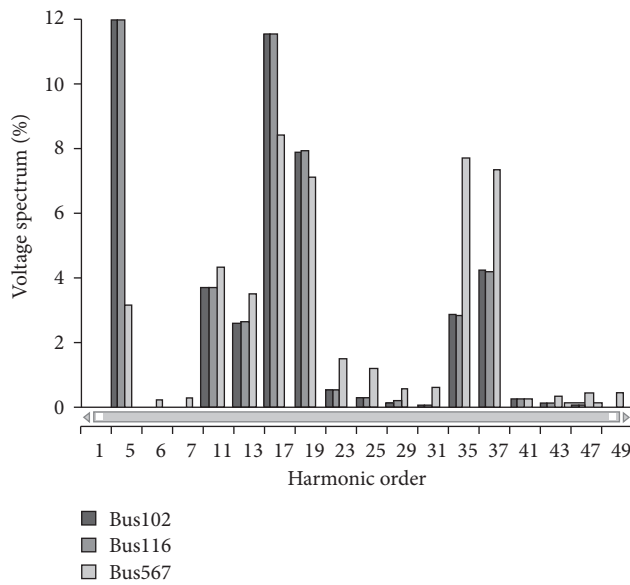
Here, another power flow is performed after installing the decentralized system on the overloaded transformers as



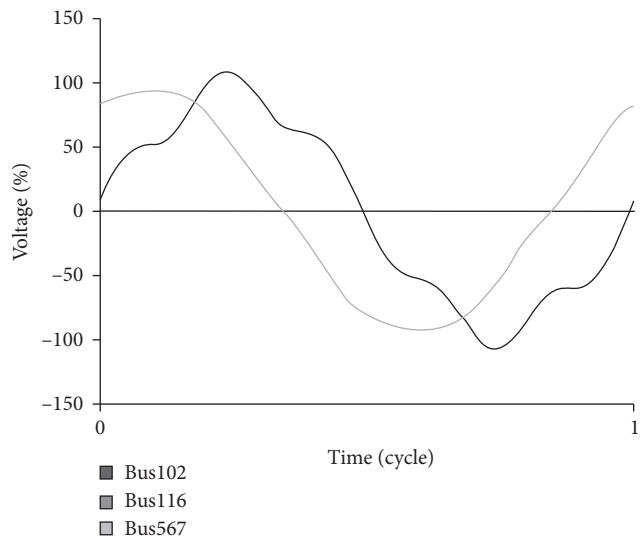
(a)



(b)



(c)



(d)

FIGURE 11: Continued.

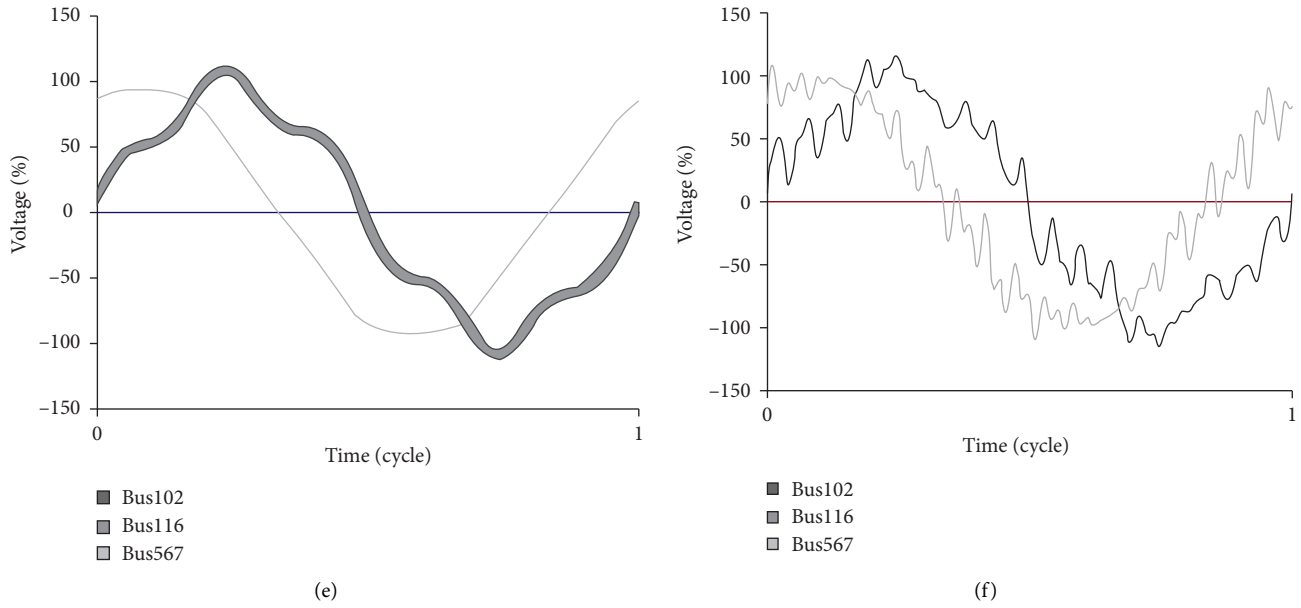


FIGURE 11: Spectrum view of harmonics order and harmonic waveform at different buses: (a, d) harmonic spectrum and waveform for the current situation, respectively; (b, e) harmonic spectrum and waveform for the centralized case, respectively; (c, f) harmonic spectrum and waveform for the decentralized case.

TABLE 5: Cost and system assumptions.

Variable	Quantity	Unit
Electricity selling price (both cases)	0.10	\$/kWh
Operation and maintenance (O & M; both cases)	25	\$/kW/year
Civil works (centralized PV system)	\$76,412.64	\$
Maintenance engineers (both cases)	1,000	\$/month
Inflation rate (both cases)	3%	—
Minimum attractive rate of return (both cases)	12%	—
Tax rate (both cases)	10%	—
Price of PV system (rooftop)	700	\$/kW
Price of PV system (land)	850	\$/kW
Plant power substation (centralized PV system)	\$45,847.58	\$
Yield factor of PV system	1750	kWh/kW/year
Roof rent	6	\$/m <sup>2</sup> /year
Land	\$42,313.65	\$/dunam
Degradation	0.8	%/year
Salvage value	0	\$
Operational period	20	Year

can be seen in Figure 6. The symbols of the photovoltaic panel are the proposed rooftop PV systems.

On the other hand, the centralized system case is represented by a new 5 MW project, Figures 7 and 8 show the thermal contouring map of the centralized and decentralized cases, respectively.

The voltage profile of the network is indicated in Figure 9. In many buses, the voltage levels are under the IEEE power networks voltage standard ( $\pm 5\%$  p.u.). Although in the decentralized case, it is much better than other arguments, as it supports the voltage of buses and overloaded transformers.

The active power loss in the base case is reduced by 4.43% when the centralized case is used, whereas it is reduced by

13.43% when the decentralized case is used. Furthermore, the reactive power loss in the base case is reduced by 2.6% when the centralized case is used, whereas it is reduced by 14.49% when the decentralized case is used. Figure 10 represents the values of losses.

From Table 2, it is very clear that the centralized PV system reduced the loading of the point of common coupling and drew more reactive power. Such a case will make this point more underloaded and may increase the frequency level there that may negatively affect the frequency level of the network.

Based on Table 2, the installation of large PV system in a single location is not recommended, because of reverse power flow, significant losses of power, and overloading of

TABLE 6: Economic analysis of the centralized system.

EOY	O & M + engineers	Savings	Net savings	Depreciation	Total	Taxable income	Tax	ATCF	ATCF with inflation	Balance
0					(\$4,837,710)			(\$4,837,710)	(\$4,837,710)	(\$4,837,710)
1	(\$137,000)	\$875,000.00	\$738,000	(\$241,886)		\$496,114	\$49,611	\$787,611	\$764,671	(\$4,073,039)
2	(\$137,000)	\$868,000.00	\$731,000	(\$241,886)		\$489,114	\$48,911	\$779,911	\$735,141	(\$3,337,898)
3	(\$137,000)	\$861,056.00	\$724,056	(\$241,886)		\$482,170	\$48,217	\$772,273	\$706,739	(\$2,631,158)
4	(\$137,000)	\$854,167.55	\$717,168	(\$241,886)		\$475,282	\$47,528	\$764,696	\$679,422	(\$1,951,736)
5	(\$137,000)	\$847,334.21	\$710,334	(\$241,886)		\$468,449	\$46,845	\$757,179	\$653,149	(\$1,298,587)
6	(\$137,000)	\$840,555.54	\$703,556	(\$241,886)		\$461,670	\$46,167	\$749,723	\$627,881	(\$670,706)
7	(\$137,000)	\$833,831.09	\$696,831	(\$241,886)		\$454,946	\$45,495	\$742,326	\$603,579	(\$67,127)
8	(\$137,000)	\$827,160.44	\$690,160	(\$241,886)		\$448,275	\$44,827	\$734,988	\$580,206	\$513,079
9	(\$137,000)	\$820,543.16	\$683,543	(\$241,886)		\$441,658	\$44,166	\$727,709	\$557,728	\$1,070,807
10	(\$137,000)	\$813,978.82	\$676,979	(\$241,886)		\$435,093	\$43,509	\$720,488	\$536,111	\$1,606,918
11	(\$137,000)	\$807,466.99	\$670,467	(\$241,886)		\$428,581	\$42,858	\$713,325	\$515,321	\$2,122,239
12	(\$137,000)	\$801,007.25	\$664,007	(\$241,886)		\$422,122	\$42,212	\$706,219	\$495,328	\$2,617,567
13	(\$137,000)	\$794,599.19	\$657,599	(\$241,886)		\$415,714	\$41,571	\$699,171	\$476,101	\$3,093,669
14	(\$137,000)	\$788,242.40	\$651,242	(\$241,886)		\$409,357	\$40,936	\$692,178	\$457,611	\$3,551,280
15	(\$137,000)	\$781,936.46	\$644,936	(\$241,886)		\$403,051	\$40,305	\$685,242	\$439,830	\$3,991,110
16	(\$137,000)	\$775,680.97	\$638,681	(\$241,886)		\$396,795	\$39,680	\$678,361	\$422,732	\$4,413,842
17	(\$137,000)	\$769,475.52	\$632,476	(\$241,886)		\$390,590	\$39,059	\$671,535	\$406,289	\$4,820,132
18	(\$137,000)	\$763,319.72	\$626,320	(\$241,886)		\$384,434	\$38,443	\$664,763	\$390,478	\$5,210,610
19	(\$137,000)	\$757,213.16	\$620,213	(\$241,886)		\$378,328	\$37,833	\$658,046	\$375,274	\$5,585,884
20	(\$137,000)	\$751,155.45	\$614,155	(\$241,886)		\$372,270	\$37,227	\$651,382	\$360,655	\$5,946,539

the network due to the low local demand at the suggested bus.

On the other hand, the suggested decentralized systems improve the voltage and reduce the losses. Table 3 illustrates the number of under-/overvoltage buses and overloaded transformers in the three cases (in the critical situation).

**5.3. Results of Short-Circuit Analysis.** The results of the three-phase short-circuit simulations performed for the grid in the current situation, centralized cases, and decentralized cases are presented in Table 4.

For the initial situation, the highest short-circuit current is 64.85 kA on the supply point. The implementation of the centralized case will lead to an increase of the short-circuit values within the analyzed network by 4.11%, while in the decentralized case, the increase in short-circuit current is 6.3%. However, the short-circuit security margin for the network will be at least 20% from the rated short-circuit current of the equipment after the implementation of the PV plant within the area. Therefore, there are no problems associated to short-circuit levels caused by the implementation of the PV plant.

**5.4. Results of Power Quality Assessment.** The impact of the proposed PV system on the harmonic content at the point of common coupling is investigated by harmonics load flow analysis. The harmonic voltages inside the PV system and at the point of common coupling are judged based on the IEC 61000-3-6 Standard by measuring the total harmonic distortions (THD). In practical considerations, the THD limit in MV and high-voltage networks is usually lowered to 5% and 2.5%, respectively, as required in the IEEE 519 Standard. In case the above limits are violating the IEEE standard, a harmonics violation case is reported in this study. The network currently faces a hard situation of harmonics,

whereas at some points and cases, it reaches 17% at the fifth and the seventh components as THD. Based on that, IEEE 18 plus CT harmonic model is implemented for all grid components to describe approximately the harmonics situation in the grid.

The PV inverters are modeled as current injection sources. The considered spectrum is taken from typical manufacturer data, multiplied by a scaling factor to obtain the current THD of 3%, which is a usual value for such equipment. The simulation results are presented in Figure 11.

According to the results, many buses exceed the limits of the allowed harmonics in the grid. The main reason for that is the current situation of the harmonics in the grid due to the presence of nonlinear loads such as saws. It is extremely so high and needs mitigation. The centralized case does not contribute that much to this critical situation. However, it is found that the decentralized case may contribute negatively to the grid as the number of inverters increase as can be seen in Figures 11(c) and 11(f).

## 6. Brief Economic Analysis of the Proposed Systems

To illustrate how the economic analysis was carried out, the houses and transformers were given from the Tubas network on GIS. Then rooftops for the suggested capacities of PVDG were chosen based on 10 m<sup>2</sup>/kWp.

The cost and system assumptions are presented in Table 5. Meanwhile, the economic analyses of both options are illustrated in Tables 6 and 7.

Capital cost includes the initial cost of installing a PV system. The operating cost includes the cost associated with maintaining and operating the PV system over its useful life. The analysis was carried out with consideration of taxes and depreciation.





TABLE 8: Results of economic assessment.

	Decentralized	Centralized
NPV	−\$768,212.88	−\$246,021.02
RoR	7%	11%
SPP	9.434	7.116

The capital cost of the system was calculated based on PV system costs in addition to costs of plant substation, civil works, and land costs. Meanwhile, in case of the installation of a decentralized PV system, the cost of PV system is assumed to be equal to PV capital cost only. The O & M and salary of maintenance engineers were also considered together. The savings indicated in Tables 6 and 7 are the amount of electricity generation from the system, which is sold to the Tubas network by considering the degradation rate for each year. The net savings are the savings minus O & M and the salary of the engineers. The depreciation was calculated based on the straight-line method, taking the initial cost minus the salvage value divided by the operational period, which is 20 years.

After that, taxable income was calculated as net savings minus depreciation to know how much taxes would be paid. After-tax cash flow is net savings minus taxes. For SPP, a balance for the cash flow considering the inflation rate was carried out to have accurate results. The NPV, RoR, and SPP are presented in Table 8.

In general, although the decentralized system exceeds the centralized system technically, the centralized system seems to be slightly more profitable than the decentralized system. However, the decentralized system is still acceptable considering the technical flows that the centralized system may cause.

## 7. Conclusion

In this paper, a grid impact assessment of a photovoltaic-based distributed generation unit is proposed for a medium voltage distribution network. The paper also proposes a comparison based on grid assessment results between centralized and decentralized photovoltaic-based distributed generation. The comparison considered the power flow analysis, short-circuit analysis, and harmonic contribution of both cases. In addition to that financial analysis was also done for both cases for better comparison. The adapted case in this research was a real case that implies the real power flow performance of a medium voltage distribution network. Results showed that the decentralized PV distributed generation systems exceeds the centralized PV systems considering power flow analysis. Meanwhile, both cases were almost equal considering short-circuit contribution. Finally, the centralized PV system contributed fewer in terms of harmonic to the grid as compared to decentralized PV systems. On the other hand, the decentralized PV systems option was less profitable as compared to the centralized system. However, considering the technical implications of the centralized system, the decentralized PV systems were recommended.

## Data Availability

Data are available upon request to the corresponding author.

## Disclosure

The article is based on a BSc final year research.

## Conflicts of Interest

The authors declare that they have no conflicts of interest.

## References

- [1] M. AlMuhaini, "Impact of distributed generation integration on the reliability of power distribution systems," in *Distributed Generation Systems*, G. B. Gharehpetian and S. M. Mousavi Agah, Eds., Butterworth-Heinemann, Oxford, UK, pp. 453–508, 2017.
- [2] K. Tamer and E. Wilfried, "PV systems in the electrical power system," in *Modeling of Photovoltaic Systems Using MATLAB®*, pp. 159–174, Wiley, Hoboken, NJ, USA, 2016.
- [3] M. Thomson and D. G. Infield, "Impact of widespread photovoltaics generation on distribution systems," *IET Renewable Power Generation*, vol. 1, no. 1, pp. 33–40, 2007.
- [4] M. Karimi, H. Mokhlis, K. Naidu, S. Uddin, and A. H. A. Bakar, "Photovoltaic penetration issues and impacts in distribution network—a review," *Renewable and Sustainable Energy Reviews*, vol. 53, pp. 594–605, 2016.
- [5] B. P. Koirala, B. Sahan, and N. Henze, "Study on MPP mismatch losses in photovoltaic applications," in *Proceedings of the Fraunhofer IWES*, Hamburg, Germany, September 2014.
- [6] S. Shivashankar, S. Mekhilef, H. Mokhlis, and M. Karimi, "Mitigating methods of power fluctuation of photovoltaic (PV) sources—a review," *Renewable and Sustainable Energy Reviews*, vol. 59, pp. 1170–1184, 2016.
- [7] M. S. ElNozahy and M. M. A. Salama, "Technical impacts of grid-connected photovoltaic systems on electrical networks—a review," *Journal of Renewable and Sustainable Energy*, vol. 5, no. 3, Article ID 032702, 2013.
- [8] D. Cheng, B. A. Mather, R. Seguin, J. Hambrick, and R. P. Broadwater, "Photovoltaic (PV) impact assessment for very high penetration levels," *IEEE Journal of Photovoltaics*, vol. 6, no. 1, pp. 295–300, 2016.
- [9] I. Taczi, B. Hartmann, and I. Vokony, "Impact study of smart grid technologies on low voltage networks with high penetration of renewable generation," *International Journal of Renewable Energy Research-IJREER*, vol. 10, no. 2, 2020.
- [10] A. Kharrazi, V. Sreeram, and Y. Mishra, "Assessment techniques of the impact of grid-tied rooftop photovoltaic generation on the power quality of low voltage distribution network—a review," *Renewable and Sustainable Energy Reviews*, vol. 120, Article ID 109643, 2020.
- [11] N. B. G. Brinkel, M. K. Gerritsma, T. A. AlSkaif et al., "Impact of rapid PV fluctuations on power quality in the low-voltage grid and mitigation strategies using electric vehicles," *International Journal of Electrical Power & Energy Systems*, vol. 118, Article ID 105741, 2020.
- [12] A. Abualkhair, "Electricity sector in the Palestinian territories: which priorities for development and peace?" *Energy Policy*, vol. 35, no. 4, pp. 2209–2230, 2007.
- [13] A. Juaidi, F. G. Montoya, I. H. Ibrik, and F. Manzano-Agugliaro, "An overview of renewable energy potential in Palestine," *Renewable and Sustainable Energy Reviews*, vol. 65, pp. 943–960, 2016.
- [14] M. S. Ismail, M. Moghavvemi, and T. M. I. Mahlia, "Analysis and evaluation of various aspects of solar radiation in the

- Palestinian territories,” *Energy Conversion and Management*, vol. 73, pp. 57–68, 2013.
- [15] A.-K. Daud and M. S. Ismail, “Design of isolated hybrid systems minimizing costs and pollutant emissions,” *Renewable Energy*, vol. 44, pp. 215–224, 2012.
- [16] M. A. Omar and M. M. Mahmoud, “Grid connected PV-home systems in Palestine: a review on technical performance, effects and economic feasibility,” *Renewable and Sustainable Energy Reviews*, vol. 82, pp. 2490–2497, 2018.
- [17] E. Ajlouni and H. Alsamamra, “A review of solar energy prospects in Palestine,” *American Journal of Modern Energy*, vol. 5, no. 3, pp. 49–62, 2019.
- [18] Y. Fathi Nassar and S. Yassin Alsadi, “Assessment of solar energy potential in Gaza Strip-Palestine,” *Sustainable Energy Technologies and Assessments*, vol. 31, pp. 318–328, 2019.
- [19] Palestinian Investment Promotion Agency, Renewable Energy Sector VP Booklet, Palestinian Investment Promotion Agency, Ramallah, Palestine, Report, <http://www.pipa.ps/files/file/Value%20Proposition/EN/PIPA-%20Renewable%20Energy%20Sector%20VP%20Booklet-%20English.pdf>.
- [20] O. A. Afolabi, W. H. Ali, P. Cofie, J. Fuller, P. Obiomon, and E. S. Kolawole, “Analysis of the load flow problem in power system planning studies,” *Energy and Power Engineering*, vol. 07, no. 10, pp. 509–523, 2015.
- [21] H. Saadat, *Power System Analysis*, Tata McGraw Hill Education Pvt. Ltd, New York, NY, USA, 2010.
- [22] D. P. Kothari and I. J. Nagrath, *Modern Power System Analysis*, Tata McGraw Hill Education Pvt., New York, NY, USA, 3rd edition, 2007.
- [23] S. A. Soman, S. A. Khaparde, and S. Pandit, “Short circuit analysis,” in *Computational Methods for Large Sparse Power Systems Analysis: An Object Oriented Approach*, S. A. Soman, S. A. Khaparde, and S. Pandit, Eds., Springer, Boston, MA, USA, pp. 179–212, 2002.
- [24] S. H. Al-Saiari, “Analysis of power systems under normal and fault conditions,” 2012, <https://www.semanticscholar.org/paper/Analysis-of-power-systems-under-normal-and-fault-Al-Saiari/160b8613325c3172c53ced3b9ed83a0193a6d044>.
- [25] J. C. Das, *Power System Analysis: Short-Circuit Load Flow and Harmonics*, CRC Press, Boca Raton, FL, USA, 2002.

## Research Article

# Stacked Autoencoder Framework of False Data Injection Attack Detection in Smart Grid

Liang Chen <sup>1</sup>, Songlin Gu,<sup>2</sup> Ying Wang,<sup>3</sup> Yang Yang,<sup>3</sup> and Yang Li <sup>4</sup>

<sup>1</sup>*School of Automation, Nanjing University of Information Science and Technology, Nanjing 210044, China*

<sup>2</sup>*State Grid Economic and Technological Research Institute Co., Ltd, Beijing 102209, China*

<sup>3</sup>*State Grid Hebei Economic Research Institute, Shijiazhuang 050011, China*

<sup>4</sup>*School of Electrical Engineering, Northeast Electric Power University, Jilin 132012, China*

Correspondence should be addressed to Liang Chen; [ch.lg@nuist.edu.cn](mailto:ch.lg@nuist.edu.cn)

Received 20 May 2021; Accepted 25 June 2021; Published 3 July 2021

Academic Editor: Bo Yang

Copyright © 2021 Liang Chen et al. This is an open access article distributed under the Creative Commons Attribution License, which permits unrestricted use, distribution, and reproduction in any medium, provided the original work is properly cited.

The advanced communication technology provides new monitoring and control strategies for smart grids. However, the application of information technology also increases the risk of malicious attacks. False data injection (FDI) is one kind of cyber attacks, which cannot be detected by bad data detection in state estimation. In this paper, a data-driven FDI attack detection framework of the smart grid with phasor measurement units (PMUs) is proposed. To enhance the detecting accuracy and efficiency, the multiple layer autoencoder algorithm is applied to abstract the hidden features of PMU measurements layer by layer in an unsupervised manner. Then, the features of the measurements and corresponding labels are taken as inputs to learn a softmax layer. Last, the autoencoder and softmax layer are stacked to form a FDI detection framework. The proposed method is applied on the IEEE 39-bus system, and the simulation results show that the FDI attacks can be detected with higher accuracy and computational efficiency compared with other artificial intelligence algorithms.

## 1. Introduction

Phasor measurement units (PMUs) can measure the voltage and current phasors directly with the help of global positioning system synchronization clock [1, 2]. Due to the ability of monitoring the transient dynamics of power systems, more and more PMUs have been installed in the smart grid. Meanwhile, the rapid developments of enhanced monitoring and information technology also facilitate the malicious cyber attacks [3]. The large-scale integration of renewable energy resources poses a challenge for the security of the system operation due to inherent uncertainties of renewables [4–6]. The cyber attacks on the power system monitoring and data acquisition systems are the main objectives for attackers to seriously threaten the power system operating safety. Attackers launch a cyber attack by sending a malicious information to the control center from measurements. One of the most important functions of a state estimator is bad data detection, by which some malicious

attacks can be detected because the value of the objective function increases dramatically when attacks are launched. However, one kind of the serious cyber attacks that cannot be detected by bad data detection in state estimations is the false data injection (FDI) attack [7].

Up to now, lots of research works have been developed on different cyber attacks. Under the assumption that the network topology and parameters are known by the attackers, the FDI attack method is proposed in [8] for the first time. However, it is hard for the attacker to obtain the full acknowledgments of power systems. Aiming at this problem, in [9], a FDI attack method is given based on only partial knowledge of the system topology and a subset of meter measurements. To reduce attack costs and detection risks, the minimal set of meters that required to be compromised is taken as the objective function in [10]. In [11], the FDI attack is combined with other kind of cyber attacks, forming an enhanced FDI attack method. Once the FDI attack is launched in power systems, it is hard to be detected. To

prevent the measurements being attacked, the meters should be protected. Lots of methods for minimizing the protection costs have been presented in [12, 13].

At the same time, the corresponding FDI attack detections are becoming a hot research topic. In [14], a reactance perturbation-based scheme is proposed to detect and identify originally covert FDI attacks on power system state estimation that enhances the security of state estimation without significantly increasing the operational cost in power systems. In [15], an online anomaly detection algorithm that utilizes load forecasts, generation schedules, and synchrophasor data to detect measurement anomalies is given. In [16], the feasibility and limitations of adopting the proactive false data detection approach to thwart FDI attacks on power grid state estimation are studied, and a framework to detect FDI attacks on power grid state estimation by using the proactive false data detection approach is proposed.

With the rapid developments of artificial intelligence technologies, the research works of data-driven technology-based detection methods are increasing dramatically. The principle component analysis is used to analyze the FDI attacks in the real-time environment [17], providing a more accurate and sensitive response than the previous FDI detection techniques. In [18], a supervised learning using labeled data called support vector machine-based FDI attacks detection method is proposed. The principal component analysis is used to reduce the dimension of the data to be processed, which leads to lower computation complexities. Use of deep learning for solving pattern classification problems is proven to be an effective way in engineering [19]. Under the FDI attack condition, spatial and temporal data correlations may deviate from those in normal operating conditions. Based on this characteristic, a discrete wavelet transform algorithm and deep neural networks' techniques are used to construct an intelligent system for AC FDI attack detection, which is proposed in [20]. In [21], the deep learning technique is applied to recognize the behavior features of FDI attacks with the historical measurement data and employ the captured features to detect the FDI attacks in real time. Although the deep learning is an effective method to detect the FDI attacks, some drawbacks, such as the heavy computation loads and bad generalization abilities with a huge amount of inputs, restrict the further applications. Autoencoders [22, 23] are one of the effective methods to cope with these problems, which can learn compressed features in an unsupervised manner, attracting more and more researchers' interests [24, 25]. However, the effectiveness of autoencoder decreases when the number of hidden units is more than the dimension of input data. To address this problem, sparse autoencoders, in which the sparsity is integrated into the autoencoder model to learn more efficient sparse features, have been developed [26]. In [27], a denoising autoencoder is used in wind turbine gearbox fault diagnosis, which can learn useful features from raw inputs by denoising. Due to the abilities of abstracting robust representations from noisy data, the denoising autoencoder is applied in many fields in recent years [27, 28]. In [29], autoencoders are used to reduce dimension and extract features from measurement datasets. Further, the

autoencoders are integrated into an advanced generative adversarial network framework, which successfully detects anomalies under FDI attacks with a few labeled measurement data. However, the single-layer autoencoder cannot abstract entire representations of the original data. Aiming at this problem, a stacked autoencoder is proposed, which is made up of multiple autoencoders. The output of the first layer of the autoencoder is taken as the input of the second layer.

In this paper, a stacked autoencoder-based FDI attack detection framework in the smart grid is proposed. The main contributions are listed:

- (1) A data-driven FDI attack detection framework is proposed. The topology errors and bad data are detected by state estimations. The hidden FDI attacks in measurements that cannot be identified by state estimation are detected by the intelligent algorithm.
- (2) The stacked autoencoder is applied to detect the FDI attacks. Compared with other methods, the performances of the stacked autoencoder are better in the condition that the amounts of ordinary and attacks' samples differ widely.
- (3) The proposed method is applied on the IEEE 39-bus testing system. The performances of the proposed method are better than the traditional deep learning methods, which are capable of practical applications.

The rest of this paper is organized as follows. Section 2 establishes the power system linear state estimation model. The bad data detection method is also given. In Section 3, the basic principle of FDI attacks is given. In Section 4, the stacked autoencoder-based FDI attack detection method is proposed. To evaluate the performance of the proposed FDI attack detection method, the case study is carried out under different conditions in Section 5. Finally, Section 6 concludes this paper.

## 2. Linear State Estimation of Power Systems

*2.1. Linear State Estimation Model.* With the rapid development of PMUs, it is possible to take the linear state estimation based on phasor measurements. The linear state estimation can be solved directly without iteration. As a result, the calculation burden of linear state estimation is lighter than nonlinear estimation. The measurements of linear state estimation include real and imaginary parts of bus voltages and currents phasors which can be measured directly. In the linear state estimation, the real and imaginary parts of bus voltages are taken as states that should be estimated. The relationships between branch current measurements and states are derived from the  $\pi$  equivalent of transmission lines, which are shown as follows:

$$\begin{cases} I_{ij,r} = (g_{ij} + g_{i0})e_i - g_{ij}e_j - (b_{ij} + b_{i0})f_i + b_{ij}f_j, \\ I_{ij,i} = (g_{ij} + g_{i0})f_i - g_{ij}f_j + (b_{ij} + b_{i0})e_i - b_{ij}e_j, \end{cases} \quad (1)$$

where  $I_{ij,r}$  and  $I_{ij,i}$  are the real and imaginary parts of the branch current phasors going from bus  $i$  to bus  $j$ ,

respectively,  $g_{ij}$  and  $b_{ij}$  are the conductance and susceptance of branch  $i$ - $j$ , respectively,  $g_{i0}$  and  $b_{i0}$  are the conductance and susceptance of the shunt branch at bus  $i$ , respectively, and  $e_i$  and  $f_i$  are the real and imaginary parts of voltage phasor of bus  $i$ , respectively.

The matrix form of (1) is

$$\begin{bmatrix} I_{ij,r} \\ I_{ij,i} \\ I_{ji,r} \\ I_{ji,i} \end{bmatrix} = \begin{bmatrix} g_{ij} + g_{i0} & -b_{ij} - b_{i0} & -g_{ij} & b_{ij} \\ b_{ij} + b_{i0} & g_{ij} + g_{i0} & -b_{ij} & -g_{ij} \\ -g_{ji} & b_{ji} & g_{ji} + g_{j0} & -b_{ji} - b_{j0} \\ -b_{ji} & -g_{ji} & b_{ji} + b_{j0} & g_{ji} + g_{j0} \end{bmatrix} \begin{bmatrix} e_i \\ f_i \\ e_j \\ f_j \end{bmatrix}. \quad (2)$$

Equation (2) can be rewritten as

$$z_B = H_B x, \quad (3)$$

where  $z_B = [\dots I_{ij,r}, I_{ij,i}, I_{ji,r}, I_{ji,i}, \dots]^T$ ,  $x = [\dots e_i, f_i, e_j, f_j, \dots]^T$ ,  $z_B$  is the vector of the branch current measurements, and  $x$  is the vector of states.

In addition to the branch current measurements, the injected currents and bus voltages can be measured by PMUs also. The measurement equation of linear state estimation is

$$\begin{bmatrix} z_U \\ z_B \\ z_{IN} \end{bmatrix} = \begin{bmatrix} I_{2m \times 2n} \\ H_B \\ Y_M \end{bmatrix} x, \quad (4)$$

where  $z_U$  and  $z_{IN}$  are the phasor measurement vectors of bus voltages and injected currents, respectively,  $I_{2m \times 2n}$  is the measurement matrix of bus voltages,  $m$  and  $n$  are the number of buses equipped with PMUs and the total bus number, respectively, and  $Y_M$  is the injected current measurement matrix.

Equation (4) can be rewritten as

$$z = Hx + v, \quad (5)$$

where  $z$  is the measurement vector,  $v$  is the measurement error, and  $v$  satisfies Gaussian distribution with zero mean and variance  $\sigma^2$ .

Equation (5) is linear, so the linear weighted least squares can be used to estimate the states. The objective function is to minimize the sum of weighted variances, which is shown as follows:

$$J(x) = [z - Hx]^T R^{-1} [z - Hx], \quad (6)$$

where  $J$  is the objective function,  $R$  is a diagonal matrix, the  $i$ th diagonal element of  $R$  is  $1/\sigma_i^2$ , and  $\sigma_i$  is the variance of  $i$ th measurement. The estimated states are

$$\hat{x} = [H^T R^{-1} H]^{-1} H^T R^{-1} z, \quad (7)$$

where  $\hat{x}$  is the estimated states.

**2.2. Bad Data Detection.** Under the normal condition (no bad data in measurements), the sum of estimated measurement variance is under a given threshold  $\varepsilon$ ; however, if

the measurements experience bad data, the threshold  $\varepsilon$  would be exceeded. The sum of estimated measurement variance is given as

$$\begin{aligned} \hat{J} &= \hat{r}^T R^{-1} \hat{r}, \\ &= (z - \hat{z})^T R^{-1} (z - \hat{z}), \\ &= (z - H\hat{x})^T R^{-1} (z - H\hat{x}), \\ &= (z - Gz)^T R^{-1} (z - Gz), \\ &= z^T (I - G)^T R^{-1} (I - G)z, \end{aligned} \quad (8)$$

where  $\hat{r}$  is the estimated measurement residual,  $\hat{r} = z - \hat{z}$ ,  $\hat{z}$  is the estimated measurement,  $\hat{z} = H\hat{x}$ ,  $I$  is an identity matrix, and  $G = H(H^T R^{-1} H)^{-1} H^T R^{-1}$ .

The bad data can be detected by the following judgement:

$$\begin{cases} \hat{J} \leq \varepsilon, & \text{no bad data,} \\ \hat{J} > \varepsilon, & \text{bad data exist.} \end{cases} \quad (9)$$

If the measurements experience bad data, the measurements would be removed one by one, and the states are estimated again until all bad data are removed.

### 3. False Data Injection Attacks

Aiming at the above bad data detection, FDI attack can construct an attack vector to the measurements that are able to bypass the bad data detection, but the estimated states deviate from the true values seriously. Assuming that the attackers can obtain the system typologies and parameters, the FDI attacks are formulated as follows:

$$z_a = z + a, \quad (10)$$

where  $z_a$  is the attacked measurement and  $a$  is the attack vector. If  $a$  is not artificially designed, the sum of estimated measurement variance would exceed the threshold, and the attack would be detected. As a result, the attacker must find out a proper vector  $a$  that will satisfy the following constrain:

$$\begin{aligned} \hat{r}_a - \hat{r} &= (z_a - H\hat{x}_c) - (z - H\hat{x}), \\ &= z_a - H(\hat{x} + c) - (z - H\hat{x}), \\ &= z + a - H\hat{x} - Hc - z + H\hat{x}, \\ &= a - Hc, \\ &= 0, \end{aligned} \quad (11)$$

where  $\hat{r}_a$  is the estimated measurement residual under the bad data condition,  $\hat{x}_c = \hat{x} + c$ ,  $\hat{x}_c$  is the estimated states under attack condition, and  $c$  is the estimated deviation with attacked measurements. It can be seen from (11) that estimated measurement residual  $\hat{r}_a$  under attack condition is equal to the residual  $\hat{r}$  if the FDI attack vector  $a$  satisfies  $a = Hc$ . As a result, the FDI attack can bypass the bad data detection of (9). If the attacker obtains the overall structure and parameters, he can launch the attack by injecting malicious vectors to the measurements to change the

estimating results as he wanted. This will cause serious consequences on power systems, while it cannot be detected.

The attacked measurements satisfy all constraints as the normal measurements, which can be presented as follows:

$$\begin{aligned} z_a &= z + a, \\ &= Hx + Hc, \\ &= H(x + c). \end{aligned} \quad (12)$$

Equation (12) shows that if the attacked measurement  $z_a$  satisfies constraints (5), the estimated states will deviate from actual values. This character leads to the hardness of detecting the FDI attacks using the traditional methods. In this paper, the stacked autoencoder is proposed to abstract the intrinsic features of the attacked measurements.

## 4. False Data Injection Attack Detection

**4.1. Stacked Autoencoder.** The autoencoder is a typical unsupervised learning neural network; the inputs of it are a set of unlabeled data. An autoencoder includes two parts: encoder and decoder. A reduced dimensional feature representation can be obtained by the encoder, which is taken as the inputs of decoders. The decoder tries to reconstruct the original input according to the reduced dimensional feature. The structure of the autoencoder is shown in Figure 1.  $z$  is the measurement vector, which is taken as inputs of the autoencoder.  $y$  is the reduced dimensional feature of  $z$  abstracted by the encoder, which is the decoder input. The output  $\tilde{z}$  is the reconstruction of the original input  $z$ . The objective of the autoencoder is to try to copy its input to its output by two transformations:

$$\begin{aligned} y &= f(W_1 z + b_1), \\ \tilde{z} &= g(W_2 y + b_2), \end{aligned} \quad (13)$$

where  $f$  and  $g$  are the activation functions of the encoder and decoder, respectively,  $W_1$  and  $W_2$  are the weight matrixes, and  $b_1$  and  $b_2$  are the bias vectors.

$W_1$ ,  $W_2$ ,  $b_1$ , and  $b_2$  can be obtained by training the autoencoder using the unlabeled data  $z$ . It must be noted that the autoencoder can reconstruct different original inputs accordingly, which means that the feature representation  $y$  contains all information of the original input  $z$  in a lower dimensional form. As a result, the objective of the autoencoder is to minimize the gap between the output  $\tilde{z}$  and input  $z$ . Thus, in the training process, the reconstruction loss function is

$$J_a(W_1, W_2, b_1, b_2) = \arg \min \|z - \tilde{z}\|^2, \quad (14)$$

where  $J_a$  is the loss function of autoencoders.

In our FDI attack detection, once an autoencoder is trained, the output layer is useless. Only the hidden layer of the encoder is used to abstract the features of inputs. However, the application of a single encoder is limited. Aiming at this problem, the stacked autoencoder is proposed; the structure of it is shown in Figure 2. It can be seen that the outputs of one encoder are taken as the inputs of the

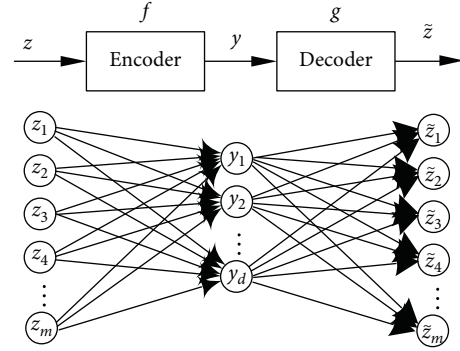


FIGURE 1: Basic structure of autoencoders.

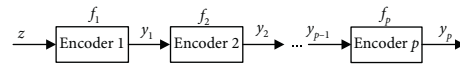


FIGURE 2: Structure of stacked autoencoders.

next encoder. By this way, several encoders are stacked together to form a multilayer autoencoder. The features of original data are abstracted layer by layer. The stacked autoencoder is trained by the layer-wise unsupervised pretraining method. The encoder 1 is trained using the original data  $z$  by (14). The output of encoder 1  $y_1$  is taken as the input for training encoder 2. This process continues until the last encoder is trained. The output of each encoder is less than the former one. In the last, a softmax layer is trained by supervised learning using the output of the last encoder as input. The softmax layer function maps input scalars to a probability distribution; the values of it range from 0 to 1. The softmax layer is always used as the output layer for the classification problem. The probability function of the softmax layer is

$$\phi(s) = \frac{e^{s_l}}{\sum_{c=1}^C e^{s_c}}, \quad l = 1, 2, \dots, C, \quad (15)$$

where  $\phi$  is the probability function of the softmax layer,  $s$  is the input of the softmax layer,  $s_l$  is the  $l$ th input element, and  $C$  is the total number of inputs. The sum of the softmax layer output elements is 1, and the value of each element represents the probability of the according classification.

**4.2. Framework of False Data Injection Attack Detection.** The flowchart of the proposed FDI attack detection is shown in Figure 3. After the measurement  $z_k$  is obtained, the linear state estimation should be taken first. Then, the value of the objective function is used to detect bad data. If the value exceeds the threshold, the bad data is deleted, and the state estimation is taken again, until all bad data are deleted. FDI attacks can bypass the bad data detection, so the proposed FDI attack detection is taken in the next step. If the attack is detected, the attacked measurements should be identified, which is not the research topic of this paper.

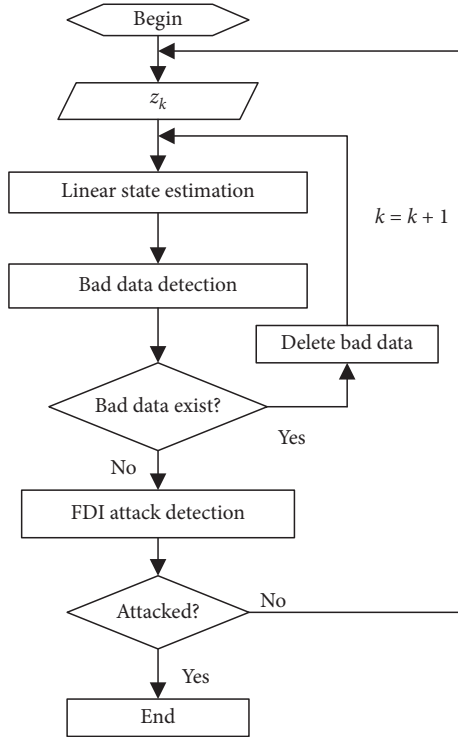


FIGURE 3: Flowchart of the FDI attack detection.

## 5. Case Studies

**5.1. Descriptions of the Testing System and Data.** To testify the validity of the proposed FDI attack detection method, the IEEE 39-bus testing system [16, 19] is used in this study. The voltage and current phasors can be measured by PMUs, which are taken as the inputs of the FDI attack detector. The power system states are obtained by power flow calculation using MATPOWER [30]. To simulate the practical operating condition, the generator and load powers are created by Monte Carlo simulations. The simulated values are true values, while the measured values are generated by adding specific distributed random numbers to the true values. The measurement errors of amplitudes and angles are 2% and 2°, respectively. Assume that the attacker chooses 5 states to be attacked, and the estimated deviation  $c$  ranges from  $-2$  to  $2$ . The attacked value  $a = Hc$  is added to measurement  $z$  to form  $z_a$ . In practice, the attacked measurements are far less than the normal measurements. In this simulation, the training set includes 5000 normal measurement samples and 500 attacked samples; the testing set includes 3000 normal samples and 300 attacked samples.

In this study, two encoders and a softmax layer are stacked to form the stacked autoencoder-based FDI attack detection framework. The overall structure as well as the input and output numbers of the stacked encoders are shown in Figure 4.

**5.2. The Performances of the Method.** To evaluate the performance of the detection method, the confusion matrix is used to analyze the detection results quantitatively, which

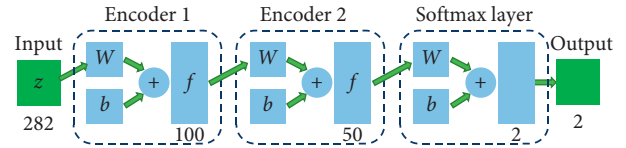


FIGURE 4: Structure of the stacked encoder.

are defined in Figure 5. The true positives (TP) means that actual attacks are correctly classified as attacks; the true negatives (TN) means that actual normal measurements are correctly classified as no attack; the false positives (FP) means that actual normal measurements are incorrectly classified as attacks; the false negatives (FN) means that actual attacks are incorrectly classified as no attacks. The following three indexes are used to evaluate the ability of the proposed method, which are defined as

$$\begin{aligned} \text{Acc} &= \frac{\text{TP} + \text{TN}}{\text{TP} + \text{TN} + \text{FP} + \text{FN}}, \\ \text{Pre} &= \frac{\text{TP}}{\text{TP} + \text{FP}}, \\ \text{Rec} &= \frac{\text{TP}}{\text{TP} + \text{FN}}, \end{aligned} \quad (16)$$

where Acc, Pre, and Rec are the accuracy, precision, and recall, respectively, Acc represents the overall performances of the method, Rec evaluates performances of the attack detection, and Pre evaluates the probability that the normal measurements are not detected as attacks.

The confusion matrix of the detection results is shown in Figure 6. It can be seen that the 300 attacks are detected out; the others are detected as normal measurements. The index values of Acc, Pre, and Rec are 100%, 100%, and 100%, respectively.

**5.3. Comparison with Other Methods.** Three other detection methods, i.e., multilayer perceptron (MLP), support vector machines (SVM), and deep neural network (DNN), are applied in the simulation. The neuron number in the hidden layer of MLP is 15. If the output of MLP is smaller than 0.5, the classification is no attack; otherwise, the classification is being attacked. For the DNN, the number of hidden layers is 4, and the unit number of each hidden layer is 150. The confusion matrixes and the methods are shown in Figure 7. It shows that the TN numbers of the three methods are 3000, meaning that all normal measurements are correctly detected. However, the 300 attacks are not detected accurately; the detection performance of which can be evaluated by the index of Rec shown in Table 1. Among the three methods, the performance of the DNN method is better than the other two methods. However, it is still worse than the proposed detection method.

**5.4. Sensitivity Analysis.** In this section, the influences of the following factors to the detection performances will be studied:



True positives	False positives
False negatives	True negatives

FIGURE 5: Confusion matrix.

TP 300	FP 0
FN 0	TN 3000

FIGURE 6: Confusion matrix of detection results.

TP 97	FP 0	TP 155	FP 0	TP 279	FP 0
FN 203	TN 3000	FN 145	TN 3000	FN 21	TN 3000
(a)	(b)	(c)			

FIGURE 7: Confusion matrixes of three different methods. (a) MLP. (b) SVM. (c) DNN.

TABLE 1: The values of indexes of three methods.

	Acc (%)	Pre (%)	Rec (%)
MLP	93.8	100.0	32.3
SVM	95.6	100.0	51.7
DNN	99.4	100.0	93.0
Stacked encoder	100	100	100

- (1) The number of neurons: the influence of neuron numbers of the encoders is studied in this section. The neuron numbers of encoder 1 and encoder 2 are set in the following cases:

- Case 1: 50 and 10
- Case 2: 80 and 40
- Case 3: 20 and 200

The confusion matrixes of detection results are shown in Figure 8. It shows that 20 attacks are not detected in Case 1, meaning that the performance of the proposed method decreases if the neuron is less. In Case 3, 16 attacks are not detected. The reason is that the neuron number of encoder 1 is 20, which cannot abstract the full features in the measurements, although the neuron number of encoder 2 is 200.

TP 280	FP 0	TP 300	FP 0	TP 284	FP 0
FN 20	TN 3000	FN 0	TN 3000	FN 16	TN 3000
(a)	(b)	(c)			

FIGURE 8: Confusion matrixes of different neurons. (a) Case 1. (b) Case 2. (c) Case 3.

TP 291	FP 0	TP 300	FP 0	TP 293	FP 0
FN 9	TN 3000	FN 0	TN 3000	FN 7	TN 3000
(a)	(b)	(c)			

FIGURE 9: Confusion matrixes of different encoder numbers. (a) Case 1. (b) Case 2. (c) Case 3.

- (2) The number of encoders: the influence of the encoder number stacked in the detection algorithm is studied. The following 3 cases are considered:

- Case 1: 1 encoder; 100 neurons
- Case 2: 3 encoders; 200, 100, and 50 neurons for each encoder
- Case 3: 3 encoders; 50, 20, and 10 neurons for each encoder

The confusion matrixes of detection results are shown in Figure 9. It can be seen that 9 attacks are not detected in Case 1 because there is only one encoder, and the features cannot be abstracted fully. Although there are 3 encoders in Case 3, 7 attacks are not detected because the neurons of each encoder are less.

- (3) Attack proportions of the training set: in practice, the attacked samples are much less than the normal samples. The influence of attack proportions in the training set is studied also. The detection framework of Figure 4 is applied, and the testing samples include 3000 normal measurements and 300 attacks. The following training sets are considered:

- Case 1: 7000 normal samples; 500 attacks
- Case 2: 9000 normal samples; 500 attacks
- Case 3: 9500 normal samples; 200 attacks

The confusion matrixes are shown in Figure 10. It shows that, with the decreasing proportion of attack samples, more attacks cannot be detected. The proposed method is sensitive to the proportion of attacks in the training set. The reason is that the features of FDI attacks are hard to be abstracted by the encoder when the attack proportion is low.



TP 300	FP 0	TP 254	FP 0	TP 229	FP 0
FN 0	TN 3000	FN 46	TN 3000	FN 71	TN 3000
(a)		(b)		(c)	

FIGURE 10: Confusion matrixes of different attack proportions. (a) Case 1. (b) Case 2. (c) Case 3.

## 6. Conclusion

In this paper, a stacked autoencoder-based FDI attack detection framework is proposed, and it is applied on the IEEE 39-bus testing system under different conditions. The confusion matrix and 3 indexes are used to evaluate the performances of the detection methods. The simulation results show that the neuron numbers of encoders influence the detection performance. If the neurons are less, the features cannot be abstracted fully, resulting in the low Rec values. The encoder number is another aspect influencing the detection performances. If the encoders are less, some attacks cannot be detected. It should be noted that if the neurons are less, the detection performances still decrease even when many encoders are stacked. The proposed detection method is sensitive to the attack sample proportion in the training set. If too few attacks are in the training sets, the features of FDI attacks cannot be abstracted fully, and the detection performance is decreased.

The FDI attack detection based on stacked autoencoders can be carried out in the following areas: the method of determining the optimal number of encoders and neurons, denoising function of the detectors, robustness to the wrong labeled samples, and detection with unbalanced data. Another interesting topic is to extend this work for detecting cyber attacks in integrated energy systems [31–36].

## Data Availability

The IEEE 39-bus system data used to support the findings of this study are included within the article.

## Conflicts of Interest

The authors declare that they have no conflicts of interest.

## Acknowledgments

This work was partly supported by the Natural Science Foundation of Jilin Province, China, under Grant no. 2020122349JC.

## References

- [1] A. G. Phadke, "Synchronized phasor measurements in power systems," *IEEE Computer Applications in Power*, vol. 6, no. 2, pp. 10–15, 1993.
- [2] Y. Li and Z. Yang, "Application of EOS-ELM with binary Jaya-based feature selection to real-time transient stability assessment using PMU data," *IEEE Access*, vol. 5, pp. 23092–23101, 2017.
- [3] Y. Xiang, L. Wang, and N. Liu, "Coordinated attacks on electric power systems in a cyber-physical environment," *Electric Power Systems Research*, vol. 149, pp. 156–168, 2017.
- [4] Y. Li, Z. Yang, G. Li, D. Zhao, and W. Tian, "Optimal scheduling of an isolated microgrid with battery storage considering load and renewable generation uncertainties," *IEEE Transactions on Industrial Electronics*, vol. 66, no. 2, pp. 1565–1575, 2019.
- [5] J. Li, B. Lu, Z. Wang, and M. Zhu, "Bi-level optimal planning model for energy storage systems in a virtual power plant," *Renewable Energy*, vol. 165, pp. 77–95, 2021.
- [6] Y. Li and K. Li, "Incorporating demand response of electric vehicles in scheduling of isolated microgrids with renewables using a bi-level programming approach," *IEEE Access*, vol. 7, pp. 116256–116266, 2019.
- [7] Y. Li, Z. Li, and L. Chen, "Dynamic state estimation of generators under cyber attacks," *IEEE Access*, vol. 7, pp. 125253–125267, 2019.
- [8] Y. Liu, P. Ning, and M. K. Reiter, "False data injection attacks against state estimation in electric power grids," *ACM Transactions on Information and System Security*, vol. 14, no. 1, pp. 1–33, 2011.
- [9] M. A. Rahman and H. Mohsenian-Rad, "False data injection attacks with incomplete information against smart power grids," in *Proceedings of the IEEE Global Communications Conference (GLOBECOM)*, pp. 3153–3158, Anaheim, CA, USA, December 2012.
- [10] K. C. Sou, H. Sandberg, and K. H. Johansson, "Electric power network security analysis via minimum cut relaxation," in *Proceedings of the 2011 50th IEEE Conference on Decision and Control and European Control Conference (CDC-ECC)*, pp. 4054–4059, Orlando, FL, USA, December 2011.
- [11] M. N. Kurt, Y. Yilmaz, and X. Wang, "Real-time detection of hybrid and stealthy cyber-attacks in smart grid," *IEEE Transactions on Information Forensics and Security*, vol. 14, no. 2, pp. 498–513, 2019.
- [12] J. Chen and A. Abur, "Placement of PMUs to enable bad data detection in state estimation," *IEEE Transactions on Power Systems*, vol. 21, no. 4, pp. 1608–1615, 2006.
- [13] T. T. Kim and H. V. Poor, "Strategic protection against data injection attacks on power grids," *IEEE Transactions on Smart Grid*, vol. 2, no. 2, pp. 326–333, 2011.
- [14] C. Liu, J. Wu, C. Long, and D. Kundur, "Reactance perturbation for detecting and identifying FDI attacks in power system state estimation," *IEEE Journal of Selected Topics in Signal Processing*, vol. 12, no. 4, pp. 763–776, 2018.
- [15] A. Ashok, M. Govindarasu, and V. Ajarapu, "Online detection of stealthy false data injection attacks in power system state estimation," *IEEE Transactions on Smart Grid*, vol. 9, no. 3, pp. 1636–1646, 2019.
- [16] B. Li, G. Xiao, R. Lu, R. Deng, and H. Bao, "On feasibility and limitations of detecting false data injection attacks on power grid state estimation using D-FACTS devices," *IEEE Transactions on Industrial Informatics*, vol. 16, no. 2, pp. 854–864, 2020.
- [17] A. S. Musleh, M. Debouza, H. M. Khalid, and A. Al-Durra, "Detection of false data injection attacks in smart grids: a real-time principle component analysis," in *Proceedings of the IECON 2019—45th Annual Conference of the IEEE Industrial Electronics Society*, pp. 2958–2963, Lisbon, Portugal, October 2019.

- [18] M. Esmalifalak, L. Liu, N. Nguyen, R. Zheng, and Z. Han, "Detecting stealthy false data injection using machine learning in smart grid," *IEEE Systems Journal*, vol. 11, no. 3, pp. 1644–1652, 2017.
- [19] M. Zhang, J. Li, Y. Li, and R. Xu, "Deep learning for short-term voltage stability assessment of power systems," *IEEE Access*, vol. 9, pp. 29711–29718, 2021.
- [20] J. J. Q. Yu, Y. Hou, and V. O. K. Li, "Online false data injection attack detection with wavelet transform and deep neural networks," *IEEE Transactions on Industrial Informatics*, vol. 14, no. 7, pp. 3271–3280, 2018.
- [21] Y. He, G. J. Mendis, and J. Wei, "Real-time detection of false data injection attacks in smart grid: a deep learning-based intelligent mechanism," *IEEE Transactions on Smart Grid*, vol. 8, no. 5, pp. 2505–2516, 2017.
- [22] Y. Lin and J. Wang, "Probabilistic deep autoencoder for power system measurement outlier detection and reconstruction," *IEEE Transactions on Smart Grid*, vol. 11, no. 2, pp. 1796–1798, 2020.
- [23] A. Majumdar, "Blind denoising autoencoder," *IEEE Transactions on Neural Networks and Learning Systems*, vol. 30, no. 1, pp. 312–317, 2019.
- [24] X. Han, Y. Zhong, and L. Zhang, "Spatial-spectral unsupervised convolutional sparse auto-encoder classifier for hyperspectral imagery," *Photogrammetric Engineering and Remote Sensing*, vol. 83, no. 3, pp. 195–206, 2017.
- [25] G. Abdi, F. Samadzadegan, and P. Reinartz, "Spectral-spatial feature learning for hyperspectral imagery classification using deep stacked sparse autoencoder," *Journal of Applied Remote Sensing*, vol. 11, no. 4, pp. 1–15, 2017.
- [26] J. Deng, Z. Zhang, E. Marchi, and B. W. Schuller, "Sparse autoencoder based feature transfer learning for speech emotion recognition," in *Proceedings of Humaine Association Conference on Affective Computing and Intelligent Interaction*, pp. 511–516, Geneva, Switzerland, September 2013.
- [27] G. Jiang, H. He, P. Xie, and Y. Tang, "Stacked multilevel-denoising autoencoders: a new representation learning approach for wind turbine gearbox fault diagnosis," *IEEE Transactions on Instrumentation and Measurement*, vol. 66, no. 9, pp. 2391–2402, 2017.
- [28] J. Yu, "Enhanced stacked denoising autoencoder-based feature learning for recognition of wafer map defects," *IEEE Transactions on Semiconductor Manufacturing*, vol. 32, no. 4, pp. 613–624, 2019.
- [29] Y. Zhang, J. Wang, and B. Chen, "Detecting false data injection attacks in smart grids: a semi-supervised deep learning approach," *IEEE Transactions on Smart Grid*, vol. 12, no. 1, pp. 623–634, 2021.
- [30] R. D. Zimmerman, C. E. Murillo-Sánchez, and R. J. Thomas, "MATPOWER: steady-state operations, planning, and analysis tools for power systems research and education," *IEEE Transactions on Power Systems*, vol. 26, no. 1, pp. 12–19, 2011.
- [31] Y. Li, C. Wang, G. Li, and C. Chen, "Optimal scheduling of integrated demand response-enabled integrated energy systems with uncertain renewable generations: a Stackelberg game approach," *Energy Conversion and Management*, vol. 235, Article ID 113996, 2021.
- [32] Y. Liu, Y. Li, H. B. Gooi et al., "Distributed robust energy management of a multimicrogrid system in the real-time energy market," *IEEE Transactions on Sustainable Energy*, vol. 10, no. 1, pp. 396–406, 2019.
- [33] Y. Li, C. Wang, G. Li, J. Wang, D. Zhao, and C. Chen, "Improving operational flexibility of integrated energy system with uncertain renewable generations considering thermal inertia of buildings," *Energy Conversion and Management*, vol. 207, Article ID 112526, 2020.
- [34] Y. Li, T. Zhao, P. Wang et al., "Optimal operation of multimicrogrids via cooperative energy and reserve scheduling," *IEEE Transactions on Industrial Informatics*, vol. 14, no. 8, pp. 3459–3468, 2018.
- [35] Y. Li, Z. Yang, D. Zhao, H. Lei, B. Cui, and S. Li, "Incorporating energy storage and user experience in isolated microgrid dispatch using a multi-objective model," *IET Renewable Power Generation*, vol. 13, no. 6, pp. 973–981, 2019.
- [36] Y. Li, Z. Han, D. Yang, and G. Li, "Coordinating flexible demand response and renewable uncertainties for scheduling of community integrated energy systems with an electric vehicle charging station: a bi-level approach," *IEEE Transactions on Sustainable Energy*, 2021.

## *Retraction*

# **Retracted: A Stochastic Rolling Horizon-Based Approach for Power Generation Expansion Planning**

### **Mathematical Problems in Engineering**

Received 13 April 2023; Accepted 13 April 2023; Published 19 April 2023

Copyright © 2023 Mathematical Problems in Engineering. This is an open access article distributed under the Creative Commons Attribution License, which permits unrestricted use, distribution, and reproduction in any medium, provided the original work is properly cited.

*Mathematical Problems in Engineering* has retracted the article titled “A Stochastic Rolling Horizon-Based Approach for Power Generation Expansion Planning” [1], as substantial overlap has been identified with a manuscript by different authors which had previously been submitted to another journal and has since been published [2].

### **References**

- [1] H. Wang, T. Wang, X. Wang, B. Li, and C. Ye, “A Stochastic Rolling Horizon-Based Approach for Power Generation Expansion Planning,” *Mathematical Problems in Engineering*, vol. 2021, Article ID 6635829, 11 pages, 2021.
- [2] E. F. Bødal, A. Botterud, M. Korpås, “Capacity Expansion Planning with Stochastic Rolling Horizon Dispatch,” *Electric Power Systems Research*, vol. 205, 2022.

## Review Article

# A Stochastic Rolling Horizon-Based Approach for Power Generation Expansion Planning

Hanyun Wang <sup>1</sup>, Tao Wang <sup>1</sup>, Xinyi Wang <sup>2</sup>, Bing Li <sup>2</sup>, and Congmin Ye <sup>2</sup>

<sup>1</sup>Huzhou Power Supply Company of SGCC, Huzhou 313000, China

<sup>2</sup>North China Electric Power University, Beijing 102206, China

Correspondence should be addressed to Xinyi Wang; [120171010324@ncepu.edu.cn](mailto:120171010324@ncepu.edu.cn)

Received 23 November 2020; Revised 29 December 2020; Accepted 6 February 2021; Published 30 June 2021

Academic Editor: Xiao-Shun Zhang

Copyright © 2021 Hanyun Wang et al. This is an open access article distributed under the Creative Commons Attribution License, which permits unrestricted use, distribution, and reproduction in any medium, provided the original work is properly cited.

Variable renewable energy sources introduce significant amounts of short-term uncertainty that should be considered when making investment decisions. In this work, we present a method for representing stochastic power system operation in day-ahead and real-time electricity markets within a capacity expansion model. We use Benders' cuts and a stochastic rolling-horizon dispatch to represent operational costs in the capacity expansion problem (CEP) and investigate different formulations for the cuts. We test the model on a two-bus case study with wind power, energy storage, and a constrained transmission line. The case study shows that cuts created from the day-ahead problem gives the lowest expected total cost for the stochastic CEP. The stochastic CEP results in 3% lower expected total cost compared to the deterministic CEP capacities evaluated under uncertain operation. The number of required stochastic iterations is efficiently reduced by introducing a deterministic lower bound, while extending the horizon of the operational problem by persistence forecasting leads to reduced operational costs.

## 1. Introduction

The increasing penetration of variable renewable energy (VRE) sources is introducing new challenges in modern power systems. Central to these challenges is the increased level of the short-term uncertainty and the need for more flexibility in operation [1, 2]. To balance supply and demand for electricity in the power system, we need a certain share of flexible resources that can reliably change their energy output in a few seconds or minutes to counteract variations in VRE electricity production [3]. The level of VRE that can be integrated into a power system in a cost-effective manner is directly dependent on the level of flexibility in the system [4].

The need for more flexibility, changes in market structures, and operational rules have been evident in countries which are integrating large amounts of VRE such as Denmark, China, Ireland, and Spain [5, 6]. As power systems are aspiring to increase the share of clean energy sources towards 100%, even more and cleaner flexible sources are needed.

Traditionally, the long-term power system capacity expansion problem (CEP) focuses on long-term uncertainties in investment costs, yearly electricity demand, and policy decisions, but neglect short-term uncertainties [7]. In fact, all kinds of uncertainties must be accurately captured and reasonably described to ensure the rationality of planning [8]. This can lead to inaccurate results as using a deterministic representation of operations in investment models overvalues fluctuating VRE [9] and undervalues flexible resources and can also lead to insufficient investments for both thermal generation [10] and transmission capacities [11]. In these types of models, short-term uncertainties from VRE are often implicitly accounted for by using deterministic reserve constraints based on forecast errors [12, 13]. Representing the short-term uncertainty explicitly in the model as a stochastic parameter is expected to give significantly better results compared to using reserve constraints [14], but there are few long-term models for the CEP that do this as it is much more computationally demanding.

The computational complexity of stochastic CEPs can be reduced by either reducing the number of scenarios

[13, 15, 16] or reducing the time dimension by using representative operational periods [17]. Reducing the time dimension from a full year to some representative periods of one to several days is a common approach and allows for more detailed operational models that include the uncertainty in wind and solar power [9, 18]. However, studies show that the temporal resolution and chronology is especially important in CEPs with large shares of VRE [19] where simple operational representations might lead to overinvestments in solar and underinvestments in wind and natural gas. Furthermore, the chronology will become more important as energy storage becomes more relevant as a flexible asset due to reduced storage costs and increasing VRE integration. Evidently, insufficient representation of short-term uncertainty, temporal resolution, and chronology can be significant factors in undervaluing flexibility and overestimating the optimal VRE levels in power systems [20].

In power system applications, rolling-horizon frameworks are extensively used in operational models and case studies that focus on short-term VRE uncertainty and flexibility, for example, to study VRE integration, for large-scale battery operation [21] and for local energy storage in proximity to VRE electricity production [22]. Models using this framework are suitable for representing the short-term uncertainty in an accurate and realistic way and can therefore capture the need for flexibility during operation.

Stochastic rolling-horizon dispatch (SRHD) models are formulated by a series of two-stage economic dispatch problems integrated in a rolling-horizon framework [23], thereby accounting for operational details such as market products, time stages, and uncertain VRE power production. SRHD within the CEP is previously used for assessing the effect of VRE on different CO<sub>2</sub>-emission policies [24]. It has also been used for assessing VRE and storage investments in microgrids, using various heuristic methods [25, 26]. To the knowledge of the authors, the work of Fortenbacher et al. (2018) is the only study where a SRHD has been integrated in the CEP using Benders' cuts [27]. The CEP model corresponds to a large-scale MILP problem, which is difficult to solve directly in mathematics, due to its heterogeneous nature in variable types and large number of decision variables involved. The Benders' cuts method is dedicated to solving large-scale MILP problems by decomposing them into a master problem and multiple subproblems. Generally, the master program is an integer problem, and subproblems are the linear programs. This reformulation makes the whole problem to be easily manageable by using iterative-based methods. In addition, through the Benders' decomposition, the lower-bound solution of the master problem may involve fewer constraints, which makes the computational complexity, and the time for solving the problem can be significantly reduced, as compared to conventional algorithms. Because of the abovementioned advantages, the Benders' cuts method can be highly suitable to be used in CEP studies, which is helpful to improve the computational efficiency of the proposed problem.

In this work, we formulate a model for the CEP with SRHD, focusing on the representation of the operational decisions in both the day-ahead and real-time markets. The market representation is an important difference compared to [27] as we model that generators commit to a schedule in the day-ahead market that can be adjusted in the real-time market. This market representation resembles the market representation used by Pineda et al. (2016), who use forecast errors and duration curves to study the impact of the short-term uncertainty on the CEP [28]. We improve on the dispatch strategy of [27] by including a perfect information deterministic model in the algorithm that gives end-of-horizon storage values and accelerate the decomposition algorithm by providing a lower bound to the operational costs. The operational model in this paper is based on the existing works in [29, 30].

Compared with the extant literatures, the main contributions of this paper are as follows:

- (a) We propose an algorithm for representing two-stage stochastic rolling-horizon dispatch in CEP using Benders' cuts, where a lower bound for the operational problem is derived from a deterministic model
- (b) We investigate different approaches for using Benders' cuts to extract operational values in the context of day-ahead and real-time electricity markets
- (c) We evaluate the impact of the short-term uncertainty and forecast horizon for operations on optimal investments in a realistic case study

The rest of the paper is organized as follows: in Section 2, we describe the investment model with the rolling-horizon operation. Section 3 presents a case study, and we present the corresponding results in Section 4, and finally, the conclusions are drawn in Section 5.

## 2. Methods

The mathematical formulation of the CEP with energy storage is shown in equations (1)–(10). Investment and operational costs are minimized as formulated in the objective function in equation (1). Operational costs consist of fuel, load shedding, and exchange costs for power traded with market nodes (system boundary). Investments in power plants and storage are limited by an upper threshold in equations (2) and (3). The sum of electricity production and curtailment is equal to the production capacity for each power plant as stated in equation (4). Equation (5) keeps track of the energy level in the storage, accounting for losses. The storage level is limited by the installed storage energy capacity in equation (6). Storage charge or discharge is limited by the storage power capacity in equation (7). The energy balance in equation (8) accounts for the balance between energy injected and extracted from the bus. Curtailment of demand may occur during shortages, but at a significant cost:



$$\min \sum_{i \in R} C_i^w w_i^{\max} + \sum_{i \in \varepsilon} (C_i^s s_i^{\max} + C_i^e e_i^{\max}) + \sum_{t \in T} \left[ \sum_{i \in P} O_i^f p_{ti} + \sum_{n \in B} O^n r_{tn} + \sum_{n \in M} O_{tn}^{ex} p_{tn}^{ex} \right], \quad (1)$$

$$w_i^{\max} \leq W_i^{\text{Pot}}, \quad \forall i \in R, \quad (2)$$

$$s_i^{\max} \leq S_i^{\text{Pot}}, e_i^{\max} \leq E_i^{\text{Pot}}, \quad \forall i \in S, \quad (3)$$

$$p_{ti} + c_{ti} = P_{ti} w_i^{\max}, \quad \forall t \in T, \forall i \in P, \quad (4)$$

$$s_{ti} = s_{(t-1)i} + \eta e_{ti}, \quad \forall t \in T, \forall i \in \varepsilon, \quad (5)$$

$$s_{ti} \leq S_i^{\max}, \quad \forall t \in T, \forall i \in \varepsilon, \quad (6)$$

$$e_{ti} \leq e_i^{\max}, \quad \forall t \in T, \forall i \in \varepsilon, \quad (7)$$

$$\sum_{j \in P_n} p_{tj} - p_{tis}^{ex} + r_{ti} + \sum_{j \in \varepsilon_n} e_{tj} = D_{tn}, \quad \forall t \in T, \forall n \in N, \quad (8)$$

$$p_{tns}^{ex} = \sum_{m \in C_n} B_{nm} (\delta_n - \delta_m), \quad \forall t \in T, \forall n \in B, \quad (9)$$

$$-T_{nm} \leq B_{nm} (\delta_n - \delta_m) \leq T_{nm}, \quad \forall t \in T, \forall n \in B, \forall m \in C_n. \quad (10)$$

Equation (9) states the nodal balance, where the net exchange with other buses equals the flow on all the lines connected to the bus. The line flow is represented by the linearized power-flow equation and is equal to the difference in the voltage angle between the buses and proportional to the susceptance of the transmission line. The power flow on the transmission lines is constrained by the transmission capacity, as shown in equation (10).

### 3. Benders' Decomposition for the Discussed Problem

A common method for solving the CEP is to decompose investments and operation into two different parts [31], a master problem and a subproblem, which is solved by iterating between them until the upper and lower bounds of the problem converge. We formulate the master problem, as shown in equations (11), (12), (2), and (3):

$$\min \sum_{i \in R} C_i^w w_i^{\max} + \sum_{i \in \varepsilon} (C_i^s s_i^{\max} + C_i^e e_i^{\max}) + \alpha, \quad (11)$$

$$\alpha \geq \alpha^k + \sum_{i \in P} \pi_i^k P_i (w_i^{\max} - W_i^k) + \sum_{i \in \varepsilon} \beta_i^k (s_i^{\max} - S_i^k) + \gamma_i^k (e_i^{\max} - E_i^k), \quad \forall k \in K, \quad (12)$$

s.t. equations (2) and (3).

In the master problem, the operational costs are estimated by  $\alpha$ , which is constrained by Benders' cuts in equation (12) [32]. For a given solution of the investments in the master problem, the subproblem becomes as stated in equations (13)–(16), in addition to equations (5) and (8)–(10). Here, the capacities are no longer variables but fixed parameters,  $W_i^k$ ,  $S_i^k$ , and  $E_i^k$ :

$$\min \sum_{t \in T} \left[ \sum_{i \in P} O_i^f p_{ti} + \sum_{n \in B} O^n r_{tn} + \sum_{n \in M} O_{tn}^{ex} p_{tn}^{ex} \right], \quad (13)$$

$$p_{ti} + c_{ti} = P_{ti} W_i^k \pi_{ti}, \quad \forall t \in T, \forall i \in P, \quad (14)$$

$$s_{ti} \leq S_i^k \beta_{ti}, \quad \forall t \in T, \forall i \in \varepsilon, \quad (15)$$

$$e_{ti} \leq E_i^k \gamma_{ti}, \quad \forall t \in T, \forall i \in \varepsilon, \quad (16)$$

s.t. equations (5) and (8)–(10).

The cuts in the master problem consist of the optimal objective value of the subproblem, the installed capacities used in the operational model for the current iteration, and the dual of the capacity constraints in equations (14), (15), and (16) summed over all times. The upper bound is the objective of the best solution found so far calculated by summing up the values from the master and subproblem according to the original objective function in equation (1). The lower bound is the best solution that can be found and is

the same as the objective of the master problem in equation (11).

#### 4. Stochastic Rolling-Horizon Dispatch

To include the short-term VRE uncertainty, we substitute the deterministic operational subproblem with a stochastic rolling-horizon dispatch (SRHD). The basic element of the SRHD is a two-stage problem which is implemented in a rolling-horizon framework as illustrated in Figure 1, where parameters are updated as new information becomes available.

In the rolling-horizon framework, we introduce day-ahead schedules for energy production and storage. In the first stage, a fixed day-ahead schedule has to be followed. In the second stage, a schedule is created (day-ahead) for the real-time operation in the following two-stage model. One day-ahead schedule is made considering a range of scenarios for VRE production and passed on to the first stage of the next instance of the two-stage model, typically the next day, in the rolling-horizon framework. Deviations from the day-ahead schedules have a cost which is representing a ‘premium-of-readiness’ for changing production close to real time [33]. This is analogous to how the electricity markets are currently organized, illustrated in Figure 1, where a day-ahead schedule is made the day before in the day-ahead market (second stage of the first two-stage model), and deviations from this plan is accounted for continuously in

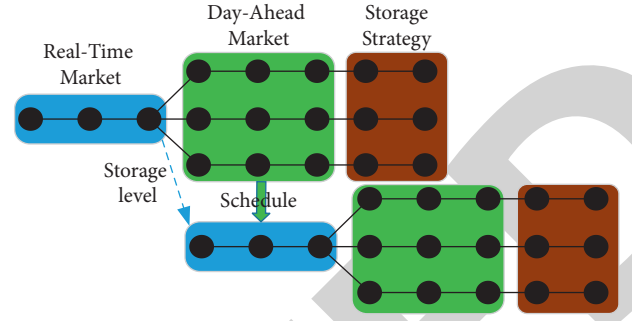


FIGURE 1: Illustration of the two-stage stochastic operation subproblem of the SRHD.

the real-time market (first stage of the second two-stage model).

The two-stage operation subproblem is formulated in equations (17)–(27). The new features compared to the deterministic model in equations (13)–(16) is the day-ahead schedules enforced by equations (19) and (20), where positive and negative deviations incur equal costs in the objective. Additionally, we have the scenario index,  $s$ , defining the two-stage structure where  $S_1$  is the realized first-stage ‘scenario’ and  $S_2$  is the set of future scenarios for the second stage. In the objective function described by equation (17), we add the value of the remaining energy in the storage at the end of the two-stage model horizon (calculated externally by the deterministic model):

$$\min \sum_{s \in S} \sum_{t \in T_s} \left[ \sum_{i \in P} O_i^f p_{tis} + \sum_{n \in B} O_{tns}^s r_{tns} + \sum_{n \in M} O_{tns}^{es} p_{tns}^{ex} + \sum_{i \in P, \varepsilon} O_{ti}^r (d_{tis}^m + d_{tis}^p) \right] - \sum_{i \in \varepsilon} V_{T^s} s_{Tis}, \quad (17)$$

$$p_{tis} + c_{tis} = P_{tis} W_i^*, \quad \forall t \in T_s, \forall i \in P, \forall s \in S, \quad (18)$$

$$p_{tis} - d_{tis}^n + d_{tis}^p = P_{ti}^{sch}, \quad \forall t \in T_s, \forall i \in P, \forall s \in S_1, \quad (19)$$

$$p_{tis} - d_{tis}^n + d_{tis}^p = P_{ti}^{sch}, \quad \forall t \in T_s, \forall i \in P, \forall s \in S_2, \quad (20)$$

$$s_{0is} = S^{prev}, \quad \forall i \in \varepsilon, \forall s \in S, \quad (21)$$

$$s_{tis} \leq S_i^*, \quad \forall t \in T_s, \forall i \in \varepsilon, \forall s \in S, \quad (22)$$

$$s_{tis} = s_{(t-1)is} + e_{tis}, \quad \forall t \in T_s, \forall i \in \varepsilon, \forall s \in S, \quad (23)$$

$$e_{tis} \leq E_i^*, \quad \forall t \in T_s, \forall i \in \varepsilon, \forall s \in S, \quad (24)$$

$$\sum_{i \in P_n} p_{tis} - p_{tns}^{ex} + r_{tns} + \sum_{i \in \varepsilon_n} e_{tis} = D_{tns}, \quad \forall t \in T_s, \forall i \in N, \forall s \in S, \quad (25)$$

$$p_{tns}^{ex} = \sum_{m \in C_n} B_{nm} (\delta_{tns} - \delta_{tns}), \quad \forall t \in T_s, \forall i \in B, \forall s \in S, \quad (26)$$

$$-T_{nm} \leq B_{nm} (\delta_{tns} - \delta_{tns}) \leq T_{nm}, \quad \forall t \in T_s, \forall i \in B, \forall m \in C_n, \forall s \in S. \quad (27)$$



## 5. Rolling-Horizon Dispatch in Capacity Expansion with Benders' Decomposition

Benders' decomposition has slow convergence if initialized with an inaccurate description of the operational costs in the master problem [34]. A good lower bound on operational costs can greatly improve the solution time of the algorithm by reducing the number of iterations. This is especially important if solving the operational problem is time consuming such as for the SRHD. The algorithm for solving the investment problem with SRHD operation is illustrated by the flowchart in Figure 2. It consists of two loops solved in sequence, first L1 and then L2. The deterministic operations' problem with perfect foresight can be considered a relaxation of the SRHD, as the problems are identical except for the constraints in (19) and (20) and the short-term uncertainty. Thus, solving the decomposed deterministic CEP (D-CEP) first in L1 creates cuts for the investment problem that are a good lower bound for the operational costs in the SRHD (L2). This significantly reduces the computational time for the algorithm as it requires fewer iterations of L2.

In L2, the deterministic operations' problem from L1 is included to reduce the impact of the limited horizon of the two-stage problem by providing end-of-horizon storage values obtained from the duals of the storage balance in equation (5). This enables the SRHD to operate storage with dynamics beyond the horizon of the VRE forecasts. The impact of the end-of-horizon storage values on real-time and day-ahead operations is low if the two-stage model horizon is sufficiently long compared to the storage types considered.

The implementation of SRHD-CEP introduces three main challenges: (1) cut generation in the context of short-term commitments and overlapping time stages, (2) end-of-horizon effects in the two-stage model, and (3) accurate representation of expected wind power production by forecasts over time. We investigate the impact of these challenges (especially 1 and 2) on the performance of the SRHD-CEP and the effect of the short-term wind power uncertainty on investments in a two-bus case study.

## 6. Case Study

We use the SRHD-CEP to find the optimal capacity expansion in a two-bus case study where local electricity demand is served by a combination of wind power, energy storage, and a transmission line, as shown in Figure 3(a). The transmission line has limited capacity and is connected to the electricity market, represented by a price series as illustrated in Figure 3(b). A combination of energy storage and wind power is needed to supply the electric load as the transmission capacity of 130 MW is not large enough to supply all the electricity (1000 GWh/year) needed for the load in the winter, as shown in Figure 3(c).

We use a technology cost scenario for 2050 for new investments [35], as shown in Table 1. In this scenario, we assume that the transmission line capacity cannot be expanded, and energy storage costs are sufficiently low to make storage an interesting alternative to transmission line upgrades. Other important parameters include losses of 5% for

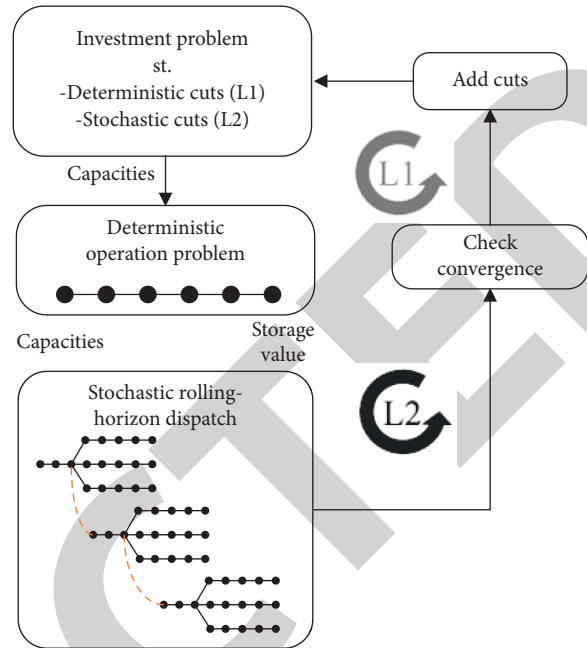


FIGURE 2: Flowchart of the solution algorithm.

both charging and discharging and a value of lost load (VOLL) of 10 000 \$/MWh.

Data series for wind and load are obtained from northern Norway where wind power is well suited to supply the electric load as the wind-load seasonal correlation is high. However, the wind power plant has significant short-term variation and uncertainty in power output. Storage can be valuable to alleviate these issues by balancing and improving security of supply. We assume that load, wind power, and energy storage are balancing their power collectively as one unit, which results in one aggregate day-ahead schedule for exchange with the market bus. Thus, the storage can be used for internal balancing that might be less costly than purchasing balancing power from the market. We assume a real-time balancing premium at 30% of the spot price for the power exchanged over the transmission line, which is higher than the current market prices but in line with expectations for future systems with high VRE shares [36].

Forecasts of the future wind power production are essential for efficient dispatch to ensure that sufficient storage levels are maintained ahead of time to avoid load shedding in deficit situations and wind power curtailment in surplus situations. Wind power scenarios are created by using historical weather forecasts and historical wind power production to create quantile forecasts for each day [37]. From the quantile forecasts, we sample 90 scenarios for each day [38], which is reduced to 30 scenarios using SCENRED2 [39].

We use this case study to investigate how to best calculate the parameters for the Benders' cuts, by selecting dual and operational costs from the different stages of the SRHD, resulting in two different cut types: (a) cuts obtained from expected (day-ahead) values; (b) cuts obtained from the average of realized (real-time) and expected values (day-ahead).

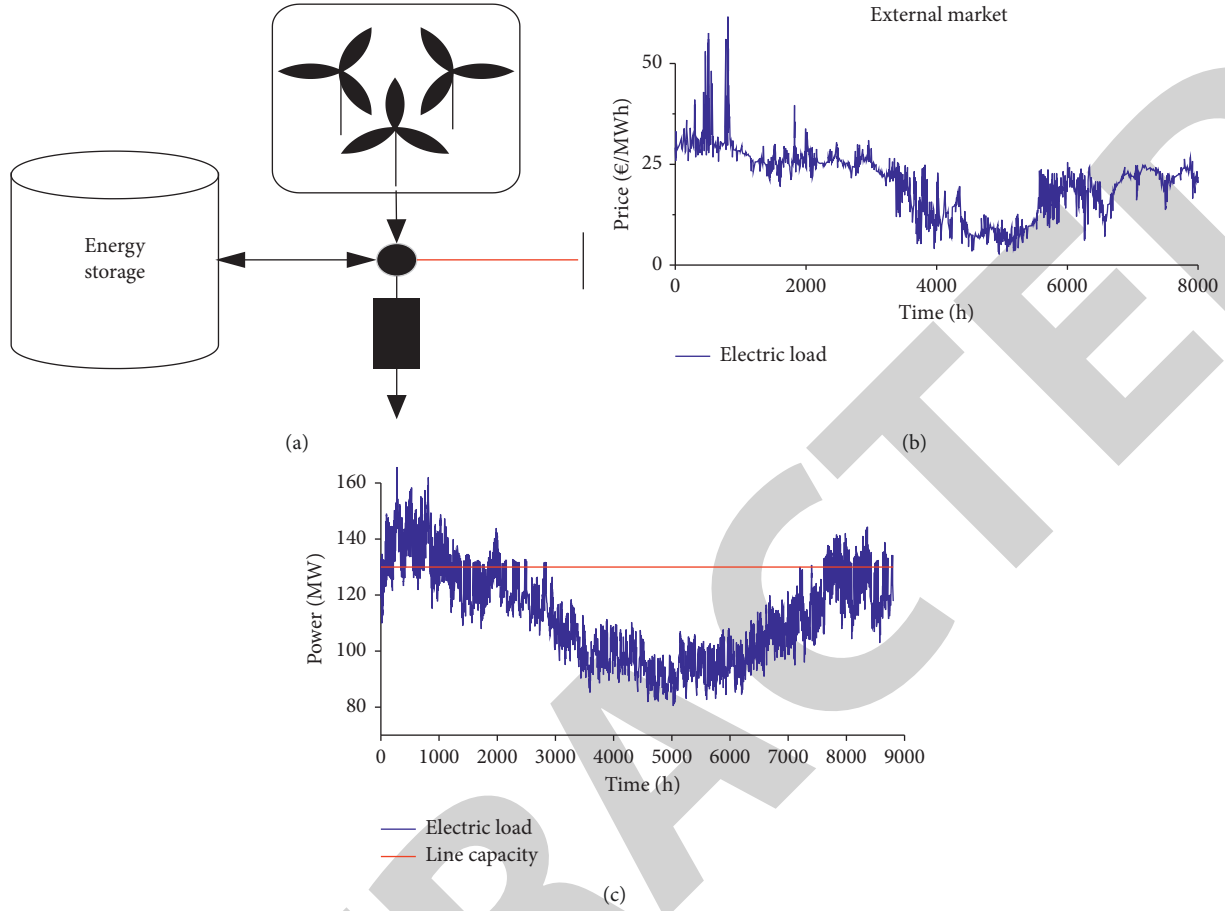


FIGURE 3: Information of the test system. (a) System structure. (b) Price series of the external market. (c) Load profile and capacity limit of the transmission line.

TABLE 1: Wind power, storage costs, and unit size.

	Investment cost (€/kW)	O&M cost (€/kW·yr)	Size (MW/unit)
Wind power	930	30	3
Storage power	250	6	1
Storage energy	80	2	10

Cut type *b* is similar to the cuts used in [27], where they generate cuts from the weighted values of the cut parameters from all the time stages. However, the market commitments used in our model will affect the dual values in the first stage. Thus, type *a* cuts are introduced to investigate the significance of these commitments on the optimal investments.

The models are implemented in Python using the PYOMO modeling framework [40] and the Gurobi solver. The simulations are performed on a shared server with 28 cores and 56 logical processors of the type Intel Xeon E5-2690 v4 at 2.6 GHz.

## 7. Results

*7.1. Impact of Uncertainty and SRHD Horizon on Investments.* We find the realistic D-CEP operating costs by running the SRHD model with the optimal capacities from the D-CEP.

The resulting total cost of the D-CEP/SRHD is compared against the SRHD-CEP solutions for the two cut types and different SRHD horizons. The pure D-CEP solution (with the deterministic operation) is used as a benchmark as it has perfect information of the future and is a lower limit for the total realized costs. The total costs are shown in Figure 4 as the percentage increase from the benchmark. The operational costs are calculated by two different metrics from the SRHD, on the left by realized costs (first stage) and on the right by expected costs (expected value of the second-stage scenarios).

It is not surprising that the D-CEP/SRHD result in the lowest total realized costs, 2.3–3.9% more than the benchmark, as the D-CEP investments are optimized with perfect information. In contrast, the two SRHD-CEP solutions result in realized total costs of 4.4–13% higher than the benchmark. However, the better metric for the operational

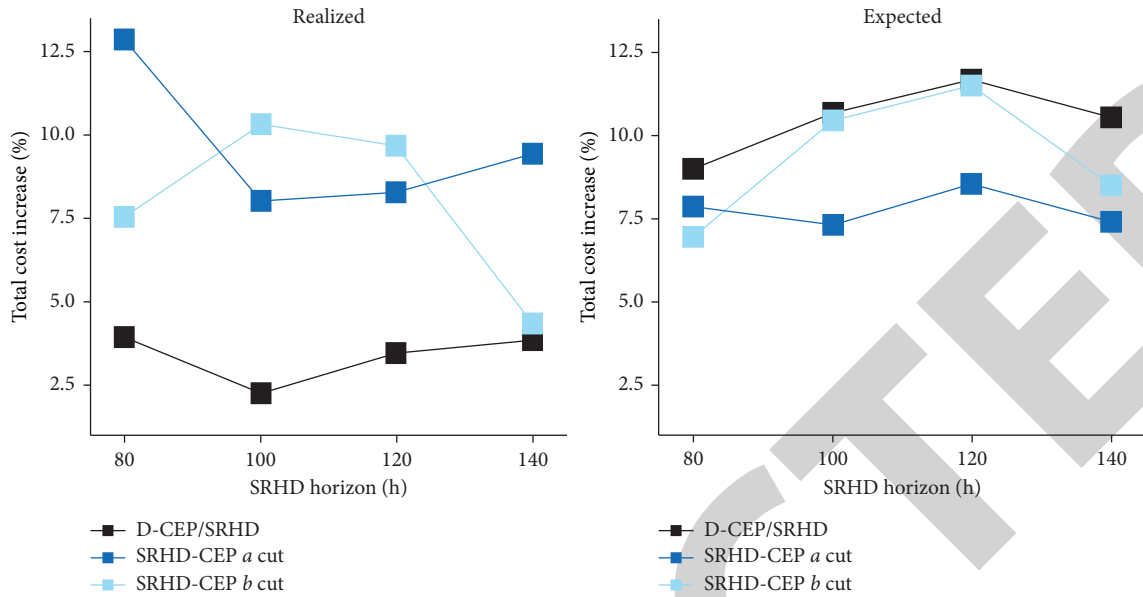


FIGURE 4: Total costs for D-CEP and the two cases of SRHD-CEP.

costs in a CEP is the expected value, as the operational costs will be close to the expectation across the 30 scenarios over time. The D-CEP/SRHD gives significantly higher expected total costs, 9–11.6% above the benchmark, because the D-CEP expansion plan results in operations close to the capacity limits and have a higher risk of load shedding. The expected cost is clearly lowest for the SRHD-CEP with *a* cuts with total costs of 7.3–8.5% relative to the benchmark. The SRHD-CEP expansion plans result in similar realized and expected costs as the capacities are higher which is better for robust operation under realistic conditions, which generally guarantees a safer operating condition.

A sufficiently long SRHD horizon is important for the storage strategy and gives a more realistic storage value in the presence of the significant wind power uncertainty than the end-of-horizon value given by the deterministic model. In Figure 4, we evaluate the impact of the SRHD horizon by adding persistence forecasts, in increments of 20 hours, at the end of the 80 hours given by the weather forecasts. Note that the persistence forecast extends each of the scenarios for the next *x* hours with the average of the last *x* hours of the original scenario. Extending the horizon to 100 hours is beneficial for the D-CEP/SRHD and the SRHD-CEP with *a* cuts as it results in a better storage strategy and lower realized costs. For the SRHD-CEP with *a* cuts, better storage handling in the first stage result in lower expected costs. Longer horizons over 100 hours are less beneficial as the persistence forecasts are not accurate, and it is better to use the end-of-horizon storage value.

The optimal capacities from the D-CEP and the two versions of the SRHD-CEP with a horizon of 100 hours are shown in Figure 5. The wind power capacity in the D-CEP is 60 MW, while the capacities are dependent on the cut type in the SRHD-CEP, 69 MW at *a* cut and 54 MW at *b* cut. The SRHD-CEP results in more storage capacity than the D-CEP due to the higher risk of load shedding when the uncertainty

is accounted for in the operation. The storage power capacity is increased from 32 MW in the D-CEP to 36 MW at *a* cut and 58 MW at *b* cut in the SRHD-CEP, whereas the energy capacity increased from 930 MWh to 1120 at *a* cut and 1340 MWh at *b* cut.

The type of cuts used in the SRHD-CEP makes a significant difference for the investments, where *a* cuts give more wind power capacity and *b* cuts give more storage energy capacity (see Figure 5). For *b* cuts, fixed day-ahead schedules lead the first stage to give the wrong investment signal which skews investments from wind power to storage as it can be used for internal balancing (no regulation penalty). The *a* cuts represent the operational costs without taking into account the first stage, instead it obtains the dual values only from the second stage where day-ahead schedules are variable. In general, *a* cuts are superior to *b* cuts because (1) fixed day-ahead schedules will not distort investments and (2) capacities should be built to minimize the expected operational cost. In this case, where the transmission grid is constrained without an option to expand the transmission capacity, the D-CEP also underinvests in wind power contrary to less constrained case studies in the literature.

**7.2. Representation of Stochastic Operation.** The cutting planes used to represent operational costs in the investment model are shown for the wind-storage energy dimension in Figure 6, where the storage power is fixed at the D-CEP solution of 32 MW. The operational costs estimated by the D-CEP are shown in grey (L1 in Figure 2), while the estimation from the SRHD *a* cuts (L2) are shown in a red-blue color gradient. Points in the red-blue plane indicate where operational costs are calculated by the SRHD-CEP. In Figure 6, the differences between the stochastic (black/solid) and deterministic (red/dotted) planes are highlighted by lines of fixed storage energy capacity. Points indicate the

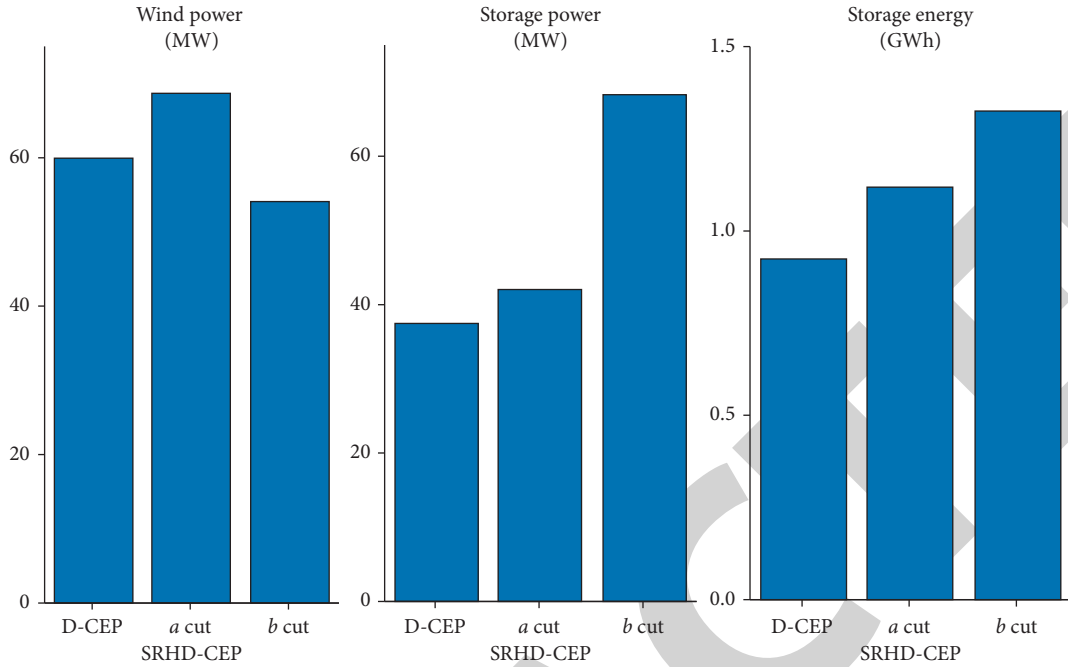


FIGURE 5: Optimal investments for D-CEP and SRHD-CEP models with L2 cuts and 100-hour SRHD horizon.

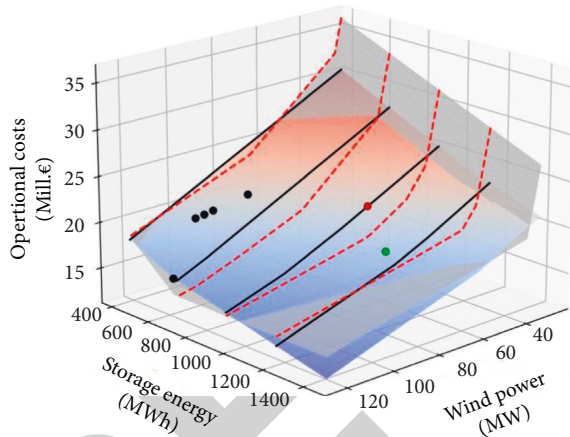


FIGURE 6: Cutting planes show the difference between the stochastic (red-blue) and deterministic (grey) operational cost as a function for the storage energy and wind power capacity.

capacities searched by the SRHD-CEP, where the D-CEP (red) and SRHD-CEP (green) solutions are highlighted.

Figure 6 shows that the operational costs are under-represented by the cuts from the D-CEP compared to SRHD-CEP. The differences between the two planes are especially large around the optimal D-CEP solution (red point), where the wind power capacity is relatively low and the storage energy capacity is high. This leads the SRHD-CEP to search for alternative solutions with more wind power and less energy storage capacity that potentially gives lower operational costs (black points). However, these solutions prove to be more costly, and the SRHD-CEP solution (green point) is found closer to the D-CEP solution but with higher wind power and storage energy capacity.

Initializing the algorithm with a lower bound from the deterministic cuts helps to significantly reduce the area that is searched when using SRHD for cut generation, resulting in only 7 additional iterations to find the SRHD-CEP solution, thereby saving significant computational time. The operational costs are higher at every point where the operational costs are calculated by the SRHD compared to deterministic operation, which supports the use of the deterministic operational model as a lower bound.

Figure 7 shows the result comparison between deterministic operation and SRHD for the first 20 days of the year using the capacities from the SRHD-CEP solution (*a* cut and 100-hour horizon). The SRHD is represented by the realized values (start of each two-stage problem is marked with a point), and day-ahead scenarios are illustrated by the 50% and 95% confidence intervals. The wind power uncertainty is significant, while realized production is the same for both deterministic operation and SRHD. On the contrary, storage operation is much more restricted in the SRHD than under deterministic operation, where the SRHD leads to slower storage charge/discharge and generally does not operate as close to the capacity limits due to the higher risk of load shedding arising from uncertain wind power production. System operation between hours 250 and 300 is defining for the system capacities as wind power production is low, while demand is high, leading to constraints on the transmission line (Figure 7(c)) and maximum discharge from the storage. In the SRHD, an extension of the horizon from 80 to 100 hours is critical for obtaining a sufficient storage level and avoiding load curtailment. Using the deterministic model to set an end-of-horizon storage value in the SRHD with an 80-hour horizon does not give the sufficient storage strategy as indicated by the realized costs in Figure 4.

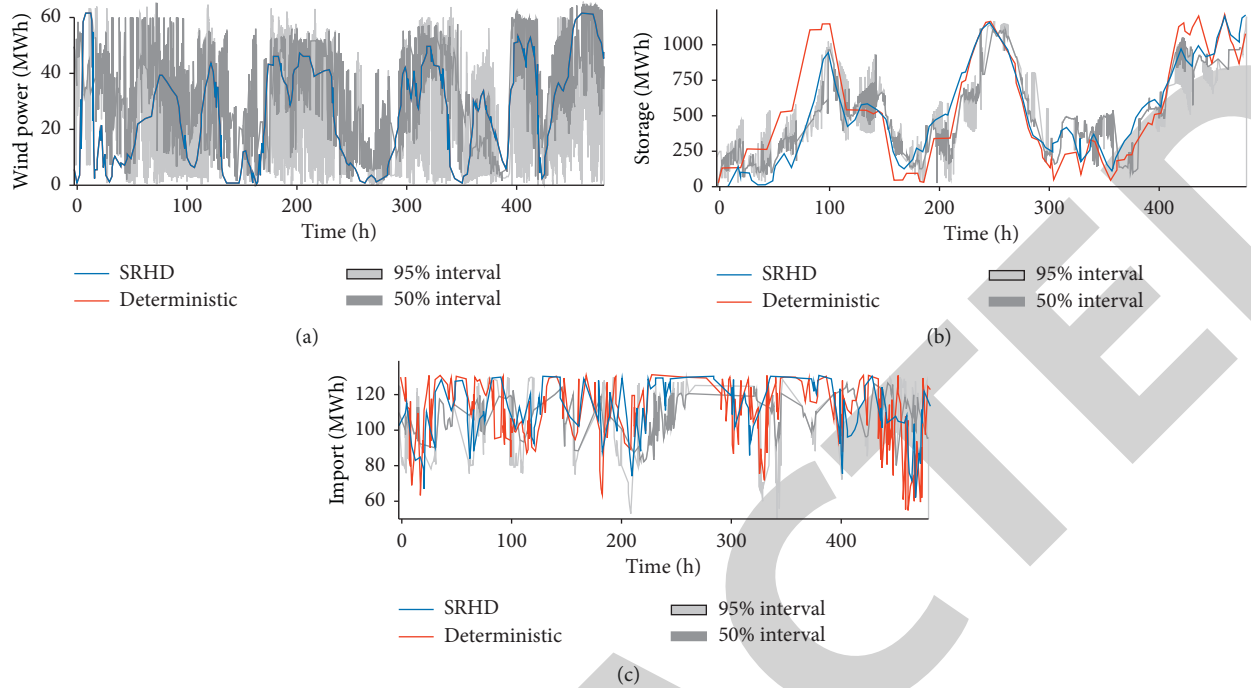


FIGURE 7: Deterministic and SRHD system operation for the first 20 days of the year and SRHD-CEP investments are represented by the following. (a) Wind power. (b) Storage level. (c) Import from the market bus.

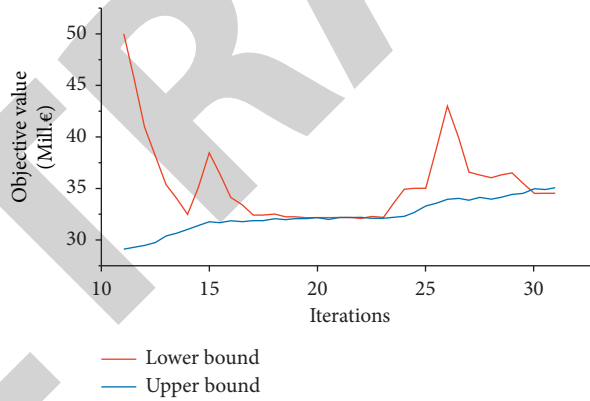


FIGURE 8: Convergence of the proposed algorithm.

TABLE 2: Computation efficiency for different SRHD horizons.

SRHD horizon (h)		80	100	120	140
Conventional Benders' decomposition method	Stochastic iterations	86	95	106	114
	Total time (hours)	14.8	18.5	24.8	30.1
Proposed method	L1 time (sec/itr)	31	31	32	30
	L2 time (min/itr)	42	57	75	94
	L2 iterations	7	8	9	11
	Total time (hours)	5.1	7.8	11.4	17.5

7.3. *Performance of the Applied Algorithm.* The convergence performance of the proposed algorithm is shown in Figure 8, which depicts the upper bounds and lower bounds of each iteration. The deterministic solution in L1 is found after 22 iterations, while an additional 7 iterations are needed to

obtain the stochastic solution in iteration 30 (iteration 23 and 31 are redundant and are only used to confirm convergence). The computational time and iterations of conventional Benders' decomposition and our proposed method have been shown in Table 2, which indicates our



algorithm spends much less time required for the stochastic iterations which ranges from 42 to 94 minutes depending on the SRHD horizon compared to the conventional Benders' cut method. A longer SRHD horizon also leads to more iterations, thus resulting in larger increase in SRHD-CEP computational times than the increased SRHD times indicate.

## 8. Conclusions

This paper proposes a new methodological framework to include SRHD with a representation of the real-time and day-ahead electricity markets in CEP, in which the impact of the short-term VRE uncertainty on optimal capacity expansion has been explicitly captured and considered. Through the simulation results from numerical studies, we showed how to link the operational model to the investment model in the presence of short-term market commitments by using Benders' cuts derived from the day-ahead values. The expected total costs are reduced by 2.5–3% compared to a deterministic investment model without stochastic representation of operation. The resulting capacities of wind power, storage power, and storage energy from the SRHD-CEP are 12.5–20% higher than in the deterministic case. The model is initialized by a lower bound generated from a deterministic operational model, which reduces the number of iterations with the more time-consuming SRHD.

In the future work, the capacity expansion with stochastic operations should be tested on a larger system with more sources of uncertainty to see if the effects of including the short-term uncertainty results in larger differences from the deterministic solution in a more complex setting. For larger systems, it could be beneficial to also decompose the two-stage operational model in order to avoid prohibitive increases in computational times.

## Nomenclature

### Indices and Sets

$i$ :	Index of power plants in set P
$j$ :	Index of energy storage in set $\epsilon$
$k$ :	Index of cuts in set K
$n$ and $m$ :	Indices of system buses in set B
$s$ :	Index of scenarios in set S
$t$ :	Index of time steps in set T.

### Parameters

$\rho_s$ :	Probability of renewable power scenario
$B_{nm}$ :	Susceptance between bus $n$ and $m$ (p.u.)
$C^{w/sl/p}$ :	Investment cost for wind ( $w$ ), storage energy ( $s$ ), or power ( $p$ ) (€/MW, €/MWh)
$D_{tn}$ :	Electricity demand (MW)
$E_i$ and $S_i$ :	Storage power and energy capacity (MW/MWh)
$O^{w/sl/p}$ :	Operational cost for fuel ( $f$ ), regulation ( $r$ ), load shedding ( $s$ ), or exchange ( $ex$ ) (€/MWh)
$P_{tis}$ :	Power profile (MW)
$T_{nm}$ :	Transmission capacity from bus $n$ to $m$ (MW)
$V_T$ :	End-of-horizon storage value (€/MWh)
$W^{Pot}$ :	VRE resource capacity (MW).

### Variables

$\alpha$ and $\alpha^k$ :	Estimated/actual operational cost (€)
$\beta_{tis}$ and $\gamma_{tis}$ :	Dual values of storage energy and power constraints
$\delta_{tms}$ :	Voltage phase angle
$\pi_{tis}$ :	Dual values of production constraints
$c_{tis}$ :	Curtailement of VRE (MW)
$d_{tis}^{-/+}$ :	Negative or positive regulation (MW)
$e_i^{max}/s_i^{max}$ :	Storage power/ energy capacity (MW/MWh)
$e_{ti}$ :	Energy from or to the energy storage (MWh)
$P_{tms}^{ex}$ :	Power exchange with other buses (MW)
$p_{tis}$ :	Power production (MW)
$r_{tms}$ :	Curtailement of load (MW)
$w_i^{max}$ :	Installed generation capacity (MW).

## Data Availability

The data used to support the findings of this study are included within this article.

## Conflicts of Interest

The authors declare that there are no conflicts of interest regarding the publication of this paper.

## Acknowledgments

This work was funded by Huzhou Power Supply Company of SGCC (Research on Theoretical Framework of Diversified and High Elastic Power Grid, SGZJHU00FZJS2000611).

## References

- [1] N. E. Koltsaklis and A. S. Dagoumas, "State-of-the-art generation expansion planning: a review," *Applied Energy*, vol. 230, no. 11, pp. 563–589, 2018.
- [2] B. Zeng, Y. Liu, F. Xu, Y. Liu, X. Sun, and X. Ye, "Optimal demand response resource exploitation for efficient accommodation of renewable energy sources in multi-energy systems considering correlated uncertainties," *Journal of Cleaner Production*, vol. 288, Article ID 125666, 2021.
- [3] E. Lannoye, D. Flynn, and M. O'Malley, "Evaluation of power system flexibility," *IEEE Transactions on Power Systems*, vol. 27, no. 2, pp. 922–931, 2012.
- [4] M. Huber, D. Dimkova, and T. Hamacher, "Integration of wind and solar power in Europe: assessment of flexibility requirements," *Energy*, vol. 69, pp. 236–246, 2014.
- [5] H. Lund and B. Mathiesen, "Energy system analysis of 100% renewable energy systems—The case of Denmark in years 2030 and 2050," *Energy*, vol. 34, no. 5, pp. 524–531, 2009.
- [6] L. Bird, D. Lew, M. Milligan et al., "Wind and Solar Energy Curtailement: A Review of International Experience," *Renewable and Sustainable Energy Reviews*, vol. 65, pp. 577–586, 2016.
- [7] S. Collins, J. P. Deane, K. Poncelet et al., "Integrating short term variations of the power system into integrated energy system models: a methodological review," *Renewable and Sustainable Energy Reviews*, vol. 76, pp. 839–856, 2017.
- [8] L. V. Pérez, G. R. Bossio, D. Moitre et al., "Optimization of power management in an hybrid electric vehicle using dynamic programming," *Mathematics & Computers in Simulation*, vol. 73, no. 1-4, pp. 244–254, 2014.

## Research Article

# Identification of Permanent Faults and Disturbance Induced by Deicing Based on Permutation Entropy for the Large-Scale Clean Energy Transmission in Winter

Yunlong Wang , Tiejun Tang, Xiang Ju, and Dingding Hong

Kunming Branch of EVC CSG, Kunming 650000, China

Correspondence should be addressed to Yunlong Wang; 041603@ymu.edu.cn

Received 6 May 2021; Revised 24 May 2021; Accepted 1 June 2021; Published 21 June 2021

Academic Editor: Bo Yang

Copyright © 2021 Yunlong Wang et al. This is an open access article distributed under the Creative Commons Attribution License, which permits unrestricted use, distribution, and reproduction in any medium, provided the original work is properly cited.

Ice shedding may induce isolated ground wires' temporary grounding, which can cause electric quantities of direct current (DC) deicing devices to fluctuate. Hence, the disturbance of ice shedding is able to trigger the protective relay frequently and unnecessarily, which adversely affects the deicing process. Due to the randomness of ice shedding, the grounding resistance varies quickly; thus, the disturbance in poles of deicing devices can be detected multiple times in a short time. Moreover, the permanent fault requires steady arc plasma because of the low output voltage and current of deicing devices, which cannot bring out multiple-time disturbances in the poles. This paper proposes the identification of permanent faults and disturbance induced by deicing based on the permutation entropy, which is verified by a large number of simulations.

## 1. Introduction

The ground wire is usually applied for the lightning shield and communication, which transmits little energy. Therefore, the cold rain in the plateau may induce ice freezing along the ground wire. If there is no operation to melt or eliminate ice along the ground wire, ice may be too heavy, which exceeds the affordability of ground wires. Actually, the tower destruction caused by heavy ice is the severest problem in the extreme weather in winter. In order to decrease the adverse effect of the ice freezing in ground wires, the deicing device is widely equipped in China.

In the process of deicing, melting ice drops from the ground wire. Melting ice can significantly reduce the isolation between the ground wire and transmission lines; hence, the discharge may occur if transmission lines are still transmitting the energy. The swing of transmission lines induced by ice melting is analyzed in the experiment environment in [1–5]. Zhuang et al. and Nie et al. [6, 7] applied a trend prediction model for the ice freezing and development of deicing based on the micrometeorology monitor. The cause and the process of deicing faults are studied in [8–20], and the reinforcement of isolators of transmission lines is proposed.

The filter is usually unset for the DC deicing device, so there are a large number of high-frequency harmonics in the output voltage. Furthermore, the disturbance induced by deicing cannot be detected by time-frequency domain methods, e.g., the wavelet and the short-window Fourier transformation. This paper analyzes the difference of circuits between the disturbance and the fault induced by deicing, and the permutation entropy is employed to obtain the trend of the waveform. At last, the variance is utilized to identify the disturbance and the fault by weighing the complexity of permutation waveforms.

## 2. Permutation Entropy Identification Method for Deicing Disturbance and Fault of the Ice-Melting Line

**2.1. Permutation Entropy Algorithm.** Permutation entropy is a numerical calculation method to estimate the dynamic mutation and stochastic time series. It can quantitatively evaluate the random noise contained in the time series and detect the sudden change which is different from the noise. It can obtain a higher resolution, the output results of its



calculation are clear, and the prominent information can be intuitively identified [21, 22].

Let a time series be  $X(i)$ ,  $i = 1, 2, 3, \dots, n$ ; then, the time series is reconstructed in the phase space, and the resulting matrix is

$$Z = \begin{bmatrix} x(1) & x(1+t) & \cdots & x(1+(d-1)t) \\ x(2) & x(2+t) & \cdots & x(2+(d-1)t) \\ \vdots & \vdots & \ddots & \vdots \\ x(k) & x(k+t) & \cdots & x(k+(d-1)t) \end{bmatrix}. \quad (1)$$

In the formula,  $j = 1, 2, \dots, k$ ,  $k$  is the number of rows in the matrix,  $d$  is the embedded digit capacity,  $t$  is the delay time, and  $k = n - (d-1)t$ . Every row  $\{x(j), x(j+t), \dots, x(j+(d-1)t)\}$  in the matrix can be regarded as a reconstructed component, and there are a total of  $k$  reconstructed components. The elements of each reconstructed component are arranged in the ascending order according to their numerical size;  $j_1, j_2, \dots, j_d$  denote the index of the column of each element in the reconstructed component; that is,

$$x(i + (j_1 - 1)t) \leq x(i + (j_2 - 1)t) \leq \cdots \leq x(i + (j_d - 1)t). \quad (2)$$

If there are equal values in the reconstructed components, which are

$$x(i + (j_1 - 1)t) = x(i + (j_2 - 1)t), \quad (3)$$

at this time, they are sorted according to the subscript  $i$  of  $j_i$ . For each row of the matrix reconstructed by any time series  $X(i)$ , a group of symbol sequences can be obtained:

$$S(l) = (j_1, j_2, \dots, j_d). \quad (4)$$

In the formula,  $l = 1, 2, \dots, k$ , and  $k \leq d!$ ,  $d$ -dimensional phase space maps different symbol sequences  $(j_1, j_2, \dots, j_d)$ , and there are  $d!$  kinds. The symbol sequence  $S(l)$  is one of these permutations. If the probability of  $k$  different symbol sequences appearing is  $P_1, P_2, \dots, P_k$ , the permutation entropy can be defined as

$$H_p(d) = - \sum_{j=1}^k P_j \ln P_j. \quad (5)$$

Normalize  $H_p(d)$ , and the results are as follows:

$$0 \leq H_p = \frac{H_p}{\ln(d!)} \leq 1. \quad (6)$$

The magnitude of the  $H_p$  value indicates the randomness of the time series  $X(i)$ . The larger the  $H_p$  value is, the more complex and random the time series will be; the smaller the  $H_p$  value is, the more orderly and regular the time series will be. Besides, the  $H_p$  waveform can be used to reflect the mutation degree of time series  $X(i)$ .

*2.2. Variance Analysis of the Permutation Entropy Waveform of the Output DC Voltage of the Ice-Melting System.* Variance is often used to measure the degree of deviation between a random variable and its mathematical expectations,

and the variance calculation can be used to further verify the degree of randomness, dispersion, and mutation of the DC voltage permutation entropy waveform. Assuming that  $X$  is a discrete random variable, the calculation formula of variance of the discrete random variable is as follows:

$$D(X) = E((X - E(X))^2) = E(X^2) - E^2(X). \quad (7)$$

In the formula,  $E(X)$  is the expected value;  $X$  is the value of the variable. The larger the variance is, the greater the fluctuation of the data is and the more unstable and discrete it is. The smaller the variance is, the smaller the fluctuation of the data is and the more stable it is. In the ice-melting process of the ice-melting device, the variance of the DC voltage permutation entropy obtained when the negative pole of the deicing line has a disturbance and a permanent fault is calculated, and the results can be characterized such that, in the process of disturbance, the overall voltage fluctuation range is large and its variance is large, while in the case of permanent fault, the overall voltage variation law tends to be stable, the fluctuation is small, and the variance is small. According to this characteristic, permanent faults and disturbances can be identified. At present, the protection delay of DC melting ice can reach hundreds of milliseconds, so it takes a long time to identify the disturbance and permanent fault in the process of DC melting ice.

The fault type can be confirmed by the following criteria:

$$\begin{cases} D(X) \geq D_{th}, & \text{disturbance,} \\ D(X) < D_{th}, & \text{fault.} \end{cases} \quad (8)$$

In this formula,  $D_{th}$  is the variance threshold.

### 3. Simulation Modeling

Taking the DC ice-melting system of Kunbei Converter Station as an example, a simulation model is built in PSCAD/EMTDC. The overall structure is shown in Figure 1, and the parameters of relevant components are shown in Table 1 [23–25].

The 12-pulse converter consists of two six-pulse three-phase bridge fully controlled rectifiers. For one of the three-phase bridge fully controlled rectifiers, the structure is shown in Figure 2. There are six thyristors in total. The top three thyristors are the common cathode group, and the bottom three thyristors are the common anode group. Two thyristors need to conduct at the same time at each time, one in the common cathode group and the other in the common anode group, and cannot be in the same phase. The pulses of six thyristors conduct in the order of 1~6 as shown in Figure 2, and the trigger phase difference is  $60^\circ$ . The output voltage of each cycle has 6 pulsations, and the waveform of each pulsation is the same, so it is a 6-pulse rectifier circuit. The 12-pulse converter valve is also the 12-pulse rectifier circuit.

### 4. Simulation Cases

*4.1. Disturbance in the Ice-Melting Line.* Set up that when the disturbance occurs, the short-circuit fault is located at 20 km from the rectifying device to the negative ice-melting line. A

TABLE 1: Parameters of each element of the ice-melting system of the converter station.

Element	Parameter
AC power supply	500 kV
Step-down transformer	500 kV/38.5 kV
AC filter	20 MVar
Three-winding converter transformer	35 kV/15 kV/15 kV
Rated current of the 12-pulse converter valve	4.5 kA
Rated voltage of the 12-pulse converter valve	20 kV
Smoothing reactor	0.025 H
Length of the ground wire	70 km
Unit length resistance of the ground wire: $R$	0.2 $\Omega$
Range of the resistance of the disturbance	0~1000 $\Omega$

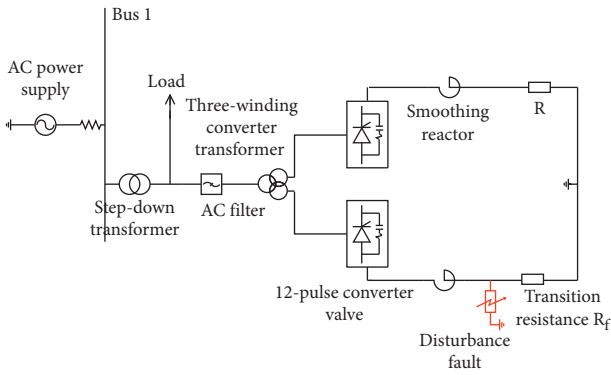


FIGURE 1: Overall structure diagram of the ice-melting system.

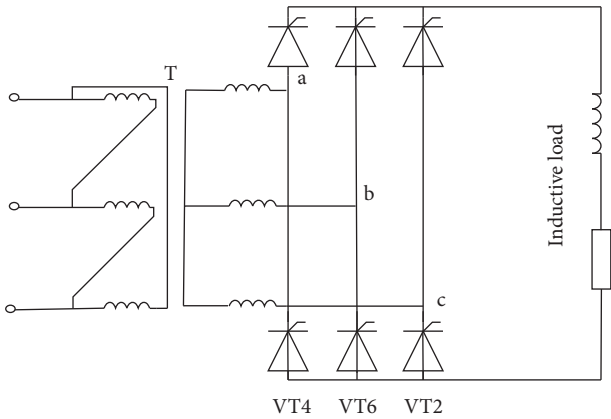


FIGURE 2: Three-phase bridge fully controlled rectifier circuit.

set of deicing circuit disturbance transition resistances varying with thawing time is randomly set, and the corresponding ice-melting voltage waveform can be obtained, as shown in Figure 3. Permutation entropy is calculated for the negative poles of the perturbation, and the results are shown in Figure 4.

By analyzing the graphics and simulation results, one can get the following: in the process of ice melting, disturbance may occur when the line deicing, resulting in a short-time grounding short circuit. However, the change of the resistance value caused by deicing will lead to many sudden changes of ice-melting voltage in a short time. In Figure 3, set in the

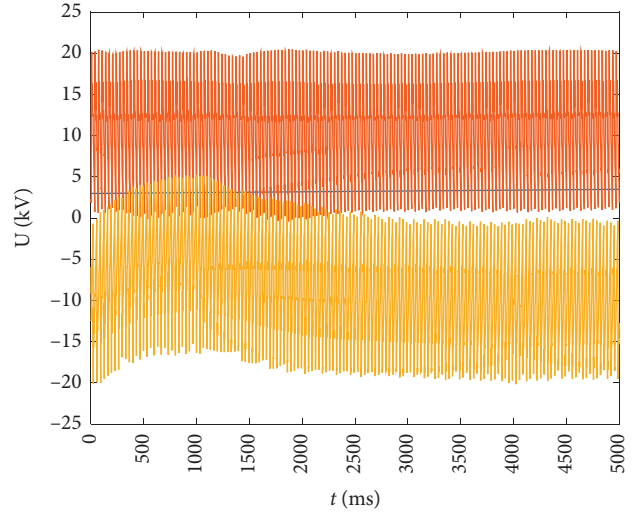


FIGURE 3: Ice-melting voltage waveform of the random disturbance fault.

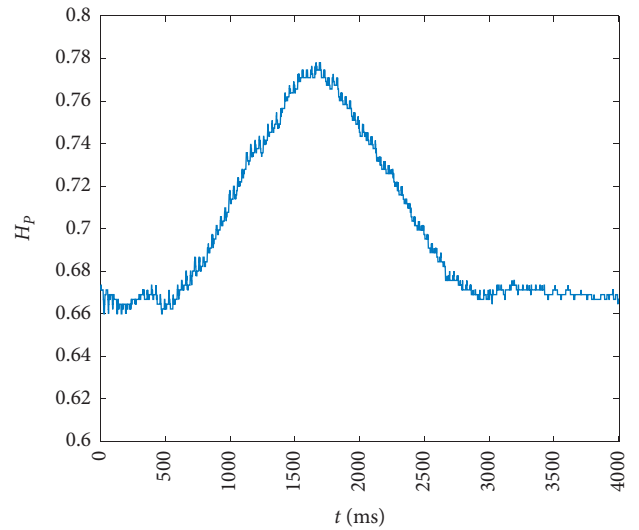


FIGURE 4: Permutation entropy waveform of thawing voltage for random disturbance faults.

negative pole due to the short-circuit fault, so the negative ice-melting voltage is particularly obvious, the change of the positive ice-melting voltage is relatively small, and it can be approximately ignored. There are a lot of high-frequency mutations in the output voltage of the DC ice-melting device due to harmonic influence; therefore, it is difficult to extract the disturbance directly from the waveform. However, disturbances can be easily detected from harmonics by using permutation entropy. The waveform variance calculated in Figure 4 is 0.014 according to equation (7).

4.2. *Permanent Failure of the Ice-Melting Line.* Set up that the permanent fault is located 5 km away from the negative pole of the ice-melting device, and the resulting ice-melting voltage waveform is shown in Figure 5. The permutation

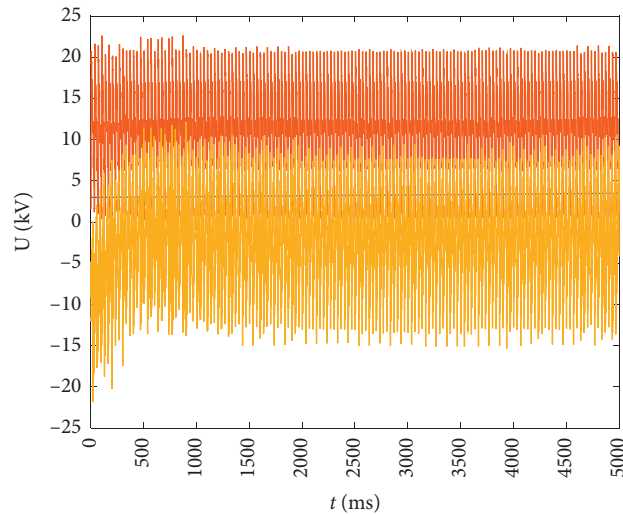


FIGURE 5: Ice-melting voltage waveform for permanent failure at 5 km.

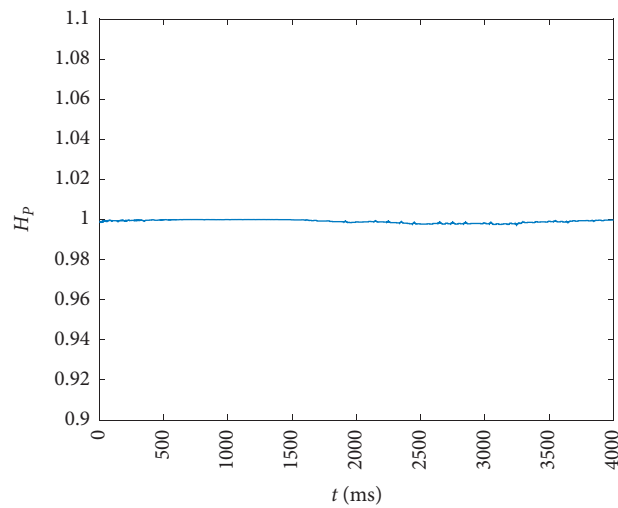


FIGURE 6: Permutation entropy waveform of thawing voltage for the permanent fault at 5 km.

TABLE 2: Permanent failure of the ice-melting line.

Type	Fault distance (km)	Positive and negative poles	Variance
Disturbance	10	Negative	0.013
Disturbance	25	Positive	0.032
Disturbance	30	Negative	0.028
Disturbance	45	Positive	0.021
Disturbance	50	Negative	0.061
Disturbance	65	Positive	0.036
Fault	15	Negative	$1.7129 \times 10^{-6}$
Fault	20	Positive	$3.2447 \times 10^{-6}$
Fault	35	Negative	$1.3610 \times 10^{-4}$
Fault	40	Positive	$6.5241 \times 10^{-4}$
Fault	55	Negative	$1.4890 \times 10^{-5}$
Fault	60	Positive	$7.0781 \times 10^{-5}$

entropy waveform obtained by calculating the fault pole voltage is shown in Figure 6.

When a permanent fault occurs, the transition resistance at the fault point remains constant. The output voltage of the DC ice-melting device is relatively stable, which does not contain the abrupt change outside the harmonic wave. Though its permutation entropy value is large, the value is quite stable compared with the perturbation. The variance calculated according to equation (7) is  $6.13 \times 10^{-4}$ , which is quite small compared with the disturbance.

In the simulation system shown in Figure 1, set up a variety of faults and disturbances, and then test them. The results are shown in Table 2.

By analyzing the results, the following can be obtained: after the permanent failure of the ice-melting line, the voltage fluctuation is very small, which is greatly different from the disturbance, and the variance of its permutation entropy is stable and less than 0.01. However, due to the influence of random transition resistance, the output voltage of the DC ice-melting device will change many times under the disturbance condition, and its variance value of permutation entropy is large and easy to distinguish from permanent failures.

## 5. Conclusion

- (1) When a deicing disturbance occurs, the voltage waveform of the DC ice-melting device will fluctuate many times, and such voltage fluctuations will not occur for permanent faults due to the stability of the fault point.
- (2) Without the suppression of the DC filter, the output voltage of the DC deicing device contains a large number of high-order harmonics, so it is difficult to accurately find the voltage fluctuation caused by disturbance or fault using traditional time-frequency analysis methods.
- (3) Through permutation entropy calculation, the voltage fluctuation caused by disturbance and permanent fault can be accurately extracted. Through the variance estimation of permutation entropy calculation results, disturbance and permanent fault can be accurately identified.

## Data Availability

All the data supporting the results of our study are available within the manuscript.

## Conflicts of Interest

The authors declare no conflicts of interest.

## Acknowledgments

This work was supported by the China Southern Power Grid Project (no. 0109002021030103SJ00002).

## References

- [1] W. Hao, S. Peng, and J. Lu, "Research on DC ice-melting technologies for 500 kV AC transmission lines," in *Proceedings of the 2015 5th International Conference on Electric Utility Deregulation and Restructuring and Power Technologies (DRPT)*, pp. 1663–1666, Changsha, China, November 2015.
- [2] X. Jiang, S. Fan, Z. Zhang, C. Sun, and L. Shu, "Simulation and experimental investigation of DC ice-melting process on an iced conductor," *IEEE Transactions on Power Delivery*, vol. 25, no. 2, pp. 919–929, 2010.
- [3] G. He, Q. Hu, L. Shu et al., "Impact of icing severity on corona performance of glaze ice-covered conductor," *IEEE Transactions on Dielectrics and Electrical Insulation*, vol. 24, no. 5, pp. 2952–2959, 2017.
- [4] L. E. Kollar, M. Farzaneh, and P. Van Dyke, "Modeling ice shedding propagation on transmission lines with or without interphase spacers," *IEEE Transactions on Power Delivery*, vol. 28, no. 1, pp. 261–267, 2013.
- [5] M. Yan, Z. Zhou, J. Wen et al., "Risk assessment method of power grid icing disaster based on short-term icing prediction," *Automation of Electric Power Systems*, vol. 40, no. 21, pp. 168–175, 2016.
- [6] W. Zhuang, C. Qi, J. Wang et al., "Dynamic ice process estimation model of transmission line based on micrometeorological monitoring," *Power System Protection and Control*, vol. 47, no. 14, pp. 87–94, 2019.
- [7] S. Nie, G. Qu, H. Ye, and X. Jiang, "On-line monitoring system for icing state of overhead transmission line," in *Proceedings of the 2012 Power Engineering and Automation Conference*, pp. 1–5, Bali, Indonesia, September 2012.
- [8] F. Jafarishadeh, F. Mohammadi, and M. Sahraei-Ardakani, "Preventive dispatch for transmission de-icing," *IEEE Transactions on Power Systems*, vol. 35, no. 5, pp. 4104–4107, 2020.
- [9] L. Shunxin, G. Guangsong, Y. Lichao, and Z. Songwei, "Research on conductor icing of overhead transmission lines," in *Proceedings of the 2011 International Conference on Consumer Electronics, Communications and Networks (CECNet)*, pp. 606–609, Xianning, China, April 2011.
- [10] Z. Wang, S. He, Q. Li et al., "A full-scale experimental validation of electromagnetic time reversal applied to locate disturbances in overhead power distribution lines," *IEEE Transactions on Electromagnetic Compatibility*, vol. 60, no. 5, pp. 1562–1570, 2018.
- [11] F. Cui, X. Liu, S. Zhang, A. Zhou, and B. Huo, "The impact of interphase spacers on galloping control of three-phase iced eight-bundled transmission lines: an experimental study," *IEEE Transactions on Power Delivery*, vol. 36, no. 1, pp. 371–382, 2021.
- [12] S. Xiong, Y. Liu, J. Fang, J. Dai, L. Luo, and X. Jiang, "Incipient fault identification in power distribution systems via human-level concept learning," *IEEE Transactions on Smart Grid*, vol. 11, no. 6, pp. 5239–5248, 2020.
- [13] G. Huang, E. F. Fukushima, J. She, C. Zhang, and J. He, "Estimation of sensor faults and unknown disturbance in current measurement circuits for PMSM drive system," *Measurement*, vol. 137, pp. 580–587, 2019.
- [14] M. Parsi and P. A. Crossley, "Optimized time for travelling wave fault locators in the presence of different disturbances based on real-world fault data," *IEEE Open Access Journal of Power and Energy*, vol. 8, pp. 138–146, 2021.
- [15] F. Zhen, M. Site, L. Bo et al., "Design method of modular multilevel real-time on-line anti-icing and ice-melting

- equipment based on self-ice-melting conductors,” in *Proceedings of the 2019 IEEE 3rd Conference on Energy Internet and Energy System Integration (EI2)*, pp. 877–882, Changsha, China, November 2019.
- [16] Z. Ye, “The application analysis of ice-melting technical measures for OPGW,” in *Proceedings of the 2018 2nd IEEE Conference on Energy Internet and Energy System Integration (EI2)*, pp. 1–6, Beijing, China, October 2018.
- [17] F. Bin, Z. Lixing, and T. Zhe, “The study on factors influencing the ice-melting performance of transmission line,” in *Proceedings of the 2013 Fourth International Conference on Intelligent Systems Design and Engineering Applications*, pp. 710–713, Zhangjiajie, China, November 2013.
- [18] C. Wang, J. Wen, S. Li, X. Ma, and J. Wang, “Design on DC de-icing schemes for high voltage transmission line,” in *Proceedings of the 2010 5th International Conference on Critical Infrastructure (CRIS)*, pp. 1–5, Beijing, China, September 2010.
- [19] H. Yang and Y. Chen, “Analysis of line deicing jump fault,” *Transactions of China Electrotechnical Society*, vol. 10, pp. 102–103, 2017.
- [20] B. Niu, C. Wang, and W. Liang, “Application research on anti-deicing jumping fault measures of 220 kV double circuit line with the same tower,” *Shanxi Electric Power*, vol. 4, pp. 46–48, 2020.
- [21] H. Zhang and S. He, “Analysis and comparison of permutation entropy, approximate entropy and sample entropy,” in *Proceedings of the 2018 International Symposium on Computer, Consumer and Control (IS3C)*, pp. 209–212, Taichung, Taiwan, December 2018.
- [22] A. Dávalos, M. Jabloun, P. Ravier, and O. Buttelli, “Theoretical study of multiscale permutation entropy on finite-length fractional Gaussian noise,” in *Proceedings of the 2018 26th European Signal Processing Conference (EUSIPCO)*, pp. 1087–1091, Rome, Italy, September 2018.
- [23] H. Zhang, L. Wang, and S. He, “The comparison of several kinds of permutation entropy,” in *Proceedings of the 2018 International Conference on Intelligent Transportation, Big Data & Smart City (ICITBS)*, pp. 432–435, Xiamen, China, January 2018.
- [24] X. Chen, Z. Yang, and W. Lou, “Fault diagnosis of rolling bearing based on the permutation entropy of VMD and decision tree,” in *Proceedings of the 2019 3rd International Conference on Electronic Information Technology and Computer Engineering (EITCE)*, pp. 1911–1915, Xiamen, China, October 2019.
- [25] P. Sun, S. Chen, and S. Zhang, “The study of DC melting ice for overhead ground wire,” in *Proceedings of the 2011 International Conference on Electronics, Communications and Control (ICECC)*, pp. 2960–2963, Ningbo, China, September 2011.



## Research Article

# Neutral-Point Potential Balance Control Strategy on Three-Level Active Power Filters

Fei Li , Na Geng , Guifeng Wang , Chunjie Li , Zhan Liu , and Zhenglong Xia 

*School of Electrical Engineering and Automation, Jiangsu Normal University, Xuzhou 221116, China*

Correspondence should be addressed to Na Geng; gengna@126.com

Received 13 March 2021; Revised 7 May 2021; Accepted 2 June 2021; Published 15 June 2021

Academic Editor: Xiao-Shun Zhang

Copyright © 2021 Fei Li et al. This is an open access article distributed under the Creative Commons Attribution License, which permits unrestricted use, distribution, and reproduction in any medium, provided the original work is properly cited.

This paper presents a simplified strategy in neutral-point (NP) potential balance of the neutral-point-clamped (NPC) three-level three-wire active power filter (APF). By introducing a simplified carrier-based pulse width modulation (CB-PWM) strategy and analysing the occurrence mechanism of NP potential unbalance, we proposed a NP potential balancing control strategy based on the simplified strategy. With this strategy, the NP current in a sampling period can be calculated through the detection of compensating current of APF. The three phase's duration time of reference voltage can also be computed through detecting the voltage fluctuation of upper and lower capacitors accurately, according to the law of charge conservation. Experiment results show that this proposed approach with simplified computation can effectively achieve NP potential balance.

## 1. Introduction

As the power electronics technology develops fast in recent decades, much attention has been given to the study of power grid optimization [1]. The active power filter (APF) is an important device for harmonic suppression in optimizing power quality, which can compensate the dynamic reactive power and harmonic distortion on the frequency and amplitude in real time [2]. In medium-voltage and high-power applications, multilevel topology has been widely adopted in APF for its numerous advantages, especially the higher DC-bus voltage utilization [3].

The neutral-point-clamped (NPC) three-level converter [4–6] is one of the preferred options in high-power medium-voltage applications for its simple topology and mature control technology. However, the neutral-point (NP) potential unbalance still remains as a major limitation.

Therefore, various modulation strategies have been proposed to solve the problem of NP potential unbalancing in NPC converters. These proposals can be classified into two categories according to their PWM modulation strategies [7]. The first category is space vector PWM (SVPWM) strategy [8–16], including nearest three space vector pulse width modulation (NTSVPWM) and virtual space vector pulse width modulation (VSVPWM). These strategies

allocate the duration time of small vector to balance the NP potential. The second category adopts the carrier-based PWM [17–20] which injects zero-sequence voltage in three-phase reference voltage.

The balancing method presented in [13, 14] was based on the opposite effects of a pair of small vectors on neutral-point potential under the SVPWM algorithm. The neutral-point potential is balanced by selecting the positive or negative short vectors in a switching period. Such a method rearranges the time distribution of the short vectors and changes the switching sequence. Thus, the balance of neutral-point voltage is achieved but with prolonged switching transitions due to its complicated and intensive control algorithms.

In [17–20], researchers proposed a strategy that injected zero-sequence voltage in three-phase reference voltage based on carrier-based PWM. However, the NP potential balancing of this strategy requires too complex calculation of zero-sequence voltage. The NP potential control algorithm based on SVPWM was applied in the three-level shunt APF system in [21], which, however, was only simulated in modelling but not verified with experiments.

The present research, aiming to optimize the NP potential balancing, introduces a novel simplified CB-PWM strategy with NP potential balance control to the three-level

three-wire APF system. Compared to the traditional CB-PWM, this strategy is more simplified and can significantly reduce the execution time, compensate the harmonic current, and effectively solve the NP potential offset problem. The effectiveness of this novel control strategy is verified with experiments.

## 2. Simplified CB-PWM Strategy

**2.1. Principle of NPC Three-Level Three-Wire APF.** A structural schematic diagram of typical NPC three-level three-wire APF is shown in Figure 1. The NPC three-level converter is connected to power grid through a reactor  $L_s$ .  $C_1$  and  $C_2$  are DC-bus capacitors of three-level converter, respectively.

The control diagram of the three-level three-wire APF system is shown in Figure 2. The system consists of current loop with a PI (proportional integral) regulator, a voltage loop with a PR (proportional resonant) regulator and a NP potential balance controller, and grid voltage and load current detection. Besides, simplified CB-PWM strategy for the NPC three-level converter is adopted to generate PWM signals to drive the NPC converter.

Compared to the traditional converter system, the APF system is more complex because it involves an extra step of harmonic detecting including the low-pass filter and the current controller with the PR regulator. The precision of the compensation will be determined by the execution speed of the algorithm.

**2.2. Principle of Simplified CB-PWM Strategy.** Structural schematic diagram of NPC three-level APF is shown in Figure 1. Each phase of the converter has three switching states as P, O, and N, signifying that the output terminal voltages are  $U_{dc}$ , 0, and  $-U_{dc}$ , respectively. Table 1 presents the terminal voltage of each phase and switching states of each bridge.

The reference voltage space vector  $\vec{V}_{ref}$  is then introduced in Figure 3. It can be calculated with the terminal voltage of three phases,  $V_a$ ,  $V_b$ , and  $V_c$ :

$$\vec{V}_{ref} = \frac{2}{3} (V_a + V_b e^{j(2/3)\pi} + V_c e^{-j(2/3)\pi}). \quad (1)$$

Figure 3 shows voltage space vector diagram of the NPC three-level converter. There are 27 switching states on the three-level converter, which means it has a much larger quantity of basic vectors than the two-level converter. As to traditional SVPWM schemes, it takes over long time to select sectors (or triangle region) and calculate the space vector duration. The researchers, based on the two aspects above, propose a simplified CB-PWM strategy, which is applied in a three-level three-wire APF system to reduce the amount of computation greatly.

Figure 3 shows that all vectors are divided into 6 sectors. An easier way for selecting sectors in space voltage vectors is proposed, and the principles that it follows is shown in Table 2.

$u_{A\_ref}$ ,  $u_{B\_ref}$ , and  $u_{C\_ref}$  are reference voltages of three phases. For example, reference voltage space vector  $\vec{V}_{ref}^*$  locates in sector I ( $S=1$ ), which means  $u_{A\_ref} > 0$ ,  $u_{B\_ref} < 0$ , and  $u_{C\_ref} < 0$ , as shown in Figure 4. Reference voltage space vector  $\vec{V}_{ref}^*$  can be obtained from  $\vec{V}_1$  (including  $\vec{V}_{1P}$  and  $\vec{V}_{1N}$ ),  $\vec{V}_7$ , and  $\vec{V}_8$ .

Based on traditional voltage-second balance, it can be expressed that

$$\begin{cases} \vec{V}_{ref} \cdot T_s = \vec{V}_{1P} \cdot T_{1P} + \vec{V}_7 \cdot T_7 + \vec{V}_8 \cdot T_8 + \vec{V}_{1N} \cdot T_{1N}, \\ T_s = T_{1P} + T_7 + T_8 + T_{1N}. \end{cases} \quad (2)$$

According to simplified CB-PWM strategy, reference voltages of three phases can be obtained:

$$\begin{cases} u_{A\_ref} \cdot T_s = \int_0^{T_s} u_{AO}(t) dt, \\ u_{B\_ref} \cdot T_s = \int_0^{T_s} u_{BO}(t) dt, \\ u_{C\_ref} \cdot T_s = \int_0^{T_s} u_{CO}(t) dt. \end{cases} \quad (3)$$

Equation (3) and Figure 3 show that when  $u_{A\_ref} > 0$ , terminal voltage of phase A  $u_{AO}$  consists of  $U_{dc}$  and 0 (indicated by state P and O); when  $u_{B\_ref} < 0$ , terminal voltage of phase B  $u_{BO}$  consists of  $-U_{dc}$  and 0 (indicated by state N and O). Similarly, terminal voltage of phase C  $u_{CO}$  consists of  $-U_{dc}$  and 0 (indicated by state N and O).

Therefore, the phases' duration time could be obtained as follows:

$$\begin{cases} T_A = \frac{(u_{A\_ref} \cdot T_s)}{U_{dc}}, \\ T_B = T_s + \frac{(u_{B\_ref} \cdot T_s)}{U_{dc}}, \\ T_C = T_s + \frac{(u_{C\_ref} \cdot T_s)}{U_{dc}}. \end{cases} \quad (4)$$

According to (4), the switching sequence in Sector I is shown in Figure 5.

Thus, three phase's duration time of reference voltage can be concluded as

$$\begin{cases} T_X = \frac{U_{X\_ref} T_s}{U_{dc}} (u_{X\_ref} \geq 0) \\ T_X = T_s + \frac{U_{X\_ref} T_s}{U_{dc}} (u_{X\_ref} < 0) \end{cases}, \quad (X = A, B, C). \quad (5)$$

## 3. Analysis of Neutral-Point Potential Offset and the Balancing Strategy

**3.1. Analysis on Neutral-Point Potential Offset of NPC Three-Level Three-Wire APF.** As shown in Figure 3, there are 27 switching states and 19 space vectors in the space vector



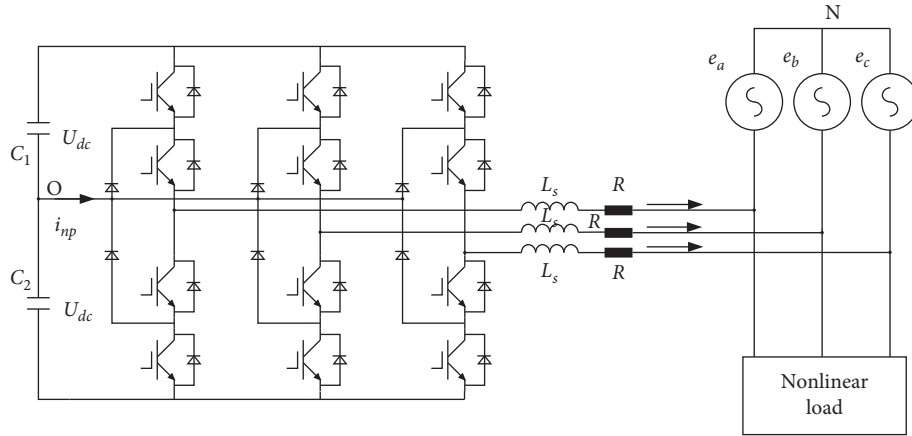


FIGURE 1: Structural schematic diagram of three-level APF.

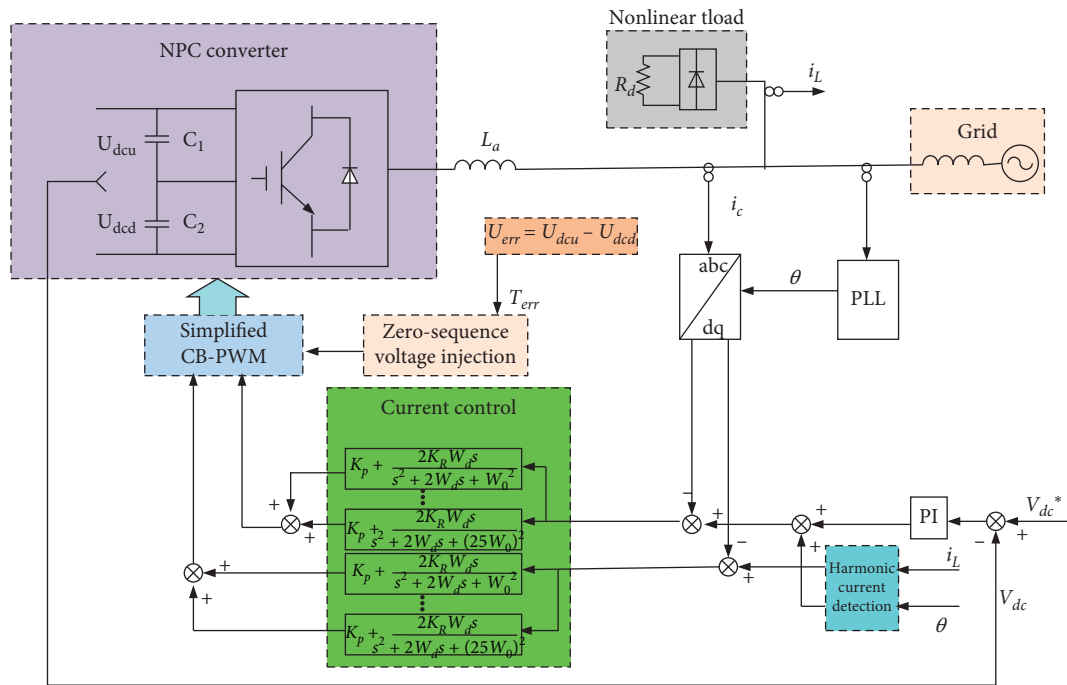


FIGURE 2: Block diagram of the APF system.

TABLE 1: Switching states of the three-level NPC converter ( $X = A, B, C$ ).

SX1	SX2	SX3	SX4	Terminal voltage	Switching state
ON	ON	OFF	OFF	$U_{dc}$	P
OFF	ON	ON	OFF	0	O
OFF	OFF	ON	ON	$-U_{dc}$	N

diagram of the NPC three-level converter. These vectors can be divided into four different types, zero vector, small vector, medium vector, and large vector, based on the different influences of neutral-point potential. The detail will be discussed separately in the following.

When zero vector works, such as PPP, the three-phase load is connected to the positive terminal of DC-bus directly. As shown in Figure 6, no current flows into/out of the

neutral point O. Therefore, the zero vector does not have any effect on the neutral-point potential.

As shown in Figure 7, when the large vector (PNN) works, the three-phase load is connected to the positive and negative terminal of DC-bus, respectively. It can be seen that no current flows into/out of the neutral-point O. So, the large vector does not influence the neutral-point potential, either.

Figures 8 and 9 show that when the small or medium vector works, the neutral point O is connected to the load. There is some current flowing into/out of the neutral point O, which will affect the neutral-point potential. The small or the medium vector always have the switching state "O," so there is at least one phase load connected to the neutral point. In such a circumstance, the phase current is equal to the current which flows into/out of the neutral point O. There is the neutral-point potential offset because of the neutral-point current.

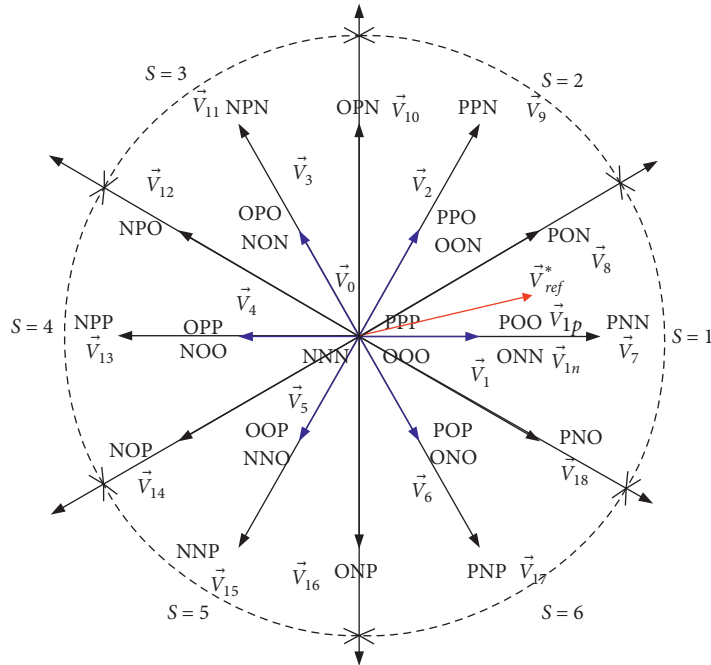


FIGURE 3: Voltage space vector diagram of the NPC three-level converter.

TABLE 2: Principles of sector selection.

$u_{A\_ref}$	$u_{B\_ref}$	$u_{C\_ref}$	S
>0	<0	<0	1
>0	>0	<0	2
<0	>0	<0	3
<0	>0	>0	4
<0	<0	>0	5
>0	<0	>0	6

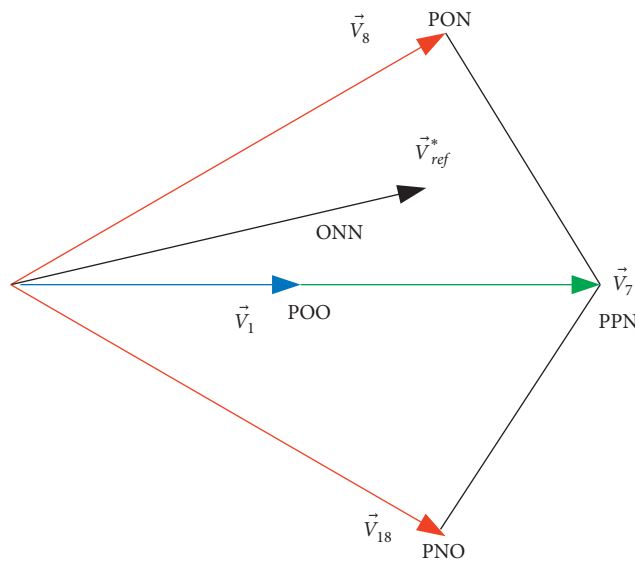


FIGURE 4:  $\vec{V}_{ref}^*$  locating in sector I.

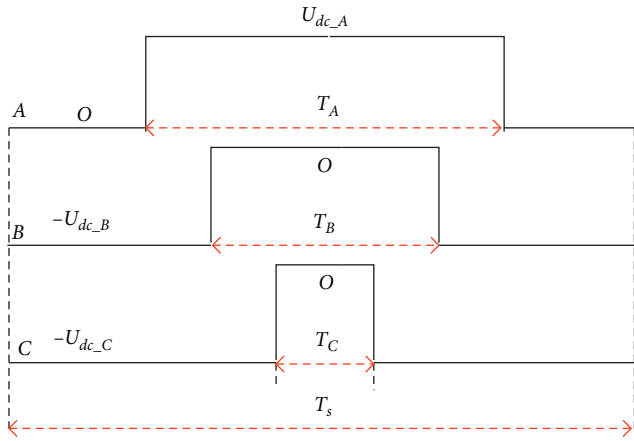


FIGURE 5: Diagram of PWM waveform in Sector I.

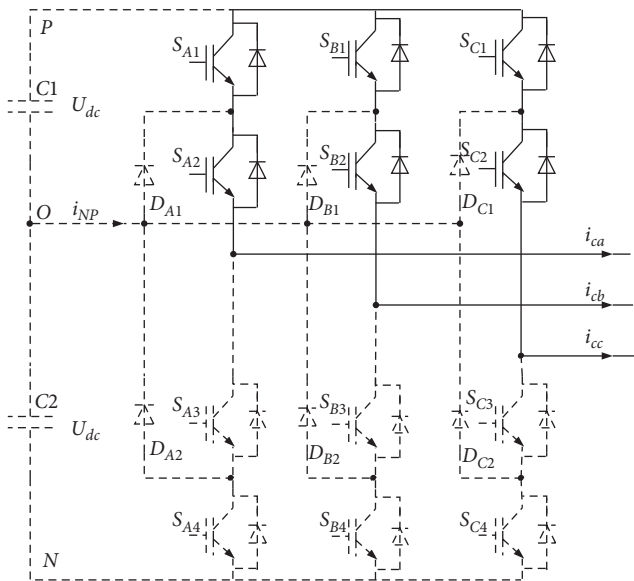


FIGURE 6: Zero vector (PPP).

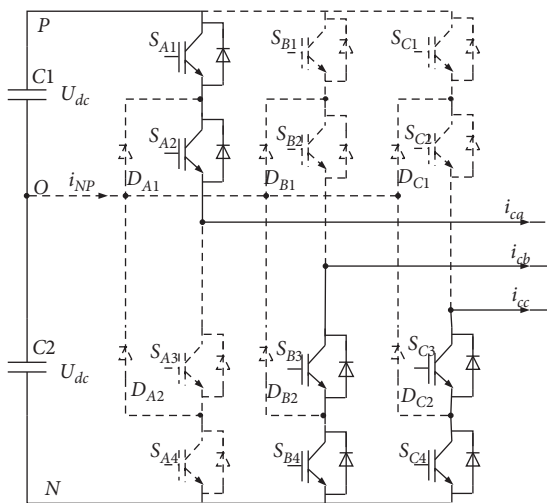


FIGURE 7: Large vector (PNN).

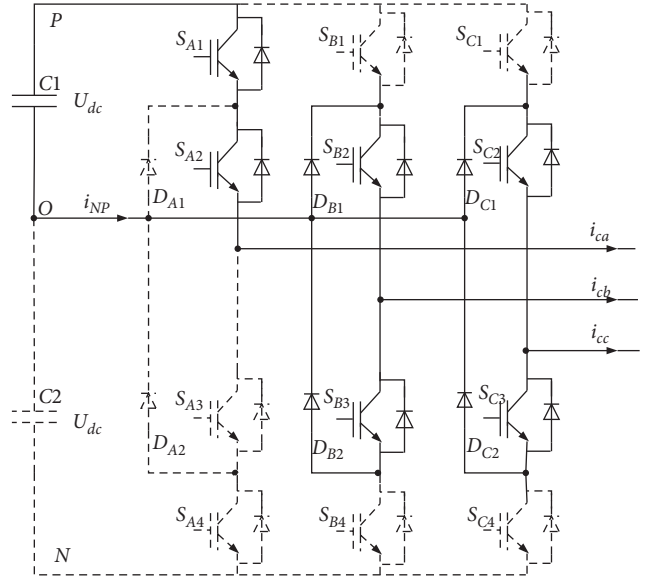


FIGURE 8: Small vector (POO).

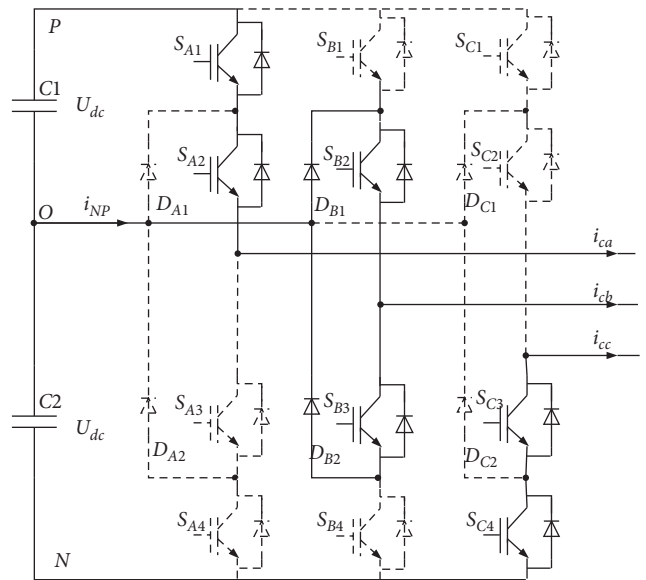


FIGURE 9: Medium vector (PON).

Table 3 shows the neutral-point current corresponding to different vectors. It can be inferred that small vectors appear in pairs, but the two have opposite effects on neutral-point potential. The PWM waveform can be generated by the seven-stage modulation method by combining the original PWM waveform in Figure 5 and the data in Table 3, as shown in Figure 10.

When the sampling period is small enough, the current of phase current can be considered as constant in a sampling period. According to Figure 10, the average value of neutral-point current  $i_{NP}$  can be calculated as

TABLE 3: Neutral-point current corresponding to different vectors.

Positive small vectors	$i_{NP}$	Negative small vectors	$i_{NP}$	Medium vectors	$i_{NP}$
ONN	$i_a$	POO	$-i_a$	OPN	$i_a$
NON	$i_b$	OPO	$-i_b$	PON	$i_b$
NNO	$i_c$	OOP	$-i_c$	PNO	$i_c$
OPP	$i_a$	NOO	$-i_a$	ONP	$i_a$
POP	$i_b$	ONO	$-i_b$	NOP	$i_b$
PPO	$i_c$	OON	$-i_c$	NPO	$i_c$

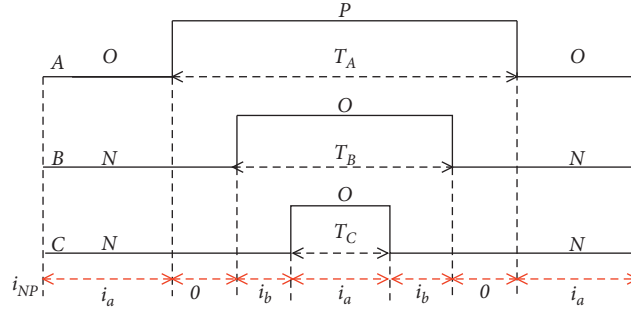


FIGURE 10: Neutral-point current in a switching period.

$$\begin{cases} i_{NP} = \frac{i_a \cdot (T_s - T_A) + i_b \cdot (T_B - T_C) + (-i_a) \cdot T_C}{T_s}, \\ i_a + i_b + i_c = 0. \end{cases} \quad (6)$$

By solving (6), the neutral-point current  $i_{NP}$  can be obtained as

$$i_{NP} = \frac{i_a \cdot (T_s - T_A) + i_b \cdot T_B + i_c \cdot T_C}{T_s}. \quad (7)$$

**3.2. The Neutral-Point Potential Balancing Strategy.** In traditional CB-PWM, zero-sequence voltage is injected into three-phase reference voltage to balance the neutral-point

potential, which requires complicated calculation. The present study proposes a novel strategy, aiming to make the calculation convenient and simpler.

Compare to the injection of zero-sequence component, we add the common time  $T_{err}$  to three phase's duration time  $T_X$  ( $X = A, B, C$ ) to balance the neutral-point potential offset. After  $T_{err}$  is added, the new three phase's duration time can be obtained as

$$\begin{cases} T'_A = T_A + T_{err}, \\ T'_B = T_B + T_{err}, \\ T'_C = T_C + T_{err}. \end{cases} \quad (8)$$

Thus, the new neutral-point current is

$$i'_{NP} = \frac{i_A \cdot [T_s - T'_A] + i_B \cdot T'_B + i_C \cdot T'_C}{T_s} = \frac{i_A \cdot [T_s - (T_A + T_{err})] + i_B \cdot (T_B + T_{err}) + i_C \cdot (T_C + T_{err})}{T_s} = i_{NP} - \frac{2i_A}{T_s} \cdot T_{err}. \quad (9)$$

Based on the principle of charge conservation, the following equation can be obtained:

$$i'_{NP} \cdot T_s = U_{err} \cdot C, \quad (10)$$

where  $U_{err} = U_{dcd} - U_{dcu}$  is the voltage difference between lower and upper DC-link capacitors,  $U_{dcu}$  and  $U_{dcd}$  the upper and lower DC-link capacitor voltage, respectively, and  $C = C_1 = C_2$  is the capacitance of DC-link. Thus,  $T_{err}$  can be derived from (9) and (10) directly:

$$T_{err} = \frac{i_{NP} \cdot T_s - C \cdot U_{err}}{2 \cdot i_A}. \quad (11)$$

Equation (9) shows that  $T_{err}$  can affect the neutral-point current and can adjust the neutral-point potential. When  $i_{NP}$  is positive, the neutral-point potential will decrease. Thus,  $T_{err}$  can be modified by equation (11) to suppress the neutral-point potential offset in theory. The process of modification is shown in Figure 11.

When  $\vec{V}_{ref}$  is located in the other sectors,  $T_{err}$  can be expressed as follows:

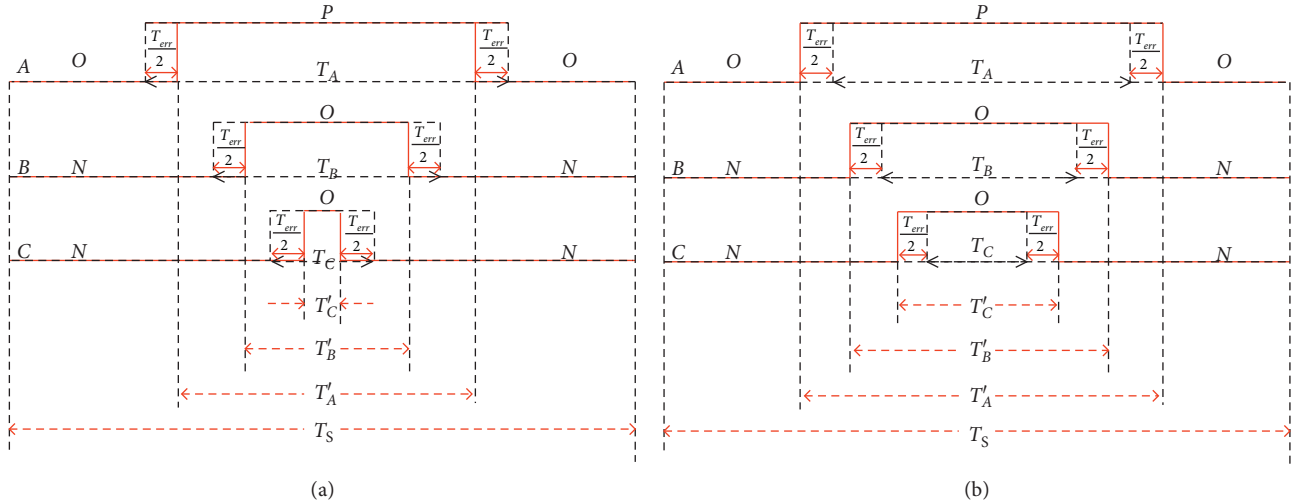


FIGURE 11: Procedure of duration time modification of PWM waveforms. (a) Neutral-point potential to be decreased. (b) Neutral-point potential to be increased.

$$T_{err} = \begin{cases} \frac{i_{NP} \cdot T_s - C \cdot U_{err}}{2 \cdot i_A}, & S = 1, \\ \frac{i_{NP} \cdot T_s - C \cdot U_{err}}{2 \cdot i_C}, & S = 2, \\ \frac{i_{NP} \cdot T_s - C \cdot U_{err}}{2 \cdot i_B}, & S = 3, \\ \frac{i_{NP} \cdot T_s - C \cdot U_{err}}{2 \cdot i_A}, & S = 4, \\ \frac{i_{NP} \cdot T_s - C \cdot U_{err}}{2 \cdot i_C}, & S = 5, \\ \frac{i_{NP} \cdot T_s - C \cdot U_{err}}{2 \cdot i_B}, & S = 6, \end{cases} \quad (12)$$

where  $S$  is the sector number. Figure 11 shows that the range of common time  $T_{err}$  should follow

$$\begin{cases} T_{err} \leq T_s - \max(T_A, T_B, T_C), & (\text{when } T_{err} \geq 0), \\ \text{abs}(T_{err}) \leq \min(T_A, T_B, T_C), & (\text{when } T_{err} < 0). \end{cases} \quad (13)$$

#### 4. Experimental Verification

In order to verify the effectiveness of the proposed balancing strategy, experiments for NPC three-level three-wire APF are conducted. The parameters of the experimental platform are listed in Table 4.

Figure 12 shows the photograph of the experiment equipment including AC supply from the grid, nonlinear load, sensor board connected to controller board, and NPC three-level converter board.

TABLE 4: Parameters of the experimental platform.

Parameters	Value
Phase voltage ( $V_s$ )	110 V (RMS)
Frequency of phase voltage	50 Hz
DC-link voltage ( $2U_{dc}$ )	400 V
DC-link capacitance ( $C_1, C_2$ )	1350 $\mu$ F
Output inductor ( $L_s$ )	4 mH
Switching frequency ( $f_s$ )	10 kHz
Load resistance ( $R_d$ )	30 $\Omega$

Figure 13 shows some waveforms before and after compensation by APF. The three-phase uncontrolled rectifier bridge connecting serially with a 30  $\Omega$  resistor is selected as the typical nonlinear load. The typical load current waveforms can be found from Figure 13(a). Figure 13(b) shows the load current, the grid current after compensation, and the reference current and output current of APF, respectively. The grid current, compared with the distorted load current, is approximately sinusoidal and symmetrical after the compensation. The same conclusion can be drawn after the THD analysis. The THD of load current reaches up to maximum 24.01%. However, the THD of grid-side current sharply falls to 4.5% because of the compensation. Meanwhile, the actual output compensating current is nearly the same as the reference current, suggesting that APF is with good performance. The experiments and analysis above have verified that the three-level three-wire NPC APF has significant positive performance on improving the quality of power grid.

Figure 14 shows the waveforms of upper and lower DC-link voltage. It can be seen that when the neutral-point potential control strategy is not working, the upper and lower voltage  $U_{dcu}/U_{dcd}$  diverge in opposite directions. Then, the proposed neutral-point potential scheme starts working. It shows that the differential value between upper and lower DC-link voltage is less than 2 V, suggesting that the neutral-point potential offset is suppressed effectively.

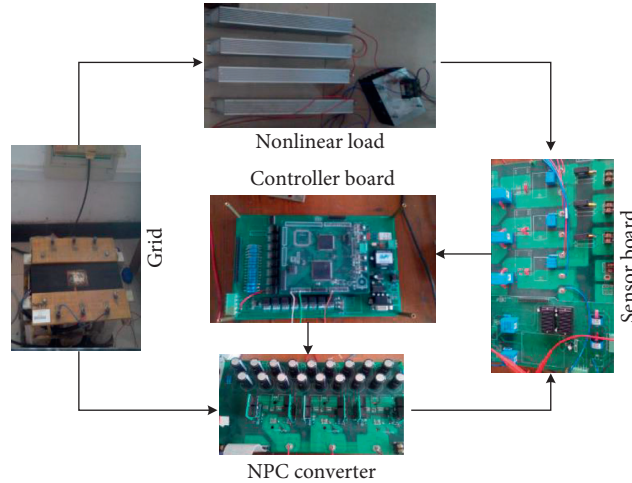


FIGURE 12: Photograph of the experimental platform.

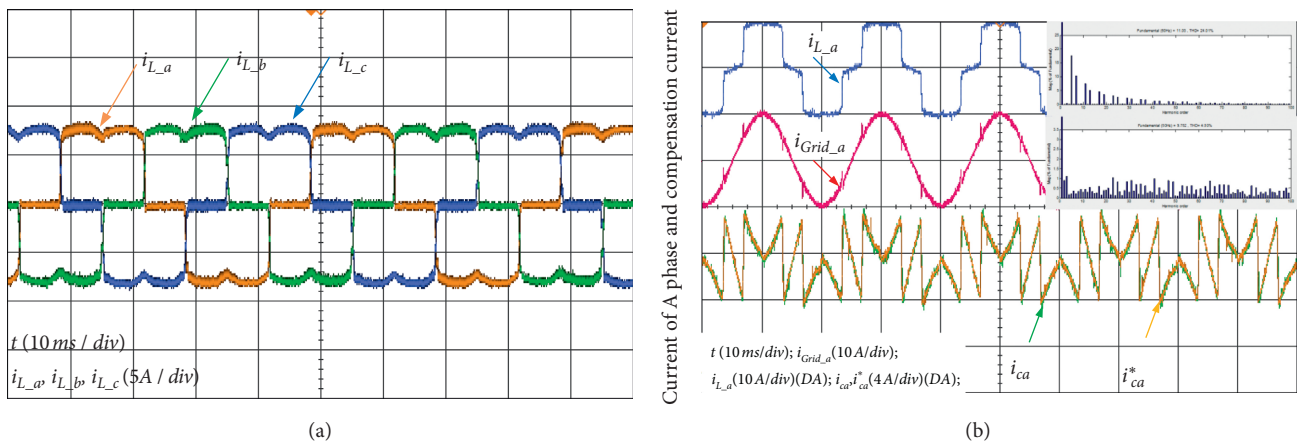


FIGURE 13: Waveforms of some currents. (a) Load current before compensation. (b) Harmonic reference current.

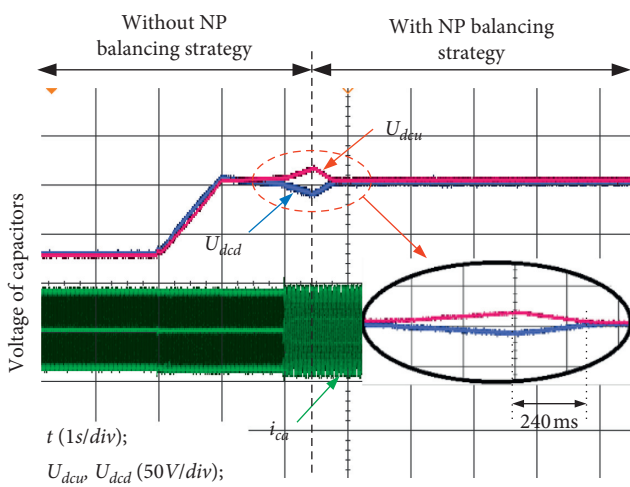


FIGURE 14: Waveforms of upper and lower DC-link voltage.

The proposed scheme and conventional SVPWM were both programmed on the same TMS320F28335 DSP board to check which algorithm can simplify the calculation. Meanwhile, the same code style and composer

configuration were adopted, and all extra optimal measures during the programming were strictly controlled. The results of the experiments showed that it only took DSP  $6.4\ \mu\text{s}$  in the proposed scheme to finish the whole calculation, while in conventional SVPWM, it was  $9.6\ \mu\text{s}$ , indicating a significant simplification.

### 5. Conclusions

The present paper, based on a new voltage-second rule for the three-level converter on three-phase three-wire APF systems, proposes a novel simplified neutral-point balancing scheme and verifies its performance in balancing NP potential. Firstly, the duration time of three phases can be calculated directly with this scheme to avoid the complicated selection of space vector sectors by conventional SVPWM. The calculations in the proposed strategy cover multiplication, addition, and few amounts of division. Compared with the large quantity of divisions, even trigonometry operations in conventional SVPWM, the proposed strategy represents a simplified algorithm when applied in the DSP plant.

Secondly, this proposed strategy reconstructs the switching sequence of every phase by modifying the duration time. Its operation is significantly simpler than the traditional method of zero-sequence voltage injection. The experiments in Section 4 have verified the feasibility and effectiveness of the proposed strategy.

## Data Availability

The raw/processed data required to reproduce these findings cannot be shared at this time as the data also forms part of an ongoing study.

## Conflicts of Interest

The authors declare that there are no conflicts of interest regarding the publication of this paper.

## Acknowledgments

This work was supported by the Natural Science Research Project of Jiangsu Higher Education Institutions of China (19KJB470020).


## References

- [1] C. Eyisi, A. S. Al-Sumaiti, K. Turitsyn, and Q. Li, "Mathematical models for optimization of grid-integrated energy storage systems: a review," in *Proceedings of the 2019 North American Power Symposium (NAPS)*, pp. 1–5, Wichita, KS, USA, October 2019.
- [2] C. Liu, Y. He, K. Dai, and Y. Kang, "Industrial power distribution system harmonic resonance problem and solution with shunt active power filter," in *Proceedings of the IECON 2017-43rd Annual Conference of the IEEE Industrial Electronics Society*, pp. 1243–1248, Beijing, China, November 2017.
- [3] H. Abu-Rub, J. Holtz, J. Rodriguez, and G. Ge Baoming, "Medium-voltage multilevel converters-state of the art, challenges, and requirements in industrial applications," *IEEE Transactions on Industrial Electronics*, vol. 57, no. 8, pp. 2581–2596, 2010.
- [4] Z. Hao, X. Wang, and X. Cao, "Harmonic control for variable-frequency aviation power system based on three-level NPC converter," *IEEE Access*, vol. 8, pp. 132775–132785, 2020.
- [5] A. Pal and K. Basu, "A three-phase three-level isolated DC-AC converter with line frequency unfolding," *IEEE Transactions on Power Electronics*, vol. 35, no. 11, pp. 11758–11769, 2020.
- [6] Z. Xia, Z. Liu, and J. M. Guerrero, "Multi-objective optimal model predictive control for three-level ANPC grid-connected inverter," *IEEE Access*, vol. 8, pp. 59590–59598, 2020.
- [7] B. Zhang, Q. Ge, L. Tan, X. Wang, Y. Yu, and J. Liu, "A New PWM scheme for loss balancing and neutral-point voltage balancing in three-level active NPC converter," in *Proceedings of the 2015 IEEE 10th Conference on Industrial Electronics and Applications (ICIEA)*, pp. 1128–1133, Auckland, New Zealand, June 2015.
- [8] G. Liu, L. Qu, W. Zhao, Q. Chen, and Y. Xie, "Comparison of two SVPWM control strategies of five-phase fault-tolerant permanent-magnet motor," *IEEE Transactions on Power Electronics*, vol. 31, no. 9, pp. 6621–6630, 2016.
- [9] R. Stala, "A natural DC-link voltage balancing of diode-clamped inverters in parallel systems," *IEEE Transactions on Industrial Electronics*, vol. 60, no. 11, pp. 5008–5018, 2013.
- [10] S. Wang, J. Ma, B. Liu, N. Jiao, T. Liu, and Y. Wang, "Unified SVPWM algorithm and optimization for single-phase three-level NPC converters," *IEEE Transactions on Power Electronics*, vol. 35, no. 7, pp. 7702–7712, 2020.
- [11] F. Bu, T. Pu, W. Huang, and L. Zhu, "Performance and evaluation of five-phase dual random SVPWM strategy with optimized probability density function," *IEEE Transactions on Industrial Electronics*, vol. 66, no. 5, pp. 3323–3332, 2019.
- [12] A. Gopinath, "A triangular 3-D coordinate system for multilevel SVPWM generation," *IEEE Transactions on Industry Applications*, vol. 56, no. 4, pp. 4061–4070, 2020.
- [13] H. Lin, Z. Shu, J. Yao et al., "A simplified 3-D NLM-based SVPWM technique with voltage-balancing capability for 3LNPC cascaded multilevel converter," *IEEE Transactions on Power Electronics*, vol. 35, no. 4, pp. 3506–3518, 2020.
- [14] V. Janaki Ramaiah and S. Keerthipati, "Hybrid PWM scheme for Pole-phase modulation induction motor drive using carrier-based hexagonal and octadecagonal SVPWM," *IEEE Transactions on Industrial Electronics*, vol. 67, no. 9, pp. 7312–7320, 2020.
- [15] L. Gu and K. Jin, "A three-phase isolated bidirectional AC/DC converter and its modified SVPWM algorithm," *Journal of Power Electronics*, vol. 30, no. 10, pp. 989–999, 2019.
- [16] B. Sakthisudhursun, J. K. Pandit, and M. V. Aware, "Simplified three-level five-phase SVPWM," *IEEE Transactions on Power Electronics*, vol. 19, no. 7, pp. 2429–2436, 2016.
- [17] J.-S. Lee and K.-B. Lee, "Carrier-based discontinuous PWM method for vienna rectifiers," *IEEE Transactions on Power Electronics*, vol. 30, no. 6, pp. 2896–2900, 2015.
- [18] J. Pou, J. Zaragoza, S. Ceballos, M. Saeedifard, and D. Boroyevich, "A carrier-based PWM strategy with zero-sequence voltage injection for a three-level neutral-point-clamped converter," *IEEE Transactions on Power Electronics*, vol. 27, no. 2, pp. 642–651, 2012.
- [19] C. Yongdong Li and Y. Li, "Analysis and calculation of zero-sequence voltage considering neutral-point potential balancing in three-level NPC converters," *IEEE Transactions on Industrial Electronics*, vol. 57, no. 7, pp. 2262–2271, 2010.
- [20] J. Zaragoza, J. Pou, S. Ceballos, E. Robles, C. Jaen, and M. Corbalan, "Voltage-balance compensator for a carrier-based modulation in the neutral-point-clamped converter," *IEEE Transactions on Industrial Electronics*, vol. 56, no. 2, pp. 305–314, 2009.
- [21] T. Abdelkrim, E. M. Berkouk, A. Benkhalifa, K. Benamrane, and T. Benslimane, "Neutral point potential balancing algorithm for autonomous three-level shunt active power filter" *journal of electrical and control engineering*, *IEEE*, vol. 5, no. 2, pp. 20–26, 2012.



## Research Article

# Coordinated Planning and Energy Conservation for Distribution Network with Renewable Energy: Standardized Information Model and Software

Tianlin Wang,<sup>1</sup> Huazhen Cao,<sup>1</sup> Chong Gao,<sup>1</sup> Zhuohuan Li,<sup>2</sup> Tao Yu ,<sup>2</sup> and Ran Cheng<sup>1</sup>

<sup>1</sup>Grid Planning & Research Center, Guangdong Power Grid Co., Ltd., CSG, Guangzhou 510030, China

<sup>2</sup>Electric Power College of South China University of Technology, Guangzhou 510640, China

Correspondence should be addressed to Tao Yu; [taoyu1@scut.edu.cn](mailto:taoyu1@scut.edu.cn)

Received 30 April 2021; Accepted 28 May 2021; Published 12 June 2021

Academic Editor: Bo Yang

Copyright © 2021 Tianlin Wang et al. This is an open access article distributed under the Creative Commons Attribution License, which permits unrestricted use, distribution, and reproduction in any medium, provided the original work is properly cited.

In recent years, energy conservation and environmental protection have attracted great attention by the state, and many efforts have been made from the policy and planning level. In view of the current distribution network planning requirements about energy-saving and environmental protection attributes such as loss reduction, carbon reduction, and environmental friendliness, this study proposes a set of energy-saving and environmental protection evaluation indicators for distribution network. Then, the CIM file library is constructed for typical equipment. Based on the CIM file, the digital planning technology for distribution network is designed. Besides, the feature library of energy conservation and environmental protection indicators, power flow calculation module, carbon flow calculation module, and renewable energy integration planning module are described.

## 1. Introduction

In December 2016, China issues the development plan for energy conservation and environmental protection industries during the 13th five-year plan period, which points out that environmentally friendly industries are the key to promote economic growth and enhance green competitiveness, as well as support ecological conservation. And, the development and reform commission of Guangdong province proposes the 13th five-year plan for energy development of Guangdong province (2016–2020) in January 2017, which puts forward the development goals of improving the green and low-carbon energy system, promoting energy conservation, and reducing carbon emission. Meanwhile, Guangdong province government presents that it is vital to implement energy-saving and low-carbon power dispatching considering economic, energy-saving, and environmental protection factors and then make the reasonable competition rules of power market. Besides, China Southern Power Grid Corporation has established a complete index evaluation system about energy conservation and

environmental protection, which helps to combine market transaction with energy-saving and low-carbon power dispatching. Hence, it can be predicted that improving renewable energy penetration rate, developing low-carbon planning technology, and promoting distributed energy (such as solar, wind, and geotherm) are the development trends of the power system in the future [1–3].

Distribution network is the link between the power plant and end users. The scientific planning of distribution network can ensure the reasonable structure and economical operation of the power grid. Moreover, it is important to realize dual carbon control (carbon peaking and carbon neutralization) of the power system by improving the power supply quality, improving environment, and optimizing energy consumption structure. From the perspective of planning, electric energy should be delivered to the user terminal with high quality. And, the reliable supply of electric energy is supported by large-scale distribution equipment. Therefore, the economic and technical cost-benefit analysis of distribution network investment is essential for the efficient and economic operation of the power

system [4]. From the perspective of operation, the voltage at the load side of distribution network is low with large load current, which makes the loss of transformers and lines. These power losses even can reach about 10% or even higher of the transmission power. Hence, the energy-saving and loss reduction measures should be carried out to improve the economic operation level and equipment utilization rate of distribution network [5].

Recently, higher requirements have been raised for distribution network planning with the economy development, power system reformation, and energy conservation and environmental protection initiative. Distribution network planning not only requires the minimize the construction and operation costs with the safe and reliable power supply but also concentrates on the coordination between distribution network and environment to reduce carbon emission and protect environment [6]. At present, lots of works on energy saving and loss reduction of distribution network [7–9] have been studied, which design a series of new technologies and equipment and establish the relevant evaluation index. However, these research studies ignore the environmental problems in the construction and operation of distribution network equipment, such as the greenhouse effect caused by sulfur dioxide, nitrogen oxide, and carbon dioxide emission. On the contrary, the electromagnetic radiation from distribution transformer, overhead lines, and cable lines may affect nearby residents which leads to a great deal of criticism. Furthermore, the research on renewable energy access planning of distribution network mainly includes planning algorithm [10–12], planning model [13–15], renewable energy siting and sizing [16–20], and collaborated planning between renewable energy and power system [21, 22]. And, the evaluation indexes and intelligent planning software of distribution network environmental protection planning need to be further studied.

To make up for the above deficiencies, this paper establishes an index system that can guide the distribution network planning and evaluate the energy conservation and environmental protection attributes. Then, a typical equipment library is established to systematically model the distribution network equipment based on the CIM file. Finally, the function modules of energy-saving and environmental protection software are designed which lays the foundation for the digital distribution network planning.

## 2. Energy Conservation and Environmental Protection Indexes

The purpose of establishing the index system is to better evaluate the energy conservation and environmental protection characteristics of the distribution network, and the following content will analyse and elaborate on these two aspects.

*2.1. Energy Conservation Indexes.* Energy conservation indexes mainly include equipment life cycle, line loss, equipment loss, and operation loss; the structure of them is

shown in Figure 1. In particular, the whole life cycle denotes the overall costs of equipment (such as transformer, overhead line, cable line, circuit breaker, load switch, switch cabinet, outdoor switch box, cable distribution box, ring network cabinet, reactive power compensation device, and lightning rod) from production to recycle. Line loss and equipment loss fully describe the actual operation loss caused by line heating and equipment heating in the actual operation of distribution network. Moreover, the three-phase unbalanced additional loss, unreasonable operating voltage additional loss, high-order harmonic additional loss, and equipment aging additional loss should be further considered in the operational additional level.

*2.2. Environmental Protection Indexes.* Environmental protection indexes mostly compose of equipment environmental protection index, high harmonic content, green distribution network index, carbon emission flow, and electric energy substitution index; the sketch map of them is given in Figure 2. Specially, equipment environmental protection index focuses on the radiation intensity and noise intensity. And, the distributed power penetration rate, electric vehicle charging (replacement) power station area density, capacity proportion of public electric vehicle charging and swapping facilities, annual consumption rate of distributed power generation, and cost of waste gas treatment in distribution network, as well as green equipment proportion, are the subindexes of the green distribution network indicator. In addition, the carbon emission stream regards the carbon emission flow rate and node carbon potential as the evaluation criterion. And, the electricity substitution index denotes the potential of “replace oil, gas, and coal with electricity.”

## 3. CIM File and Its Analytical Process

The CIM model is a collection of various subsystems, and the main purpose of using CIM file is to establish a unified and standard information model to provide effective model support for distribution network research and planning. It is necessary to determine the relationship between each subsystem and then build an integrated framework that is easy to understand for users. There are three kinds of CIM models:

- (1) Core model: this model is the basic to describe and analyse management system. It defines the control range of each subsystem, which also is the starting point of all the public models.
- (2) General model: this model is independent of the system, which helps to develop management applications such as setting program and Internet program.
- (3) Extended model: this model is a technical extension of the general model, which is mostly used in the specific environment.

As an information-based model, designers can realize visual CMI modelling through unified modelling language

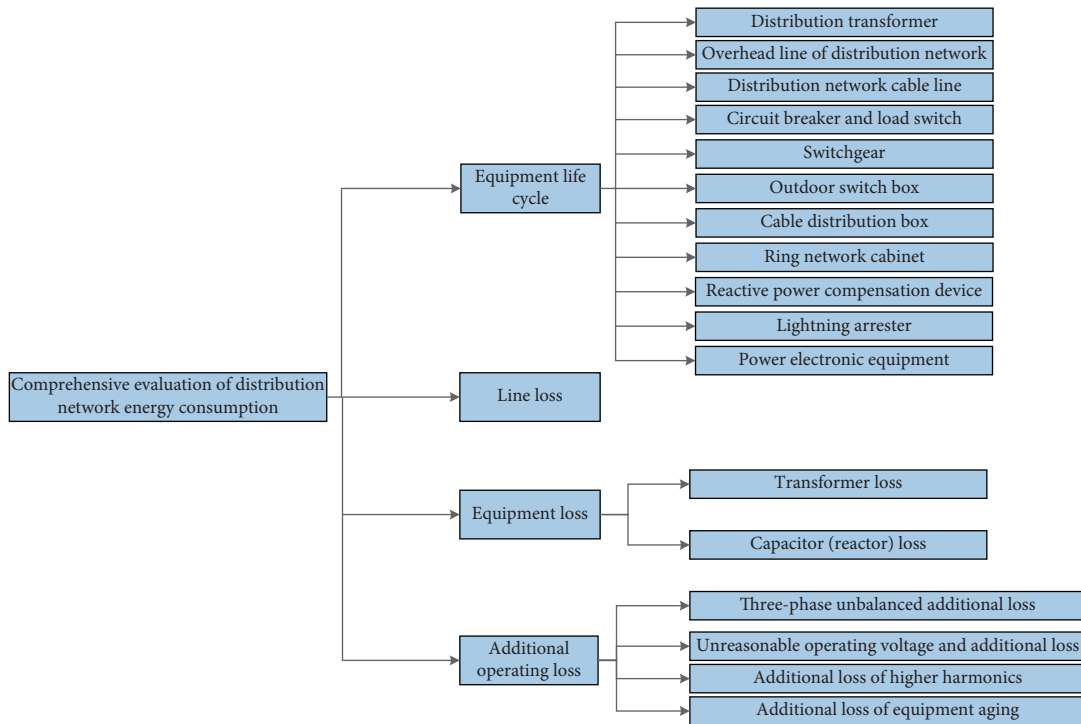


FIGURE 1: The diagram of the energy conservation index system.

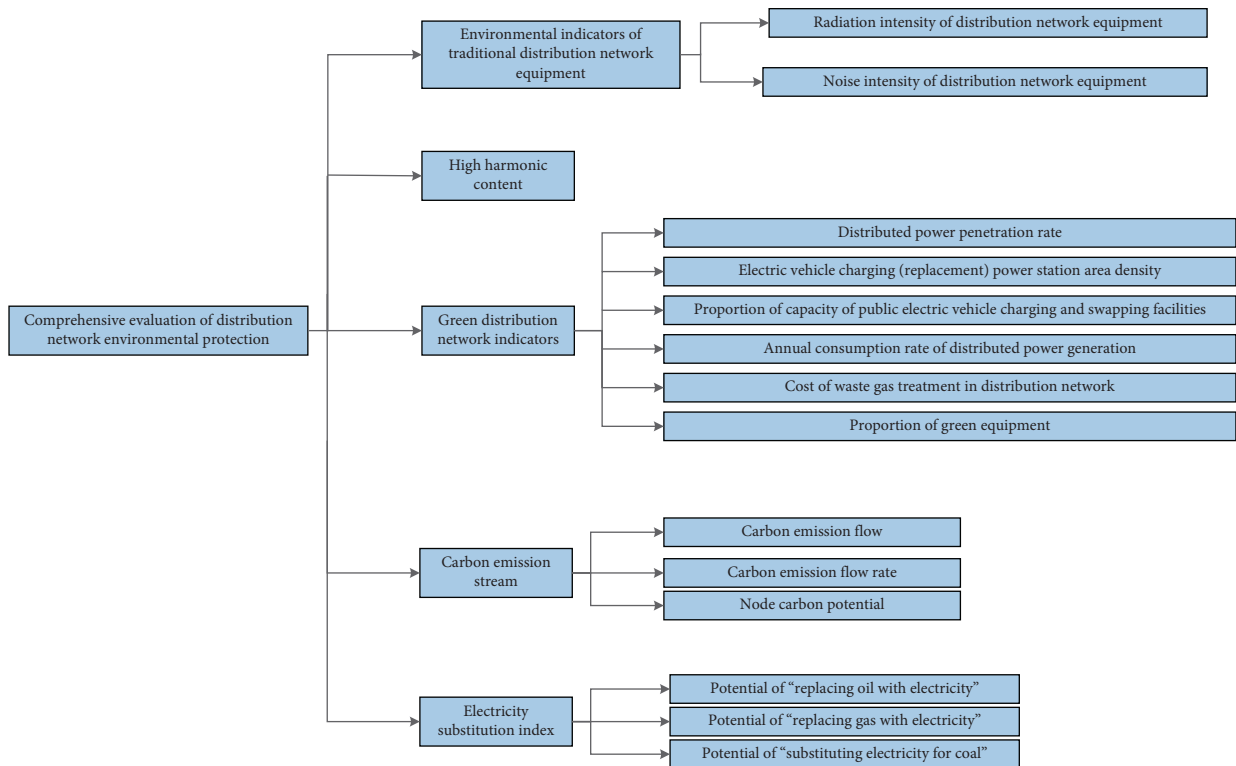


FIGURE 2: The diagram of the environmental protection index system.

(UML). The autoinformation exchange of the CIM model is achieved by Internet; then, an intelligent distribution network planning technology can be established. Besides, the CIM model avoids the problem of large subclasses caused by

various definitions. The generic class is used to identify the attribute of each subclass and their name. Hence, this model can describe the specific attribute of monitoring content via integer, Boolean variable, floating-point number, string, etc.

This paper analyses the CIM file and investigates the main objects involved in the distribution network planning. Then, the following analytical process of the CIM file can be given:

- (1) Read CIM file and extract CIM component object, including station, wire, bus, switch, transformer, and terminal
- (2) Find the connected component according to the terminal head of circuit breaker
- (3) Determine the terminal head according to the component and read the component set
- (4) Traverse component set and identify bus node, distribution node, and contact switch
- (5) Repeat step (4) until the recursive traversal is completed
- (6) Implement skeleton analysis including the main line marking and the insufficient assessment of main cross section and branch line; then, the problem library can be generated
- (7) SVG element node mapping
- (8) Save CIM data in library

#### 4. CIM File Library of Typical Distribution Network Equipment

The distribution network model usually has large data and complex structure. And, the theory and practice of this paper are based on the modelling of power grid equipment (e.g., topology, line, load, equipment, and feeder), which can be described as follows:

- (1) Line model: the line model can be classified according to the conductor type, wiring method, conductor kind, and wire style. However, the definition of the conductor type shows that this model is only suitable for the three-phase symmetric system which employs positive sequence and zero sequence components to describe line impedance. And, the distribution system is three-phase asymmetric system, which needs to consider more geometric attributes, electrical attributes, and electrical information to establish the integrated line model.
- (2) Transformer model: the transformer model is composed of equipment container, transformer winding, and so on. In the CIM model, the winding type of the transformer is replaced by the end type which is associated with star impedance type and admittance type to represent the parameter matrix of the transformer.
- (3) Load model: this model depicts the load of the power grid, which is able to (a) show the characteristics of load access point, (b) express multiphase connection and its connection type, (c) reflect constant impedance, constant power, and constant current load, and (d) represent three-phase balance and three-phase imbalance in distribution network.

- (4) Feeder model: The feeder model is extended by the CIM model. Feeder is a combination of power lines with the same voltage level in the distribution network which contains lots of power equipment. And, feeder modelling can build the overall or partial relationship between composite equipment and single equipment in distribution network.

#### 5. The Design of Coordinated Planning and Energy Conservation Software

This proposed software is a novel distribution network planning technology, which can realize the digital and intelligent planning and decision-making with renewable energy connected. And, the energy conservation and environment protection factors are fully considered to satisfy the requirement of green distribution network construction. The algorithms and functions of the platform are compiled from the bottom layer, packaged, and encapsulated so that the platform interface can call these function packages. The system login page and technical framework are shown in Figures 3 and 4, respectively.

Moreover, the design of this software mainly includes four modules: energy-saving and environmental protection indexes feature library, power flow calculation, carbon flow calculation, and renewable energy connected planning.

*5.1. Energy-saving and Environmental Protection Indexes' Feature Library.* This library is dynamic which stores the typical energy-saving and environmental protection indexes from the engineering cases. The prominent advantage of this library is that the computation efficiency of software and the data capacity of library are improved simultaneously. Specially, the scale of database is increased based on the outcomes of engineering cases' analysing. Then, the engineering cases can extract characteristic data from the library to estimate the relevant indexes of equipment which saves computation time in large.

And, the visual interface of the indicator feature library is given in Figure 5. It is observed that the energy-saving and environmental protection indexes are exhibited via analysing engineering cases. And, the database can be continuously enriched by the increasing engineering cases to establish indicator feature library of equipment.

*5.2. Power Flow Calculation.* CIM expand package defines the connection mode of each equipment in distribution network, which can be described by "equipment-terminal-connection point." The terminal is the end of the device. A device has multiple terminals, and the connection point aggregates the related terminals without impedance according to network operation status. Taking the model library of the network layer as the middle layer, the CIM model is analysed to the middle layer database and a real-time synchronous computing database can be generated to achieve the automatic modelling of the whole physical model. Besides, the interface layer is established based on the secondary development and encapsulation of API

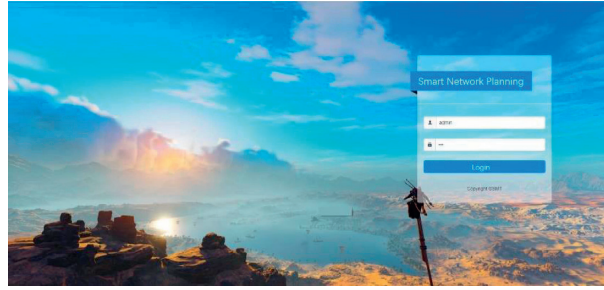


FIGURE 3: The system login page.

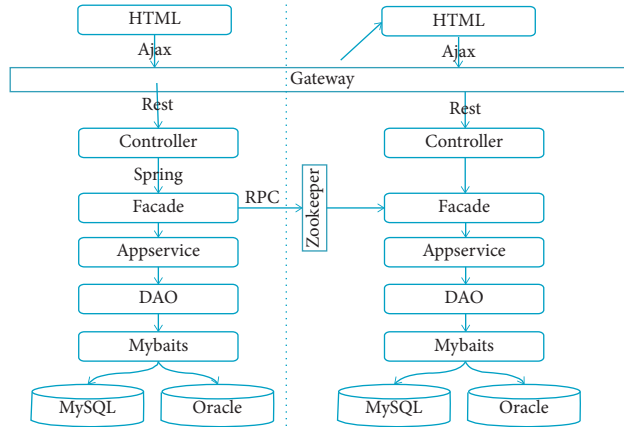


FIGURE 4: The overall technical framework.

Indicator feature library

Engineering example
v
Enter
Save

Energy saving of equipment   
  Environmental protection of equipment

Device ID	Device model	Indicator 1	Indicator 2	Indicator 3

Description column

FIGURE 5: The visual interface of indicator feature library.

interface, which can realize the auto-periodic operation of power flow calculation.

The graph-based network topology subsystem can identify electrical equipment, which also supports the automatic

topology program calling, network topology analysing, node numbering, and topology results updating. And, this system has the function of automatic network tracking, state network analysing, dynamic network diving, and region segmenting.



The power flow calculation module is a built-in calculation module. Its calculation parameters are obtained by parse CIM file with distribution network information. Then, the relevant calculation parameters are input to the power flow calculation interface. And, the final calculation results are output and displayed on the front-end topology interface via the built-in calculation module developed by Python language. The power flow calculation module is compiled from the bottom of the code by us, without the use of software packages from other institutions or companies.

**5.3. Carbon Flow Calculation.** The carbon flow calculation module mainly involves the following indicators.

**5.3.1. Branch Carbon Flow.** The branch carbon flow is the most basic physical quantity of carbon flow, which is represented by  $F$ . It is defined as the cumulative amount of carbon emission corresponding to the carbon flow that passes through a branch along with the load flow in the given time. And, the unit of carbon flow is the same as carbon emission.

**5.3.2. Branch Carbon Flow Rate.** The carbon flow rate of a branch in unit time is called the branch carbon flow rate, which is represented by  $R$ . Its value is equal to the derivative of the branch carbon flow, and the unit is t-CO<sub>2</sub>/h or kg-CO<sub>2</sub>/s:

$$R = \frac{dF}{dt}. \quad (1)$$

**5.3.3. Branch Carbon Flux Density.** The carbon emission flow of the power system is related to active power flow, so it is necessary to combine the above concepts to implement research. The branch carbon flux density is defined as the ratio of the carbon flow rate to the active power flow in a branch, which can be denoted by  $\rho$ . It is easy to find that the unit of branch carbon flow density is the same as the carbon emission intensity on the power generation side, i.e., kg-CO<sub>2</sub>/kWh.

**5.3.4. Node Carbon Potential.** The node carbon potential of the power system describes the linear relationship between the carbon flow and the active power flow through a node, which is written as  $e$ . And, the expression is given by

$$e_n = \frac{\sum_{i \in N^+} P_i \rho_i}{\sum_{i \in N^+} P_i} = \frac{\sum_{i \in N^+} R_i}{\sum_{i \in N^+} P_i}, \quad (2)$$

where  $N^+$  is the set of all branches whose flow flows into node  $n$  and  $i$  is the branch number. It can be observed that the unit of node carbon potential is the same as branch carbon flux density, and its value is equal to the weighted average of carbon flow density  $\rho_i$  of the branches flowing into node  $n$  for the active power flow  $P_i$ .

The essence of the power system carbon emission flow calculation is to quantitatively determine the flow state of

carbon emission flow based on load flow distribution. The differences and relation between load flow analysing and carbon emission flow analysing can be summarized as follows: (a) the carbon emission flow depends on the existence of load flow, and the factors affecting load flow distribution also will have an impact on carbon emission flow; (b) the carbon emission flow is related to the carbon emission characteristics of the generator unit. Therefore, the carbon emission flow is not only restricted by load flow distribution but also affected by some parameters and boundary conditions about the generator unit.

The active power, reactive power, voltage, and phase angle of all nodes, as well as the load flow of all branches, can be obtained via the load flow calculation based on the CIM file. According to the nature of carbon emission flow, the carbon flow density on the all branches is equal to the carbon potential of the node connected to the branches. When the carbon potential of all nodes is obtained, the carbon flow rate of all branches can be calculated from the carbon potential of the starting node and branch load flow. Then, the carbon flow rate of each branch and key section can be acquired based on the carbon potential of each node.

Similar to the load flow calculation module, carbon flow calculation is carried out by the built-in calculation module using Python language, and the calculation outcomes are shown in the front-end topology interface (see Figure 6). Moreover, two practical engineering cases are introduced to assess the performance of designed load flow and carbon flow calculation platform. And, the sketch maps of these engineering cases are shown in Figure 7. Note that the detailed information is hidden in the maps due to confidentiality needs. Besides, the display interface of calculated feeders is denoted in Figure 8.

**5.4. Renewable Energy Connected Planning.** With the advancement and popularization of power electronics technology and the continuous advancement of China's energy conservation and emission reduction strategy, the scale and proportion of new energy access to the distribution network is increasing. In order to cope with the situation that the proportion of new energy access in the distribution network has increased year by year in recent years, the new energy access module is designed here.

The photovoltaic system has an important role and large market in distribution network with renewable energy connected. Hence, this proposed module is developed considering solar power.

Photovoltaic cell is the basic component of photovoltaic system, and its output power value is related to energy conversion efficiency, solar irradiation, panel area, and so on. The active power of the photovoltaic system can be approximately expressed as follows:

$$P_{PV} = rA\eta, \quad (3)$$

where  $A$  is panel area,  $r$  is solar irradiation, and  $\eta$  is energy conversion efficiency.

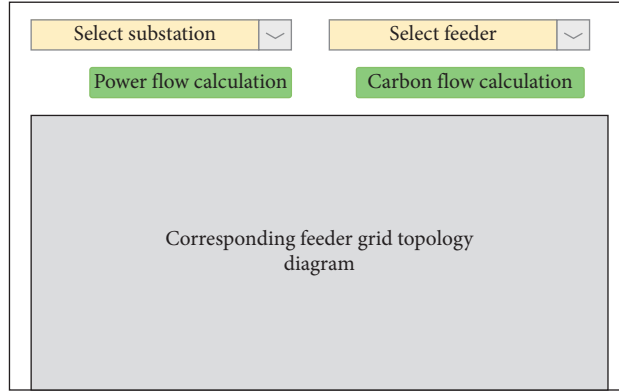


FIGURE 6: The visual interface of the carbon flow calculation module.

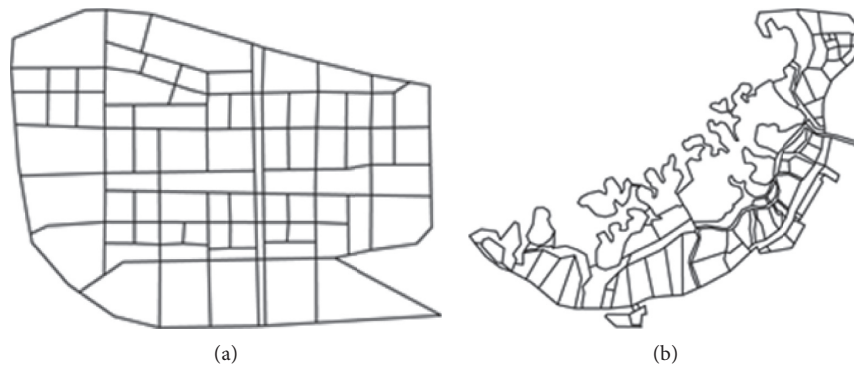


FIGURE 7: The sketch maps of two engineering cases. (a) Case one. (b) Case two.

The photovoltaic system usually works in the daytime. And, the solar irradiation meets beta distribution, and probability density it is

$$f(r) = \frac{\Gamma(\alpha + \beta)}{\Gamma(\alpha)\Gamma(\beta)} \left(\frac{r}{r_{\max}}\right)^{\alpha-1} \left(1 - \frac{r}{r_{\max}}\right)^{\beta-1}, \quad (4)$$

where  $r_{\max}$  is the maximum solar irradiation and  $\alpha$  and  $\beta$  both are the shape parameters of beta distribution.

Therefore, the probability density of output power is given by

$$f(P_{PV}) = \frac{\Gamma(\alpha + \beta)}{\Gamma(\alpha)\Gamma(\beta)} \left(\frac{P_{PV}}{P_{\max}}\right)^{\alpha-1} \left(1 - \frac{P_{PV}}{P_{\max}}\right)^{\beta-1}. \quad (5)$$

The idea of the photovoltaic module based on the CIM file is to establish a front-end input interface. Then, the model and parameters of photovoltaic equipment can be input manually or read in the text and stored in the database.

Especially, the selection of photovoltaic equipment directly affects the properties and parameters of equipment. And, the related parameters are as follows:

- (1) Shape parameter  $\alpha$
- (2) Shape parameter  $\beta$
- (3) Single square array area  $A$
- (4) Energy conversion efficiency  $\eta$
- (5) Maximum solar irradiation  $r_{\max}$
- (6) PV capacity  $S$

There are engineering restrictions on the location and capacity determination of PV equipment in actual scenarios. Hence, the location and capacity determination in photovoltaic system depends on manual operation in this software module. And, the built-in module can assess the operation status of distribution network, and its visual interface is shown in Figure 9.



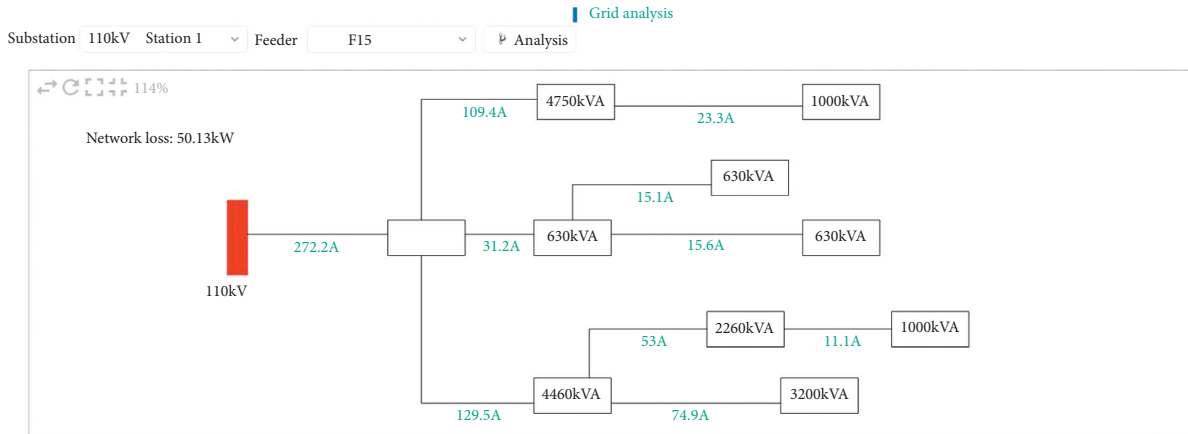


FIGURE 8: The display interface of calculated feeders.



FIGURE 9: The display interface of renewable energy connected planning.

## 6. Conclusion

This paper proposes the standardized information model and software of coordinated planning and energy conservation for distribution network, and the main contributions are as follows:

- (1) The comprehensive index system of energy conservation and environmental protection for distribution network is presented, which provides a

powerful tool to implement the evaluation and planning of the power system.

- (2) The CIM file library of typical equipment in distribution network is established. This library is helpful for the intelligent planning of distribution network.
- (3) The energy conservation and environmental protection software module is designed based on the CIM file which can be regarded as a general design scheme.

- (4) The designed indexes feature library can realize the improvement of software performance and background data capacity.
- (5) The constructed power flow calculation module, carbon flow calculation module, and renewable energy connected planning module serve as the foundation for visual planning of distribution network.

Our next work will be promoted from the following two aspects:

- (1) The functional modules of the software platform will continue to be expanded.
- (2) The digitization and automation capabilities of the software will be enhanced, and a variety of machine learning core algorithms should be added.

### Data Availability

The research data used to support the findings of this study are included within the article.

### Conflicts of Interest

The authors declare that they have no conflicts of interest.

### Authors' Contributions

T. W. conceptualized the study, developed to the methodology of the study, and wrote the original draft. H. C., C. G., and Z. L. carried out formal analysis, visualized the study, and obtained resources. T. Y. and R. C. reviewed and edited the article.

### Acknowledgments

The authors gratefully acknowledge the support of the Science and Technology Project of China Southern Power Grid Corporation (GDKJXM20173256).

### References

- [1] J. A. Turner, "A realizable renewable energy future," *Science*, vol. 285, no. 5428, pp. 687–689, 1999.
- [2] H. Lund, "Renewable energy strategies for sustainable development," *Energy*, vol. 32, no. 6, pp. 912–919, 2007.
- [3] S. Kazemlou and S. Mehraeen, "Novel decentralized control of power systems with penetration of renewable energy sources in small-scale power systems," *IEEE Transactions on Energy Conversion*, vol. 29, no. 4, pp. 851–861, 2014.
- [4] J. T. Boardman and C. C. Meckiff, "A branch and bound formulation to an electricity distribution planning problem," *IEEE Transactions on Power Apparatus & Systems*, vol. 104, no. 8, pp. 2112–2118, 2007.
- [5] S. K. Goswami, "Distribution system planning using branch exchange technique," *IEEE Transactions on Power Systems*, vol. 12, no. 2, pp. 718–723, 1997.
- [6] N. Ponnaivaikko, K. S. P. Rao, and S. S. Venkata, "Distribution system planning through a quadratic mixed integer programming approach," *IEEE Transactions on Power Delivery*, vol. 2, no. 4, pp. 1157–1163, 1987.
- [7] I. J. Ramfrez-Rosado and J. A. Dominguez-Navarro, "New multiobjective tabu search algorithm for fuzzy optimal planning of power distribution systems," *IEEE Transactions on Power Systems*, vol. 21, no. 1, pp. 224–233, 2006.
- [8] M. Shahbaz, C. Raghutla, K. R. Chittedi, Z. L. Jiao, and X. V. Vo, "The effect of renewable energy consumption on economic growth: evidence from the renewable energy country attractive index," *Energy*, vol. 207, Article ID 118162, 2020.
- [9] P. S. N. Rao and R. Deekshit, "Energy loss estimation in distribution feeders," *IEEE Transactions on Power Delivery*, vol. 21, no. 3, pp. 1092–1100, 2006.
- [10] V. Miranda, J. V. Ranito, and L. M. Proenca, "Genetic algorithms in optimal multistage distribution network planning," *IEEE Transactions on Power Systems*, vol. 9, no. 4, pp. 1927–1933, 1994.
- [11] V. F. Martins and C. L. T. Borges, "Active distribution network integrated planning incorporating distributed generation and load response uncertainties," *IEEE Transactions on Power Systems*, vol. 26, no. 4, pp. 2164–2172, 2011.
- [12] A. Soroudi and M. Ehsan, "A distribution network expansion planning model considering distributed generation options and techno-economical issues," *Energy*, vol. 35, no. 8, pp. 3364–3374, 2010.
- [13] E. Miguez, J. Cidras, E. Diaz-Dorado, and J. L. Garcia-Dornelas, "An improved branch exchange algorithm for large scale distribution network planning," *IEEE Power Engineering Review*, vol. 22, no. 9, p. 58, 2002.
- [14] I. J. Ramirez-Rosado and J. A. Dominguez-Navarro, "Possibilistic model based on fuzzy sets for the multiobjective optimal planning of electric power distribution networks," *IEEE Transactions on Power Systems*, vol. 19, no. 4, pp. 1801–1810, 2004.
- [15] A. Soroudi, M. Ehsan, and H. Zareipour, "A practical eco-environmental distribution network planning model including fuel cells and non-renewable distributed energy resources," *Renewable Energy*, vol. 36, no. 1, pp. 179–188, 2011.
- [16] M. Sedghi, A. Ahmadian, and M. Aliakbar-Golkar, "Assessment of optimization algorithms capability in distribution network planning: review, comparison and modification techniques," *Renewable and Sustainable Energy Reviews*, vol. 66, pp. 415–434, 2016.
- [17] S. Essallah, A. Bouallegue, and A. Khedher, "Optimal sizing and placement of DG units in radial distribution system," *International Journal of Renewable Energy Research (IJRER)*, vol. 8, no. 1, pp. 166–177, 2018.
- [18] N. Acharya, P. Mahat, and N. Mithulananthan, "An analytical approach for dg allocation in primary distribution network," *International Journal of Electrical Power & Energy Systems*, vol. 28, no. 10, pp. 669–678, 2006.
- [19] M. F. Alhajri, M. R. Alrashidi, and M. E. El-Hawary, "Improved sequential quadratic programming approach for optimal distribution generation deployments via stability and sensitivity analyses," *Electric Power Components and Systems*, vol. 38, no. 14, pp. 1595–1614, 2010.
- [20] Y. M. Atwa, E. F. El-Saadany, M. M. A. Salama, and R. Seethapathy, "Optimal renewable resources mix for distribution system energy loss minimization," *IEEE Transactions on Power Systems*, vol. 25, no. 1, pp. 360–370, 2010.
- [21] K. M. S. Alzaidi, O. Bayat, and O. N. Uçan, "Multiple DGs for reducing total power losses in radial distribution systems using hybrid WOA-SSA algorithm," *International Journal of Photoenergy*, vol. 2019, Article ID 2426538, 20 pages, 2019.

- [22] M. M. Aman, G. B. Jasmon, A. H. A. Bakar, and H. Mokhlis, "A new approach for optimum simultaneous multi-DG distributed generation Units placement and sizing based on maximization of system loadability using HPSO (hybrid particle swarm optimization) algorithm," *Energy*, vol. 66, pp. 202–215, 2014.

## Research Article

# Compulsory Islanding Transition Strategy Based on Fuzzy Logic Control for a Renewable Microgrid System

Jiexing Wan , Wei Hua, and Baoan Wang

*School of Electrical Engineering, Southeast University, Nanjing 210096, China*

Correspondence should be addressed to Jiexing Wan; 230179195@seu.edu.cn

Received 3 March 2021; Accepted 5 May 2021; Published 18 May 2021

Academic Editor: Xiao-Shun Zhang

Copyright © 2021 Jiexing Wan et al. This is an open access article distributed under the Creative Commons Attribution License, which permits unrestricted use, distribution, and reproduction in any medium, provided the original work is properly cited.

Advantages of microgrid integrated with a renewable energy system have been acknowledged in more and more applications. Operating steadily during different modes is of great significance, and different modes transferring must be transient, seamless, and reliable to maintain the continuous electricity supply for loads, especially sensitive ones. As a semiconrolled switch that is unable to shut instantly until the zero point of its current, thyristors should be forced to be turned off by certain strategies to minimise the influence brought by the delay of modes transferring. In this paper, a compulsory turn-off strategy based on fuzzy logic control of converter output voltage is proposed. With the strategy, an alterable reverse voltage is applied across the conducting thyristor by dynamically adjusting the output voltage reference instruction and closed-loop control parameters depending on the changing rate rather than detecting the polarity of voltage or current. Constraints from acquisition of analog data and error of digital calculation will be eliminated. Finally, simulation and experimental results verify the effectiveness of the proposed strategy.

## 1. Introduction

In recent years, motivated by the climate change and unsustainable consumption on fossil fuels for electricity generation, establishment of the microgrid (MG) system with renewable energy conversion such as distributed generating (DG) or battery storing (BS) has steadily increased [1–3]. The MG system is capable of supplying uninterrupted power for critical loads independently with the flexibility of multiple working modes under planned outage or unintentional faults such as short circuit, disturbance, and blackout [4–7]. Because of different control objectives, the mode transition of the MG system, especially when it disconnects from the utility, must be transient, seamless, and reliable so that influence caused by the intermediate process can be mitigated or avoided even better without any current surge or voltage fluctuation [8].

Studies have been carried out on smooth transferring of output. In [9], a master inverter is set to build up the AC voltage and other inverters can still work in the grid-tied mode to supply continuous power. Unified schemes based on indirect current control are devised to impose no

alteration to the control structure so that the output voltage and injected current can transmit smoothly with no shock [10–12]. In [13, 14], smooth transition mechanisms based on state observer are discussed to maintain the system variables within acceptable limits. In [15–18], a unified scheme based on droop control is designed to only change the voltage reference rather than control structure so that inrush currents and voltage distortions of mode transfer can be eliminated. In [19–22], fuzzy-based parameter regulation is implemented to improve the performance of dynamic response and stability when transferring.

However, before getting power supply from the MG system, loads should disconnect from the utility completely [23, 24]. Inadequate attention has been applied on switch-over transients of the connecting devices between the utility and the MG system, which leaves several challenges to be further researched. Generally, it takes around 1 s (second) for the relays to switch off completely and around 0.5 s for mechanical breakers [25] while power electronic switches have much faster on-off response [26]. In spite of this, the MG system is usually connected to the utility through switches consisting of thyristors rather than IGBTs, GTOs

etc., in AC bus from current-carrying capability and the practicability point of view, especially in high voltage and current occasions [27, 28]. In [29–31], it takes from 1/4 to 1/2 line cycle for the MG system to disconnect from the utility at zero crossing of the grid current and 5 line cycle to ensure the whole procedure at most, which is far beyond the requirement of power continuity for sensitive loads [32]. Even worse, power quality of the MG system may be further deteriorated by the turn-off delay. So, it is of great significance to take measures to ensure the fast and smooth switching of thyristors.

Compensation strategies are introduced in [33, 34] that the injecting current of the inverter is regulated to follow the instantaneous value of load when the off-grid transfer signal starts up; then, the current of thyristors can be reduced to zero and enter the blocking state quickly. But, the deficiencies are also obvious. For one thing, the injecting current of the inverter is difficult to be controlled exactly as the load current, especially when the load is nonlinear or light. On the contrary, if the load is heavy, the voltage will undergo a distortion because of the current surge. An LC series resonance circuit is designed to reverse the deviation of voltage on thyristors to accelerate the current decaying [35] while it can be implemented simply in the case of voltage sag rather than any other anomalies and the resonance is susceptible to variation of characteristics. In [36], two control methods for the transition by means of inverter output voltage amplitude and phase regulation, which depend heavily on the accurate polarity of the static transfer switch current, and measures dealing with inaccurate judgment are not explained. When the instantaneous amplitude of conducting current is too small to be sampled by the sensors (e.g., near zero) of the system controller, the polarities will not be recognized accurately. Then, there will be a high probability that the MG system fails to disconnect from the utility before working as a voltage source. To solve this problem, the MG system controller can equip a high-precision and wide-range sampling circuit in its detecting section, which may take much more cost. On the other hand, it can also set a minimum threshold to escape transition when the current or voltage is beyond the linear sampling region, which may jeopardize the power continuity and stability of local loads.

Taking the limitations of research mentioned above into consideration, this paper proposes a new strategy based on fuzzy logic control of converter output voltage to force to turn the MG thyristors off without detecting the voltage or the current polarity at the moment of islanding so that the transitory time of utility disconnecting can be minimized effectively. Firstly, an initial voltage conference is set for the MG converter to form a voltage deviation between the anode and cathode of the conducting thyristor. Then, the voltage conference is regulated according to fuzzy logic rules based on the following variation trends of its current until the conducting thyristor is turned off. The proposed method makes sure that the MG system can accomplish islanding transition rapidly at any time and any circumstance and can ensure the reliability for MG customers more comprehensively during the occurrence of utility anomaly.

The main contributions of this paper are listed as follows:

- (1) The mathematical model of compulsory turning off for thyristors in the MG system is demonstrated
- (2) In contrast to the existing control methods, an islanding transition strategy without detecting the polarity is introduced on the basis of the mathematical relationship between the time of compulsory turnoff with the parameters of main circuit and control system
- (3) Fuzzy rules of the compulsory disconnecting strategy for the thyristors through the output voltage of the MG converter are proposed to ensure islanding transition rapidly at any time and any circumstance

The remainder of this paper is organized as follows. Four different operational modes of the MG system are presented in Section 2 with a brief review about the necessity of control scheme studied in this paper. Section 3 demonstrates the control principle of compulsory turnoff for the thyristors in the MG system by the equipped converter and formulates the mathematical relationship between turn-off time with the main circuit and control parameters on the basis of a single-phase schematic diagram of the MG system. The strategy of compulsory islanding based on fuzzy logic to regulate the output voltage of the converter in the MG system is presented in Section 4. Simulation with four voltage and current situations and, practically, experimental results are displayed in Section 5 to prove the validity and effectiveness of the proposed method. Finally, conclusions are duly down.

## 2. System Description

*2.1. Structure and Working Modes of the MG System.* A typical single-phase structure diagram and controlling block of the MG power supply system integrated with the utility is mapped in Figure 1. In detail, local loads and the MG system are connected in parallel to the utility by thyristors. A solar cell and energy storage battery are connected to the DC bus and provide energy support for different operational modes of the MG system. The converter is connected to the utility through the LC filter. The MG power controller monitors the voltage of the public grid as well as the DC bus in real time and outputs driving signals to turn on/off the thyristors in order to change the connecting state between the MG system and the utility. Space vector pulse width modulation (SVPWM) is used to reduce the switching harmonics and to improve the utilization of DC voltage.

Two operational modes of the MG system are further depicted in Figure 1, which are utility-connected mode and stand-alone mode. The MG power controller changes the strategy with a software switch for the converter to achieve different output targets by working as a controlled current or voltage source relatively according to the ON/OFF state of thyristors. However, the utility-connected and stand-alone mode, which can be also defined as steady-state modes, should not transfer from one to another directly in order to avoid saturation or mutation of controlling. As is shown in

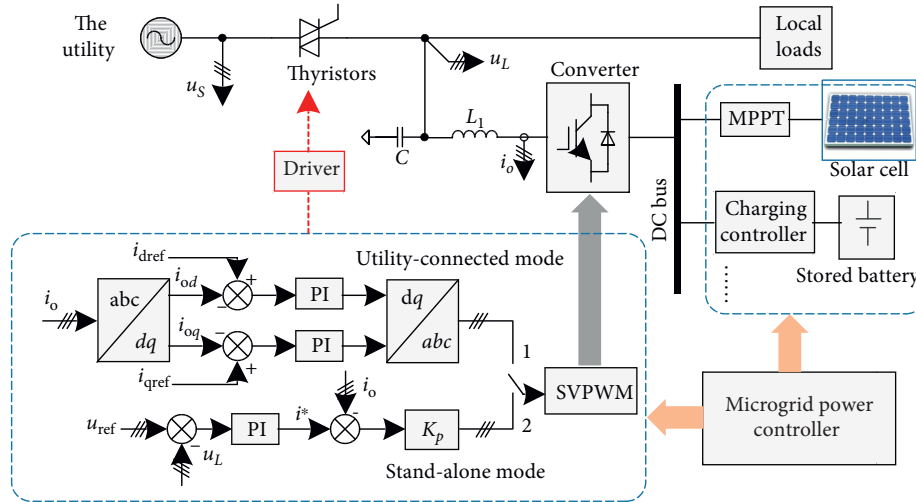


FIGURE 1: Typical single-phase structure diagram and control methods of the MG system.

Figure 2, between the utility-connected mode (mode 1) and the stand-alone mode (mode 2), there are other two transient-state modes for smooth transferring to help to prevent any sudden voltage or current changes to the load as well as to the grid, which are presynchronization (mode 3) and islanding transition (mode 4).

**2.1.1. Mode 1: Utility-Connected Mode.** If the utility is stiff, thyristors are turned ON and the MG system works at the utility-connected mode. Local loads get voltage supply from the utility. The MG converter works as a current source, which can both maintain the inactive power balance and provide active power to reduce electricity cost from the main grid if necessary. In addition, the stored battery of the distributed generating part can get charged during this mode.

**2.1.2. Mode 2: Stand-Alone Mode.** When an abnormal grid condition occurs, the thyristors are turned OFF and the MG system disconnects from the utility. In this situation, the MG system is working at the stand-alone mode and local loads get power from the MG system independently. The MG converter transfers its control strategy from current control to voltage control to ensure the continuous voltage supply for the operation of local loads.

**2.1.3. Mode 3: Presynchronization.** When the MG system is transferring from the stand-alone mode to utility-connected mode, the thyristors are switching from the OFF state to ON state and the converter adjusts the referencing instruction in accordance with the voltage of the utility [7]. If the deviation between the MG converter output and the utility voltage reduces to an acceptable range, the thyristors will be turned on and the converter will get reconnected to the utility along with local loads. This process is presynchronization [13, 33–37]. Presynchronization is the operational process that the converter regulates its output voltage (including amplitude, frequency, and phase) constantly as a controlled

voltage source after the utility is restored normally, which is totally controllable and predictable.

**2.1.4. Mode 4: Islanding Transition.** In contrast, the transition that is from utility-connected to stand-alone mode brings much more uncertainties due to the switching state of thyristors from the ON state to OFF state. When there is scheduled maintenance or planned islanding, the MG power controller can schedule the transferring of working modes in advance. If it is unplanned, which might be occasional voltage sag, swell, interruption, or even worse, then the MG system must respond in time to ensure the consecutiveness of power supply. Firstly, the thyristors should be shut off so that local loads can disconnect from the utility, and then, the MG controller should change the strategy to transfer its operation to the stand-alone mode.

However, for the MG system with thyristors as AC switches, the turn-off time ranges from microseconds to half of the fundamental cycle, which is far beyond the acceptance of sensitive loads. Therefore, it is of great significance to realize the fast switching of the working mode at any moment and to reduce the impact of the switching interval.

**2.2. Compulsory Turnoff of Thyristors in the MG System.** As a kind of semicontrolled power electronic device, once the thyristor begins to conduct, the gate loses control and the switch-on process continues until the anode-cathode current reduces to zero or below the holding value [36]. This zero-crossing turn-off prototype can be defined as natural turnoff while measures that applied to accelerate the decay of  $I_{AK}$  can be defined as compulsory turnoff.

Figure 3 shows the equivalent single-phase schematic of the integrated power supply system. The positive direction of the current in each branch is determined as the arrows in the figure. The voltage of the utility is represented as  $u_s$ , while the equivalent line impedance of the utility is  $Z_s$ . The symbol  $i_s$  is the current crossing thyristors. The load of the MG system is  $Z_L$ , while the voltage and current are  $u_L$  and  $i_L$ . As for the DG



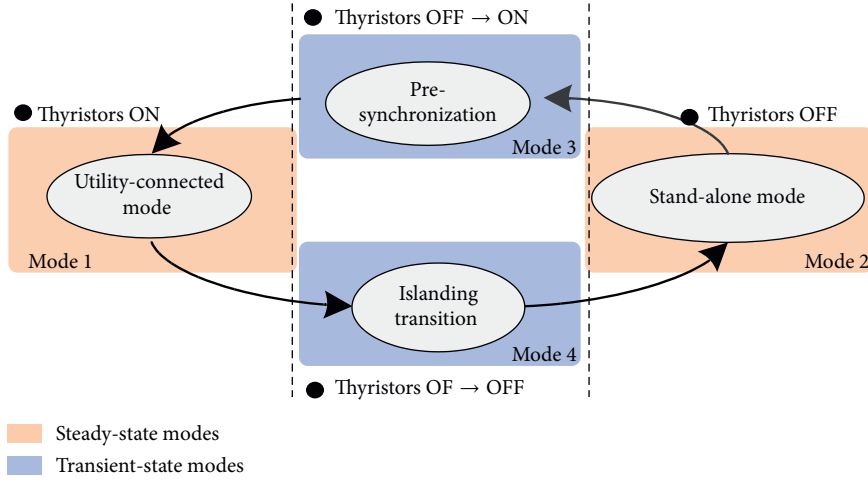


FIGURE 2: Converting relationship of different operational modes in the MG system.

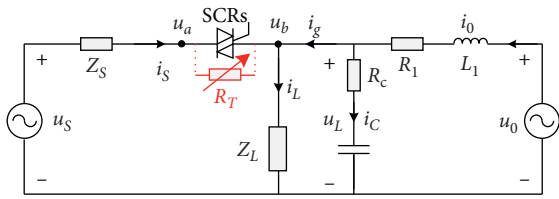


FIGURE 3: Equivalent single-phase schematic of the MG system.

system,  $u_0$  and  $i_0$  are the output voltage and current of the converter, respectively, while  $R_1$  and  $R_c$  are the parasitic resistances of the LC filter.

When the converter works as a voltage source, the amplitude and phase of the output voltage  $u_0$  are adjustable through the MG controller. If the voltage output of converter makes the anode-cathode voltage  $U_{AK}$  positive, the thyristor will continue to conduct until the next zero point of current. Even worse, an inrush and uncontrolled current caused by the parallel connecting of two voltage sources will trigger the protection mechanism [7]. If the MG converter makes the voltage  $U_{AK}$  negative, the thyristor can be turned off in a very short time and adverse effects of modes transferring on local loads, especially sensitive loads, can be eliminated [37]. Ignoring the voltage drop of thyristors, there are four situations according to the instantaneous value of the current and the voltage to satisfy the condition of compulsory turnoff:

- (1) If  $i_s > 0$  and  $u_a > 0$ , then  $u_b > u_a > 0$
- (2) If  $i_s > 0$  and  $u_a < 0$ , then  $u_b > u_a$
- (3) If  $i_s < 0$  and  $u_a > 0$ , then  $u_b < u_a$
- (4) If  $i_s < 0$  and  $u_a < 0$ , then  $u_b < u_a < 0$

This can be summarized as

$$\begin{cases} u_b - u_a > 0, & i_s > 0, \\ u_b - u_a < 0, & i_s < 0. \end{cases} \quad (1)$$

During compulsory turnoff, the output voltage reference  $u_{ref}$  of the MG converter can be expressed as

$$u_{ref} = u_a + \Delta u, \quad (2)$$

where  $\Delta u$  is a kind of regulative variable that can form a voltage deviation between the utility and the converter and  $u_a$  is the measuring point of system voltage.

When the conducting thyristor begins to turn off, it can be seen as a variable resistor  $R_T$  equivalently [28], of which the relationship between resistance and current under different voltage is shown in Figure 4.  $I_{AK}$  represents the current flowing from the anode to cathode of the conducting thyristor while  $U_{KA}$  represents the reverse voltage. It is indicated that the resistance  $R_T$  increases as  $I_{AK}$  decreases. In addition, if the resistance keeps its value in  $R_1$ , a greater  $U_{KA}$  will bring a faster decaying speed for  $I_{AK}$ . Meanwhile, if the current keeps its value in  $I_2$ , the resistance will increase along with the  $U_{KA}$ , which means a greater suppression for  $I_{AK}$ .

The relationship between the output voltage and the decaying time of current can be calculated during the compulsory turn-off process. For the studied system in Figure 3, there are equations as follows:

$$\begin{cases} u_L = u_0 - R_1 i_0 - L_1 \frac{di_0}{dt}, \\ i_L = \frac{u_L}{Z_L} = i_s + i_o - i_c. \end{cases} \quad (3)$$

The parasitic resistances  $R_1$  and  $R_c$  are omitted in order to facilitate the analysis; then, the current  $i_c$  can be represented as

$$\begin{aligned} i_c &= C \frac{du_C}{dt}, \\ &= C \frac{du_L}{dt}. \end{aligned} \quad (4)$$

Applying equation (4) to equation (3), the voltage  $u_L$  can be expressed as

$$u_L = u_0 - \frac{L_1}{Z_L} \frac{du_L}{dt} - L_1 C \frac{d^2 u_L}{dt^2} + L_1 \frac{di_s}{dt}. \quad (5)$$

If the voltage referring instruction  $u_{ref}$  and the system current  $i_s$  are both defined as sinusoidal variables,



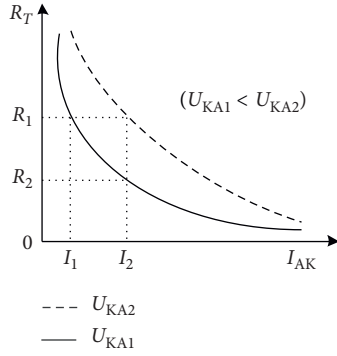


FIGURE 4: The equivalent relationship curves of resistance and current for thyristors.

$$\begin{cases} u_{\text{ref}} = U_m \sin \omega t, \\ i_s = I_m \sin(\omega t + \theta), \end{cases} \quad (6)$$

where  $\omega$  is the angular frequency and  $\theta$  is the phase angle. In addition, if  $i_s$  decays to zero in a very short time  $\Delta t$  and  $u_L$  tracks the  $u_{\text{ref}}$  with no deviation ( $u_L = u_{\text{ref}}$ ), then equation (5) can be converted as

$$L_1 \frac{I_m \sin(\omega t + \theta)}{\Delta t} = A \sin \omega t - B \cos \omega t, \quad (7)$$

where  $A = (\omega^2 L_1 C + K_U - 1)U_m$ ,  $B = \omega U_m L_1 / Z_L$ .

Output voltage  $u_0$  is replaced by  $u' = K_U U_m \sin \omega t$ , which can be seen as an ideal linear proportional control model.

Then, the turn-off time of the conducting thyristor  $\Delta t$  can be calculated as

$$\Delta t = \frac{L_1 I_m \sin(\omega t + \theta)}{U_m [(\omega^2 L_1 C + K_U - 1) \sin \omega t - L_1 \omega \cos \omega t / Z_L]}. \quad (8)$$

Regardless of the unchangeable variables ( $L_1$ ,  $I_m$ ,  $C$ ,  $\omega$ ,  $\theta$ , and  $Z_L$ ), it is indicated that the turn-off time depends on three elements:

- (1) Amplitude of the referring instruction,  $U_m$
- (2) Proportional control factor,  $K_U$
- (3) Occurring time of islanding transition,  $t$

Anyway, the occurring time  $t$  of an islanding event is unpredictable, but  $U_m$  and  $K_U$  can be calculated and then regulated by the controller. In equation (8), the decaying time of current  $\Delta t$  is in an inverse proportion with  $U_m$  and  $K_U$ , which means the bigger the value of  $U_m$  and  $K_U$ , the faster the conducting thyristor will be turned off. Also, it is also corresponded with Figure 4 that the current  $I_{AK}$  has a greater equivalent resistance under  $U_{KA2}$  when the value is greater than  $U_{KA1}$ .

The value of  $\Delta u$  in equation (2) depends on the polarity of  $i_s$ , which can be recognized correctly only when the value of sampling is valid. As is shown in Figure 5, the hatched section is the linear region of sampling. For the positive part (vice versa), if the instantaneous value of the actual waveform is over the superior limit of the linear region sampling ( $t_2 \sim t_3$ ), then the sampling value will be clamped in the maximum and

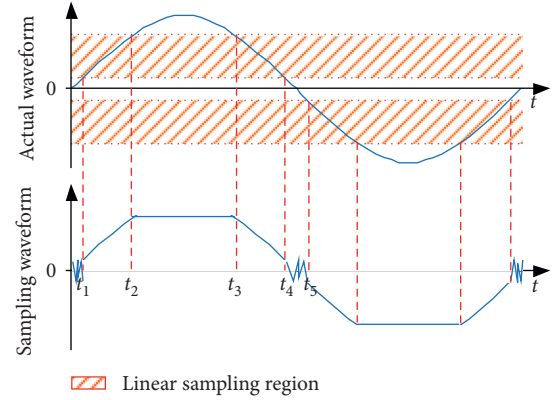


FIGURE 5: Actual and resulting waveforms beyond the linear region of sampling.

the sampling waveform will be distorted. If the instantaneous value of the actual waveform is below the inferior limit of the linear sampling region ( $0 \sim t_1$  and  $t_4 \sim t_5$ ), then the sampling value will be overwhelmed by noise. Generally, different kinds of filter will be designed for the sampling data to obtain a smooth waveform. But, the phase delay of filters will also bring influence on the accuracy of polarity judgment.

For the studied system in this paper, when the instantaneous value of  $i_s$  is near zero, the polarity is hard to be acquired accurately because of sampling noise. If the polarity of  $i_s$  that the MG power controller detecting is contrary to actuality when islanding occurs, the voltage between the anode and the cathode of the thyristor is still positive and the thyristor will keep conducting. There are two consequences as follows.

On one hand, if the converter retains the current control strategy or shuts off its output until the conducting thyristor turns off, it will result in a longer shutdown time or an interruption of power supply for local loads even worse. On the other hand, if the converter changes the strategy to voltage control before the thyristor turning off completely, then it will connect parallelly with the public grid as a voltage source. In this case, it might cause a surge of current of the converter and a further deterioration for the voltage quality, which may trigger the local protection mechanism.

In order to get rid of the limitations of polarity detection mentioned above, a compulsory turn-off strategy based on fuzzy control of converter output voltage is proposed in this paper. This strategy is especially applicable when the polarity of the current flowing across the thyristor cannot be recognized accurately by the sampling circuit. In detail, an initial value of voltage reference instruction is given firstly to formulate a planned voltage and attempt to turn off the conducting thyristor. Then, the voltage reference and the control parameters will be adjusted dynamically according to the variation trend of the thyristors' current during the turn-off process.

### 2.3. Islanding Transition Strategy with Fuzzy Control

2.3.1. *Foundation of Fuzzy Logic Control.* The fuzzy logic controller relates the controller output and the inputs by

using a list of inference rules. A basic structure of a typical fuzzy control block diagram is given in Figure 6. The inputs of the fuzzy controller consist of the deviation  $e$  and the change rate of the deviation  $ec$  between the output  $r$  and input  $r^*$ . The output of the fuzzy controller is carried out according to the fuzzy rules and is converted into variables that can be identified by the controlled system, which finally regulate the output.

**2.3.2. Design of Fuzzy Control for Island Transition.** According to the on-off characteristics of the thyristors, the decreasing speed of the current is related to the instantaneous value of itself before switching off and the reverse voltage between the anode and cathode. The smaller the instantaneous current value and the larger the reverse voltage are, the faster the current attenuation will be. As shown in Figure 3, the voltage  $u_a$  is clamped by the utility. However, a fuzzy controller can be designed according to the basic characteristics of thyristors and the connecting relation of the MG system, with which the current  $i_s$  can be regulated through  $u_L$  indirectly and the referring instruction can be adjusted dynamically according to the instantaneous value of  $i_s$  in order to realize the compulsory turnoff of the thyristors. In addition, the output voltage of the MG converter, which is working as a voltage source, is also affected by the closed-loop control parameters. Hence, as shown in Figure 7, the inputs of the fuzzy controller are set as the deviation value and its rate of change between two adjacent sampling values of  $i_s$ , and the outputs of the fuzzy controller are the amount of changes for the amplitude of the instruction  $u_{\text{ref}}$  and the voltage closed-loop control factor  $K_p$ .

The inputs of the fuzzy controller  $e(k)$  and  $ec(k)$  are obtained, respectively, as equations (9) and (10), of which the values are directly related to the instantaneous current  $i_s$  and the sampling period  $T$ . To prevent an overcurrent between two adjacent sampling points in time,  $T$  and  $\Delta U$  should be restricted as equation (11), where  $Z_s$  is the short-circuit impedance of the utility and  $I_p$  is the trigger threshold of overcurrent protection for the MG system.

$$e(k) = |i_s(k) - i_s(k-1)|, \quad (9)$$

$$ec(k) = \frac{de(k)}{dt} = \frac{e(k) - e(k-1)}{T}, \quad (10)$$

$$\frac{\Delta U}{T|Z_s|} \leq I_p. \quad (11)$$

Due to the actual range of the inputs and outputs variables, the basic level in the continuous domain and the quantitative level in discrete domains are shown in Table 1, respectively.

The fuzzy subset of  $e$ ,  $ec$ , and  $\Delta U$  are set as {NB, NM, NS, PS, PM, PB} and the subset of  $\Delta K_p$  is set as {NB, NM, NS, ZE, PS, PM, PB}. In addition, each input and output follows the triangle subjection function, which is shown in Figures 8(a) and 8(b).

**2.3.3. Fuzzy Logic Rules.** According to the fuzzy idea of compulsory turnoff and the principle of "if  $A$  and  $B$  and then  $C$ ", the fuzzy control rule is shown in Tables 2 and 3.

If the deviation as well as its rate of change between the absolute values of two adjacent sampling for  $i_s$  is positive and increasing, it indicates that the voltage on the anode and the cathode of the thyristor is still positive as a conducting state. In this case, the polarity of  $\Delta U$  should be changed. If the rate of change tends to decrease with positive deviation, the amplitude of  $\Delta U$  should be increased properly. If the deviation change of  $i_s$  is almost constant or increasing gradually,  $\Delta K_p$  and  $\Delta U$  should be both increased so that the divergent trend of  $i_s$  can be slowed down. But, an improper value of  $\Delta K_p$  will bring unexpected overshoot during the control process and affect the stability of the voltage output by the MG converter. So,  $\Delta K_p$  should be selected properly.

If the deviation between the absolute values of two adjacent sampling for  $i_s$  is negative, it indicates that the current  $i_s$  has begun to move towards zero. When the changing rate of  $i_s$  is large, it indicates that the A-K current is decaying very fast, then the parameter should be just kept as the former size. If the changing rate of  $i_s$  decreases from a large value to a small value gradually, the amplitude of  $\Delta U$  can be increased properly to accelerate the decay of  $i_s$ . In addition, the value of  $\Delta K_p$  should increase properly if the deviation of  $i_s$  keeps a small rate.

The referencing instruction of the voltage and close-loop controlling coefficient after regulating by the fuzzy control can be obtained as follows:

$$u_{\text{ref}}(k) = u_{\text{ref}}(k-1) + \Delta U(k), \quad (12)$$

$$K_p(k) = K_p(k-1) + \Delta K_p(k). \quad (13)$$

### 3. Simulation and Results

Simulated performances of the proposed strategy for compulsory islanding transition are evaluated in this section compared to the cases of natural turnoff and traditional forced turnoff with false polarity detecting. As discussed before, there are four possible combinations with different polarities of  $i_s$  and  $u_s$  when an islanding event occurs. To demonstrate the implementation process of the studied strategy, a specific time is selected, respectively, for instance in each case. In spite of different loads, it is universally applicable to any other time when the instantaneous values of  $i_s$  and  $u_s$  meet each condition of polarities under the four scenarios mentioned in equation (1).

Assume that, initially, the MG converter is operating in the grid-connected mode and each scenario takes the same initial value of  $\Delta U$ . Before the sag of the utility, there is simply a small deviation between the utility and the local loads voltage, which can also be seen as the sum of thyristor conduction voltage and line loss drop equivalently. Main parameters of the simulation model are in Table 4.

**3.1. Natural Turnoff.** Figure 9 shows the natural turn-off process of thyristors when there is voltage sag at an instant of 0.0601 s. It can be discovered from Figure 9(a) that it takes

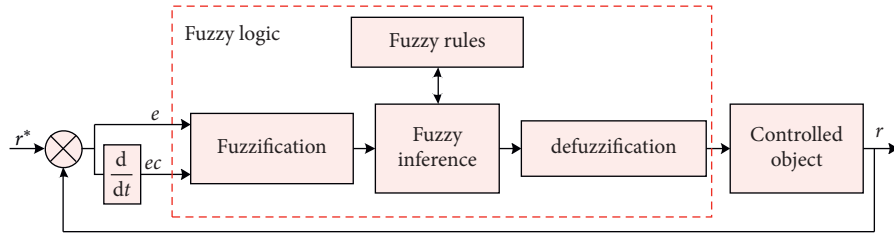


FIGURE 6: Block diagram of fuzzy control.

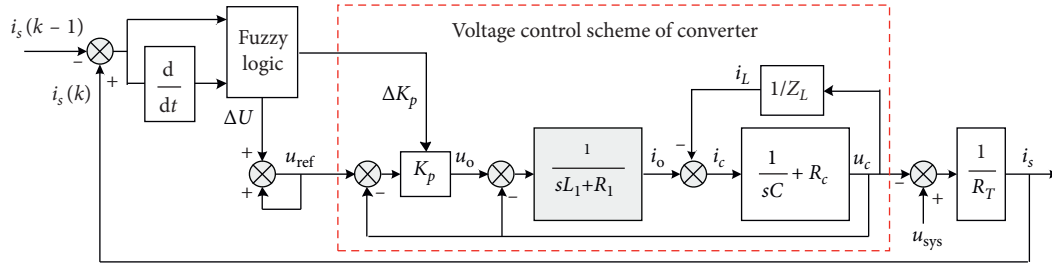


FIGURE 7: Control diagram of fuzzy control for islanding transition.

TABLE 1: The basic level and the quantitative level of variables in fuzzy control.

Variables	Basic level	Quantitative level
$e$	$\{-60, 60\}$	$\{-3, -2, -1, 1, 2, 3\}$
$ec$	$\{-200, 200\}$	$\{-3, -2, -1, 1, 2, 3\}$
$\Delta U$	$\{-60, 60\}$	$\{-3, -2, -1, 1, 2, 3\}$
$\Delta K_p$	$\{-3, 3\}$	$\{-3, -2, -1, 0, 1, 2, 3\}$

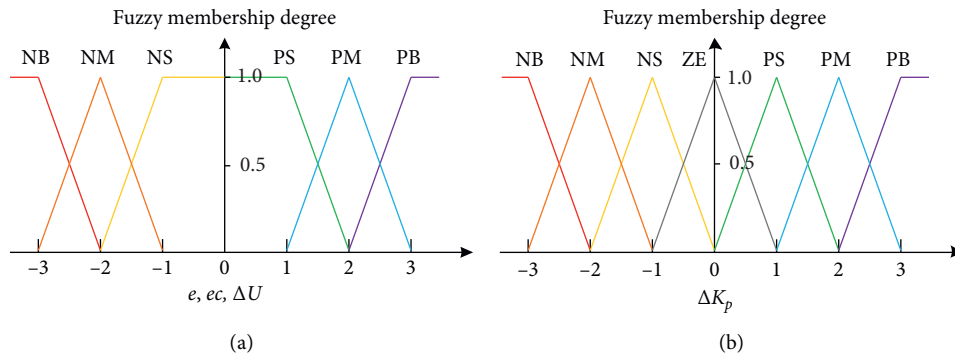


FIGURE 8: Membership functions of the input and output variables of the fuzzy controller: (a) Membership functions of  $e$ ,  $ec$ , and  $\Delta U$ . (b) Membership functions of  $\Delta K_p$ .

TABLE 2: Fuzzy control rule of  $\Delta U$ .

$\Delta U$	EC						
	NB	NM	NS	PS	PM	PB	
E	NB	NM	NM	NB	PB	PM	PM
	NM	NS	NS	NM	PM	PS	PS
	NS	NS	NS	NS	PS	PS	PS
	PS	NS	NS	NM	NM	NB	NB
	PM	NS	NM	NM	NB	NB	NB
	PB	NM	NM	NM	NB	NB	NB

TABLE 3: Fuzzy control rule of  $\Delta K_p$ .

$\Delta K_p$	EC						
	NB	NM	NS	PS	PM	PB	
E	NB	PB	PM	PS	ZE	ZE	NB
	NM	PM	PS	ZE	ZE	ZE	NS
	NS	PS	ZE	ZE	ZE	NS	NM
	PS	NS	ZE	ZE	ZE	ZE	PS
	PM	ZE	PS	PM	PM	PM	PB
	PB	PS	PS	PM	PM	PB	PB

TABLE 4: Main parameters of simulation.

Parameters	Initial values (unit)
Phase voltage value of the utility, $U_{sys}$	220 (V)
Frequency of the utility voltage, $f$	50 (Hz)
Effective value of voltage sag, $U_{sag}$	60 (V)
Resistance of simulated load, $R_L$	2 ( $\Omega$ )
Inductance of simulated load, $L$	4 (mH)
Inductor of the LC filter, $L_1$	0.4 (mH)
Capacitor of the LC filter, $C$	20 ( $\mu$ F)
Sampling frequency, $f_s$	10 (kHz)
Voltage closed-loop control factor, $K_p$	4
Adjustment of voltage control factor, $\Delta K_p$	0
Adjustment of voltage reference, $\Delta U$	20 (V)

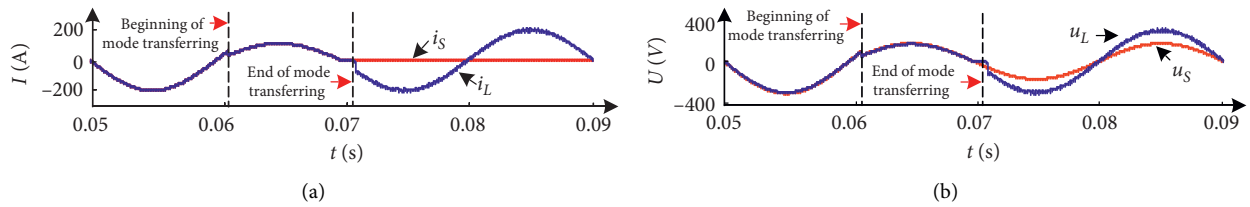


FIGURE 9: Simulation waveforms of natural turnoff for islanding transition: (a) simulation waveforms of the system and load current. (b) Simulation waveforms of the utility and load voltage.

almost half of the line cycle for the conducting thyristor to shut off completely. Then, the converter in the MG system works as a voltage source, which leads an interruption to continuity for the load in Figure 9(b).

### 3.2. Compulsory Turnoff with False Polarity Detecting.

Figure 10 shows the unsuccessful disconnecting process when the recognition of current polarity is false. In Figure 10(a), the current  $i_s$  is undergoing a surge during the turning-off process of the conducting thyristor in that case. Furthermore, as shown in Figure 10(b), the output voltage of the converter is seriously deteriorated because of the short-term large current injection. After that, distortion is brought to the load current and the continuity and stability of the load operation are affected at the same time, which is consistent with the foregoing content in this paper.

### 3.3. Successful Compulsory Disconnection

**3.3.1. Islanding Transition at the Moment When  $i_s > 0$  and  $u_s > 0$  (E.g., the Instant of 0.062 s).** If the polarity of the current  $i_s$  is beyond the sampling linear region with positive

polarity actually at the time of 0.062 s and the output voltage of the converter is equal to the referring instruction, then the condition of compulsory turnoff is satisfied as the initial value of +20 (V) for  $\Delta U$ . So, the current  $i_s$  decays to zero rapidly as is shown in Figure 11(a). Figure 11(b) shows that the value of  $\Delta U$  has not changed for the stability of the MG system. When the thyristors have been turned off completely, the referring instruction will be switched to the state before the occurrence of islanding. Then, the converter will supply power for the local loads independently. It takes a very short time to obtain the whole process of islanding transfer and leads to no mutation or other abnormal scenarios no matter for the voltage or the current of local loads.

**3.3.2. Islanding Transition at the Moment When  $i_s > 0$  and  $u_s < 0$  (E.g., the Instant of 0.0505 s).** If the islanding mode transfers at the time of 0.0505 s, the initial value of +20 (V) for  $\Delta U$  will lead the thyristor to continue to conduct. Then, the current  $i_s$  tends to increase, as is shown in Figure 12(a). When the MG power controller detects that the thyristor current does not decay, the fuzzy controller adjusts the polarity of  $\Delta U$ , and the converter reference instruction responds to the change of polarity quickly. Figure 12(b) shows

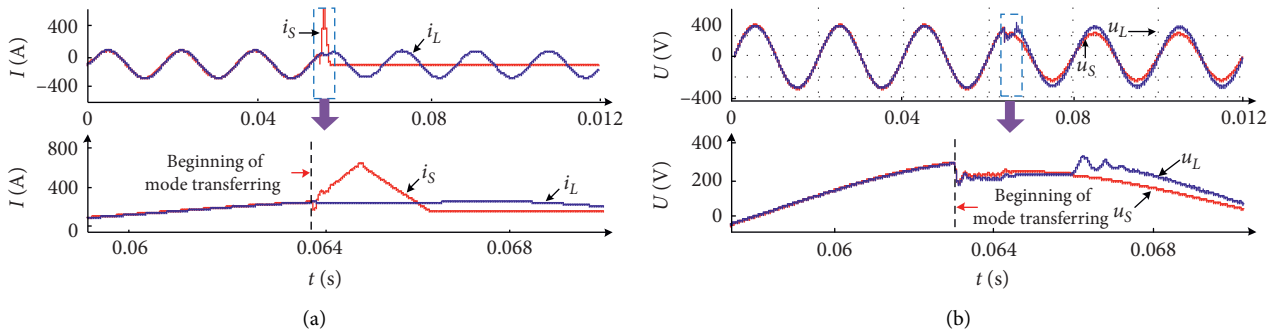


FIGURE 10: Simulation waveforms of compulsory turnoff with false polarity detecting: (a) simulation waveforms of the system and load current. (b) Simulation waveforms of the utility and load voltage.

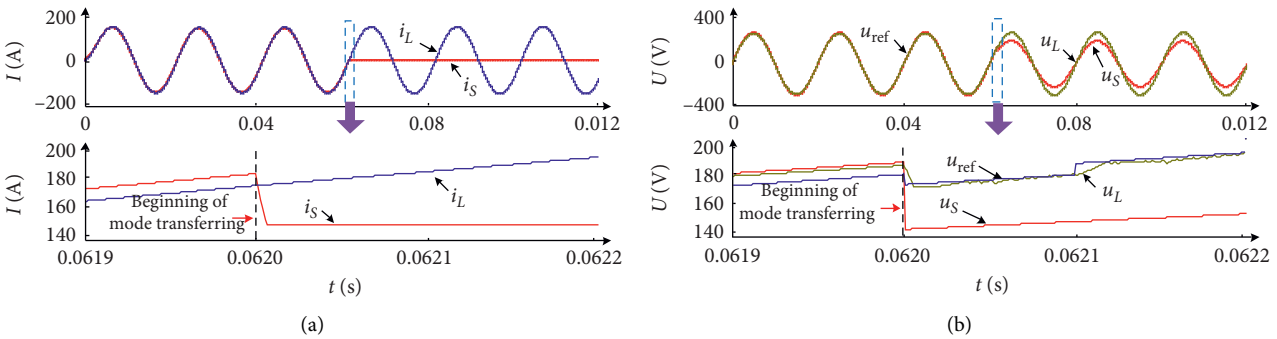


FIGURE 11: Simulation waveforms of islanding transition at time 0.062 s: (a) simulation waveforms of the system and load current. (b) Simulation waveforms of the utility, reference, and load voltage.

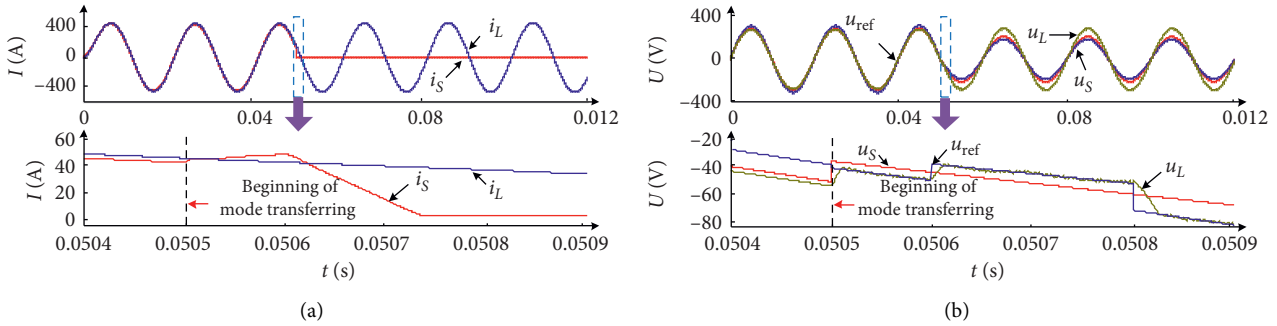


FIGURE 12: Simulation waveforms of islanding transition at time 0.0505 s: (a) simulation waveforms of the system and load current. (b) Simulation waveforms of the utility, reference, and load voltage.

that the current  $i_S$  begins to decay as the backpressure between the anode and cathode rapidly appears after the output voltage of the converter tracking the reference instruction. At the time of 0.0508 s, the conducting thyristor can be considered turned off completely. Then, the converter readjusts the reference instruction to provide standard voltage to local loads.

3.3.3. *Islanding Transition at the Moment When  $i_S < 0$  and  $u_S > 0$  (E.g., the Instant of 0.0615 s).* Figure 13 shows the islanding mode transfer occurs when the instantaneous value of the current  $i_S$  is negative and the utility voltage is positive. Because the initial value of  $\Delta U$  is +20 (V) and the

initial situation is considered to be  $u_L > u_S$ , the condition of compulsory turnoff cannot be met and the current  $i_S$  experiences a trend of gradual increase in Figure 13(a). After detecting the abnormal increasing current, the fuzzy controller adds the opposite polarity of  $\Delta U$  to the voltage referring instruction to obtain the reserve voltage in a very short time.

3.3.4. *Islanding Transition at the Moment When  $i_S < 0$  and  $u_S < 0$  (E.g., the Instant of 0.0059 s).* Similar to the curves in Figure 11, the initial value of  $\Delta U$  makes voltage across the conducting thyristor negative at the time of 0.059 s, which can ensure the compulsory turn-off process. In Figure 14(a),

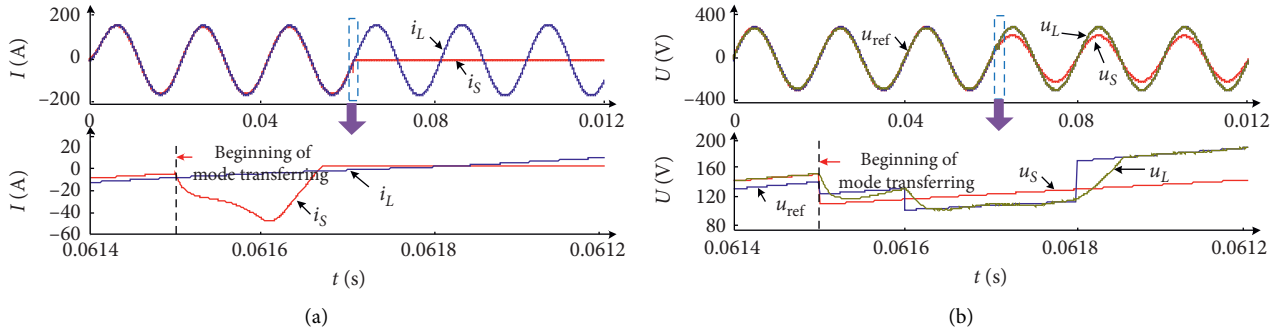


FIGURE 13: Simulation waveforms of islanding transition at time 0.0615 s: (a) simulation waveforms of the system and load current. (b) Simulation waveforms of the utility, reference, and load voltage.

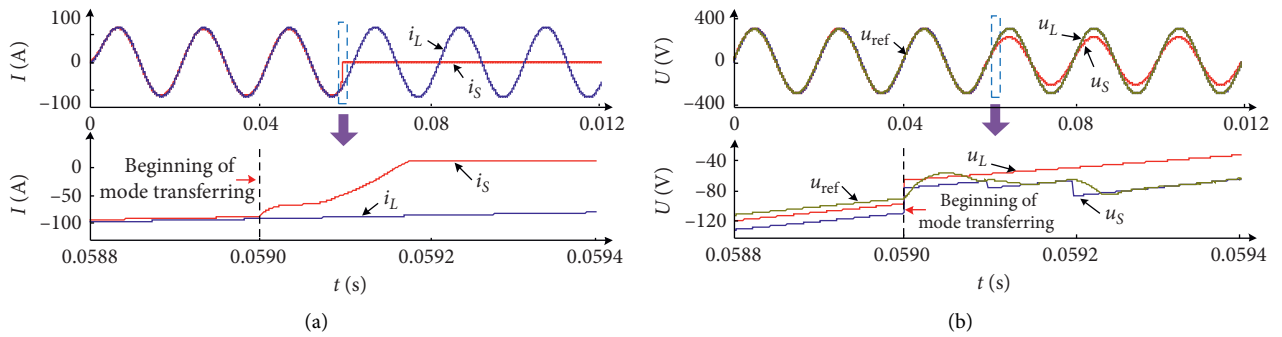


FIGURE 14: Simulation waveforms of islanding transition at time 0.059 s: (a) simulation waveforms of the system and load current. (b) Simulation waveforms of the utility, reference, and load voltage.

the current  $i_S$  does not increase to the reverse direction but falls rapidly. Meanwhile, it is shown in Figure 14(b) that the original parameters of voltage control closed-loop fail to make the output voltage track referring instruction well and the changing rate of the current  $i_S$  is declined at the beginning of the compulsory turn-off process. So, the proportional coefficient  $K_p$  is regulated by the designed fuzzy controller in order to improve the dynamic response speed of the voltage control loop.

#### 4. Practical Experiment and Results

Practical experiment is conducted to prove the effectiveness of the disconnecting strategy proposed in this paper. In actual MG systems, the kinds of sensitive loads are diverse and the voltage-current curves vary as well. Without loss of generality, a common resistance type and a nonlinear single-phase rectifier bridge are selected as the experimental load with low current level, so the time of disconnection can be unspecified in practical experiment to verify the applicability of the studied strategy. Parameters of the controller are the same as in Table 4.

Figure 15 shows the load current with natural turnoff of thyristors when the MG system disconnects from the utility. As it can be seen, the load current is discontinuous and the stand-alone mode of the MG system begins until load current reaches the first zero crossing. It takes almost 1/4 fundamental cycle. For sensitive loads, this kind of discontinuity might be intolerable.

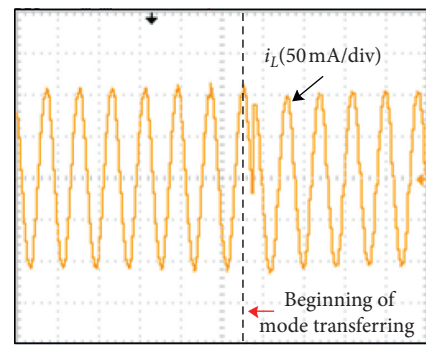


FIGURE 15: Waveform of load current with natural turnoff for thyristors.

Figure 16 shows the system current  $i_S$  and the load current  $i_L$  during the transferring from the utility-connected mode to stand-alone mode when the recognition of polarity is incorrect. It shows that the thyristor is still conducting when the recognition of polarity for the current  $i_S$  is incorrect and undergoes an inrush. Meanwhile, the load current is oscillating periodically, which will affect the stable operation of the load.

With the strategy proposed in this paper, experimental results based on fuzzy logic indicate the correctness and validity in Figures 17 and 18 with linear load and nonlinear load, respectively. It shows that the transient progress of islanding barely bring any impact on the continuity and



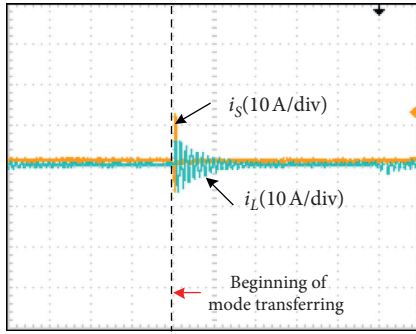


FIGURE 16: Waveforms of the system and load current with compulsory turnoff when the recognition of polarity is incorrect.

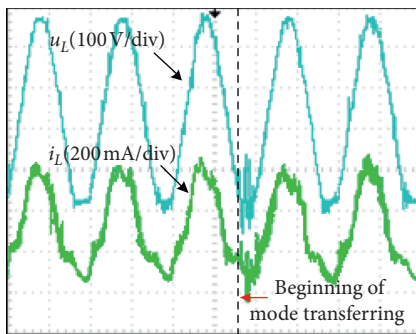


FIGURE 17: Waveforms of voltage and current with compulsory turnoff for linear load.

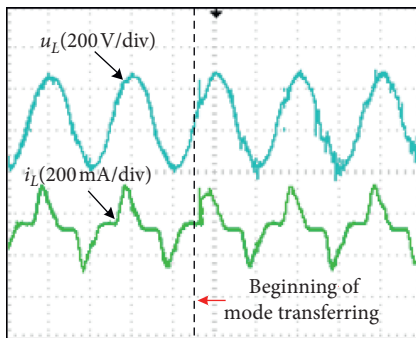


FIGURE 18: Waveforms of voltage and current with compulsory turnoff for nonlinear load.

stability of load without detecting the polarity of voltage or current, which can be accepted for almost all of the existing sensitive loads.

## 5. Conclusions

For the microgrid system, the mode transition, especially when it disconnects from the utility, must be transient, seamless, and reliable. If the current exceeds the linear sampling region of the system, it is difficult to ensure the rapidity and stability of mode transition.

In this paper, it proposes a compulsory turn-off strategy for the thyristors when the MG system

disconnects from the utility. Rather than detecting the voltage or current polarity, the proposed strategy can realize fast turning off for the thyristors at any time by adjusting the converter reference instruction and closed-loop control parameters dynamically with fuzzy logic. Then, the disconnection process will not be affected by the software or hardware of the MG system and will be more applicable and efficient. However, a more sophisticated strategy can be extended from future studies, and there are still problems, which need to be further researched at the same time.

## Nomenclature

MG:	Microgrid
DG:	Distributed generating
BS:	Battery storing
SSR:	Solid-state relay
PI:	Proportional integral
SVPWM:	Space vector pulse width modulation
NB:	Negative big
NM:	Negative middle
NS:	Negative small
PS:	Positive small
PM:	Positive middle
PB:	Positive big
$u_s, i_s$ :	Voltage and current of the utility (V, A)
$I_m$ :	Amplitude of $i_s$ (A)
$Z_s$ :	Equivalent impedance of the utility ( $\Omega$ )
$u_L, i_L$ :	Voltage and current of local loads (V, A)
$Z_L$ :	Equivalent impedance of local loads ( $\Omega$ )
$u_o, i_o$ :	Output voltage and output current of the converter (V, A)
$L_1, R_1$ :	Inductor and parasitic resistance of the LC filter (H, $\Omega$ )
$C, R_c$ :	Capacitor and parasitic resistance of the LC filter (F, $\Omega$ )
$i_{dref}, i_{qref}$ :	Current reference in the $d$ -axis and $q$ -axis (A)
$i_{0d}, i_{0q}$ :	Component of $i_o$ in the $d$ -axis and $q$ -axis (A)
$u_{ref}$ :	Voltage reference of the converter (V)
$U_m$ :	Amplitude of voltage reference (V)
$i^*$ :	Current reference of the voltage control loop (A)
$i_g$ :	Grid-connected current of the converter (A)
$u_a$ :	Voltage near the side of the utility
$u_b$ :	Voltage near the side of the MG converter
$R_T$ :	Equivalent resistance of the thyristor when shutting off ( $\Omega$ )
$U_{AK}, I_{AK}$ :	Anode-cathode voltage and current of the thyristor (V, A)
$U_{KA}$ :	Cathode-anode voltage of the thyristor (V)
$K_U$ :	Equivalently proportional coefficient
$e, ec$ :	Inputs of the fuzzy controller
$\Delta U, \Delta K_p$ :	Outputs of the fuzzy controller
$K_p$ :	Proportional coefficient of the voltage loop.

## Data Availability

The data used to support the findings of this study are included within the article.

## Conflicts of Interest

The authors declare that there are no conflicts of interest regarding the publication of this paper.

## References

- [1] E. Unamuno and J. A. Barrena, "Hybrid AC/DC microgrids-part I: review and classification of topologies," *Renewable and Sustainable Energy Reviews*, vol. 52, pp. 1251–1259, 2015.
- [2] A. Cagnano, E. D. Tuglie, and P. Mancarella, "Microgrids: overview and guidelines for practical implementations and operation," *Applied Energy*, vol. 258, Article ID 114039, 2020.
- [3] P. Li, X. Guan, J. Wu, and D. Wang, "An integrated energy exchange scheduling and pricing strategy for multi-microgrid system," in *Proceedings of the IEEE Region 10 Conference*, pp. 1–5, IEEE, Xi'an, China, October 2013.
- [4] D. S. Ramos, T. E. D. Carpio-Huayllas, and R. L. Vasquez-Arnez, "Load shedding application within a microgrid to assure its dynamic performance during its transition to the islanded mode of operation," *Energy and Power Engineering*, vol. 5, no. 7, pp. 437–445, 2013.
- [5] I. Serban, "A control strategy for microgrids: seamless transfer based on a leading inverter with supercapacitor energy storage system," *Applied Energy*, vol. 221, pp. 490–507, 2018.
- [6] S. Huang, W. Pei, and L. Kong, "Control algorithm research on seamless transfer for PV system during intentional islanding," in *Proceedings of the ISES Solar World Congress 2007 III*, pp. 1637–1641, Springer, Beijing, China, September 2008.
- [7] R. Tirumala, N. Mohan, C. Henze, and I. O. E. A. Engineer, "Seamless transfer of grid-connected PWM inverters between utility-interactive and stand-alone modes," in *Proceedings of the Applied Power Electronics Conference and Exposition Seventeenth Annual IEEE*, vol. 2, pp. 1081–1086, IEEE, Dallas, TX, USA, March 2002.
- [8] B. Singh, G. Pathak, and B. K. Panigrahi, "Seamless transfer of renewable-based microgrid between utility grid and diesel generator," *IEEE Transactions on Power Electronics*, vol. 33, no. 10, pp. 8427–8437, 2018.
- [9] C. Chang and Y. Chang, "Energy storage systems for seamless mode transfer in microgrid," in *Proceedings of the 2011 IEEE International Conference on Power Electronics and Drive Systems*, pp. 799–802, Singapore, December 2011.
- [10] L. Jia, Y. Zhu, S. Du, and Y. Wang, "Analysis of the transition between multiple operational modes for hybrid AC/DC microgrids," *CSEE Journal of Power and Energy Systems*, vol. 4, no. 1, pp. 49–57, 2018.
- [11] I. Ahmed, L. Sun, and X. Chen, "A novel control scheme for microgrid inverters seamless transferring between grid-connected and islanding mode," in *Proceedings of the 2017 (China) International Electrical and Energy Conference*, pp. 75–80, IEEE, Beijing, China, October 2017.
- [12] M. Abadi and S. M. Sadeghzadeh, "A control approach with seamless transition capability for a single-phase inverter operating in a microgrid," *International Journal of Electrical Power & Energy Systems*, vol. 111, pp. 475–485, 2019.
- [13] G. Lou, W. Gu, J. Zhu, P. Li, and X. Zhang, "A novel control strategy for the seamless transfer of microgrids based on disturbance observer," *International Journal of Electrical Power & Energy Systems*, vol. 118, Article ID 105804, 2020.
- [14] A. H. Etemadi and R. Iravani, "Supplementary mechanisms for smooth transition between control modes in a microgrid," *Electric Power Systems Research*, vol. 142, pp. 249–257, 2017.
- [15] W. Issa, A. E. Khateb, N. Anani, and M. Abusara, "Smooth mode transfer in AC microgrids during unintentional islanding," *Energy Procedia*, vol. 134, pp. 12–20, 2017.
- [16] W. Zhang, H. Liu, W. Wang, and P.C. Loh, "Seamless transfer scheme for parallel PV inverter system," *IET Power Electronics*, vol. 13, no. 5, Article ID 101049, 2020.
- [17] J. Hmad, A. Houari, H. Trabelsi, and M. Machmoum, "Fuzzy logic approach for smooth transition between grid-connected and stand-alone modes of three-phase DG-inverter," *Electric Power Systems Research*, vol. 175, Article ID 105892, 2019.
- [18] M. Ganjian-Aboukheili, M. Shahabi, Q. Shafiee, and J. M. Guerrero, "Seamless transition of microgrids operation from grid-connected to islanded mode," *IEEE Transactions on Smart Grid*, vol. 11, no. 3, pp. 2106–2114, 2020.
- [19] H. Ameli, E. Abbasi, M. T. Ameli, and G. Strbac, "A fuzzy-logic-based control methodology for secure operation of a microgrid in interconnected and isolated modes," *International Transactions on Electrical Energy Systems*, vol. 27, no. 11, Article ID e2389, 2017.
- [20] H. Lhachimi, Y. Sayouti, and Y. E. Kouari, "Control of a flexible microgrid during both modes of operations with presence of nonlinear loads," *Journal of the Franklin Institute*, vol. 357, no. 11, pp. 6498–6538, 2020.
- [21] S. Choudhury, T. P. Dash, P. Bhowmik, and P. K. Rout, "A novel control approach based on hybrid fuzzy logic and seeker optimization for optimal energy management between micro-sources and supercapacitor in an islanded microgrid," *Journal of King Saud University-Engineering Sciences*, vol. 32, no. 1, pp. 27–41, 2020.
- [22] J. P. Roselyn, A. Ravi, D. Devaraj, R. Venkatesan, M. Sadees, and K. Vijayakumar, "Intelligent coordinated control for improved voltage and frequency regulation with smooth switchover operation in LV microgrid," *Sustainable Energy, Grids and Networks*, vol. 22, Article ID 100356, 2020.
- [23] J. Xiang, F. Ji, H. Nian, J. Zhang, and H. Deng, "Seamless transfer of single-phase utility interactive inverters with a synchronized output regulation strategy," *Journal of Power Electronics: A Publications of The Korean Institute Of Power Electronics*, vol. 16, no. 5, pp. 1821–1832, 2016.
- [24] X. Liao, Z. Guo, and D. Sha, "Voltage magnitude and frequency control of three-phase voltage source inverter for seamless transfer," *IET Power Electronics*, vol. 7, no. 1, pp. 200–208, 2014.
- [25] C. Sun, G. Joos, S. Q. Ali et al., "Design and real-time implementation of a centralized microgrid control system with rule-based dispatch and seamless transition function," *IEEE Transactions on Industry Applications*, vol. 56, no. 3, pp. 3168–3177, 2020.
- [26] S. Lee, K. Sung, T. Lee, and W. Lee, "UPS/APF power conversion equipment with a seamless mode transfer," in *Proceedings of the IEEE 8th International Conference on Power Electronics*, pp. 2769–2776, IEEE, Jeju, South Korea, June 2011.
- [27] B. Kroposki, C. Pink, J. Lynch et al., "Development of a high-speed static switch for distributed energy and microgrid applications," in *Proceedings of the 2007 Power Conversion Conference*, pp. 1418–1423, IEEE, Nogaya, Japan, April 2007.
- [28] G. F. Reed, M. Takeda, and I. Iyoda, "Improved power quality solutions using advanced solid-state switching and static compensation technologies," in *Proceedings of the IEEE Power Engineering Society 1999 Winter Meeting*, vol. 2, pp. 1132–1137, New York, NY, USA, February 1999.
- [29] C. Chen, Y. Wang, J. Lai, Y. Lee, and D. Martin, "Design of parallel inverters for smooth mode transfer microgrid

- applications,” *IEEE Transactions on Power Electronics*, vol. 25, no. 1, pp. 6–15, 2010.
- [30] W. U. Tareen and S. Mekhilef, “Transformer-less 3P3W SAPF (three-phase three-wire shunt active power filter) with line-interactive UPS (uninterruptible power supply) and battery energy storage stage,” *Energy*, vol. 109, pp. 525–536, 2016.
- [31] K.-R. Kim, C.-Y. Oh, T.-J. Kim, J.-P. Lee, and H.-J. Kim, “Implementation of a smart power conditioning system for energy storage system with a novel seamless transfer strategy,” *Energies*, vol. 11, no. 5, p. 1108, 2018.
- [32] K.-Y. Lo and Y.-M. Chen, “Design of a seamless grid-connected inverter for microgrid applications,” *IEEE Transactions on Smart Grid*, vol. 11, no. 1, pp. 194–202, 2020.
- [33] Y. Chen, Z. Wang, X. Zhou et al., “Seamless transfer control strategy for three-phase inverter in microgrid,” in *Proceedings of the IEEE 8th International Power Electronics and Motion Control Conference*, pp. 1759–1763, IEEE, Hefei, China, May 2016.
- [34] B. Tian, C. Mao, D. Wang et al., “Control strategy of grid-connected/grid-disconnected seamless transfer of energy storage converter in microgrid,” *Proceedings of the CSU-EPSA*, vol. 26, no. 11, pp. 1–27, 2014.
- [35] L. Hou, L. Xu, Y. Wei et al., “Passive network optimization design of seamless switching of controllable switches in microgrid,” *Automation of Electric Power System*, vol. 42, no. 7, pp. 171–177, 2018.
- [36] G. Shen, D. Xu, and D. Xi, “Novel seamless transfer strategies for fuel cell inverters from grid-tied mode to off-grid mode,” in *Proceedings of the IEEE Applied Power Electronics Conference & Exposition*, vol. 1, pp. 109–113, IEEE, Austin, TX, USA, March 2005.
- [37] N. W. A. Lidula and A. D. Rajapakse, “Behavior of a microgrid during the transition from grid connected to islanded mode,” in *Proceedings of the 2nd Annual International Conference on Sustainable Energy and Environmental Sciences*, pp. 28–33, Singapore, February 2013.

## Research Article

# Machine-Learning-Based Intelligent Mechanical Fault Detection and Diagnosis of Wind Turbines

Qiang Gao <sup>1</sup>, Xinhong Wu <sup>2</sup>, Junhui Guo <sup>1</sup>, Hongqing Zhou <sup>1</sup> and Wei Ruan <sup>3</sup>

<sup>1</sup>State Grid Zhejiang Electric Power Co., Ltd., Taizhou Power Supply Company, Taizhou 318000, China

<sup>2</sup>State Grid Zhejiang Integrated Energy Service Company, Hangzhou 310007, China

<sup>3</sup>College of Control Science and Engineering, Zhejiang University, Hangzhou 310027, China

Correspondence should be addressed to Wei Ruan; 2191724107@qq.com

Received 19 March 2021; Revised 3 April 2021; Accepted 15 April 2021; Published 27 April 2021

Academic Editor: Bo Yang

Copyright © 2021 Qiang Gao et al. This is an open access article distributed under the Creative Commons Attribution License, which permits unrestricted use, distribution, and reproduction in any medium, provided the original work is properly cited.

Wind power has gained wide popularity due to the increasingly serious energy and environmental crisis. However, the severe operational conditions often bring faults and failures in the wind turbines, which may significantly degrade the security and reliability of large-scale wind farms. In practice, accurate and efficient fault detection and diagnosis are crucial for safe and reliable system operation. This work develops an effective deep learning solution using a convolutional neural network to address the said problem. In addition, the linear discriminant criterion-based metric learning technique is adopted in the model training process of the proposed solution to improve the algorithmic robustness under noisy conditions. The proposed solution can efficiently extract the features of the mechanical faults. The proposed algorithmic solution is implemented and assessed through a range of experiments for different scenarios of faults. The numerical results demonstrated that the proposed solution can well detect and diagnose the multiple coexisting faults of the operating wind turbine gearbox.

## 1. Introduction

In recent decades, wind power generation has become one of the dominating sustainable and renewable energy sources and achieved high popularity and significant expansion [1]. Due to the increasing CO<sub>2</sub> emissions and the ever-increasing demand for energy, renewable power generation sources have been considered as one of the most important means to alleviate the urgent power demand in a low-carbon fashion. In practice, the deployment of wind turbines is generally located in some rural areas, remote sites, or even offshore. This brings about direct challenges for the inspection and maintenance of wind power generation infrastructures. Due to the harsh operating environment and extreme working conditions, wind turbines are prone to various faults, resulting in high maintenance efforts [2]. Gearbox, being a critical transmission component in wind turbines, shows a high fault rate in practice. The statistics provided in [3] indicated that 76% of the failures are observed at the bearings, and the faults in gears and other components are

17.1% and 6.9%, respectively. Therefore, efficient health condition monitoring is of paramount importance to reduce maintenance costs as well as downtimes for reliable system operation and low economic losses [4, 5].

In practice, the mechanical fault detection and diagnosis of wind turbines in large-scale wind farms is a nontrivial task due to the operating conditions and complex operational characteristics. In general, the manual condition monitoring methods were based on signal processing and analysis, which required skilled expert knowledge and consequently leading to time-consuming remedies [6]. In the literature, to effectively address the technical challenge of fault detection and analysis, the solutions of operational condition monitoring and online fault detection and diagnosis have been investigated (e.g., [7–10]).

It can be observed from the literature that the intelligent fault diagnosis process generally consists of three key steps: (1) signal acquisition by field sensors; (2) feature extraction through the signal preprocessing; and (3) fault classification using machine-learning algorithms, regarded collectively as

a typical pattern recognition problem. During the process of signal acquisition, various signals, including the measurements of vibration signals, acoustic emission signals, current, and infrared thermal, can be acquired from the field [11]. In particular, the condition monitoring and diagnosis through the analysis of vibration signals has been considered useful for the rotating machines as the vibration signal contains the most intrinsic characteristics related to health conditions [12]. During the process of the feature extraction, it is required to understand the characteristics of signals collected from various field sensors and generate the proper sensitive features to address specific diagnosis issues. As suggested by the existing studies (e.g., [13]), the extraction of intrinsic features from the available vibration signals can be generally carried out through the analysis in the time domain, frequency domain, and time-frequency domain. Time-domain features include some statistical parameters, for example, the root mean square, variance, kurtosis, skewness, impulse factor, and crest factor. For the analysis in the frequency domain, the fast Fourier transform (FFT) is a widely used technique for signal processing, while the short-time Fourier transform (STFT) and wavelet packet transform (WPT) is often adopted for the analysis of nonstationary signals [14]. Also, some other advanced techniques have been adopted for the time-frequency analysis, for example, local mean decomposition (LMD), ensemble empirical mode decomposition (EEMD), Hilbert–Huang transform (HHT), and sparse representation [15–18]. For fault classification, many machine-learning-based solutions have been developed in previous studies, such as support vector machine (SVM) [19], random forest (RF) [20],  $k$ -nearest neighbor ( $k$ -NN) [21], and artificial neural networks (ANN) [22]. The existing methods generally combine advanced signal processing techniques and machine-learning-based approaches to obtain the sensitive features from the collected field signals and make the diagnostic decisions efficiently, achieving remarkable results in various fault diagnosis applications. In [23], the statistical parameters were extracted and characterized from the measured vibration signals and the roller bearing operation conditions were analyzed based on an SVM-based approach to recognize the. The authors in [24] adopted the energy entropy of empirical mode decomposition (EMD) as the input feature and used the ANN for fault classification. The authors in [25] presented an algorithmic solution to calculate the multiscale permutation entropy of vibration signals that are further used as the inputs for the SVM classifier to carry out the bearing fault diagnosis. In [26], the authors proposed to integrate the ensemble empirical mode decomposition with the independent component analysis (ICA) for the classification of the component faults for carrying out the diagnosis of bearing failures in wind turbines.

The conventional machine-learning-based approaches have obtained great success in fault diagnosis. However, there are still a set of limitations that can be summarized as follows: (1) the feature extraction is generally needed for every specific fault diagnosis task. This demands expert knowledge of signal processing and is generally time-consuming; (2) some features may be redundant and it is very

difficult to select the most sensitive features without prior knowledge; and (3) the shallow architectures of learning models, for example, ANN, may potentially limit the capability of the classifiers to learn sophisticated nonlinear relationship during complicated fault scenarios. To overcome existing limitations, more advanced deep learning-based techniques need to be further investigated and assessed.

In recent years, deep learning-based techniques that can automatically and efficiently learn the high-level feature representations from the raw input data have been developed rapidly (e.g., [27, 28]). Also, a collection of deep learning methods, such as deep belief network (DBN) [29], sparse autoencoder (SAE) [30], denoising autoencoder (DAE) [31], sparse filtering [32], convolutional neural network (CNN) [33], and recurrent neural network (RNN) [34], have shown extraordinary feature learning capacity and significant diagnosis results in mechanical fault diagnosis. In [33], the study calculated 256 statistic features and reshaped them into a square matrix and then adopted 2D CNN for gearbox fault diagnosis. In [35], the authors applied various time-frequency methods including short-time Fourier transform, discrete wavelet transform, and S transform to generate time-frequency images and fed them into a CNN to evaluate the performance. The authors in [36] converted a 1D raw vibration signal into 2D vibration grey-scale image directly, utilized LeNet-5-based CNN for data-driven intelligent fault diagnosis of mechanical equipment, and resulted in remarkable accuracy. Besides, a one-dimensional CNN structure has also attracted significant attention due to its straightforward fitness in coping with time-series analysis. The solutions proposed in [37, 38] have adopted the 1D CNN for the fault detection and analysis of real-time signals through capturing the low-frequency features.

Based on the observation and analysis of the existing literature, there are still some challenges that are summarized as follows:

- (1) The early fault signal is very faint, easy to be interfered with by the environmental noise, even submerged. Thus, the fault signal may have a low signal-noise ratio, which is a challenge for fault prognostics.
- (2) Various faults may occur simultaneously which is referred to as multifault and must be taken into consideration.

This work attempts to address the aforementioned problems and proposed a deep learning-based intelligent fault detection and analysis solution of wind turbine gearboxes using the linear discriminant convolutional neural network. A linear discriminant criterion-based linear discriminating loss is introduced into the loss function to enhance the discriminative power of learned features during the training process. The enhanced discriminating power is a promising factor to strengthen the generalization capability and robustness against noise. The experimental results demonstrated that the proposed LDCNN solution can not

only efficiently extract the features from vibration measurements but also provide accurate fault detection and diagnosis in comparison with the existing solutions.

In this work, compared with the aforementioned existing solutions, the main technical contributions made in this work are described as follows:

- (1) A deep learning-based solution is proposed and implemented to extract and learn the various forms of fault features and characteristics from the vibration measurements.
- (2) The linear discriminant loss is introduced and integrated into the loss function to address the technical challenge of diagnosing slight mechanical faults under a noisy environment. This effectively minimizes the negative impact of noises in the process of fault detection and classification.
- (3) The proposed linear discriminant convolutional neural network (LDCNN) solution is extensively evaluated through experiments for a range of fault scenarios through experimental studies based on simulation signals, bearing testbed, and realistic measurements. It demonstrated that the proposed LDCNN can provide a diagnosis accuracy of 98.75%.

The rest of this work is organized as follows: the convolutional neural network is firstly overviewed in Section 2. Section 3 provides a detailed description of our proposed fault diagnosis scheme. Section 4 presents case studies and the analysis of experimental results. Finally, future research directions and conclusive remarks are given in Section 5.

## 2. Preliminaries and Models

**2.1. Overview of CNN.** The convolutional neural network (CNN) is considered a multilayer neural network (convolutional layer, pooling layer, and fully connected layer) with a deep supervised learning architecture and has demonstrated prominent performance in many pattern recognition tasks.

The convolutional layer performs a convolution of the input local regions with filter kernels and then generates the output features by the activation unit. Every kernel has the same size. We use  $W_i^l$  and  $b_i^l$  to denote the weights and bias of the  $i$ -th filter kernel in the layer  $l$ , respectively, and use  $a_j^l$  to denote the  $j$ -th region in layer  $l$ . The convolutional process can be described as follows:

$$a_{ij}^{l+1} = f(W_i^l \cdot a_j^l + b_i^l), \quad (1)$$

where  $a_{ij}^{l+1}$  represents the input of  $j$ -th neuron in frame  $i$  of layer  $l+1$  and  $f$  denotes the activation function that may include the sigmoid function, rectified linear units (ReLU), and others.

The max-pooling layer is one of the most commonly used layers on CNN. Let  $M_j$  denote the  $j$ -th pooling window, the max-pooling transformation then can be formulated as follows:

$$p_i^l(j) = \max_{k \in M_j} (a_i^l(k)). \quad (2)$$

For classification tasks, the deep neural network is followed by a classifier, for example, a multilayer perceptron (MLP), a softmax classifier, or a support vector machine (SVM). Here, the softmax function-based classifier is adopted in the proposed solution. The output of the softmax classifier for a given dataset of  $k$  classes can be obtained based on the probability distribution function, as given in the following:

$$\sigma(x)_i = \frac{e^{W_i x + b_i}}{\sum_i^K e^{W_i x + b_i}}, \quad \text{for } i = 1, 2, \dots, k. \quad (3)$$

**2.2. LDA-Based Distance Metric Learning.** A reasonable distance metric between classes is usually helpful to improve the efficiency and accuracy in pattern recognition. Metric learning is widely used in machine-learning tasks due to its capability to learn suitable metrics from training data automatically. In terms of feature learning, metric learning can learn a new discriminative feature space by feature transformation [39]. Given the training dataset  $D = \{\mathbf{x}_1, \mathbf{x}_2, \dots, \mathbf{x}_N\}$ , with label  $y_i \in \{1, 2, \dots, c\}$  and using  $D_i$  to represent the set of training samples in  $i$ -th class, the distance between two samples under projection is formulated in

$$d(\mathbf{x}_i, \mathbf{x}_j) = \sqrt{(\mathbf{x}_i, \mathbf{x}_j)^T \mathbf{W}^T \mathbf{W} (\mathbf{x}_i - \mathbf{x}_j)}. \quad (4)$$

Here,  $\mathbf{W}$  is the projection matrix and the symmetric matrix  $\mathbf{W}^T \mathbf{W}$  is called a Mahalanobis distance metric. Distance metric learning aims to learn the matrix  $\mathbf{W}$  automatically.

The linear discriminant analysis (LDA) has been widely used in dimension reduction and pattern recognition applications [40]. It enables identifying the linear transformation matrix  $\mathbf{W}$  that is called the Fisher criterion. Let  $\mathbf{S}_b$  denote the interclass scatter matrix and  $\mathbf{S}_w$  denote the intraclass scatter matrix, as described by equations (5)–(7). Then, the Fisher criterion function can be expressed as equation (8):

$$\mathbf{S}_w = \sum_{i=1}^c \sum_{\mathbf{x} \in D_i} (\mathbf{x} - \boldsymbol{\mu}_c) (\mathbf{x} - \boldsymbol{\mu}_c)^T, \quad (5)$$

$$\mathbf{S}_b = \sum_{i=1}^c N_i (\boldsymbol{\mu}_i - \boldsymbol{\mu}) (\boldsymbol{\mu}_i - \boldsymbol{\mu})^T, \quad (6)$$

$$\boldsymbol{\mu}_i = \frac{1}{N_i} \sum_{\mathbf{x} \in D_i} \mathbf{x}, \quad \boldsymbol{\mu} = \frac{1}{N} \sum_{\mathbf{x} \in D} \mathbf{x}, \quad (7)$$

$$J_F(\mathbf{W}) = \max_{\mathbf{W}} \frac{\det(\mathbf{W}^T \mathbf{S}_b \mathbf{W})}{\det(\mathbf{W}^T \mathbf{S}_w \mathbf{W})}. \quad (8)$$



The linear transformation matrix  $W$  obtained by the fisher criterion could be used as a distance metric. As to deep learning tasks, better clustering of each class and separability between classes of the extracted features is promising to strengthen the diagnostic capability. Motivated by the metric learning and fisher criterion, this work introduces the linear discriminating loss to address fault diagnosis tasks that are described in detail in the following sections.

### 3. Proposed Method for Fault Diagnosis

This section developed a deep learning-based fault diagnosis solution for wind turbines, as illustrated in Figure 1. The overall procedure of the proposed linear discriminant convolutional neural network- (LDCNN-) based solution can be described as follows: firstly, the data argumentation is carried out to increase the sample numbers by sampling the raw signals with overlap. Through such data argumentation, a sufficient number of data samples can be obtained for the training process. Then, the LDCNN is designed based on one-dimensional CNN combining improved loss function to learn the highly abstracted features from the input data in an automatic fashion. Finally, the fault classification is carried out through a softmax classifier for different operating conditions with a range of fault scenarios. The implementation details of the proposed solution, including the data sample argumentation, feature extraction, and fault classification, are further explained in the following subsections.

**3.1. Sample Acquisition.** The raw signal measurements can be collected by the field accelerometers, and the overlap sampling is used to produce more samples for the training and testing processes, as illustrated in Figure 1. In this work, the data augmentation through slicing the original data with overlap is used to produce a sufficient number of training samples, as suggested in [33]. Here, the segment length and overlapping rate are set as 1024 and 0.3, respectively.

**3.2. The Architecture of the Proposed Model.** There are no deterministic criteria for the CNN structure and parameters for the fault diagnosis in the existing literature. To reduce the network complexity and enhance the efficiency of the proposed model, this work simplifies the network structure through rigorous experiments. In this work, the proposed model consists of three pairs of one-dimensional convolution and pooling layers and two fully connected layers. The wide kernels [33] are adopted in the first convolutional layer. The numbers of nodes of fully connected layers are set as 512 and 128, respectively.

**3.3. Loss Function Design.** In fact, the adopted loss function in the proposed solution combines both softmax loss and the proposed linear discriminant loss, and hence it can improve the classification efficiency. The target distribution and the estimated distribution are denoted as  $p(x)$  and  $q(x)$ , respectively. The cross-entropy between them can be defined as

$$H(p, q) = - \sum_x p(x) \log q(x). \quad (9)$$

Specifically, combining equation (3), the softmax loss can be written as

$$L_s = - \sum_{i=1}^m \log \frac{e^{W_{y_i} x_i + b_{y_i}}}{\sum_{j=1}^n e^{W_j x_i + b_j}}. \quad (10)$$

To simultaneously minimize the intraclass and maximize the interclass variations of the extracted features, a linear discriminant loss function is proposed and implemented based on the distance metric defined in

$$L_{ld} = \frac{D_w}{D_b}, \quad (11)$$

Here,  $L_{ld}$  is defined as the ratio of intraclass variations and interclass variations, and the metric of intraclass and interclass variations can be calculated as follows:

$$D_w = \frac{1}{2} \sum_{i=1}^m \|x_i - c_{y_i}\|_2^2, \quad (12)$$

$$D_b = \frac{1}{2} \sum_{i=1}^m \|x_{y_i} - c\|_2^2, \quad (13)$$

where  $x_i$  denotes the features generated from the top layer,  $c$  denotes the center of feature space for all samples, and  $c_{y_i}$  denotes the center of samples that belong to class  $y_i$  in the feature space. In this way, the weights of the top layer can be regarded as a linear transformation matrix and optimized in training.

The loss function can be written in the following form:

$$L = L_s + \alpha \cdot L_c. \quad (14)$$

Here,  $L_s$  is the softmax loss,  $L_c$  represents the linear discriminant loss for each epoch, and  $\alpha$  is a hyperparameter used for balancing the two parts of the loss function.

**3.4. Vibration Signal and LDCNN-Based Fault Diagnosis.** Figure 1 shows that the sliced one-dimensional vibration signal segment is fed directly into the one-dimensional CNN for feature learning and classification. In the forward-propagation, features are extracted by successive convolutional and pooling layers followed by the fully connected layers, and the feature classification is carried out by using a softmax classifier. In the backpropagation, the model is optimized by minimizing the improved loss function based on the stochastic gradient descent (SGD) algorithm. After the training process, the testing dataset is used to evaluate the proposed solution, and the accuracy of fault detection and diagnosis is used as the main metric in the evaluation.

## 4. Experimental Assessment and Result Analysis

The developed fault detection and diagnosis solution is extensively assessed through a range of experiments. The experiments are carried out based on the 10-fold cross-

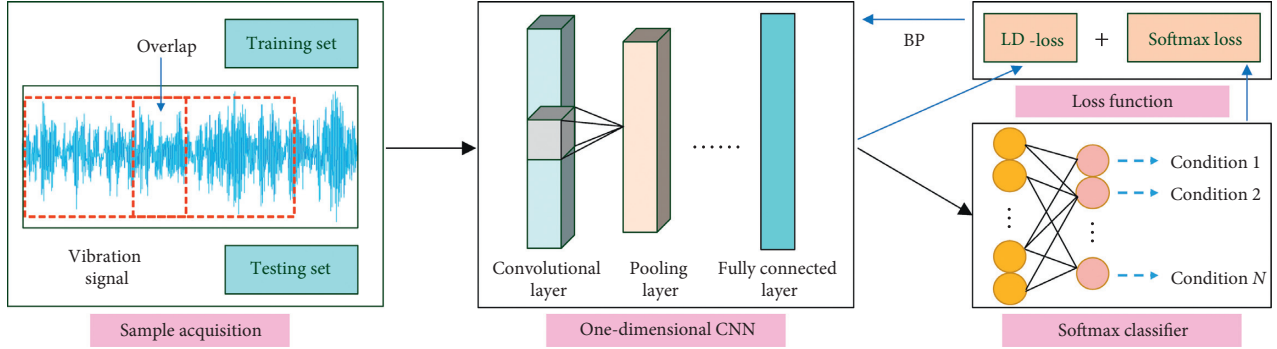


FIGURE 1: Flowchart of the proposed fault detection and diagnosis method.

validation and using a PC with the hardware configuration of Intel Core i5 CPU, 12 GB RAM, and GEFORCE GTX 940M GPU.

**4.1. Case 1: Validation with Simulation Signals.** This work firstly carries out the performance evaluation based on the simulated signals as adopted in [41]. The simulated signals can be expressed as

$$x(t) = \sum_i A_i s(t - T_i) + \sum_k B_k \cos(2\pi k f + \phi_k) + n(t). \quad (15)$$

Here,  $A_i$  is the amplitude of the  $i^{\text{th}}$  impulse excited by the defect and  $T_i$  is the time of its occurrence,  $B_k$  and  $\phi_k$  are the amplitude and initial phase of the  $k^{\text{th}}$  harmonic caused by bearing imbalance or gear meshing; and  $n(t)$  is the white noise in the measurement.

The vibration signals under both normal and fault scenarios are considered. Also, two vibration harmonics are generated under normal conditions. The simplified mathematical expressions are given by

$$\begin{aligned} s_1 &= 0.7 \sin(2\pi f_1 t), \\ s_2 &= 0.3 \sin(2\pi f_2 t), \end{aligned} \quad (16)$$

where  $f_1 = 200$  Hz and  $f_2 = 400$  Hz represent two gear vibration harmonic frequencies,  $t$  represents the time, and  $t = n/f_s$  where  $n$  is sample point and  $f_s$  is sampling frequency which is kept 10 kHz in this experiment.

In addition, the signals for both outer-race and inner-race fault scenarios are simulated as follows [41, 42]:

$$\begin{aligned} s_3 &= 2e^{-200\pi t_1} \sin(2\pi f_{ro} t), \\ s_4 &= 1.5(\cos(2\pi f_o t) + 1) \cdot e^{-500\pi t_2} \sin(2\pi f_{ri} t), \end{aligned} \quad (17)$$

$$t_1 = \text{mod}\left(\frac{t, 1}{f_i}\right), \quad t_2 = \text{mod}\left(\frac{t, 1}{f_o}\right),$$

where  $f_{ro} = 2000$  Hz and  $f_{ri} = 3000$  Hz,  $f_o = 30$  Hz, and  $f_i = 150$  Hz represent the resonance frequency and fault characteristic frequency for the two kinds of faults, respectively. Here,  $f_o = 20$  Hz is the bearing shaft rotating frequency. The simulated fault signals of the outer-race and inner-race fault are presented in Figure 2, respectively.

In simulations, the vibration signals can be generated using the aforementioned source signals based on (14), and four kinds of vibration signals are shown in Figure 3.

In this case, in total, 500 samples are used for each class and each sample consists of 400 data points, and hence the dataset contains 2000 ( $500 \times 4$ ) samples, where 70% of the samples are used for training and the remainder is used for the performance test. In experiments, different solutions are implemented as the comparison benchmarks: the 1D CNN [37], traditional 2D CNN [35], WDCNN with the wide kernel in the first layer [38], and two machine-learning models with 15 time-domain statistical features [43]. Figure 4 presents the numerical results of the evaluated solutions in terms of the detection accuracy based on the test datasets.

In Figure 4, the numerical results demonstrate that the proposed fault detection and diagnosis methods can efficiently detect and diagnose both single and multiple coexisting faults. The superiority of the proposed LDCNN-based solution is confirmed compared with other existing solutions.

**4.2. Case 2: Validation Using the Bearing Testbed.** The performance of the proposed algorithmic solution is further evaluated using the tested at the Case Western Reserve University Bearing Data Centre [44]. In detail, the CWRU testbed consists of a 2 hp motor, a torque transducer, and a dynamometer, as illustrated in Figure 5. This work considers three types of single mechanical faults, that is, inner race fault (IRF), outer race fault (ORF), and ball fault (BF), which are introduced to the test bearings using electrical discharge machining with different fault diameters. In this study, the bearing data with a fault diameter of 0.007 inches and 0.014 inches are selected and used for performance evaluation. Here, the bearing signals are collected from the drive end of the motor by the use of accelerometers with a sampling rate of 12 kHz under four different load conditions, that is, 0, 1, 2, and 3 hp, respectively.

The data of the aforementioned three fault categories with two fault diameters as well as normal operating condition data are directly adopted to evaluate our proposed solution. There are seven categories in total and for each health condition; 150 samples are generated in each load condition, where each sample consists of 1024 data points in

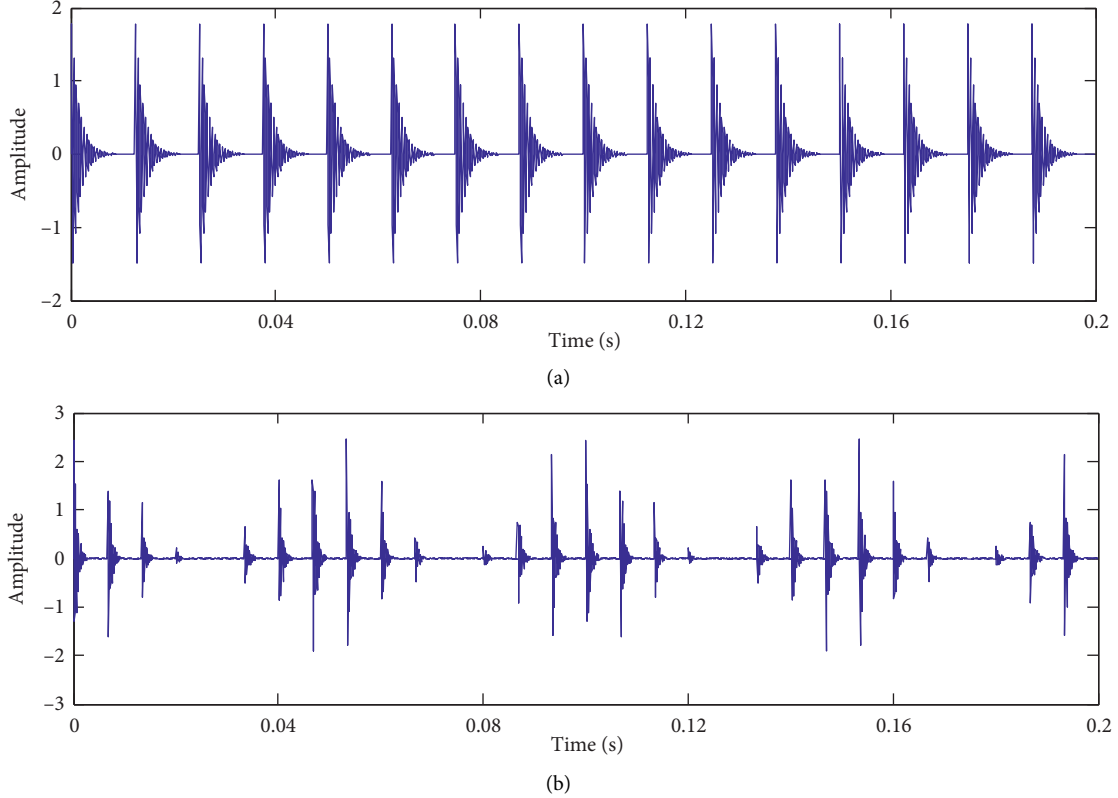


FIGURE 2: Fault signals in simulation experiments: (a) outer race fault; (b) inner race fault.

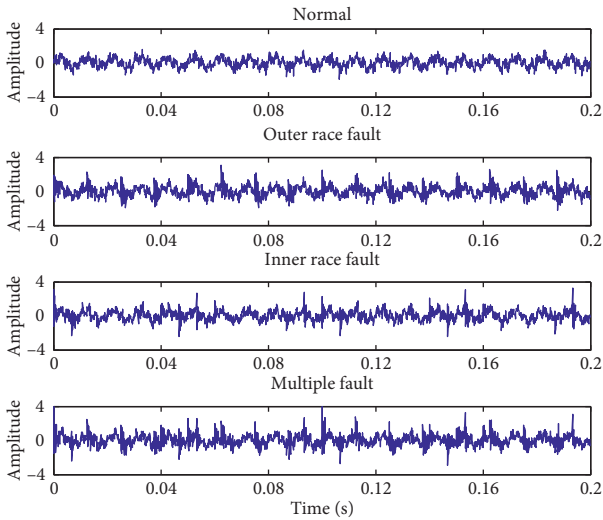


FIGURE 3: Vibration signals of different conditions in simulation experiments.

this work. Therefore, the constructed dataset contains 4200 samples in total, where 70 percent of them are used for training and 30 percent for testing. As in case 1, four deep learning models and two machine-learning models with manual feature extraction are applied and compared. Here, the adopted deep learning models are optimized by stochastic gradient descent (SGD) algorithm with a minibatch size of 64 samples. As a result, the 2D CNN-based method

achieved a high accuracy of 99.52%, while other deep learning models ended with 100%. In contrast, machine-learning-based methods resulted in an accuracy of 94.76% and 95.36%. Hence, the effectiveness and advantages of deep learning can be confirmed due to its higher accuracy despite the lack of manual feature extraction.

In addition, the effectiveness and robustness of the proposed solution are evaluated by adding the Gaussian white noise to the collected data samples. It can be observed that the noisy condition can bring about difficulty for fault detection and diagnosis, particularly in the presence of multiple simultaneously coexisting mechanical faults. Therefore, robustness against noise disturbance is essentially required and needs to be evaluated. In practice, noise-added data are generated for different signal-to-noise ratio (SNR) defined in

$$\text{SNR} = 10 \log_{10} \left( \frac{P_{\text{signal}}}{P_{\text{noise}}} \right). \quad (18)$$

Here,  $P_{\text{signal}}$  and  $P_{\text{noise}}$  represent the powers of the original signal and the additive Gaussian white noise, respectively.

In this work, the data measurements are used in the training phase to train the intelligent models and the noise-added samples with various SNR are used for the testing phase. In the training stage, the hyperparameter of the loss function for LDCNN is set as  $\alpha=0.2$ . Figure 5 shows the experimental results of deep learning methods. Low SNR values represent greater noise power which, as a result,

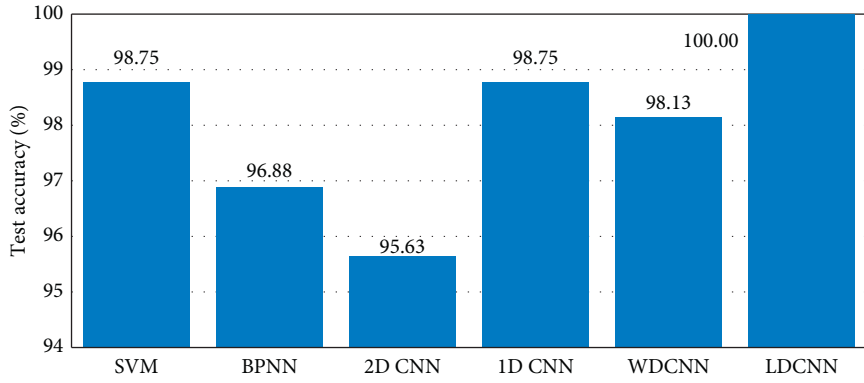


FIGURE 4: The mean detection accuracy of different machine-learning approaches.

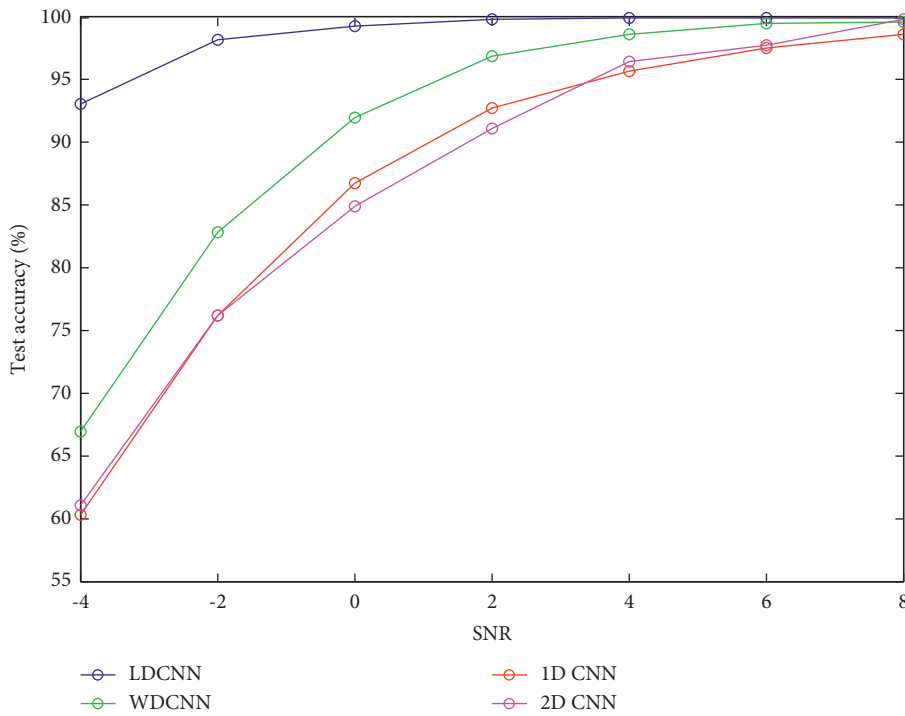


FIGURE 5: Performance of fault detection accuracy under different SNR conditions.

hinders the efficient fault diagnosis. It is evident from Figure 5 that the proposed LDCNN outperforms other intelligent methods with 100% and 93.07% testing accuracy for 8 dB and -4 dB SNR values, respectively.

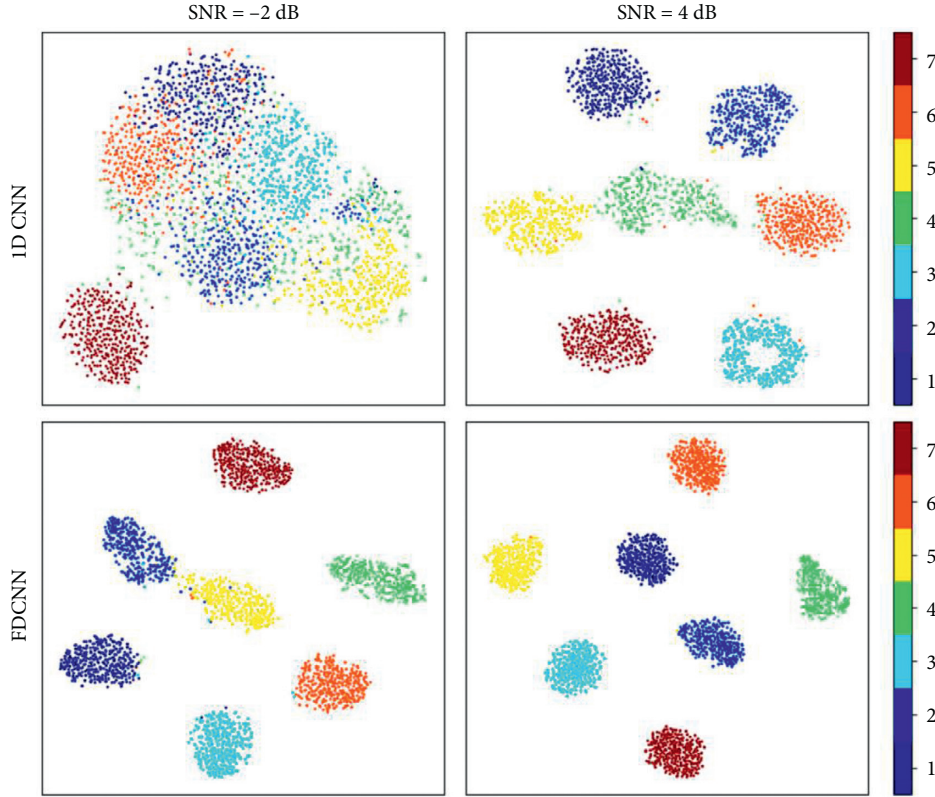
This work adopted the *t*-distributed Stochastic Neighbor Embedding (*t*-SNE) to represent the exacted features. Figure 6 illustrates the extracted high-dimensional features for 7 different conditions under two noisy conditions. The extracted features can be differentiated for SNR = 4 dB, whereas for SNR = -2 dB, features extracted by traditional 1D CNN are heavily overlapped, while features extracted by the proposed LDCNN are fairly distinguishable. This confirmed the performance of the proposed solution in terms of robustness under different noisy conditions.

It should be noted that although the effectiveness of the developed solution is confirmed by the numerical

experiments, the proposed solution for multifault analysis needs to be further evaluated. To assess its performance in multiple fault scenarios, this work utilizes the single fault signals to construct multiple fault vibration signals by employing mixing matrix [45] and nonlinear function [46] given by

$$X = \tan h(A \cdot S), \tag{19}$$

where *S* is the set of single fault signals and *A* and  $\tan h(\cdot)$  are the linear mixing matrix and the nonlinear function, respectively. The nonlinear mixture is employed to mimic the vibration signals of realistic multiple faults. This work considers multifault signals based on only two types of faults to eradicate the combinational complexity. Specifically, any two of the three types of single faults with any fault size are selected to form various multiple faults to generate the

FIGURE 6: Extracted features visualization using  $t$ -SNE.

dataset. The obtained measurement datasets are given in detail in Table 1. There are in total 13 categories and 7800 samples used in this study. Here, 5460 randomly selected samples and the remaining 2340 samples are used as the training set and testing set, respectively.

Figure 7 provides the detection accuracy of the training dataset and testing dataset for deep learning-based solutions. It is clearly seen from the training and testing results that the proposed LDCNN and 1D CNN have a faster convergence rate as compared to 2D CNN. Moreover, the testing accuracy of LDCNN is higher than 1D CNN, which demonstrates the effectiveness of improved loss function. Considering the fact that the multifault data are manually constructed and have already introduced noises and errors, evaluating noise immunity by adding Gaussian white noises may not be consistent with realistic situations and valueless, which is left out for the present.

**4.3. Case 3: Validation with Realistic Data.** The proposed method is further evaluated through the adoption of realistic wind farm measurements. In this case, the realistic vibration signals are measured and collected from the operating wind turbines with the sampling rate at 25.6 kHz and the rotating speed of each selected wind turbine is about 1100 rpm. In addition to the bearing fault, the gearbox is also prone to gear failure caused by harsh operation state and extreme environmental conditions. Here, five different conditions are measured from a group of fault-diagnosed wind turbine gearboxes, including the bearing rolling ball fault (B), the

TABLE 1: The selected dataset.

Fault location	Diameter (inch)	Train/test	Label
None	0	420/180	1
Ball	0.007	420/180	2
	0.014	420/180	3
Inner race	0.007	420/180	4
	0.014	420/180	5
Outer race	0.007	420/180	6
	0.014	420/180	7
Ball and inner race	0.007/0.007	420/180	8
	0.007/0.014	420/180	9
Ball and outer race	0.007/0.007	420/180	10
	0.007/0.014	420/180	11
Inner and outer race	0.007/0.007	420/180	12
	0.007/0.014	420/180	13

inner raceway fault (I), the gear fault (G), and the multiple faults compounded by the ball and gear fault (B&G), and the inner race and gear fault (I&G), respectively. The measurements of the accelerometer installed at high-speed shaft bearing on the motor side are recorded. As a result, 300 measurement samples of each operating condition are obtained to set up the measurement dataset containing in total 1500 samples.

The performance of the proposed LDCNN is compared with the existing solutions, and the performance in terms of accuracy is provided in Table 2. It is evident from the numerical results that the developed LDCNN can achieve

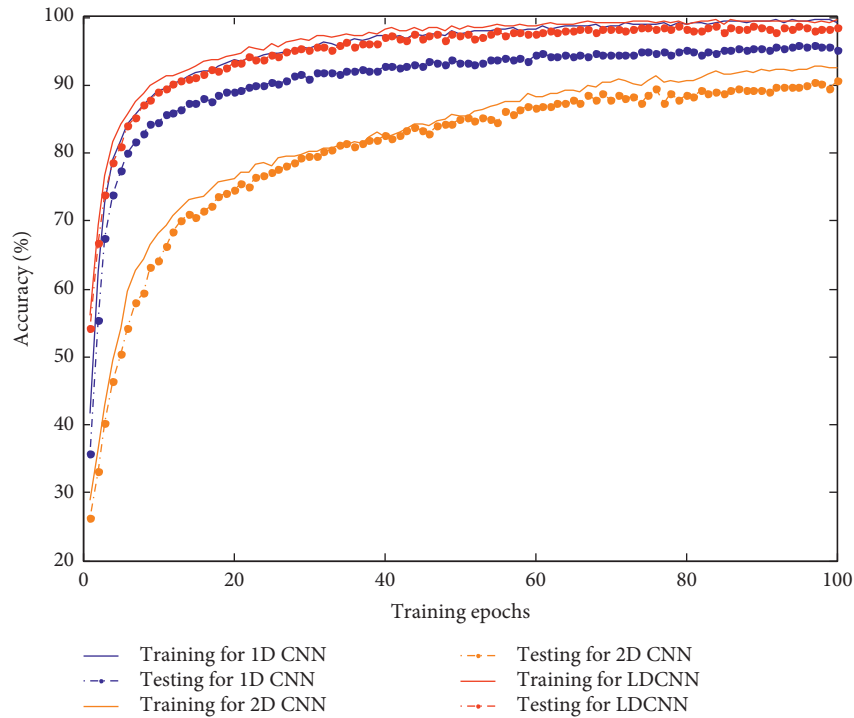


FIGURE 7: Accuracy curve during the training process.

TABLE 2: Method evaluation.

Methods	Mean accuracy (%)
SVM	75.49
BPNN	90.42
2-D CNN	93.57
1-D CNN	90.83
WDCNN	96.56
<b>LDCNN</b>	<b>98.75</b>

of one of the test results is presented in Figure 8. It is noteworthy from the confusion matrix that the multiple faults may be diagnosed as a single fault due to the variability in the size of each single fault. However, such fault detection cannot be ruled out as a misclassification case because multiple fault condition is also one of the fault conditions.

### 5. Conclusion and Remarks

In this paper, a linear discriminant CNN-based diagnostic solution is proposed for efficient detection and diagnosis of multiple coexisting mechanical faults in the operational wind turbines. The proposed solution is extensively assessed through simulation and experiments. In addition to the accurate performance of diagnosis for multiple faults, the noises immunity of the proposed algorithmic model is enhanced to provide excellent performance under the conditions with a low signal-to-noise ratio.

For future considerations, the following two research directions will be particularly examined. To further facilitate the proposed solution, the scalable data samples argumentation and accurate classification are required. Thus, the effectiveness and efficiency of the proposed solution need to be further validated and extensively assessed with massive data measurements of various other kinds of faults and operating conditions. A physical testbed that can simulate various kinds of bearing and gear faults should be established and used for further research. Also, more advanced data-driven optimization and machine-learning-based techniques can be developed and incorporated into the fault feature characterization and recognition.

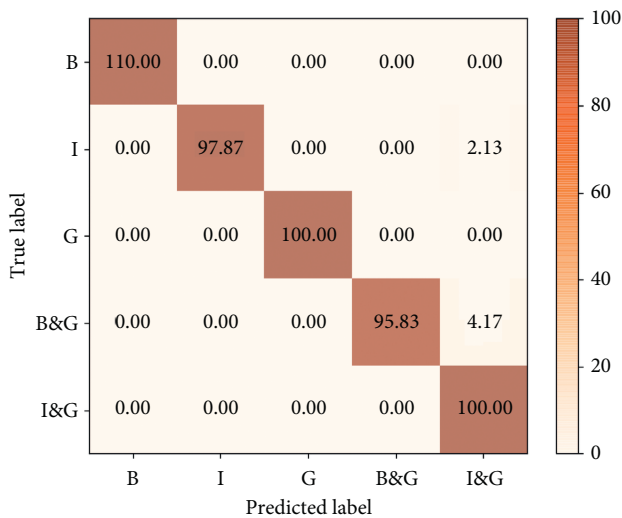


FIGURE 8: Confusion matrix of the proposed LDCNN solution.

the detection accuracy of 98.75%, which outperforms the compared machine-learning and deep learning-based methods. For the proposed solution, the confusion matrix



## Data Availability

The experiments are supported by the data source from Case Western Reserve University, Cleveland, Ohio, America, available online at <http://csegroups.case.edu/bearingdatacenter/pages/bearing-information>.

## Conflicts of Interest

The authors declare that they have no conflicts of interest.

## Acknowledgments

This work was supported by the Science and Technology Project of State Grid Zhejiang Electric Power Co., Ltd. (research on the evaluation of the distributed renewable energy consumption based on the generation-network-demand coordination in the electricity market).

## References

- [1] M. Nie and L. Wang, "Review of condition monitoring and fault diagnosis technologies for wind turbine gearbox," *Procedia CIRP*, vol. 11, pp. 287–290, 2013.
- [2] W. Qiao and D. Lu, "A survey on wind turbine condition monitoring and fault diagnosis-part I: components and subsystems," *IEEE Transactions on Industrial Electronics*, vol. 62, no. 10, pp. 6536–6545, 2015.
- [3] National Renewable Energy Laboratory (NREL), *Statistics Show Bearing Problems Cause the Majority of Wind Turbine Gearbox Failures*, National Renewable Energy Laboratory (NREL), Golden, CO, USA, 2015, <http://energy.gov/eere/wind/articles/statistics-show-bearing-problems-cause-majority-wind-turbine-gearbox-failures>.
- [4] X. M. Zhao, Q. H. Hu, Y. G. Lei, and M. J. Zuo, "Vibration-based fault diagnosis of slurry pump impellers using neighbourhood rough set models," *Proceedings of the Institution of Mechanical Engineers, Part C: Journal of Mechanical Engineering Science*, vol. 224, no. 4, pp. 995–1006, 2010.
- [5] Y. G. Lei and Z. J. He, "Advances in applications of hybrid intelligent fault diagnosis and prognosis technique," *Journal of Vibration and Shock*, vol. 30, no. 9, pp. 129–135, 2011.
- [6] Z. Hameed, Y. S. Hong, Y. M. Cho, S. H. Ahn, and C. K. Song, "Condition monitoring and fault detection of wind turbines and related algorithms: a review," *Renewable and Sustainable Energy Reviews*, vol. 13, no. 1, pp. 1–39, 2009.
- [7] W. Qiao and D. Lu, "A survey on wind turbine condition monitoring and fault diagnosis-part II: signals and signal processing methods," *IEEE Transactions on Industrial Electronics*, vol. 62, no. 10, pp. 6546–6557, 2015.
- [8] Z. Zhang, A. Verma, and A. Kusiak, "Fault analysis and condition monitoring of the wind turbine gearbox," *IEEE Transactions on Energy Conversion*, vol. 27, no. 2, pp. 526–535, 2012.
- [9] B. Lu, Y. Li, X. Wu, and Z. Yang, "A review of recent advances in wind turbine condition monitoring and fault diagnosis," in *Proceedings of the 2009 IEEE Power Electronics and Machines in Wind Applications*, pp. 1–7, Lincoln, NE, USA, June 2009.
- [10] W. Y. Liu, B. P. Tang, J. G. Han et al., "The structure healthy condition monitoring and fault diagnosis methods in wind turbines: a review," *Renewable and Sustainable Energy Reviews*, vol. 44, pp. 466–472, 2014.
- [11] F. P. G. Márquez, A. M. Tobias, J. M. P. Pérez, and M. Papaelias, "Condition monitoring of wind turbines: techniques and methods," *Renewable Energy*, vol. 46, pp. 169–178, 2012.
- [12] J. Zarei, M. A. Tadjedini, and H. R. Karimi, "Vibration analysis for bearing fault detection and classification using an intelligent filter," *Mechatronics*, vol. 24, no. 2, pp. 151–157, 2014.
- [13] A. K. S. Jardine, D. Lin, and D. Banjevic, "A review on machinery diagnostics and prognostics implementing condition-based maintenance," *Mechanical Systems and Signal Processing*, vol. 20, no. 7, pp. 1483–1510, 2006.
- [14] H. O. A. Ahmed, M. L. D. Wong, and A. K. Nandi, "Intelligent condition monitoring method for bearing faults from highly compressed measurements using sparse over-complete features," *Mechanical Systems and Signal Processing*, vol. 99, pp. 459–477, 2018.
- [15] H. Liu and M. Han, "A fault diagnosis method based on local mean decomposition and multi-scale entropy for roller bearings," *Mechanism and Machine Theory*, vol. 75, pp. 67–78, 2014.
- [16] X. Zhang, Y. Liang, J. Zhou, and Y. Zang, "A novel bearing fault diagnosis model integrated permutation entropy, ensemble empirical mode decomposition and optimized SVM," *Measurement*, vol. 69, pp. 164–179, 2015.
- [17] A. Soualhi, K. Medjaher, and N. Zerhouni, "Bearing health monitoring based on hilbert-huang transform, support vector machine, and regression," *IEEE Transactions on Instrumentation and Measurement*, vol. 64, no. 1, pp. 52–62, 2015.
- [18] L. Ren, W. Lv, S. Jiang, and Y. Xiao, "Fault diagnosis using a joint model based on sparse representation and SVM," *IEEE Transactions on Instrumentation and Measurement*, vol. 65, no. 10, pp. 2313–2320, 2016.
- [19] A. Widodo and B.-S. Yang, "Support vector machine in machine condition monitoring and fault diagnosis," *Mechanical Systems and Signal Processing*, vol. 21, no. 6, pp. 2560–2574, 2007.
- [20] D. Cabrera, F. Sancho, R.-V. Sánchez et al., "Fault diagnosis of spur gearbox based on random forest and wavelet packet decomposition," *Frontiers of Mechanical Engineering*, vol. 10, no. 3, pp. 277–286, 2015.
- [21] Z. Hu, L. X. Duan, and L. B. Zhang, "Application of improved KNNC method in fault pattern recognition of rolling bearings," *Journal of Vibration & Shock*, vol. 32, pp. 84–87+105, 2013.
- [22] L. Eren, A. Karahoca, and M. J. Devaney, "Neural network based motor bearing fault detection," in *Proceedings of the 21st IEEE Instrumentation and Measurement Technology Conference*, vol. 3, pp. 1657–1660, Como, Italy, May 2004.
- [23] X. Zhang, B. Wang, and X. Chen, "Intelligent fault diagnosis of roller bearings with multivariable ensemble-based incremental support vector machine," *Knowledge-Based Systems*, vol. 89, pp. 56–85, 2015.
- [24] Y. Yu, D. J. YuDejie, and C. Junsheng, "A roller bearing fault diagnosis method based on EMD energy entropy and ANN," *Journal of Sound and Vibration*, vol. 294, no. 1-2, pp. 269–277, 2006.
- [25] S.-D. Wu, P.-H. Wu, C.-W. Wu, J.-J. Ding, and C.-C. Wang, "Bearing fault diagnosis based on multiscale permutation entropy and support vector machine," *Entropy*, vol. 14, no. 8, pp. 1343–1356, 2012.
- [26] J. Wang, R. X. Gao, and R. Yan, "Integration of EEMD and ICA for wind turbine gearbox diagnosis," *Wind Energy*, vol. 17, no. 5, pp. 757–773, 2014.

- [27] S. Yin and O. Kaynak, "Big data for modern industry: challenges and trends [point of view]," *Proceedings of the IEEE*, vol. 103, no. 2, pp. 143–146, 2015.
- [28] Y. LeCun, Y. Bengio, and G. Hinton, "Deep learning," *Nature*, vol. 521, no. 7553, pp. 436–444, 2015.
- [29] H. Shao, H. Jiang, X. Zhang et al., "Rolling bearing fault diagnosis using an optimization deep belief network," *Measurement Science and Technology*, vol. 26, no. 11, p. 115002, 2015.
- [30] W. Sun, S. Shao, R. Zhao, R. Yan, X. Zhang, and X. Chen, "A sparse auto-encoder-based deep neural network approach for induction motor faults classification," *Measurement*, vol. 89, pp. 171–178, 2016.
- [31] C. Lu, Z.-Y. Wang, W.-L. Qin, and J. Ma, "Fault diagnosis of rotary machinery components using a stacked denoising autoencoder-based health state identification," *Signal Processing*, vol. 130, pp. 377–388, 2017.
- [32] Y. Lei, F. Jia, J. Lin, S. Xing, and S. X. Ding, "An intelligent fault diagnosis method using unsupervised feature learning towards mechanical big data," *IEEE Transactions on Industrial Electronics*, vol. 63, no. 5, pp. 3137–3147, 2016.
- [33] Z. Chen, C. Li, and R.-V. Sanchez, "Gearbox fault identification and classification with convolutional neural networks," *Shock and Vibration*, vol. 2015, no. 2, 10 pages, Article ID 390134, 2015.
- [34] T. de Bruin, K. Verbert, and R. Babuska, "Railway track circuit fault diagnosis using recurrent neural networks," *IEEE Transactions on Neural Networks and Learning Systems*, vol. 28, no. 3, pp. 523–533, 2017.
- [35] R. Chen, X. Huang, L. Yang, X. Xu, X. Zhang, and Y. Zhang, "Intelligent fault diagnosis method of planetary gearboxes based on convolution neural network and discrete wavelet transform," *Computers in Industry*, vol. 106, pp. 48–59, 2019.
- [36] L. Wen, X. Li, L. Gao, and Y. Zhang, "A new convolutional neural network-based data-driven fault diagnosis method," *IEEE Transactions on Industrial Electronics*, vol. 65, no. 7, pp. 5990–5998, 2018.
- [37] T. Ince, S. Kiranyaz, L. Eren, M. Askar, and M. Gabbouj, "Real-time motor fault detection by 1-D convolutional neural networks," *IEEE Transactions on Industrial Electronics*, vol. 63, no. 11, pp. 7067–7075, 2016.
- [38] W. Zhang, G. Peng, C. Li et al., "A new deep learning model for fault diagnosis with good anti-noise and domain adaptation ability on raw vibration signals," *Sensors*, vol. 17, no. 2, p. 425, 2017.
- [39] W. B. Li, J. Huo, Y. H. Shi et al., "Online deep metric learning," 2018, <http://arxiv.org/abs/1805.05510v1>.
- [40] Y. Chen, X. G. Zhao, and J. D. Han, "Distance metric learning with penalized linear discriminant analysis," in *Proceedings of the 2010 IEEE International Conference on Progress in Informatics and Computing*, pp. 170–174, Shanghai, China, December 2010.
- [41] M. Zhao, J. Lin, X. Xu, and X. Li, "multi-fault detection of rolling element bearings under harsh working condition using IMF-based adaptive envelope order analysis," *Sensors*, vol. 14, no. 11, pp. 20320–20346, 2014.
- [42] X. A. Yan, M. P. Jia, and L. Xiang, "Compound fault diagnosis of rotating machinery based on OVMD and a 1.5-dimension envelope spectrum," *Measurement Science and Technology*, vol. 27, no. 7, p. 075002, 2016.
- [43] Z. Chen and W. Li, "Multisensor feature fusion for bearing fault diagnosis using sparse autoencoder and deep belief network," *IEEE Transactions on Instrumentation and Measurement*, vol. 66, no. 7, pp. 1693–1702, 2017.
- [44] Case Western Reserve University. Cleveland, OH, USA [Online]. Available: <http://csegroups.case.edu/bearingdatacenter/pages/bearing-information>.
- [45] H. Hong and M. Liang, "Separation of fault features from a single-channel mechanical signal mixture using wavelet decomposition," *Mechanical Systems and Signal Processing*, vol. 21, no. 5, pp. 2025–2040, 2007.
- [46] W. Li and H. Yang, "A maximum entropy based nonlinear blind source separation approach using a two-layer perceptron network," in *Proceedings of the 2013 10th IEEE International Conference on Control and Automation (ICCA)*, pp. 978–982, Hangzhou, China, June 2013.

## Research Article

# Small-Signal Stability Analysis for Power System Frequency Regulation with Renewable Energy Participation

Tingyi He,<sup>1</sup> Shengnan Li,<sup>1</sup> Shuijun Wu,<sup>1</sup> and Ke Li<sup>2,3</sup> 

<sup>1</sup>Yunnan Power Grid Co., Ltd., Electric Power Research Institute, Kunming 650200, China

<sup>2</sup>Department of Electronic Engineering, Shantou University, Shantou 515041, China

<sup>3</sup>Key Lab of Digital Signal and Image Processing of Guangdong Province, Shantou 515041, China

Correspondence should be addressed to Ke Li; [ericlee@stu.edu.cn](mailto:ericlee@stu.edu.cn)

Received 6 January 2021; Revised 20 January 2021; Accepted 22 March 2021; Published 5 April 2021

Academic Editor: Bo Yang

Copyright © 2021 Tingyi He et al. This is an open access article distributed under the Creative Commons Attribution License, which permits unrestricted use, distribution, and reproduction in any medium, provided the original work is properly cited.

With the improvement of the permeability of wind and photovoltaic (PV) energy, it has become one of the key problems to maintain the small-signal stability of the power system. Therefore, this paper analyzes the small-signal stability in a power system integrated with wind and solar energy. First, a mathematical model for small-signal stability analysis of power systems including the wind farm and PV station is established. And the characteristic roots of the New England power system integrated with wind energy and PV energy are obtained to study their small-signal stability. In addition, the validity of the theory is verified by the voltage drop of different nodes, which proves that power system integrated with wind-solar renewable energy participating in the frequency regulation can restore the system to the rated frequency in the shortest time and, at the same time, can enhance the robustness of each unit.

## 1. Introduction

Recently, with the exhaustion of fossil energy and the deterioration of the natural environment, renewable energy has attracted wide attention [1]. Wind energy and solar energy are the most widely used intermittent clean energy, and they are highly complementary in terms of resource and time distribution [2]. If wind and solar energy are integrated to form a wind-solar complementary energy system and participate in the frequency regulation of the power system, the utilization efficiency of intermittent energy can be improved to a certain extent and the global energy shortage can be alleviated [3, 4].

However, the random fluctuation of the output of wind and solar energy causes huge regulatory peak pressure to the power balance of the power system [5, 6]; on the other hand, the power system is disturbed by small-signal all the time during operation [7, 8]. An unstable system is difficult to operate properly in practice [9, 10]. Thus, the analysis of small-signal stability of power system becomes one of the important tasks of power system [11, 12]. Literature [13]

establishes a small-signal model of PV generation connected to a weak AC grid. The stability of PV power generation under different power grid strength and control parameters is studied by means of eigenvalue analysis. Literature [14] studies the influence of a large number of wind power generation on small-signal stability and corresponding control strategies to alleviate this negative influence. In [15], the Lyapunov stability criterion is used to analyze the stability research method of the integrated hybrid system. Stability research can be carried out for different renewable energy sources, such as the wind power generation system, photovoltaic system, and micro hydropower system. However, the above analysis regards wind-solar and other renewable energy sources as a perturbation of the power system and does not consider their participation in the frequency regulation of the power system. Therefore, it is not effective in analyzing the stability of the power system in which wind-solar renewable energy participate in the frequency regulation.

Thus, this paper studies the integrated energy system including wind power and PV system with the method of

eigenvalue analysis and studies the oscillation modes of the power system when wind and solar power are connected separately, and when the wind farm is connected first and then the PV system is connected. The simulation model of the system is established and the New England power system is used to verify the correctness of the small-signal stability analysis.

The remaining of this paper is organized as follows: Section 2 develops the system modelling. In Section 3, small-signal stability analysis is described. Comprehensive case studies are undertaken in Section 4. The different systems are discussed in Section 5 and Section 6 summarizes the main contributions of the paper.

## 2. System Modelling

**2.1. Multimachine Power System Modelling.** The third-order model of the  $i$ th generator in a multimachine power system can be expressed by the following formula:

$$\begin{cases} \dot{\delta}_i = \omega_i - \omega_0, \\ \dot{\omega}_i = \frac{\omega_0}{2H_i} \left[ P_{mi} - \frac{D_i}{\omega_0} (\omega_i - \omega_0) - P_{ei} \right], \\ \dot{E}'_{qi} = \frac{1}{T_{d0i}} (u_{f di} + E_{f0i} - E_{qi}), \quad i = 1, 2, \dots, n, \end{cases}$$

$$E_{qi} = E'_{qi} - (x_{di} - x'_{di})I_{di},$$

$$P_{ei} = \sum_{j=1}^n E'_{qi} E'_{qj} \beta_{ij},$$

$$Q_{ei} = \sum_{j=1}^n E'_{qi} E'_{qj} \alpha_{ij},$$

$$I_{di} = \sum_{j=1}^n E'_{qi} \alpha_{ij},$$

$$I_{qi} = \sum_{j=1}^n E'_{qj} \beta_{ij},$$

$$V_{ti} = \sqrt{V_{di}^2 + V_{qi}^2},$$

$$V_{di} = x_{qi} I_{qi}, \quad V_{di} = E'_{qj} - x'_{di} I_{di},$$

$$\alpha_{ij} = B_{ij} \cos(\delta_i - \delta_j) + G_{ij} \sin(\delta_i - \delta_j),$$

$$\beta_{ij} = B_{ij} \sin(\delta_i - \delta_j) + G_{ij} \cos(\delta_i - \delta_j),$$
(1)

where subscript  $i$  denotes the variables of the  $i$ th machine;  $\delta_i$  is the relative rotor angle;  $\omega_i$  is the generator rotor speed;  $\omega_0$  is the system speed;  $E'_{qi}$  and  $E_{qi}$  are the voltage and transient voltage on the  $q$ -axis;  $P_{mi}$  is the constant mechanical power

input;  $P_{ei}$  is the electric power output;  $V_{ti}$  is the generator terminal voltage;  $V_{di}$  and  $V_{qi}$  are the  $d$ -axis and  $q$ -axis generator terminal voltages;  $x_{di}$  and  $x'_{di}$  are the  $d$ -axis synchronous and transient impedances;  $x_{qi}$  is the  $q$ -axis synchronous impedance;  $H_i$  is the rotor inertia;  $T_{d0i}$  is the  $d$ -axis transient short-circuit time constant;  $I_{di}$  and  $I_{qi}$  are the  $d$ -axis and  $q$ -axis generator currents;  $Y_{ij}$  is the equivalent admittance between the  $i$ th and  $j$ th nodes;  $B_{ij}$  is the susceptance between  $i$  and  $j$  nodes;  $G_{ij}$  is the conductance between  $i$  and  $j$  nodes; and  $u_{f di}$  and  $E_{f0i}$  are the excitation voltage and the initial excitation voltage, respectively.

**2.2. System Modelling of DFIG Based Wind Turbine.** DFIG is connected to the power system through the voltage source converter, as shown in Figure 1 [16].

The aerodynamic mathematical model of the wind turbine can be described as [16]

$$P_m = \frac{1}{2} \rho \pi R^2 C_p(\lambda, \beta) v_{\text{wind}}^3,$$

$$\lambda = \frac{\omega_m R}{v_{\text{wind}}},$$
(2)

$$C_p(\lambda, \beta) = c_1 \left( \frac{c_2}{\lambda_i} - c_3 \beta - c_4 \right) e^{-(c_5/\lambda_i)} + c_6 \lambda,$$

with

$$\frac{1}{\lambda_i} = \frac{1}{\lambda + 0.08\beta} - \frac{0.035}{\beta^3 + 1},$$
(3)

where  $\rho$  is the air density,  $R$  denotes the radius of the wind turbine, and  $v_{\text{wind}}$  means the wind speed.  $C_p(\lambda, \beta)$  is a function of tip-speed-ratio  $\lambda$  and blade pitch angle  $\beta$  representing the power coefficient. A specific wind speed corresponds to a wind turbine rotational speed to obtain  $C_{p\text{max}}$ , namely, the maximum power coefficient and therefore tracks the maximum mechanical (wind) power.  $\omega_m$  denotes the wind turbine rotational speed [17].

The 4<sup>th</sup>-order mathematical model of DFIG can be described as

$$\begin{cases} \frac{di_{qs}}{dt} = \frac{\omega_b}{L'_s} \left( -R_1 i_{qs} + \omega_s L'_s i'_{qs} + \frac{\omega_r}{\omega_s} e'_{qs} - \frac{1}{T_r \omega_s} e'_{ds} - v_{qs} + \frac{L_m}{L_{rr}} v_{qr} \right), \\ \frac{di_{ds}}{dt} = \frac{\omega_b}{L'_s} \left( -\omega_s L'_s i'_{ds} - R_1 i_{ds} + \frac{1}{T_r \omega_s} e'_{qs} + \frac{\omega_r}{\omega_s} e'_{ds} - v_{ds} + \frac{L_m}{L_{rr}} v_{qr} \right), \\ \frac{de'_{qs}}{dt} = \omega_b \omega_s \left[ R_2 i_{ds} - \frac{1}{T_r \omega_s} e'_{qs} + \left( 1 - \frac{\omega_r}{\omega_s} \right) e'_{ds} - \frac{L_m}{L_{rr}} v_{dr} \right], \\ \frac{de'_{ds}}{dt} = \omega_b \omega_s \left[ -R_2 i_{qs} - \left( 1 - \frac{\omega_r}{\omega_s} \right) e'_{qs} - \frac{1}{T_r \omega_s} e'_{ds} + \frac{L_m}{L_{rr}} v_{qr} \right], \end{cases}$$
(4)

where  $\omega_b$  represents the electrical base speed,  $\omega_s$  denotes the synchronous angle speed, and  $\omega_r$  means the rotor angle speed;  $e'_{ds}$  and  $e'_{qs}$  denote the equivalent  $d$ -axis and  $q$ -axis

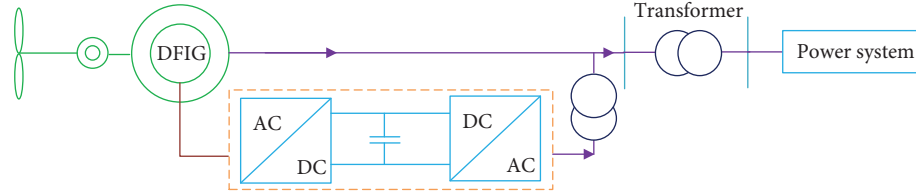


FIGURE 1: The grid-connected structure of wind turbine.

( $dq$ -) internal voltages;  $i_{ds}$  and  $i_{qs}$  are the  $dq$ -stator currents;  $v_{ds}$  and  $v_{qs}$  represent the  $dq$ -stator terminal voltages; and  $v_{dr}$  and  $v_{qr}$  are the  $dq$ -rotor voltages.  $L_m$  means mutual inductance.

The pitch angle control system is designed to improve wind energy conversion efficiency and make wind turbine output stable. Its model can be described as follows:

$$\frac{d\beta}{dt} = \frac{1}{T_\beta} (\beta_{\text{ref}} - \beta), \quad (5)$$

where  $\beta_{\text{ref}}$  is the reference value of pitch angle;  $T_\beta$  is the inertia time constant of the pitch control system.

The grid-side converter which is directly connected with the power system has the main function of maintaining constant capacitive voltage under the control of the DC regulating system and the function of adjusting the power factor. The DC sides of both converters are supported by a common capacitor. The power equation of the converter can be described as [18]

$$\begin{cases} P_r = P_g + P_{DC}, \\ P_r = v_{dr}i_{dr} + v_{qr}i_{qr}, \\ P_g = v_{dg}i_{dg} + v_{qg}i_{qg}, \\ P_{DC} = v_{DC}i_{DC} = -Cv_{DC}\frac{dv_{DC}}{dt}, \end{cases} \quad (6)$$

where  $P_r$  is the active power of the AC terminal of the machine side converter and  $P_g$  is the active power of the AC terminal of the grid-side converter.  $P_{DC}$  is the active power of the capacitor tie line;  $i_{dr}$  and  $i_{qr}$  are the  $d$ - $q$  axis components of rotor current respectively;  $i_{dg}$  and  $i_{qg}$  are the  $d$ - $q$  axis components of the system side converter current, respectively;  $v_{dg}$  and  $v_{qg}$  are the  $d$ - $q$  axis components of the system side converter voltage respectively;  $v_{DC}$  and  $i_{DC}$  are the current and voltage of the DC link in the converter;  $C$  is the capacity of the capacitor.

Equation (6) can be rewritten as

$$Cv_{DC}\frac{dv_{DC}}{dt} = v_{dg}i_{dg} + v_{qg}i_{qg} - (v_{dr}i_{dr} + v_{qr}i_{qr}). \quad (7)$$

**2.3. Modelling of PV System.** The control structure of the PV system is shown in Figure 2 [19].

According to Kirchhoff's law, the  $U$ - $I$  equation of PV cell can be described as

$$I = I'_{sc} \left\{ 1 - C_1 \left[ e^{(U/I)(C_2 U_{oc})} - 1 \right] \right\},$$

$$C_1 = \left( 1 - \frac{I'_m}{I'_{sc}} \right) e^{(-U'_m / (C_2 U_{oc}))},$$

$$C_2 = \left( \frac{U'_m}{U'_{oc}} - 1 \right) \left[ \ln \left( 1 - \frac{I'_m}{I'_{sc}} \right) \right]^{-1},$$

$$I'_{sc} = I_{sc} \Delta I,$$

$$I'_m = I_m \Delta I,$$

$$U'_{oc} = U_{oc} \Delta U,$$

$$U'_m = U_m \Delta U,$$

$$\Delta I = \frac{[1 + \alpha(T - T_{\text{ref}})]S}{S_{\text{ref}}},$$

$$\Delta U = [1 - \gamma(T - T_{\text{ref}})] \ln [e + \beta(S - S_{\text{ref}})],$$

where  $I_{sc}$  is the short-circuit current;  $U_{oc}$  is the open-circuit voltage;  $U_m$  is the voltage at maximum power;  $I_m$  is the current at maximum power;  $S_{\text{ref}}$  is the illumination intensity under standard environment, which is  $1 \text{ kW/m}^2$ .  $T_{\text{ref}}$  is the temperature in the standard environment, which is  $25^\circ\text{C}$ .  $I'_{sc}$ ,  $U'_{oc}$ ,  $I'_m$ , and  $U'_m$  are, respectively, the correction values of  $I_{sc}$  and  $U_m$  under different environments.  $\alpha$  and  $\gamma$  are temperature compensation coefficients; and  $\beta$  is the compensation coefficient of PV irradiation.

In addition, DC/DC converter mainly plays the role of Boost and power transformation, it can be described as

$$\begin{cases} P_{pv2} = f_1(P_{pv1}) = P_{pv1}, \\ V_{pv1} = f_2(V_D, V_{pvm1}) = V_D. \end{cases} \quad (9)$$

DC link is the intermediate link connecting DC side and AC side, namely, the DC bus capacitance model. According to the capacitance energy and voltage relationship, the DC link model can be described as

$$\begin{cases} \frac{dE_C}{dt} = P_{PV2} - P_{De}, \\ E_C = \frac{1}{2CV_D^2}. \end{cases} \quad (10)$$

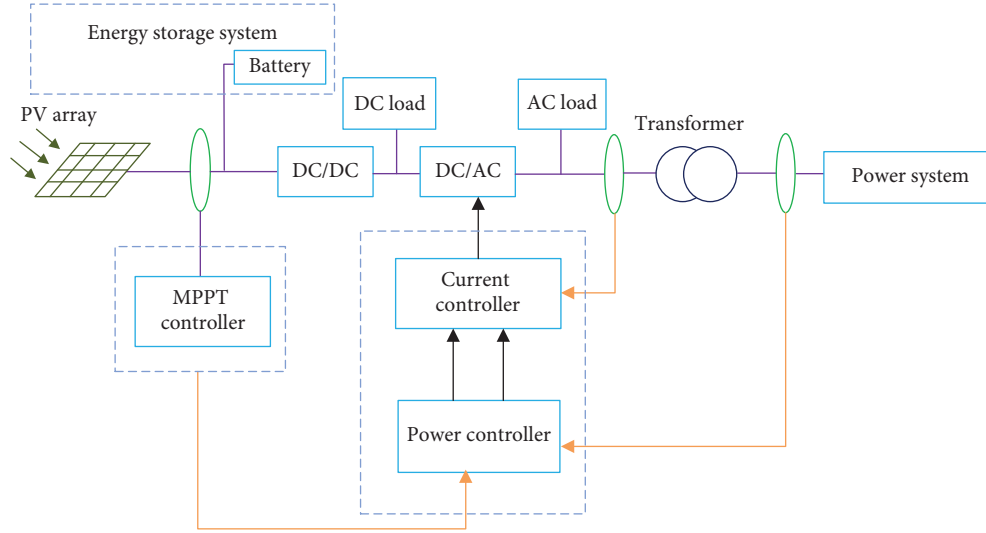


FIGURE 2: The control structure block diagram of the PV system.

where  $P_{PV2}$  is the DC side input power of the DC link;  $P_{pve}$  is the output power of the DC link inverter side;  $C$  is the capacitance value of the DC link capacitance;  $V_D$  is the voltage value of the dc link; the  $E_C$  is the amount of energy stored on a capacitor.

The wind-solar complementary energy system has three operating states: first, the wind turbine generated independently; second, the PV array independent power generation state; and third, wind-solar complementary power generation. Wind speed, solar radiation, load power consumption, and charging and discharging capacity of the energy storage device all determine the operation state of the wind-solar complementary energy system. Due to the randomness of these factors, the stability of the power system is bound to be affected to some extent. Therefore, it is necessary to analyze the stability of the small-signal of the power system integrated with renewable energy. The control structure diagram of the wind-solar energy system is giving in Figure 3.

### 3. Small-Signal Stability Analysis

The Lyapunov linearization method is related to the local stability of nonlinear systems. The basic idea is to obtain the local stability of nonlinear systems near their equilibrium operation points from the linear approximation stability property of nonlinear systems [20–22].

For the dynamic characteristic differential-algebraic equation of the power system, linearization at the steady-state operating point  $(x_0, y_0)$  can be obtained as follows [23–25]:

$$\begin{bmatrix} \frac{d\Delta x}{dt} \\ 0 \end{bmatrix} = \begin{bmatrix} \tilde{A} & \tilde{B} \\ \tilde{C} & \tilde{D} \end{bmatrix} \begin{bmatrix} \Delta x \\ \Delta y \end{bmatrix}, \quad (11)$$

where  $\Delta x$  represents the state variable that describes the dynamic characteristics of the power system in the system of

differential equations and  $\Delta y$  represents the operating parameters of the system in algebraic equations.  $\tilde{A}$ ,  $\tilde{B}$ ,  $\tilde{C}$ ,  $\tilde{D}$  are, respectively, their partial derivatives at steady-state operating point  $(x_0, y_0)$ .

Omitting operation parameter  $y$ , the following equation can be obtained:

$$\frac{d\Delta x}{dt} = A\Delta x, \quad (12)$$

with

$$\begin{aligned} A &= \tilde{A} - \tilde{B}\tilde{D}^{-1}\tilde{C}, \\ \tilde{A} &= \begin{bmatrix} A_1 & 0 & 0 & 0 \\ 0 & A_2 & 0 & 0 \\ 0 & 0 & A_3 & 0 \\ 0 & 0 & 0 & A_{10} \end{bmatrix}, \\ \tilde{B} &= \begin{bmatrix} B_1 & 0 & 0 & 0 & 0 \\ 0 & B_2 & 0 & 0 & 0 \\ 0 & 0 & B_3 & 0 & 0 \\ 0 & 0 & 0 & B_{10} & 0 \end{bmatrix}, \\ \tilde{C} &= \begin{bmatrix} -C_1 & 0 & 0 & 0 \\ 0 & -C_2 & 0 & 0 \\ 0 & 0 & -C_3 & 0 \\ 0 & 0 & 0 & -C_{10} \\ 0 & 0 & 0 & 0 \end{bmatrix}, \\ \tilde{D} &= \begin{bmatrix} Y_{GG} - D_G & Y_{GL} \\ Y_{LG} & Y_{LL} \end{bmatrix}. \end{aligned} \quad (13)$$

Matrix  $A$  is usually called the state matrix of the system. The stability of the analyzed system at the steady-state operating point  $(x, y)$  can be judged by obtaining the eigenvalue of matrix  $A$  [26–28]:



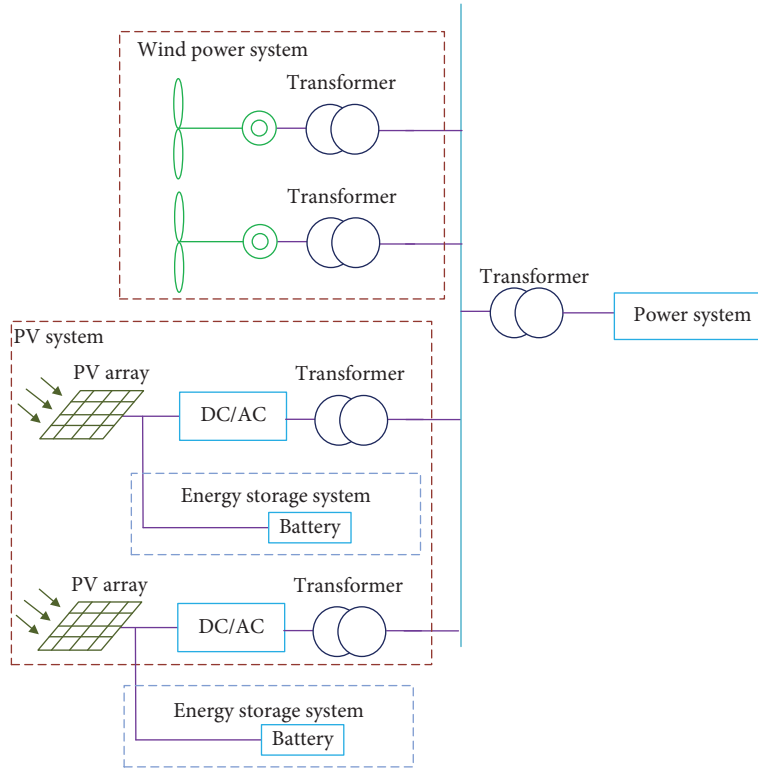


FIGURE 3: Control structure diagram of the wind-solar energy system.

- When the real part of all eigenvalues of  $A$  is negative, it means that the actual power system can maintain stability when the equilibrium point encounters a small-signal.
- When at least one real part of all eigenvalues of  $A$  is positive, it means that the actual power system will lose stability when it encounters a small-signal at the equilibrium point.
- When all eigenvalues of  $A$  have no positive eigenvalue of the real part, but at least one eigenvalue of the real part is zero, then the linearized system is in  $A$  critical stable state, but it cannot be used to judge whether the actual power system is stable at the equilibrium point.
- A real characteristic root corresponds to a non-oscillating mode. The modes represented by negative real characteristic roots are attenuated, and the greater the absolute value, the faster the corresponding modes decay.
- Complex characteristic roots always appear as conjugate pairs and can be described as

$$\lambda = \sigma \pm j\omega. \quad (14)$$

Complex eigenvalues are always composed of conjugate pairs, which can be described as the negative real part represents the damping oscillation mode [29–31]. The positive real part represents the increased oscillation, and the real part of the eigenvalue represents the damping of the

system oscillation, while the imaginary part represents the frequency of the system oscillation [32]. The frequency of oscillation can be expressed as [33]

$$f = \frac{\omega}{2\pi}. \quad (15)$$

The damping ratio is defined as

$$\zeta = \frac{-\sigma}{\sqrt{\sigma^2 + \omega^2}}. \quad (16)$$

It represents the attenuation characteristic of the oscillation amplitude.

#### 4. Case Studies

The proposed methodology is tested on the New England power system, as shown in Figure 4. It consists of 39 buses and 10 generators, and the New York grid connected to the New England power system is represented by the first generator. In addition, detailed system parameters are shown in literature [16]. The proposed methodology has been developed in MATLAB 2017 b environment. In order to analyze the damping characteristics of interconnected systems when wind farm and PV system are connected to the power system, the eigenvalue analysis is carried out for the following four working conditions:

- Initial system
- Only wind farms are connected on bus #1 and output 5 MW

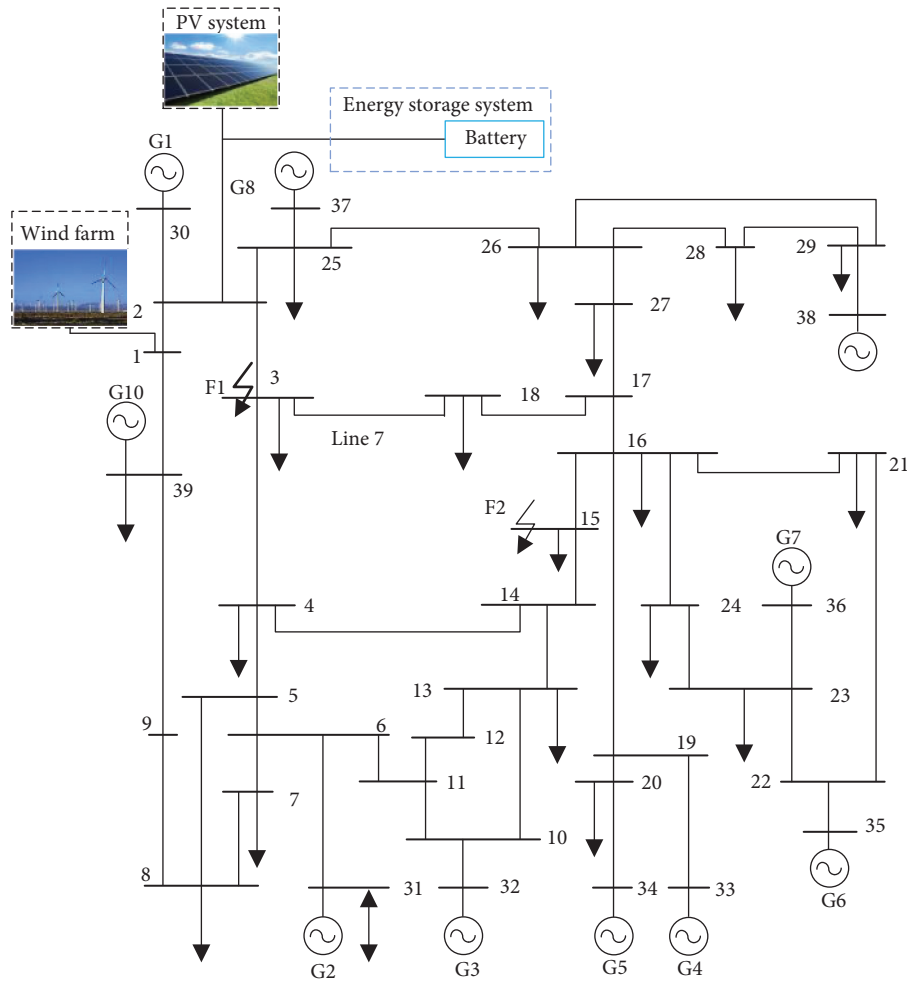


FIGURE 4: The configuration of the New England power system.

TABLE 1: Eigenvalues of the system.

Case	Characteristic root	Fluctuating frequency (Hz)	Damping ratio	Relevant units
Without wind or PV	$-0.9789 \pm j6.8784$	1.0947	0.1408	G1, G2
	$-1.2415 \pm j7.4895$	1.2332	0.1582	G1, G3
	$-0.3021 \pm j4.1298$	0.6573	0.0730	G1, G5
	$-0.8243 \pm j7.1776$	1.0065	0.1292	G1, G8
	$-0.5194 \pm j7.9844$	0.9476	0.0869	G1, G9
	$-0.4123 \pm j4.4777$	0.7937	0.0824	G1, G10
	$-0.6512 \pm j6.6744$	0.8156	0.1260	G2, G3
	$-1.1654 \pm j6.2732$	0.7402	0.2430	G2, G4
	$-0.9426 \pm j5.0038$	1.1116	0.1337	G2, G5
Only wind	$-1.1584 \pm j7.1777$	1.1423	0.1593	G1, G2
	$-1.3828 \pm j7.9844$	1.2707	0.1706	G1, G3
	$-0.5108 \pm j4.4778$	0.7126	0.1133	G1, G5
	$-1.0342 \pm j6.6744$	1.0622	0.1531	G1, G8
	$-0.7109 \pm j6.2732$	0.9984	0.1126	G1, G9
	$-0.4223 \pm j5.0038$	0.7963	0.0841	G1, G10
	$-0.6718 \pm j5.1594$	0.8211	0.1291	G2, G3
	$-1.2612 \pm j4.8112$	0.7657	0.2535	G2, G4
	$-1.1018 \pm j7.2496$	1.1538	0.1502	G2, G5
	$-0.4291 \pm j0.7962$	0.1267	0.4744	G1-G10, DFIG

TABLE 1: Continued.

Case	Characteristic root	Fluctuating frequency (Hz)	Damping ratio	Relevant units
Only PV	$-1.3548 \pm j7.5049$	1.1944	0.1776	G1, G2
	$-1.5051 \pm j8.1882$	1.3031	0.1807	G1, G3
	$-0.7568 \pm j4.8878$	0.7779	0.1530	G1, G5
	$-1.2497 \pm j7.0336$	1.1194	0.1749	G1, G8
	$-1.0015 \pm j6.7575$	1.0755	0.1466	G1, G9
	$-0.5817 \pm j5.2695$	0.8386	0.1097	G1, G10
	$-0.7693 \pm j5.3220$	0.8470	0.1431	G2, G3
	$-1.2929 \pm j4.8640$	0.7741	0.2569	G2, G4
	$-1.2851 \pm j7.5551$	1.2024	0.1677	G2, G5
	$-0.6627 \pm j1.1856$	0.1886	0.4879	G1-G10, PV
Combination of wind and PV	$-1.4818 \pm j7.7166$	1.2281	0.1885	G1, G2
	$-1.5323 \pm j8.2336$	1.3104	0.1829	G1, G3
	$-0.8368 \pm j5.0210$	0.7991	0.1643	G1, G5
	$-1.2958 \pm j7.1105$	1.1316	0.1792	G1, G8
	$-1.0858 \pm j6.8981$	1.0978	0.1554	G1, G9
	$-0.7138 \pm j5.4895$	0.8736	0.1289	G1, G10
	$-0.9275 \pm j5.5855$	0.8889	0.1638	G2, G3
	$-1.4302 \pm j5.0927$	0.8105	0.2703	G2, G4
	$-1.5478 \pm j7.9928$	1.2721	0.1901	G2, G5
	$-0.8182 \pm j1.4446$	0.2299	0.4928	G1-G10, DFIG
	$-0.7283 \pm j5.0665$	0.8064	0.1423	G1-G10, PV

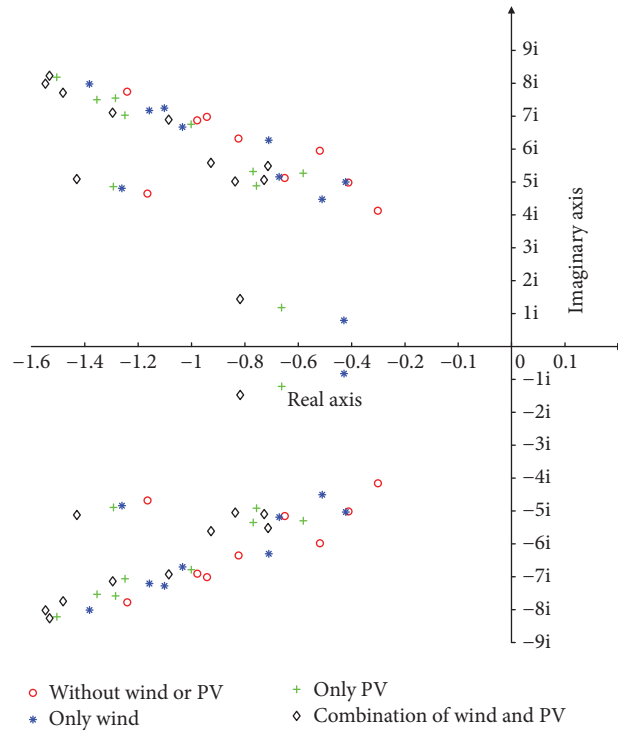


FIGURE 5: Root loci distribution of different conditions.

- (c) Only the PV system is connected on bus #2 and output 5 MW
- (d) Wind farms and the PV system are both connected on bus #1 and bus #2, respectively, and the output is 2.5 MW and 2.5 MW, respectively

Table 1 shows the partial eigenvalues of the system in four cases. It can be seen that when wind farm and PV

system are connected separately, their characteristic roots are all far away from the imaginary axis. In particular, after the addition of wind and solar energy, the characteristic root distribution was well improved, which indicates that wind power and PV system independent access system both can significantly improve the stability and, at the same time, are complementary to each other. And Root loci distribution of different conditions is given in Figure 5.

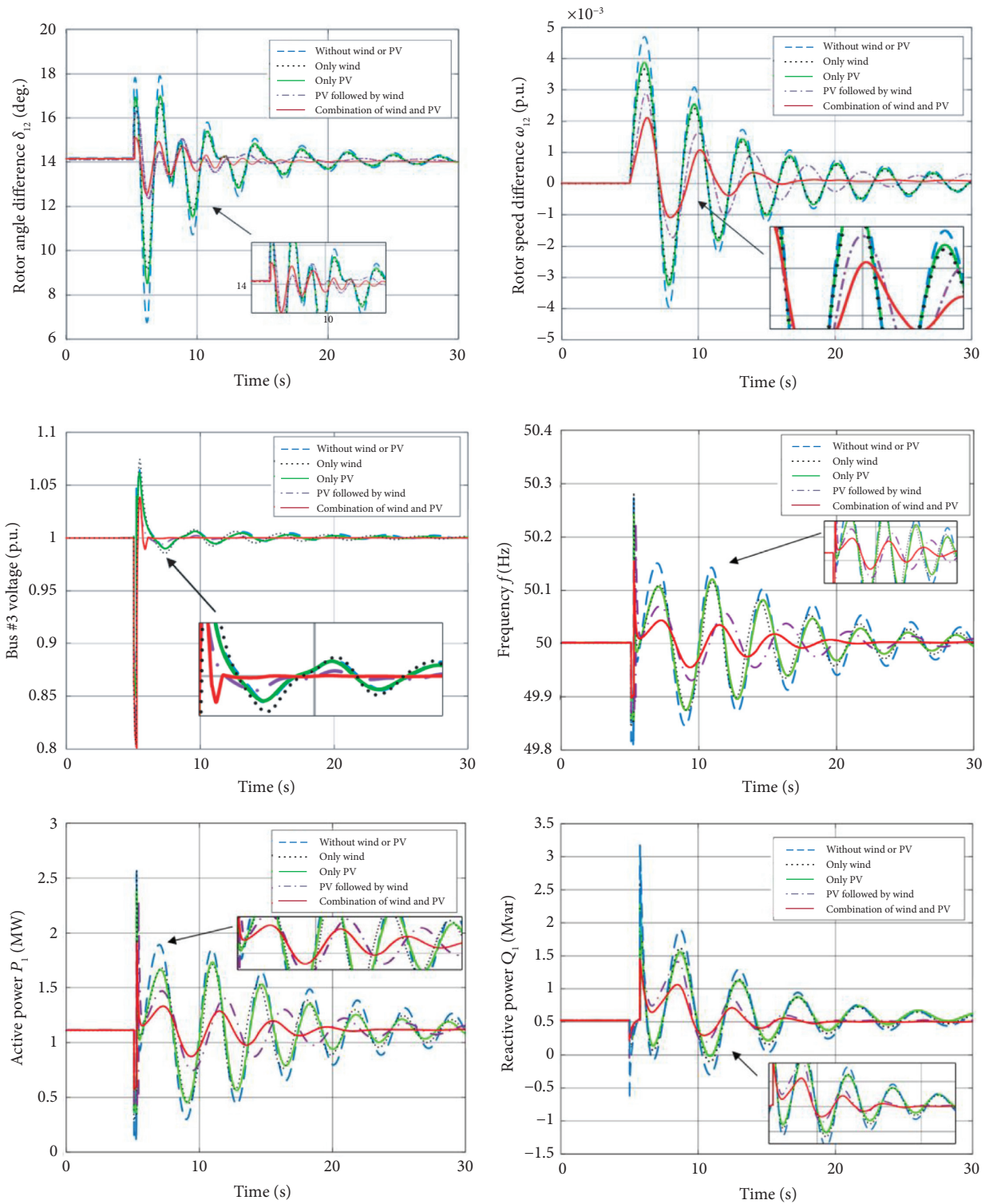


FIGURE 6: System responses obtained under bus #3 voltage drop.

**4.1. Bus #3 Voltage Drop.** In order to further verify the validity of the characteristic roots above, voltage drop 0.8 p.u. occurred at bus #3 when  $t = 5$  s and recovered after 0.1 s. The corresponding system response is shown in Figure 6. It can be seen that the system that does not involve wind-solar renewable energy in frequency modulation has

the worst recovery ability after small-signal, while, with the connection of wind and solar energy, the recovery ability of the system after small-signal is improved. In particular, the system combination of wind and solar energy has the best recovery from small-signal and the ability to adjust the system frequency to near the rated frequency in the shortest amount of time.

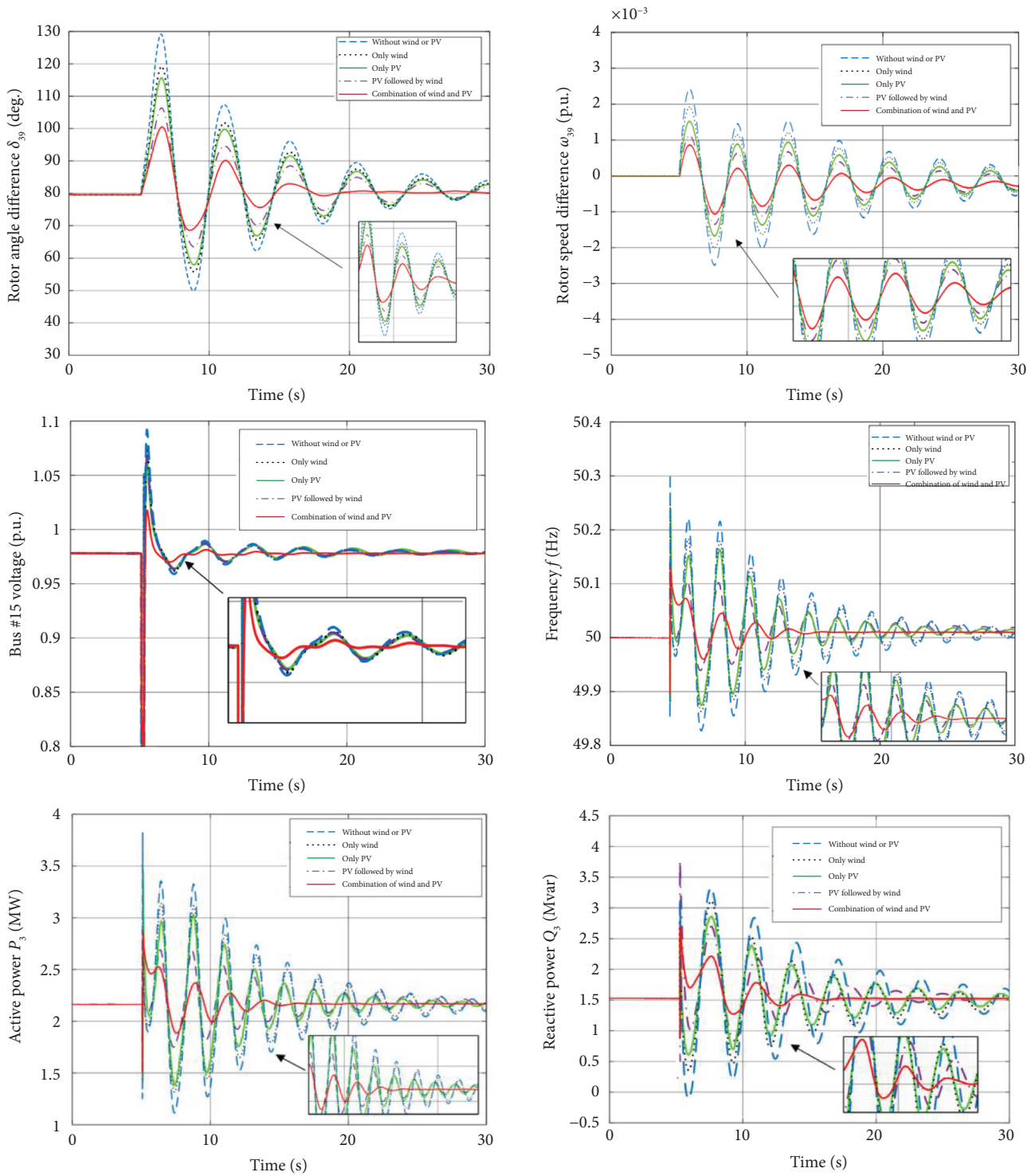


FIGURE 7: System responses obtained under bus #15 voltage drop.

**4.2. Bus #15 Voltage Drop.** In order to verify the recovery ability of the system after receiving small-signal at different positions, voltage drop 0.8 p.u. occurred at bus #15 when  $t = 5$  s and recovered after 0.1 s. And the voltage was restored after 0.1 s. The corresponding system response is shown in Figure 7. It can be found that, with the system combination of wind and PV, the rotor angle difference regulation

capacity of generator  $G_1$  is significantly improved, its oscillation amplitude is significantly reduced, and it is restored to the rated value in the shortest time. In addition, it has the best regulation ability for active power and reactive power and will adjust the system to the steady-state in the shortest period, so that the system subject to small-signal has the strongest frequency regulation ability.

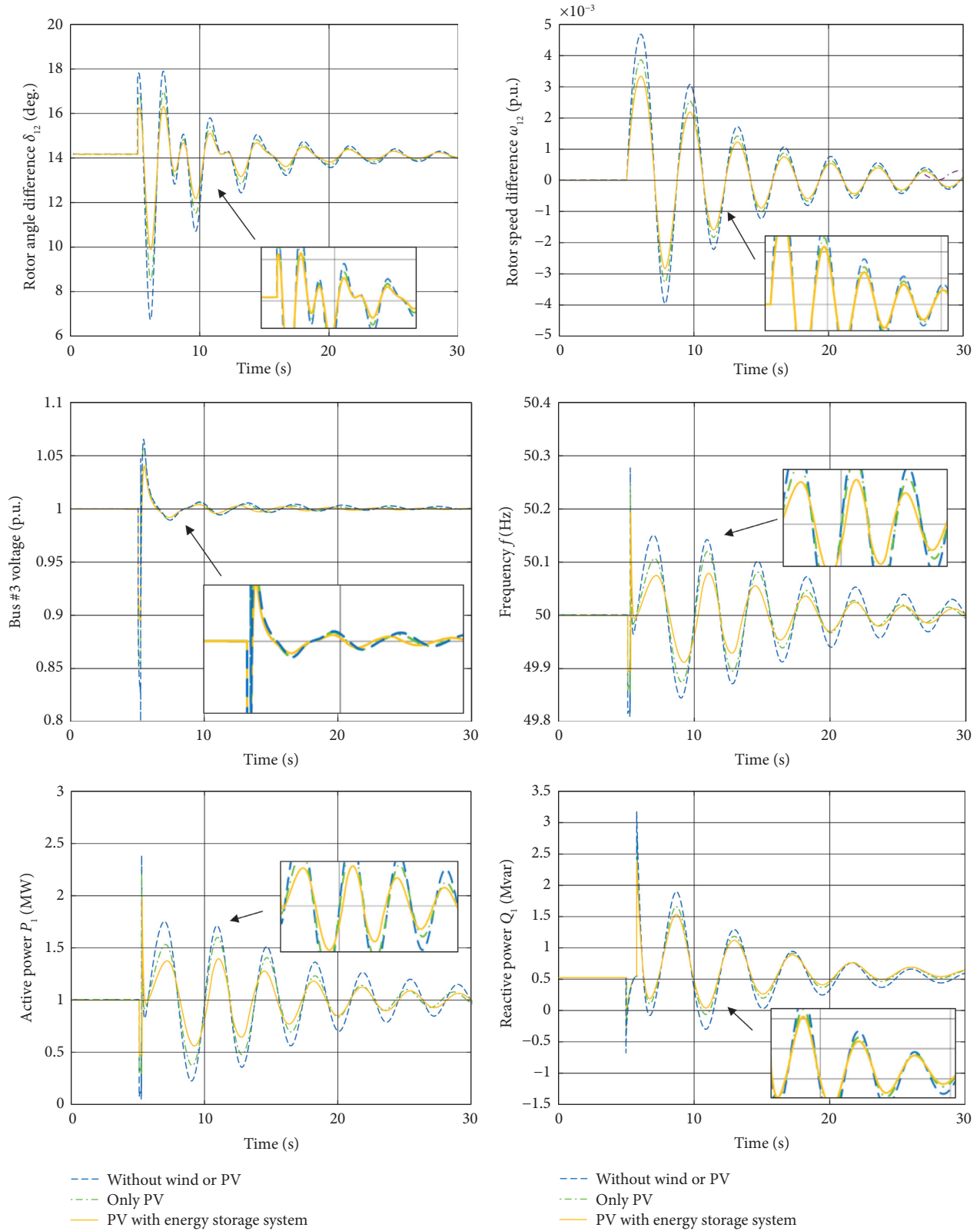


FIGURE 8: System responses obtained under bus #3 voltage drop.

## 5. Discussion

**5.1. Bus #3 Voltage Drop.** In order to further study the positive effect of the energy storage system on the PV station,

based on the above case, this paper considers that the energy storage system is configured in the PV station connected to bus #2. In addition, voltage drop 0.8 p.u. occurred at bus #3 when 5 s and recovered after 0.1 s, and its system response is



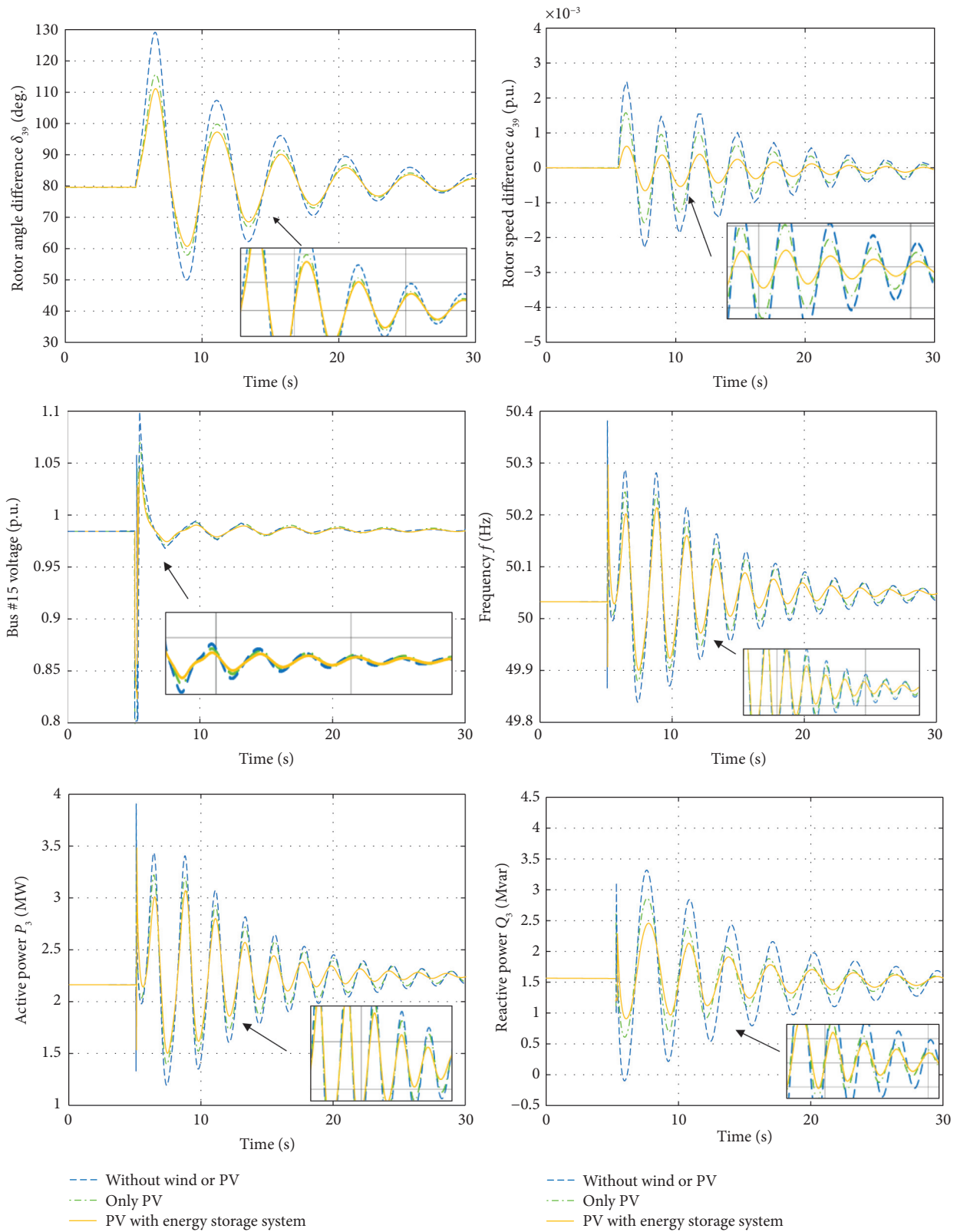


FIGURE 9: System responses obtained under bus #15 voltage drop.

shown in Figure 8. It can be seen that after the PV system is configured with the energy storage system, the stability of small-signal is better. Compared with the initial PV system, it can restore system frequency in a relatively short time.

**5.2. Bus #15 Voltage Drop.** Consider the following fault: voltage drop 0.8 p.u. occurred at bus #15 with 5 s and recovered after 0.1 s. To verify the stability of the system in case of failure at different locations, its system response is shown

TABLE 2: IAE indices of six parameters acquired in two fault locations (in p.u.).

Cases: bus #3 voltage drop	$IAE_{\delta_{12}}$	$IAE_{\omega_{12}}$	$IAE_{U_3}$	$IAE_f$	$IAE_{P_1}$	$IAE_{Q_1}$
Without wind or PV	1.155	$1.239 \times 10^{-2}$	0.785	0.094	0.545	0.759
Only wind	0.956	$1.058 \times 10^{-2}$	0.696	0.089	0.516	0.694
Only PV	0.911	$1.042 \times 10^{-2}$	0.677	0.087	0.505	0.696
PV with energy storage system	0.870	$1.024 \times 10^{-2}$	0.651	0.083	0.489	0.675
PV followed by wind	0.810	$0.985 \times 10^{-2}$	0.594	0.081	0.470	0.648
Combination of wind and PV	0.715	$0.898 \times 10^{-2}$	0.452	0.076	0.441	0.617
Cases: bus #15 voltage drop	$IAE_{\delta_{39}}$	$IAE_{\omega_{39}}$	$IAE_{U_{15}}$	$IAE_f$	$IAE_{P_3}$	$IAE_{Q_3}$
Without wind or PV	1.196	$1.314 \times 10^{-2}$	0.818	0.098	0.559	0.776
Only wind	0.928	$1.082 \times 10^{-2}$	0.734	0.095	0.542	0.746
Only PV	0.897	$1.066 \times 10^{-2}$	0.695	0.092	0.524	0.714
PV with energy storage system	0.846	$1.034 \times 10^{-2}$	0.669	0.088	0.516	0.701
PV followed by wind	0.797	$0.997 \times 10^{-2}$	0.619	0.086	0.490	0.692
Combination of wind and PV	0.731	$0.921 \times 10^{-2}$	0.481	0.078	0.445	0.658

in Figure 9. It can be found that the frequency regulation ability of the PV station equipped with the energy storage system is greatly improved, which can well suppress the frequency fluctuation of the power system subjected to small-signal disturbance. In addition, it can help the synchronous generator to recover to the stable state in a short time.

**5.3. Comparative Analysis.** The integral of absolute error (IAE) of each index in different fault locations is given in Table 2, in which  $IAE_x = \int_0^T |x - x^*| dt$  and  $x^*$  denotes the reference of variable  $x$ , respectively. In particular,  $IAE_{\delta_{12}}$  of the system of combination of wind and PV is merely 61.90%, 74.79%, 78.49%, 82.84%, and 88.27% of that without wind and PV, only wind, only PV, PV station with energy storage system, and PV followed by wind, respectively, acquired in #3 bus voltage drop (bold colour indicates the best results in Table 2).

## 6. Conclusions

More and more large- and medium-sized renewable energy power stations have been built and connected to the power system, and they account for an increasing proportion of the power system. It affects the stability and damping characteristics of the traditional power system. In this paper, the influence of wind power and photovoltaic energy on the stability of the power system is studied, and the main conclusions are as follows:

- Based on the calculation of characteristic roots, it is proved that power system integrated with wind and solar energy participating in frequency regulation has better stability.
- Based on the New England power system, the damping characteristics of the system can be effectively improved and the system can be more stable after the wind-solar renewable energy is incorporated into the power system.
- Based on the New England power system test, it is verified that the photovoltaic power station can improve its stability to a certain extent after installing

the energy storage system. Particularly,  $IAE_f$  acquired by PV with energy storage system is merely 88.30% and 95.40% of that without wind or PV and only PV, respectively, on the case of bus #3 voltage drop.

## Data Availability

The data that support the findings of this study are available upon request from the corresponding author. The data are not publicly available due to privacy or ethical restrictions.

## Conflicts of Interest

The authors declare no conflicts of interest.

## Acknowledgments

The authors gratefully acknowledge the support of the Research and Development Start-Up Foundation of Shantou University (NTF19028) and Research on Regional Power Grid Frequency Regulation with Renewable Energy Participation (YNKJXM20191240).

## References

- H. Zhang, Z. Lu, W. Hu, Y. Wang, L. Dong, and J. Zhang, "Coordinated optimal operation of hydro-wind-solar integrated systems," *Applied Energy*, vol. 242, pp. 883–896, 2019.
- M. Sara, E. Ahmed, N. Tamou, and B. I. Badr, "NA direct power control of a DFIG based-WECS during symmetrical voltage dips," *Protection and Control of Modern Power Systems*, vol. 5, no. 1, pp. 36–47, 2020.
- D. Xie, Y. Lu, J. Sun, and C. Gu, "Small signal stability analysis for different types of PMSGs connected to the grid," *Renewable Energy*, vol. 106, pp. 149–164, 2017.
- J. Liu, W. Yao, J. Wen et al., "Impact of power grid strength and PLL parameters on stability of grid-connected DFIG wind farm," *IEEE Transactions on Sustainable Energy*, vol. 11, no. 1, pp. 545–557, 2020.
- D. Song, X. Fan, J. Yang, A. Liu, S. Chen, and Y. H. Joo, "Power extraction efficiency optimization of horizontal-axis wind turbines through optimizing control parameters of yaw control systems using an intelligent method," *Applied Energy*, vol. 224, pp. 267–279, 2018.

- [6] D. R. Song, S. Y. Zheng, S. Yang et al., "Annual energy production estimation for variable-speed wind turbine at high-altitude site," *Journal of Modern Power Systems and Clean Energy*, 2020.
- [7] B. Mokhtar, B. Antonio, C. Pierluigi, C. Guido, C. Mauro, and D. F. Pasquale, "Bayesian bootstrap quantile regression for probabilistic photovoltaic power forecasting," *Protection and Control of Modern Power Systems*, vol. 5, no. 3, pp. 36–47, 2020.
- [8] L. Ruisheng, W. K. Peter, B. L. Wang, and F. Y. Fang, "Power quality enhancement and engineering application with high permeability distributed photovoltaic access to low-voltage distribution networks in Australia," *Protection and Control of Modern Power Systems*, vol. 5, no. 3, pp. 1–7, 2020.
- [9] X. Yan, "A review of cyber security risks of power systems: from static to dynamic false data attacks," *Protection and Control of Modern Power Systems*, vol. 5, no. 3, pp. 8–19, 2020.
- [10] J. I. A. Qi, Y. A. N. Gangui, C. A. I. Yuru, L. I. Yonglin, and J. Zhang, "Small-signal stability analysis of photovoltaic generation connected to weak AC grid," *Journal of Modern Power Systems and Clean Energy*, vol. 7, no. 2, pp. 254–267, 2019.
- [11] P. He, F. Wen, G. Ledwich, and Y. Xue, "Small signal stability analysis of power systems with high penetration of wind power," *Journal of Modern Power Systems and Clean Energy*, vol. 1, no. 3, pp. 237–244, 2013.
- [12] S. G. Sathana, S. Ashok, and S. Kumaravel, "Small signal stability analysis of grid connected renewable energy resources with the effect of uncertain wind power penetration," *Energy Procedia*, vol. 117, pp. 769–776, 2017.
- [13] L. Xu and Y. Wang, "Dynamic modeling and control of DFIG-based wind turbines under unbalanced network conditions," *IEEE Transactions on Power Systems*, vol. 22, no. 1, pp. 314–323, 2017.
- [14] A. Bektache and B. Boukhezzer, "Nonlinear predictive control of a DFIG-based wind turbine for power capture optimization," *International Journal of Electrical Power & Energy Systems*, vol. 101, pp. 92–102, 2018.
- [15] M. Fei and B. Pal, "Modal analysis of grid-connected doubly fed induction generators," *IEEE Transactions on Energy Conversion*, vol. 22, pp. 728–736, 2007.
- [16] K. H. Lam, T. M. Lai, W. C. Lo, and W. M. To, "The application of dynamic modelling techniques to the grid-connected PV (photovoltaic) systems," *Energy*, vol. 46, no. 1, pp. 264–274, 2012.
- [17] D. S. H. Chan and J. C. H. Phang, "Analytical methods for the extraction of solar-cell single- and double-diode model parameters from I-V characteristics," *IEEE Transactions on Electron Devices*, vol. 34, no. 2, pp. 286–293, 1987.
- [18] D.-J. Lee and L. Wang, "Small-signal stability analysis of an autonomous hybrid renewable energy power generation/energy storage system part I: time-domain simulations," *IEEE Transactions on Energy Conversion*, vol. 23, no. 1, pp. 311–320, 2008.
- [19] Q. Wu, Y. Huang, C. Li, Y. Gu, H. Zhao, and Y. Zhan, "Small signal stability of synchronous motor-generator pair for power system with high penetration of renewable energy," *IEEE Access*, vol. 7, pp. 166964–166974, 2019.
- [20] O. A. Ajeigbe, J. L. Munda, and Y. Hamam, "Optimal allocation of renewable energy hybrid distributed generations for small-signal stability enhancement," *Energies*, vol. 12, no. 24, p. 4777, 2019.
- [21] S. Gurung, S. Naetiladdanon, and A. Sangswang, "Coordination of power-system stabilizers and battery energy-storage system controllers to improve probabilistic small-signal stability considering integration of renewable-energy resources," *Applied Sciences*, vol. 9, no. 6, p. 1109, 2019.
- [22] Z. Zeng, H. Yang, and R. Zhao, "Study on small signal stability of microgrids: a review and a new approach," *Renewable and Sustainable Energy Reviews*, vol. 15, no. 9, pp. 4818–4828, 2011.
- [23] S. Wei, Y. Zhou, Y. Zhou, S. Li, and Y. Huang, "A possible configuration with motor-generator pair for renewable energy integration View Document," *CSEE Journal of Power and Energy Systems*, vol. 3, no. 1, pp. 93–100, 2017.
- [24] A. U. Krismanto, N. Mithulanathan, and O. Krause, "Stability of renewable energy based microgrid in autonomous operation," *Sustainable Energy Grids and Networks*, vol. 13, pp. 134–147, 2018.
- [25] A. Krismanto, N. Mithulanathan, and K. Y. Lee, "Comprehensive modelling and small signal stability analysis of RES-based microgrid," *IFAC-PapersOnLine*, vol. 48, no. 30, pp. 282–287, 2015.
- [26] M. Amin and M. Molinas, "Small-signal stability assessment of power electronics based power systems: a discussion of impedance- and eigenvalue-based methods," *IEEE Transactions on Industry Applications*, vol. 53, no. 5, pp. 5014–5030, 2017.
- [27] K. Adirak, C. K. Vira, and A. Kenneth, "Small-signal stability enhancement of power systems with renewable distributed energy resources," *IFAC Proceedings Volumes*, vol. 44, no. 1, pp. 513–518, 2011.
- [28] Y. Pan, F. Liu, L. Chen et al., "Towards the robust small-signal stability region of power systems under perturbations such as uncertain and volatile wind generation," *IEEE Transactions on Power Systems*, vol. 33, no. 2, pp. 1790–1799, 2017.
- [29] W. Du, Q. Fu, X. Wang, and H. F. Wang, "Small-signal stability analysis of integrated VSC-based DC/AC power systems - a review," *International Journal of Electrical Power & Energy Systems*, vol. 103, pp. 545–552, 2018.
- [30] X. Xi, H. Geng, and G. Yang, "Enhanced model of the doubly fed induction generator-based wind farm for small-signal stability studies of weak power system," *IET Renewable Power Generation*, vol. 8, no. 7, pp. 765–774, 2014.
- [31] T. Knüppel, J. N. Nielsen, K. H. Jensen, A. Dixon, and J. Østergaard, "Small-signal stability of wind power system with full-load converter interfaced wind turbines," *IET Renewable Power Generation*, vol. 6, no. 2, pp. 79–91, 2012.
- [32] A. U. Krismanto and N. Mithulanathan, "Identification of modal interaction and small signal stability in autonomous microgrid operation," *IET Generation Transmission & Distribution*, vol. 12, no. 1, pp. 247–257, 2017.
- [33] D. C. Das, N. Sinha, and A. K. Roy, "Small signal stability analysis of dish-Stirling solar thermal based autonomous hybrid energy system," *International Journal of Electrical Power & Energy Systems*, vol. 63, pp. 485–498, 2014.

## Research Article

# Robust Kalman Filter-Based Dynamic State Estimation of Natural Gas Pipeline Networks

Liang Chen <sup>1</sup>, Peng Jin,<sup>2</sup> Jing Yang,<sup>2</sup> Yang Li <sup>3</sup>, and Yi Song<sup>4</sup>

<sup>1</sup>School of Automation, Nanjing University of Information Science and Technology, Nanjing 210044, China

<sup>2</sup>State Grid Customer Service Center, Tianjin 300309, China

<sup>3</sup>School of Electrical Engineering, Northeast Electric Power University, Jilin 132012, China

<sup>4</sup>StateGrid Economic and Technological Research Institute Co., Ltd., Beijing 102209, China

Correspondence should be addressed to Yang Li; [liyang@neepu.edu.cn](mailto:liyang@neepu.edu.cn)

Received 28 January 2021; Revised 10 February 2021; Accepted 27 February 2021; Published 8 March 2021

Academic Editor: Xiao-Shun Zhang

Copyright © 2021 Liang Chen et al. This is an open access article distributed under the Creative Commons Attribution License, which permits unrestricted use, distribution, and reproduction in any medium, provided the original work is properly cited.

To obtain the accurate transient states of the big scale natural gas pipeline networks under the bad data and non-zero mean noises conditions, a robust Kalman filter-based dynamic state estimation method is proposed using the linearized gas pipeline transient flow equations in this paper. Firstly, the dynamic state estimation model is built. Since the gas pipeline transient flow equations are less than the states, the boundary conditions are used as supplementary constraints to predict the transient states. To increase the measurement redundancy, the zero mass flow rate constraints at the sink nodes are taken as virtual measurements. Secondly, to ensure the stability under bad data condition, the robust Kalman filter algorithm is proposed by introducing a time-varying scalar matrix to regulate the measurement error variances correctly according to the innovation vector at every time step. At last, the proposed method is applied to a 30-node gas pipeline network in several kinds of measurement conditions. The simulation shows that the proposed robust dynamic state estimation can decrease the effects of bad data and achieve better estimating results.

## 1. Introduction

In comparison with the traditional coal-fired power units, gas-fired electric generators can respond to the power load fluctuation rapidly, enhancing the operating flexibility of electrical energy systems [1–3]. This may help to improve security of power system with large-scale renewable energy. The random change of the natural gas consumptions due to the uncertainties of renewable energies makes it essential for obtaining the accurate dynamic states just like the pressures and mass flow rates of the natural gas pipeline networks to ensure the security and optimal operation of the integrated energy system containing electric powers and natural gases [4–7]. To capture the states, the pipeline networks have to be equipped with a mount of measuring devices, which requires heavy investments. Even so, it is impossible to install sensors at every node of the networks and obtain all states. On the other hand, the measuring devices experience random errors and bad data unavoidably, so the measured data cannot be

applied directly to the leak detections [8, 9] and control problems [10] before state estimations.

In recent years, some research works about state estimations for natural gas pipeline networks have appeared [11–15]. These works are based on the nonlinear partial differential equation (PDE) describing the characteristics of transient gas flow [16, 17]. To linearize the PDEs of gas systems, in [18, 19], the dynamic states are redefined as deviations from steady states for linearization purpose. In [20], an iterative linear approximation is proposed, which is used to solve optimal power flow problem, rather than the linearization of PDEs. In [11], a state estimation method for natural gas pipe lines by using the linearization of PDEs [20–22] is proposed. To improve the estimating performance, the state estimation with a pair of Kalman filter-based estimators running in parallel is carried out. Some researchers established the state estimation model applying the PDEs directly, and solved the model by nonlinear algorithms. In [12], the extended Kalman filter (EKF) is



chosen to design an efficient observer for natural gas transmission system, and then an algorithm is proposed to handle the discontinuities that appear in the dynamic model of a gas transmission networks. In [13], a two-step Lax-Wendroff method is used for the discretization of the PDEs to obtain finite-dimensional discrete-time state-space representations, and the particle filter that fits for the nonlinear filter problems is applied to estimate the transient states. These methods can capture the accurate states in the transient processes. However, as the scale expands, the centralized implementation of the Kalman filter has severe limitations such as tuning, scalability, unacceptable calculating loads, and lack of robustness in the case of sensor failures. Aiming at this problem, a strategy for the distributed and decentralized state estimation of state variables in big scale systems is proposed in [14]. In addition, the algorithm for a joint state and parameter estimation problem for large-scale networks of pipelines is presented in [15], and the gradient descent algorithm is applied to solve the optimization problem.

In practical systems, the supervisory control and data administration system experience random errors and bad data inevitably due to the sensor error and electromagnetic interference. The existing state estimation methods based on Kalman filter can reduce the random errors to some extent but are vulnerable to bad data. To solve this problem, a variety of improved Kalman filter algorithms are proposed. Based on variational Bayesian technique, an adaptive Kalman filter for linear Gaussian state-space models is proposed in [23, 24], which has better robustness to resist the uncertainties of process and measurement noise covariance matrices, as well as the colored measurement noise. In [25], a robust filter in a batch-mode regression form is developed to process the observations and predictions together, making it very effective in suppressing multiple outliers. To ensure the stability of the unscented Kalman filter, the unknown time-varying matrix is introduced to describe the prediction error of the unscented transformation in [26]. It can be seen that the robustness of the Kalman filter is a big challenge for its practical applications, attracting more and more researchers' attentions.

The existing gas pipeline network state estimation methods based on Kalman filter solve the transient flow equations by using a numerical approximation technique called finite element methods. These estimation methods have the following drawbacks:

- (1) The gas pipe lines are divided into several linear elements, and the number of variables increases accordingly. For large-scale networks with long pipes, to ensure the estimating accuracy, many linear elements have to be created, as well as the states, causing low measurement redundancy and heavy computation load.
- (2) The algorithm robustness against bad data is not considered. Once the measurements in the practical system experience bad data or non-zero mean noises, the estimating performances cannot be guaranteed.

To cope with the above problems, and obtain accurate transient states of large-scale gas pipeline networks under practical operating conditions, this paper focuses on the robust dynamic state estimation method along with the following contributions:

- (1) To deal with the problem that the transient equations are less than the states, the boundary conditions are used as supplementary constraints, and the linear process functions are established. The zero mass flow rates at the sink nodes are taken as virtual measurements, improving the measurement redundancy.
- (2) A time-varying scalar matrix is proposed to regulate the measurement variance matrix according to the innovations, where the measurements can correct the predicted states accurately, and then increasing the robustness of the Kalman filter against the bad data and non-zero mean noises.
- (3) The proposed dynamic state estimation method is tested on a 30-node natural gas pipeline network under the normal measurement condition, bad data condition, and non-zero mean noises condition. The simulation results show that the proposed approach manages to perform robust DSE of natural gas pipeline networks and the performance of the proposed method is better than the traditional Kalman filter.

The rest of this paper is organized as follows. Section 2 builds the mathematical model of the DSEs for gas pipelines. Section 3 proposes the robust Kalman filter algorithm based on the time-varying scalar matrix. Section 4 shows and analyzes the simulation results under various conditions. Finally, Section 5 concludes this paper.

## 2. DSE Modeling of Gas Pipeline Network

As the basic components of natural gas systems, the pipelines can store a certain amount of natural gases due to the compressibility, which is called the linepack storage. For the natural gas systems with a large number of pipelines, the linepack storage drives the dynamic process of the nodal pressure and mass flow of the natural gas in the pipelines. To describe the above physical dynamic mathematically, the state space representation of transient gas flows is introduced.

*2.1. State Space Representation of Transient Gas Flow.* Under stable operating conditions, the gas states such as the nodal pressure and mass flow rate in pipelines are constant. However, in practical natural gas systems, the stable operating condition can be disrupted easily due to the continuous changes of gas loads, supplies of gas companies, and other operational activities, causing the fluid dynamic process along pipelines, which can be represented by a set of nonlinear partial differential equations (PDEs). These PDEs are derived from the momentum conservation principles

and material balances, which is given as the following state space form [4, 11, 27]:

$$\frac{\partial \rho}{\partial t} + \frac{\partial(\rho u)}{\partial x} = 0, \quad (1a)$$

$$\frac{\partial(\rho u)}{\partial t} + \frac{\partial(\rho u^2)}{\partial x} + \frac{\partial p}{\partial x} = -\frac{f \rho u |u|}{2d} - \rho g \sin \theta, \quad (1b)$$

where,  $\rho$ ,  $p$ , and  $u$  are the density, pressure, and gas velocity, respectively;  $t$  and  $x$  are the time and spatial coordinate, respectively;  $f$  is the friction factor;  $g$  is the gravitational constant;  $\theta$  is the pipe inclination angle; and  $d$  is the pipe diameter. The second term on the left-hand side of (1b) describes the convective effect of the natural gas, which can be omitted when the gas velocity is significantly smaller than the sound speed in practical operation [4, 11]. Further, we assume that the pipelines are horizontal, hence the inclination angle is zero, and the second term on the right-hand side of (1b) can also be omitted. Under the condition that the gas pressure is less than 10 bar and the temperature is lower than 20°C, the functions between the pressure, mass flow rate, and the gas density are as follows [4, 11]:

$$\begin{aligned} p &= c^2 \rho, \\ \dot{m} &= \rho u a, \end{aligned} \quad (2)$$

where  $c^2 = ZRT$ ;  $\dot{m}$  and  $a$  are the mass flow rate and cross section area of pipelines, respectively, and  $Z$ ,  $R$ , and  $T$  are the gas compressibility factor, the specific gas constant, and the gas temperature, respectively. For the natural gas,  $c^2$  is constant if the temperature is not changing. Here, the absolute value of average gas velocity  $|\bar{u}|$  is used instead of  $|u|$ . Under the aforementioned assumptions, equations (1a) and (1b) can be rewritten as the following equation [4]:

$$\frac{\partial \rho}{\partial t} + \frac{\partial \dot{m}}{a \partial x} = 0, \quad (3a)$$

$$\frac{\partial \dot{m}}{a \partial t} + c^2 \frac{\partial \rho}{\partial x} + \frac{f \dot{m} |\bar{u}|}{2da} = 0. \quad (3b)$$

The simplified partial differential equations (3a) and (3b) are able to describe the practical natural gas dynamic process in continuous form, which should be transformed to difference equation before numerical solving.

**2.2. Discretization of PDE.** A generalized model of natural gas pipelines is shown in Figure 1. Assume that the node numbers of the three nodes of pipelines are  $i$ ,  $j$ , and  $k$ , respectively, and  $k < i < j$ . The gas flow direction is defined as from the smaller node to the bigger node. Thus, the gas flow directions of pipeline  $k-i$  and  $i-j$  are  $k \rightarrow i$  and  $i \rightarrow j$ , respectively. The gas densities are  $\rho_k$ ,  $\rho_i$ , and  $\rho_j$ , while the mass flow rates on the two sides of the pipeline  $i-j$  are  $\dot{m}_{ij}$  and  $\dot{m}_{ji}$ , respectively. The mass flow rate of gas load at node  $i$  is  $\dot{m}_i$ . For simplification, the compressor at  $k$  end of pipeline  $ki$  is modeled as a constant ratio of densities  $c_{rki}$ . The positive direction is defined as flowing out; thus the mass flow rate values are negative for the source nodes. Every natural gas pipeline can be modeled according to Figure 1 and satisfy the PDEs (3a) and (3b). One of the common methods for solving PDEs is the Euler finite difference technique, which is applied to solve (3a) and (3b) in our works. The differencing scheme is [28]

$$\frac{\partial X}{\partial t} \approx \frac{1}{2} \left( \frac{X_{s+1,t+1} - X_{s+1,t}}{\Delta t} + \frac{X_{s,t+1} - X_{s,t}}{\Delta t} \right), \quad (4a)$$

$$\frac{\partial X}{\partial x} \approx \frac{1}{2} \left( \frac{X_{s+1,t+1} - X_{s,t+1}}{\Delta x} + \frac{X_{s+1,t} - X_{s,t}}{\Delta x} \right), \quad (4b)$$

$$X \approx \frac{1}{4} (X_{s+1,t+1} + X_{s,t+1} + X_{s+1,t} + X_{s,t}), \quad (4c)$$

where  $X$  represents the generalized states;  $\Delta t$  and  $\Delta x$  are the time and spatial step widths respectively; and the subscripts  $s$  and  $t$  represent the  $s$ th node and time step  $t$ , respectively. Equations (3a) and (3b) can be transformed to (5a) and (5b) according to the differencing scheme (4a)–(4c) for pipeline  $i-j$ .

$$c_{rji} \rho_{j,t+1} - c_{rji} \rho_{j,t} + c_{rij} \rho_{i,t+1} - c_{rij} \rho_{i,t} + \frac{\Delta t}{L_{pij} a_{ij}} (\dot{m}_{ji,t+1} - \dot{m}_{ij,t+1} + \dot{m}_{ji,t} - \dot{m}_{ij,t}) = 0, \quad (5a)$$

$$\dot{m}_{ji,t+1} - \dot{m}_{ij,t+1} + \dot{m}_{ji,t} - \dot{m}_{ij,t} + \frac{a_{ij} \Delta t c^2}{L_{pij}} (c_{rji} \rho_{j,t+1} - c_{rij} \rho_{i,t+1} + c_{rji} \rho_{j,t} - c_{rij} \rho_{i,t}) + \frac{\gamma |\bar{v}_G| \Delta t}{4d_{ij} a_{ij}} (\dot{m}_{ij,t+1} + \dot{m}_{ji,t+1} + \dot{m}_{ij,t} + \dot{m}_{ji,t}) = 0, \quad (5b)$$

where the subscript  $ij$  represents the pipeline  $i-j$  and  $L_{ij}$  is the length of pipeline  $i-j$ . In addition to the difference equations, some boundary conditions should be satisfied.

**2.3. Boundary Conditions.** The gas flow dynamic processes and gas density distribution are influenced by the changes of operating conditions at both the source and sink nodes.



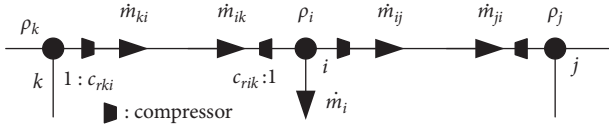


FIGURE 1: The general model of natural gas pipelines.

Under the practical operating condition, the mass flow rates at sink nodes are changing, while the gas density is constant at the source nodes. These constraints are defined as boundary conditions.

The boundary condition of the mass flow rate balance at sink nodes is represented as

$$\sum_{k \in i, k < i} \dot{m}_{ik,t} - \sum_{j \in i, j > i} \dot{m}_{ij,t} = \dot{m}_{i,t}, \quad i \in N_{\text{Sink}}, \quad (6)$$

where  $k \in i$  means the node  $k$  connected to node  $i$  with pipeline  $i-k$ ;  $i \in N_{\text{Sink}}$  represents  $i$  is the source node. The first and second terms of (6) represent the sum of mass flow rates from node  $i$  and to node  $i$ , respectively.

For the source nodes, the assumption is made that the gas capacities are big enough so that the gas density is able to maintain constant in the dynamic process. This forms the following boundary condition:

$$\rho_{i,t} = \rho_{Si,0}, \quad i \in N_{\text{Source}}, \quad (7)$$

where  $\rho_{Si,0}$  is the gas density at source node  $i$  at initial time;  $i \in N_{\text{Source}}$  represents  $i$  is the source node.

The boundary conditions supply more constraints, making it possible to build the mathematical model of DSE for the natural gas pipeline networks.

**2.4. Mathematical Model of DSE.** The DSE based on Kalman filter includes two basic steps, the prediction and filtering. In the prediction step, the difference equations and boundary conditions are used to predict the states. In this work, the gas densities at nodes and mass flow rates at the two ends of pipelines are taken as states. Hence, for a natural gas pipeline network with  $n_N$  nodes and  $n_L$  pipelines, the number of states is  $n_N + 2n_L$ . The state vector at time step  $t$  is  $\mathbf{x}_t = [\mathbf{x}_{r,t}, \mathbf{x}_{m,t}]^T$ ,  $\mathbf{x}_{r,t} = [\rho_{1,t}, \rho_{2,t}, \dots, \rho_{n_N,t}]^T$ ,  $\mathbf{x}_{m,t} = [\dots, \dot{m}_{ij,t}, \dot{m}_{ji,t}, \dots]^T$ ,  $i < j$ .  $\mathbf{x}_{r,t}$  is the state vector of gas densities;  $\mathbf{x}_{m,t}$  is the state vector of mass flow rates, and the dimension of  $\mathbf{x}_{m,t}$  is  $2n_L$ . Based on the above state definition, (5a) and (5b) can be rewritten as

$$\begin{bmatrix} \mathbf{A}_{11} & \mathbf{A}_{12} \\ \mathbf{A}_{21} & \mathbf{A}_{22} \end{bmatrix} \begin{bmatrix} \mathbf{x}_{r,t+1} \\ \mathbf{x}_{m,t+1} \end{bmatrix} = \begin{bmatrix} \mathbf{A}_{11} & -\mathbf{A}_{12} \\ -\mathbf{A}_{21} & -\mathbf{A}_{22} \end{bmatrix} \begin{bmatrix} \mathbf{x}_{r,t} \\ \mathbf{x}_{m,t} \end{bmatrix}, \quad (8)$$

$$\mathbf{A}_{11}(l, i) = \begin{cases} c_{rij}, & \text{if } i \in l, j \in l, \\ 0, & \text{else,} \end{cases} \quad \mathbf{A}_{11} \in \mathbb{R}^{n_p \times n_N}, \quad (9)$$

$$\mathbf{A}_{12} = \begin{bmatrix} -\alpha_1 & \alpha_1 & & & & \mathbf{0} \\ & -\alpha_2 & \alpha_2 & & & \\ & & & \ddots & & \\ \mathbf{0} & & & & -\alpha_{n_L} & \alpha_{n_L} \end{bmatrix}, \quad \mathbf{A}_{12} \in \mathbb{R}^{n_L \times 2n_L}, \quad (10)$$

$$\alpha_l = \frac{\Delta t}{L_{ij} a_{ij}}, \quad i \in l, j \in l, \quad (11)$$

$$\mathbf{A}_{21}(l, i) = \begin{cases} -c_{rij} \beta_l, & \text{if } i \in l, j \in l, i < j, \\ c_{rji} \beta_l, & \text{if } i \in l, j \in l, i > j, \\ 0, & \text{else,} \end{cases} \quad \mathbf{A}_{21} \in \mathbb{R}^{n_p \times n_N}, \quad (12)$$

$$\beta_l = \frac{a_{ij} \Delta t c^2}{L_{ij}}, \quad i \in l, j \in l, \quad (13)$$

$$\mathbf{A}_{22}(l, i) = \begin{cases} \gamma_l - 1, & \text{if } i \in l, j \in l, i < j, \\ \gamma_l + 1, & \text{if } i \in l, j \in l, i > j, \\ 0, & \text{else,} \end{cases} \quad \mathbf{A}_{22} \in \mathbb{R}^{n_L \times 2n_L}, \quad (14)$$

$$\gamma_l = \frac{f|\bar{u}|\Delta t}{4d_{ij} a_{ij}}, \quad i \in l, j \in l, \quad (15)$$

where  $(l, i)$  represents the row  $l$  and column  $i$ ;  $i \in l$  means node  $i$  is one end of pipeline  $l$ . For the natural gas pipeline systems, the total number of state variables is  $n_N + 2n_L$ , but the number of equations in (8) is  $2n_L$ . Equation (8) cannot be solved because the states are more than the equations. The boundary conditions can be applied as the supplementary constraints. Similarly, (6) and (7) can be rewritten in the matrix form.

$$\begin{bmatrix} \mathbf{B}_{11} & \mathbf{0}_{n_{in} \times 2n_L} \\ \mathbf{0}_{n_{out} \times n_N} & \mathbf{B}_{22} \end{bmatrix} \begin{bmatrix} \mathbf{x}_{r,t+1} \\ \mathbf{x}_{m,t+1} \end{bmatrix} = \begin{bmatrix} \mathbf{u}_{r,t+1} \\ \mathbf{u}_{m,t+1} \end{bmatrix}, \quad (16)$$

$$\mathbf{B}_{11}(s, i) = \begin{cases} 1, & i \in N_{\text{Source}}, \\ 0, & \text{else,} \end{cases} \quad \mathbf{B}_{11} \in \mathbb{R}^{n_{in} \times n_{out}}, \quad (17)$$

$$\mathbf{B}_{22}(j, 2l) = \begin{cases} 1, & j \in N_{\text{Sink}}, j \in l, \\ 0, & \text{else,} \end{cases} \quad \mathbf{B}_{22} \in \mathbb{R}^{n_{out} \times 2n_L}, \quad (18a)$$

$$\mathbf{B}_{22}(i, 2l-1) = \begin{cases} -1, & \text{if } i \text{ is a outlet node, } i \in l, \\ 0, & \text{else,} \end{cases} \quad (18b)$$

where  $\mathbf{u}_{r,t+1} = [\dots, \rho_{Si,0}, \dots]^T$ ,  $i \in N_{\text{Source}}$ ,  $\mathbf{u}_{r,t+1} \in \mathbb{R}^{n_{\text{Source}}}$ ;  $\mathbf{u}_{m,t+1} = [\dots, \dot{m}_{j,t+1}, \dots]^T$ ,  $i \in N_{\text{Sink}}$ ,  $\mathbf{u}_{m,t+1} \in \mathbb{R}^{n_{\text{Sink}}}$ ;  $n_{\text{Source}}$  and  $n_{\text{Sink}}$  are the numbers of source and sink nodes, respectively;  $s$  is the source nodes number,  $s = 1, 2, \dots, n_{\text{Source}}$ ;  $\mathbf{0}$  is the zero matrix and the subscript of  $\mathbf{0}$  is the dimension.

Equations (8) and (16) can be written as the following concentrated form:

$$\mathbf{A}\mathbf{x}_{t+1} = \mathbf{B}\mathbf{x}_t + \mathbf{U}_{t+1}, \quad (19)$$

where  $\mathbf{A} = \begin{bmatrix} \mathbf{A}_{11} & \mathbf{A}_{12} \\ \mathbf{A}_{21} & \mathbf{A}_{22} \\ \mathbf{B}_{11} & \mathbf{0}_{n_{in} \times 2n_L} \\ \mathbf{0}_{n_{out} \times n_N} & \mathbf{B}_{22} \end{bmatrix}$ ,  $\mathbf{B} = \begin{bmatrix} \mathbf{A}_{11} & -\mathbf{A}_{12} \\ -\mathbf{A}_{21} & -\mathbf{A}_{22} \\ \mathbf{0}_{n_{in} \times n_N} & \mathbf{0}_{n_{in} \times 2n_L} \\ \mathbf{0}_{n_{out} \times n_N} & \mathbf{0}_{n_{out} \times 2n_L} \end{bmatrix}$ ,  $\mathbf{U}_{t+1} = \begin{bmatrix} \mathbf{0}_{n_L \times 1} \\ \mathbf{0}_{n_L \times 1} \\ \mathbf{u}_{r,t+1} \\ \mathbf{u}_{m,t+1} \end{bmatrix}$ .

Then multiplied by the inverse matrix of the left matrix, (19) becomes

$$\mathbf{x}_{t+1} = \mathbf{F}\mathbf{x}_t + \mathbf{u}_{t+1}, \quad (20)$$

where  $\mathbf{F} = \mathbf{A}^{-1}\mathbf{B}$ ,  $\mathbf{u}_{t+1} = \mathbf{A}^{-1}\mathbf{U}_{t+1}$ .

Equation (20) is the system equation of the gas pipeline networks, which is used to represent the dynamic processes. Additionally, the measured pressure and mass flow rate information from supervisory control and data administration systems provide redundant constraints for the DSE. In this work, assume that all of the nodes are equipped with flow meters and barometers; hence such information is taken as the measurement vectors. The measurement function is

$$\mathbf{z}_{t+1} = \mathbf{H}_{t+1}\mathbf{x}_{t+1}, \quad (21)$$

$$\mathbf{H}_{t+1} = \begin{bmatrix} c^2 \mathbf{I}_{n_N \times n_N} & \mathbf{0}_{n_N \times 2n_L} \\ \mathbf{0}_{n_N \times n_N} & \mathbf{H}' \end{bmatrix},$$

where  $\mathbf{H}'(j, 2l) = \begin{cases} 1, & j \propto l, \\ 0, & \text{else,} \end{cases}$ ,  $\mathbf{H}'(i, 2l-1) = \begin{cases} -1, & i \propto l, \\ 0, & \text{else,} \end{cases}$ ,  $\mathbf{H}' \in \mathbb{R}^{n_N \times 2n_L}$ ,  $\mathbf{z}_{t+1} = [z_{r1,t+1}, z_{r2,t+1}, \dots, z_{rn_N,t+1}, z_{m1,t+1}, z_{m2,t+1}, \dots, z_{mm_N,t+1}]^T$ ;  $\mathbf{I}$  is an identity matrix; and  $z_{ri,t+1}$  and  $z_{mi,t+1}$  are the note pressure and mass flow rate measurements at time instant  $t+1$ , respectively.

Up to now, the DSE model of gas pipeline networks is formed:

$$\begin{cases} \mathbf{x}_{t+1} = \mathbf{F}\mathbf{x}_t + \mathbf{u}_{t+1} + \mathbf{v}_t, \\ \mathbf{z}_{t+1} = \mathbf{H}\mathbf{x}_{t+1} + \mathbf{w}_{t+1}, \end{cases} \quad (22)$$

where  $\mathbf{v}_t$  and  $\mathbf{w}_{k+1}$  are the system and measurement error vectors, respectively,  $\mathbf{v}_t \in \mathbb{R}^{n_N+2n_L}$ ,  $\mathbf{w}_{t+1} \in \mathbb{R}^{2n_N}$ . The variance matrixes of  $\mathbf{v}_{t+1}$  and  $\mathbf{w}_{k+1}$  are  $\mathbf{Q}_{t+1}$  and  $\mathbf{R}_{t+1}$ , respectively. In this paper, the errors are assumed to satisfy the normal distribution. However, the practical measurement experiences bad data inevitably due to the electromagnetic interference or transmission errors. Additionally, in some cases, the mean values of the measurement errors are not zero, so the errors are non-zero mean noises.

The states in (22) should be estimated by the DSE algorithm based on Kalman filter.

### 3. Robust Dynamic State Estimation Algorithm

One of the commonly used dynamic state estimation algorithms is Kalman filter, which is used in this work.

**3.1. Kalman Filter.** Kalman filter algorithm [29] includes two basic steps: prediction and filtering.

**3.1.1. Prediction Step.** Given the initial estimated state  $\hat{\mathbf{x}}_0$  and its covariance matrix  $\mathbf{P}_{t|t}$ , the state prediction  $\tilde{\mathbf{x}}_{t+1}$  and predicting covariance matrix  $\mathbf{P}_{t+1|t}$  can be calculated by

$$\tilde{\mathbf{x}}_{t+1} = \mathbf{F}\hat{\mathbf{x}}_t + \mathbf{u}_{t+1}, \quad (23)$$

$$\mathbf{P}_{t+1|t} = \mathbf{F}\mathbf{P}_{t|t}\mathbf{F}^T + \mathbf{Q}_t. \quad (24)$$

**3.1.2. Filtering Step.** The predicted state  $\tilde{\mathbf{x}}_{t+1}$  should be corrected, and the estimated state  $\hat{\mathbf{x}}_{t+1}$  and covariance matrix  $\mathbf{P}_{t+1|t+1}$  are obtained.

$$\mathbf{K}_{k+1} = \mathbf{P}_{t+1|t}\mathbf{H}^T(\mathbf{H}\mathbf{P}_{t+1|t}\mathbf{H}^T + \mathbf{R}_{t+1})^{-1}, \quad (25)$$

$$\hat{\mathbf{x}}_{t+1} = \tilde{\mathbf{x}}_{t+1} + \mathbf{K}_{t+1}(\mathbf{z}_{t+1} - \mathbf{H}\tilde{\mathbf{x}}_{t+1}), \quad (26)$$

$$\mathbf{P}_{t+1|t+1} = \mathbf{P}_{t+1|t} - \mathbf{K}_{k+1}\mathbf{H}\mathbf{P}_{t+1|t}. \quad (27)$$

The right part of (25),  $\mathbf{P}_{e,t+1} = \mathbf{H}\mathbf{P}_{t+1|t}\mathbf{H}^T + \mathbf{R}_{t+1}$ , is the innovation covariance matrix, which represents the errors between measurements and their predicting values. When the measurements experience bad data,  $\mathbf{P}_{e,t+1}$  cannot represent the real errors correctly. Thus, the estimating performance of Kalman filter decreases. In this work, we introduce a time-varying scalar to regulate the measurement variance matrix, making Kalman filter robust.

**3.2. Time-Varying Scalar.** Kalman filter estimates the states by trading off the predicted states against the measurements according to the measurement and prediction variances. If the measurements experience bad data, Kalman filter would not correct the predicted states accurately and result in a poor estimation results. Aiming at this problem, to make the algorithm robust to the bad data, a time-varying scalar matrix  $\boldsymbol{\mu}_t$  is proposed to regulate the measurement variance matrix. The objective of  $\boldsymbol{\mu}_t$  is to fulfill

$$\mathbf{P}_{e,t+1} = \mathbf{H}\mathbf{P}_{t+1|t}\mathbf{H} + \boldsymbol{\mu}_{t+1}\mathbf{R}_{t+1}. \quad (28)$$

To obtain the value of  $\boldsymbol{\mu}_{t+1}$ , the sliding window method is used to estimate the innovation covariance matrix:

$$\mathbf{P}_{e,t+1} = \frac{1}{m_W} \sum_{i=0}^{m_W-1} \mathbf{e}_{t+1-i}\mathbf{e}_{t+1-i}^T = \mathbf{H}\mathbf{P}_{t+1|t}\mathbf{H} + \boldsymbol{\mu}_{t+1}\mathbf{R}_{t+1}, \quad (29)$$

where  $\mathbf{e}_{t+1} = \mathbf{z}_{t+1} - \mathbf{H}\tilde{\mathbf{x}}_{t+1}$  is the innovation vector and  $m_W$  is the window length. By solving (29),  $\boldsymbol{\mu}_{t+1}$  can be obtained as

$$\boldsymbol{\mu}_{t+1} = \left( \frac{1}{m_w} \sum_{i=0}^{m_w-1} \mathbf{e}_{t+1-i}\mathbf{e}_{t+1-i}^T - \mathbf{H}\mathbf{P}_{t+1|t}\mathbf{H} \right) \mathbf{R}_{t+1}^{-1}. \quad (30)$$

The obtained  $\boldsymbol{\mu}_{t+1}$  by (30) may be non-diagonal; as a result, the inversion of the innovation covariance matrix is singular probably. Aiming at this problem, a diagonal matrix  $\boldsymbol{\mu}_{t+1}$  is defined

$$\boldsymbol{\mu}'_{t+1} = \text{diag}(\mu'_1, \mu'_2, \dots, \mu'_{2n_N}), \quad (31)$$

where  $\mu'_i = \max(1, \mu_{t+1,ii})$ ,  $i = 1, 2, \dots, 2n_N$ ,  $\mu_{t+1,ii}$  is the  $i$ th diagonal element. Equation (25) becomes

$$\mathbf{K}_{k+1} = \mathbf{P}_{t+1|t} \mathbf{H}^T (\mathbf{H} \mathbf{P}_{t+1|t} \mathbf{H}^T + \boldsymbol{\mu}'_{t+1} \mathbf{R}_{t+1})^{-1}. \quad (32)$$

With the help of the scalar, the modified robust Kalman filter can decrease the influence of bad data, and a better performance can be obtained than the traditional Kalman filter.

#### 4. Case Study

In this section, the proposed DSE method is applied to a 30-node natural gas pipeline network shown in Figure 2. The time-varying mass flow rates of gas loads are simulated artificially and the dynamic processes of the node pressures and mass flow rates are calculated by (5a)~(7). The simulation results are taken as true values, and the measurements are derived by adding random numbers to the real values. The traditional Kalman filter and the proposed algorithm are used to estimate the states of the gas pipeline system. The DSE is carried out in the following three measurement conditions: normal condition, bad data condition, and non-zero mean noises condition.

*4.1. Description of the Test System.* The test system includes 30 nodes and 29 pipelines, which is used to evaluate the performances of DSE methods. The lengths and cross-sectional diameters are given in Table 1. The friction factor  $f$  and the gas speed  $c^2$  are 0.015 and 340 m/s, respectively. Gas is supplied at the source node 1 and 2, and the pressures of these two nodes are 27.8 bar and 28.5 bar, respectively. We assume that the capacities of gas sources are infinite, which means the pressures are constant in the dynamic processes.

The simulation interval is 15 minutes over the time horizon of 24 hours. All nodes are equipped with flow meters and barometers, so the pressures and mass flow rates can be measured. The standard deviations of pressure and mass flow rate measurements are 0.01 bar and 2%, respectively. Note that the mass flow rates at the conjunction nodes are zero, which can be taken as virtual measurements. The errors of virtual measurements are smaller than others, and the errors are set to 0.001 in our work.

*4.2. Normal Measurement Condition.* In this section, the DSE is carried out under the normal measurement condition that the measurement errors obey the Gauss distribution with zero mean. The traditional Kalman filter and robust Kalman filter are used to estimate the states, and the results are compared by the filter coefficient  $\varepsilon$  [30, 31].

$$\varepsilon = \frac{\sum_t (\widehat{z}_t - \mathbf{z}_t^+)^2}{\sum_t (\mathbf{z}_t - \mathbf{z}_t^+)^2}, \quad (33)$$

where  $\widehat{z}_t$  is the estimated value of measurements, which can be calculated by the estimated states and  $\mathbf{z}_t^+$  is the true value of measurements without errors.

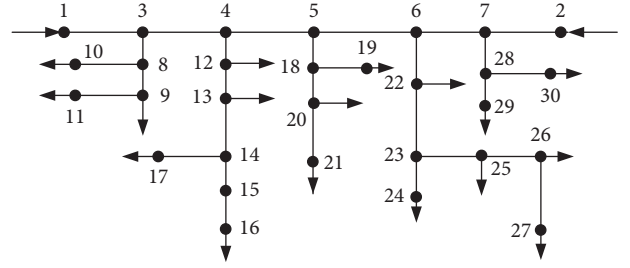


FIGURE 2: The 30-node test system. The tiny black points are pipeline conjunction nodes. Nodes 1 and 2 are the inlet nodes, and the others are the outlet nodes. The outlet nodes without arrows mean that the gas loads are zero.

TABLE 1: Parameters of gas pipelines.

Pipeline	Length (km)	Diameter (m)
1, 3	5	0.6
3, 4	3	0.6
4, 5	4	0.5
5, 6	6	0.5
6, 7	7	0.5
2, 7	2	0.5
3, 8	3	0.4
8, 9	5	0.2
8, 10	7	0.2
9, 11	5	0.4
4, 12	4	0.4
12, 13	8	0.4
13, 14	10	0.4
14, 15	9	0.2
15, 16	10	0.2
14, 17	4	0.2
5, 18	10	0.4
18, 20	3	0.2
20, 21	7	0.2
18, 19	2	0.2
6, 22	10	0.4
22, 23	6	0.2
23, 24	7	0.2
23, 25	4	0.2
25, 26	9	0.2
26, 27	4	0.2
7, 28	2	0.2
28, 29	7	0.2
28, 30	5	0.2

The filter coefficients of the two kinds of DSE methods are shown in Table 2. Nodes 1 and 2 are source nodes, the pressures of which are constant, so the filter coefficients are not computed. All results in Table 2 are smaller than 1, meaning that both the DSEs based on Kalman filter and robust Kalman filter are effective. It should be noted that the virtual measurement errors of mass flow rates at the sink nodes are very small and the denominator of (33) is approximately equal to the numerator; as a result, the filter coefficients are almost 1. Besides that, most of the coefficients of the robust Kalman filter are smaller than the traditional Kalman filter, meaning that the performance of the robust Kalman filter is better.

TABLE 2: Filter coefficients of DSEs.

Node	Pressure		Mass flow rate	
	KF	RKF	KF	RKF
1	—	—	0.1111	0.1084
2	—	—	0.4831	0.4492
3	0.0001	0.0001	0.9888	0.9888
4	0.0001	0.0001	0.9888	0.9888
5	0.0002	0.0001	0.9888	0.9888
6	0.0002	0.0001	0.9888	0.9888
7	0.0003	0.0002	0.9888	0.9888
8	0.0003	0.0002	0.9888	0.9888
9	0.0014	0.0011	0.5619	0.5161
10	0.0061	0.0049	0.5101	0.3902
11	0.0011	0.0008	0.1394	0.0706
12	0.0011	0.0007	0.4301	0.3681
13	0.0016	0.0011	0.2984	0.1957
14	0.0027	0.0021	0.5032	0.4625
15	0.0187	0.0245	0.6488	0.6339
16	0.0355	0.0363	0.0405	0.0151
17	0.0308	0.0206	0.0061	0.0021
18	0.0006	0.0004	0.9888	0.9888
19	0.0331	0.0144	0.1634	0.0956
20	0.0388	0.0293	0.2903	0.2361
21	0.0601	0.0473	0.2087	0.1523
22	0.0004	0.0003	0.4232	0.3063
23	0.0064	0.0042	0.9888	0.9888
24	0.0372	0.0249	0.0661	0.0281
25	0.0361	0.0298	0.4338	0.2521
26	0.0501	0.0363	0.3376	0.2185
27	0.0687	0.0365	0.1316	0.0748
28	0.0193	0.0114	0.9888	0.9888
29	0.0551	0.0318	0.0944	0.0606
30	0.0543	0.0394	0.1021	0.0661

**4.3. Bad Data Condition.** In practical systems, the measuring equipments experience bad data inevitably [32], which should be considered in DSEs. In this section, based on the normal measurement condition, the bad data are added to the measurement vectors artificially to test the performances of the proposed DSE for gas pipeline networks. Here, the value of the pressure measurements at node 30 is set to 12, 10.7, and 13.8 bar at time 5, 5.25, and 5.5 hours, and 13, 15.5, and 23 bar at time 13.25, 13.5, and 13.75 hours, respectively. Meanwhile, the mass flow rate measurements at node 11 are reset to 3, 2.1, 3, and 2.2 kg/s at time 7.5, 7.75, 8, and 8.25 hours, and 3, 2.1, and 1.7 kg/s at time 15.75, 16, and 16.25 hours, respectively.

The estimating results of Kalman filter and robust Kalman filter are shown in Figure 3, and the time-varying scalars are shown in Figure 4. It can be seen that the curve of Kalman filter (the green dotted line) is deviated from the true value (the blue solid line) when the bad data appeared. This is because the measurement error variance matrix does not correspond with the truth in the bad data condition. However, with the help of the time-varying scalar, the curve of robust Kalman filter (the yellow dotted line) and the true value curve are well coincident all the time. The time-varying scalar can regulate the measurement error variance matrix according to the actual errors precisely and the accurate estimating results can be obtained. When the bad data

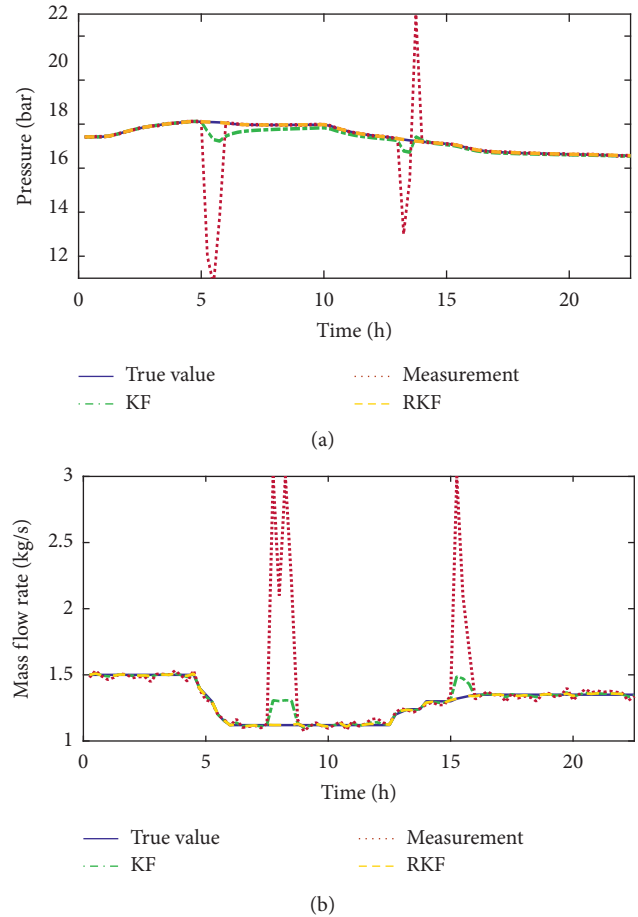


FIGURE 3: Estimating results of the pressure and mass flow rate under bad data condition.

appear, the values of the scalar increase dramatically, causing the reduction of the corresponding elements in Kalman gain matrix  $K_{t+1}$ . As a result, the correcting effects of the measurements decrease and the estimated values are little affected by the bad data.

**4.4. Non-Zero Mean Noises Condition.** The errors of measurements in the above two sections are Gaussian white noises, but in practice the non-zero mean noises are more common, which are considered in this section. Based on the condition of section B, we added constant deviations 0.2 bar and 0.1 kg/s to the pressure measurements and mass flow rate measurements from 10~19.75 hours and 5~12.5 hours, respectively.

The estimating results are shown in Figures 5 and 6. It can be seen that the estimating curves of Kalman filter deviate from the true value curves obviously under the non-zero mean noises condition. At the same time, we can notice that the scalars increase obviously while the measurement mean values are deviating from zero, and the estimating curves based on robust Kalman filter fit with the true value all the time. Furthermore, the Kalman filter curves deviate from true value gradually at the beginning of the non-zero

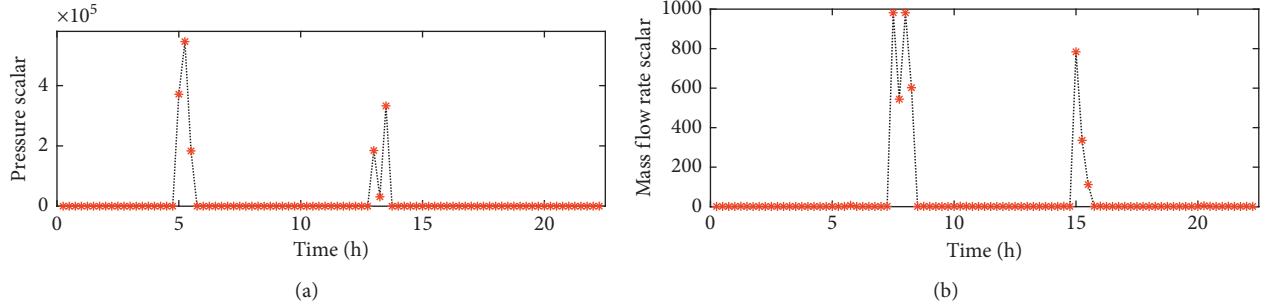


FIGURE 4: Time-varying scalars of the pressure and mass flow rate under bad data condition.

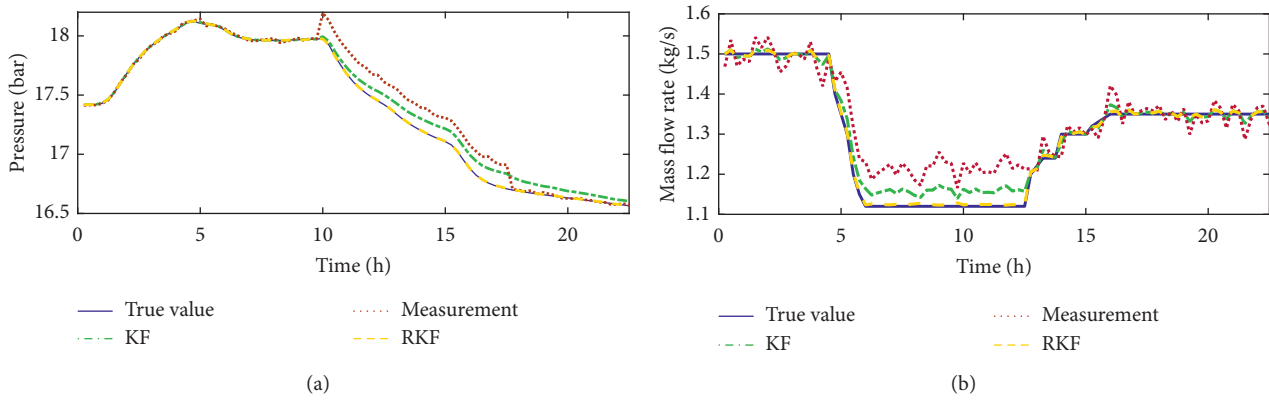


FIGURE 5: Estimating results of the pressure and mass flow rate under non-zero mean noises condition.

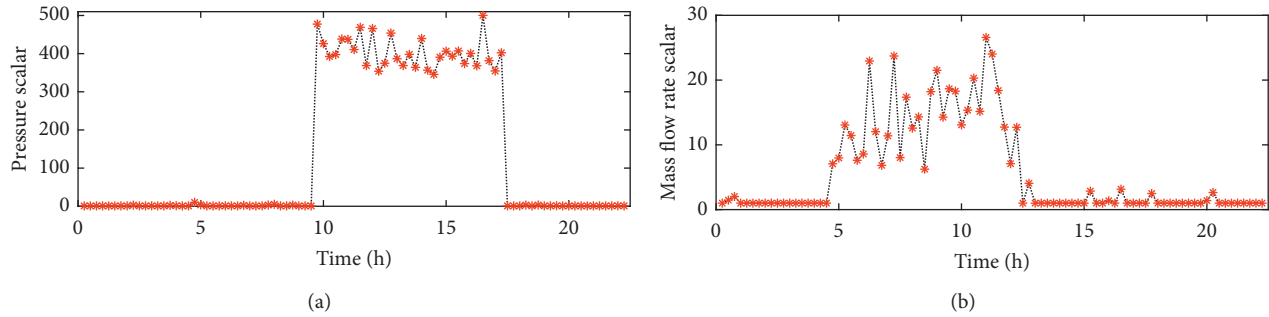


FIGURE 6: Time-varying scalars of the pressure and mass flow rate under non-zero mean noises condition.

mean noises. This is because the negative effects of the non-zero mean noises are accumulating continuously throughout the whole process. If the non-zero mean noises exist all the time, eventually, the estimated value of the Kalman filter will coincide with the deviation.

## 5. Conclusion

This paper proposes a robust dynamic state estimation method against bad data for natural gas pipeline networks. The method is applied on a 30-node pipeline network in several conditions, and the filter coefficient is used to evaluate the performances of the dynamic state estimation based on the traditional Kalman filter and the proposed

robust method. The results show that most of the filter coefficient values of the proposed method are smaller than the traditional Kalman filter in the normal measurement condition. This means that the filtering efficiency of the robust method is better. Furthermore, the two methods are studied under the bad data and non-zero mean measurement noises conditions, and the results show that the proposed method can decrease the effects of bad data, obtaining accurate estimating states under these two conditions.

Future work will focus on the accurate DSE modeling based on the nonlinear transient equations of the pipeline networks with compressors under the operating limitation constraints, and calculating method of predicting error



covariance; another interesting topic is the adaptive DSE algorithm that can cope with the model uncertainty due to parameter errors and malicious cyber attacks [33, 34]. Besides, it is interesting to extend the presented approach to the DSE of integrated energy systems with integration of new elements such as cogeneration units [35], electrical vehicles [36], modular multilevel converter based high-voltage direct current systems [37], and uncertain renewable generations [38].

## Data Availability

The data used to support the findings of this study are included within the article.

## Conflicts of Interest

The authors declare that they have no conflicts of interest.

## Acknowledgments

This work was partly supported by the Natural Science Foundation of Jilin Province, China, under grant no. 2020122349JC.

## References

- [1] S. Sreenu, C. S. Kailash, and B. Rohit, "Gumbel copula based multi interval ramp product for power system flexibility enhancement," *International Journal of Electrical Power & Energy Systems*, vol. 112, pp. 417–427, 2019.
- [2] P. Jin, Y. Li, G. Li, Z. Chen, and X. Zhai, "Optimized hierarchical power oscillations control for distributed generation under unbalanced conditions," *Applied Energy*, vol. 194, pp. 343–352, 2017.
- [3] Y. Li, C. Wang, G. Li, J. Wang, D. Zhao, and C. Chen, "Improving operational flexibility of integrated energy system with uncertain renewable generations considering thermal inertia of buildings," *Energy Conversion and Management*, vol. 207, Article ID 112526, 2020.
- [4] J. Fang, Q. Zeng, X. Ai, Z. Chen, and J. Wen, "Dynamic optimal energy flow in the integrated natural gas and electrical power systems," *IEEE Transactions on Sustainable Energy*, vol. 9, no. 1, pp. 188–198, 2018.
- [5] W. Liu, P. Li, W. Yang, and C. Y. Chung, "Optimal energy flow for integrated energy systems considering gas transients," *IEEE Transactions on Power Systems*, vol. 34, no. 6, pp. 5076–5079, 2019.
- [6] K. Rashid and K. M. Powell, "Dynamic simulation, control, and performance evaluation of a synergistic solar and natural gas hybrid power plant," *Energy Conversion and Management*, vol. 179, pp. 270–285, 2018.
- [7] Y. Wang, Y. Wang, Y. Huang et al., "Operation optimization of regional integrated energy system based on the modeling of electricity-thermal-natural gas network," *Applied Energy*, vol. 251, Article ID 113410, 2019.
- [8] F. Chraim, Y. Bugra Erol, and K. Pister, "Wireless gas leak detection and localization," *IEEE Transactions on Industrial Informatics*, vol. 12, no. 2, pp. 768–779, 2016.
- [9] L. Dong, Z. Qiao, H. Wang et al., "The gas leak detection based on a wireless monitoring system," *IEEE Transactions on Industrial Informatics*, vol. 15, no. 12, pp. 6240–6251, 2019.
- [10] N. Y. Chiang and V. M. Zavala, "Large-scale optimal control of interconnected natural gas and electrical transmission systems," *Applied Energy*, vol. 168, pp. 226–235, 2016.
- [11] D. İsmail and M. Kemal Leblebicioğlu, "State estimation of transient flow in gas pipelines by a Kalman filter-based estimator," *Journal of Natural Gas Science and Engineering*, vol. 35, pp. 189–196, 2016.
- [12] H. A. Behrooz and R. B. Boozarjomehry, "Modeling and state estimation for gas transmission networks," *Journal of Natural Gas Science and Engineering*, vol. 22, pp. 551–570, 2015.
- [13] F. E. Uilhoorn, "State-space estimation with a Bayesian filter in a coupled PDE system for transient gas flows," *Applied Mathematical Modelling*, vol. 39, no. 2, pp. 682–692, 2015.
- [14] H. A. Behrooz and R. B. Boozarjomehry, "Distributed and decentralized state estimation in gas networks as distributed parameter systems," *ISA Transactions*, vol. 58, pp. 552–566, 2015.
- [15] K. Sundar and A. Zlotnik, "State and parameter estimation for natural gas pipeline networks using transient state data," *IEEE Transactions on Control Systems Technology*, vol. 27, no. 5, pp. 2110–2124, 2019.
- [16] C. Fletcher, *Computational Techniques for Fluid Dynamics 2: Specific Techniques for Different Flow Categories*, Springer-Verlag, Berlin, Germany, 2012.
- [17] S. Mokhtab and W. A. Poe, *Handbook of Natural Gas Transmission and Processing*, Gulf, Houston, TX, USA, 2012.
- [18] H. Aalto, "Transfer functions for natural gas pipeline systems," *IFAC Proceedings Volumes*, vol. 41, pp. 889–894, 2018.
- [19] K. Wen, Z. Xia, W. Yu et al., "A new lumped parameter model for natural gas pipelines in state space," *Energies*, vol. 11, pp. 1–17, 2018.
- [20] X. Fang, M. T. Craig, and B. S. Hodge, "Linear approximation line pack model for integrated electricity and natural gas systems OPF," in *Proceedings of the 2019 IEEE Power & Energy Society General Meeting*, Atlanta, GA, USA, 2019.
- [21] M. G. Larson and F. Bengzon, *The Finite Element Method: Theory, Implementation, and Applications*, Springer, Berlin, Germany, 2013.
- [22] R. Alamian, M. Behbahani-Nejad, and A. Ghanbarzadeh, "A state space model for transient flow simulation in natural gas pipelines," *Journal of Natural Gas Science and Engineering*, vol. 9, pp. 51–59, 2012.
- [23] Y. Huang, Y. Zhang, Z. Wu, N. Li, and J. Chambers, "A novel adaptive Kalman filter with inaccurate process and measurement noise covariance matrices," *IEEE Transactions on Automatic Control*, vol. 63, no. 2, pp. 594–601, 2018.
- [24] Y. Zhang, G. Jia, N. Li, and M. Bai, "A novel adaptive Kalman filter with colored measurement noise," *IEEE Access*, vol. 6, pp. 74569–74578, 2018.
- [25] M. A. Gandhi and L. Mili, "Robust Kalman filter based on a generalized maximum-likelihood-type estimator," *IEEE Transactions on Signal Processing*, vol. 58, no. 5, pp. 2509–2520, 2010.
- [26] K. Xiong, L. D. Liu, and H. Y. Zhang, "Modified unscented Kalman filtering and its application in autonomous satellite navigation," *Aerospace Science and Technology*, vol. 13, no. 4–5, pp. 238–246, 2009.
- [27] J. F. Helgaker, A. Oosterkamp, L. I. Langelandsvik, and T. Ytrehus, "Validation of 1D flow model for high pressure offshore natural gas pipelines," *Journal of Natural Gas Science and Engineering*, vol. 16, pp. 44–56, 2014.
- [28] A. R. Gourlay and J. L. Morris, "Finite difference methods for nonlinear hyperbolic systems," *Mathematics of Computation*, vol. 22, no. 101, pp. 28–39, 1968.



- [29] S. Dan, "Kalman filtering for fuzzy discrete time dynamic systems," *Applied Soft Computing*, vol. 3, pp. 191–207, 2003.
- [30] Y. Li, Z. Li, and L. Chen, "Dynamic state estimation of generators under cyber attacks," *IEEE Access*, vol. 7, pp. 125253–125267, 2019.
- [31] Y. Li, J. Li, J. Qi, and L. Chen, "Robust cubature Kalman filter for dynamic state estimation of synchronous machines under unknown measurement noise statistics," *IEEE Access*, vol. 7, pp. 29139–29148, 2019.
- [32] J. Zhao and L. Mili, "A theoretical framework of robust H-infinity unscented Kalman filter and its application to power system dynamic state estimation," *IEEE Transactions on Signal Processing*, vol. 67, no. 10, pp. 2734–2746, 2019.
- [33] J. Qi, A. F. Taha, and J. Wang, "Comparing Kalman filters and observers for power system dynamic state estimation with model uncertainty and malicious cyber attacks," *IEEE Access*, vol. 6, pp. 77155–77168, 2018.
- [34] G. Abdu, M. H. Mohammad, H. Shamsul et al., "A robust cyberattack detection approach using optimal features of SCADA power systems in smart grids," *Applied Soft Computing*, vol. 96, Article ID 106658, 2020.
- [35] Y. Li, J. Wang, D. Zhao, G. Li, and C. Chen, "A two-stage approach for combined heat and power economic emission dispatch: combining multi-objective optimization with integrated decision making," *Energy*, vol. 162, pp. 237–254, 2018.
- [36] Y. Li and K. Li, "Incorporating demand response of electric vehicles in scheduling of isolated microgrids with renewables using a bi-level programming approach," *IEEE Access*, vol. 7, pp. 116256–116266, 2019.
- [37] J. Chen, C. Sun, Y. Li, Y. Xin, B. Li, and G. Li, "The analysis of DC fault mode effects on MMC-HVDC system," in *Proceedings of the 2017 IEEE Power & Energy Society General Meeting*, Chicago, IL, USA, 2017.
- [38] Y. Li, C. Wang, G. Li, and C. Chen, "Optimal scheduling of integrated demand response-enabled integrated energy systems with uncertain renewable generations: a Stackelberg game approach," *Energy Conversion and Management*, In press, 2021.

## Research Article

# Biobjective Optimization-Based Frequency Regulation of Power Grids with High-Participated Renewable Energy and Energy Storage Systems

Tingyi He,<sup>1</sup> Shengnan Li,<sup>1</sup> Shuijun Wu,<sup>1</sup> Chuangzhi Li,<sup>2</sup> and Biao Xu <sup>2</sup>

<sup>1</sup>Yunnan Power Grid Co., Ltd., Electric Power Research Institute, Kunming 650200, China

<sup>2</sup>College of Engineering, Shantou University, Shantou 515063, China

Correspondence should be addressed to Biao Xu; xubiao@stu.edu.cn

Received 3 February 2021; Revised 16 February 2021; Accepted 23 February 2021; Published 1 March 2021

Academic Editor: Bo Yang

Copyright © 2021 Tingyi He et al. This is an open access article distributed under the Creative Commons Attribution License, which permits unrestricted use, distribution, and reproduction in any medium, provided the original work is properly cited.

Large-scale renewable energy sources connected to the grid bring new problems and challenges to the automatic generation control (AGC) of the power system. In order to improve the dynamic response performance of AGC, a biobjective of complementary control (BOCC) with high-participation of energy storage resources (ESRs) is established, with the minimization of total power deviation and the minimization of regulation mileage payment. To address this problem, the strength Pareto evolutionary algorithm is employed to quickly acquire a high-quality Pareto front for BOCC. Based on the entropy weight method (EWM), grey target decision-making theory is designed to choose a compromise dispatch scheme that takes both of the operating economy and power quality into account. At last, an extended two-area load frequency control (LFC) model with seven AGC units is taken to verify the effectiveness and the performance of the proposed method.

## 1. Introduction

Automatic generation control (AGC) is one of the important tools to maintain the contact line exchange power and real-time network frequency of the power system within the schedule when the grid experiences load disturbances [1]. Traditional AGC units mainly include thermal and hydro units, which are hard to fast track the dynamic power input commands due to their low regulation performance [2]. With the development of renewable energy, a large number of wind power and photovoltaic (PV) units are connected to the grid. On the one hand, as the outputs of wind power and PV units are regulated by power electronics equipment, they can quickly respond to the dynamic power input regulation commands. On the other hand, since the large-scale wind power and PV units are subject to climate conditions, their generation outputs have large random fluctuations, which aggravates the pressure on frequency regulation of power system. In addition, more and more new energy storage resources (ESRs) are joining the grid, such as chemical

battery energy storage, electric vehicles, and grid-scale battery storage.

Currently, there is a worldwide effort to balance the intermittency of renewable energy in the grid with high-capacity batteries, in which these ESRs have considerably faster regulation performance than conventional power generators. In China, a vast 200 MW, 800 MWh Vanadium Redox Flow Battery in the Dalian High-Tech zone is currently being readied for operation, which is the largest chemical energy storage plant in the world [3]. In California, the largest battery energy storage project in the world, Gateway Energy Storage, is in progress [4]. The addition of energy storage can improve the economic operation of the system. It can help reduce the pressure on frequency regulation of power system caused by PV units. Wind power and PV units generate electricity by storing excess energy in large-capacity battery sets, which are fed back into the grid when the batteries are not generating electricity to relieve the pressure on frequency regulation of the power system.

Besides, the traditional frequency regulation compensation scheme does not effectively stimulate fast response resources to be engaged in AGC because it fails to provide fair compensation in terms of actual regulation performance [5]. The Federal Energy Regulatory Commission (FERC) published Order No. 755 in 2011 to establish a more reasonably priced compensation framework [6]. This command document showed that the compensation payment in the performance-based frequency regulation market is not only determined by the regulation capacity, but also by the actual regulation volume and unit performance [7]. However, some independent system operators (ISOs) implemented 755 negatively and did not establish fair and dynamic markets, because they adopted existing rules that protect existing resources such as liquefied natural gas (LNG) units from competition that is created by ESRs with lower regulation mileage payment and faster regulation performance. And then in February 2018, the FERC issued a landmark order for ESRs, Order No. 841, setting standards for ESR participation in frequency regulation [8]. The regulation units such as ESRs with higher regulation performance will be preferred for ISOs when receiving the same power regulation command. And it will be paid more compared to the regulation unit with lower regulation performance.

So far, few research studies have addressed the complementary control between wind, PV, ESRs, and other frequency regulation resources. In [9], a new biobjective optimization model of real-time AGC dispatch (BOAD) was constructed, with the minimization of the total power deviation and the regulation mileage payment. However, it did not consider ESRs to participate in AGC. Hence, this paper presents a new biobjective of complementary control (BOCC) for AGC with the high participation of ESRs.

To solve the BOCC with high nonlinearity, the meta-heuristic-based multiobjective optimization algorithms show stronger global searching ability than the traditional mathematical optimization methods [10–15]. Widely used multiobjective algorithms include the improved strength Pareto evolutionary algorithm (SPEA2) [16] and a non-dominated sorting genetic algorithm II (NSGA-II) [17]. Compared with NSGA-II, the fitness function of SPEA2 is not calculated directly from the value of the objective function, which is indirectly linked to the value of the objective function but to the Pareto strength. SPEA2 ensures that the converged solution set is a set of noninferior solutions and considers the density of individuals in the solution space to maintain the diversity of the population and ensure the uniform distribution of the solution set. Therefore, this paper adopts SPEA2 to solve BOCC.

In addition, since ISOs can allocate only one AGC dispatch signal to each unit at each control interval, the ISOs should select the best suitable solution from the multiple solutions obtained on the Pareto front. This requires the application of a decision-making method to help the ISOs select a best compromise dispatch scheme from the set of obtained Pareto solutions. Grey target decision-making is one of the methods to solve multiobjective optimization by using the grey systematic theory to select a best compromise solution. In [18], a transformation operator of rewarding the

good and punishing the bad was proposed to classify the index of effect sample matrix into three categories. Furthermore, some subjective weighting methods such as the analytic hierarchy process method (AHP) [19] and Delphi method [20] are usually used to determine the weights of indexes by the experts' evaluation matrix, but they easily lead to deviations in indicator weights, while the objective weighting method such as the entropy weight method (EWM) is based on inherent information of decision-making matrix to determine the weights of indexes. And then grey target decision-making theory with EWM is designed to choose a dispatch plan that takes into account both of the operating economy and power quality, which can provide an objective decision without a subjective judgment.

The remaining of this work is organized as follows: Section 2 presents the mathematical model of BOCC. Section 3 gives the detailed implementation of SPEA2 and grey target decision-making with EWM for BOCC. The simulation results and discussions are given in Section 4. Finally, Section 5 concludes the paper.

## 2. Mathematical Model of BOCC

**2.1. AGC Dispatch Framework.** AGC mainly consists of two operations. Figure 1 displays an extended two-area load frequency control (LFC) model.  $\Delta P_T$  is the junction line power exchange deviation;  $\Delta f$  is the real-time frequency deviation;  $\Delta P_{\text{out}}$  is the actual regulated power output; and  $\Delta P_D$  is the power disturbance. The goal of the first operation is to approximate the real-time power disturbance by a PI controller with the inputs of the real-time frequency deviation  $\Delta f$  and the junction line power exchange deviation  $\Delta P_T$ . In the second operation, the ISO assigns the total generation command  $\Delta P_C$  to all the AGC units. Note that this paper focuses on the specific allocation process of the second operation, which is addressed by the proposed SPEA2 and grey target decision-making with EWM. The specific framework of the AGC dispatch model has been given in reference [9], and the ESRs are added to participate in the AGC scheduling process.

**2.2. Constraints.** In BOCC, it should consider various constraints, including the power balance constraint, dynamic response process with generation ramp constraint (GRC), regulation capacity constraint, and energy transfer constraint [9], as follows:

- (1) Power balance constraint: at the  $k^{\text{th}}$  control interval, the total power regulation command output by the controller should be equal to the sum of the power regulation input signals received by all AGC units, as follows:

$$\sum_{i=1}^n \Delta P_i^{\text{in}}(k) - \Delta P_c(k) = 0, \quad (1)$$

where  $\Delta P_i^{\text{in}}(k)$  denotes the input power command received by the  $i^{\text{th}}$  unit at  $k^{\text{th}}$  control interval and  $\Delta P_c(k)$  denotes the output of the PI controller.

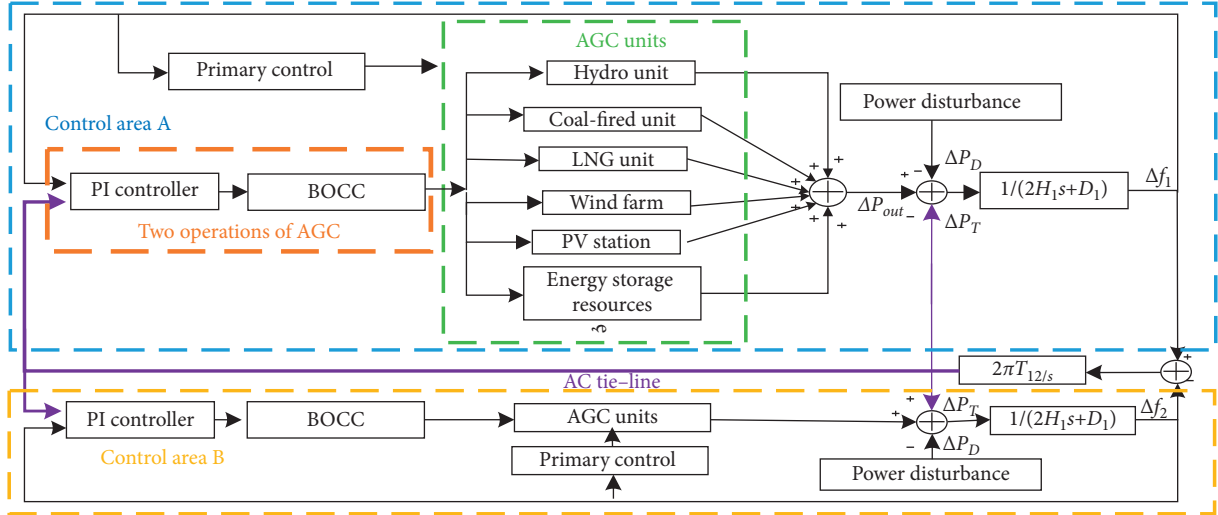


FIGURE 1: Framework of AGC on the extended two-area LFC model.

(2) GRC: depending on the response time delay, AGC units can be sorted into different types of units [21]. Like wind power and PV units, the dynamic response model of ESRs has no a generation ramp constraint (GRC), as shown in Table 1. And the dynamic response function is shown in Figure 2. Without considering the GRC and power limiter, the actual regulated power output is relating to a Laplacian inverse transfer function, as follows:

$$\Delta P_i^{\text{out}}(t) = L^{-1} \left\{ \frac{G_i(s)}{s(1 + T_d^i s)} \sum_{k=1}^N [e^{-\Delta T(k-1)s} M_i^{\text{in}}(k)] \right\}, \quad (2)$$

$$\Delta P_i^{\text{out}}(k) = \Delta P_i^{\text{out}}(t = k \cdot \Delta T), \quad (3)$$

$$M_i^{\text{in}}(k) = \Delta P_i^{\text{in}}(k) - P_i^{\text{in}}(k-1), \quad (4)$$

where  $G_i(s)$  is the energy transfer function of the  $i^{\text{th}}$  AGC unit;  $\Delta T$  is the delay time constant of the  $i^{\text{th}}$  unit; and  $M_i^{\text{in}}(k)$  is the regulation mileage input of the  $i^{\text{th}}$  AGC unit at  $k^{\text{th}}$  control interval.

If the GRC and power limiter are considered, then the output of the AGC unit can be calculated, as follows:

$$\Delta P_i^{\text{out}}(k) = \begin{cases} \Delta P_i^{\text{out}}(k-1) + R_i^{\text{min}}, & \text{if } \Delta P_i^{\text{out}}(k) < R_i^{\text{min}}, \\ \Delta P_i^{\text{out}}(k), & \text{if } R_i^{\text{min}} \leq \Delta P_i^{\text{out}}(k) \leq R_i^{\text{max}}, \\ \Delta P_i^{\text{out}}(k-1) + R_i^{\text{max}}, & \text{if } \Delta P_i^{\text{out}}(k) > R_i^{\text{max}}, \end{cases} \quad (5)$$

$$R_i^{\text{min}} = \begin{cases} 0, & \text{if } M_c(k) \geq 0, \\ \max[-\Delta P_i^{\text{rate}} \cdot \Delta T, \Delta P_i^{\text{min}} - \Delta P_i^{\text{out}}(k-1)], & \text{if } M_c(k) < 0, \end{cases} \quad (6)$$

$$R_i^{\text{max}} = \begin{cases} \min[\Delta P_i^{\text{rate}} \cdot \Delta T, \Delta P_i^{\text{max}} - \Delta P_i^{\text{out}}(k-1)], & \text{if } M_c(k) \geq 0, \\ 0, & \text{if } M_c(k) < 0, \end{cases} \quad (7)$$

where  $\Delta P_i^{\text{min}}$  and  $\Delta P_i^{\text{max}}$  are the minimum and maximum regulation capacities of the  $i^{\text{th}}$  unit, respectively;  $R_i^{\text{min}}$  and  $R_i^{\text{max}}$  are the minimum and maximum power regulation variations of the  $i^{\text{th}}$  unit, respectively; and  $\Delta P_i^{\text{rate}}$  is the maximum ramp rate of the  $i^{\text{th}}$  unit.

**2.3. Objective Function.** Since the proposed BOCC is intended to minimize the total power deviation between the regulation command and the actual power regulation output and minimize the regulation mileage payment, the objective functions can be written as follows:

TABLE 1: Types of transfer functions for various units.

Type	Transfer function $G(s)$
Non-reheat steam unit	$1/1 + T_1s$
Reheat steam unit	$1 + T_2s/(1 + T_3s)(1 + T_4s)(1 + T_5s)$
Hydro unit	$(1 - T_6s)(1 + T_7s)/(1 + 0.5T_6s)(1 + T_8s)$
WT and PV	$1/1 + T_9s$
ESRs	$1/1 + T_{10}s$

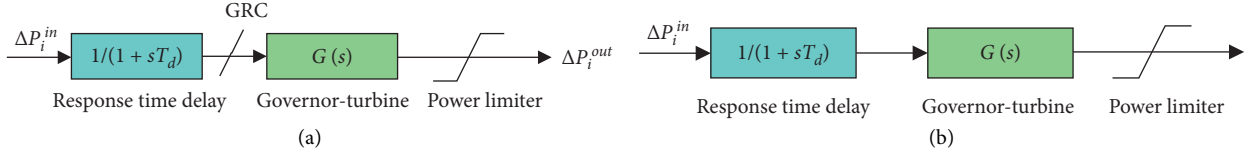


FIGURE 2: Dynamic response models: (a) conventional units; (b) renewable units and ESRs.

$$\begin{cases} \min f_1 = \sum_{k=1}^N \left| \Delta P_c(k) - \sum_{i=1}^n \Delta P_i^{\text{out}}(k+1) \right|, \\ \min f_2 = \sum_{i=1}^n R_i, \end{cases} \quad (8)$$

where  $R_i$  represents the regulation mileage payment for the  $i^{\text{th}}$  AGC unit, as follows:

$$R_i = \sum_{k=1}^N \gamma S_i^p M_i^{\text{out}}(k), \quad (9)$$

$$M_i^{\text{out}}(k) = \left| \Delta P_i^{\text{out}}(k) - \Delta P_i^{\text{out}}(k-1) \right|, \quad (10)$$

where  $\lambda$  is the price of regulation mileage;  $S_i^p$  is the performance score;  $\Delta P_i^{\text{out}}(k)$  is the actual regulation power output of  $i^{\text{th}}$  unit at the  $k^{\text{th}}$  time control interval; and  $M_i^{\text{out}}(k)$  is the regulation mileage output at the  $k^{\text{th}}$  control interval.

### 3. Design of SPEA2 and Grey Target Decision-Making for BOCC

#### 3.1. Principle of SPEA2

3.1.1. Optimization Operations. In general, SPEA2 mainly contains four operations, as follows:

$$\begin{cases} F_2(X_j) = F_1(X_j) = \left\{ [x_d - \Delta P_d^{\text{max}}][x_d - \Delta P_d^{\text{min}}] + 1 \right\} \cdot 10^8, & \text{if } x_d > \Delta P_d^{\text{max}} \text{ or } x_d < \Delta P_d^{\text{min}}, \\ F_1(X_j) = f_1(X_j), F_2(X_j) = f_2(X_j), & \text{else,} \end{cases} \quad (11)$$

where  $\Delta P_d^{\text{min}}$  and  $\Delta P_d^{\text{max}}$  are the minimum and maximum regulation capacities of the  $d^{\text{th}}$  unit, respectively.

- (3) Sorted by actual fitness function and copy: the actual fitness function can be calculated by equations (11)–(15). Then, the results can be sorted by adaptation value. When the number of noninferior

- (1) Initialization: generating a random set of solutions in the solution space  $X_j = \Delta P_i^{\text{in}}$  ( $i = 1, 2, \dots, n, j = 1, 2, \dots, N$ )  $X_j$  forms the initialized population  $P_0$ , and the size of the population is  $N$ . And then creating the empty archive  $P'_0 = \emptyset$ , and the size of the archive is  $\bar{N}$ . In addition, at the  $k^{\text{th}}$  control interval, the lower and upper boundary of all optimization variables are set equally to the lower and upper adjustment capacity of all units, respectively.

- (2) Fitness calculation: based on the equation power balance constraint in (1), the variable  $x_d = \Delta P_c(k) - \sum_{i=1}^n (i \neq d) \Delta P_i^{\text{in}}(k)$  can be regarded as a known quantity during optimization. By considering the constraint of the  $d^{\text{th}}$  unit output, if the boundary conditions are violated, the fitness function of  $j^{\text{th}}$  individual should be given with a large penalty value. Hence, the fitness function can be designed as follows:

solutions is less than the number of archive size  $\bar{N}$ , copy the first  $\bar{N} - |\bar{P}_{t+1}|$  individuals  $X_j$  with  $F(X_j) \geq 1$  from the resulting ordered list to  $\bar{P}_{t+1}[11]$ , and  $|\cdot|$  corresponds to the number of elements of a set.

- (4) Archive truncation procedure: when the number of noninferior solutions exceeds the number of archive

size  $\overline{N}$ , some of the solutions should be removed from  $\overline{P}_{t+1}$  until  $|\overline{P}_{t+1}| = \overline{N}$ .

3.1.2. *Parameters of SPEA2.* (1) *Strength Value*  $S(X_i)$ . Denote the number of solutions that  $j^{\text{th}}$  individual dominates:

$$S(X_j) = |\{X_i | X_i \in \mathbf{P}_t + \overline{P}_t \wedge X_j \succ X_i\}|, \quad (12)$$

where  $X_j$  denotes the  $i^{\text{th}}$  individual of the nondominated set  $\mathbf{A}$ ;  $\mathbf{P}_t$  denotes the  $t^{\text{th}}$  generation population;  $\overline{P}_t$  denotes the  $t^{\text{th}}$  generation archived population;  $|\cdot|$  corresponds to the number of elements of a set;  $+$  represents the sum of two sets and the symbol; and  $\succ$  indicates that the latter is dominated by the former.

(2) *Raw Fitness*  $R(X_j)$ . Denote the quality of other solutions that are better than the  $i^{\text{th}}$  solution. Its lower value means better solution. In particular, when  $R(X_j)$  is 0, it means that there is no solution strictly better than this solution in the internal and external populations, and it is a noninferior solution. It is calculated as follows:

$$R(X_j) = \sum_{X_i \in \mathbf{P}_t + \overline{P}_t, X_j \succ X_i} S(X_i). \quad (13)$$

(3) *Density*  $D(x_i)$ . A number less than 1 indicates the density of the solution around the individual, and the larger the value is, the denser the solution set is. When the number of noninferior solutions exceeds the number of archive size  $\overline{N}$ , some of the solutions should be rejected in the dense area. However, the individuals in the sparser regions are retained to evolve in the next generation, so that the diversity of solutions can be maintained:

$$D(X_j) = \frac{1}{\delta_j^k + 2}, \quad (14)$$

$$k = \sqrt{N + \overline{N}}, \quad (15)$$

where  $\delta_j^k$  means the distance between  $X_j$  individuals and the  $k^{\text{th}}$  nearest individuals;  $N$  denotes the population size; and  $\overline{N}$  denotes the archive size.

(1) *Actual fitness function*  $F(x_i)$ : it can be calculated as follows:

$$F(x_i) = R(x_i) + D(x_i). \quad (16)$$

3.2. *Design of Grey Target Decision-Making with EWM.* In this paper, grey target decision-making based on EWM is used to filter out the compromise solutions of the Pareto solution set. A bullseye is selected in grey target decision-making region formed by the solution set. The distance between each solution and the bullseye is taken as an important basis for grey target decision-making, and then the solutions are ranked according to the distance. Each solution of the solution set is considered as a separate decision solution. The weights and distances to the bullseye of each solution obtained by EWM do not rely on the evaluation and preference of experts, so that the decision is credible.

3.2.1. *Design of the Effect Sample Matrix.* The Pareto solution set  $\mathbf{X}$  based on the SPEA2 algorithm is a matrix of  $n$  rows and  $m$  columns, which is also the set of unit outputs. Here, the absolute values of each solution in  $\mathbf{X}$  can be taken as one of the decision indicators, as follows:

$$X'(i, j) = |X(i, j)|, \quad i = 1, 2, \dots, n, j = 1, 2, \dots, N. \quad (17)$$

To consider the reduction of total power deviation and regulation mileage payment, two objective function values  $F_1$  and  $F_2$  are used as one of the evaluation indicators.

In this paper, we consider the limiting the variation of the output of each unit by adding an index  $D$ , representing the Euclidean distance of each solution of  $\mathbf{X}'$  to the origin, as follows:

$$D_i = \sqrt{\sum_{j=1}^m X'(i, j)^2}. \quad (18)$$

Therefore, there are  $m + 3$  evaluation indicators, which are  $m$  unit outputs, two objective function values, and Euclidean distance squared  $D$ . Therefore, the matrix of effect samples containing  $n$  decision options and  $m + 3$  decision objectives is expressed as follows:

$$\mathbf{X}'' = [\mathbf{X}' \quad F_1 \quad F_2 \quad D]. \quad (19)$$

3.2.2. *Design of the Bullseye Vector.* The operator  $Z_j$  based on the principles of rewarding the best and punishing the worst is calculated as follows:

$$Z_j = \frac{1}{n} \sum_{i=1}^n \mathbf{X}''(i, j), \quad j = 1, 2, \dots, m + 3. \quad (20)$$

Since the indicators are positive and the smaller they are, the better the program is, so this paper selects the cost-type indicator formula, the decision-making matrix  $\mathbf{V}$  is calculated as follows:

$$v_{ij} = \frac{z_{ij} - x_{ij}}{\max\{\max_{1 \leq i \leq n}\{x_{ij}\} - z_j, z_j - \min_{1 \leq i \leq n}\{x_{ij}\}\}}. \quad (21)$$

Then, the decision matrix can be obtained  $\mathbf{V} = (v_{ij})_{n \times (m+3)}$ .  $v_j^0 = \max\{v_j^i | 1 \leq i \leq n\}$ ,  $j = 1, 2, \dots, m + 3$ . Therefore, the selected bullseye vector is  $v^0 = \{v_1^0, v_2^0, \dots, v_{m+3}^0\}$ .

3.2.3. *Design of Bullseye.* In this paper, EWM is used to calculate the weights of the decision indicators, which is an objective method that does not depend on expert judgments or decision makers' preferences and helps to filter an objective solution from numerous solutions of the Pareto solution set and use this objective solution as the best compromise dispatch scheme. The weight  $y_{ij}$  and entropy value  $E_j$  are calculated based on the index values of each program, respectively, as follows:



$$y_{ij} = \frac{x_{ij}}{\sum_{i=1}^n x_{ij}}, \quad x_{ij} \geq 0, \quad (22)$$

$$E_j = -\frac{1}{\ln n} \sum_{i=1}^n y_{ij} \ln y_{ij}, \quad E_j > 0, \quad (23)$$

$$\omega_j = \frac{(1 - E_j)}{\sum_{j=1}^{m+3} (1 - E_j)}. \quad (24)$$

According to the bullseye vector  $v^0 = \{v_1^0, v_2^0, \dots, v_{m+3}^0\}$  [13], the bullseye distances of each program can be expressed as follows:

$$d_i = |v_i - v^0| = \sqrt{\sum_{j=1}^{m+3} \omega_j (v_{ij} - v_j^0)^2}. \quad (25)$$

The principle of the screening program is that the closer the indicator is to the bullseye, the better the solution.

**3.2.4. Selection of Decision Options.** When three consecutive AGC time intervals are taken, the set of three Pareto solution sets obtained by the SPEA2 algorithm is allowed to compare with the change in the decision solution, and the results are shown in Figure 3. It can be concluded from Figure 3 that the optimal rational point obtained by applying this decision is not necessarily in the geometric center of the set but is the result of combining the output of each unit as well as the biobjective value.

**3.3. Calculation Flow.** The whole calculation flow of solving BOCC by SPEA2 and grey target decision-making with EWM is provided in Table 2, where the termination condition of SPEA2 is set to the maximum number of iterations.

## 4. Case Studies

In this paper, the SPEA2 and grey target decision-making based BOCC are evaluated via the static test and dynamic test on the extended two-area LFC model by expanding the original single equivalent generating unit in area A into seven AGC units. The control time cycle of AGC is equal to 4 s, and the price of regulation mileage is equal to 2 \$/MW. The main parameters of transfer function parameters of the units are given in Table 3. And the main parameters of regulation of the units are given in Table 4. The population size and the maximum number of iteration steps of all the algorithms are set to 50 and 50, respectively. And the archive size of SPEA2 is set to 50.

**4.1. Static Test Experiments.** In the static test, two load disturbances are applied to the dynamic model, with  $\Delta P_D = 50$  MW and  $\Delta P_D = -50$  MW. Here, 10 algorithms including

the multiobjective immune algorithm with nondominated neighbor-based selection (NNIA) [22], NSGA-II, strength Pareto evolutionary algorithm based on reference direction for multiobjective (SPEAR) [23], SPEA2, a decision variable clustering-based evolutionary algorithm for large-scale many-objective (LMEA) [24], a cellular genetic algorithm for multiobjective optimization (MOCELL) [25], a proposal for multiple-objective particle swarm optimization (MOPSO) [26], an evolutionary many-objective optimization algorithm using reference point-based nondominated (NSGA-III) [27], many-objective evolutionary optimization based on reference points (PREA) [28], and region-based selection in evolutionary multiobjective optimization (PESAI) [29] are selected for comparison.

Figure 4 provides the comparison of the local Pareto front of the ten algorithms. Figure 4(a) shows that the solutions obtained by LMEA and PESAI deviate obviously from the ideal Pareto front, in which the Pareto front obtained by SPEA2 tends to be better than the fronts of NSGA-II and NSGA-III. Figure 4(b) shows that the solutions obtained by LMEA, SPEAR, and PESAI deviate obviously from the ideal Pareto front, while the Pareto front obtained by SPEA2 tends to be better than the fronts of NSGA-II, MOCELL, and NSGA-III. Meanwhile, the Pareto solutions of SPEA2 are evenly and widely distributed on the local Pareto front.

Figure 4(c) shows that Pareto fronts obtained by 10 algorithms with 10 runs are converted into an approximate ideal Pareto surface. To better compare the convergence and diversity of the algorithms, the performance indexes of four algorithms are evaluated in Table 5, including inverted generational distance (IGD) [30], generational distance (GD) [31], pure diversity (PD) [32], hyper volume (HV) [33], DM (diversity metric) [34], spread [35], and spacing [36], where IGD [37] and HV denote the accuracy and diversity of algorithm; GD considers the accuracy of the algorithm; PD and spread denote the diversity of the algorithm; spacing denotes the evenness of the solutions obtained by algorithm; GD, IGD, spread, and spacing are the negative indexes, while DM, HV, and PD are the positive indexes [38–40].

It is evident that the SPEA2 outperforms the other three algorithms in the extend two-area LFC model at the two disturbances:

- (1) The SPEA2 has the smallest GD value among the average data of the algorithm metrics, representing that it has a good merit of convergence performance.
- (2) It has the largest DM and HV average, which demonstrates that SPEA2 has the largest objective space covered by the Pareto front.
- (3) It has the smallest spread and spacing average, i.e., which indicates that the Pareto solutions obtained by SPEA2 are evenly and widely distributed on the Pareto front.
- (4) It also has the smallest running average time and satisfies the requirement that the time interval of

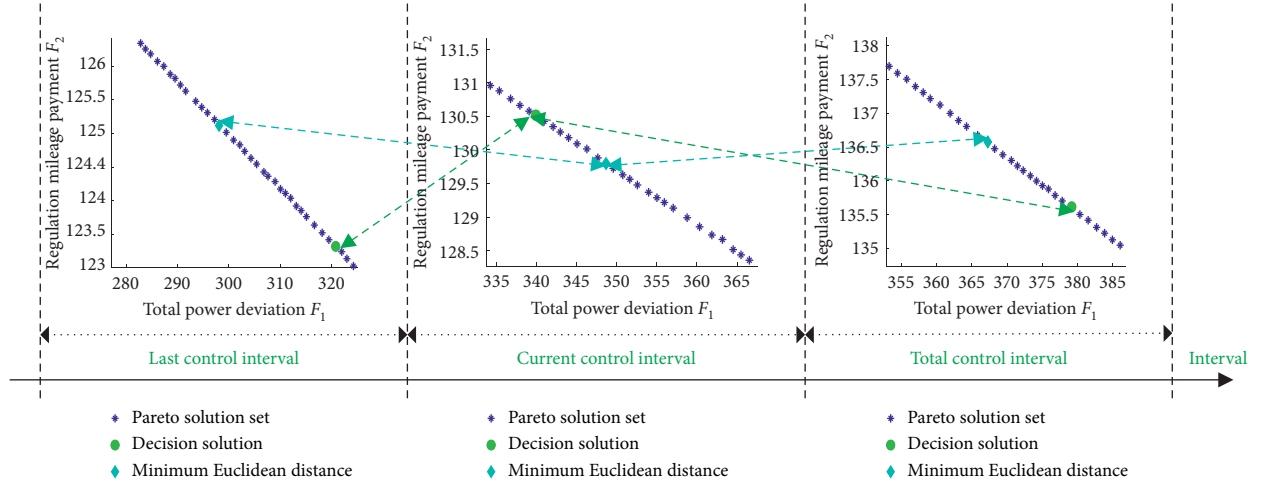


FIGURE 3: The selection of decision options.

TABLE 2: The execution procedure of SPEA2 for BOCC.

Input: The total power regulation command for the current control interval.	
1:	Initialize the parameters of SPEA2;
2:	Initialize the parent population and archive of SPEA2;
3:	Calculate the initial dispatch solution by equations (1)–(7);
4:	Compute the objective function for each individual by equations (8)–(10);
5:	Evaluate the fitness function for each individual by equation (11);
6:	Merge the generation population and the generation archived population into one.
7:	Calculate the parameters of the new set by equations (12)–(16);
8:	Compare the number of noninferior solutions and archive size, and then perform the truncation or reproduction to fill the archive set.
9:	Generate the offspring population by applying recombination and mutation operators to the set
10:	If the termination condition of SPEA2 is satisfied, then go to the next step; otherwise, return to Step 4;
11:	Find the best compromise solution from multiple solutions in Pareto solution set by grey target decision-making theory in equation (17)–(25).
Output: The best power regulation inputs for all AGC units.	

TABLE 3: Transfer function parameters of AGC units.

Generation type	Parameters (s)
Coal-fired	$T2 = 5, T3 = 0.08, T4 = 10, T5 = 0.3$
LNG	$T2 = 2, T3 = 0.05, T4 = 5, T5 = 0.2$
Hydro	$T6 = 1, T7 = 5, T8 = 0.513$
WT, PV	$T1 = 0.01$
ESRs	$T1 = 2$

AGC dispatch is less than 4 s, which means that SPEA2 can converge to the Pareto front much faster than other three algorithms.

#### 4.2. Dynamic Test

**4.2.1. Step Load Disturbance.** To better verify the superiority of SPEA2 and grey target decision-making, the following dynamic simulation tests are performed in real-time optimization of BOCC. This paper introduces a comparison using the adjustable capacity method, called the proportional (PROP) method [41]. PROP is an engineering calculation method, which distribute the dispatching signal of the unit by using the proportion of the adjustable capacity of

the unit. Therefore, the output of the  $i^{\text{th}}$  AGC unit at  $k^{\text{th}}$  time interval is calculated as follows:

$$\Delta P_i^{\text{out}}(k) = \begin{cases} \Delta P_c(k) \cdot \frac{\Delta P_i^{\text{max}}}{\sum_{i=1}^n \Delta P_i^{\text{max}}}, & \text{if } \Delta P_c(k) \geq 0, \\ \Delta P_c(k) \cdot \frac{\Delta P_i^{\text{min}}}{\sum_{i=1}^n \Delta P_i^{\text{min}}}, & \text{if } \Delta P_c(k) < 0. \end{cases} \quad (26)$$

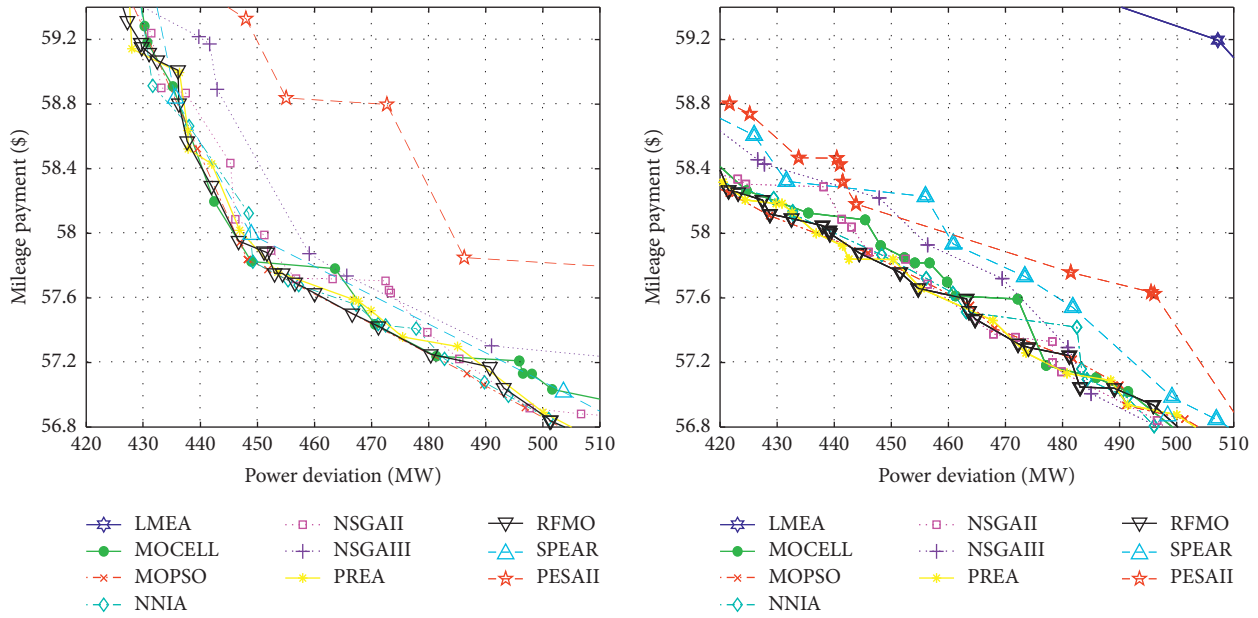
Then, two load disturbances (see Figures 5 and 6) are applied to the extended two-area LFC model, which are  $\Delta P_D = 70$  MW and  $\Delta P_D = -50$  MW.

Figure 5(a) reveals that the proposed SPEA2 with grey target decision-making and EWM can get a more minor error between the total input power and total output power than PROP via the regulation coordination between ESRs and other units, as shown in Figure 5(b). Hence, it slightly reduces the peak of frequency deviation due to it can match the total regulation command closely. Moreover, it results a lower regulation mileage payment than PROP, as illustrated in Figure 7(a).

Figure 6(a) shows that compared to the PROP, the proposed method obtains a less power deviation, reduces the overshoot of the total power command, and makes the total

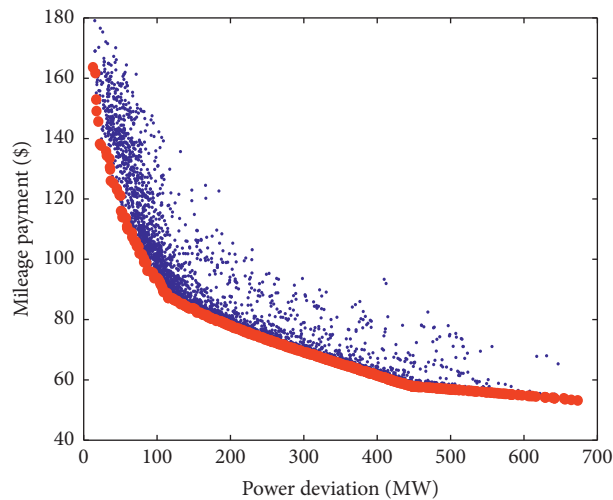
TABLE 4: Main parameters of AGC units in area A of the two-area LFC model.

Unit no.	Type	Td (s)	$\Delta P^{rate}$ (MW/min)	$\Delta P_{max}$ (MW)	$\Delta P_{min}$ (MW)
$G_1$	Coal-fired	60	30	50	-50
$G_2$	LNG	20	18	30	-30
$G_3$	Hydro	5	150	20	-10
$G_4$	WT	1	—	15	-5
$G_5$	PV	1	—	10	-10
$G_6$	ESRs1	1	—	8	-12
$G_7$	ESRs2	1	—	7	-13



(a)

(b)



· Data points of the ten algorithms  
 ● Approximate idea pareto surface

(c)

FIGURE 4: Comparison of the Pareto front surface obtained by 10 algorithms on the extended two-area LFC model: (a)  $\Delta P_D = 70$  MW, (b)  $\Delta P_D = 70$  MW, and (c) select the approximate ideal Pareto surface.

TABLE 5: Comparison of performance metrics of algorithms.

$\Delta P_D$	Function		IGD	GD	PD	HV	DM	Spread	Spacing	$T$ (s)	
50 W	NNIA	Ave	8.50	1.01	$3.36E+05$	0.572	0.726	0.663	6.04	$7.33E-02$	
		Std	2.96	0.29	$7.18E+04$	0.004	0.059	0.085	1.06	$1.34E-03$	
	NSGAI	Ave	11.23	0.94	$2.99E+05$	0.571	0.684	0.696	4.96	$6.50E-02$	
		Std	5.16	0.26	$5.21E+04$	0.008	0.047	0.064	0.69	$2.58E-03$	
	SPAR2	Ave	11.08	<b>0.64</b>	$2.85E+05$	<b>0.573</b>	<b>0.752</b>	<b>0.475</b>	<b>3.62</b>	<b><math>6.49E-02</math></b>	
		Std	5.33	<b>0.17</b>	$7.60E+04$	0.007	0.076	0.090	0.79	$1.92E-03$	
	SPEAR	Ave	12.20	0.98	$2.47E+05$	0.562	0.634	0.826	9.01	$6.63E-02$	
		Std	4.17	0.34	$3.47E+04$	0.006	0.057	0.076	2.06	$2.98E-03$	
	-50 W	NNIA	Ave	12.54	0.66	$2.18E+05$	0.485	0.689	0.735	5.44	$7.79E-02$
			Std	11.87	0.15	$2.47E+04$	0.003	0.065	0.070	1.23	$5.13E-03$
NSGAI		Ave	14.68	0.37	$2.15E+05$	0.485	0.663	0.759	4.73	$6.48E-02$	
		Std	11.37	0.14	$3.38E+04$	0.007	0.079	0.056	1.05	$2.87E-03$	
SPAR2		Ave	22.35	<b>0.45</b>	$1.74E+05$	<b>0.479</b>	<b>0.692</b>	<b>0.523</b>	<b>2.96</b>	<b><math>6.47E-02</math></b>	
		Std	25.49	<b>0.11</b>	$3.52E+04$	0.009	0.151	0.143	<b>0.87</b>	<b><math>2.46E-03</math></b>	
SPEAR		Ave	13.12	0.61	$2.15E+05$	0.487	0.612	0.879	7.76	$6.70E-02$	
		Std	6.04	0.15	$4.79E+04$	0.004	0.062	0.067	2.30	$2.84E-03$	

power output curve markedly closer to the total command curve. However, it results a higher regulation mileage payment (see Figure 7(a)), because it assigns larger commands to the AGC units with fast performance scores.

**4.2.2. Continuous Step Load Disturbance.** In the following dynamic simulation test, two continuous step load disturbances with 120 control intervals a step and 300 control intervals a step (see Figures 8(b) and 9(c)) are applied to the extended two-area LFC mode.

At the short-time interval step, Figure 8(a) illustrates that the proposed method can also gain a slightly smaller power deviation. After the 460 control interval (see Figure 8(a)), the mileage payment of PROP quickly exceeds that of SPEA2. After reaching the lower limit capacity, the outputs of the PV unit and wind power remain almost static (see Figure 8(b)). However, for PROP, those outputs continue to change dramatically during the simulation.

At the long-time interval step, Figure 9(a) shows that the proposed method also gets a smaller power deviation and a smaller frequency deviation. Moreover, it makes a lower regulation mileage payment (see Figure 7(a)) because PROP distributes more input power command to the PV unit and wind power, while the disturbance borne by wind power and PV unit is shared by ESR units after SPEA2 optimization. It can be concluded that at the short-time interval step, the proposed method can help significantly reduce the mileage payment for IOSs. On the contrary, at the long-time interval step, it can make the total output command well close to the total input command.

To further discuss the relationship between the regulation mileage payment and regulated output power of new energy units and ESRs, Figure 7(a) displays the payment changes under the four disturbance cases. In case of ideal single-step disturbance, due to the stochastic character of the calculation results of the multiobjective algorithm, SPEA2 has uncertainty in reducing the regulation mileage payment,

but in the continuous step disturbance case, the algorithm plays a significant role in reducing the regulation mileage payment. In case of successive step disturbance, the two curves before and after the optimization have an intersection point (see Figure 7(a)) due to the changes of the total command assignment scheme (see Figures 7(b) and 7(c)). In the starting phase of the disturbance, because the proposed method assigns mainly units with fast performance scores and high regulation price to participate in the AGC dispatch, it can obtain a slightly higher regulation mileage payment than PROP. However, in the middle stage of disturbance, the PROP still involves wind power and PV unit in regulation frequency, and the regulation capacity of ESR units is not fully utilized. However, in the dispatch with SPEA2 participation, the disturbance borne by wind power and PV units is shared by ESR units, and the superior regulation performance of ESR units is still maximized, so the dispatching payment with SPEA2 participation will be lower than the payment before optimization. In conclusion, ESRs play an important role in AGC dispatch, and the proposed method can make full use of this advantage.

To further test the performance of the SPEA2 algorithm, this example compares the online optimization results of the four cases separately, as shown in Table 6, where accuracy is used to measure the approximate degree of the actual regulation output and the regulation command curve during the simulation time. It can be found two main points from Table 5 compared with PROP, as follows:

- (1) The proposed method can significantly improve the power quality for power grid by reducing the power deviation and improving each performance index of the system dynamic response, especially in the case of continuous short-time interval step disturbances. The power deviation, average  $|\Delta f|$ , and  $|ACE|$  reduce 66.8%, 8.0%, and 5.2%, respectively, in the case of continuous and long-time interval step load disturbance. The power deviation, average  $|\Delta f|$ , and  $|$

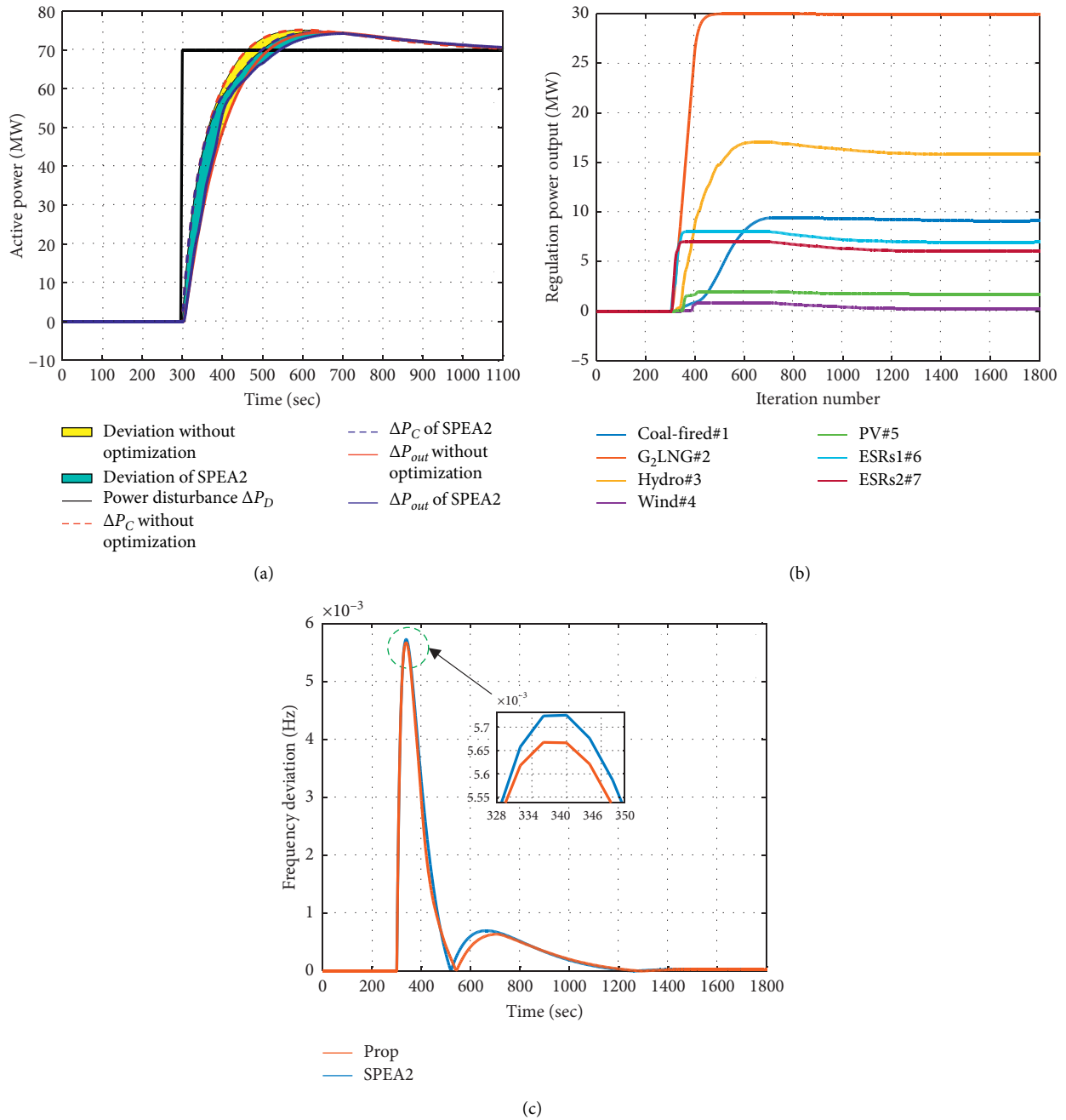


FIGURE 5: Real-time optimization results obtained on the extended two-area LFC model when  $\Delta P_D = 70$  MW, (a) overall power deviation, (b) regulation power output obtained by SPEA2 with grey target decision-making, and (c) frequency deviation.

ACE| reduce 45.9%, 5.9%, and 6.4%, respectively, in the case of continuous and short-time interval step load disturbance.

(2) The proposed method can obviously reduce the regulation mileage payment and thus rise the economy operating for ISOs, especially in the case of

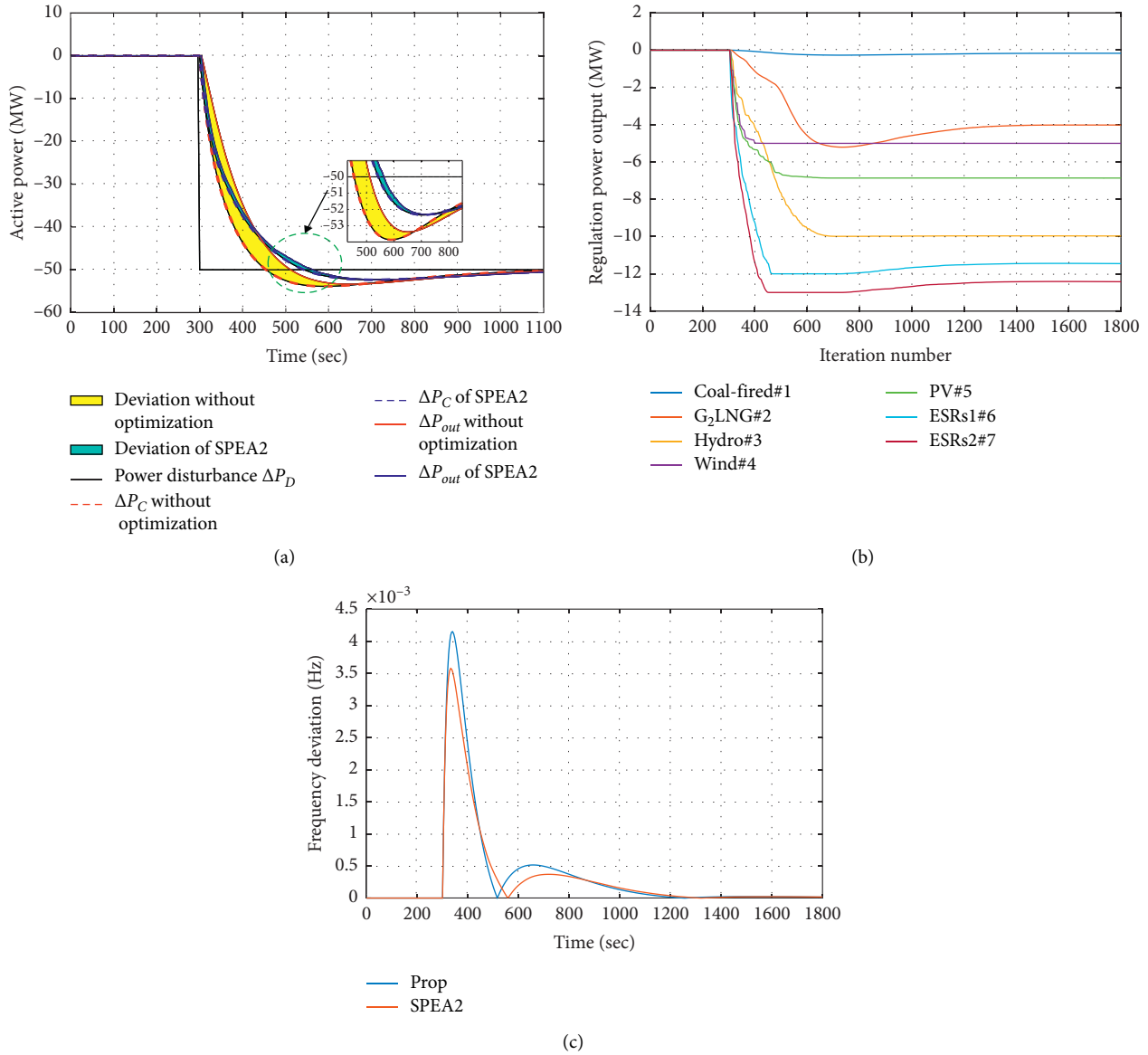


FIGURE 6: Real-time optimization results obtained on the extended two-area LFC model when  $\Delta P_D = -50$  MW, (a) overall power deviation, (b) regulation power output obtained by SPEA2 with grey target decision-making, and (c) frequency deviation.

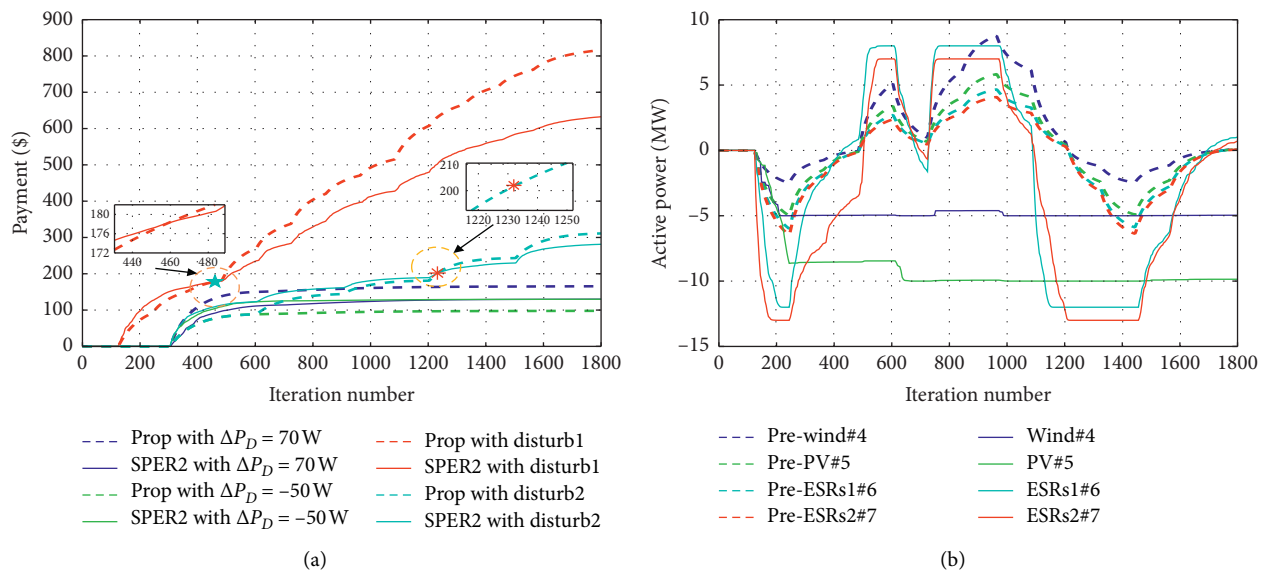


FIGURE 7: Continued.



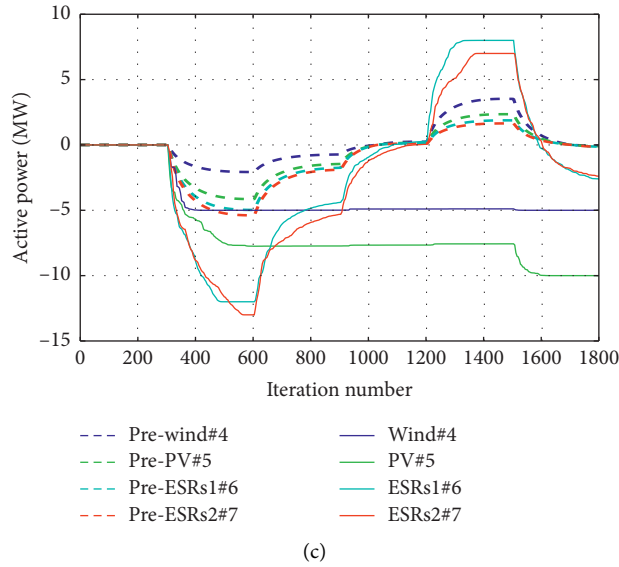


FIGURE 7: (a) The payment under four disturbance cases. Comparison of regulated output power of new energy units and ESRs before and after optimization: (b) under a continuous and short-time interval step load disturbance and (c) under a continuous and long-time interval step load disturbance.

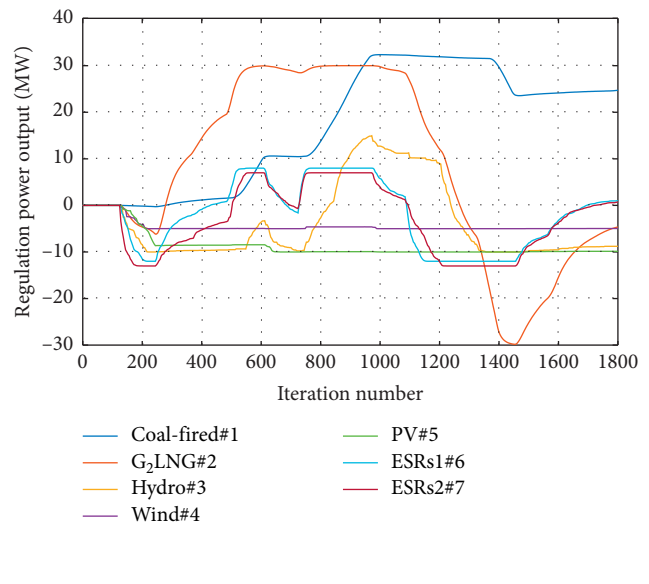
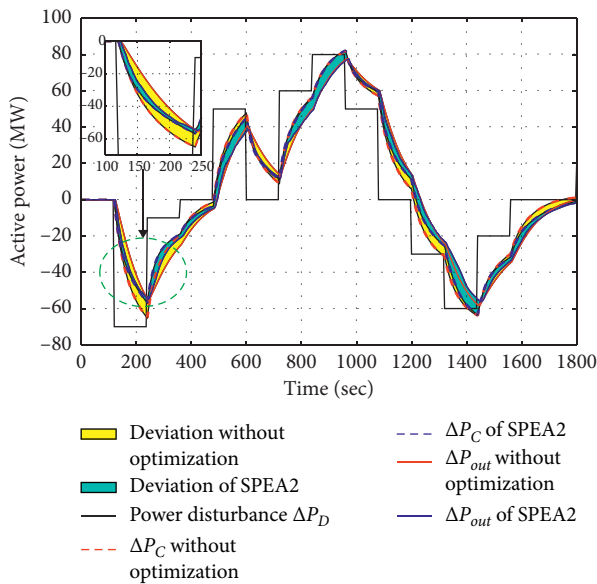
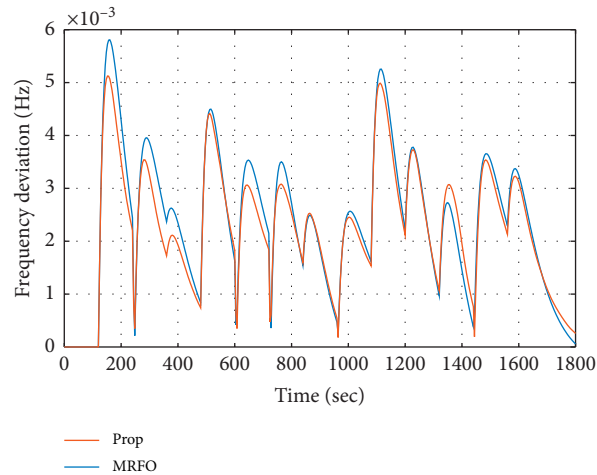
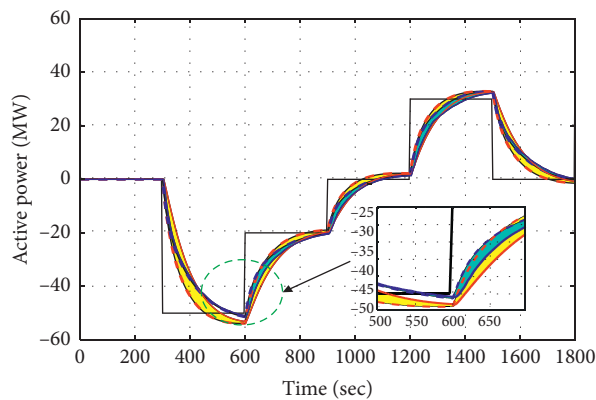


FIGURE 8: Continued.



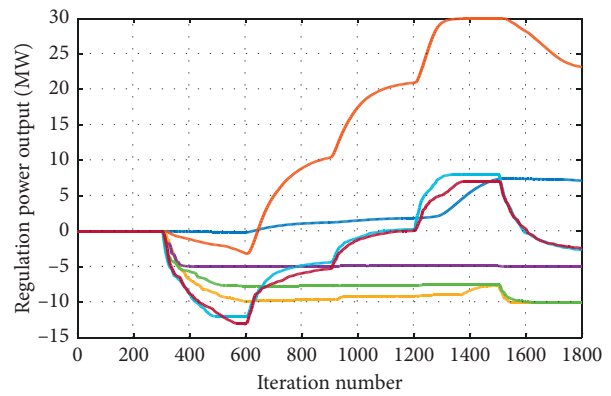
(c)

FIGURE 8: Online optimization results obtained by SPEA2 under a continuous and short-time interval step load disturbance in the extended two-area LFC model, (a) overall power deviation, (b) regulation power output obtained by SPEA2 with grey target decision-making, and (c) frequency deviation.



- █ Deviation without optimization
- █ Deviation of SPEA2
- Power disturbance  $\Delta P_D$
- $\Delta P_C$  without optimization
- $\Delta P_C$  of SPEA2
- $\Delta P_{out}$  without optimization
- $\Delta P_{out}$  of SPEA2

(a)



- Coal-Fired#1
- $G_2LNG\#2$
- Hydro#3
- Wind#4
- PV#5
- ESRs1#6
- ESRs2#7

(b)

FIGURE 9: Continued.

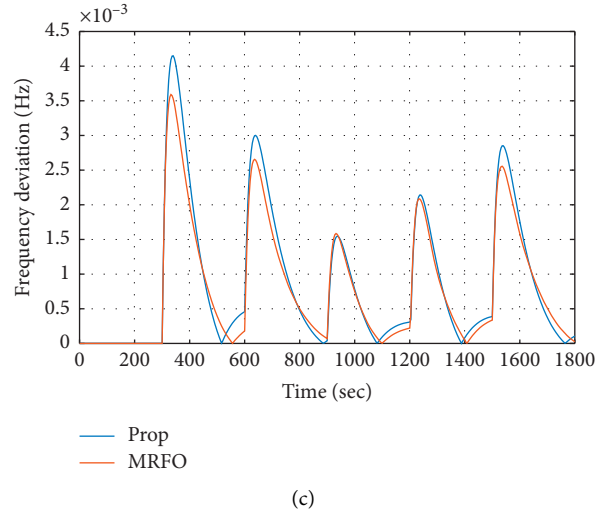


FIGURE 9: Online optimization results obtained by SPEA2 under a continuous and long-time interval step load disturbance in the extended two-area LFC model, (a) overall power deviation, (b) regulation power output obtained by SPEA2 with grey target decision-making, and (c) frequency deviation.

TABLE 6: Result comparison of online optimization under different disturbances.

$\Delta P_D$	Method	ACE  (MW)		$\Delta f$   (Hz)		CPS1 (%)		Deviation (MW)	Accuracy (%)	Payment (\$)
		Avg	Max	Avg	Max	Avg	Min			
70 MW	PROP	0.89	11.17	$4.78E-04$	$5.73E-03$	199.99	199.82	550.06	81.34	<b>165.58</b>
	SPEA2	0.88	11.06	$4.52E-04$	$5.67E-03$	199.99	199.82	383.36	81.87	130.09
-50 MW	PROP	0.64	8.09	$3.46E-04$	$4.15E-03$	199.99	199.90	426.14	81.19	97.87
	SPEA2	0.61	6.93	$3.04E-04$	$3.58E-03$	199.99	199.93	53.36	82.87	<b>126.95</b>
Disturb 1 (see Figure 8(a))	PROP	4.72	11.33	$2.38E-03$	$5.81E-03$	199.96	199.81	2854.38	74.23	816.35
	SPEA2	4.42	9.95	$2.24E-03$	$5.12E-03$	199.96	199.85	1544.57	<b>82.73</b>	632.56
Disturb 2 (see Figure 9(a))	PROP	1.92	8.09	$8.71E-04$	$4.15E-03$	199.99	199.90	1240.69	70.31	311.12
	SPEA2	1.82	6.95	$8.01E-04$	$3.59E-03$	199.99	199.93	411.56	78.75	281.25

continuous long-time interval step disturbances. Particularly, in the two continuous disturbance test, the regulation mileage payments reduce by 22.5% and 9.6%.

## 5. Conclusions

In summary, the presented work includes the following three contributions:

- (1) The proposed BOCC can effectively coordinate various frequency regulation resources and ESRs for AGC, which can simultaneously reduce the total power deviation and the regulation mileage payment.
- (2) The presented SPEA2 can converge to a high-quality Pareto front for BOCC in the relatively short time, while grey target decision-making with EWM can effectively select a compromise dispatch scheme that makes full use of the advantage of ESRs in frequency regulation to consider both of the operating economy and power quality.

- (3) The simulation results of the extended two-area LFC model verify that the combination of SPEA2 and grey target decision-making with EWM can effectively solve BOCC. It can effectively improve the response performance by reducing the |ACE|, average | $\Delta f$ |, and total power deviation and simultaneously rise the operating economy for IOSs by reducing the total regulation mileage payment.

To further improve the operating economy and power quality, the future studies will focus on the higher-participated renewable energy and smaller control periodic. Furthermore, the method based on model predictive control or deep learning will be the key technology to solve BOCC.

## Data Availability

The data that support the findings of this study are available on request from the corresponding author. The data are not publicly available due to privacy or ethical restrictions.

## Conflicts of Interest

The authors declare that they have no conflicts of interest.

## Acknowledgments

This work was jointly supported by Research on Regional Power Grid Frequency Regulation with Renewable Energy Participation (YNKJXM20191240), the Project of the Scientific Research Starting Foundation of Shantou University (no. NTF20009), and the Open Project of Key Laboratory of Computational Intelligence and Signal Processing for Ministry of Education (no. 2019A002).

## References

- [1] L. Xi, J. Chen, Y. Huang et al., "Smart generation control based on multi-agent reinforcement learning with the idea of the time tunnel," *Energy*, vol. 153, pp. 977–987, 2018.
- [2] V. Lakshmanan, M. Marinelli, J. Hu, and H. W. Bindner, "Provision of secondary frequency control via demand response activation on thermostatically controlled loads: solutions and experiences from Denmark," *Applied Energy*, vol. 173, pp. 470–480, 2016.
- [3] Z. Liu, H. Zhang, S. Gao, X. Ma, and Y. Lu, "The world's largest all-vanadium redox flow battery energy storage system for a wind farm," *Energy Storage Science and Technology*, vol. 3, no. 1, pp. 71–77, 2014.
- [4] D. M. Davies, M. G. Verde, O. Mnyshenko et al., "Combined economic and technological evaluation of battery energy storage for grid applications," *Nature Energy*, vol. 4, no. 1, pp. 42–50, 2019.
- [5] B. Xu, Y. Dvorkin, D. S. Kirschen, C. A. Silva-Monroy, and J. P. Watson, "A comparison of policies on the participation of storage in U.S. frequency regulation markets," in *Proceedings of the 2016 IEEE Power and Energy Society General Meeting (PESGM)*, pp. 1–5, Boston, MA, USA, July 2016.
- [6] U. S. Federal Energy Regulatory Commission, *FERC 755, Dockets RM11-7-000 AD10-11-000*, U. S. Federal Energy Regulatory Commission, Washington, DC, USA, 2011.
- [7] A. D. Papalexopoulos and P. E. Andrianesis, "Performance-based pricing of frequency regulation in electricity markets," *IEEE Transactions on Power Systems*, vol. 29, no. 1, pp. 441–449, 2014.
- [8] Federal Energy Regulatory Commission, *Electric Storage Participation In Markets Operated by Regional Transmission Organizations and Independent System Operators, Order No. 841, 162 FERC ¶ 61*, p. 127, Federal Energy Regulatory Commission, Washington, DC, USA, 2018.
- [9] X. Zhang, T. Tan, T. Yu, B. Yang, and X. Huang, "Bi-objective optimization of real-time AGC dispatch in a performance-based frequency regulation market," *CSEE Journal of Power and Energy Systems*, 2020.
- [10] D. Gong, B. Xu, Y. Zhang, Y. Guo, and S. Yang, "A similarity-based cooperative Co-evolutionary algorithm for dynamic interval multiobjective optimization problems," *IEEE Transactions on Evolutionary Computation*, vol. 24, no. 1, pp. 142–156, 2020.
- [11] Y. Tian, C. Lu, X. Zhang, K. Tan, and Y. Jin, "Solving large-scale multi-objective optimization problems with sparse optimal solutions via unsupervised neural networks," *IEEE Transactions on Cybernetics*, 2020.
- [12] C. Wang, R. Xu, J. Qiu, and X. Zhang, "AdaBoost-inspired multi-operator ensemble strategy for multi-objective evolutionary algorithms," *Neurocomputing*, vol. 384, pp. 243–255, 2020.
- [13] F. Cheng, Q. Zhang, Y. Tian, and X. Zhang, "Maximizing receiver operating characteristics convex hull via dynamic reference point-based multi-objective evolutionary algorithm," *Applied Soft Computing*, vol. 86, pp. 1–11, 2020.
- [14] L. Zhang, J. Xia, F. Cheng, J. Qiu, and X. Zhang, "Multi-objective optimization of critical node detection based on cascade model in complex networks," *IEEE Transactions on Network Science and Engineering*, vol. 7, no. 3, pp. 2052–2066, 2020.
- [15] F. Cheng, J. Chen, J. Qiu, and L. Zhang, "A subregion division based multi-objective evolutionary algorithm for SVM training set selection," *Neurocomputing*, vol. 394, pp. 70–83, 2020.
- [16] E. Zitzler, M. Laumanns, and L. Thiele, "SPEA2: improving the strength pareto evolutionary algorithm," TIK-Report, vol. 103, Eidgenössische Technische Hochschule Zürich, Zürich, Switzerland, 2001.
- [17] K. Deb, A. Pratap, S. Agarwal, and T. Meyarivan, "A fast and elitist multiobjective genetic algorithm: NSGA-II," *IEEE Transactions on Evolutionary Computation*, vol. 6, no. 2, pp. 182–197, 2002.
- [18] Z. Gu, D. Niu, and H. Wang, "Multiple attribute grey target decision making model based on linear combination weights determining and entropy," *International Journal of Business and Management*, vol. 3, no. 1, pp. 106–111, 2008.
- [19] J. W. Ra, "Hierarchical decision process," technology management: the new international language," in *Proceedings of the-PICMET '91*, pp. 595–599, Portland, OR, USA, October 1991.
- [20] D. Norman and H. Olaf, "An experimental application of the Delphi method to the use of experts," *Management Science*, vol. 9, no. 3, pp. 458–467, 1963.
- [21] T. Yu, Y. M. Wang, W. J. Ye, B. Zhou, and K. W. Chan, "Stochastic optimal generation command dispatch based on improved hierarchical reinforcement learning approach," *IET Generation, Transmission & Distribution*, vol. 5, no. 8, pp. 789–797, 2011.
- [22] M. Gong, L. Jiao, H. Du, and L. Bo, "Multi-objective immune algorithm with nondominated neighbor-based selection," *Evolutionary Computation*, vol. 16, no. 2, 2008.
- [23] S. Jiang and S. Yang, "A strength Pareto evolutionary algorithm based on reference direction for multiobjective and many-objective optimization," *IEEE Transactions on Evolutionary Computation*, vol. 21, no. 3, pp. 329–346, 2017.
- [24] X. Zhang, Y. Tian, R. Cheng, and Y. Jin, "A decision variable clustering-based evolutionary algorithm for large-scale many-objective optimization," *IEEE Transactions on Evolutionary Computation*, vol. 22, no. 1, pp. 97–112, 2016.
- [25] H. Kor, H. Iranmanesh, H. Haleh, and S. M. Hatefi, "A multi-objective genetic algorithm for optimization of cellular manufacturing system," in *Proceedings of the 2009 International Conference on Computer Engineering and Technology*, pp. 252–256, Singapore, January 2009.
- [26] C. C. Coello and M. S. Lechuga, "MOPSO: a proposal for multiple objective particle swarm optimization," in *Proceedings of the 2002 IEEE Congress on Evolutionary Computation*, pp. 1051–1056, Honolulu, HI, USA, May 2002.
- [27] K. Deb and H. Jain, "An evolutionary many-objective optimization algorithm using reference-point-based non-dominated sorting approach, part I: solving problems with

- box constraints,” *IEEE Transactions on Evolutionary Computation*, vol. 18, no. 4, pp. 577–601, 2014.
- [28] Y. Liu, D. Gong, X. Sun, and Y. Zhang, “Many-objective evolutionary optimization based on reference points,” *Applied Soft Computing*, vol. 50, pp. 344–355, 2017.
- [29] D. W. Corne, N. R. Jerram, J. D. Knowles, and M. J. Oates, “PESA-II: region-based selection in evolutionary multi-objective optimization,” in *Proceedings of the 3rd Annual Conference on Genetic and Evolutionary Computation*, pp. 283–290, San Francisco, CA, USA, January 2001.
- [30] A. Zhou, Y. Jin, Q. Zhang, B. Sendhoff, and E. Tsang, “Combining model-based and genetics-based offspring generation for multi-objective optimization using a convergence criterion,” in *Proceedings of the 2006 IEEE International Conference on Evolutionary Computation*, pp. 892–899, Vancouver, Canada, July 2006.
- [31] L. C. Bezerra, M. López-Ibáñez, and T. Stützle, “An empirical assessment of the properties of inverted generational distance on multi- and many-objective optimization,” in *Proceedings of the International Conference on Evolutionary Multi-Criterion Optimization*, pp. 31–45, Munster, Germany, February 2017.
- [32] H. Wang, Y. Jin, and X. Yao, “Diversity assessment in many-objective optimization,” *IEEE Transactions on Cybernetics*, vol. 47, no. 6, pp. 1510–1522, 2017.
- [33] L. While, P. Hingston, L. Barone, and S. Huband, “A faster algorithm for calculating hypervolume,” *IEEE Transactions on Evolutionary Computation*, vol. 10, no. 1, pp. 29–38, 2006.
- [34] K. Deb and S. Jain, “Running performance metrics for evolutionary multi-objective optimizations,” in *Proceedings of the Fourth Asia-Pacific Conference on Simulated Evolution and Learning (SEAL’02)*, pp. 13–20, Singapore, 2002.
- [35] Y.-N. Wang, L.-H. Wu, and X.-F. Yuan, “Multi-objective self-adaptive differential evolution with elitist archive and crowding entropy-based diversity measure,” *Soft Computing*, vol. 14, no. 3, pp. 193–209, 2010.
- [36] J. R. Schott, *Fault Tolerant Design Using Single and Multi-criteria Genetic Algorithm Optimization*, Massachusetts Institute of Technology, Cambridge, MA, USA, 1995.
- [37] N. Riquelme, C. Von Lücken, and B. Baran, “Performance metrics in multi-objective optimization,” in *Proceedings of the 2015 Latin American Computing Conference (CLEI)*, pp. 1–11, Arequipa, Peru, December 2015.
- [38] Y. Tian, T. Zhang, J. Xiao, X. Zhang, and Y. Jin, “A coevolutionary framework for constrained multi-objective optimization problems,” in *Proceedings of the IEEE Transactions on Evolutionary Computation, CEC 2011*, New Orleans, LA, USA, June 2011.
- [39] Y. Tian, X. Zhang, R. Cheng, C. He, and Y. Jin, “Guiding evolutionary multiobjective optimization with generic front modeling,” *IEEE Transactions on Cybernetics*, vol. 50, no. 3, pp. 1106–1119, 2020.
- [40] L. Zhang, X. Wu, H. Zhao, F. Cheng, and Q. Liu, “Personalized recommendation in P2P lending based on risk-return management: a multi-objective perspective,” in *Proceedings of the IEEE Transactions on Big Data*, p. 1, San Francisco, CA, USA, 2020.
- [41] Y. Xichang and Z. Quanren, “Practical implementation of the SCADA+AGC/EDC system of the Hunan power pool in the central China power network,” *IEEE Transactions on Energy Conversion*, vol. 9, no. 2, pp. 250–255, 1994.

## Research Article

# Optimal Power Allocation for Cooperative Pattern Division Multiple Access Systems

Xiurong Zhang,<sup>1</sup> Shaoli Kang,<sup>2</sup> and Xueqian Fu <sup>3</sup>

<sup>1</sup>School of Electronic and Information Engineering, Beihang University, Beijing 100083, China

<sup>2</sup>State Key Laboratory of Wireless Mobile Communications, China Academy of Telecommunications Technology, Beijing 100191, China

<sup>3</sup>College of Information and Electrical Engineering, China Agricultural University, Beijing 100083, China

Correspondence should be addressed to Xueqian Fu; fuxueqian@cau.edu.cn

Received 4 February 2021; Revised 11 February 2021; Accepted 20 February 2021; Published 26 February 2021

Academic Editor: Bo Yang

Copyright © 2021 Xiurong Zhang et al. This is an open access article distributed under the Creative Commons Attribution License, which permits unrestricted use, distribution, and reproduction in any medium, provided the original work is properly cited.

This study focuses on the power allocation (PA) problem in code division multiple access (PDMA) networks with amplify-and-forward (AF) relays. We provide two wireless communication technical performance indexes, which are system throughput and outage probability. A multiobjective version of particle swarm optimization is proposed to solve Pareto-optimal solutions for optimal PA problems. A novel programming model is built based on improvement of constraint functions, and the accuracy and efficiency of solution can be improved via compact constraints. The technique for order preference by similarity to an ideal solution is proposed to balance the performance indicators, which include outage probability and system throughput. It has been calculated that the proposed approach for optimal PA is verified and performs better than a genetic algorithm approach.

## 1. Introduction

Renewable energy has become a trend in smart grid development. Wind power and photovoltaic are representatives of renewable energy. To address the randomness of wind power, robust sliding mode control [1], maximum power point tracking control [2, 3], and passivity-based sliding-mode control [4] are presented to maximize the availability of wind power. Maximum power point tracking is also used in the photovoltaic system, which can get the maximum power output under partial shading condition [5, 6]. The reliability of the renewable energy communication system has significant engineering significance for optimization and control in distribution networks integrated with renewable energy.

With the development of 5G networks, wireless communication technology will support the intellectualization of the renewable energy system. 5G networks can deliver superfast speeds and support extremely low-latency connections. Power communication adopts both optical fiber communication and wireless communication, which are

applied to new energy monitoring systems. 5G networks can meet the real-time data acquisition and transmission and realize data measurement, state awareness, and scheduling control. Nonorthogonal multiple access (NOMA) has emerged as a key component of 5G networks and has attracted extensive attention and research for its superior spectral efficiency performance [7]. The core concepts of NOMA are to service multiple users on the same resource simultaneously by utilizing power allocation (PA) and to separate multiplexed users at the receiver side by using the successive interference canceller (SIC) technique [8]. Different from the traditional orthogonal transmission, NOMA uses nonorthogonal transmission at the transmitter and actively introduces interference information. At the receiving end, the correct demodulation is realized by a SIC technology. Huawei, ZTE, and Datang Telecom have presented their own multiple access technologies, which are called sparse code multiple access (SCMA) [9], multiuser shared access (MUSA) [10], and pattern division multiple access (PDMA) [11], respectively. Although these technical details are different, they basically belong to NOMA



schemes. SCMA, MUSA, and PDMA [11] have been studied in both academia and industry. PDMA is a multicarrier NOMA scheme that has attracted significant attention due to its unequal diversity design at the transmitting side, and its ability to obtain almost equal or approximately equal diversity benefits at the receiving side. PDMA combined with relay technology can enhance system performance [12]. PDMA is a significant NOMA technology, which defines sparse mapping from data to a great sum of resources. Compared with other multiple access technologies, such as SCMA and MUSA, the advantage of PDMA is that PDMA patterns provide unequal classification to meet the communication requirements of different users [13]. Different diversity orders are provided for multiple users to alleviate the error propagation problem of the SIC receiver in PDMA-based systems.

The programming problem is a common problem in wireless communication systems, including optimal parameter setting and optimal power allocation (OPA). Bae and Han joined power and time allocation to minimize system outage probability for two-way cooperative NOMA [14]. Cao et al. [15] presented two PA schemes to improve the secrecy of wireless transmissions in a NOMA system. One scheme jammed eavesdropping attempts, and the other optimized the PA power. Zhu et al. presented a PA method to achieve max-min fairness, weighted sum rate maximization, sum rate maximization with quality of service (QoS) constraints, and energy efficiency maximization with weights or QoS constraints under a given channel assignment in NOMA systems [16]. Cui et al. investigated PA in multicell multicarrier NOMA (MC-NOMA) networks by considering maximizing the sum mean opinion scores (MOSs) of users and proposed a low-complexity suboptimal approach based on successive convex approximation techniques, which attained a good computational complexity-optimality trade-off [17]. Ni et al. developed a centralized minimum power control algorithm to minimize the total transmit power by considering the user data rate requirements for multicell MC-NOMA networks where the user assignment is fixed [18]. Khan et al. presented an iterative local optimal solution to calculate the optimal PA and enhance the sum capacity, which considered the transmission power in sending node, the user PA, and the minimum rate requirements per user [19]. Zhao et al. presented a joint problem of spectrum allocation and power control to maximize the sum rate of small-cell users in a NOMA network by considering user fairness. The PA problem used sequential convex programming to update the result iteratively. The spectrum allocation problem used a many-to-one matching game with peer effects [20]. Song et al. presented a PA algorithm based on a bisection search algorithm and a gradient value to maximize the energy efficiency in downlink NOMA networks with imperfect channel state information. The nonconvex problem was transformed to a convex problem by sequential convex programming, and the PA factors were attained by the Lagrangian multiplier method [21]. He et al. presented a deep reinforcement learning framework where PA and channel assignment were combined to allocate resources to users in a near optimal way.

Specifically, an attention-based neural network was exploited to perform the channel assignment [22]. Xiao et al. presented an improved PSO algorithm to improve the energy efficiency of the systems while guaranteeing the spectral efficiency [23]. Except GA, particle swarm optimization (PSO) is another artificial intelligence algorithm that can be used for wireless communication system optimization [24]. From the point of view of the programming solution method, the following comparison can be summarized [24], and the proposed methods are artificial intelligence algorithms. The main difference between this study and [24] is that, in this study, OPA is a multiobjective optimization problem rather than a single-objective optimization problem as in [24]. High system throughput is a major target in [24]. Both high system throughput and low outage probability are targets in this study. We not only improve the constraint functions in [24] but also propose an effective method for multiobjective programming.

The existing OPA methods only consider a single performance objective, that is, the system throughput, but single-objective optimization cannot meet the requirements of multiple performance indicators of wireless communication. Beside system throughput, outage probability is another important index to measure the performance of the communication system. Multiobjective optimization can make power allocation meet the requirements of different performance indexes of PDMA at the same time, that is, the significance of this work. Multiobjective optimization is of vital importance in a wireless communication system, but it is more complex and time-consuming than single-objective optimization. This motivates us to find an OPA algorithm in amplify-and-forward (AF) relaying with PDMA (AF-PDMA) networks to improve multiple system performances. The first challenge is that OPA is a nonconvex problem, which cannot be solved effectively by the gradient descent method. The second challenge is that how to balance the optimization needs of different system performance indicators. It was proved that different performance objectives make the optimization problem become a constrained multiobjective optimization problem in PDMA systems [25].

The contributions of this study can be outlined as follows. (1) We present a multiobjective PSO algorithm considering a Pareto-optimal solution to solve the complicated PA solution problems in an AF-PDMA network. The benefit is that the feasible region of the PSO algorithm is greatly reduced by modifying the original constraint functions, and the convergence efficiency is greatly improved. The iteration in the infeasible region is also avoided. (2) We analyse the relationship of user outage probabilities and system throughput from which a trade-off between the outage probability of a single user and system throughput is attained. The benefit is that different requirements of users and systems on OPA are taken into consideration, and the proposed multiobjective evaluation theory can be extended to other wireless communication systems for equilibrium optimization.

Notation: the notation  $\odot$  represents the dot multiple.  $(\cdot)^{-1}$  denotes the matrix inversion.  $(\cdot)^H$  denotes the matrix

conjugate transpose.  $\mathbf{I}_N$  represents an identity matrix with an  $N \times N$  vector.

## 2. System Model

In this section, we consider an AF-PDMA downlink network as outlined in [26]. A PDMA pattern matrix  $\mathbf{G}_{\text{PDMA}}^{N,K} = [\mathbf{g}_1, \mathbf{g}_2, \dots, \mathbf{g}_K]$  denotes a  $K$  pattern with  $\mathbf{g}_i$  mapping on  $N$  resources, where  $\mathbf{g}_i$  is the  $i^{\text{th}}$  user's PDMA pattern.

$$\begin{aligned} \mathbf{y}_{\text{bu}_k} &= \mathbf{h}_{\text{bu}_k} \odot \sum_{i=1}^K \sqrt{\alpha_i P} \mathbf{g}_i x_i + \mathbf{n}_{\text{bu}_k} = \sum_{i=1}^K \sqrt{\alpha_i P} \tilde{\mathbf{h}}_{\text{bu}_k} x_i + \mathbf{n}_{\text{bu}_k} = \mathbf{H}\mathbf{x} + \mathbf{n}_{\text{bu}_k}, \\ \mathbf{y}_{\text{ru}_k} &= G \tilde{\mathbf{h}}_{\text{ru}_k} \odot \left( \mathbf{h}_{\text{br}} \sum_{i=1}^K \sqrt{\alpha_i P} \mathbf{g}_i x_i + \mathbf{n}_{\text{br}} \right) + \mathbf{n}_{\text{ru}_k}, \end{aligned} \quad (1)$$

where  $\mathbf{y}_{\text{bu}_k}$  and  $\mathbf{y}_{\text{ru}_k}$  are the signals from the BS or relaying node, respectively.  $\mathbf{n}_{\text{bu}_k}$  and  $\mathbf{n}_{\text{ru}_k}$  are the noises from the BS and relaying node, respectively.  $\tilde{\mathbf{h}}_{\text{bu}_k}$  and  $\tilde{\mathbf{h}}_{\text{ru}_k}$  are the channel responses from the BS and relaying node, respectively.  $\tilde{\mathbf{h}}_{\text{bu}_k} = \mathbf{h}_{\text{bu}_k} \odot \mathbf{g}_k$ ,  $\tilde{\mathbf{h}}_{\text{ru}_k} = \mathbf{h}_{\text{ru}_k} \odot \mathbf{g}_k$ , and  $\tilde{H}$  is the PDMA equivalent channel response matrix.  $x_i$  is the  $i^{\text{th}}$  user's signal.  $\alpha_i$  is the PA coefficient, where  $\alpha_1 + \alpha_2 + \dots + \alpha_K = 1$ .  $\mathbf{x} = [\sqrt{\alpha_1 P} x_1 \ \sqrt{\alpha_2 P} x_2 \ \dots \ \sqrt{\alpha_K P} x_K]^T$  is the modulated symbol.  $G$  is the amplifying gain factor in which  $G = \sqrt{P / (P |\tilde{\mathbf{h}}_{\text{br}}|^2 + N_0)}$ .

The corresponding SINR for the  $k^{\text{th}}$  user who receives a signal from the BS is represented as follows:

$$\gamma_{\text{bu}_k} = P_k (\tilde{\mathbf{h}}_{\text{bu}_k})^H \left( N_0 \mathbf{I}_N + \sum_{i=k+1}^K P_i \tilde{\mathbf{h}}_i (\tilde{\mathbf{h}}_i)^H \right)^{-1} \tilde{\mathbf{h}}_{\text{bu}_k}. \quad (2)$$

$P_k = \alpha_k P$  denotes the  $k^{\text{th}}$  user's transmit power.

The corresponding SINR for the  $k^{\text{th}}$  user who receives the signal from the relaying node is represented as follows:

The transmission powers for the BS and relaying node are equal ( $P_s = P_r = P$ ). The channel coefficients among the BS, the  $k^{\text{th}}$  user, and the AF relaying node are denoted as  $h_{\text{mn}_k}$ , ( $\text{mn}_k \in \{\text{bu}_k, \text{br}, \text{ru}_k\}$ ), in which  $h_{\text{mn}_k} \sim \text{CN}(0, \mu_{\text{mn}_k})$ .  $n_{\text{br}} \sim \text{CN}(0, N_0)$  and  $n_{\text{bu}_k} \sim \text{CN}(0, N_0)$  represent additive white Gaussian noise at the relaying node and the  $k^{\text{th}}$  user, respectively.  $\gamma \triangleq (P/N_0)$  is a transmit SNR.

The received signals at  $k^{\text{th}}$  user from the BS or relaying node are denoted as follows:

$$\gamma_{\text{ru}_k} = \alpha_k \gamma^2 (\tilde{\mathbf{h}}_{\text{ru}_k} \odot \tilde{\mathbf{h}}_{\text{br}_k})^H [\mathbf{K}_{Z_k}]^{-1} (\tilde{\mathbf{h}}_{\text{ru}_k} \odot \tilde{\mathbf{h}}_{\text{br}_k}), \quad (3)$$

where  $Z_k$  is the noise plus the interference from the relaying node.  $\mathbf{K}_{Z_k}$  is the covariance of  $Z_k$ , which is calculated as follows:

$$\begin{aligned} \mathbf{K}_{Z_k} &= \gamma^2 \sum_{i=k+1}^K \alpha_i (\tilde{\mathbf{h}}_{\text{ru}_i} \odot \tilde{\mathbf{h}}_{\text{br}_i}) (\tilde{\mathbf{h}}_{\text{ru}_i} \odot \tilde{\mathbf{h}}_{\text{br}_i})^H + \gamma \tilde{\mathbf{h}}_{\text{ru}_k} (\tilde{\mathbf{h}}_{\text{ru}_k})^H \\ &\quad + \gamma \tilde{\mathbf{h}}_{\text{br}} (\tilde{\mathbf{h}}_{\text{br}})^H + \mathbf{I}_N. \end{aligned} \quad (4)$$

The metrics are defined as follows. Generally, outage probability is defined as the probability by which SINR is smaller than a specified threshold value in both BS-to-user and relay-to-user channels. An outage occurs if neither the direct nor the relay transmission succeeds [24]. System throughput is defined as the product of the transmission rate and the probability of successful transmission [27].

To simplify the outage expressions, we define function  $G_k(x)$  as (5).

$$G_k(x) = \begin{cases} 1 - e^{-(x/\gamma) \left( (1/\mu_{\text{br}}) + (1/\mu_{\text{ru}_k}) \right)} \sqrt{\frac{4x(x+1)}{\mu_{\text{br}} \mu_{\text{ru}_k} \gamma}} K_1 \left( \frac{4\phi(x+1)}{\mu_{\text{br}} \mu_{\text{ru}_k} \gamma} \right), & x \neq 0, \\ 0, & x = 0, \end{cases} \quad (5)$$

where  $K_1(\cdot)$  is the first-order modified Bessel function of the second type, and  $\mu_{\text{mn}_k}$  is the channel coefficient where  $\text{mn}_k \in \{\text{bu}_k, \text{br}, \text{ru}_k\}$ .

The matrix with two rows ( $N=2$ ) and three columns ( $k=3$ ) is the most representative matrix with the minimum

degree of unequal diversity. Other larger dimension matrices can be extended similarly. The PSO algorithm has a good applicability. When the number of users and channels change, we only need to modify the PSO parameters, constraints, and objective functions, rather than the

algorithm mechanism. Taking the PDMA pattern matrix  $G_{\text{PDMA}}^{2,3}$  as an example, the outage expressions for users are as follows:

$$\begin{aligned} \mathcal{O}_1 &= \begin{cases} (1 - e^{-\tau_1/\mu_{bu1}} + e^{-\tau_2/\mu_{bu1}}) \times (1 + G_1(\tau_1) - G_1(\tau_2)), & \text{if } a < 0, \\ (e^{-\tau_1/\mu_{bu1}} - e^{-\tau_2/\mu_{bu1}}) \times (G_1(\tau_2) - G_1(\tau_1)), & \text{if } a > 0, \end{cases} \\ \mathcal{O}_2 &= \begin{cases} (1 - e^{-\varsigma_1/\mu_{bu2}} + e^{-\varsigma_2/\mu_{bu2}}) \times (1 + G_2(\varsigma_1) - G_2(\varsigma_2)), & \text{if } a < 0, \\ (1 - e^{-\varsigma/\mu_{bu2}} + e^{-\varsigma_1/\mu_{bu2}} - e^{-\varsigma_2/\mu_{bu2}}) \times (G_2(\varsigma) - G_2(\varsigma_1) + G_2(\varsigma_2)), & \text{if } a > 0, \end{cases} \\ \mathcal{O}_3 &= \begin{cases} (1 - e^{-\xi_1/\mu_{bu3}} + e^{-\xi_2/\mu_{bu3}}) \times (1 + G_3(\xi_1) - G_3(\xi_2)), & \text{if } a < 0, \\ (1 - e^{-\xi/\mu_{bu3}} + e^{-\xi_1/\mu_{bu3}} - e^{-\xi_2/\mu_{bu3}}) \times (G_3(\xi) - G_3(\xi_1) + G_3(\xi_2)), & \text{if } a > 0, \end{cases} \end{aligned} \quad (6)$$

where  $\tau_1 = \max\{0, x_1\}$ ,  $\tau_2 = \max\{0, x_2\}$ ,  $\varsigma = (\phi_2/\alpha_2\gamma)$ ,  $\varsigma_1 = \max\{(\phi_2/\alpha_2\gamma), x_1\}$ ,  $\varsigma_2 = \max\{(\phi_2/\alpha_2\gamma), x_2\}$ ,  $\psi_1 = \max\{x_1, (\phi_2/\alpha_2\gamma), (\phi_3/\alpha_3\gamma)\}$ ,  $\psi_2 = \max\{x_2, (\phi_2/\alpha_2\gamma), (\phi_3/\alpha_3\gamma)\}$ ,  $\psi = \max\{(\phi_2/\alpha_2\gamma), (\phi_3/\alpha_3\gamma)\}$ , and  $a = [\alpha_1(\alpha_2 + \alpha_3) - \alpha_2\alpha_3\phi_1]\gamma^2$ .

$\phi_k$  is the targeted SNR of the  $k^{\text{th}}$  user;  $x_1$  and  $x_2$  stand for different values of  $|h_{bu1}|^2$ , and they can be obtained by solving the following equation.

$$\begin{aligned} &[\alpha_1(\alpha_2 + \alpha_3) - \alpha_2\alpha_3\phi_1]\gamma^2|h_{bu1}|^4 \\ &+ [2\alpha_1 - (\alpha_2 + \alpha_3)\phi_1]\gamma|h_{bu1}|^2 - \phi_1 = 0. \end{aligned} \quad (7)$$

The AF-PDMA system throughput expression is denoted as

$$\mathcal{R}_{\text{sum}} = \mathcal{R}_1(1 - \mathcal{O}_1) + \mathcal{R}_2(1 - \mathcal{O}_2) + \mathcal{R}_3(1 - \mathcal{O}_3). \quad (8)$$

### 3. Optimal Power Allocation

The optimal PA is mathematically equivalent to the optimal PA factor setting. Multiobjective programming is an effective way to solve complicated PA problems.

**3.1. Programming Model.** Two typical objectives, based on system throughput and outage probability, have been proposed for optimal PA in a downlink network. Hence, the PA allocation problem is an optimization problem with two objective functions, and it can be formulated as

$$\min f(\boldsymbol{\alpha}, \boldsymbol{\theta}) = [\mathcal{O}_3(\boldsymbol{\alpha}, \boldsymbol{\theta}), -R_{\text{sum}}(\boldsymbol{\alpha}, \boldsymbol{\theta})], \quad (9)$$

where  $\boldsymbol{\alpha}$  is the three PA coefficients (i.e.,  $\alpha_1$ ,  $\alpha_2$ , and  $\alpha_3$ ),  $\boldsymbol{\theta}$  is a system parameter vector in the downlink network,  $\mathcal{O}_3$  is the outage probability of the third user, the significance ensures the reliability of single-user communication, and  $R_{\text{sum}}$  is the system throughput.

The inequality constraints are given as follows:

$$1 > \alpha_1 > \alpha_2 > \alpha_3 > 0. \quad (10)$$

The equality constraint is given as follows:

$$\alpha_1 + \alpha_2 + \alpha_3 = 1. \quad (11)$$

The challenge of PSO is that once the initial value and update particles are not in the feasible region, all the particles may be updated in the infeasible region. We propose a new approach to address this issue by revising the existing constraints through logic. After the constraint conditions are modified, the decision variables are changed from three coefficients to two coefficients. The third coefficient is calculated as a parameter by (11). The inequality constraints are improved as follows:

$$\frac{1}{3} < \alpha_1 < 1, \quad (12a)$$

$$0 < \alpha_2 < \frac{1}{2}, \quad (12b)$$

$$0 < \alpha_2 < \alpha_1, \quad (12c)$$

$$1 - \alpha_1 - \alpha_2 < \alpha_2. \quad (12d)$$

Equations (13) and (14) are broad constraints, but (12a)–(12d) make the constraints narrow. The point is that the constraint conditions are very important for the efficiency and accuracy of the evolutionary algorithm. With respect to PSO, the programming model based on (13) and (14) is easy to iterate in the infeasible region, but the model based on (12a)–(12d) can avoid this problem.

**3.2. PSO Theory.** PSO exhibits strong randomness and covers most solution spaces to avoid reaching a local optimum [28]. The advantage of an artificial intelligence algorithm is that it is amenable to almost all stochastic programming models. Its disadvantage is that it cannot guarantee that a global optimal solution can be found. Even if the global optimal solution is found, it is impossible to provide a strict mathematical proof. In addition, adjusting the parameters, including the step size and penalty coefficients, is difficult. Reasonable parameters are necessary conditions for obtaining the optimal solution, and the PSO parameters in this study are listed in Table 1.

TABLE 1: Simulation parameters for PSO.

Item	Value
The PSO particle size	30
The PSO iteration number	15
The penalty function factor	$10^6$

**3.3. Pareto Frontier.** The Pareto frontier is a key to solving the multiobjective programming problem [29]. A Pareto-optimal solution can include a noninferior solution set, a nondominated solution set, and a nondominant solution set. Based on the Pareto dominance, we present a multiobjective PSO algorithm considering a Pareto-optimal solution. The procedure of the multiobjective PSO algorithm is given as follows: Algorithm 1.

**3.4. TOPSIS.** The technique for order preference by similarity to an ideal solution (TOPSIS) is an effective double benchmark evaluation method [30] that can be used to balance the outage probability of a single user and system throughput. TOPSIS can calculate the positive and negative ideal solutions of each index (i.e., outage probability of a single user or system throughput). The relative closeness of each evaluation object to positive and negative ideal solutions can be used to evaluate the comprehensive performance of the system. The optimal TOPSIS should be close to the positive ideal solution, and the distance from the negative ideal solution should be large. The decision problem of two objectives is shown in Figure 1.

$A^+$  and  $A^-$  denote the positive ideal solution and negative ideal solution, respectively. The feasible solution  $A_1$  is closest to the ideal solution  $A^+$  but not the farthest solution from the negative ideal solution  $A^-$ . The feasible solution  $A_2$  is further away from the negative ideal  $A^-$ . The disadvantage of TOPSIS is that the weight is not reflected in the distance calculation. The calculated Euclidean distance can be weighted using an entropy-weighting method to overcome this shortcoming.

The calculation steps of an entropy TOPSIS method are as follows. A standard treatment of the evaluation matrix data using 0-1 transformation is implemented.

When the index is positive, the following formula is used for standardized transformation.

$$b_{ij}^* = \frac{b_{ij} - \min_j b_{ij}}{\max_j b_{ij} - \min_j b_{ij}}, \quad 1 \leq i \leq m, 1 \leq j \leq n, \quad (13)$$

where  $b_{ij}$  is an optimal system throughput in step 3 in section C, and  $n$  is equal to two. When the index is an inverse index, the following formula is used for standardized transformation.

$$b_{ij}^* = \frac{\max_j b_{ij} - b_{ij}}{\max_j b_{ij} - \min_j b_{ij}}, \quad 1 \leq i \leq m, 1 \leq j \leq n, \quad (14)$$

where  $b_{ij}$  is an optimal outage probability in step 3 in section C.

According to the standardized decision matrix, the characteristic proportion of the  $j^{\text{th}}$  index and the  $i^{\text{th}}$  evaluation sample can be calculated using

$$cP_{ij} = \frac{b_{ij}^*}{\sum_{i=1}^m b_{ij}^*}. \quad (15)$$

The entropy of the index is calculated using

$$e_j = -\frac{1}{\ln m} \sum_{i=1}^m cP_{ij} \ln cP_{ij}, \quad 1 \leq j \leq n. \quad (16)$$

Note that when  $cP_{ij} = 0$ , we set  $\ln(cP_{ij})$  equal to zero. The entropy weight formula is

$$w_j = \frac{1 - e_j}{\sum_{i=1}^n 1 - e_j}, \quad 1 \leq j \leq n. \quad (17)$$

From here, it follows that

$$\begin{aligned} c_{ij} &= w_j \times b_{ij}, \quad i = 1, 2, \dots, m; j = 1, 2, \dots, n, \\ C^+ &= \max c_{ij}, \quad 1 \leq i \leq m, \\ C^- &= \min c_{ij}, \quad 1 \leq i \leq m, \end{aligned} \quad (18)$$

where  $C = (c_{ij})_{m \times n}$  is the weighted normal matrix,  $C^+$  is the set of positive ideal solutions, and  $C^-$  is the set of negative ideal solutions.

Then, the weighted Euclidean distances from each evaluation object to the positive and negative ideal solutions are calculated separately.

$$\begin{aligned} d_i^+ &= \sqrt{\sum_{j=1}^n w_j^2 (c_{ij} - c_j^+)^2}, \quad i = 1, 2, \dots, m, \\ d_i^- &= \sqrt{\sum_{j=1}^n w_j^2 (c_{ij} - c_j^-)^2}, \quad i = 1, 2, \dots, m, \\ f_i &= \frac{d_i^-}{d_i^+ + d_i^-}, \quad i = 1, 2, \dots, m, \end{aligned} \quad (19)$$

where  $f_i$  is the evaluation result of the comprehensive performances. One can find the best solution at the Pareto frontier by finding the greatest  $f_i$ .

The implementation process of the proposed algorithm is shown in Figure 2.

## 4. Results and Discussion

**4.1. Subheadings.** We use a step-by-step validation method to demonstrate the power optimization method for AF-PDMA in a downlink network. First, we compare GA with the proposed PSO algorithm. Then, system throughput performance and the minimum outage probability of the third user are taken as planning objectives, and different

Step 1. Single-objective optimization

- (i) Find the optimal solution of the maximum system throughput using the PSO algorithm
- (ii) Find the optimal solution of the minimum outage probability of user3 using the PSO algorithm

Step 2. Probability distribution calculation

- (i) Calculate the system throughput using the solutions, which ensures the minimum outage probability of user3
- (ii) Generate a row vector of  $m$  linearly equally spaced points between the optimal system throughput and the system throughput, which is solved in the last step

Step 3. Obtain the Pareto frontier

- (i) Add inequality constraint  $R_{\text{sum}}(\alpha, \theta) > a$ , which is an element of the above equally spaced points. For each solution, a constraint is added in order.
- (ii) Find the optimal solution of the minimum outage probability of user3 using the PSO algorithm based on the above added inequality constraint
- (iii) Repeat the above process  $m$  times to obtain  $m$  groups of optimization target values

ALGORITHM 1: Process for multiobjective optimization.

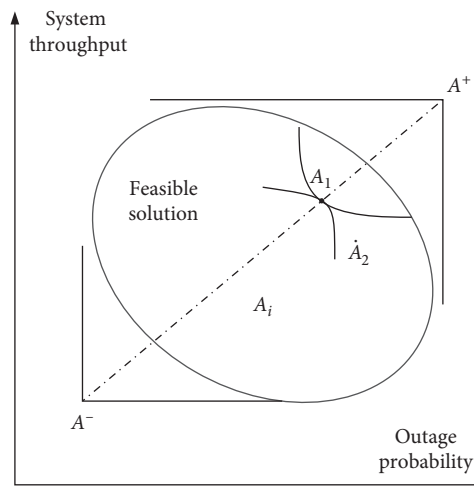


FIGURE 1: Positive ideal solution and negative ideal solution.

solutions for OPA are derived. To balance the need for system throughput with the desire to minimize outage probabilities, a Pareto frontier consisting of a set of possible solutions is found. The Pareto solutions are further evaluated with the TOPSIS approach to help the decision-maker find the desired OPA solution. The simulation in this study is performed on a Lenovo laptop with an Intel(R) Core (TM) i7-1065G7 CPU operating at 1.30 GHz with 15.7 GB of available memory.

An internal function of MATLAB, i.e., a GA solver for mixed-integer or continuous-variable optimization, constrained or unconstrained, is used to solve the OPA problem. Because GA internal function is installed in Matlab, the solution performance is reliable and can be used to verify the accuracy and effectiveness of the proposed PSO algorithm.

PSO and GA are used to solve the OPA problem to obtain the maximum system throughput. As shown in Figures 3–5, the performances of this method are better than those of the GA. It should be noted that it is important to adjust parameters in an artificial intelligence algorithm

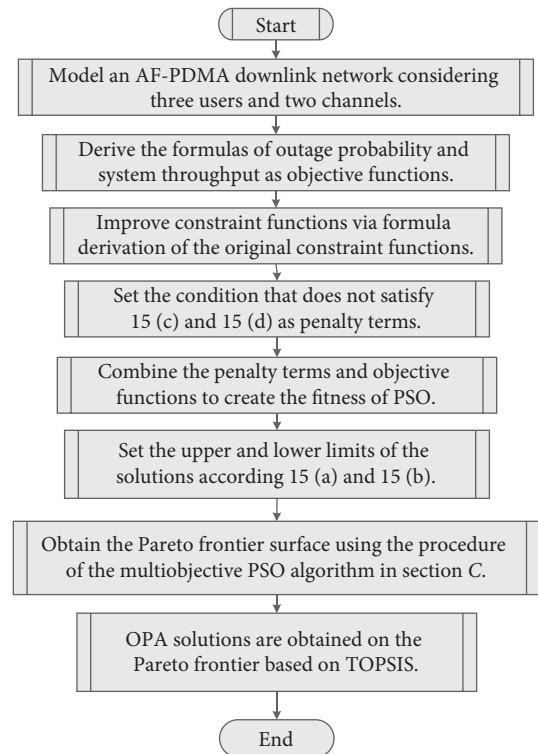


FIGURE 2: Implementation process of the proposed algorithm.

according to the programming model. The simulation results do not demonstrate that PSO is more efficient and accurate than GA but demonstrate that the solution performance of the artificial intelligence algorithm depends on the parameter setting. Noted that the PSO algorithm uses the modified constraints, the GA uses the constraints before modification. The feasible region of GA solution is original and broad, and the solution is limited by (13)–(14). The feasible region of the PSO algorithm is modified and compact, and the solution is limited by (12a)–(12d). It will greatly improve the efficiency and accuracy of the solution via transforming (10)–(11) to (12a)–(12d). With respect to



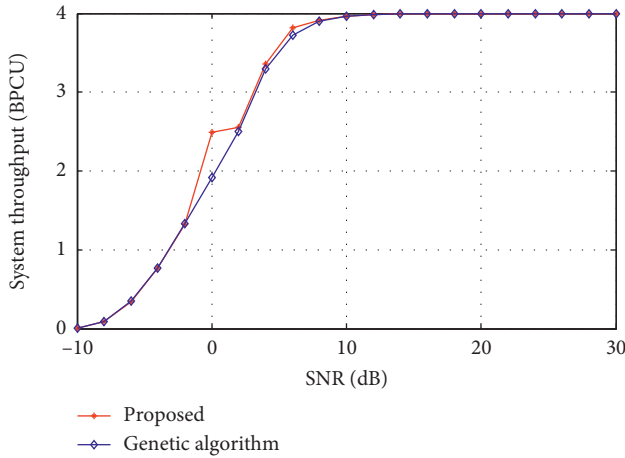


FIGURE 3: System throughput (BPCU) versus SNR (dB) using different solutions.

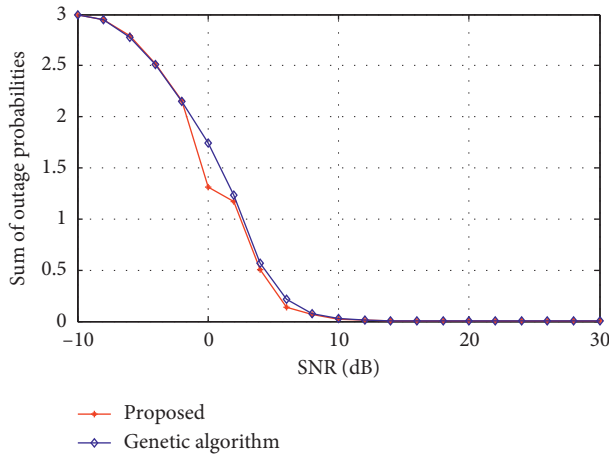


FIGURE 4: Sum of outage probabilities versus SNR (dB) using different solutions.

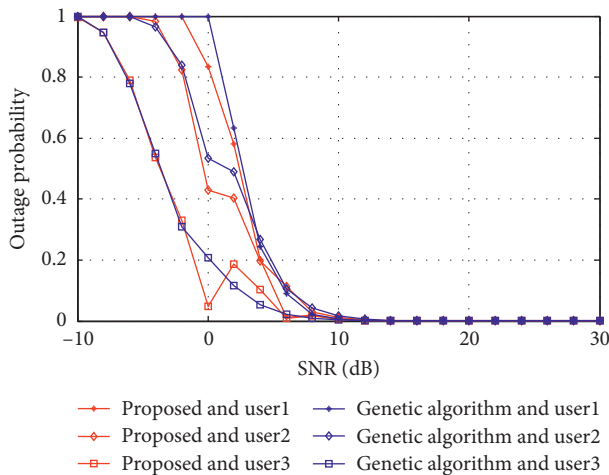


FIGURE 5: Outage probabilities versus SNR (dB) using different solutions.

the proposed method, the feasible regions of  $\alpha_1$  and  $\alpha_2$  have been reduced to improve the calculation efficiency.  $\alpha_3$  is no longer used as a solution, and it is directly calculated using  $\alpha_1$  and  $\alpha_2$ . The benefit of such a treatment is that the equality constraint (11) is avoided when generating fitness function. This result shows that rigorous mathematical derivations and reductions of the feasible region are important for an intelligent optimization algorithm.

Figures 3–5 show the different evaluation metrics, but their optimization objectives are the same. System throughput is taken as the single-objective function. According to the formulas for outage probabilities and system throughput, there is no contradiction between them. When the outage probability is very low, the system throughput performance can be guaranteed. However, this does not mean that the outage probability of each user is completely consistent with the system throughput performance of the downlink network. It has been calculated that the individual user may be sacrificed to maximize the system throughput. With the increasing of outage probability (power reduction) of the individual user, the total outage probability and system throughput may be improved. Although some GA results are better than the PSO results for user3, system throughput of GA optimization is definitely worse than that of the proposed PSO optimization. There exist balance and game problems between system throughput performance and a user outage probability. To illustrate this problem, the outage probability of user3 is taken as the objective function, and the proposed PSO method is used to solve the OPA.

As shown in Figures 6–8, the system performances vary depending on the target functions. It can be seen that the optimal system throughput performance does not guarantee the best performance for every user. Even if multiple users have the lowest total outage probability, there is no guarantee that each user will have the lowest outage probability. With regards to the solution results, it should be noted that it is difficult for an artificial intelligence algorithm to find the global optimal solution. In terms of few individual points, the system throughput of the curve targeting the best system throughput can be less than that of the curve targeting the best user3. Also, these locally optimal solutions are few and reasonable when PSO is used. To solve the biobjective programming problem, we use the weighted ideal method to evaluate Pareto frontier using 500 solutions, which is shown in Figure 9.

At the Pareto frontier, user3 outage probability and system throughput performances need to be balanced. OPA should balance the two to achieve a balance of the two indicators.

The index of outage probability is an inverse index and has a cost type attribute. The smaller the outage probability value is, the better the system performance. The index of system throughput is positive and has a benefit type attribute. The larger the index value, the better the system performance. According to formulas (9) and (10), the system throughput and outage probability values in Figure 9 are standardized. The weight matrix is determined by the entropy weight method, and the matrix is



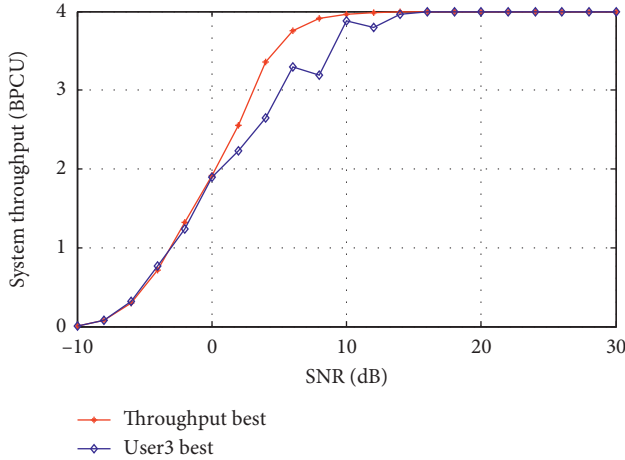


FIGURE 6: System throughput (BPCU) versus SNR (dB) considering different optimization objectives.

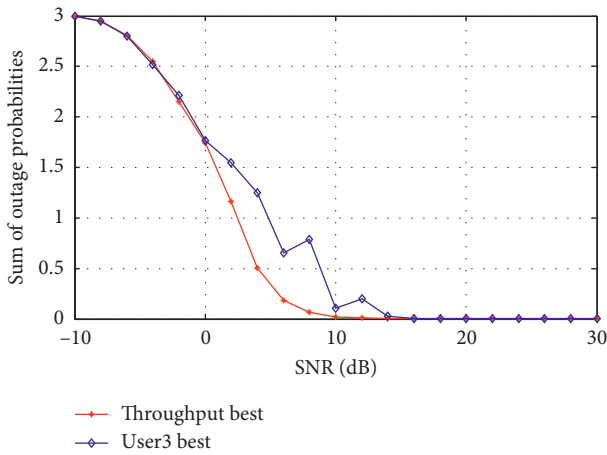


FIGURE 7: Sum of outage probabilities versus SNR (dB) considering different optimization objectives.

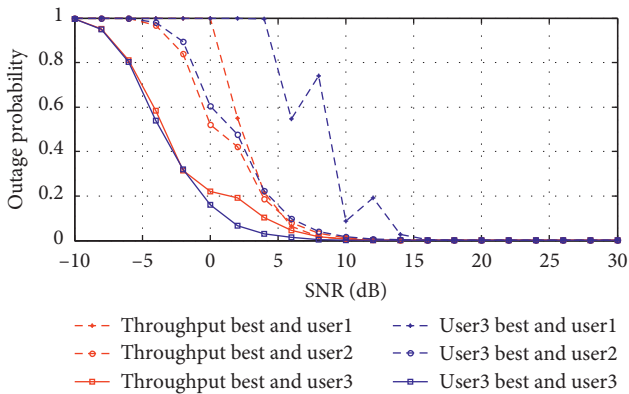


FIGURE 8: Sum of outage probabilities versus SNR (dB) considering different optimization objectives.

[0.1408, 0.8592]. The TOPSIS approach is a double benchmark that can reduce the probability of the same evaluation results. We can obtain the best power distribution

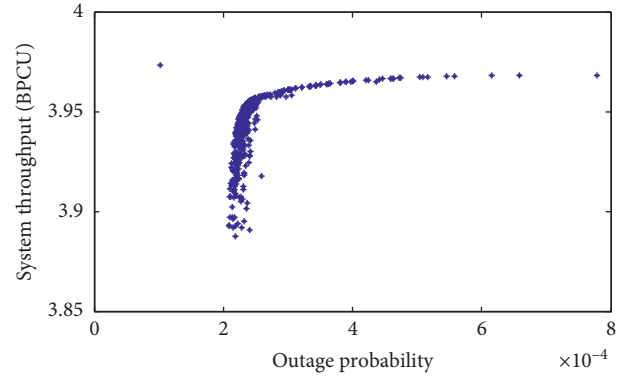


FIGURE 9: Pareto frontier for user3 outage probability versus system throughput with SNR = 10.

TABLE 2: System performances of TOPSIS.

Item	System throughput	Outage probability
Lower boundary	3.88	0.0010
Upper boundary	3.97	0.0078
TOPSIS	3.96	0.0011

scheme using the method combining entropy weight and TOPSIS, and the solution of PA coefficients is [0.7, 0.2, 0.1]. The optimal system throughput and outage probability of TOPSIS is listed in Table 2. It can be seen that each index of TOPSIS is not the best, but there is a balance between the two indexes.

Although PSO can be applied to solve nonconvex multiobjective optimization problems, it cannot avoid the complexity of parameter setting and program debugging. The setting of PA initial values and particle moving speed will affect the PSO performance. In practical programming, the biggest challenge is that the particle swarm can be updated in the infeasible region. With respect to the proposed optimization method, the updating of particle swarm is strictly limited in the feasible region via putting strict constraints on the feasible region instead of setting the penalty term in the fitness function. Of course, multi-objective will bring about the complexity problem, which can be dealt with by Pareto frontier and an effective comprehensive evaluation method.

## 5. Conclusion

The entropy method is used to determine the weight of a system index (system throughput and outage probability), which avoids the subjectivity of multifactor weight determination. Through the analysis of the comprehensive evaluation results of the system performance of a downlink network, the effectiveness and rationality of the TOPSIS approach for OPA are verified. TOPSIS can calculate the weighted distance and overcome the shortage of comprehensive evaluation results caused by the use of a single standard. The simulation results ensure that the outage probability of a single user is low, and the system throughput performance is good.

## Data Availability

The data used to support the findings of this study are available from the corresponding author upon request.

## Conflicts of Interest

The authors declare that they have no conflicts of interest.

## Acknowledgments

This work was supported by the National Natural Science Foundation of China (52007193).

## References

- [1] B. Yang, T. Yu, H. Shu, J. Dong, and L. Jiang, "Robust sliding-mode control of wind energy conversion systems for optimal power extraction via nonlinear perturbation observers," *Applied Energy*, vol. 210, pp. 711–723, 2018.
- [2] B. Yang, X. Zhang, T. Yu, H. Shu, and Z. Fang, "Grouped grey wolf optimizer for maximum power point tracking of doubly-fed induction generator based wind turbine," *Energy Conversion and Management*, vol. 133, pp. 427–443, 2017.
- [3] B. Yang, L. Jiang, L. Wang, W. Yao, and Q. H. Wu, "Nonlinear maximum power point tracking control and modal analysis of DFIG based wind turbine," *International Journal of Electrical Power & Energy Systems*, vol. 74, pp. 429–436, 2016.
- [4] B. Yang, T. Yu, H. Shu et al., "Passivity-based sliding-mode control design for optimal power extraction of a PMSG based variable speed wind turbine," *Renewable Energy*, vol. 119, pp. 577–589, 2018.
- [5] B. Yang, L. Zhong, X. Zhang et al., "Novel bio-inspired memetic salp swarm algorithm and application to MPPT for PV systems considering partial shading condition," *Journal of Cleaner Production*, vol. 215, pp. 1203–1222, 2019.
- [6] B. Yang, T. Yu, X. Zhang et al., "Dynamic leader based collective intelligence for maximum power point tracking of PV systems affected by partial shading condition," *Energy Conversion and Management*, vol. 179, pp. 286–303, 2019.
- [7] Y. Ye, R. Q. Hu, G. Lu, and L. Shi, "Enhance latency-constrained computation in MEC networks using uplink NOMA," *IEEE Transactions on Communications*, vol. 68, no. 4, pp. 2409–2425, 2020.
- [8] Z. Ding, Y. Liu, J. Choi et al., "Application of non-orthogonal multiple access in LTE and 5G networks," *IEEE Communications Magazine*, vol. 55, no. 2, pp. 185–191, 2017.
- [9] L. Lu, Y. Chen, W. Guo, H. Yang, Y. Wu, and S. Xing, "Prototype for 5G new air interface technology SCMA and performance evaluation," *China Communications*, vol. 12, pp. 38–48, 2015.
- [10] ZTE, *Discussion on Multiple Access for New Radio Interface 3GPP TSG RAN WG1 Meeting 84bis, Doc.R1-162226*, ZTE, Busan, Korea, 2016.
- [11] X. Dai, Z. Zhang, B. Bai, S. Chen, and S. Sun, "Pattern division multiple access: a new multiple access technology for 5G," *IEEE Wireless Communications*, vol. 25, no. 2, pp. 54–60, 2018.
- [12] B. Ren, Y. Wang, X. Dai, K. Niu, and W. Tang, "Pattern matrix design of PDMA for 5G UL applications," *China Communications*, vol. 13, no. Supplement2, pp. 159–173, 2016.
- [13] S. Chen, B. Ren, Q. Gao, S. Kang, S. Sun, and K. Niu, "Pattern division multiple access—a novel nonorthogonal multiple access for fifth-generation radio networks," *IEEE Transactions on Vehicular Technology*, vol. 66, no. 4, pp. 3185–3196, 2017.
- [14] J. Bae and Y. Han, "Joint power and time allocation for two-way cooperative NOMA," *IEEE Transactions on Vehicular Technology*, vol. 68, no. 12, pp. 12443–12447, 2019.
- [15] Y. Cao, S. Wang, M. Jin et al., "Power optimization for enhancing secrecy of cooperative user relaying NOMA networks," *IEEE Transactions on Vehicular Technology*, vol. 69, no. 7, pp. 8008–8012, 2020.
- [16] J. Zhu, J. Wang, Y. Huang, S. He, X. You, and L. Yang, "On optimal power allocation for downlink non-orthogonal multiple access systems," *IEEE Journal on Selected Areas in Commun.*, vol. 35, no. 12, pp. 2744–2757, 2017.
- [17] J. Cui, Y. Liu, Z. Ding, P. Fan, and A. Nallanathan, "Qoe-based resource allocation for multi-cell NOMA Networks," *IEEE Transactions on Wireless Communications*, vol. 17, no. 9, pp. 6160–6176, 2018.
- [18] D. Ni, L. Hao, Q. T. Tran, and X. Qian, "Transmit power minimization for downlink multi-cell multi-carrier NOMA networks," *IEEE Communications Letters*, vol. 22, no. 12, pp. 2459–2462, 2018.
- [19] W. U. Khan, Z. Yu, S. Yu, G. A. S. Sidhu, and J. Liu, "Efficient power allocation in downlink multi-cell multi-user NOMA networks," *IET Communications*, vol. 13, no. 4, pp. 396–402, 2019.
- [20] J. Zhao, Y. Liu, K. K. Chai, A. Nallanathan, Y. Chen, and Z. Han, "Spectrum allocation and power control for non-orthogonal multiple access in hetNets," *IEEE Transactions on Wireless Communications*, vol. 16, no. 9, pp. 5825–5837, 2017.
- [21] X. Song, L. Dong, J. Wang, L. Qin, and X. Han, "Energy efficient power allocation for downlink NOMA heterogeneous networks with imperfect CSI," *IEEE Access*, vol. 7, pp. 39329–39340, 2019.
- [22] C. He, Y. Hu, Y. Chen, and B. Zeng, "Joint power allocation and channel assignment for NOMA with deep reinforcement learning," *IEEE Journal on Selected Areas in Communications*, vol. 37, no. 10, pp. 2200–2210, 2019.
- [23] H. Xiao, Y. Wang, Q. Cheng, and Y. Wang, "An improved PSO-based power allocation algorithm for the optimal EE and SE tradeoff in downlink NOMA systems," in *Proceedings of 2018 IEEE 29th Annual International Symposium on Personal, Indoor and Mobile Radio Communications (PIMRC)*, pp. 1–5, Bologna, Italy, September 2018.
- [24] X. Zhang, S. Kang, and X. Fu, "Pattern division multiple access featuring amplify-and-forward relaying in an uplink network," *IEEE Access*, vol. 8, pp. 85656–85663, 2020.
- [25] J. Tang, Y. Yu, D. So, G. Chen, X. Zhang, and M. Huang, "Multi-objective optimization of joint power allocation and splitting control for SWIPT-enabled NOMA systems," in *Proceedings of 2019 International Conference on Computing, Networking and Communications (ICNC)*, pp. 491–496, Honolulu, HI, USA, February 2019.
- [26] X. Zhang, S. Kang, X. Fu, and W. Tang, "Performance analysis of cooperative PDMA with AF relaying over Rayleigh fading channels," *IET Communications*, vol. 14, no. 13, pp. 2166–2175, 2020.
- [27] J. Choi, "Joint rate and power allocation for NOMA with statistical CSI," *IEEE Transactions on Communications*, vol. 65, no. 10, pp. 4519–4528, 2017.
- [28] X. Fu, Q. Guo, and H. Sun, "Statistical machine learning model for stochastic optimal planning of distribution networks considering a dynamic correlation and dimension reduction," *IEEE Transactions on Smart Grid*, vol. 11, no. 4, pp. 2904–2917, 2020.

- [29] X. Fu, H. Chen, R. Cai, and P. Yang, "Optimal allocation and adaptive VAR control of PV-DG in distribution networks," *Applied Energy*, vol. 137, pp. 173–182, 2015.
- [30] X. Fu, H. Chen, and X. Jin, "Study on effectiveness evaluation of the siting of DG based on a TOPSIS method-based approach," in *Proceedings of 2013 IEEE PES Asia-Pacific Power and Energy Engineering Conference (APPEEC)*, pp. 1–6, Kowloon, Kerala, 2013, November.

## Research Article

# Optimization Design of Oil-Immersed Iron Core Reactor Based on the Particle Swarm Algorithm and Thermal Network Model

Fating Yuan <sup>1,2</sup>, Kai Lv <sup>1</sup>, Bo Tang,<sup>1</sup> Yue Wang,<sup>1</sup> Wentao Yang,<sup>1</sup> Shihong Qin <sup>3</sup>, and Can Ding<sup>1</sup>

<sup>1</sup>College of Electrical Engineering & New Energy, China Three Gorges University, Yichang 443002, China

<sup>2</sup>Hubei Provincial Engineering Technology Research Center for Power Transmission Line, China Three Gorges University, Yichang 443002, China

<sup>3</sup>School of Electrical Engineering and Information, Wuhan Institute of Technology, Wuhan 430205, China

Correspondence should be addressed to Fating Yuan; [yuanfatinghss@163.com](mailto:yuanfatinghss@163.com) and Shihong Qin; [qinsh798@163.com](mailto:qinsh798@163.com)

Received 27 December 2020; Revised 12 January 2021; Accepted 22 January 2021; Published 17 February 2021

Academic Editor: Xiao-Shun Zhang

Copyright © 2021 Fating Yuan et al. This is an open access article distributed under the Creative Commons Attribution License, which permits unrestricted use, distribution, and reproduction in any medium, provided the original work is properly cited.

In this paper, according to the design parameters of oil-immersed iron core reactor, the thermal network model of windings is established by the thermo-electric analogy method, and the temperature distribution of the windings can be obtained. Meanwhile, a fluid-thermal coupled finite element model is established, the temperature and fluid velocity distribution are extracted, and the simulation results show that the error coefficient of temperature is less than 3% compared with the thermal network model, so the correctness of thermal network model has been verified. Taking the metal conductor usage and loss of windings as the optimization objects, the optimization method based on the particle swarm algorithm and thermal network model is proposed, and the Pareto optimal solutions between the metal conductor usage and loss of windings are given. The optimization results show that the metal conductor usage is reduced by 23.05%, and the loss is reduced by 20.25% compared with the initial design parameters, and the maximum temperature of winding does not exceed the expected value. Thus, the objects of low metal conductor usage and loss of windings are conflicted and cannot be optimized simultaneously; the optimization method has an important guiding significance for the design of oil-immersed iron core.

## 1. Introduction

The oil-immersed iron core reactor is an indispensable equipment in the power system, which plays the role of reactive power compensation, limiting the fault current and improving the power factor of the system [1]. However, the reactor encounters overheating and even burns out in the operation process, and the relevant studies show that the excessive temperature of the windings is the main reason [2]. The oil flow of the oil-immersed reactor enters the oil channels of the disc-type windings; the hot spot is formed as the convection heat dissipation capacity of each disc which is different; when the hot spot exceeds the limit, it will directly affect the safe and stable operation of the reactor. In order to reduce the temperature of reactor, the methods, such as increasing the cross-sectional area of conductor and oil channel width, are adopted; they can reduce the loss and

temperature of the windings, but the metal conductor usage is increased. The loss and the metal conductor usage of windings are two key parameters in the design of reactor; in order to realize the low loss and the metal conductor usage simultaneously, the temperature calculation is needed and the optimization design method about the reactor is essential.

Currently, the relevant studies mainly include (1) the temperature calculation of the reactor. The finite-difference method is used to calculate the temperature of the reactor [3, 4], and it is merely suitable for the situations that the temperature and heat flux distribution of the coil surface are the same, which limits its practical application. The finite element model is adopted [5–7], and the detailed temperature and fluid velocity distribution of the reactor can be obtained, but the calculation process is complex and

calculation time is long. The thermal network model is put forward, and it was applied to the transformer windings [8]. On the basis, the optimization model of transformer windings is proposed [9–12]. In [13], the complex model of oil channels in windings is simplified to an approximate matrix of hydraulic channel, and the correctness has been verified. (2) The optimization design of the reactor. In [14], the finite element method is adopted to improve the heat dissipation efficiency of the windings by adjusting the oil channel width and the thickness of the coils, but the calculation time is large and the principle is not clear. In [15, 16], the thermal-electromagnetic combined optimization method is proposed to reduce the metal conductor, but the influence of air duct's width on the heat dissipation efficiency is not considered. In [17–21], the genetic algorithm and particle swarm optimization are applied to minimize the metal conductor usage or the loss of the transformer, but it can only realize the optimization of a single target, the overall optimization of the reactor cannot be achieved.

In this paper, taking the metal conductor usage and loss of windings as the optimization objects, the thermal network model of windings is established by the thermo-electric analogy method, the temperature distribution of the windings can be obtained, and the correctness has been verified by the fluid-thermal coupled finite element method. Meanwhile, the optimization method based on particle swarm algorithm and thermal network model is proposed, and the Pareto optimal solutions between the metal conductor usage and loss of windings are given. The optimization results show that the metal conductor usage is reduced by 23.05%, and the loss is reduced by 20.25% compared with the initial design parameters, and the maximum temperature of windings does not exceed the expected value, and the correctness has been verified.

## 2. The Structure and Equivalent Model of Windings

**2.1. The Structure and Parameters of Core Reactor.** The oil-immersed core reactor with a rated voltage of 26.4 kV and rated capacity of 66 MVA is selected as a research object. The disc-type windings are made of wires with insulating layer, which are surrounded on the iron core column. In the windings, the horizontal oil channels are formed between disc-type windings in the axial direction; the inside and outside of the windings are the vertical insulation paper tubes. Meanwhile, a baffle for oil is set up at intervals of a certain number of discs, so as to lead the oil flow in the vertical direction to the horizontal direction, which can enhance the cooling effect of windings. According to the structure characteristic of iron reactor, the influence of iron column and iron yoke on the heat dissipation of windings can be ignored; thus, the windings of iron reactor are only considered in this paper, and the basic structure of windings is given in Figure 1.

**2.2. The Equivalent Model of Windings.** The total windings consist of 60 layers of disc, and they were divided into 4 channels by the oil guiding washer. Each channel consists of

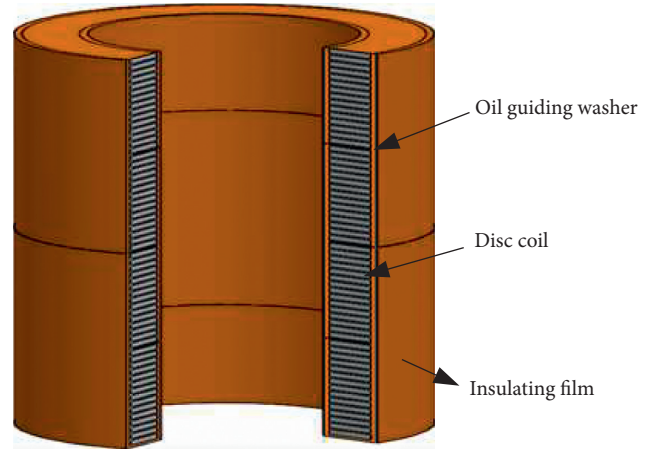


FIGURE 1: The basic structure of windings.

15 layers of disc, each layer of disc consists of 23 turns of conductor with insulating layers, and the thickness of the insulating layer is 0.4 mm. Considering the temperature and fluid velocity distribution in each channel of the windings are basically the same, thus, one of the channels is selected to research the temperature distribution of windings, and the equivalent model and parameters are given in Figure 2.

The characteristics of metal conductor and insulating materials are given in Table 1.

## 3. The Temperature Calculation of Windings Based on the Thermal Network Model

**3.1. The Establishment of Thermal Network Model.** The heat transfer model of windings can be equivalent to the circuit node network, which adopts the analogy method between the circuit and the heat transfer system. The basic idea of thermo-electric analogy is to compare the transfer of heat between media to the transfer of electric current in a conductor. The related physical essence of the temperature field is analogized to the heat transfer parameters, such as temperature difference, heat flux, heat resistance, and heat capacity. So, the topology of the thermal network can be established, and it is similar to the circuit [22]. In order to obtain the temperature distribution of each conductor and oil flow node, a thermal network model with each conductor as the basic unit is established based on the equivalent model of windings, as shown in Figure 3.

In Figure 3,  $T_{\text{disc}}$  and  $T_{\text{oil}}$  are the node temperature of conductor and oil flow, respectively,  $R_{\text{cir}}$  is the conduction thermal resistance between conductors and insulating layers,  $R_{\text{oor}}$  is the conduction thermal resistance of oil flow,  $R_{\text{ior}}$  is the convection thermal resistance between the insulation layers and oil, and  $q$  is the heat source of the conductor.

**3.2. The Calculation of Thermal Resistance.** In the actual operation process of oil-immersed iron core reactor, the influence of the leakage magnetic on the eddy current loss of each turn is basically the same, so it is considered that each turn conductor has the same heat source. Considering the temperature difference between the adjacent conductors is



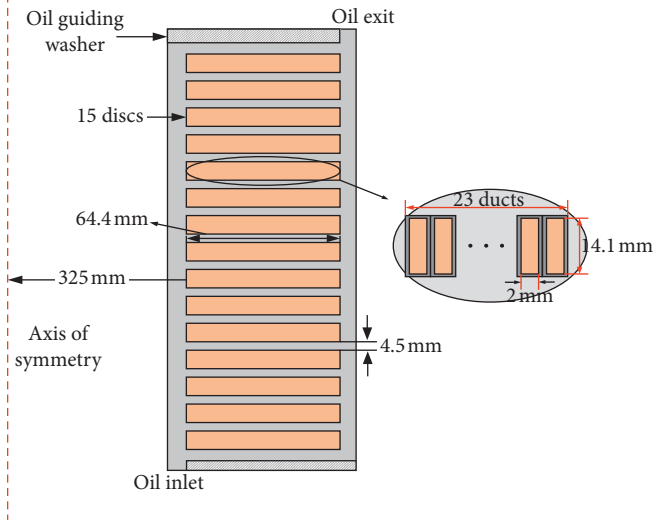


FIGURE 2: The equivalent model of windings.

TABLE 1: The characteristics of metal conductor and insulating materials.

Materials	Attribute	Value
Copper	Heat conductivity ( $\text{W}\cdot\text{M}^{-1}\cdot\text{K}^{-1}$ )	400
	Specific heat ( $\text{W}\cdot\text{kg}^{-1}\cdot\text{K}^{-1}$ )	385
	Density ( $\text{Kg M}^{-3}$ )	8940
Insulating materials	Heat conductivity ( $\text{W}\cdot\text{M}^{-1}\cdot\text{K}^{-1}$ )	0.21
	Specific heat ( $\text{W}\cdot\text{kg}^{-1}\cdot\text{K}^{-1}$ )	1250
	Density ( $\text{Kg M}^{-3}$ )	870

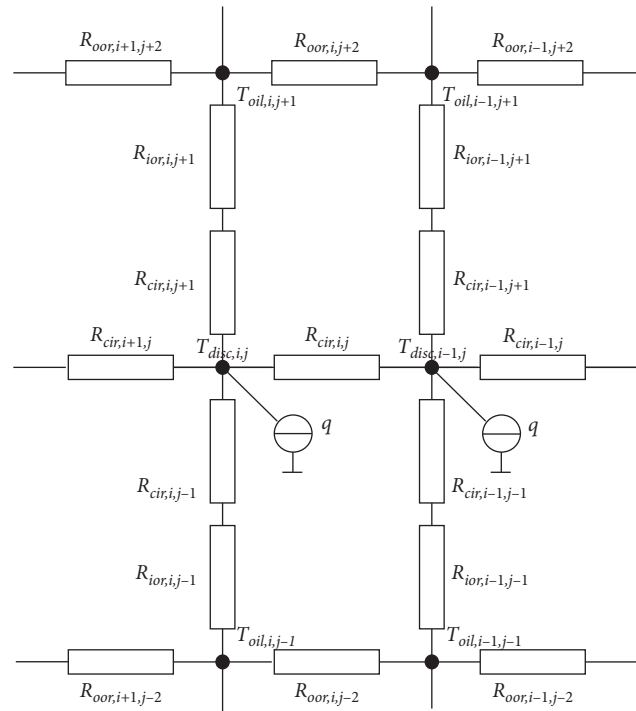


FIGURE 3: The thermal network model.

small, the radiation heat transfer can be ignored, so the heat transfer modes of heat flux in the four directions of the conductor are merely the heat conduction and heat convection. In order to establish the thermal network model, the calculation of thermal resistance is essential.

- (1) The conduction thermal resistance: in the inner of conductors and insulating material, the conduction thermal resistance depends on the geometric structure and material properties. When the heat flux is transferred to the oil channel, the heat transfer will occur in the oil flow, and the conduction thermal resistance of the oil flow is related to the geometric shape of the oil channel and physical properties of the oil. The conduction thermal resistance in the conductors, insulation layers and oil can be calculated, as shown in the following equation:

$$R_{(\text{cir/or})} = \frac{L_q}{k_m S}, \quad (1)$$

where  $L_q$  is the thickness of the conductor in the direction in which the heat flows,  $k_m$  is the thermal conductivity of material,  $S$  is the surface area, which is perpendicular to heat flow direction,  $R_{\text{cir}}$  is the conduction thermal resistance of metal conductor and insulating layers, and  $R_{\text{oor}}$  is the conduction thermal resistance of oil.

- (2) The convection thermal resistance: the convection heat transfer is formed between the discs and the horizontal and vertical oil channel, and the thermal resistance is related to the fluid velocity and temperature of oil. According to the Newton's law of cooling, the convection thermal resistance between the surfaces of the insulating layers and the oil channels can be expressed, as shown in the following equation:

$$R_{\text{ior}} = \frac{1}{\alpha A}, \quad (2)$$

where  $R_{\text{ior}}$  is the convection thermal resistance between the insulation layer and oil,  $A$  is the area of the insulating layer, and  $\alpha$  is the convection coefficient, which is related to the geometric structure, material, and fluid characteristics of oil, and it can be written as follows:

$$\alpha = \frac{N_u k_{\text{oil}}}{L_{io}}, \quad (3)$$

where  $L_{io}$  is the geometric characteristic length of the convection heat transfer surface,  $k_{\text{oil}}$  is the thermal conductivity of transformer oil, and  $N_u$  is the Nusselt number, and the expression is [23]

$$N_u = 1.86 \left( \frac{R_e P_r D}{L} \right)^{(1/3)} \left( \frac{\mu}{\mu_s} \right)^{0.14}, \quad (4)$$

where  $L$  is the horizontal length,  $D$  is the diameter of oil channel,  $\mu$  is the kinetic viscosity of oil with the ambient temperatures,  $\mu_s$  is the kinetic viscosity of



oil,  $R_e$  is the Reynolds number, and  $P_r$  is the Prandtl number. The parameters,  $R_e$  and  $P_r$ , can be calculated by the following equation:

$$\begin{cases} R_e = \frac{\rho_{\text{oil}} v_i D}{\mu_s}, \\ P_r = \frac{c_p \mu_s}{k_{\text{oil}}}, \end{cases} \quad (5)$$

where  $\rho_{\text{oil}}$  and  $c_p$  are the density and specific heat capacity of oil, respectively, and  $v_i$  is the fluid velocity of horizontal oil channel in the  $i_{th}$  layer.

**3.3. The Temperature Calculation of Windings.** According to the thermal network model in Figure 3, it contains  $N$  nodes, so the  $n-1$  node equations can be listed [21], which is similar to the node voltage equation in the circuit. The temperature equations of each node can be written [24], as shown in the following equation:

$$\begin{cases} \left( \sum \frac{1}{R_{\text{self-impedance}}} \right) T_{\text{disc},i,j} - \sum \left( \frac{1}{R_{\text{mutual-impedance}}} T_{\text{disc},m_i,j} \right) - \sum \left( \frac{1}{R_{\text{mutual-impedance}}} T_{\text{oil},i,n_j} \right) = q, \\ \left( \sum \frac{1}{R_{\text{self-impedance}}} \right) T_{\text{oil},i,j} - \sum \left( \frac{1}{R_{\text{mutual-impedance}}} T_{\text{disc},m_i,j} \right) - \sum \left( \frac{1}{R_{\text{mutual-impedance}}} T_{\text{oil},i,n_j} \right) = 0, \end{cases} \quad (6)$$

$$T = G^{-1}Q, \quad (7)$$

where  $R_{\text{self-impedance}}$  is the node self-thermal resistance,  $R_{\text{mutual-impedance}}$  is the node mutual thermal resistance,  $T_{\text{disc},i,j}$  and  $T_{\text{oil},i,j}$  are the conductor and oil flow nodes of the  $i_{th}$  row and  $j_{th}$  column in the model, respectively,  $m_i$  and  $n_j$  are the numbers of adjacent nodes,  $m_i = (i-1, i+1)$ ,  $n_j = (j-1, j+1)$ . The above equation can be solved by the MATLAB software, and the node temperature can be expressed as

where  $T$  is the temperature of node,  $Q$  is the heat source matrix of the conductor, and  $G$  is the heat conductivity matrix, which is composed by the self-thermal resistance and mutual thermal resistance, as shown in the following equation:

$$G = \begin{bmatrix} \frac{1}{R_{sa-1}} & -\frac{1}{R_{ma1-1}} & 0 & \cdot & -\frac{1}{R_{ma2-1}} & \cdot & 0 & 0 \\ -\frac{1}{R_{ma1-1}} & \frac{1}{R_{sa-2}} & -\frac{1}{R_{ma1-2}} & 0 & \cdot & \cdot & \cdot & 0 \\ 0 & -\frac{1}{R_{ma1-2}} & \frac{1}{R_{sa-2}} & -\frac{1}{R_{ma1-3}} & \cdot & \cdot & \cdot & \cdot \\ \cdot & 0 & -\frac{1}{R_{ma1-3}} & \cdot & \cdot & \cdot & \cdot & -\frac{1}{R_{ma2-t}} \\ \frac{1}{R_{ma2-1}} & \cdot & \cdot & \cdot & \cdot & \cdot & 0 & \cdot \\ \cdot & \cdot & \cdot & \cdot & \cdot & \frac{1}{R_{sa-n-2}} & -\frac{1}{R_{ma1-n-1}} & 0 \\ 0 & \cdot & \cdot & \cdot & 0 & -\frac{1}{R_{ma1-n-1}} & \frac{1}{R_{sa-n-1}} & -\frac{1}{R_{ma1-n}} \\ 0 & 0 & \cdot & -\frac{1}{R_{ma2-t}} & \cdot & 0 & -\frac{1}{R_{ma1-n}} & \frac{1}{R_{sa-n}} \end{bmatrix}, \quad (8)$$

where,  $(1/R_{ma1-i})$  and  $(1/R_{ma2-j})$  are the sum of mutual admittance of the  $i_{th}$  and  $j_{th}$  nodes, respectively, and the

parameter,  $(1/R_{sa-i})$ , is the sum of self-admittance of the node.

According to the structure and electrical parameters of windings, combined with the above calculation method, the temperature of each node can be obtained by solving equation (7).

### 3.4. The Calculation Results Based on Thermal Network Model.

The settings of thermal network model are as follows: the loss of each turn conductor is 34.5 W, the temperature in the inlet of the oil channel is 303.15 K, and the velocity is 0.3 m/s; the boundary conditions of the upper and lower surfaces of each channel are heat insulation as the low thermal conductivity of the oil guide baffle. In the thermal network model, there exist 437 conductor nodes and 460 oil channel nodes; the number of the discs is sorted from top to bottom; combined with the thermal resistance calculation method and node temperature equation, the temperature of each node can be obtained, and the maximum temperature of each disc is given, as shown in Table 2.

In Table 2, it can be seen that the maximum temperature of discs is gradually increased from the bottom to the top, but there is a downward trend when nearing the top, the maximum temperature is 62.65°C, and the maximum temperature area is mainly concentrated in the upper middle position of winding; the main reason is that the fluid velocity of oil is large in the inlet and outlet, and the convection heat transfer degree is high. When the oil flows in the long channel, the temperature is increased and the fluid velocity of oil is decreased, which leads to the accumulation of heat in the middle of windings, so the temperature of the middle discs is higher than the upper and lower discs.

## 4. Model Validation

**4.1. The Finite Element Simulation Calculation.** According to the structure parameters and material characteristics of the windings, the two-dimensional model is established based on the COMSOL, as shown in Figure 4.

The governing equations and boundary conditions settings are the key steps of simulation calculation.

**4.1.1. Governing Equation.** The heat conduction and heat convection are the main heat transfer processes in the windings region, and the governing equation of heat conduction can be expressed by the following equation [25]:

$$\frac{\partial^2 T}{\partial r^2} + \frac{\partial^2 T}{\partial z^2} + \frac{q}{k_m} = 0. \quad (9)$$

The heat convection between windings and oil channels satisfies mass, momentum, and energy conservation, as shown in the following equation [26]:

$$\left\{ \begin{array}{l} \frac{1}{r} \frac{\partial(ur)}{\partial r} + \frac{1}{z} \frac{\partial(vr)}{\partial z} = 0, \\ \rho_{oil} \left( u \frac{\partial u}{\partial r} + v \frac{\partial u}{\partial z} \right) = F_r - \frac{\partial p}{\partial r} + \mu_s \left( \frac{\partial^2 u}{\partial r^2} + \frac{\partial^2 u}{\partial z^2} \right), \\ \rho_{oil} \left( u \frac{\partial v}{\partial r} + v \frac{\partial v}{\partial z} \right) = F_z - \frac{\partial p}{\partial z} + \mu_s \left( \frac{\partial^2 v}{\partial r^2} + \frac{\partial^2 v}{\partial z^2} \right), \\ u \frac{\partial T}{\partial r} + v \frac{\partial T}{\partial z} = \frac{k_{oil}}{\rho_{oil} c_p} \left( \frac{\partial^2 v}{\partial r^2} + \frac{\partial^2 v}{\partial z^2} \right), \end{array} \right. \quad (10)$$

where  $u$  and  $v$  are the radial and axial fluid velocities of oil, respectively,  $F_r$  and  $F_z$  are the radial and axial components of fluid gravity, and  $p$  is the pressure of fluid.

**4.1.2. The Boundary Conditions Setting.** The boundary conditions are set as follows: (1) the heat transfer between the insulating paper and the outer transformer oil can be ignored, and it sets as an adiabatic boundary. (2) The discs surface is regarded as the stationary, the axial and radial velocity are zero, the inlet velocity of oil is 0.3 m/s, and the temperature is 303.15 K. (3) The outlet boundary condition of oil flow is natural pressure outlet boundary and the axis of rotation is axisymmetric boundary condition. The heat source of each turn conductor is setting the same; the value is 34.5 W. Meanwhile, the characteristic parameters of oil are given in Table 3.

**4.2. The Simulation Results.** The transient field is applied in the simulation, the total calculation time is 10 h, and the time step is 0.1 h, which can be considered that it has reached the steady state. The temperature of windings and fluid velocity distribution of oil are given in Figure 5.

In Figure 5, the temperature of discs in the inlet is lower than in the middle, and the maximum temperature reaches 66.20°C in the 8th disc; the fluid velocity of oil is relatively large in the inlet and outlet. In order to analyze the heat transfer process of discs, the radial and axial direction paths are extracted, as shown in Figure 6.

According to the paths selected and simulation results, the temperature distribution with the different paths is plotted, as shown in Figures 7–9.

From Figures 7–9, it can be seen that the temperature of discs is increased first and then decreased in axial and radial directions. On the contrary, the fluid velocity along the axial direction is decreased first and then increased, which is opposite to the trends of temperature. Meanwhile, the maximum temperature locates the eighth disc, and the fluid velocity is the lowest on the both sides of the discs with the maximum temperature, the main reasons are that the fluid velocity in lower channels is relatively large when the oil passes the inlet, and the temperature is low. The heat

TABLE 2: The maximum temperature of each disc.

Disc number	1	2	3	4	5	6	7	8
Temperature (°C)	40.79	45.58	50.47	55.49	59.33	61.35	62.32	62.65
Disc number	9	10	11	12	13	14	15	
Temperature (°C)	62.56	62.17	61.54	60.73	59.77	58.68	57.47	

dissipation conditions are weak because of the high temperature and low velocity of the oil in the middle discs; the temperature of the middle discs is the highest. In the upper discs, the oil converges in the outlet; it leads to the increase of the fluid velocity, so the temperature of the upper discs is lower compared with the middle discs.

**4.3. Model Validation.** In order to verify the accuracy of the thermal network model, the maximum temperature of each disc is obtained in both the thermal network model and finite element method, as shown in Figure 10.

In Figure 10, it can be seen that the maximum temperature is basically the same based on the thermal network model and finite element method, and the maximum error coefficient of the disc is only 5.30%, which locates the 8th disc, so the correctness of the thermal network model is verified.

The error coefficient is defined as follows:

$$\varepsilon = \left| \frac{T_{\text{hot}} - T_{\text{COM}}}{T_{\text{COM}}} \right|, \quad (11)$$

where  $\varepsilon$  is the error coefficient,  $T_{\text{hot}}$  is the temperature based on the thermal network model, and  $T_{\text{COM}}$  is the temperature based on the finite element method. Meanwhile, the thermal network model is a multivariate linear equation related to thermal resistance, and the calculation speed is fast compared with the finite element method; thus, the thermal network model is adopted to optimize the windings in this paper.

## 5. The Optimization Design of Windings Based on Particle Swarm Algorithm and Thermal Network Model

According to actual engineering requirements of the oil-immersed iron core reactor, the metal conductor usage and loss of windings are the two major optimization objects; however, these goals are in conflict with each other, the performance improvement of one object results in the reduction of the other object. In order to achieve the optimal design parameters of windings, the optimization design of iron reactor is needed.

**5.1. The Particle Swarm Optimization Algorithm.** The particle swarm optimization is one of the most influential multi-objective algorithms, including the prominent characteristics: the optimal solution of multiobjective can be easily obtained for its efficient search ability, and the algorithm has good multipeak search ability, which means it has a good ability to search for a global optimal value and it converges

quickly. The flow chart of particle swarm optimization method is given in Figure 11.

The formulas of particle update in particle swarm optimization are as follows [27]:

$$\begin{aligned} V^{k+1} &= wV^k + c_1r_1(P_i^k - X^k) + c_2r_2(P_g^k - X^k), \\ X^{k+1} &= X^k + V^{k+1}, \end{aligned} \quad (12)$$

where  $w$  is the inertia weight,  $r_1, r_2$  are the random numbers distributed in  $[0, 1]$ ,  $k$  is the current iteration number,  $P_i$  is the individual optimal particle position,  $P_g$  is the global particle position,  $c_1, c_2$  are the acceleration constants,  $V$  is the velocity of the particle, and  $X$  is the position of the particle.

The optimization object is to obtain the minimum metal conductor usage and loss of windings; according to the structural characteristics of the windings, the size of the conductor  $W_{\text{coil}}$ , the height of horizontal channels  $H_{\text{coil}}$ , and the thickness of insulation layer  $L_{\text{ins}}$  are selected as the optimization variables. The object functions of metal conductor usage  $M_{\text{cu}}$  and loss  $P_{\text{loss}}$  can be written as

$$\begin{cases} \min M_{\text{cu}} = \pi \rho m \sum_{i=1}^{n_{\text{disc}}} d_i W_{\text{coil}} H_{\text{coil}}, \\ \min P_{\text{loss}} = \pi I^2 \gamma \sum_{i=1}^{n_{\text{disc}}} \frac{d_i}{W_{\text{coil}} H_{\text{coil}}}, \end{cases} \quad (13)$$

where  $\rho$  is the density of metal conductor,  $m$  is the number of discs,  $n_{\text{disc}}$  is the number of conductors in each disc,  $d_i$  is the average diameter of the  $i_{\text{th}}$  conductor,  $I$  is the current of the conductor, and  $\gamma$  is the resistance of the conductor.

The inequality constraints are

$$\begin{cases} T_{\text{Hot\_max}} \leq T_{\text{max}}, \\ L_{\text{min}} \leq L \leq L_{\text{max}}, \\ W_{\text{coil\_min}} \leq W_{\text{coil}} \leq W_{\text{coil\_max}}, \\ H_{\text{coil\_min}} \leq H_{\text{coil}} \leq H_{\text{coil\_max}}, \\ H_{\text{duct\_min}} \leq H_{\text{duct}} \leq H_{\text{duct\_max}}, \end{cases} \quad (14)$$

where  $T_{\text{Hot\_max}}$  is the maximum temperature of discs by calculation methods,  $T_{\text{max}}$  is the maximum temperature constraints of the discs,  $L$  is the inductance of the reactor, and  $W_{\text{coil\_min}}, W_{\text{coil\_max}}, H_{\text{coil\_min}}, H_{\text{coil\_max}}, H_{\text{duct\_min}},$  and  $H_{\text{duct\_max}}$  are the minimum and the maximum values of variables.

**5.2. The Optimization Results.** In particle swarm optimization algorithm, the variable parameters are set as follows: the radial width of the conductor is  $[1.6, 2.6]$  mm, the axial

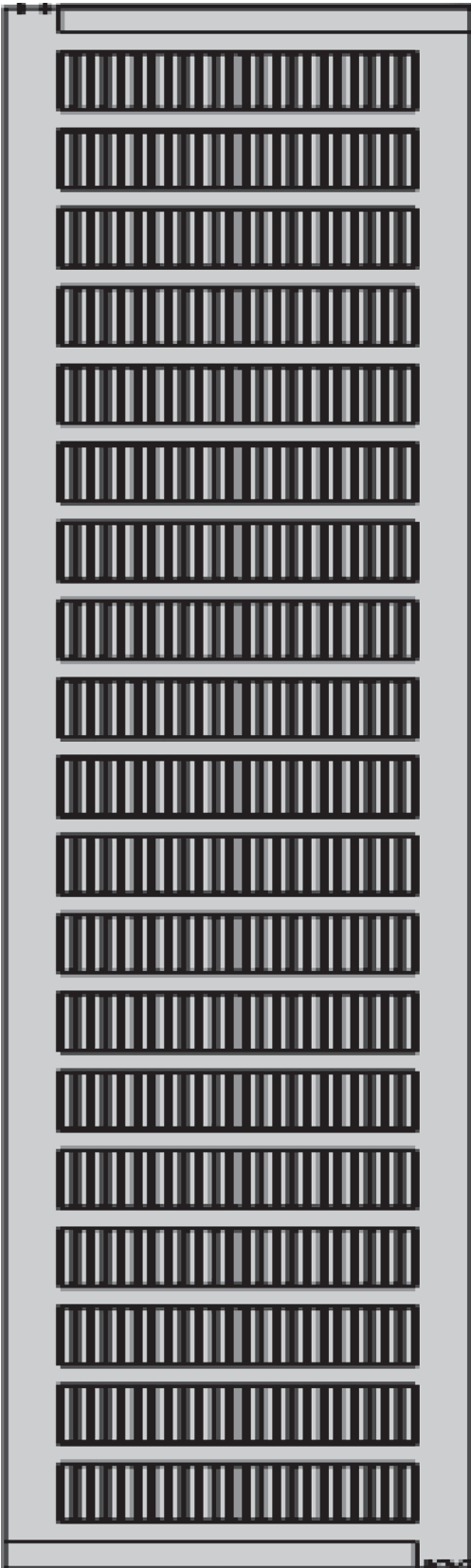


FIGURE 4: The simulation model of windings.

TABLE 3: The characteristics of oil.

Materials	Attribute	Value
Oil	Heat conductivity ( $\text{W}\cdot\text{M}^{-1}\cdot\text{K}^{-1}$ )	$0.134 - 8.05 \times 10^{-5}T$
	Specific heat ( $\text{W}\cdot\text{kg}^{-1}\cdot\text{K}^{-1}$ )	$-13408.15 + 123.04T - 0.33T^2$
	Density ( $\text{Kg M}^{-3}$ )	$1055.05 - 0.58T - 6.4 \times 10^{-5}T^2$
	Dynamic viscosity ( $\text{kg}\cdot\text{M}^{-1}\cdot\text{S}^{-1}$ )	$91.45 - 1.33T + 0.01T^2$

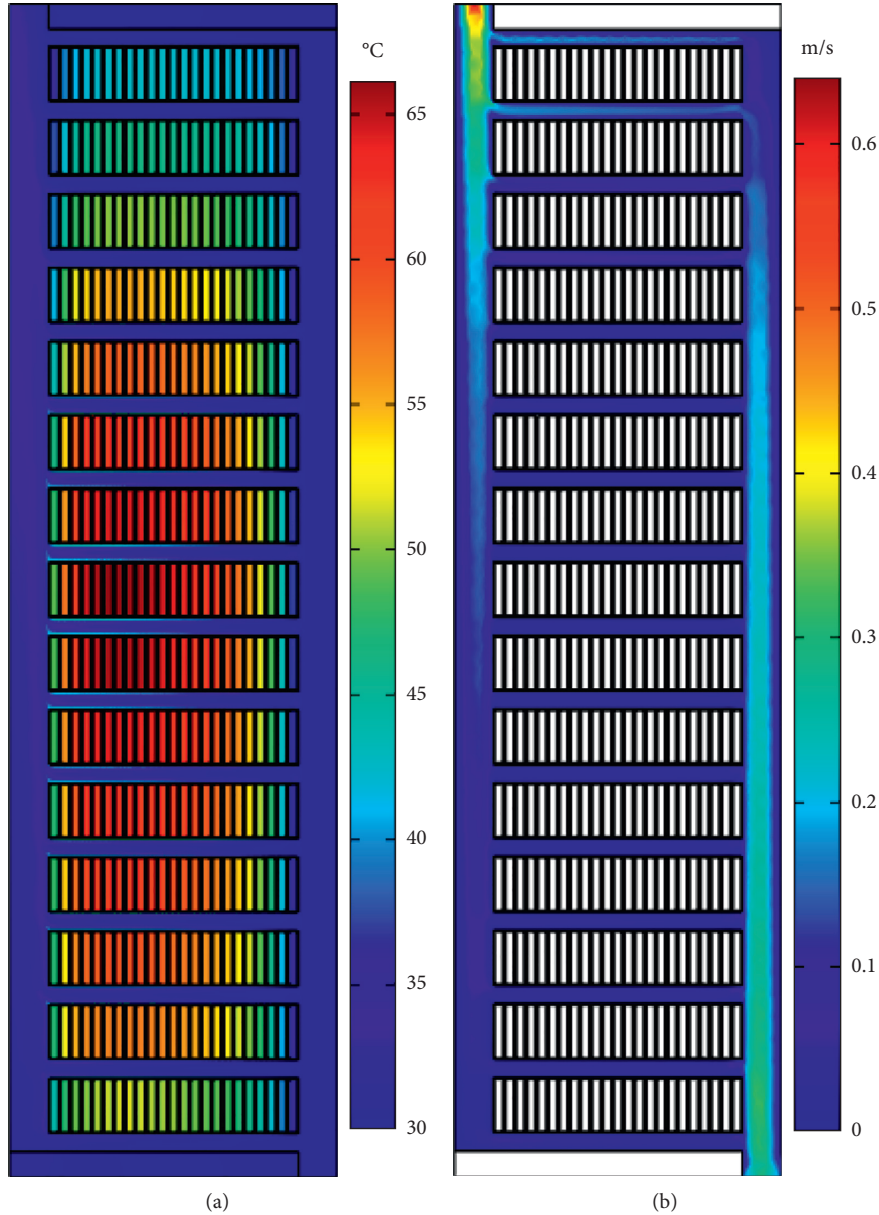


FIGURE 5: Simulation results: (a) temperature distribution; (b) fluid velocity distribution.

height of the conductor is [12, 14.6] mm, the thickness of the insulation layer is [0.25, 0.5] mm, and the height of horizontal channels is [3.9, 5.4] mm. The expected inductance difference is less than 2%, and the maximum temperature of winding is 75°C. The settings of particles in particle swarm optimization are as follows: the acceleration constants  $c_1$  and  $c_2$  are 0.8, the iteration time is 200, and the inertia weight

value is 0.8–1.2. The Pareto optimum results are shown in Figure 12,

The change rate of metal conductor usage and loss,  $K_M$  and  $K_{\text{loss}}$ , is defined as the following equation:

$$K_x = \frac{x}{x_0}, \quad (15)$$

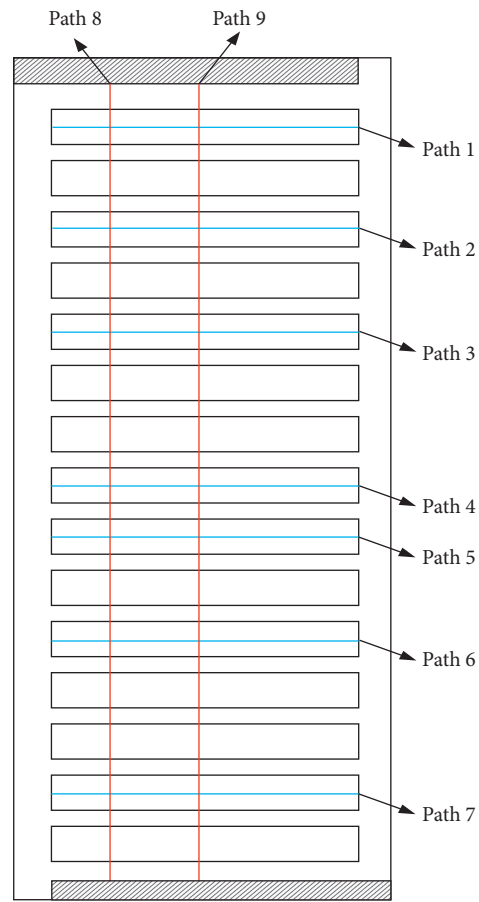


FIGURE 6: The extract path of the model.

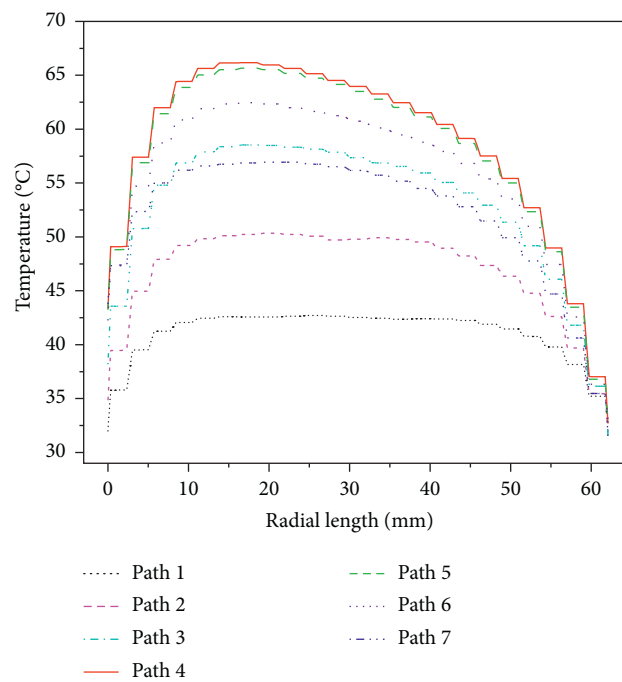


FIGURE 7: The temperature rise distribution along the radial paths.



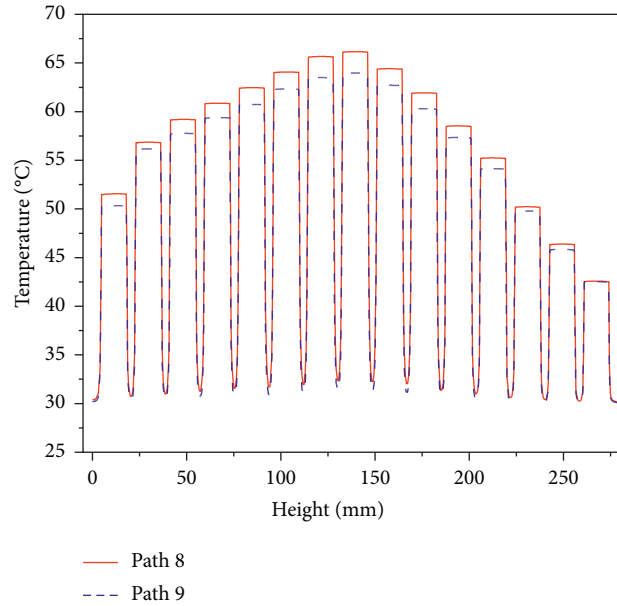


FIGURE 8: The temperature rise distribution along the axial paths.

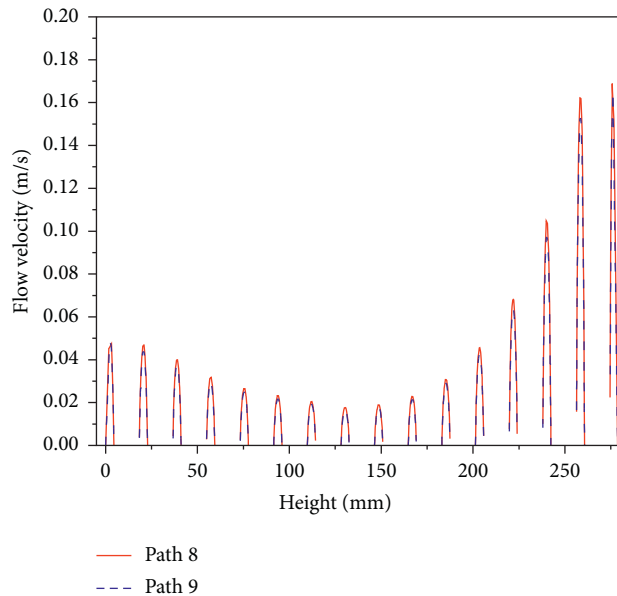


FIGURE 9: The fluid velocity distribution along the horizontal paths.

where  $x_0$  is the initial design parameter and  $x$  is the design parameter with the optimization method. In the initial parameters, the metal conductor usage and loss of windings are 90.98 kg and 11.9 kW before optimization, respectively.

In Figure 12, it can be seen that there exists an opposite trend between the metal conductor usage and loss of windings. Combined with the particle swarm optimization algorithm and thermal network model, the representative results can be obtained, as shown in Table 4. The inductance change rate is less than 1% compared with the initial parameters.

In order to verify the correctness of the optimization results, taking the groups 2, 9, 17, and 20 in Table 4 as an example,

the maximum temperatures of windings are 54.91°C, 67.74°C, 68.56°C, and 73.40°C, respectively, based on the thermal network model. Meanwhile, the simulation results based on the finite element method are given in Figure 13; the maximum temperatures of windings are 55.10°C, 68.20°C, 70.00°C, and 72.63°C respectively; it can be seen that the temperature distribution laws of the four groups are basically the same, and the error coefficient is less than 3%; thus, the correctness of the optimization method has been verified.

In Table 4, it can be seen that the metal conductor usage of windings is reduced by 23.05%, and the loss of the windings is reduced by 20.25% compared with the initial design parameters. As the purpose of low metal conductor

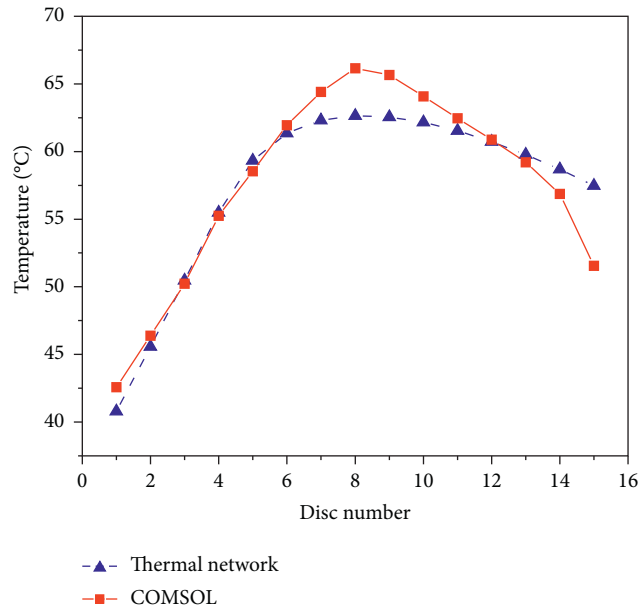


FIGURE 10: The maximum temperature of each disc.

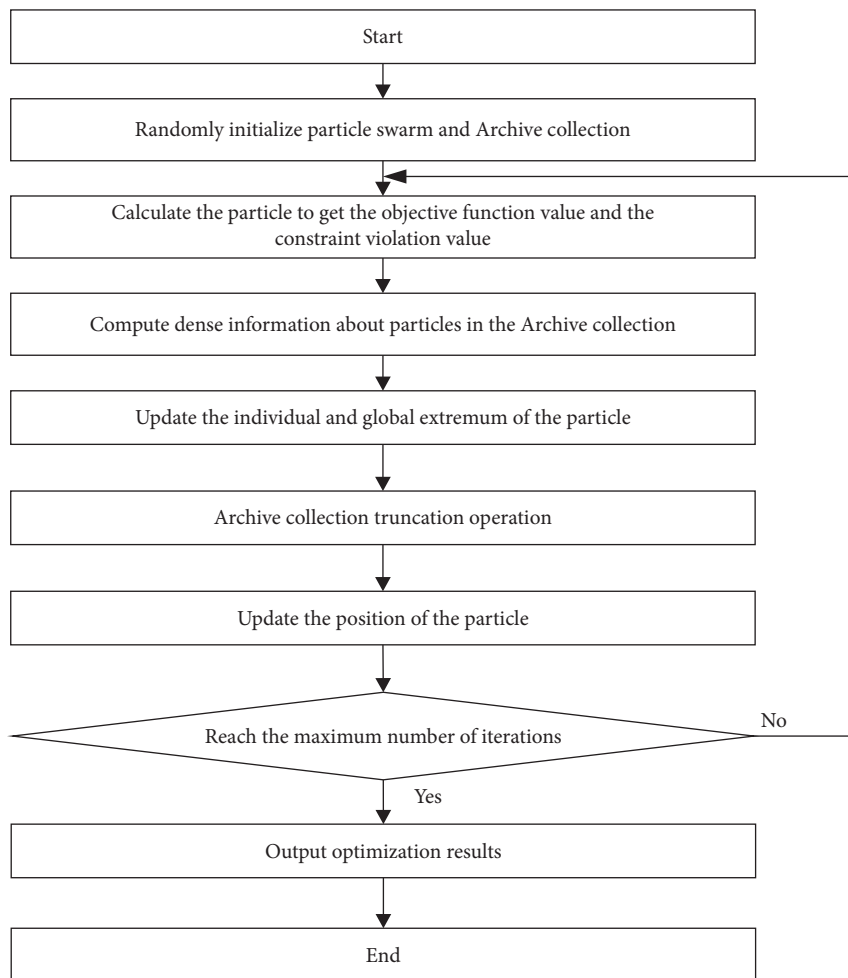


FIGURE 11: The flow chart of particle swarm optimization algorithm.

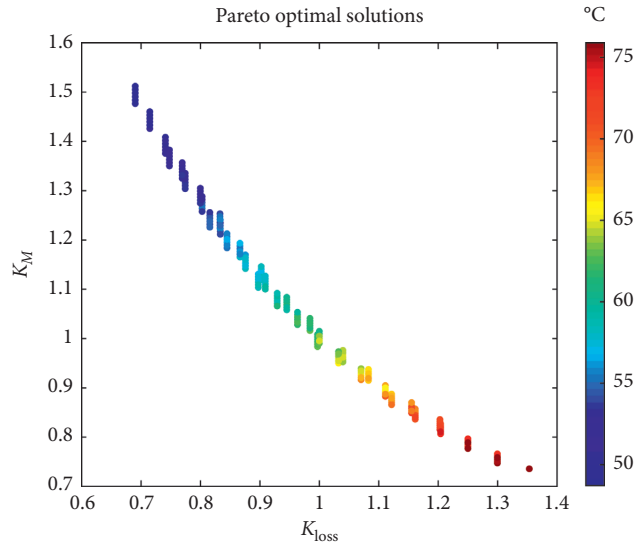


FIGURE 12: Pareto Frontier of particle swarm optimization.

TABLE 4: The pareto optimum solutions.

Case	Wcoil (mm)	Hcoil (mm)	Lins (mm)	Hduct (mm)	Loss (kW)	Weight (kg)
1	1.6	13.6	0.35	4.5	15.04	75.57
2	2.6	12.1	0.40	5.1	11.06	109.25
3	1.6	13.1	0.45	4.5	15.61	74.45
4	1.8	12.1	0.45	4.8	15.21	75.64
5	2.4	14.6	0.40	4.2	9.81	121.68
6	1.6	14.1	0.50	3.9	14.51	78.34
7	1.8	13.6	0.40	3.9	13.54	85.01
8	1.8	13.1	0.35	4.8	14.05	81.89
9	1.8	12.6	0.35	3.9	14.61	78.76
10	1.8	13.1	0.50	4.2	14.05	81.89
11	1.6	12.6	0.50	4.2	16.23	70.01
12	2.0	12.1	0.50	4.2	13.87	84.04
13	2.4	13.1	0.40	4.2	10.94	109.18
14	2.6	14.1	0.25	4.2	9.49	127.31
15	1.8	13.1	0.50	4.5	14.06	81.89
16	2.4	14.6	0.40	3.9	9.81	121.68
17	1.8	12.6	0.35	4.2	14.61	78.76
18	2.0	12.1	0.25	5.1	13.86	84.04
19	2.0	12.6	0.30	5.1	13.32	78.75
20	1.6	13.1	0.30	3.9	15.61	72.79

usage and loss of winding are conflicted and cannot be optimized simultaneously, therefore, in the actual design process of the iron reactor, it is necessary to select the

suitable structural parameter to realize the optimization of one objective with the other objectives which are not deteriorating.

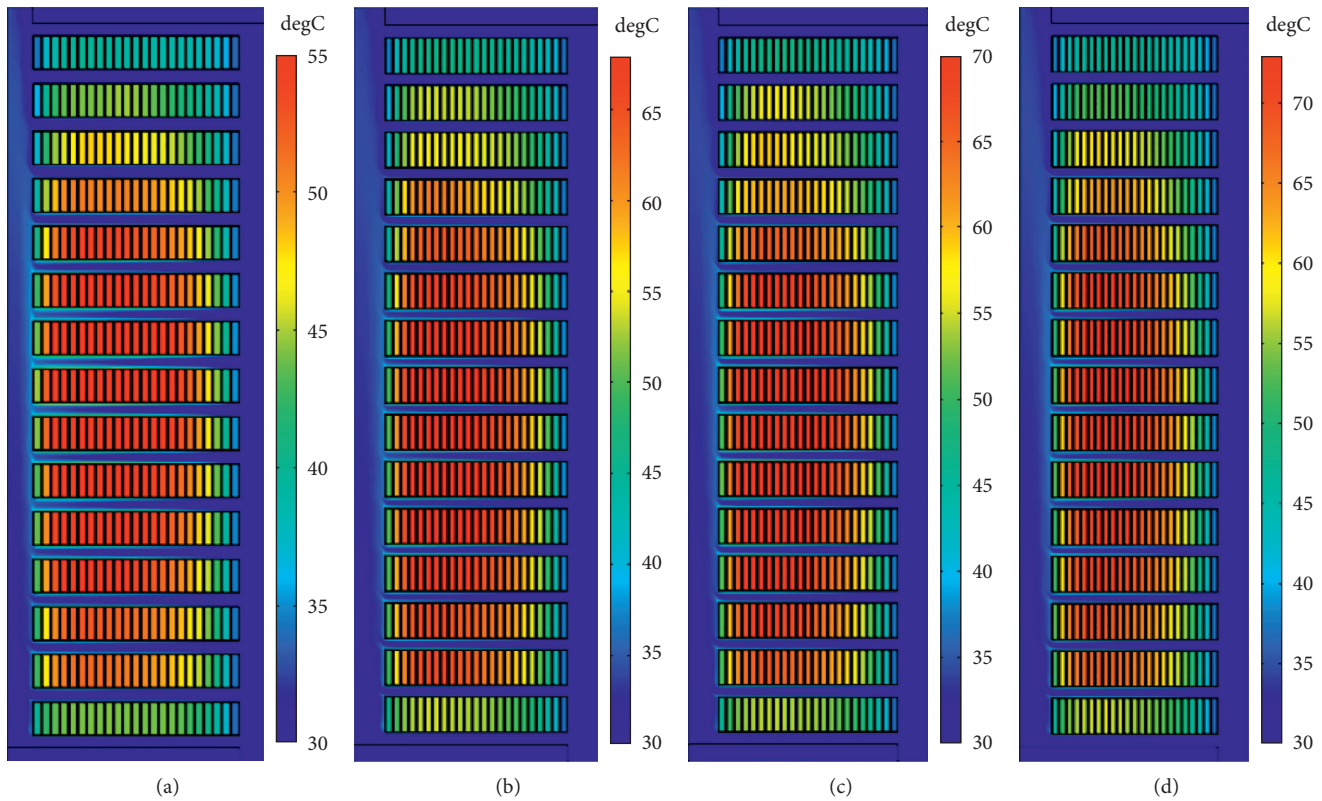


FIGURE 13: Simulation results: (a) Case 2; (b) Case 9; (c) Case 17; (d) Case 20.

## 6. Conclusions

According to the structure and parameters of oil-immersed iron core reactor, a multiobjective optimization method based on particle swarm optimization and thermal network model is proposed, and the following conclusions can be obtained:

- (1) The maximum temperature error of discs is less than 3% between the thermal network model and finite element method, and the position of the temperature is basically the same; the correctness of thermal network model has been verified
- (2) The maximum temperature region is mainly concentration of the middle of windings; the reasons are given by analyzing the fluid velocity distribution of oil, so this area is the main focus to monitoring temperature for the windings
- (3) The optimization design of windings based on particle swarm algorithm and thermal network model is proposed, the metal conductor usage is decreased by 23.05%, and the loss of the windings is reduced by 20.25% compared with the initial design parameters, so the optimization method has an important guiding significance for the design of oil-immersed iron core

## Data Availability

The data used to support the findings of this study are included in this paper and available without any restriction.

## Conflicts of Interest

The authors declare no conflicts of interest.

## Acknowledgments

This work was supported by the Natural Science Foundation of Hubei Province (no. 2020CFB376), Hubei Provincial Engineering Technology Research Center for Power Transmission Line Open Fund Project, China Three Gorges University (no. 2019KXL09), and National Natural Science Foundation of China (no. 51977121).

## References

- [1] H. Yuzhu, *Design Optimization and Multi Physical Field Analysis of Oil Immersed Series Iron-Core Reactor*, Harbin University of Science and Technology, Harbin, China, 2018.
- [2] Y. Fating, Y. Zhao, L. Junxiang, W. Yong, and H. Junjia, "Research on temperature field simulation of dry type Air core reactor," in *Proceedings of International Conference on Electrical Machines and Systems Sydney*, IEEE, Australia, August 2017.
- [3] X. Tianwei, C. Yundong, J. Wei, and G. Yuanzhi, "The analysis of temperature field in dry air core reactor," *High Voltage Engineering*, vol. 25, no. 4, pp. 86–88, 1999.
- [4] D. Qiu, *The Research on Thermal Field Calculation of Tightly Coupled Dry Type Air-Core Split Reactor*, Huazhong University of Science and Technology, Wuhan, China, 2011.
- [5] Y. Fating, T. Bo, D. Can, Q. Shihong, H. Li, and Y. Zhao, "Optimization design of a high-coupling split reactor in a

- parallel-type circuit breaker," *IEEE Access*, vol. 7, pp. 33473–33480, 2019.
- [6] C. Rong, S. W. Yang, and Q. Q. Yan, "Electromagnetic-fluid-temperature coupling calculation and analysis of dry type Air-core shunt reactor," *High Voltage Engineering*, vol. 43, no. 9, pp. 3021–3028, 2017.
  - [7] J. Zhipeng, W. Xishan, W. Yu, C. Ruizhen, C. Jifeng, and C. Tuteng, "Test and coupling calculation of temperature field for UHV dry type Air-core smoothing reactor," *Proceedings of the CSEE*, vol. 35, no. 20, pp. 5344–5350, 2015.
  - [8] A. J. Oliver, "Estimation of transformer winding temperatures and coolant flows using a general network method," *IEE Proceedings C Generation, Transmission and Distribution*, vol. 127, no. 6, pp. 395–405, 1980.
  - [9] C. Joris, V. Wim, and B. Martine, "Assessment of a hydraulic network model for zig zag cooled power transformer windings," *Applied Thermal Engineering*, vol. 80, pp. 220–228, 2015.
  - [10] A. Weinlader, W. Wu, S. Tenbohlen et al., "Prediction of the oil flow distribution in oil-immersed transformer windings by network modelling and computational fluid dynamics," *IET Electric Power Applications*, vol. 6, no. 2, pp. 82–90, 2012.
  - [11] Z. Xiang, W. Zhongdong, and L. Qiang, "Prediction of pressure drop and FlowDistribution in disc type transformer windings in an OD cooling mode," *IEEE Transactions on Power Delivery*, vol. 32, no. 4, pp. 1655–1664, 2017.
  - [12] Z. Jiahui and L. Xianguo, "Coolant flow distribution and pressure loss in ONAN transformer windings-Part II: optimization of design parameters," *IEEE Transactions on Power Delivery*, vol. 19, no. 1, pp. 194–199, 2004.
  - [13] Z. Xiang and W. Zhongdong, "Assessment of hydraulic network models in predicting reverse flows in OD cooled disc type transformer windings," *IEEE Access*, vol. 7, pp. 139249–139257, 2019.
  - [14] J. Smolka and A. J. Nowak, "Shape optimization of coils and cooling ducts in dry-type transformers using computational fluid dynamics and genetic algorithm," *IEEE Transactions on Magnetics*, vol. 47, no. 6, pp. 1726–1731, 2011.
  - [15] Y. Zhao, H. Junjia, P. Yuan, Y. Xiaogen, L. Chujun, and C. Sizhe, "Research on electromagnetic efficiency optimization in the design of air-core coils," *International Transactions on Electrical Energy Systems*, vol. 25, no. 5, pp. 789–798, 2015.
  - [16] Y. Fating, T. Bo, D. Can, Q. Shihong, Y. Zhao, and H. Li, "Optimization design of oil-immersed air core coupling reactor for a 160 kV mechanical direct current CircuitBreaker," *Energies*, vol. 12, no. 6, 2019.
  - [17] L. Zhigang, G. Yingsan, and W. Jianhua, "Optimum design of dry-type air-core series reactor based on modified adaptive genetic algorithm," *Proceedings of the CSEE*, vol. 23, no. 9, pp. 103–106, 2003.
  - [18] I. Mohamed, A. Abdelwanis, R. Abaza, and A. Elsehiemy, "Parameter estimation of electric power transformers using coyote optimization algorithm with experimental verification," *IEEE Access*, vol. 8, pp. 50036–50043, 2020.
  - [19] V. D. Shabnam and H. Hossein, "A diversified multi-objective simulated annealing and genetic algorithm for optimizing a three-phase HTS transformer," *IEEE Transactions on Applied Superconductivity*, vol. 26, no. 2, p. 5500210, 2016.
  - [20] M. S. Mohammed, R. A. Vural, and R. A. Vural, "NSGA-II+FEM based loss optimization of three-phase transformer," *IEEE Transactions on Industrial Electronics*, vol. 66, no. 9, pp. 7417–7425, 2019.
  - [21] B. Xia, G. G. Jeong, and C. S. Koh, "Cokriging assisted PSO algorithm and its application to optimal transposition design of power transformer windings for the reduction of circulating current loss," *IEEE Transactions on Magnetics*, vol. 52, no. 3, Article ID 7208604, 2016.
  - [22] Z. R. Radakovic and M. S. Sorgic, "Basics of detailed thermal-hydraulic model for thermal design of oil power transformers," *IEEE Transactions on Power Delivery*, vol. 19, no. 1, pp. 194–199, 2004.
  - [23] Y. Zhao and M. S. Sorgic, *Research on Thermal and Magnetic Optimization of Carbon-type Multi-enveloped Core Reactor*, Huazhong University of Science and Technology, Wuhan, China, 2014.
  - [24] C. Bin, L. Lin, Z. Zhibin, Z. Xiwei, and Z. Pengning, "Precision design method of inductance integrated high frequency transformer with large capacity," *Proceedings of the CSEE*, vol. 38, no. 5, pp. 1356–1368, 2015.
  - [25] Y. Fangting, Y. Zhao, W. Yong, L. Junxiang, and H. Junjia, "Thermal optimization for nature convection cooling performance of air core reactor with the rain cover," *IEEJ Transactions on Electrical and Electronic Engineering*, 2017.
  - [26] L. Fenxia, L. Ye, and Y. Yunchang, "Numerical and experimental research of internal temperature field of oil immersed core shunt reactor with ultrahigh voltage," *High Voltage Apparatus*, vol. 53, no. 1, pp. 163–168, 2017.
  - [27] Z. Chenfen, Z. Yanzhen, Z. Jianlong, and M. Xikui, "A diversity guided modified QPSO algorithm and its application in the optimization design of dry type Air-core reactors," *Proceedings of the CSEE*, vol. 32, no. 18, pp. 108–115, 2012.

## Research Article

# Multidimensional Intelligent Distribution Network Load Analysis and Forecasting Management System Based on Multidata Fusion Technology

Weijie Cheng <sup>1</sup>, Renli Cheng <sup>1</sup>, Jinsheng Liu <sup>1</sup>, Weizhe Ma <sup>1</sup>, Jie Li <sup>2</sup>,  
Weiling Guan <sup>2</sup>, Daolu Zhang <sup>2</sup> and Tao Yu <sup>2</sup>

<sup>1</sup>Shenzhen Power Supply Bureau Co., Ltd., Shenzhen 518000, Guangdong, China

<sup>2</sup>School of Electric Power, South China University of Technology, Guangzhou 510641, Guangdong, China

Correspondence should be addressed to Renli Cheng; 1025696549@qq.com and Tao Yu; taoyu1@scut.edu.cn

Received 17 November 2020; Revised 8 December 2020; Accepted 18 December 2020; Published 13 February 2021

Academic Editor: Wei Yao

Copyright © 2021 Weijie Cheng et al. This is an open access article distributed under the Creative Commons Attribution License, which permits unrestricted use, distribution, and reproduction in any medium, provided the original work is properly cited.

In order to improve the work efficiency of load characteristic analysis and realize lean management, scientific prediction, and reasonable planning of the distribution networks, this paper develops a multidimensional intelligent distribution network load analysis and prediction management system based on the fusion of multidimensional data for the application of multidimensional big data in the smart distribution network. First, the framework of the software system is designed, and the functional modules for multidimensional load characteristic analysis are designed. Then, the method of multidimensional user load characterization is introduced; furthermore, the application functions and the design process of some important function modules of the software system are introduced. Finally, an application example of the multidimensional user load characterization system is presented. Overall, the developed system has the features of interoperability of data links between functional modules, information support between different functions, and modular design concept, which can meet the daily application requirements of power grid enterprises and can respond quickly to the issued calculation requirements.

## 1. Introduction

With the continuous socioeconomic development, the maximum load of the power grid in China's Guangdong region continues to grow, the peak-to-valley differential gradually increases, the contradiction between supply and demand of the power grid at different periods is very prominent, and the difficulty of peak adjustment continues to increase, which poses a potential hazard to the stability of the power system [1], but also brings obstacles to the planning and construction of the power grid, electricity market transactions, power load forecasting, and power market management and strategy analysis [2–7]. At the same time, under the background of industrial transformation and upgrading and gradual adjustment of economic structure, backward enterprises with high energy consumption and strong pollution in Guangdong Province have

been eliminated in large numbers, which has a significant impact on the load characteristics of the power grid. Therefore, a comprehensive study and analysis on the load characteristics of Guangdong Province is of great significance to improve the planning and construction of the overall power grid and ensure its stable operation.

In recent years, the analysis and research of load characteristics have been paid more and more attention, and researchers from local power grid companies and power industry have conducted research on load characteristics from different angles [8]. In literature [9], the Southern Power Grid Company of Yunnan adopts the sampling analysis method to study the load characteristics in different industries in Yunnan Province and makes an outlook on the development trend of load. In [10], State Grid Hunan Power Grid Company used load data to complete the calculation of several load indicators including annual maximum load and



analyzed the different load rates and their related influencing factors in different seasons based on their power load structure. Literature [11] collected real distribution network load data of Tangshan central city, focused on the analysis of residential district load, proposed indicators such as occupancy rate and demand factor to supplement the traditional load indicator system, and completed the construction of different types of district load characteristic models. The work in [12] summarizes the load characteristics indicators in the Zhengzhou Power Grid, improves the grey correlation analysis by entropy weighting, and quantifies the factors that cause changes in load characteristics to identify the main influencing factors.

On one hand, the abovementioned studies generally adopt the methods of case elimination and mean value substitution to carry out simple preprocessing on load data. These implementations may cause a waste of load data information and resources, weaken the objectivity of data, and even bring wrong results. On the other hand, the traditional load characteristic analysis often focuses on the total regional load, but lacks the analysis and comparison of the load of each industry according to the industry classification standard. In addition, in the face of the diversity of load changes and the advancement of load characteristic analysis methods, there is no comprehensive load characteristic analysis system that can keep up with the times and facilitate the development of the power grid to obtain user information and carry out reasonable planning.

To support the construction of the Greater Bay Area Smart City Cluster, China Southern Power Grid has not only accelerated the planning and construction of the Greater Bay Area Smart Grid but also adjusted its strategy and proposed “Digital China Southern Power Grid” to transform and upgrade to a comprehensive energy service provider [13]. Nowadays, the measurement system of electric power enterprises has accumulated a huge amount of fine-grained data, such as historical load data, GIS data, customer information data, and public sector service data. These data have tremendous direct and indirect value. The application of big data analysis technology and visualization and interaction technology can conduct multidimensional research and analysis of load characteristics, establish a standardized and reasonable index analysis system according to different time scales, and grasp different load change laws, while load characteristics analysis can guide the load prediction work of the distribution network. Scientific and accurate load prediction is conducive to the realization of scientific planning and management of the distribution network, to ensure the stable operation of the power grid, and to improve the economic efficiency of power grid enterprises [14].

In recent years, researchers from local power grid companies and the power industry have carried out corresponding studies from different perspectives. In [13], the airplane theory of big data in smart power distribution network application is proposed, the key technology of massive data application is sorted out, the application method of big data in different scenarios is described, and the direction of transmission and interaction of data and

energy flow is clarified through the application roadmap. Researchers in [15] studied the unified historical load data samples based on the typical daily load curves on weekdays and weekends, statistically analyzed the load characteristic indicators such as daily load rate and daily peak-to-valley differential rate, and predicted the medium- and long-term load characteristic indicators of Guizhou Power Grid to provide reference for power grid planning. In [16], the spring daily load data of Harbin are taken as a sample, and the quantitative relationship between load characteristics and meteorological factors is established by multiple regressions based on correlation analysis via the SPSS (i.e., Statistical Product and Service Solutions) software. Based on the historical load characteristic curves and meteorological data of Changde City, a statistical analysis of the main influencing factors is carried out in [17] to determine the degree of influence of specific scenarios such as small hydropower grid connection and electricity price fluctuation on regional load and the influence period and to provide revised guidance for regional load forecast based on the results. The work in [18] decomposes the residential load into basic load and seasonal load at the same time for two-level analysis, analyzes the potential size of residential load regulation based on adaptive fuzzy *c*-means algorithm clustering, and realizes the differential analysis of users' electricity consumption characteristics through a new classification method to provide data support for peak fault management and tariff formulation.

In general, although a lot of research work has been carried out on load characteristics, as well as load prediction at home and abroad, most of the current research studies separate the two separately and do not correlate them well. Most of the work uses the approaches such as case elimination or mean substitution to simply preprocess load data, which causes a waste of information and resources on load data, weakens the objectivity of the data, and may even bring wrong results. In terms of the object of analysis, most of the work is focused on the system level, lacking detailed study by industry, and the load forecast does not carry out an in-depth study on the level of substation feeder in the planning direction. In terms of engineering applications, the load management system developed at present generally has the problems of insufficient data analysis and processing ability, poor human-computer interaction performance, and low visualization degree. Therefore, in the actual application of engineering, there is a set of load characteristic comprehensive analysis system that can keep pace with the times and facilitate the grid to obtain user information and make reasonable planning.

To address the abovementioned problems, the research work of this paper is implemented based on the actual operational data in the Guangdong power grid metering system, using linear interpolation to fill in and recover the missing data in the massive load characteristic data. On this basis, a flexible and extensible multidimensional load characteristic analysis system is developed using Java development language. The system takes microservices and microapplications as the core architecture, realizes the analysis and research of load characteristics of various

industries in different time scales, and provides reference for power grid load prediction and planning and construction through comparison, statistics, and summary. Firstly, this paper introduces the overall architecture and data structure of the software system, taking into account the actual requirements of the business; then, it introduces and develops the functional implementation and logical connection of each submodule of the system; and finally, it gives an application demonstration of the software system, taking into account the actual calculation examples.

The rest of this paper is organized as follows. In Section 2, the development and design of multidimensional load characterization analysis modules are introduced. In Section 3, the multidimensional user load characteristic analysis methods are elaborated. The design process of application functions for this software system is expounded in Section 4. Furthermore, the system visualization interface development and design are demonstrated in Section 5. Section 6 conducts an application case study based on the developed software system. Finally, Section 7 concludes the paper.

## 2. Development and Design of Multidimensional Load Characterization Analysis Modules

In order to realize the load characteristic analysis based on the industry division, extract the load characteristic indexes of each user, summarize the change law, and put forward the specific suggestions for the subsequent load prediction and power grid planning, this paper develops a set of multidimensional load characteristic analysis system based on the Java language, using microservice and microapplication architecture. The system should meet the following technical requirements: flexible expansion of all functions; data sharing among various functional modules; data collection interface that supports various collection protocols; storage requirements for various data types and good security protection; rapid response to issued demands; and the underlying algorithm that supports the development of multiple languages at the same time.

This section introduces the development methodology of the multidimensional load characterization system, including microservice architecture design, functional modular development, data acquisition interface design, data storage and security, efficient data dynamic refresh technology, and algorithm integration design.

*2.1. Microservice Architecture Design.* Traditional monolithic application architectures put all functions into a single WAR/JAR package with few external dependencies to achieve centralized management and reduce development difficulty. But again, this will lead to various drawbacks such as overly centralized functionality, code and data centering; high complexity; formation of technical debt accumulation; limited scalability; and the need to refactor the project for any maintenance.

Therefore, this paper chooses to use the microservice architecture [19] as the core of software development, as shown in Figure 1. Each service is highly autonomous, and

each service focuses only on a specific business function, which makes the business clear and easy to develop and maintain [20]. At the same time, multiple services can run without waiting for the completion of other services, which achieves a smooth scalability effect and greatly reduces the start-up work time of individual microservices. In addition, when expanding a single functional module, unlike traditional architectures that require refactoring the entire project, the microservice architecture only requires the deployment of specific services that need to be expanded and modified.

The introduction of microservice architecture enables flexible expansion of the system, reduces the development cycle of each functional module, and provides great convenience for real-time updates of system functions.

*2.2. Modular Development of Functions.* Each function in the system is developed modularly, as shown in Figure 2. In particular, the front-end HTML (Vue or React) is requested through the Nginx gateway as an ajax request to the Restful API service.

The API gateway is built using Zuul to provide cross-module HTML page access and cross-domain data access, and the introduction of Nginx facilitates horizontal load balancing.

Each functional module is injected into the registry in the form of a microservice, and the data between the modules are exchanged through the API gateway, which facilitates load balancing and ensures the long-term stability of the entire system. Different functional modules use corresponding interfaces for data transmission and data sharing.

*2.3. Data Acquisition Interface Design.* As for the data acquisition interface, its design principle is shown in Figure 3. Specifically, by building a data acquisition management platform, it manages and monitors the operation state of various types of interfaces and then further implements the start/stop management of interfaces and configuration management of measurement points, so as to meet the functions of supporting various data types. The data acquisition platform supports structured data sources supported by the business system database and semistructured data sources made of electronic reports, and it also supports various acquisition protocols such as custom TCP protocol and IEC101/102/103/104 statutes. In addition, by building a data warehouse, the system integrates multisource data, uses data mining to form corresponding reports, and provides real-time query, CIM analysis, and other functions.

*2.4. Data Storage and Security Module Development.* In order to ensure to meet the requirements of multitype data storage, with large data volume and high fault-tolerance performance, the system platform has built a variety of databases to support a variety of data types, including columnar library, NoSql library, and memory library. At the same time, the platform supports database deployment using convenient

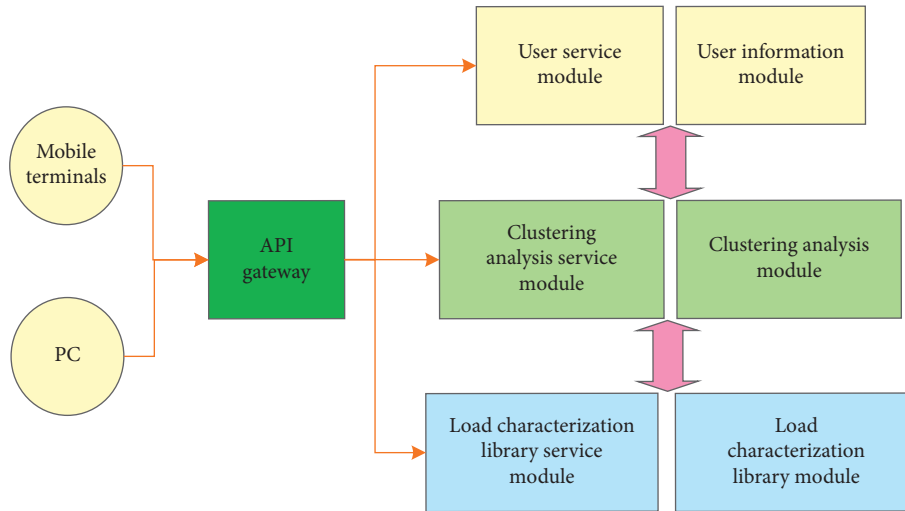


FIGURE 1: Microservice architecture design for the software system.

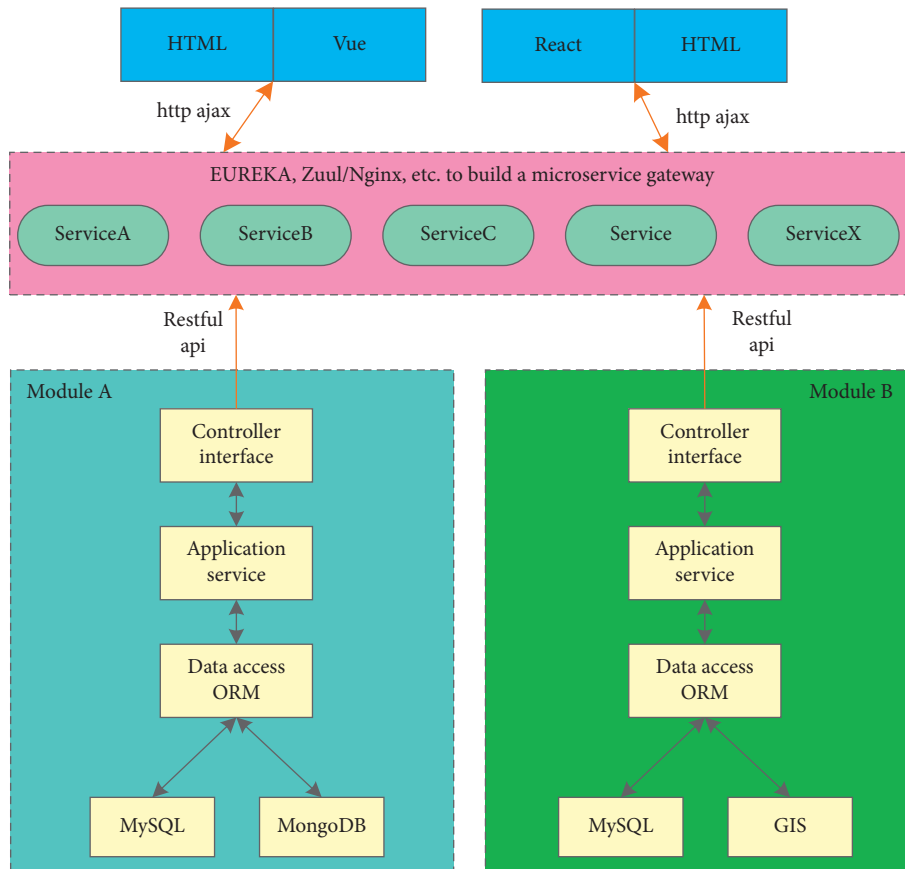


FIGURE 2: Modular development of functions for the software system.

and reliable extended multinode replica set to meet petabyte-level massive data storage, in which the master node function is set to complete the read and write of all nodes, while the rest of the replica nodes are responsible for completing the data synchronization and backup work, as shown in Figure 4. The replica nodes in the replica set use the heartbeat mechanism to monitor the state of the master node in real time and determine whether it has failed. When a

failure is detected, a master node election mechanism will be initiated within the cluster to elect a new master node to achieve automatic switching and complete the implementation of high fault tolerance.

In addition, the security part shown in Figure 4 mainly consists of two aspects: data and system. For data security, the system has established a long-term effective data backup and security management mechanism, realizing real-time

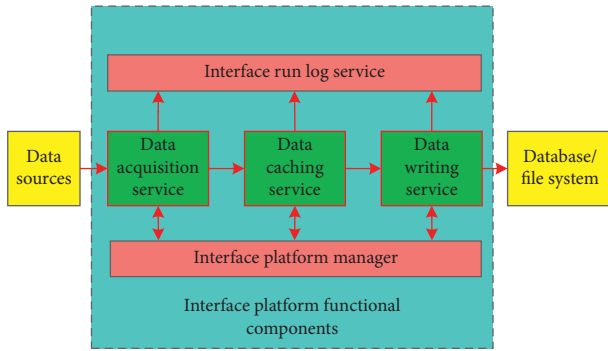


FIGURE 3: Demonstration of the design principles of the data acquisition interface.

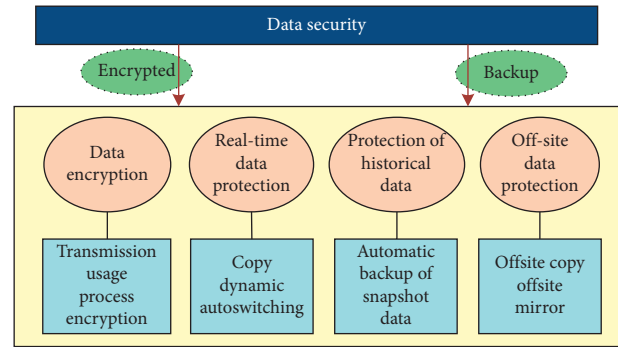


FIGURE 5: Schematic design of the data security protection module.

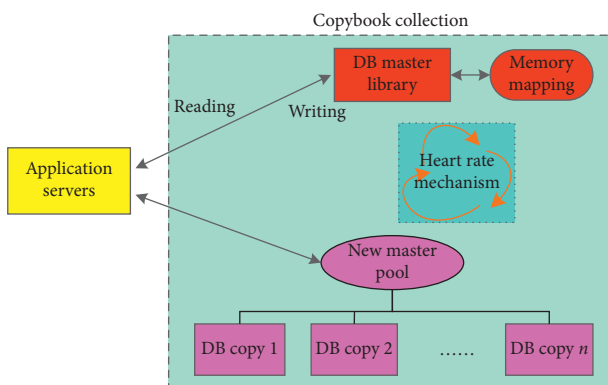


FIGURE 4: Schematic diagram of the copy set deployment model.

data protection, historical data protection, and off-site data protection, as shown in Figure 5.

In Figure 5, in terms of system security, the system ensures the stable operation of applications providing external services based on the redundant hot standby feature and adopts security protection technology to constitute Web protection against XSS cross-site script attacks and SQL script injection and other intrusions. In addition, it further strengthens protection by providing a set of authentication and authorization system for the industrial Internet platform.

2.5. Design of the Efficient Dynamic Data Refresh Technique.

In order to improve the speed of data transmission over the network when the configuration page responds to the data loading, an efficient data dynamic refresh technique is designed to improve the data loading performance, as shown in Figure 6. Specifically, we have optimized the system in the following three aspects:

- (i) Microsoft SignalR library is used based on the Web Socket duplex communication protocol to push the change data from the server to the client and improve the real-time data corresponding ability
- (ii) The configuration page supports multiple polling intervals to avoid requesting low-frequency changing data every time, such as 15-second

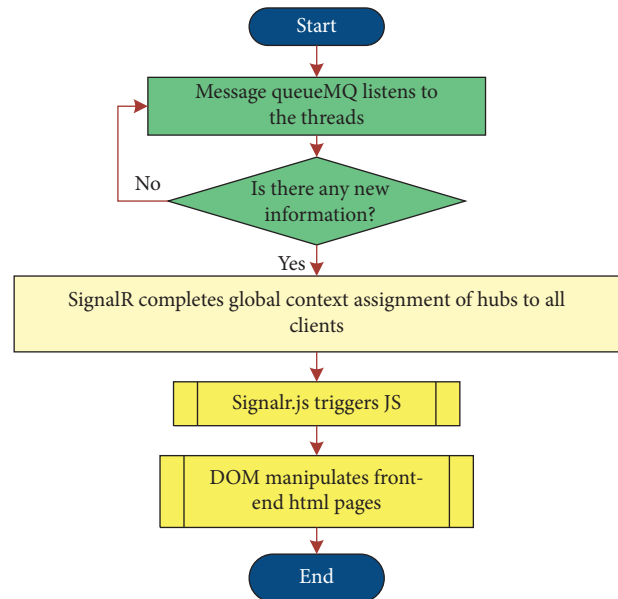


FIGURE 6: Flowchart design for dynamic data refresh.

estimates for one-hour voltage, current, and power curves

- (iii) The server side establishes correspondence with the page, and the server side compares and contrasts the real-time data of the page and only returns incremental difference data when polling the requested data

2.6. Design of Algorithm Integration. At the same time, in order to support multilingual algorithms including Java/Python/C#, the system establishes an algorithm integration platform, as shown in Figure 7. The platform architecture provides a standard unified invocation interface, http request and application/json data interaction, supports automatic identification and dynamic loading of algorithm libraries, and is integrated with microservice architecture, using Zuul gateway proxy interception to achieve algorithm access rights control. In the specific implementation of the underlying algorithm API, the system is developed in Python, taking into account the data structure specification, code simplicity, and intuition.

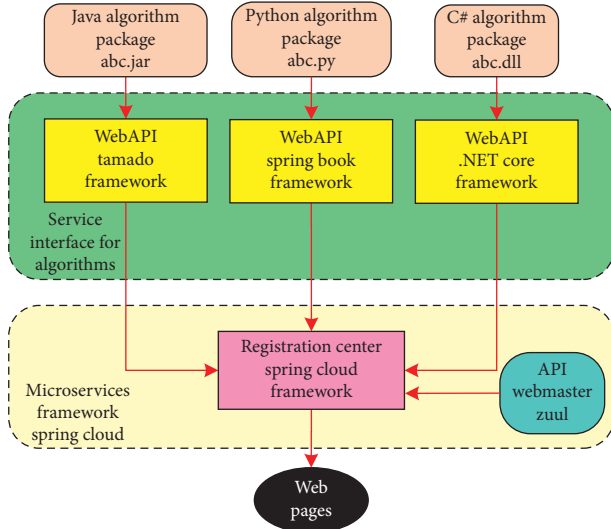


FIGURE 7: Integrated architecture design of algorithms.

### 3. Multidimensional User Load Characteristic Analysis Methods

In recent years, the load growth, industrial transformation, and economic structure adjustment have affected the load characteristics of power grid in many aspects. In the face of the complex situation of the load of today's power grid, to expand the load characteristics research ideas, fully exploiting the load characteristics from multiple angles can give more accurate and comprehensive guidance on employment expansion and installation, load prediction, and so on. With the help of the abovementioned simulation system, this paper establishes a single user's load characteristic database and then launches the research on the load characteristics of users in various industries for electricity consumption mode. The process is shown in Figure 8, with the following specific steps:

- (i) call the data preprocessing API to analyze the data obtained from the grid metering system, screen out abnormal data, and process them accordingly
- (ii) call the load characteristic index calculation API to extract the corresponding characteristic indexes according to the typical load curve of users in various industries
- (iii) call the daily load curve extraction method API, select the method according to the demand and application scenario, and extract the typical curve of a single user
- (iv) call the clustering algorithm API to cluster multiple users in an industry and analyze the typical power consumption patterns of users in the industry

**3.1. Load Characteristic Data Preprocessing.** There are various methods of data preprocessing, and considering that simple processing methods such as case exclusion and mean substitution can waste load data information and resources

and even lead to wrong conclusions, the data preprocessing API of this system adopts the linear interpolation method. The method uses a data recovery algorithm with strong continuity and autocorrelation before and after each time point on the same day, which assumes that a small number of consecutive load data points show a linear pattern of variation. The average of the complete values before and after the missing data is calculated, and the missing load is filled in. Depending on the specific location where the missing data occurs, it can be divided into two ways: first and last missing and intermediate missing. Depending on the method of missing data, there are some differences in the repair methods used. For the former, the complete data closest to the missing value will be used as the result of the repair, calculated as follows:

$$\begin{aligned} a_1 &= a_2 = \dots = a_s, \\ a_N &= a_{N-1} = \dots = a_e, \end{aligned} \quad (1)$$

where  $a_s$  is the nearest nonmissing value to the first place in the daily load curve,  $a_e$  is the nearest nonmissing value to the last place, and  $N$  is the data dimension of the single load data.

As for the latter, if it is a single missing value, then we take the average of the complete values before and after as its repair value; if it is missing at multiple consecutive points, then we find a linear expression for the nonmissing data points before and after and find out all the missing data points according to the proportion, and the formula is as follows:

$$a_x = a_m + \frac{a_n - a_m}{n - m} (x - m), \quad (2)$$

where  $a_x$  is the missing data sought and  $a_m$  and  $a_n$  are the nearest complete values before and after, respectively.

In general, the data preprocessing API of this system establishes the data preprocessing method library. The logical block diagram of the load data preprocessing method study in this method library is shown in Figure 9.

In Figure 9, the error evaluation method for data recovery uses the absolute magnitude percentage error (AMPE). In the case of multipoint loss, the mean absolute percentage error is used, which is defined as follows:

$$\text{AMPE} = \frac{1}{n} \sum_{i=1}^n \left| \frac{P'_i - P_i}{P_i} \right| \times 100\%, \quad (3)$$

where  $P'$  is the algorithm fill value,  $P$  is the true data value, and  $n$  is the number of missing points. The overall recovery effect of the algorithm can be obtained by comparing the median of the AMPE indicators of various data preprocessing methods under multiple data loss scenarios. Furthermore, the stability of the algorithm can be obtained by comparing the difference between the maximum and minimum values or the difference between the upper and lower quartiles.

**3.2. Establishing Multidimensional Load Features.** In general, conventional load characteristic indicators [21, 22] are selected and calculated according to three time spans: daily,

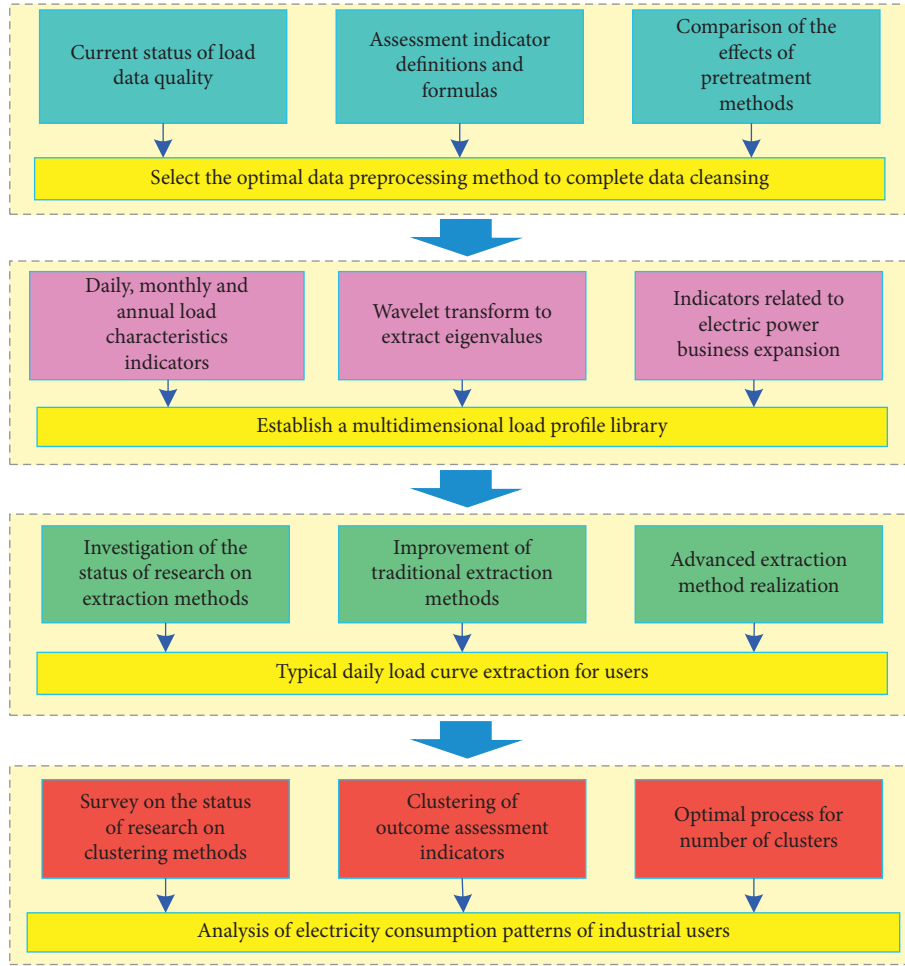


FIGURE 8: Multidimensional load characterization analysis process design.

monthly, and yearly, to describe the temporal characteristics of the load. However, the aforementioned time domain analysis results do not show the fluctuating changes of the actual load well. Therefore, the system introduces the wavelet analysis method to carry out the analysis and research of the load frequency domain. In addition, the three indicators of saturation load density, practical coefficient, and stage coefficient reflect the release law of the load after installation, which is of great significance to guide the work of industry expansion installation. The abovementioned load characteristic indexes are selected and calculated to establish the multidimensional load characteristic library, and the extraction method of each characteristic index is as follows.

**3.2.1. Extraction Method of the Daily Load Characteristic Index.** The daily load characteristic index can be used to calculate the daily load rate  $\gamma_{d,av}$ , minimum daily load rate  $\gamma_{d,min}$ , and peak-to-valley differential rate  $\epsilon_d$  for different reporting periods (year-round, summer, and winter). The formula is as follows:

$$\begin{aligned} \gamma_{d,av} &= \frac{P_{av}}{P_{max}} \times 100\%, \\ \gamma_{d,min} &= \frac{P_{min}}{P_{max}} \times 100\%, \\ \epsilon_d &= \frac{\epsilon_{max}}{P_{max}} \times 100\%, \end{aligned} \tag{4}$$

where  $P_{av}$ ,  $P_{max}$ , and  $P_{min}$  are the daily average load, daily maximum load, and daily minimum load during the reporting period, respectively, and the maximum value of daily peak-to-valley difference during the reporting period.

**3.2.2. Method of Extracting the Monthly Load Characteristic Index.** For the monthly load characteristic index, for different reporting periods (different months), the monthly average daily load rate  $\gamma_{m,av}$ , the monthly minimum load rate  $\gamma_{m,min}$ , and the monthly average daily peak-to-valley differential rate  $\epsilon_{m,av}$  can be calculated for different reporting periods. The formula is as follows:



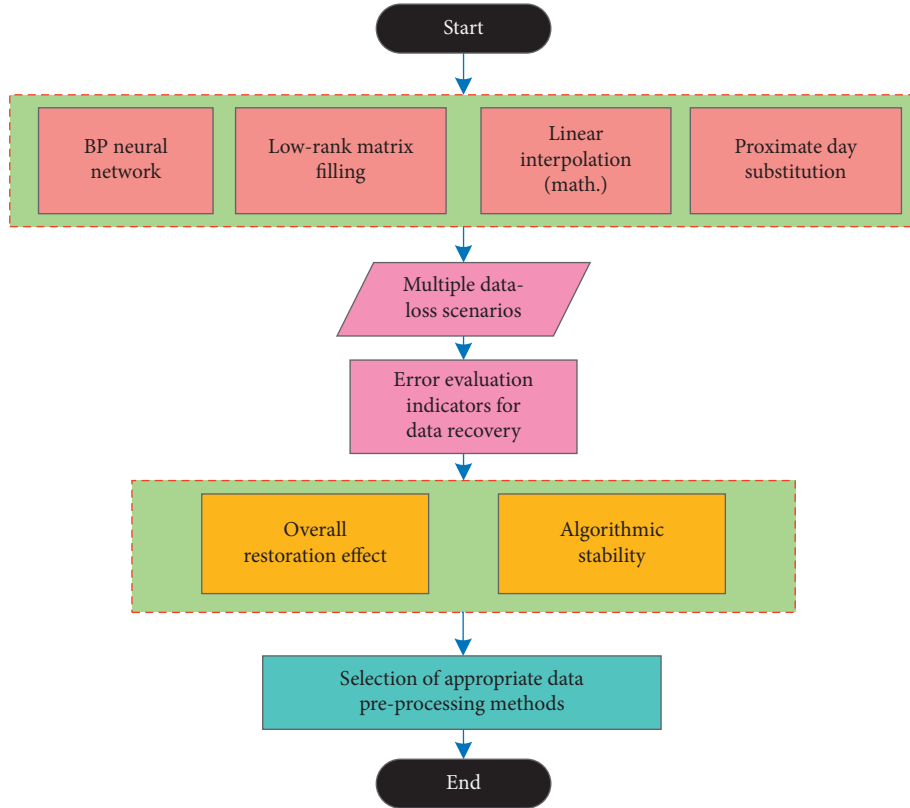


FIGURE 9: Logical block diagram of load data preprocessing method investigation.

$$\begin{aligned} \gamma_{m,av} &= \frac{\sum_{i=1}^{N_{\text{month}}} \gamma_{m,i}}{N_{\text{month}}}, \\ \gamma_{m,\min} &= \min\{\gamma_{m,1}, \gamma_{m,2}, \dots, \gamma_{m,N_{\text{month}}}\}, \\ \varepsilon_{m,av} &= \frac{\sum_{i=1}^{N_{\text{month}}} \varepsilon_{m,i}}{N_{\text{month}}}, \end{aligned} \quad (5)$$

where  $\gamma_{m,i}$  is the daily loading rate on day  $i$  of the month,  $\varepsilon_{m,i}$  is the daily peak-to-valley differential rate on day  $i$  of the month, and  $N_{\text{month}}$  is the number of days in the month.

**3.2.3. Method of Extracting the Annual Load Characteristics Indicator.** For the annual load characteristic index, the annual maximum load curve can be plotted and the annual minimum load rate, annual maximum peak-to-valley ratio, seasonal imbalance coefficient, and annual average daily peak-to-valley ratio can be calculated. The annual maximum load curve is plotted by connecting the maximum load values in each month by a polyline. The minimum annual load  $\gamma_{y-\min}$ , maximum annual peak-to-valley differential  $\varepsilon_{y-\max}$ , quarterly imbalance coefficient  $\rho$ , and average annual daily peak-to-valley differential  $\varepsilon_{y-\text{av}}$  are calculated as follows:

$$\begin{aligned} \gamma_{y-\min} &= \min\{\gamma_{y-1}, \gamma_{y-2}, \dots, \gamma_{y-i}, \dots, \gamma_{y-N_{\text{year}}}\}, \\ \varepsilon_{y-\max} &= \max\{\varepsilon_{y-1}, \varepsilon_{y-2}, \dots, \varepsilon_{y-i}, \dots, \varepsilon_{y-N_{\text{year}}}\}, \\ \rho &= \frac{P_{m,av}}{P_{m,\max}} \times 100\%, \\ \varepsilon_{y-\text{av}} &= \frac{\sum_{i=1}^{N_{\text{year}}} \varepsilon_{y-i}}{N_{\text{year}}}, \end{aligned} \quad (6)$$

where,  $\gamma_{y-i}$  is the daily load rate on day  $i$  of the year,  $\varepsilon_{y-i}$  is the daily peak-to-valley differential rate on day  $i$  of the year,  $N_{\text{year}}$  is the number of days in the year,  $P_{m,av}$  is the average value of the maximum load for each month, and  $P_{m,\max}$  is the maximum value of the maximum load for each month.

**3.2.4. Frequency Domain Load Characteristic Index Extraction Method.** As a classical algorithm in frequency domain analysis, the wavelet transform is widely used in many research fields such as power system analysis [23]. By accurately locating the time, wavelet transform analysis can truly reflect the detailed information of power loads in the

frequency domain dimension. Therefore, it plays an outstanding role in improving the overall accuracy of load clustering and user identification, and better representing the load fluctuation. The db3 wavelet is selected to carry out a three-layer wavelet decomposition of the preprocessed user load data, with the wavelet energy, root mean square value, absolute mode mean, and standard deviation of each layer coefficient, and the calculation formula of these steady-state indicators is as follows:

$$\begin{aligned}
 Ea_i &= \sum_{j=1}^{N_1} |a_{i,j}|^2, \\
 Ed_i &= \sum_{j=1}^{N_2} |d_{i,j}|^2, \\
 rms\_a_i &= \sqrt{\frac{1}{N_1} \sum_{j=1}^{N_1} |a_{i,j}|^2}, \\
 rms\_d_i &= \sqrt{\frac{1}{N_2} \sum_{j=1}^{N_2} |d_{i,j}|^2}, \\
 ua_i &= \frac{1}{N_1} \sum_{j=1}^{N_1} |a_{i,j}|, \\
 ud_i &= \frac{1}{N_2} \sum_{j=1}^{N_2} |d_{i,j}|, \\
 std\_a_i &= \sqrt{\frac{1}{N_1} \sum_{j=1}^{N_1} (a_{i,j} - \text{mean\_}a_i)^2}, \\
 std\_d_i &= \sqrt{\frac{1}{N_2} \sum_{j=1}^{N_2} (d_{i,j} - \text{mean\_}d_i)^2},
 \end{aligned} \tag{7}$$

where  $i = 1, 2, 3$ ;  $a_{i,j}$  is the  $j$ th modal value of the layer  $i$  approximation coefficient;  $d_{i,j}$  is the  $j$ th modal value of the layer  $i$  detail coefficient; and  $N_1$  and  $N_2$  are the data lengths of the approximation coefficient and detail coefficient, respectively;  $Ea_i$  represents the energy value of the layer  $i$  approximation coefficient;  $Ed_i$  represents the energy value of the layer  $i$  detail coefficient;  $rms\_a_i$  represents the RMS value of the layer  $i$  approximation coefficient;  $rms\_d_i$  denotes the root mean square value of the layer  $i$  coefficient of detail;  $ua_i$  denotes the absolute modal mean of the layer  $i$  coefficient of approximation;  $ud_i$  denotes the absolute modal mean of the layer  $i$  coefficient of detail;  $std\_a_i$  denotes the standard deviation of the layer  $i$  coefficient of approximation;  $std\_d_i$  denotes the standard deviation of the layer  $i$  coefficient of detail;  $\text{mean\_}a_i$  denotes the mean of the layer  $i$  coefficient of approximation;  $\text{mean\_}d_i$  denotes the mean

of the layer  $i$  coefficient of approximation. The average of the layer detail coefficients.

**3.2.5. Saturation Load Density, Practical Coefficients, and Phase Coefficient Extraction Methods.** In order to show the real situation of electricity consumption by users, the ratio between the size of the user's load and the size of the installed capacity is defined as the utility factor, there are a total of  $N$  electricity users, then  $P_{ij\max}$  is the maximum annual load of user  $i$  in year  $j$ ,  $P_{i\max}$  is the maximum annual load of user  $i$  in the final year, and  $S_i$  is the floor area of user  $i$ , and then, the formula for each indicator is as follows:

$$\begin{aligned}
 \rho_i &= \frac{P_{i\max}}{S_i}, \\
 \eta_i &= \frac{P_{ij\max}}{P_{ibz}}, \\
 \gamma_{ij} &= \frac{\eta_{ij}}{\eta_i},
 \end{aligned} \tag{8}$$

where  $\rho_i$  denotes the saturation load density of the user  $i$ ;  $\eta_i$  denotes the utility factor of the user  $i$ ;  $P_{ij\max}$  denotes the annual maximum load of the user  $i$  in the final year  $j$ ;  $P_{ibz}$  denotes the reported capacity of the user  $i$ ; and  $\gamma_{ij}$  is the phase factor of the user  $i$  in the  $j$ th year.

**3.3. Typical Daily Load Curve Extraction Method.** There is no uniform regulation on the typical daily load curve extraction method, and the traditional methods mainly include the daily load rate selection method, daily maximum load selection method, and fixed day selection method [24]. According to the actual situation of power grid load data, the actual demand of power grid planning work, and the insufficiency of the abovementioned methods in terms of scientificity, the fixed daily selection method with certain limitations is removed; the daily load rate selection method is improved; the typical daily load curve is selected based on the inclusion of more daily load characteristic indexes; the improvement algorithm is called daily load characteristic index selection method; and the maximum daily load selection method is retained. In addition to the improvement of the traditional method, this paper proposes a symbolic aggregation approximation method based on time-series dimensionality reduction [25] and a typical daily load curve extraction method based on nonparametric kernel density estimation [26] in combination with cutting-edge data mining techniques to extract the typical load curves more scientifically and reasonably.

Thus, it can be seen that the typical daily load curve extraction methods are various. Based on this, the daily load extraction API of this system establishes a library of typical daily load curve extraction methods, which is described as follows.

Through investigation and summarization on the traditional typical daily load curve extraction methods, we find that there is no unified regulation on the extraction method

of typical daily load curve, and the traditional methods mainly include the daily load rate selection method, daily maximum load selection method, and fixed day selection method. Based on the actual situation of power grid load data, the actual demand of power grid planning, and the insufficiency of the abovementioned methods in terms of scientificity, the fixed day selection method is used, with certain limitations eliminated.

To this end, the daily load rate selection method is improved in the developed system. Concretely speaking, more daily load characteristics indexes are included as the basis for selecting the typical daily load curves; the improvement algorithm is developed, and it is called daily load characteristics index selection method; and the daily maximum load selection method is retained.

In addition to the improvement of the traditional methods, the software system also adopts data mining techniques to form a symbolic aggregation approximation method based on time-series dimensionality reduction and a typical daily load curve extraction method based on nonparametric kernel density estimation, so as to extract the typical daily load curve more scientifically and rationally.

Finally, the system evaluates the rationality and characterization of the typical daily load curve selection by reasonably selected evaluation indexes. Overall, the logical block diagram for the study of the typical daily load curve extraction method in this system is shown in Figure 10.

Based on Figure 10, in order to further verify the effectiveness of the abovementioned single-user daily load curve extraction algorithm, we adopt a correlation calculation method to quantify the extraction effect of the software system and further choose different numbers of sample sets of load datasets for a typical daily load curve extraction experiment. The data interval of each load curve in the sample set is 15 minutes, and the day is divided into 96 time sections for analysis. The basic idea of the abovementioned correlation calculation method is to determine the degree of correlation based on the degree of similarity between curves. In practical terms, the method is an analytical comparison of the geometry between several curves, i.e., it is believed that the closer the geometry is, the closer the development and change trend is and the greater the degree of correlation is. This method can be used to compare the degree of fit between several forecast curves corresponding to several forecasting models and one actual curve. Actually, the greater the degree of correlation, the better the corresponding forecast model and the smaller the fit error.

For example, we assume that  $X_i = (x_1, x_2, \dots, x_{96})$  is the daily load curve on day  $i$ , and the typical daily load curve extracted is  $Y = (y_1, y_2, \dots, y_{96})$ . Correspondingly, the correlation coefficient between the two time series is calculated as  $r_i$  as follows:

$$r_i = \frac{\sum_{k=1}^{96} (x_k - \bar{x})(y_k - \bar{y})}{\sqrt{\sum_{k=1}^{96} (x_k - \bar{x})^2 (y_k - \bar{y})^2}}, \quad (9)$$

where  $\bar{x}$  and  $\bar{y}$  denote the mean value of the sequences of  $X_i$  and  $Y$  and the sample correlation coefficient  $r$  of the load characteristic indicator data is a consistent estimate of the overall correlation coefficient  $\rho$  of the indicator. In fact, the closer the value of  $r$  is to 1, the stronger the correlation between the typical daily load curve, denoted by  $Y$ , and the daily load curve, denoted by  $X_i$ , is for day  $i$ . The correlation coefficient between the typical daily load curve  $Y$  and the daily load curve  $X_i$  for day  $n$  of the user's daily load curve can be calculated, namely,

$$r = \frac{1}{n} \sum_{i=1}^n r_i. \quad (10)$$

Based on this, the overall extraction effect of the algorithm can be obtained by comparing the median of the correlation  $r$  index of various typical daily load curve extraction methods; the stability of the algorithm can be obtained by comparing the difference between the maximum and minimum values or the difference between the upper and lower quartiles.

**3.4. Industry-Based Load Clustering Method.** According to the standard of GB/T 4754-2017-*Classification of National Economy Industries*, multiple user loads in each industry are analyzed using multiple clustering algorithms to extract the corresponding typical load curves. Among them, the system encapsulates a variety of clustering analysis methods including hierarchical clustering algorithm [27],  $k$ -means algorithm [28, 29], and Minibatch  $k$ -means algorithm in the API of the clustering analysis module. In this paper, the description of load clustering and typical daily load curve extraction module is introduced based on the  $k$ -means method.

As one of the prototype algorithms for cluster analysis,  $k$ -means has been maturely studied and applied at this stage. Specifically, these methods usually start with an initial prototype and then iterate on the results several times according to a certain rule until convergence conditions are met.

The  $k$ -means algorithm has the advantage of being simple and easy to use, and the results are generally convincing. However, the disadvantage of the  $k$ -means algorithm is that the number of classifications depends on subjective experience and it is difficult to ensure that the number of clusters selected is the optimal number. For this reason, the software system adopts an improved  $k$ -means method based on a cluster validity evaluation index to process the load data in order to extract the relevant typical daily load curves.

Concretely speaking, this paper sets the contour coefficient as an index for evaluating the effectiveness of clustering results to determine whether the selection of the number of classifications is reasonable. To evaluate the merits of the clustering results, we need to analyze both the degree of cohesion within classes and the degree of separation between classes, and the contour coefficient effectively combines the two. The overall contour coefficient can be calculated as follows:

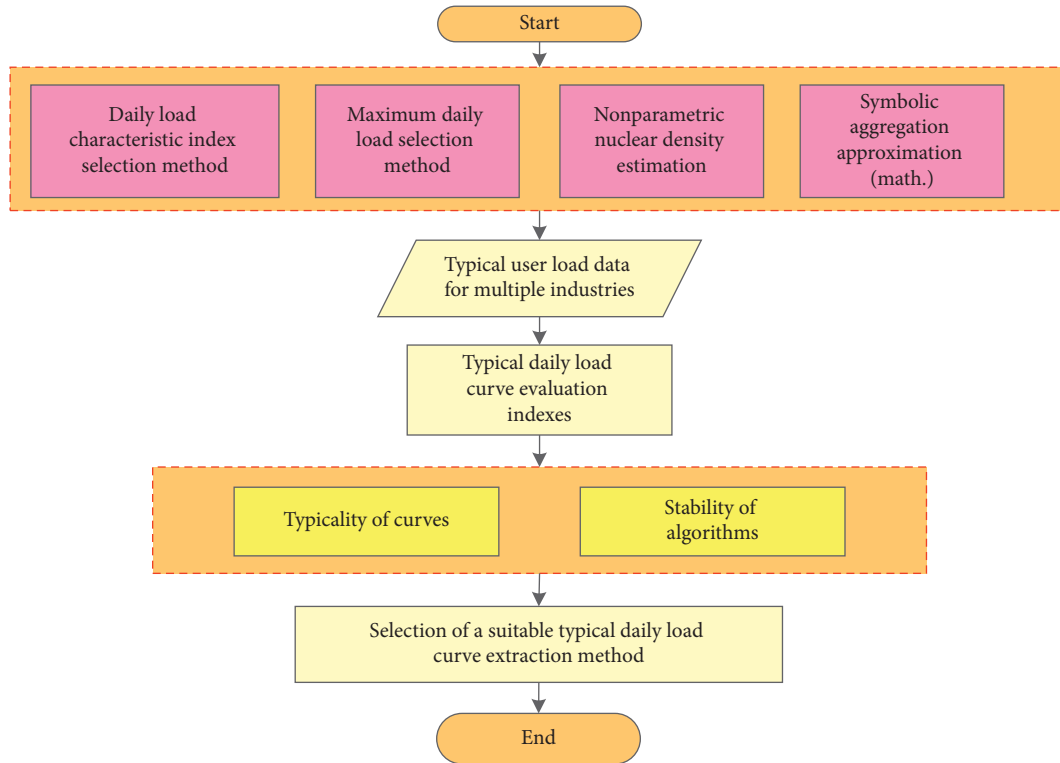


FIGURE 10: Research logic block diagram of a typical daily load curve extraction method.

$$S_{total} = \frac{\sum_{i=1}^n (b(i) - a(i)) / (\max\{a(i), b(i)\})}{n}, \quad (11)$$

where  $a(i)$  is the average distance from point  $i$  to other points in the cluster it belongs to (i.e., cohesion),  $b(i)$  is the average distance from point  $i$  to the nearest point in another cluster (i.e., separation), and  $n$  is the total number of clustering objects.

It can be seen that the value of the total contour coefficient ranges from  $-1$  to  $1$ , and a larger value represents a higher combined cohesion and separation score, which can be considered a better clustering effect. Based on the tendency of the contour coefficient to change with the number of classifications, the most reasonable number of classifications is selected to improve the abovementioned  $k$ -means drawback. Clustering analysis is performed on the load of multiple users in an industry in order to grasp the overall electricity consumption behavior of users in that industry. The specific steps of the abovementioned content are shown in Figure 11.

According to the clustering result under the optimal number of clusters obtained in the abovementioned steps, the user load in this industry can be divided into appropriate power consumption mode types, and the clustering center is the typical daily load curve of the user load under this power consumption mode.

#### 4. Application Functions Design

According to the application requirements of power grid companies, the smart distribution network load analysis and prediction management system developed in this paper contains several functional modules for data management,

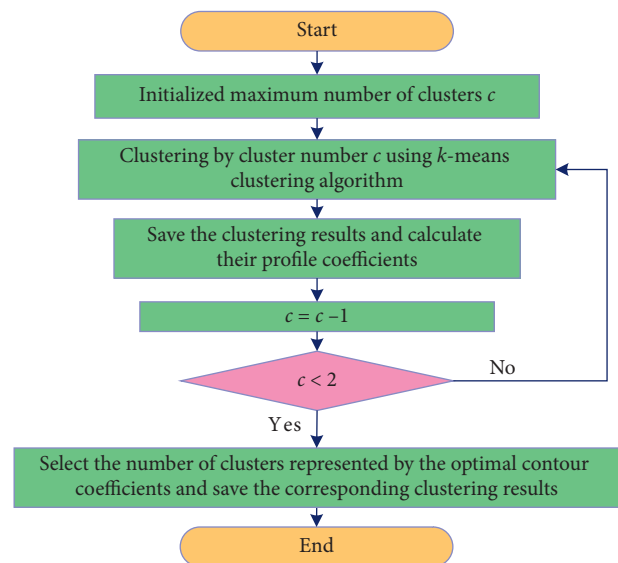


FIGURE 11: Research logic block diagram of the proposed industry-based load clustering method.

load characteristic analysis, business expansion reporting and installation, load prediction, power load optimization, distribution network planning, and system management, as demonstrated in Figure 12.

4.1. Data Management Module. The data management module is the basic module used for data processing, in which the user information function allows queries the

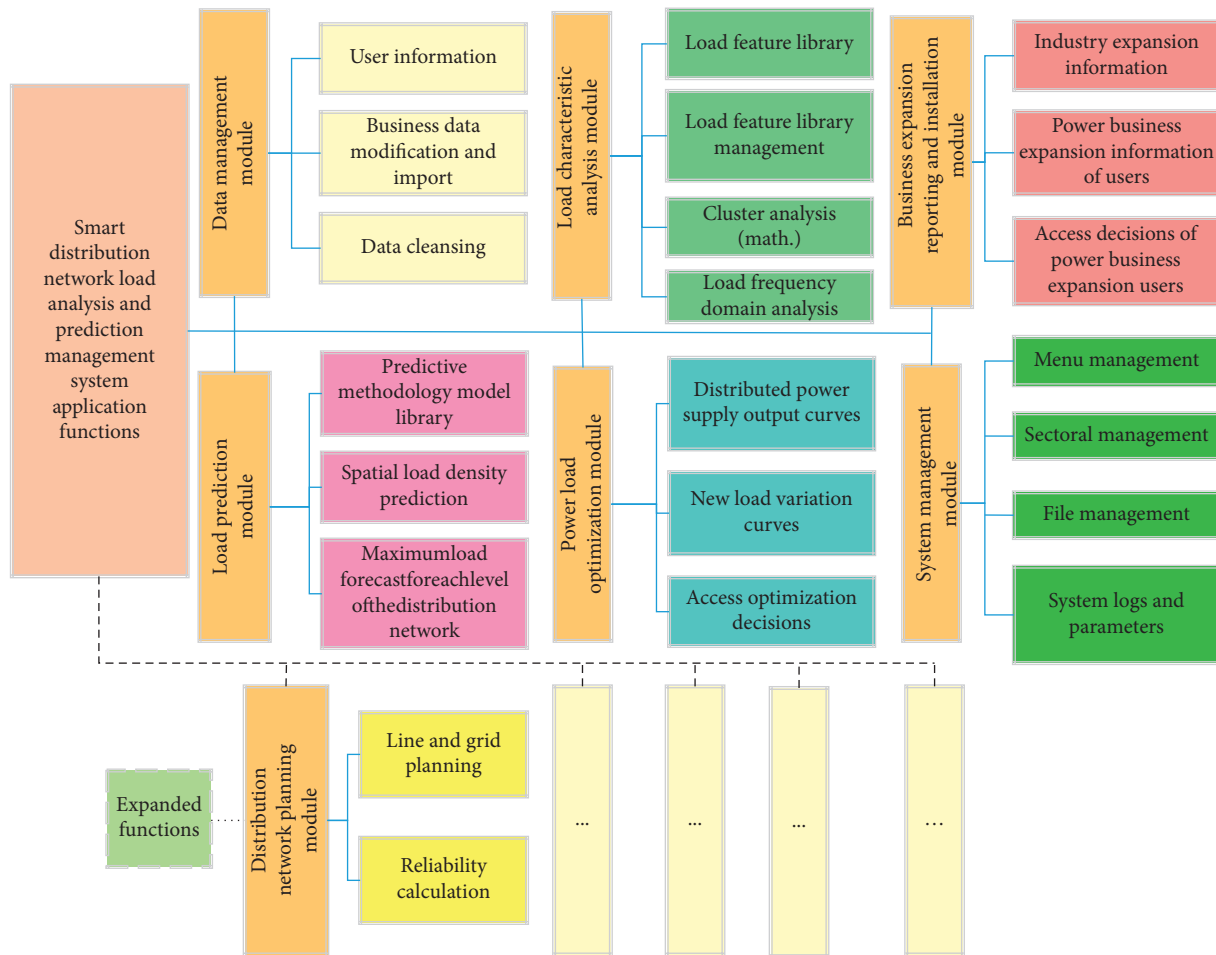


FIGURE 12: System application functional structure design.

user's name, access point, user industry type, user reported capacity, user reported installation time, floor area, scale factor, and other information, and at the same time, the data imported from the underlying database can be manually modified in this module, as well as the import of business data.

The load data are mainly data from 96 measurement points per day for distribution transformers, which requires a lot of data preprocessing operations due to the varying conditions of the measurement locations, resulting in average data quality, more bad data, and less truly usable data. Data cleaning mainly deals with missing values, zero values, sudden outliers, load curves as straight lines, and so on.

For a number of consecutive days missing a large number of data, a similar day approximation substitution method is used to repair and replace data throughout the day in order to carry out the distribution of the load addition and calculation processing functions. For single-day anomalous data, the low-rank matrix filling algorithm is used for processing, and the load curve containing the missing data and the historical load curve form a low-rank matrix, which is then calculated using the low-rank matrix filling algorithm [19], as shown in Figure 13 for the flow design of the low-rank matrix algorithm.

**4.2. Load Characteristic Analysis Module.** The load characteristic analysis module includes the establishment of load characteristic database and the management of the load characteristic database. The load characteristic database is calculated by a specific algorithm, and it can be divided into two categories of numerical characteristic indicators and curve-type indicators from the indicator type and three categories of daily characteristic indicators, monthly characteristic indicators, and annual characteristic indicators from the time dimension [20, 21], as shown in Tables 1–3, respectively.

In order to accurately identify the load and interpret the long and short period components contained in the load, the module sets up the load frequency domain analysis function on the basis of traditional load indicators, in order to improve the sensitivity of the load feature library to load fluctuations. The frequency domain analysis is based on the principle of wavelet transform and extracts the wavelet energy of the approximate signal, the wavelet energy of the detail signal, the root mean square value of the approximate signal, the root mean square value of the detail signal, the absolute mode mean of the approximate signal, the absolute mode mean of the detail signal, the standard deviation of the approximate signal, and the standard deviation of the detail signal as the analysis indexes.

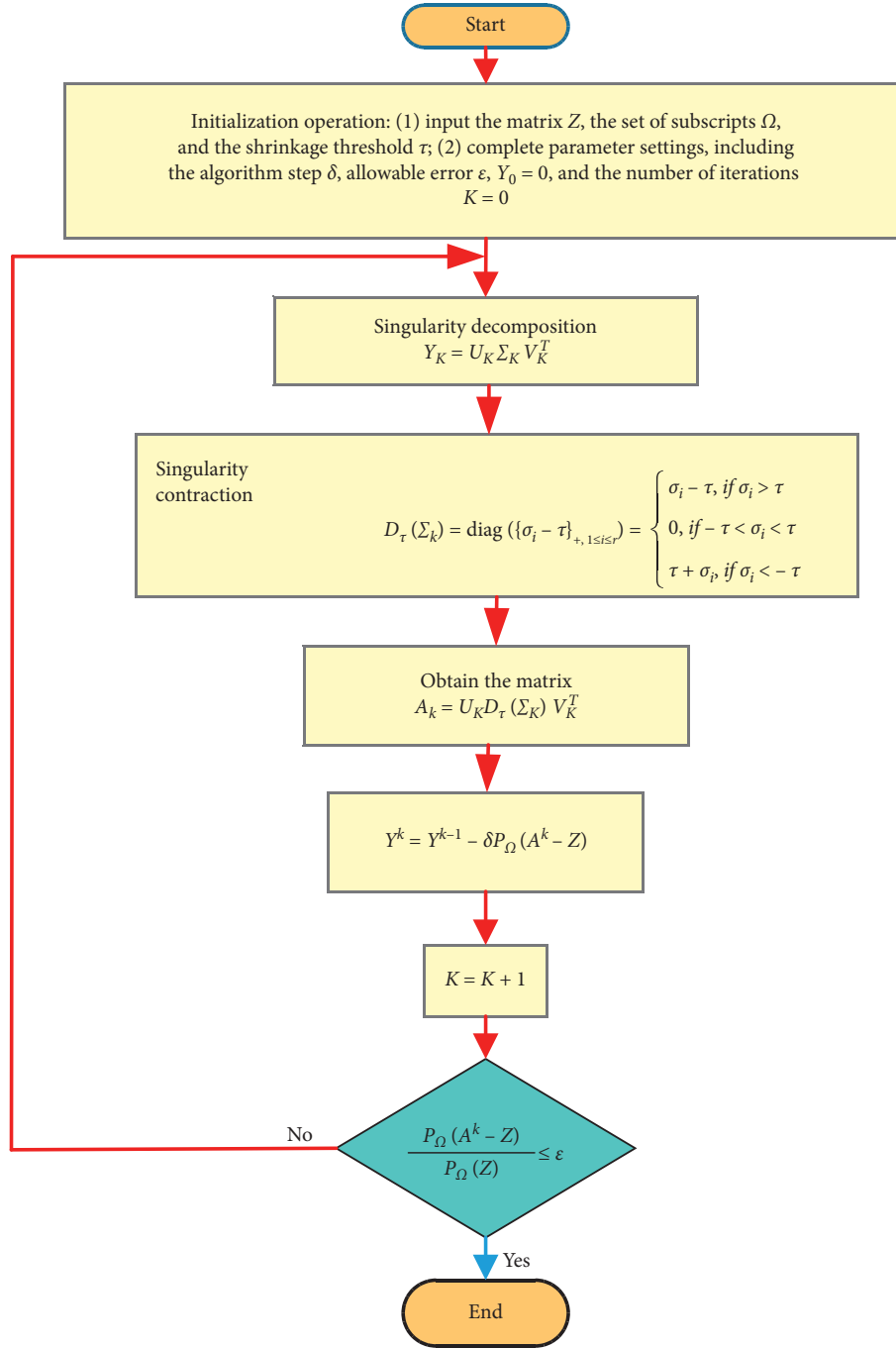


FIGURE 13: Low-rank matrix algorithm design flow.

TABLE 1: Daily load characteristics index.

Load characteristics index	Index definition
Daily maximum load	Maximum value of 96 measured point loads per day
Daily minimum load	Minimal value of 96 measured point loads per day
Average daily load	Daily average of 96 measurement point loads
Daily load rate	Ratio of average daily load to maximum daily load
Daily minimum load rate	Ratio of daily minimum load to daily maximum load
Daily peak-to-valley difference	Difference between daily maximum load and daily minimum load
Daily peak-to-valley ratio	Ratio of daily peak-to-valley difference to daily maximum load
Daily load curve	96 measurement point load connection curves per day



TABLE 2: Monthly load characteristics index.

Load characteristics index	Index definition
Monthly maximum load	Maximum load for the day of the month on maximum load day
Monthly minimum load	Minimum load for the day of the month on minimum load day
Average monthly load	Average of monthly average daily load
Monthly average daily load rate	Average of monthly daily load rates
Monthly minimum load rate	Minimum value of monthly daily load rate
Maximum monthly peak-to-valley difference	Maximum value of monthly daily peak-to-valley difference
Monthly average daily peak-to-valley ratio	Average of monthly daily peak-to-valley ratios
Monthly maximum load curve	Maximum daily load connection curve per month

TABLE 3: Annual load characteristics index.

Load characteristics index	Index definition
Annual maximum load	Maximum load for each month of the year
Annual minimum load	Minimum load for each month of the year
Annual minimum load rate	Minimum value of annual daily minimum load rate
Annual maximum peak-to-valley difference	Maximum value of annual daily peak-to-valley difference
Annual maximum peak-to-valley ratio	Maximum value of annual daily peak-to-valley rate
Quarterly imbalance coefficient	The ratio of the average of the sum of the maximum load days of the month of the year to the maximum load of the year
Annual maximum load utilization hours	Ratio of annual electricity consumption to annual maximum load
Annual maximum daily load curve	Maximum daily load connection curve per day per year

According to the industry classification, the typical daily load curves of a large number of users in the same industry are selected for clustering analysis, as shown in Figure 14, which is the typical daily load curve clustering flow chart designed in this paper.

Figure 15 demonstrates the clustering result of the summer load curves obtained from the garment industry in a certain place. Based on Figure 15, the API of the load characteristic analysis module in the developed software system encapsulates five effective clustering approaches, including fuzzy  $C$ -means clustering algorithm, fuzzy  $C$ -means clustering algorithm based on grey wolf optimization [22], hierarchy-based clustering method,  $k$ -means clustering algorithm, and Minibatch  $k$ -means clustering algorithm. Different clustering algorithms in the module will face different data samples, and they have different clustering effects; thus, the module chooses the contour coefficient as a validity indicator, which combines intraclass tightness and interclass separation as a measure of the clustering effect. The  $k$ -means algorithm, for example, has the advantage of being simple and easy to use, and the results are generally convincing. However, the disadvantage of the  $k$ -means algorithm is that the number of categories depends on subjective experience and it is difficult to guarantee that the selected number of clusters is the optimal number.

To solve the abovementioned problems, this system uses an improved  $k$ -means method based on the cluster validity evaluation index to process the load data in order to extract the relevant typical daily load curves. To solve the abovementioned problem, this paper will set the contour

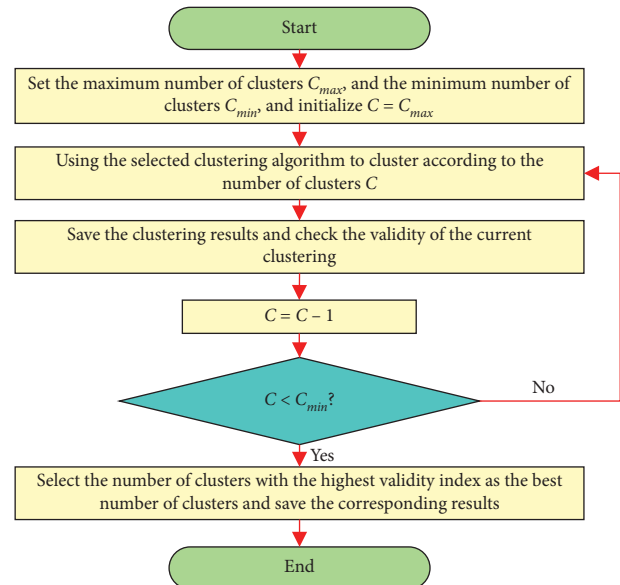


FIGURE 14: Flowchart design for clustering of typical daily load curves.

coefficient as an index for evaluating the effectiveness of clustering results to determine whether the selection of the number of classifications is reasonable. To evaluate the merits of the clustering results, we need to analyze both the degree of cohesion within classes and the degree of separation between classes, and the contour coefficient effectively

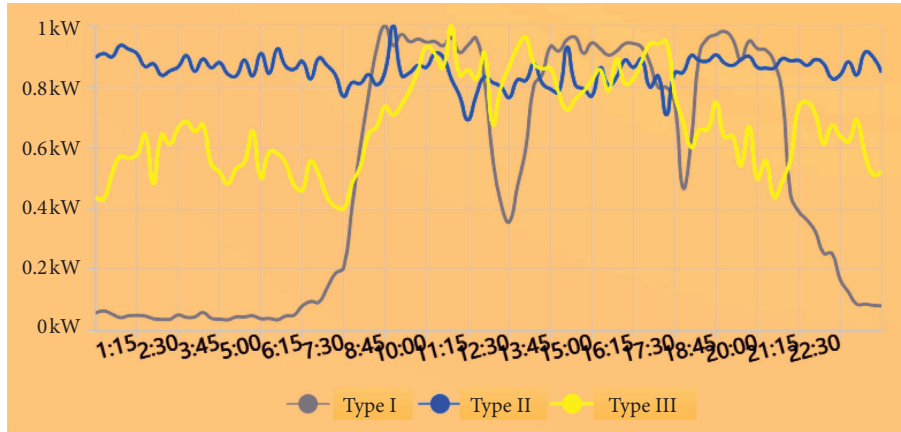


FIGURE 15: Summer daily load curve clustering results in a local garment industry.

combines the two. The overall contour coefficient [23] can be calculated by the following formula:

$$SIL_{\text{tol}} = \frac{\sum_{k=1}^{k=N} (D_1(k) - D_2(k)) / (\max\{D_1(k), D_2(k)\})}{N}, \quad (12)$$

where  $D_1(k)$  is the average distance between vector  $k$  and other points in the cluster where it is located (intracluster compactness);  $D_2(k)$  is the average distance between vector  $k$  and the points in the cluster closest to where it is located (inter-cluster separation); and  $N$  is the current number of clusters. It can be seen that the total profile coefficient values range from  $-1$  to  $1$ , and the larger value represents higher combined cohesion and separation score, which can be considered a better clustering effect.

The abovementioned  $k$ -means drawbacks can be improved by judging the trend of the contour coefficient as the number of classifications changes and selecting the most reasonable number of classifications based on this. Clustering analysis is performed on the load of multiple users in an industry to grasp the overall electricity consumption behavior of users in that industry, as shown in Figure 14.

#### 4.3. Business Expansion Reporting and Installation Module.

In this module, the distribution load data samples from the power grid SCADA systems are adopted and analyzed. According to the classification standard of GB/T 4754-2017 formulated in China, this module can be hierarchically divided into gates, major categories, medium categories, and minor categories. This division involves a total of 119 subcategories, which can be used to further realize differentiated and refined management and conduct information extraction and load analysis for the industry users.

According to the information of industry users' reporting time, reporting capacity, commissioning time, and load change in the year of commissioning from 1 to 3 years, the utility coefficient and stage coefficient of each user are calculated, and the confidence intervals of industry utility

coefficient and stage coefficient are determined by statistical methods to provide data support for reasonable load prediction [24]. Identifying the load patterns of large users is the key to developing a power access plan for large users. Only by understanding the daily load pattern of the newly connected large users can the system manager make better use of the complementary peaks and valleys between large users for reasonable planning. The system manager can enter the information of the user to be installed, such as the user's region, industry, installed capacity, floor area, volume ratio, the nature of electricity consumption, access time, production plan, peak hours of electricity consumption, production equipment, and nonproduction equipment, such as rated operating capacity.

Before the new users are connected, the typical load curve is selected scientifically from the load characteristic database based on the matching of installation information and industry expansion information, combined with the nature of user power consumption and production plan. Different matching methods are set up according to the information provided by the customers. For the information-rich customers, the load rate, minimum daily load rate, peak-to-valley differential rate, peak period load rate, flat period load rate, valley period load rate, and other calculation indexes are estimated by using the capacity of various types of equipment and information on usage behavior, and the load curves of different electricity consumption modes are selected by using artificial intelligence methods [30–36] such as random forest and probabilistic neural network. For users with fuzzy information, discrete simulated electricity consumption behavior curves are plotted and the Euclidean distance is used to discriminate. By establishing a scientific and reasonable matching method, the clustering curves in the load characteristic database can be selected with higher accuracy. At the same time, according to the existing information matching, the best recommended practical coefficients and stage coefficients are selected from the industry expansion information database, and the load prediction maximum value for new users in different years of the forecast period is obtained

by combining with the reported capacity. For a specific type of load, the system manager can also set special matching rules.

It is worth mentioning that, in the application process, the daily load curve of the new customer is selected by the matching algorithm, and the historical typical daily load curve is approximated as the future daily load curve for the load overlay analysis. The load curves in the feature library are standard curves, which only determine the shape, and the load level is still determined by the maximum value of the load forecast.

**4.4. Load Prediction Module.** Medium- and long-term load forecasting [25, 26] is a practical guide for the planning and construction of distribution networks and can initially estimate the scale of new transmission and distribution facilities to be built during the planning period. According to different forecast levels and available data sources, the model library of the medium- and long-term load forecasting method is established by integrating various forecast ideas, as shown in Figure 16.

Theoretical studies on feeder-level prediction are still scarce both at home and abroad because feeder load is smaller than system load and is subject to greater variability due to fluctuations. Feeder access to the distribution transformer load is prone to sudden changes, less stable, and difficult to seek the law of change.

In the prediction module of this paper, bottom-up distribution superposition, random forest, and top-down load allocation based on area prediction data are used as the application algorithms. Among them, the distribution overlay and random forest algorithm sink the analysis object to the level of the distribution transformer, combined with the classification criteria mentioned in the industry expansion installation module, using the data management module of the distribution transformer itself and the distribution transformer historical load data, the distribution transformer according to the public and private transformer, the nature of electricity consumption, the power supply area, the operation time, and other information to classify the distribution transformer, and different types of transformers will have different loads. For the prediction principle, the load maturity time varies for different substations, so different growth rates are set. In this case, the transformer forecasts for the same feeder are added together and multiplied by the simultaneous rate of the feeder to obtain the forecast load for the feeder.

In contrast, the top-down load allocation method first takes the 110kV substation as the object of forecast, the forecast of the 110kV main station is usually based on the current load of the 110kV main station increasing at a certain natural growth rate, and then, it adds the installed capacity of large users and the load plan transfer amount to get the result. The predicted load value is obtained for each feeder. Part of the actual feeder load data is selected for prediction [27] and then combined with the experience of experts, through manual verification and analysis of the connected distribution and other feeder state information, and the prediction results can be revised more accurately [25], as shown in Figure 17.

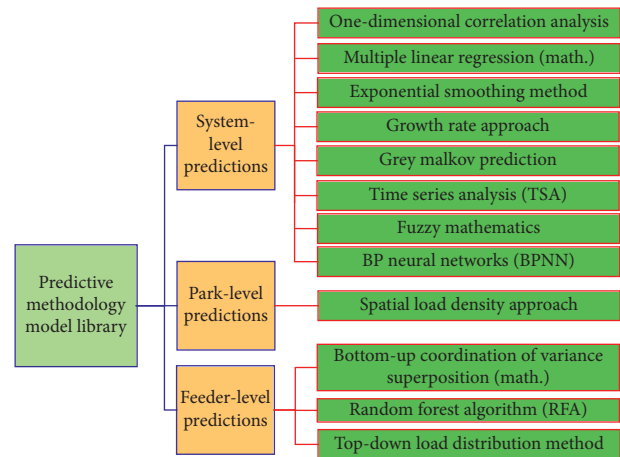


FIGURE 16: Predictive methodology model library design.

Space load density can not only calculate the maximum load value but also get the spatial distribution of the load in combination with the information of the control map of the plot, which is an important reference for the zoning of high-voltage power supply, line layout, and power supply range determination. From the calculation of historical load data, floor area, and operation time, the access load density and saturated load density of different types of users can be known, and in combination with the release coefficient of the development year, the three recommended schemes of high, medium, and low annual load value of the corresponding plot can be obtained by entering corresponding information in the function interaction column [28]. This method is used for incremental distribution network load forecasting for new parks.

The load prediction of the stock distribution network, combined with the GIS system, can clearly observe the load distribution topology and predict the maximum load of the distribution transformer in the next few years, which can roughly realize the heavy overload warning and provide data support for the capacity expansion and line modification of the existing distribution substation.

**4.5. Power Load Optimization Module.** The access to distributed energy sources, energy storage devices, and new types of loads such as electric vehicles changes the load characteristic curve of the traditional distribution network. Appropriate consideration of the timing characteristics, future increment, and commissioning costs of distributed energy and new types of load can effectively guide the commissioning of distributed power supply and electric vehicle charging stations in the region.

Considering the development of major new load electric private cars and space load demand, we make a forecast of the future electric vehicle ownership in the region based on the improved BASS model with reference to the data from the Shanghai Transportation Industry Development Report (2018) and the Shanghai New Energy Vehicle Industry Big Data Research Report (2018). With reference to the National Highway Traffic Safety Administration data, the modeling

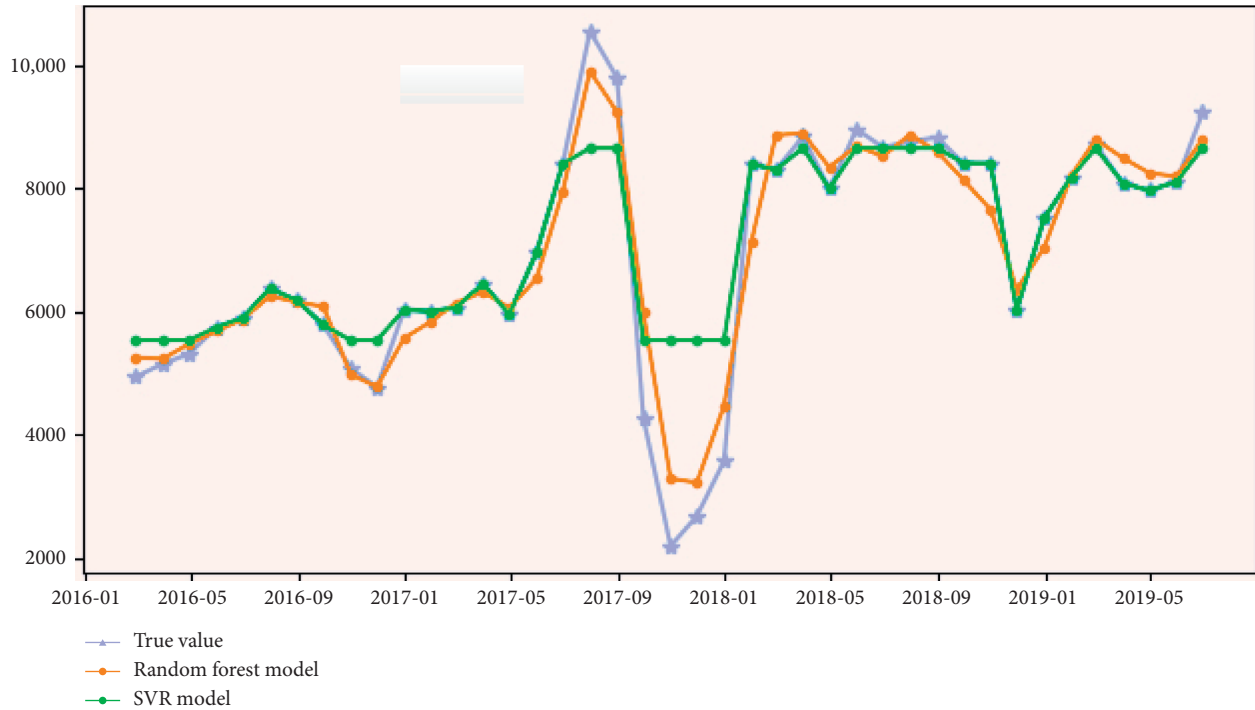


FIGURE 17: Comparative analysis of feeder-level load prediction results during Jan 2016 to May 2019.

and analysis of the temporal and spatial behavior of the vehicle based on Monte Carlo simulation is used to obtain the quantified demand of the maximum load for different charging decisions and typical EV daily load curves under different scenarios in the future forecast year [29].

The access decisions of this module are divided into load characteristic decisions, as well as economic decisions. The aforementioned industry expansion charging module can match the typical power consumption curve of new users of the industry expansion from the load characteristic analysis module through the charging information, which can be based on the load rate of the feeder near its geographic location, based on the principle of increasing the flatness of the load curve of the power supply point, to achieve the optimal decision of user access. It is also possible to make decisions on the transfer of power to existing users near the feeder to improve the load characteristic index.

At the same time, we set the initial distribution network loss, distributed power construction and operation cost, environmental benefit cost, energy storage cost simple model [37], and the access amount of PV, wind, and microgas units, combined with physical constraints to establish the solution of the multiobjective optimization function and variable weight analysis to compare the economic benefits of different conditions, for managers and investors to make a reference for decision-making.

**4.6. Distribution Network Planning Module.** This module is based on the load characteristics and load prediction module. After importing the basic data, the optimization algorithm is invoked to carry out park distribution network planning and quickly generate wiring schemes and

economic and technical indicators in various wiring modes to provide reference and basis for planners.

According to the order of the distribution network to carry out park planning, the first thing to do is to import the topology data and control map required for the primary distribution network frame planning from the GIS and then import the load characteristics of different industries from the load characteristics module, while supporting the addition, deletion, and modification of components. After importing the basic information, the user is supported to carry out grid drawing, and according to the cable corridor information on the control map, the path of the constructable transmission pipeline corridor is drawn on the control map, and the land parcel surrounded by the drawn path must be closed. The backend system will automatically identify the parcel area, path length, and other information based on the user's mapped line layer. At the same time, the road planning function column can display different layers, including the map, control map layer (mainly used for road drawing), load point layer (to display the load node and power node defined on the load prediction function module), path map layer (to display the manually drawn road network topology), and feeder map layer (to display the geographic alignment of the feeder once planned).

According to the plot information on the control plan, the location of each load node is marked on the drawing line layer, and the software automatically matches the user-marked load node with the plot load information in the control plan imported by the user and predicts the plot load by the spatial load density method of the load prediction module. The software also supports the user to manually complete or correct the process of matching the marked load nodes with the parcel load information in the imported

control regulations. The user can then select the wiring pattern and priority principle and customize the basic investment parameters and reliability parameters according to the actual requirements.

After deploying the abovementioned basic data, the optimization algorithm is invoked to optimize the distribution network planning model and generate the optimized primary grid, and the reliability and tidal current calculation results (including node voltage, line current, and line loss) of each feeder primary grid are also displayed for the planners to verify and adjust the planning results.

**4.7. System Management Module.** This module is the management operation and maintenance module of the system, though the menu management can freely adjust the system page, department management can increase the subordinate use units, and file management can download file data through the visualization of uploading, system parameters involving system copyright information and authentication code open options, and system logs to record the changes made by the user to the system operations.

Overall, as shown in Figure 18, the data full-link implementation flow of the software system is developed in this paper [38–42]. Among them, the software system selects some visual components to display the output results of the multidimensional load characteristic analysis [43]. The page of load characteristic library shows the user's typical daily load curve, day, month, year, and other regular load characteristic indexes; the page of load frequency domain analysis shows the user's load wavelet-transformed approximate signal, detailed signal, and the steady-state characteristic quantity of each layer signal; the page of the practical coefficient and stage coefficient shows the user's saturated load density, practical coefficient, and stage coefficient indexes; and the page of the practical coefficient and stage coefficient shows the user's saturated load density, practical coefficient, and stage coefficient indexes. The clustering analysis page displays the results of the electricity consumption patterns of selected industries.

Based on Figure 18, the system microservice architecture adopted in the interface of the software system developed in this paper brings flexible and expandable capabilities, and the modular development mode ensures the information interaction between each functional module, while the construction of the data acquisition management platform and the multinode replica set deployment of the database make the data interface of the system support a variety of data acquisition protocols and ensure the security of data storage. In terms of algorithm integration design, the system builds an algorithm integration platform, provides a standard unified call interface, and supports automatic identification and call of multiple languages.

## 5. System Visualization Interface Development and Design

In this paper, some visual components are used to display the output results of multidimensional load characteristic analysis [37–43]. The page of the load characteristic

database shows the user's typical daily load curve, day, month, year, and other general load characteristic indexes; the page of load frequency domain analysis shows the user's load wavelet-transformed approximate signal, detailed signal, and steady-state characteristic quantity of each signal layer; the page of the practical coefficient and stage coefficient shows the user's saturated load density, practical coefficient, and stage coefficient indexes; and the page of load frequency domain analysis shows the user's load wavelet-transformed approximate signal, detailed signal, and steady-state characteristic quantity of each signal layer. The clustering analysis page displays the results of the electricity usage patterns for the selected industry.

**5.1. Load Feature Library Page Development.** The load characteristic library analysis page developed in this system includes the typical daily load curve and characteristic index display interface, the monthly maximum load and minimum load curve interface, and the annual maximum load curve interface. As shown in Figure 19, it is the interface of the annual maximum load curve. This page adopts the nonparametric kernel density estimation method as the typical daily load curve extraction method, and the statistical time period is from 2018 to 03-01 00:00:00 to 2019-08-31 00:00:00.

This page consists of 5 sections: the typical daily load curve, daily load characteristic, maximum monthly load curve, monthly load characteristic, and annual load characteristic. The abovementioned graphical information is calculated and visualized according to the selected region, time span, user industry, user name, and typical daily load curve extraction method.

The selected region, time span, and typical daily load curve extraction method can be selected by drop-down operation, and the industry and user name provide keyword search function. The typical daily load curve section provides cursor hint function and displays specific time and data information with mouse movement.

**5.2. Load Frequency Domain Characterization Page Development.** The interface of user frequency domain analysis and characteristic coefficient is shown in Figure 20. The interface for load frequency domain analysis is mainly composed of two panels: figure and table. The load signal table shows the steady-state eigenvalues of approximate and detail signals obtained after 3-layer wavelet transformation of daily load data. The load signal diagram plots the approximate signals and detailed signals and displays the shape trend of each signal layer visually. The abovementioned graphical information is calculated and visualized according to the selected region, time span, and industry and user name.

**5.3. Utility Factor and Stage Factor Page Development.** In this system, the interface mainly consists of three panels: the practical coefficient and saturation load density, user stage coefficient, and industry stage coefficient, which are visualized



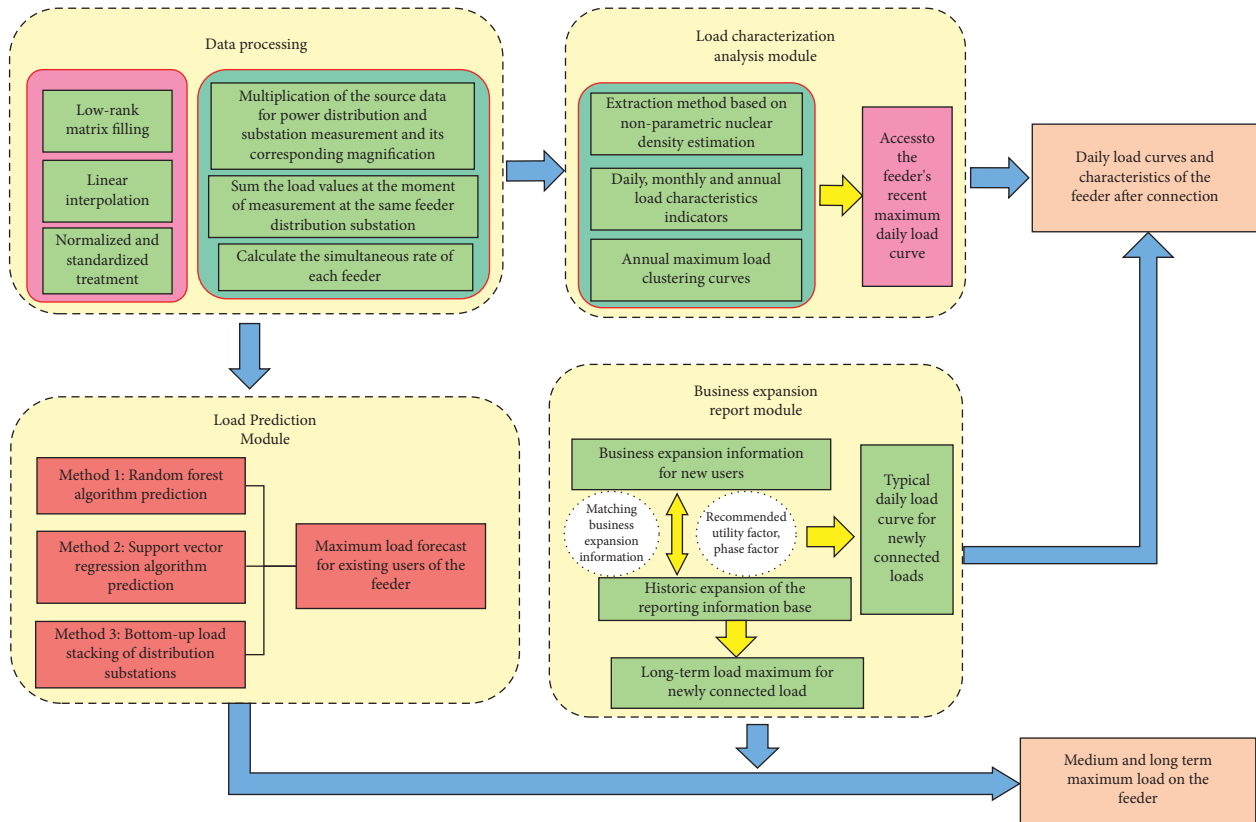


FIGURE 18: Flowchart design for the full data link implementation.

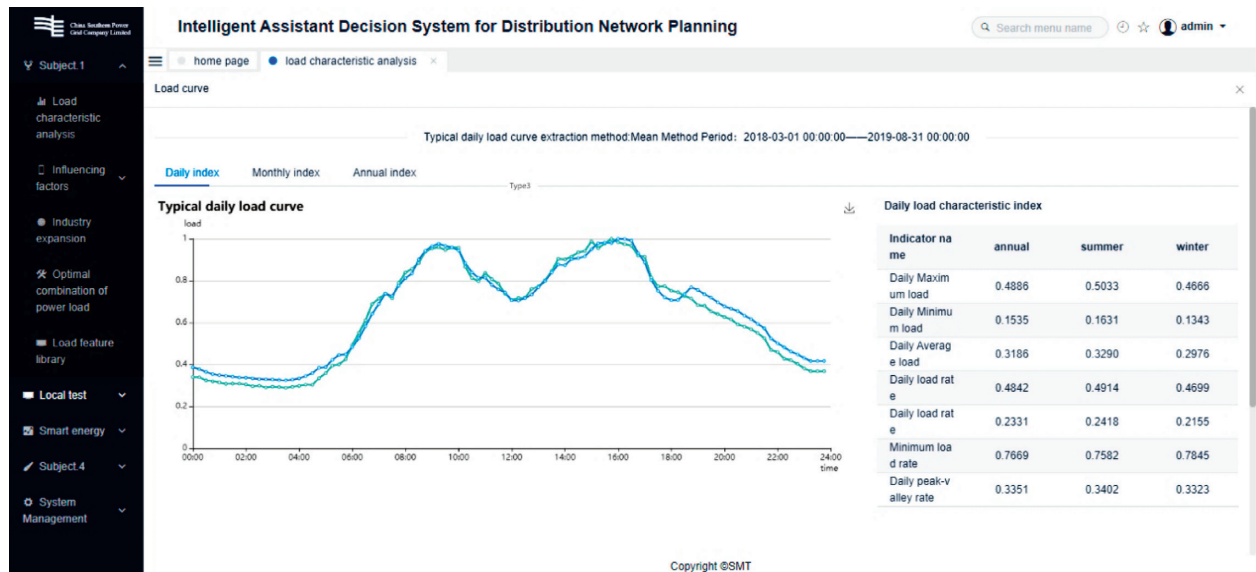


FIGURE 19: The interface display of the annual maximum load curve.

in the form of table for the specified user load and the industry to which it belongs, as demonstrated in Figure 21.

5.4. Clustering Analytics Page Development. In this system, the interface is mainly composed of two panels, namely, the industry typical daily load curve and the specified type of

load characteristic library, and the industry typical daily load curve panel plots and displays the electricity consumption patterns obtained by clustering multiple user loads in the industry. By touching the power consumption pattern legend with the mouse, you can select the power consumption pattern to be analyzed and get the characteristic database information of this type of user load. The panel



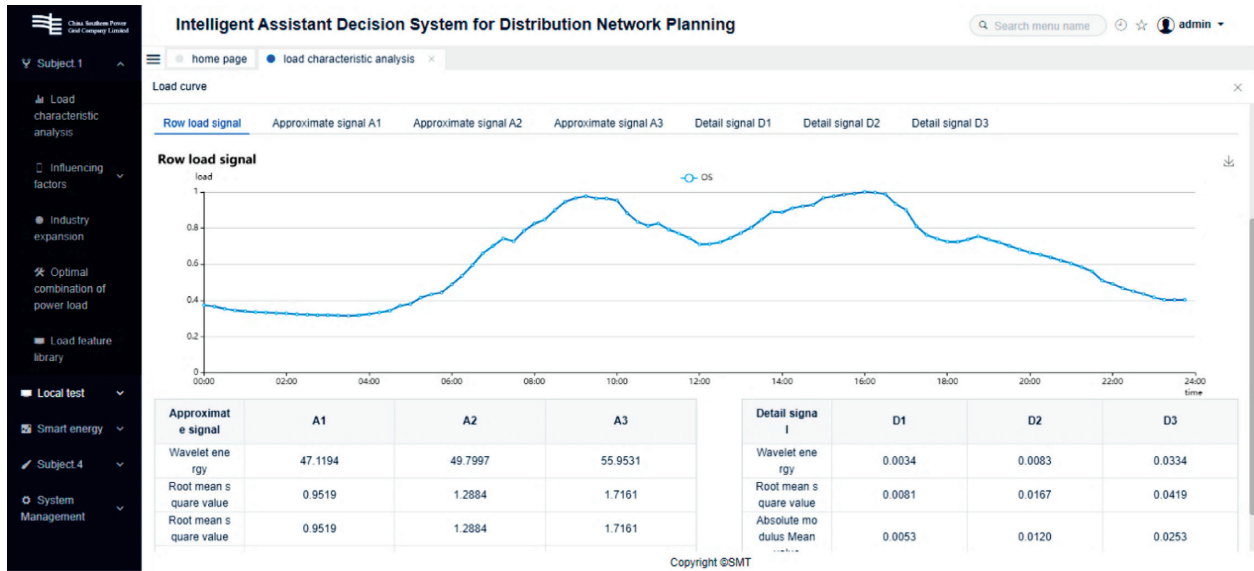


FIGURE 20: User frequency domain analysis and eigenvalue interface display.

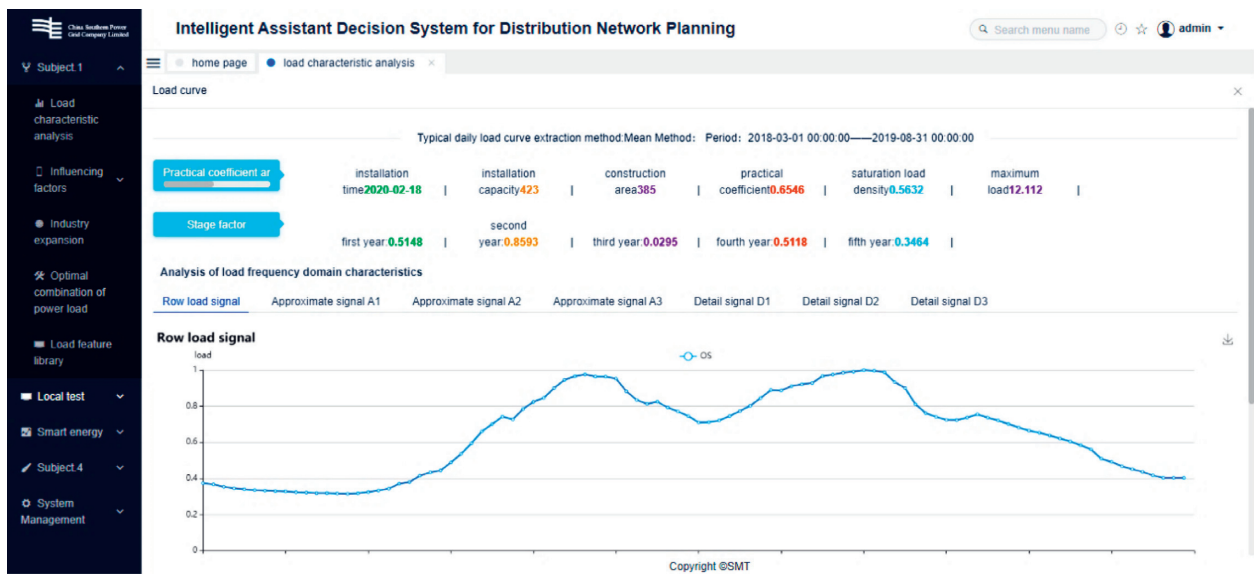


FIGURE 21: Utility factor and stage factor page display.

structure of the specified type of load characteristics database is the same as the abovementioned load characteristics database page. The abovementioned graphical information is calculated and displayed visually according to the selected region, time span, user industry, and load clustering method. Based on those mentioned above, the clustering analytics page is demonstrated in Figure 22.

### 6. Application Case Analysis of the Developed Software System

In order to realize the data link intercommunication between different modules of the software system, the application example selects a textile company as the business expansion user; its land area is 28,987 square meters, the

construction area is 29,886 square meters, the floor area ratio is 1.031, and the installed capacity is 630 kVA.

From the load characteristic library, two types of typical daily load curves are obtained according to the clustering curve of the textile industry, as shown in Figure 23. One of them is the typical load curve of an enterprise, where the load rises extremely fast at about 8 : 00 a.m. and falls back during lunch break at 12 : 00 noon, then re-enters the peak at about 14 : 00 a.m. and falls back briefly at about 17 : 00 a.m., and then re-enters the peak period and slowly decreases at 20 : 00 a.m. Finally, the load decreases slowly at 20 : 00 a.m. and falls back to the peak period.

The other typical curve shows the phenomenon of continuous peak without obvious peak and valley difference. Comparing and analyzing the two curves, it can be

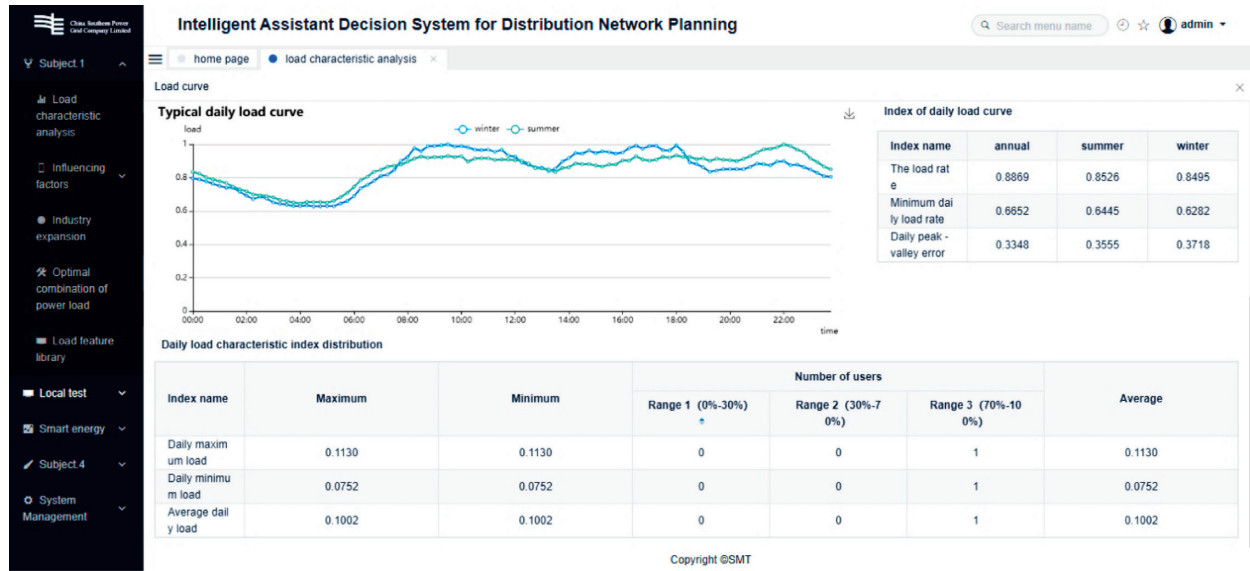


FIGURE 22: Clustering analytics page display.

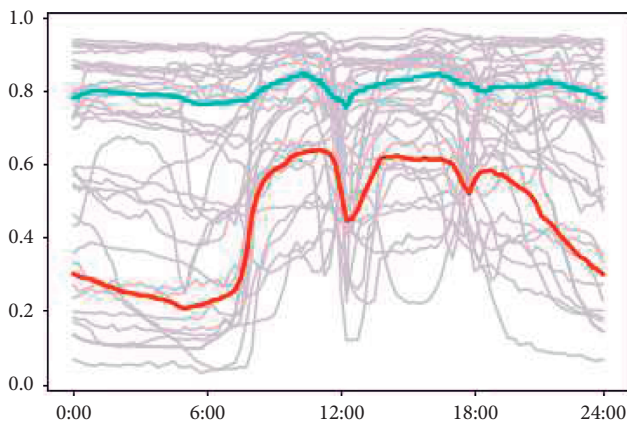


FIGURE 23: Typical daily load curve clustering results for the textile industry.

concluded that the former is a traditional hand-loom textile industry, which is not highly automated and most of the production requires human participation, so it shows a typical “three-peak” curve. But, the latter is a new type of textile industry with higher degree of automation, where most of the production work is carried out by machines instead of performing manually, and can run all day, so there is no obvious difference between time periods.

By comparing the production schedule information of the customer, this textile customer is not yet fully automated and involves other human activities; thus, a triple peak type of curve is chosen as a typical daily load curve.

The location of the user can choose two feeders 721 and 709. The load characteristic module can get the clustered typical daily load curves of these two feeders in the period where the maximum load is. By superimposing the new customer’s typical daily load curves on each of the two feeders, the new feeder load curves and characteristics can be obtained. As can be seen in Figures 24

and 25, connecting to the 721 feeder reduces the peak-to-valley differential and increases the minimum load factor, while connecting to the 709 feeder increases the peak-to-valley differential, and finally, the 721 feeder is chosen in combination with the feeder load.

The two feeders, No. 721 and No. 709, are available for this customer location. The Load Characterization module can be used to obtain clustered typical daily load curves for each of these two feeders for the time period where the maximum load is located. By superimposing the typical daily load curves for the new customer on each of the two feeders, the new feeder load curves and characteristics can be obtained. As can be seen from Figures 24 and 25, access to the 721 feeder can reduce the peak-to-valley differential ratio and increase the minimum load factor, while access to the 709 feeder will increase the peak-to-valley differential ratio, which, combined with the load of the feeder itself, is the final choice to access the 721 feeder.

The aforementioned known new user area installed capacity, industry information, and production plans, so you can match the approximate industry expansion information in the industry expansion information base to get the recommended 1~3 years of operation of the utility factor, and  $\eta_1 = 0.550$ ,  $\eta_2 = 0.734$ , and  $\eta_3 = 0.762$  according to the installed capacity can be the expected load value of each year. From the historical load information of feeder 721, three forecasting methods are applied to forecast its load maximum, and the weighted combination method is used to obtain the expected maximum load value in the following years, as shown in Table 4.

We use the principle of near large and far small and weigh the simultaneous rates for each year of feeder 721 to get the new simultaneous rate as the predicted simultaneous rate  $Sp = 0.756$ . The maximum user load is multiplied by the simultaneous rate and superimposed on the feeder load to get the predicted maximum load of the feeder in the next few years.

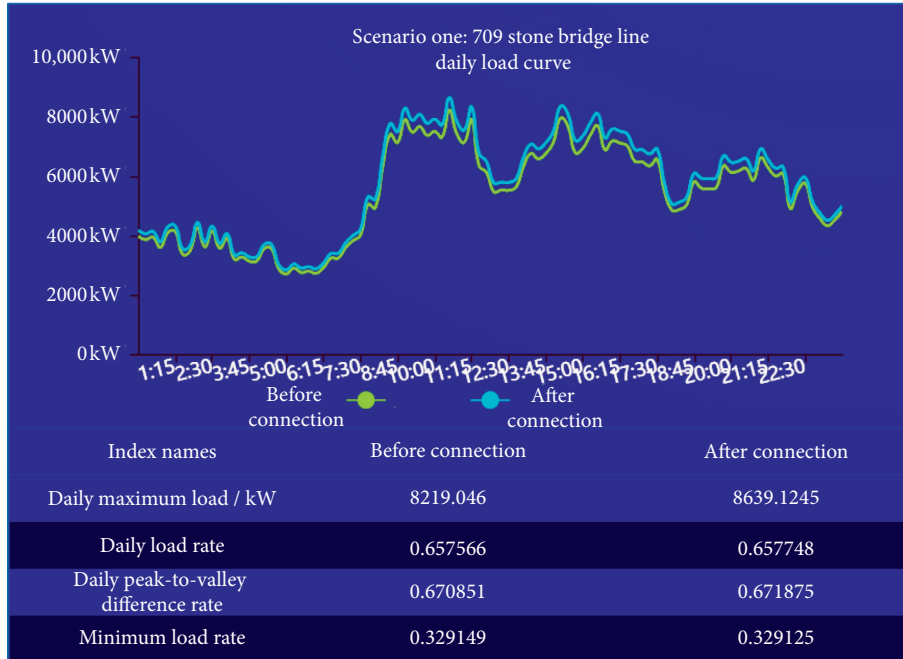


FIGURE 24: Display of the load curve No. 709 and its characteristic indicators.

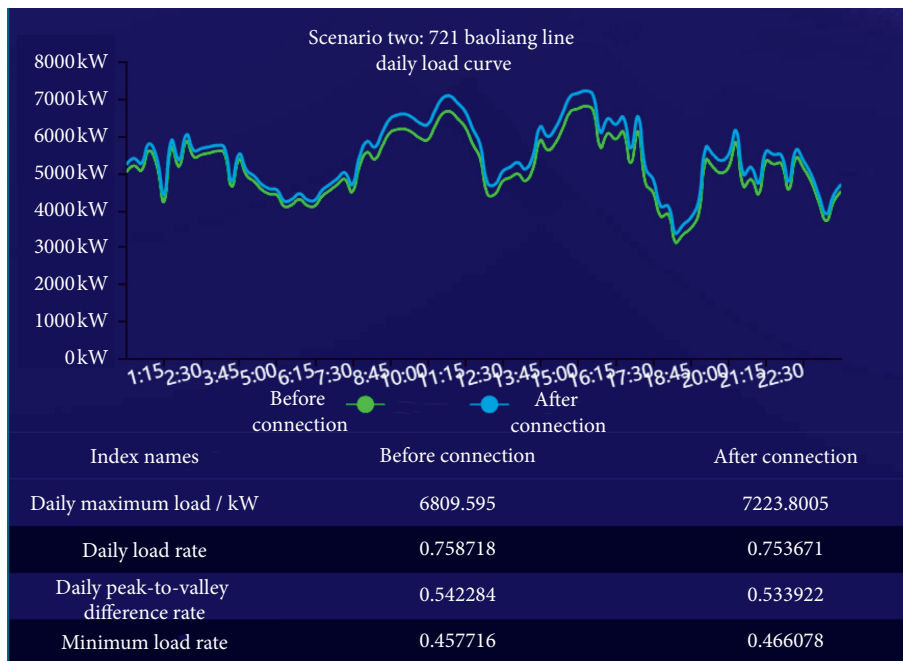


FIGURE 25: Display of the feeder load curve No. 721 and its characteristic indicators.

TABLE 4: Statistics on expected maximum load values for the year of 2020 to 2022.

Year	2020	2021	2022
Annual maximum load for new users/kW	338.4	459.35	486.22
Annual maximum load on feeder no. 721/kW	7019	7235	7604
Annual maximum load after connection/kW	7295.35	7642.25	7986.58

## 7. Conclusions

In this paper, a multidimensional load characteristic analysis system based on Java language with microservices and microapplications as the core architecture is built through a detailed analysis of the requirements of load characteristic software at the present stage. The microservice architecture of the system brings flexible and expandable capabilities, while the modular development mode ensures the information interaction between the functional modules. In terms of algorithm integration design, the system builds an algorithm integration platform, provides a standard unified invocation interface, and supports automatic identification and invocation of multiple languages.

Due to the interoperability of the data links of the software system described in this paper, the functional business platform is scalable and has new functional interfaces, so in the subsequent research, not only can we make use of richer data sources and conduct more in-depth theoretical research on modules that have not yet been fully developed, such as power optimization combinations, but also introduce the primary and secondary side coordination planning functions of the smart distribution network to provide interactive planning of the line network and generate components to serve the distribution network planning with the results of load characteristics and load forecast distribution. The solid foundation laid by diversified data management and control for functional expansion can further realize the functions of energy saving and environmental protection assessment, economic analysis, and comprehensive energy system planning for the distribution network.

At present, the system has completed the development of the load-related factor correlation analysis module and left the relevant interface of the load prediction module, and how to use the quantitative analysis results obtained from the load characteristic analysis and relevant factor correlation analysis module to further complete the prediction of regional load will be the focus of the next research and development work of this paper.

After the system is put into pilot operation and stabilized, it will continue to improve different application scenarios and eventually integrate the modules into a comprehensive decision-making management system integrating information control, distribution network index evaluation, transformer capacity determination, line network planning, and other functions and continuously improve the operation level and service capability of the smart distribution network.

## Data Availability

The underlying data supporting the results of our study can be found from the Shenzhen Power Supply Bureau Co., Ltd.

## Conflicts of Interest

The authors declare no conflicts of interest.

## Authors' Contributions

W. C. and T. Y. conceptualized the study; R. C. and T. Y. formulated the methodology; W. G. and D. Z. were responsible for software; validation was performed by W. C., J. L., W. G., and T. Y.; formal analysis was performed by J. L.; W. G. and J. L. were involved in investigation; R. C. and W. M. were responsible for resources; data curation was performed by W. G.; W. C., R. C., J. L., W. G., D. Z., and T. Y. prepared the original draft; W. C., R. C., J. L., W. M., and T. Y. were involved in review and editing; visualization was performed by W. G. and D. Z.; R. C. and T. Y. were involved in supervision; project administration was performed by W. C. and R. C.; and W. C., R. C., and T. Y. acquired fund. All authors have read and agreed to the published version of the manuscript.

## Acknowledgments

The authors would like to express their gratitude to the experts for their helpful suggestions, who have enhanced this work's content. This research was funded by the Science and Technology Project of China Southern Power Grid Co., grant no. 090000KK52190072.

## References

- [1] L. Tang, *Load Characteristics Analysis and Forecasting Research of Power System*, South China University of Technology, Guangzhou, China, 2010.
- [2] L. F. Cheng and T. Yu, "Typical scenario analysis of equilibrium stability of multi-group asymmetric evolutionary games in the open and ever-growing electricity market," *Proceedings of the CSEE*, vol. 38, no. 19, pp. 5687–5703, 2018.
- [3] X. Liu, Z. Xiao, R. Zhu, J. Wang, L. Liu, and M. Ma, "Edge sensing data-imaging conversion scheme of load forecasting in smart grid," *Sustainable Cities and Society*, vol. 62, Article ID 102363, 2020.
- [4] L. F. Cheng and T. Yu, "Decision-making behavior investigation for general multi-strategy evolutionary games in the spontaneous formation of long-term bidding equilibria of a power generation market," *Proceedings of the CSEE*, vol. 40, no. 21, pp. 6936–6955, 2020.
- [5] X. He, Q. Ai, and R. C. Qiu, "A big data architecture design for smart grids based on random matrix theory," *IEEE Transactions on Smart Grid*, vol. 8, no. 2, pp. 674–686, 2017.
- [6] L. Cheng, G. Liu, H. Huang et al., "Equilibrium analysis of general N-population multi-strategy games for generation-side long-term bidding: an evolutionary game perspective," *Journal of Cleaner Production*, vol. 276, Article ID 124123, 2020.
- [7] Y. Zhang, C. Deng, R. Zhao, and S. Leto, "A novel integrated price and load forecasting method in smart grid environment based on multi-level structure," *Engineering Applications of Artificial Intelligence*, vol. 95, Article ID 103852, 2020.
- [8] L. F. Cheng, T. Yu, X. S. Zhang, and L. F. Yin, "Machine learning for energy and electric power systems: state of the art and prospects," *Automation of Electric Power Systems*, vol. 43, no. 1, pp. 15–43, 2019.
- [9] H. L. Yan and X. Z. Zhang, "Analysis on industries load characteristic of Yunnan province," *Yunnan Electric Power*, vol. 44, no. 5, pp. 107–108+114, 2016.

- [10] G. H. Li, H. Chen, Y. Y. Chen et al., "Analysis of the load rate characteristics of Hunan power grid," *Hunan Electric Power*, vol. 36, no. 5, pp. 58–60, 2016.
- [11] F. Yun, *Characteristics Analysis and Application for Power Consumer in Cities of Tangshan*, North China Electric Power University, Baoding, China, 2018.
- [12] T. Y. Kang, S. P. Yin, X. F. Wang et al., "Load characteristics of large city power grid and analysis on its influencing factors," *Electrical Measurement & Instrumentation*, vol. 53, no. 6, pp. 51–56, 2016.
- [13] L. F. Cheng, *Theoretical Investigation on the Long-Term Evolutionarily Stable Equilibrium of Multi-Population Strategic Games in Electricity Market*, South China University of Technology, Guangzhou, China, 2019.
- [14] L. Y. Wang, J. Y. Xu, and Y. Shang, "Coordinated optimal scheduling of multi-microgrid system under mechanism of time-of-use electricity price based on multi-agent improved particle swarm optimization algorithm," *Journal of Power Supply*, vol. 17, no. 4, pp. 130–139, 2019.
- [15] X. Y. Tang, H. J. Wan, H. C. Ye et al., "Analysis and prediction of typical daily load characteristics of Guizhou power grid," *Electric Power*, vol. 48, no. 9, pp. 24–30, 2015.
- [16] D. S. Xu, W. Yang, Z. Wei et al., "Short term load characteristic analysis and prediction research based on SPSS," *Power System Protection and Control*, vol. 37, no. 21, pp. 147–151, 2009.
- [17] F. Liao, C. Y. Xu, J. G. Yao et al., "Analysis of load characteristics and influencing factors in Changde area," *Power System Technology*, vol. 36, no. 7, pp. 117–125, 2012.
- [18] D. S. Luo, Q. Du, C. H. Bie et al., "Analysis of residential differentiated electricity consumption behavior based on load decomposition," *Power System Protection and Control*, vol. 44, no. 21, pp. 29–33, 2016.
- [19] J. H. Chen, M. Chen, and Y. M. Pu, "B/S system performance analysis based on microservices architecture," *Computer Systems & Applications*, vol. 29, no. 2, pp. 233–237, 2020.
- [20] X. M. Qie and J. J. Zhang, "Design of terminal service platform based on microservice architecture," *Digital Technology & Application*, vol. 38, no. 6, pp. 124–126, 2020.
- [21] S. F. Hai, S. Y. Sun, X. H. Fan et al., "Influence of induction motor parameter change considering frequency characteristics on load characteristics," *Power System Protection and Control*, vol. 47, no. 8, pp. 17–25, 2019.
- [22] Q. Z. Zhu, Z. Dong, and N. Ma, "Forecasting of short-term power based on just-in-time learning," *Power System Protection and Control*, vol. 48, no. 7, pp. 92–98, 2020.
- [23] W. J. Zhao, L. Q. Shang, and J. F. Sun, "Power quality disturbance classification based on time-frequency domain multifeature and decision tree," *Protection and Control of Modern Power Systems*, vol. 4, pp. 337–342, 2019.
- [24] B. E. Xu and H. Lan, "Selection method of typical daily load curve based on improved fuzzy clustering," *Electrical Measurement & Instrumentation*, vol. 56, no. 4, pp. 21–26, 2019.
- [25] X. D. Wang, J. Y. Liu, Y. B. Liu et al., "Shape clustering algorithm of typical load curves based on adaptive piecewise aggregate approximation," *Automation of Electric Power Systems*, vol. 43, no. 1, pp. 110–121, 2019.
- [26] Y. J. Gao, Y. J. Sun, W. H. Yang et al., "Study on load curve's classification based on nonparametric kernel density estimation and improved spectral multi-manifold clustering," *Power System Technology*, vol. 42, no. 5, pp. 1605–1612, 2018.
- [27] W. W. Tso, C. D. Demirhan, C. F. Heuberger, J. B. Powell, and E. N. Pistikopoulos, "A hierarchical clustering decomposition algorithm for optimizing renewable power systems with storage," *Applied Energy*, vol. 270, Article ID 115190, 2020.
- [28] J. A. Liu, Y. B. Liu, and M. C. Cheng, "A distributed load clustering algorithm based on quantile radius dynamic K-means," *Power System Protection and Control*, vol. 47, no. 24, pp. 15–22, 2019.
- [29] Y. X. Wu, C. Gao, H. Z. Cao et al., "Clustering analysis of daily load curves based on GWO algorithm," *Power System Protection and Control*, vol. 48, no. 6, pp. 68–76, 2020.
- [30] L. Cheng and T. Yu, "A new generation of AI: a review and perspective on machine learning technologies applied to smart energy and electric power systems," *International Journal of Energy Research*, vol. 43, no. 6, pp. 1928–1973, 2019.
- [31] O. Dumitrascu, M. Dumitrascu, and D. Dobrotă, "Performance evaluation for a sustainable supply chain management system in the automotive industry using artificial intelligence," *Processes*, vol. 8, no. 11, p. 1384, 2020.
- [32] L. F. Cheng, T. Yu, X. S. Zhang, and B. Yang, "Parallel cyber-physical-social systems based smart energy robotic dispatcher and knowledge automation: concepts, architectures and challenges," *IEEE Intelligent Systems*, vol. 34, no. 2, pp. 54–64, 2019.
- [33] X. Zhang, Z. Xu, T. Yu, B. Yang, and H. Wang, "Optimal mileage based AGC dispatch of a GenCo," *IEEE Transactions on Power Systems*, vol. 35, no. 4, pp. 2516–2526, 2020.
- [34] X. Zhang, T. Tan, B. Zhou, T. Yu, B. Yang, and X. Huang, "Adaptive distributed auction-based algorithm for optimal mileage based AGC dispatch with high participation of renewable energy," *International Journal of Electrical Power & Energy Systems*, vol. 124, Article ID 106371, 2021.
- [35] X. S. Zhang, Q. Li, T. Yu et al., "Consensus transfer Q-learning for decentralized generation command dispatch based on virtual generation tribe," *IEEE Transactions on Smart Grid*, vol. 9, no. 3, pp. 2152–2165, 2018.
- [36] L. Cheng and T. Yu, "Smart dispatching for energy internet with complex cyber-physical-social systems: a parallel dispatch perspective," *International Journal of Energy Research*, vol. 43, no. 8, pp. 3080–3133, 2019.
- [37] Z. Wang, H. Wang, Z. Lin et al., "Modeling of regional electrical heating load characteristics considering user response behavior difference," *International Journal of Electrical Power & Energy Systems*, vol. 123, Article ID 106297, 2020.
- [38] J. Zhao, Z. Wang, T. Yang, J. Xu, Z. Ma, and C. Wang, "Design of a novel modal space sliding mode controller for electro-hydraulic driven multi-dimensional force loading parallel mechanism," *ISA Transactions*, vol. 99, pp. 374–386, 2020.
- [39] S. Lin, X. Lin, Y. Liu et al., "Development of load modeling platform for electric power system," *Electric Power*, vol. 38, no. 11, pp. 87–91, 2005.
- [40] Y. Xie, H. Zhang, C. Li et al., "Development approach of a programmable and open software package for power system frequency response calculation," *Protection Control of Modern Power Systems*, vol. 2, no. 2, pp. 189–198, 2017.
- [41] T. Yu, L. F. Cheng, and X. S. Zhang, "The weakly-centralized Web-of-Cells based on cyber-physical-social systems integration and group machine learning: theoretical investigations and key scientific issues analysis," *Scientia Sinica Technologica*, vol. 49, no. 12, pp. 1541–1569, 2019.
- [42] X. Zhou, J. Tan, and N. Shroff, "Flexible load balancing with multi-dimensional state-space collapse: throughput and heavy-traffic delay optimality," *Performance Evaluation*, vol. 127, pp. 176–193, 2018.
- [43] Y. Ma, Z. Ling, W. Cai, Y. Cui, L. Zhou, and J. Wang, "A novel coast-down no-load characteristic test and curve conversion method for large-scale synchronous condenser," *Electric Power Systems Research*, vol. 172, pp. 77–85, 2019.



## Research Article

# Prediction of Power Outage Quantity of Distribution Network Users under Typhoon Disaster Based on Random Forest and Important Variables

Min Li,<sup>1</sup> Hui Hou ,<sup>2</sup> Jufang Yu ,<sup>2</sup> Hao Geng,<sup>2,3</sup> Ling Zhu,<sup>1</sup> Yong Huang,<sup>4,5</sup> and Xianqiang Li<sup>2</sup>

<sup>1</sup>Guangdong Power Grid Co., LTD., Guangzhou 510080, China

<sup>2</sup>School of Automation, Wuhan University of Technology, Wuhan 430070, China

<sup>3</sup>Electric Power Research Institute, Yunnan Power Grid Co., Ltd., Kunming 650200, China

<sup>4</sup>GuangDong Power GRID Co., Ltd., Electric Power Research Institute, Guangzhou 510080, China

<sup>5</sup>Power Remote Sensing Technology Joint Laboratory of China Southern Power Grid, Guangzhou 510080, China

Correspondence should be addressed to Hui Hou; [hohui@whut.edu.cn](mailto:hohui@whut.edu.cn)

Received 24 November 2020; Revised 22 December 2020; Accepted 28 December 2020; Published 6 January 2021

Academic Editor: Xiao-Shun Zhang

Copyright © 2021 Min Li et al. This is an open access article distributed under the Creative Commons Attribution License, which permits unrestricted use, distribution, and reproduction in any medium, provided the original work is properly cited.

Typhoons can have disastrous effects on power systems. They may lead to a large number of power outages for distribution network users. Therefore, this paper establishes a model to predict the power outage quantity of distribution network users under a typhoon disaster. Firstly, twenty-six explanatory variables (called global variables) covering meteorological factors, geographical factors, and power grid factors are considered as the input variables. On this basis, the correlation between each explanatory variable and response variable is analyzed. Secondly, we established a global variable model to predict the power outage quantity of distribution network users based on Random Forest (RF) algorithm. Then the importance of each explanatory variable is mined to extract the most important variables. To reduce the complexity of the model and ease the burden of data collection, eight variables are eventually selected as important variables. Afterward, we predict the power outage quantity of distribution network users again using the eight important variables. Thirdly, we compare the prediction accuracy of a model called the No-model that has been used before, Linear Regression (LR), Support Vector Regression (SVR), Decision Tree Regression (DTR), RF-global variable model, and RF-important variable model. Simulation results show that the RF-important variable model proposed in this paper has a better effect. Since fewer variables can save prediction time and make the model simplified, it is recommended to use the RF-important variable model.

## 1. Introduction

Typhoon disasters may lead to a large area of power outage for distribution network users. The prediction of the power outage quantity of distribution network users under a typhoon disaster can effectively improve the accuracy of disaster prevention and reduction. It can also shorten the outage time of distribution network users, reduce power outage loss, and improve user satisfaction.

Under typhoon disaster, there are many factors affecting the power outage of distribution network users, including meteorological factors, geographical factors, power grid

factors, and so on [1]. If the traditional model-driven method is used to predict the power outage quantity, the model will be complex and difficult to solve. In addition, with the increase and normalization of power outage data of distribution network users, it is possible to predict power outage quantity of distribution network users using a data-driven method [2, 3].

At present, some scholars have successfully used the data-driven method to assess the risk to power systems under typhoon disasters. Statistical learning models, such as linear model, are firstly applied to evaluate the power outage in hurricane weather in [4]. However, they mainly focused



on the fitting effect of the model, instead of prediction accuracy. The impact of soil and terrain on power outage of distribution network users based on classification and regression trees (CART) is studied in [5]. However, it did not pay attention to the improvement of prediction accuracy. To make the model more comprehensive, many scholars decided to take more influence factors into consideration. Considering the influence factors, such as maximum wind speed, wind speed duration, rainfall, etc., a cumulative time failure model was used to predict the power grid outage under hurricane in [6]. Considering meteorological, geographical, and social information, models of equipment failure rate under natural disasters were established in [7]. On this basis, data-driven methods are widely used to assess the risk to power systems under natural disasters. An ice cover risk assessment model for power systems based on fault tree was proposed in [8]. It involved the effective assessment of transmission line risk, line break, and tower collapse. Based on the relevant public data affecting the power system, prediction models of power outage rate under disasters through data mining were established in [9–11]. In addition, a method for predicting the risk level of power outage in distribution network was presented by [12], which takes into account the weather factors. However, the risk level was classified, while factors such as region were not taken into consideration. Based on support vector machine (SVM) and grey prediction technology, a reliability prediction model for transmission line operation was proposed in [13]. It considered factors such as the running time of components and the region where the components are located. Considering storm, rainstorm, high temperature, and other weather factors comprehensively, a prediction model of the original parameters of a power system based on fuzzy clustering and similarity degree was proposed in [14]. This model considered most climatic factors but did not further evaluate the damage to the power grid.

In order to improve the prediction accuracy, the prediction area was firstly meshed in [15]. To carry out distribution network planning in a scientific and reasonable way, a multistage grid division method for distribution network was proposed [16]. Then, based on geographical grid division, the negative binomial regression model was used to predict the power outages quantity of distribution network users under Hurricane [17]. Based on the data of weather and land cover type, the spatial distribution of power outage in the 2-kilometer grid was predicted by using the Boosted Trees [18]. In addition, the support vector machine was used to predict the number of distribution towers in a 3-kilometer grid [19]. However, due to the large grid division, the eigenvalues of variables in the grid vary to a great extent, resulting in the inaccuracy of the obtained sample data, which affect the final prediction accuracy.

In the light of the aforesaid scenario, this paper proposed a prediction method of power outage quantity of distribution network users based on Random Forest (RF) algorithm. The main innovative contributions of the paper can be summarized as follows:

- (1) A data sample space with twenty-six explanatory variables covering meteorological factors, geographical factors, and power grid factors is constructed. In addition, to better understand the relationship between explanatory variables and response variables, correlation of each explanatory variable and response variable is analyzed.
- (2) To take as many variables into account as possible, we established a RF-global variable model covering all the twenty-six explanatory variables to predict the power outages quantity of distribution network users.
- (3) To accelerate the evaluation efficiency under disasters, the importance of each explanatory variable is mined in this paper. On this basis, we extract eight most important variables to establish a novel RF-important variable model to predict the power outages quantity of distribution network users.
- (4) We compare the prediction accuracy of a model called the No-model that has been used before, Linear Regression (LR), Support Vector Regression (SVR), Decision Tree Regression (DTR), RF-global variable model, and RF-important variable model. The validity and accuracy of the method based on important variable model proposed in this paper is verified. Thus, the RF-important variable model can provide guidance for emergency repair work.

The remainder of this paper is organized as follows.

The framework of the prediction model proposed in this paper is described in Section 2. In Section 3, the data sample space is introduced, and the relationship between each explanatory variable and response variable is analyzed. The RF algorithm we mainly used and the evaluation indicators are described in Section 4. In Section 5, the prediction model based on all the 26 explanatory variables and RF is built. In Section 6, the prediction model based on 8 important explanatory variables and RF is built, and the errors of No-model, LR, SVR, DTR, and the proposed two models are analyzed. Finally, Section 7 is the conclusion.

## 2. Prediction and Evaluation Framework of Power Outage Quantity of Distribution Network Users

The prediction framework of power outage quantity of distribution network users established in this paper is shown in Figure 1.

Firstly, create a data sample space. To consider as much as possible the collectible variables that may have an impact on the results, twenty-six explanatory variables are collected. The explanatory variables include meteorological factors (such as maximum wind speed, wind direction, rainfall, etc.), geographical factors (such as altitude, slope, underlay type, etc.), and power grid factors (such as number of distribution network users, number of box transformers, line

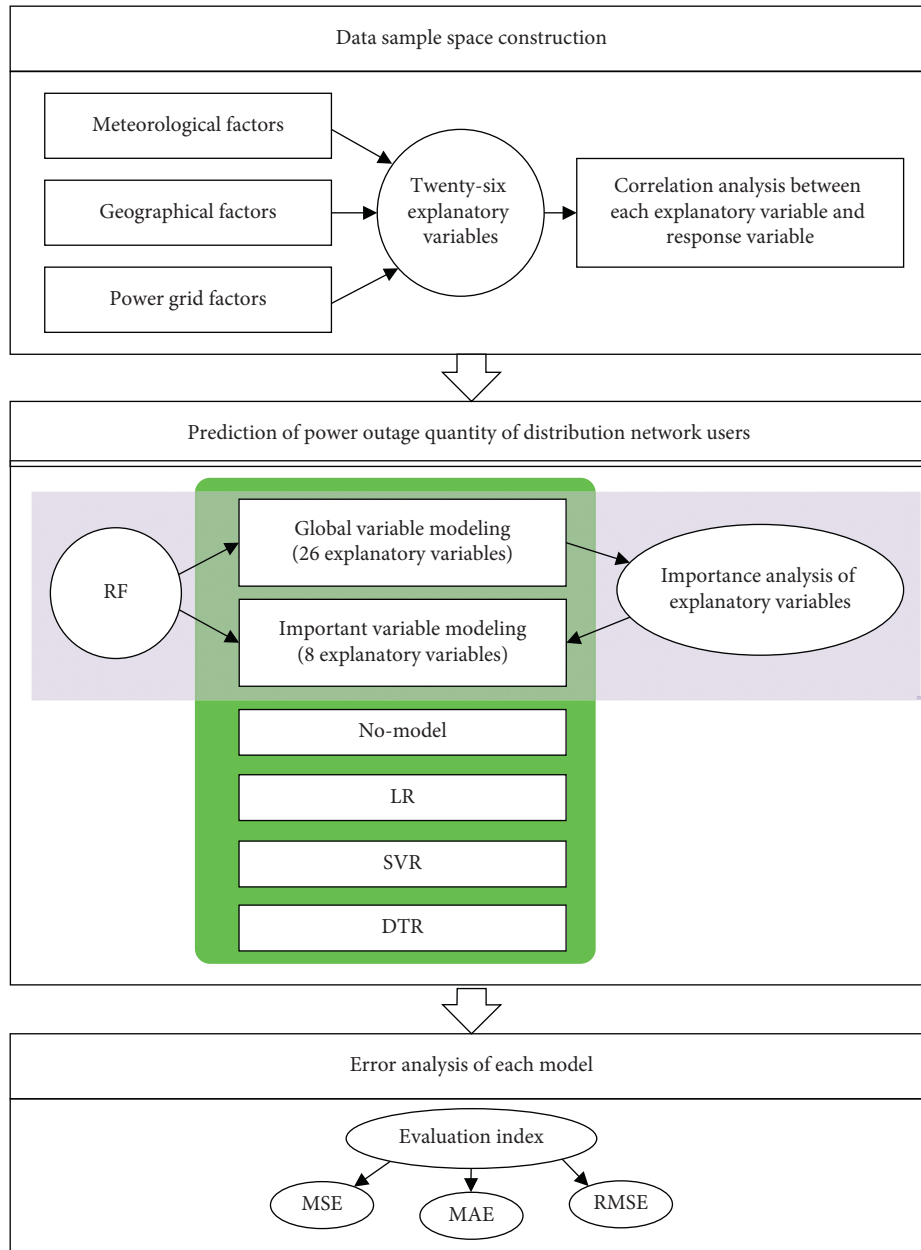


FIGURE 1: The prediction framework of power outage quantity of distribution network users.

length, etc.). Then, the correlation of explanatory variables and response variables are analyzed to mine the relationship of each variable.

Secondly, based on RF, the twenty-six explanatory variables (called global variables in this paper) are used to predict the power outage quantity of distribution network users. To reduce the complexity of the model, this paper analyzes the importance of all explanatory variables. The variables that have the greatest impact on the results are selected as important variables. This paper chose eight explanatory variables as important variables.

Finally, the important variables are used to conduct secondary modeling of power outage quantity prediction of

distribution network users. In order to compare the pros and cons of the prediction results of each model, the results of RF-important variable model are compared with those of traditional No-model, LR, SVR, DTR, and RF-global variable model. Indicators for analyzing model errors include Mean Absolute Error (MAE), Mean Square Error (MSE), and Root Mean Square Error (RMSE).

### 3. Data Sample Space Construction

The power outage quantity of distribution network users under typhoon disaster is affected by many factors.

Therefore, the data of the prediction model is firstly described and the sample data space is constructed.

**3.1. Analysis of Explanatory Variables.** Similar to distribution network users' power outage spatial distribution [1], the factors affecting the power outage quantity of distribution network users under typhoon disaster include meteorological factors, geographical factors, and power grid factors. Among the power grid factors, the failure of the distribution network line mainly refers to the failure of the 10 kV overhead line. The cable is generally laid underground with insulation and protective layers, and its failure has little to do with the impact of typhoons and rainstorms. Therefore, this article only considers the power outage of the distribution network caused by the failure of the 10 kV overhead line exposed to the outdoor environment. In this paper, explanatory variables are added as much as possible to explore the relevant factors affecting the power outages quantity of distribution network users and to improve the accuracy of the prediction model. The selected explanatory variables of the prediction model are shown in Table 1 [20].

This paper establishes the prediction model of the power outage quantity of distribution network users on the basis of the sample data of three historical typhoons (Rammasun in 2014, Kalmaegi in 2014, and Mujigae in 2015) affecting Xuwen county, Guangdong province, China [21–23]. The data are provided by meteorological bureau and Electric Power Research Institute of Guangdong Power Grid Co., Ltd, China. In this paper, the study area is divided into 1641 samples; each sample represents a grid of 1 km × km. The variable  $X_1$  is the maximum wind speed of each grid under the whole typhoon. Based on the regional grid division of 1 km × km, each typhoon produced 1641 samples with a total of 28 characteristic variables. Hence, the size of the entire sample space is  $\Phi = (X, y)_{4923 \times 28}$ . The variables in the meteorological factors and geographical factors are provided in the form of 1 km × 1 km data points. The Inverse Distance Weight Interpolation method is used to transform the data into continuous area data, and then the meteorological information and geographic information is extracted on this basis.

**3.2. Analysis of Response Variable.** In this paper, the power outage quantity of distribution network users under the typhoon disaster is predicted. Therefore, the power outage quantity of distribution network users  $Y_1$  is taken as the response variable. The sample of descriptive statistics on the power outage quantity of distribution network users is shown in Table 2.

As shown in Table 2, the distribution range of the power outage quantity of distribution network users  $Y_1$  is 0~6121. The average predicted outage quantity is 70.51, and the standard deviation is 297.12. Three quartiles of 25%, 50%, and 75% are used to explore the distribution of results. It can be seen that the samples are mainly concentrated in the range of small data values. The probability distribution diagram of the response variable  $Y_1$  is shown in Figure 2. The samples are more concentrated in the range of small

data values. The probability distribution diagram of tc response variable  $Y_1$  is shown in Figure 2.

In order to eliminate the influence of the large coverage of power outage quantity of distribution network users, this paper normalizes this value and converts the response variable into the proportion of power outage. The proportion of power outage  $Y_2$  is equal to the number of power outage users  $Y_1$  divided by the number of distribution network users  $X_{20}$ ,  $Y_2 = Y_1/X_{20}$ . Unless otherwise specified, the following response variables refer to the proportion of power outage  $Y_2$ .

**3.3. Correlation Analysis between Each Explanatory Variable and Response Variable.** In order to intuitively show the relationship between each explanatory variable and response variable  $Y_2$ , the scatter diagram between each explanatory variable and response variable is visualized, as shown in Figure 3.

As can be seen from Figure 3, there is no significant linear relationship between each explanatory variable and response variable, indicating that the effect of linear model will be poor. In order to further explore the relationship between each explanatory variable and response variable, Pearson correlation coefficient is used for quantitative correlation analysis. Assuming the existence of two variables,  $X$  and  $Y$ , the corresponding Pearson correlation coefficient [24] is calculated as follows.

$$r_{xy} = \frac{\text{COV}(X, Y)}{\sqrt{\text{Var}(X) \cdot \text{Var}(Y)}} \quad (1)$$

where COV represents covariance and Var represents variance. If  $|r_{xy}| < 0.4$ , then  $X$  and  $Y$  are weakly correlated; if  $0.4 \leq |r_{xy}| < 0.7$ , then  $X$  and  $Y$  are significantly correlated; if  $0.7 \leq |r_{xy}| < 1$ , then  $X$  and  $Y$  are strongly correlated. The correlation analysis charts of variables are shown in Figures 4 and 5.

As can be seen from Figure 4, among the explanatory variables, there is a strong positive correlation between the distribution network users ( $X_{12}$ ), maximum wind speed ( $X_1$ ), wind speed duration ( $X_6, X_7$ ), rainfall ( $X_3$ ), and the power outage proportion ( $Y_2$ ), while correlation between the other explanatory variables and the power outage proportion is weak.

In order to find out whether there is a correlation among the explanatory variables, the correlation heat map is shown in Figure 5.

As can be seen from Figure 5, there is a strong positive correlation between maximum wind speed ( $X_1$ ) and rainfall ( $X_3$ ), wind speed duration ( $X_6, X_7$ ) and landing area ( $X_{11}$ ). That is, when a typhoon lands in the study area, it will be accompanied by high wind speed and precipitation. And high wind speed makes the wind speed last longer.

## 4. The Prediction Principle of Power Outage Quantity of Distribution Network Users

**4.1. Principle of Random Forest Algorithm.** The main objective of supervised learning is to estimate the unknown

TABLE 1: The explanatory variables of the prediction model.

Factors	Variable name	Symbol	Remarks
Meteorological factors	Maximum wind speed	$X_1$	Maximum wind speed of each grid during a typhoon
	Wind direction	$X_2$	Corresponding wind direction at maximum wind speed
	Rainfall	$X_3$	Cumulative rainfall during a typhoon
	Temperature	$X_4$	Maximum temperature during a typhoon
	Humidity	$X_5$	Average humidity during a typhoon
	Wind speed duration of 20 m/s	$X_6$	Accumulated time when wind speed exceeds 20 m/s during a typhoon
	Wind speed duration of 30 m/s	$X_7$	Accumulated time when wind speed exceeds 20 m/s during a typhoon
	Wind class	$X_8$	Typhoon landing force
	Ten-level wind circle radius	$X_9$	Typhoon class 10 wind circle radius
	Landing time	$X_{10}$	Time interval from the last typhoon landing, in months
	Landing area	$X_{11}$	Indicator variable; if it is logged in the study area, it will be recorded as 1, otherwise it will be recorded as 0
Geographical factors	Whether there are distribution users	$X_{12}$	Indicating variable; the existence of distribution network users is recorded as 1, otherwise it is recorded as 0
	Altitude	$X_{13}$	/
	Slope	$X_{14}$	/
	Slope direction	$X_{15}$	/
	Underlay type	$X_{16}$	/
	Surface type	$X_{17}$	/
	Longitude	$X_{18}$	Longitude of grid center (LON)
	Latitude	$X_{19}$	Latitude of grid center (LAT)
Power grid factors	Number of distribution network users	$X_{20}$	Number of distribution network users in the grid
	Number of box transformers	$X_{21}$	Number of box transformers in the grid
	Number of desktop transformers	$X_{22}$	Number of desktop transformers in the grid
	Number of power towers	$X_{23}$	Number of 10 kV pole towers in the grid
	Number of pulling-line	$X_{24}$	/
	Number without pulling-line	$X_{25}$	/
	Line length	$X_{26}$	10 kV line length in the grid
	The power outage quantity of distribution network users	$Y_1$	Response variable
Power outage proportion	$Y_2$	The ratio between the number of distribution network users' power outages and the number of distribution network users (response variable)	

TABLE 2: Descriptive statistics of response variable.

	Mean	Std	Min	25%	50%	75%	Max
$Y_1$	70.51	297.12	0	0	0	18	6121

function  $f$  of the prediction variable  $Y$  (such as the power outage quantity) by using the  $d$ -dimensional vector of relevant input  $X$  (such as meteorological features, geographical features, and power grid features). For example,  $Y = f(X) + e$ , and  $e$  is the irremediable error. By minimizing the loss function  $L$  that represents the deviation between the observed value and the predicted value, the best unknown function  $f$  can be selected to make the prediction work best. This is the idea of supervised regression learning algorithm.

Random Forest (RF) is a nonparametric integrated data mining algorithm based on tree. Unlike a single regression tree with high variance and low bias, RF overcomes the problem of high variance by using model average. In addition, when the number of input variables is large, RF has better precision than other classical machine learning algorithms [7]. Hence, this paper establishes a prediction model for the power outage quantity of distribution network users based on the RF algorithm. The final RF output

estimate is the predicted average of all the trees, expressed as follows:

$$f_{rf}(x) = \frac{1}{M} \sum_{m=1}^M T_m(x), \quad (2)$$

where  $M$  is the number of regression trees in RF, and  $T_m(x)$  represents the model constructed by the  $m$ -th regression tree. The advantage of this method is that it can capture the nonlinear structure of data well, and it is robust to outliers and noise with a strong prediction accuracy.

**4.2. The Evaluation Indicators.** After the construction of the prediction model for the power outage quantity of distribution network users under typhoon disaster, it is necessary to evaluate the advantages and disadvantages of the model. In this paper, the evaluation indexes of the regression model are Mean Absolute Error (MAE), Mean Square Error (MSE), and Root Mean Square Error (RMSE). Suppose the data set is  $\{(x_i, y_i), i = 1, 2, \dots, n\}$ , and the prediction regression function is  $f(x)$ , then the various error expressions are as follows:

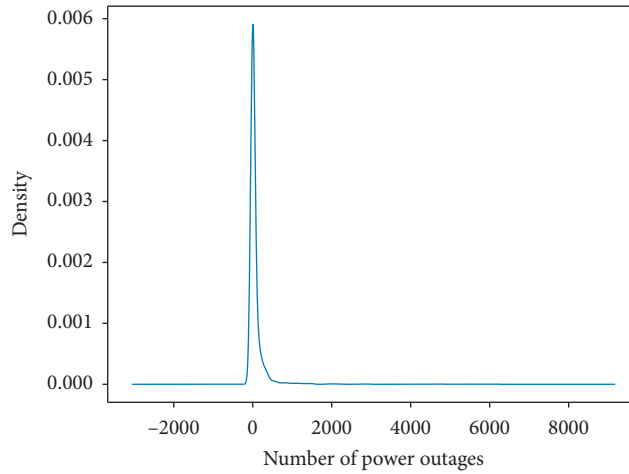


FIGURE 2: The probability distribution diagram of response variable.

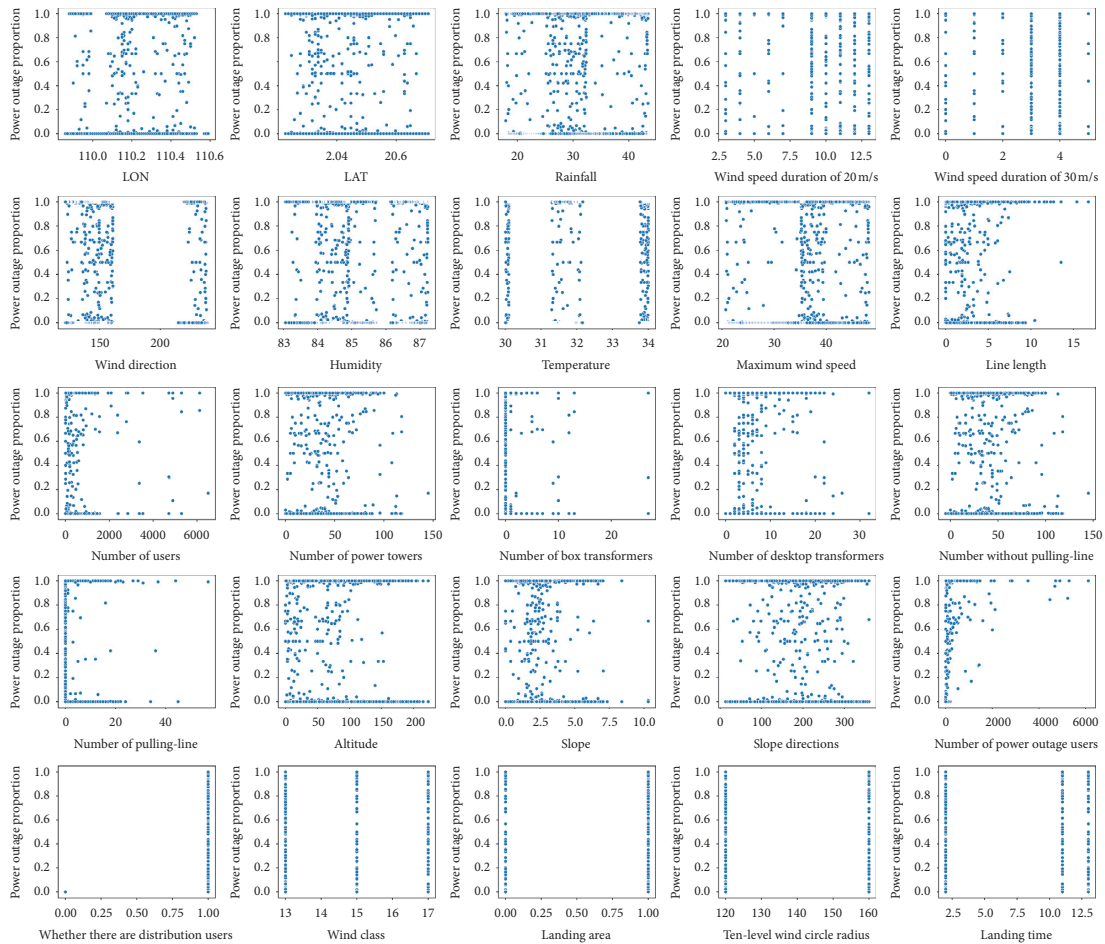


FIGURE 3: The scatter diagram between each explanatory variable and response variable.



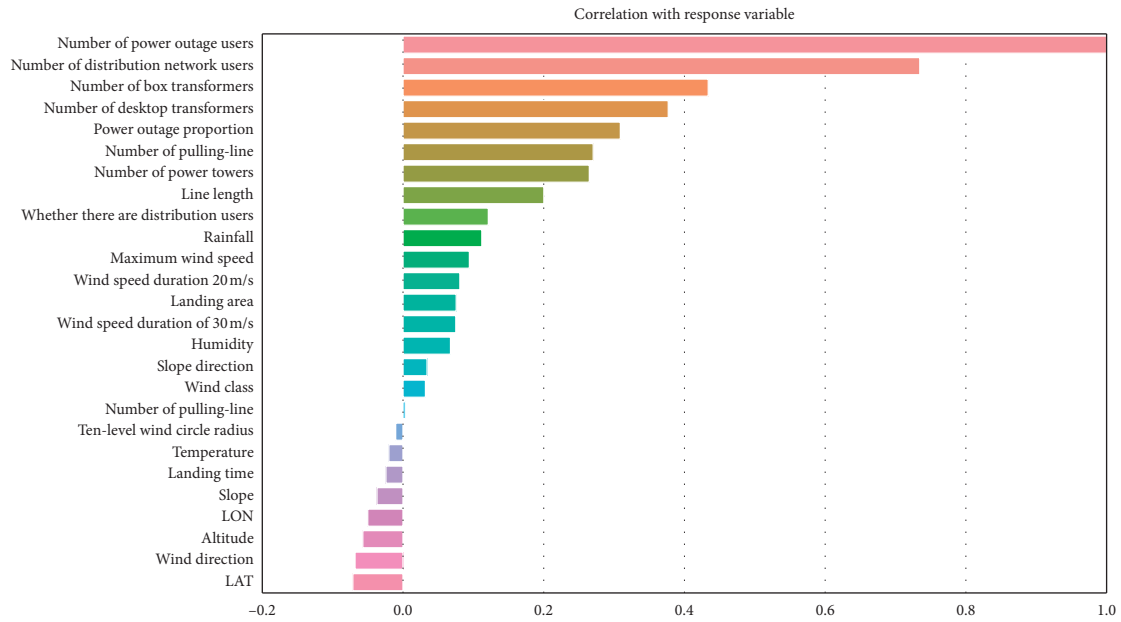


FIGURE 4: Correlation analysis of explanatory variables and response variables.

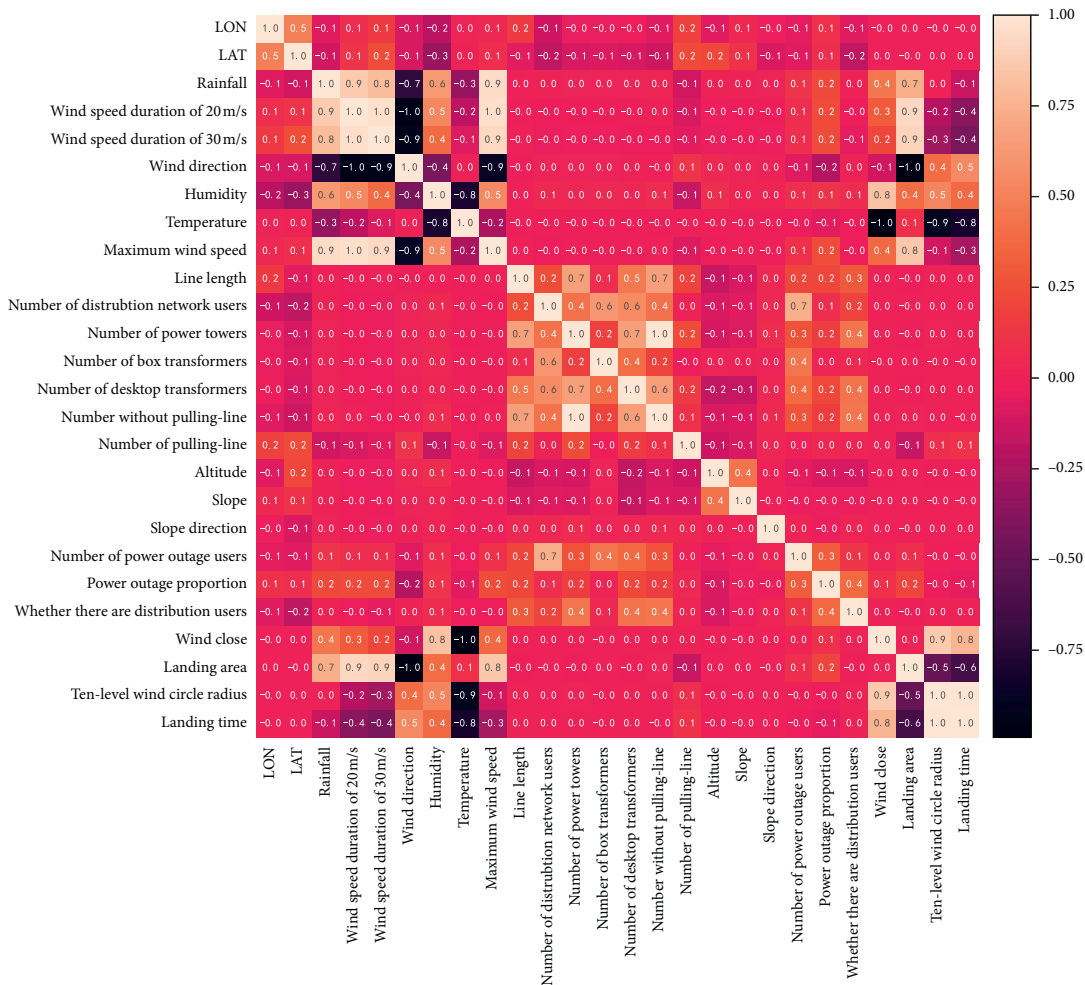


FIGURE 5: Correlation analysis among explanatory variables.



$$\begin{aligned}
MAE &= \frac{1}{n} \sum_{i=1}^n |y_i - f(x_i)|, \\
MSE &= \frac{1}{n} \sum_{i=1}^n (y_i - f(x_i))^2, \\
RMSE &= \sqrt{\frac{1}{n} \sum_{i=1}^n (y_i - f(x_i))^2}.
\end{aligned} \tag{3}$$

In this paper,  $y_i$  represents the actual power outage quantity of distribution network users in  $i$ -th grid, and  $f(x_i)$  represents the predicted power outage quantity of distribution network users in the  $i$ -th grid.

## 5. RF-Global Variable Modeling and Analysis

In order to as far as possible explore the potential relationship between each explanatory variable and response variable, the global variables (all explanatory variables) are used in this section, and the importance of variables is analyzed to identify the contribution of variables in the prediction model.

**5.1. Analysis of Prediction Results.** Firstly, 80% samples are randomly selected from the sample data for model training, and the remaining 20% samples are conducted for model test. Then, it is recycled 100 times. At last, the average values of MAE, MSE, and RMSE are obtained, as shown in Table 3.

As shown in Table 3, the prediction model of the power outage quantity is constructed with the proportion of power outage as the response variable. The MAE, MSE, and RMSE in the test errors are up to 0.1497, 0.0613, and 0.2474, respectively. To intuitively reflect the prediction effect, new model evaluation indexes  $\pm 100/\pm 200/\pm 300$  (if the deviation between the predicted quantity and the actual quantity is within 100/200/300, the prediction is considered accurate) and  $\pm 10\%/\pm 20\%/\pm 30\%$  (if the proportion of the deviation between the predicted quantity and the actual quantity is within  $\pm 10\%/\pm 20\%/\pm 30\%$ , the prediction is considered accurate) are added. The accuracy analysis of the power outage quantity prediction model is shown in Table 4.

As shown in Table 4, the accuracy rate of prediction error within  $\pm 100/\pm 200/\pm 300$  is higher than 90%. However, considering the small number of users of distribution network in most actual grids, evaluating the model with a fixed error may overestimate the predictive effect of the model. Therefore, the evaluation index  $\pm 10\%/\pm 20\%/\pm 30\%$  based on floating error is constructed, in which the accuracy of the error within  $\pm 10\%$  is 0.7546, within  $\pm 20\%$  is 0.8320, and within  $\pm 30\%$  is 0.8660. As can be seen from Tables 3 and 4, the prediction method of power outage quantity of distribution network users based on RF proposed in this paper has better performance.

**5.2. Assessment of Variable Importance.** As many explanatory variables as possible were selected in the early stage of

TABLE 3: Training and test error analysis.

Evaluation index	MAE	MSE	RMSE
Training set	0.0550	0.0083	0.0913
Test set	0.1497	0.0613	0.2474

TABLE 4: Model accuracy analysis.

Evaluation index	$\pm 100$	$\pm 200$	$\pm 300$	$\pm 10\%$	$\pm 20\%$	$\pm 30\%$
Accuracy	0.9279	0.9706	0.9831	0.7546	0.8320	0.8660

modeling. However, this may lead to a large workload of data collection and processing in the actual application of the model. In order to evaluate the contribution of each explanatory variable in the prediction model and reduce the pressure of data collection, the importance of explanatory variables is evaluated.

In the RF model, the importance ranking is calculated based on the degree of chaos (Impurity/Gini coefficient). That is to say, the criterion to measure the importance of a feature is to see how much chaos the feature reduces in the process of building a random forest through the decision tree [25]. After synthesizing all the trees, the greater the average decrease is determined as the more important feature. But the problem is that when features are continuous or there are many categories of classification factors (High-cardinality category variables), the method of feature importance analysis mentioned above will increase the importance of these features. Thus, the Permutation Importance Measure is used in this paper to solve this problem. The specific method of variable importance evaluation based on RF is as follows:

- (1) The original accuracy of test data or OOB (out of bag) data in random forest (such as the OOB data error, denoted as  $err_{OOB1}$ ) is taken as an accuracy baseline.
- (2) One of the features that need to be measured is permuted; that is, scrambling the data and rearranging them. Then run the model again with the test data (the same data set) to calculate the new accuracy rate, denoted as  $err_{OOB2}$ .
- (3) Calculate the difference between the new accuracy and the baseline accuracy. The larger the difference, the more important the feature is. Assuming that there are  $n$  trees in RF, the importance of the characteristic is  $1/n \sum (err_{OOB2} - err_{OOB1})$ .

In this process, the data do not need to be standardized, and the final importance ranking is not 1 but a relative ranking.

The importance analysis diagram of global variables is shown in Figure 6.

As can be seen from Figure 6, the explanatory variables such as longitude, latitude, maximum wind speed, wind direction, rainfall, number of users of distribution network, line length, and altitude contribute greatly to the accuracy of the prediction model. However, the explanatory variables such as landing time, landing area (whether landing in the

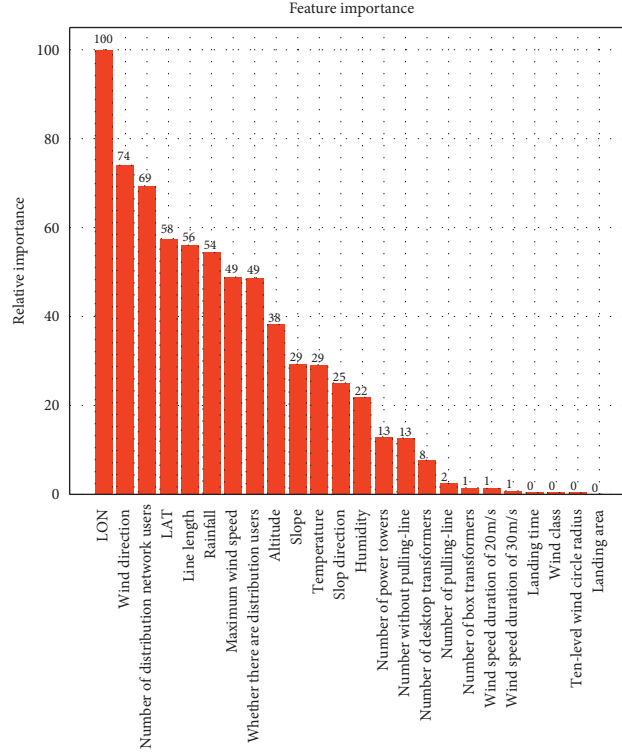


FIGURE 6: The importance analysis diagram of global variables.

research area), and wind level contributed little to the accuracy of the prediction model. Therefore, this paper focuses on the analysis of the variables that contribute a lot to the prediction model, and analyzes their impact on the power outage quantity of distribution network users. On this basis, the variation in the accuracy of the RF-important variable model and the RF-global variable model is analyzed.

**5.3. Variable Dependency Analysis.** The classical Partial Dependence Plots (PDP) [26] help visualize the average relationship between the response variable and one or more of the characteristics. When a specified characteristic changes in its marginal distribution, the PDP plots change in the average predicted value. With the help of the PDP, the trained supervised learning model can be better understood.

In order to formally define the PDP, let  $S \subset \{1, \dots, p\}$ ,  $C$  be the complement of  $S$ , and  $S \cup C = m$ . And  $m$  is the set of all characteristics. Then, the partially dependent function  $f$  of the partial characteristics set  $x_S$  is as follows:

$$f_S = E_{x_C} [f(x_S, x_C)] = \int f(x_S, x_C) dP(x_C). \quad (4)$$

Since  $f$  and  $dP(x_C)$  are unknown, equation (4) can be estimated by the following equation:

$$\hat{f}_S = \frac{1}{n} \sum_{i=1}^n \hat{f}(x_S, x_{C_i}), \quad (5)$$

where,  $n$  is the number of samples of the training set,  $\{x_{C_1}, \dots, x_{C_n}\}$  represents different values of the characteristic set  $x_C$  of the training set. When the characteristic set  $x_S$

contains only one characteristic variable  $x_j$ ,  $j = 1, 2, \dots, m$ , the partial dependency function of  $x_j$  is:

$$\hat{f}_j(x_j) = \frac{1}{n} \sum_{i=1}^n \hat{f}_j(x_j, x_{-j,i}), \quad (6)$$

where, the PDP value  $\hat{f}_j(x_j)$  of the characteristic variable  $x_j$  represents the average value of the output value of the regression prediction function when  $x_j$  is fixed and changes along its marginal distribution.

To analyze the impact of the characteristics of variables on the response variable, this paper analyses the nine most important explanatory variables for modeling (longitude  $X_{18}$ , latitude  $X_{19}$ , number of distribution network users  $X_{20}$ , maximum wind speed  $X_1$ , rainfall  $X_3$ , line length  $X_{26}$ , whether there are distribution users  $X_{12}$ , wind direction  $X_2$ , and altitude  $X_{13}$ .) based on variable importance analysis. The partial dependency is shown in Figure 7.

It can be seen from Figure 7 that the longitude and latitude have a positive influence on power outage of distribution network users; that is, the increase of longitude and latitude leads to an increase in its influence on distribution network users. The main reason may be that the region mentioned in this paper is a coastal region. The closer a region is to the sea, the stronger the typhoon attacks on its distribution network users, and the more serious the impact. However, the dependence of the model on the number of distribution network users is not obvious and the influence is relatively stable. Moreover, the greater the maximum wind speed and rainfall of a typhoon, the greater the impact of the typhoon on distribution network users. In the geographic

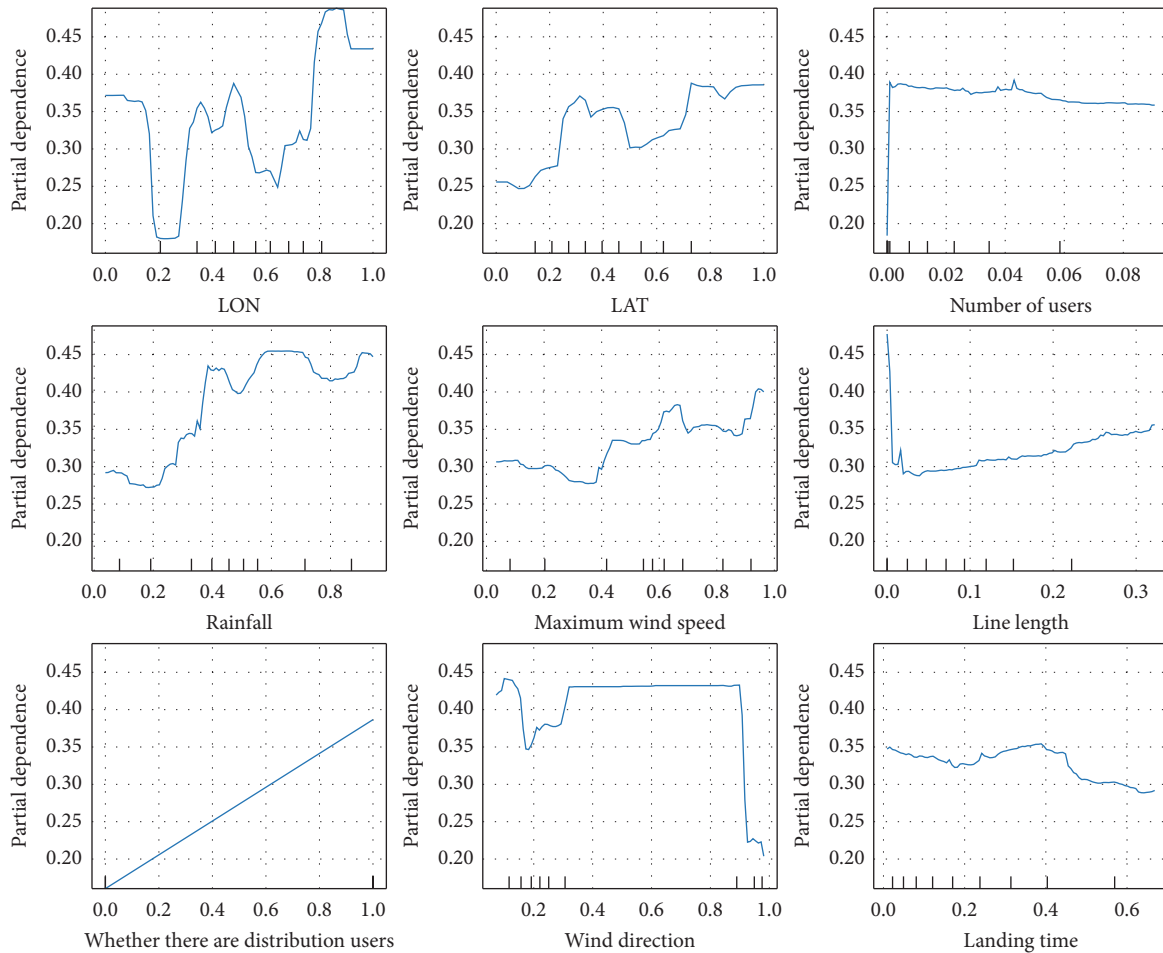


FIGURE 7: The PDP of explanatory variables.

information, the influence of altitude on power outage of distribution network users is negatively correlated; that is, the higher the altitude in the region, the smaller the influence on power outage of distribution network users, which is consistent with the influence trend of longitude and latitude. As for the line length, its influence is positively correlated with the increase of the line length. The longer the line length, the higher the probability of power outage of distribution network users will be. For classification variables with or without distribution network users, there is a relatively obvious positive correlation, because only if there are distribution network users in the grid, the distribution network users may have a power outage accident under the typhoon disaster. For the wind direction, there is no obvious correlation shown in the PDP chart. The main reason may be that the wind direction data changes rapidly and the model is not able to capture its performance characteristics. Besides, the wind direction is not a constant value under a typhoon disaster; it is difficult to select an appropriate quantitative

description. Thus, we decided not to take it as one of the values in RF-important variable model.

Since longitude and latitude, wind speed and direction, wind speed and rainfall often occur simultaneously, the characteristic dependence of the two variables of these combinations is analyzed, as shown in Figures 8–10.

As shown in Figure 8, the combination of longitude and latitude can locate an area. When the longitude is large and the latitude is small, it has a greater impact on power outage of distribution network users. The region is located in the southeast corner of the study area, closer to the landfall area of the typhoon.

In general, high wind speed tends to bring rain and aggravate the impact on power distribution network users. As shown in Figure 9, the greater the wind speed and greater the rainfall, the greater the impact on power distribution network users.

As shown in Figure 10, there is no obvious correlation between wind direction and power outage of distribution

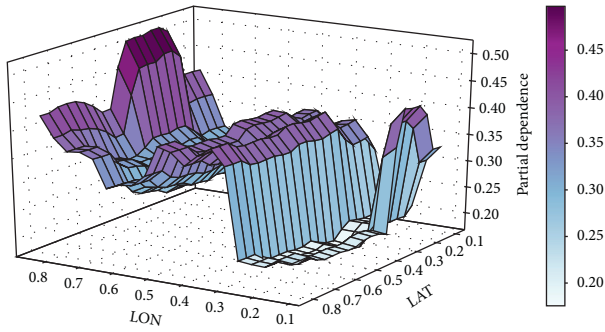


FIGURE 8: The combination of longitude and latitude.

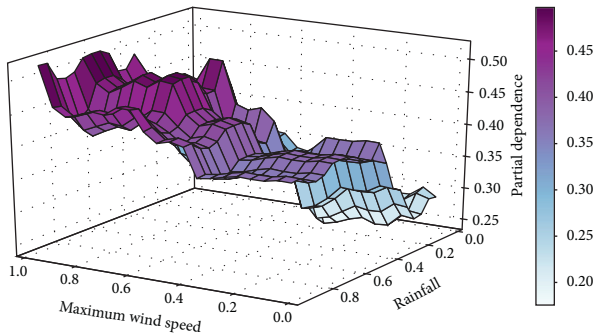


FIGURE 9: The PDP of max wind and rainfall.

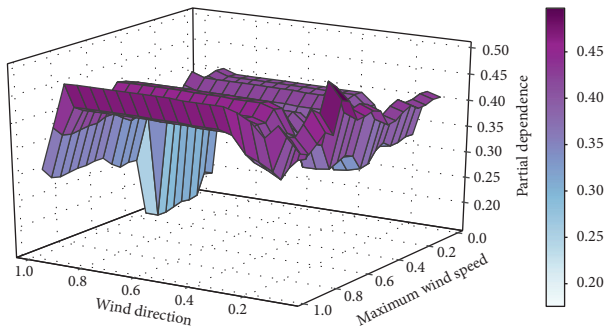


FIGURE 10: The PDP of max wind and wind direction.

network users. It shows that the wind direction has little influence on the power outage of users, so it can be removed. In addition, the higher the wind speed, the greater the probability of power outage for distribution network users.

### 6. Analysis of Modeling Important Variables

In Section 5, global variables are used for modeling, and the prediction results of power outage quantity of distribution network users are evaluated and analyzed. Based on historical data, more explanatory variables could be mined to support the accuracy of power outage quantity prediction. However, in reality, some explanatory variables are difficult to obtain, such as wind speed duration of 20 m/s and 30 m/s. In addition, many variables contribute little to prediction accuracy. Therefore, this section analyzes and compares the

prediction accuracy of models considering global variables and important variables, so as to increase the efficiency and availability of the model.

**6.1. Model Training Test Analysis.** According to the analysis results of the above section, in this section, the eight explanatory variables that are most important to the predicted results are selected as explanatory variables to carry out the training of power outage quantity prediction model: longitude  $X_{18}$ , latitude  $X_{19}$ , maximum wind speed  $X_1$ , rainfall  $X_3$ , distribution network user  $X_{20}$ , line length  $X_{26}$ , whether there are distribution users  $X_{12}$ , and altitude  $X_{13}$ . For all the samples, 80% are randomly selected as the training set and the remaining 20% as the test set, with random recycling for 100 times. The error results of the training test are shown in Table 5. The accuracy of the change of the evaluation index is shown in Table 6.

It can be seen from Table 5 that the test set MAE is 0.1366, MSE is 0.0580, and RMSE is 0.2406 for modeling analysis with important characteristic variables, and the overall prediction effect is good. The prediction accuracy of the model calculated when changing the evaluation index is shown in Table 6.

Table 6 shows that eight important variables are used for prediction model training; the accuracy of 100/ $\pm 200/\pm 300$  reaches 0.9346, 0.9706, 0.9852, and the accuracy of  $\pm 10\%/\pm 20\%/\pm 30\%$  is 0.7582, 0.8345, and 0.8822, respectively. The prediction accuracy of the model is close to that of the RF-global variable model, indicating that building a prediction model with less important variables does not significantly reduce the accuracy of the model but makes the process of predicting and evaluating the power outage quantity simpler and faster (saving time for collecting and sorting out the remaining variables). Furthermore, it accelerates the assessment of the power outage quantity of distribution network users under the typhoon disaster and prepares the conditions for further emergency decision-making. It can be seen from Figure 11 that, except for a few points, the difference between the actual value and the predicted value of most points is around 0. It indicates that the fitting data of the user outage number prediction model of the distribution network is good.

**6.2. Comparative Analysis of Models.** In order to further analyze the model built based on important variables in this paper, a No-model [27] and three other machine learning algorithms are used to compare with the trained RF model based on global variables and important variables, as shown in Table 7. The average values of the samples are used as the prediction value in No-model, LR, SVR, and DTR. At the same time, in order to visually demonstrate the prediction effect of each model, a histogram of the error analysis of each model is shown in Figure 12.

Table 7 and Figure 12 show that the prediction model of power outage quantity of distribution network users based on RF in this paper has a better prediction effect. Whether based on global variables or import variables, its MAE, MSE, and RMSE are all smaller than that of the other three

TABLE 5: Partial variable training and testing errors.

Evaluation index	MAE	MSE	RMSE
Training set	0.0503	0.0080	0.0892
Test set	0.1366	0.0580	0.2406

TABLE 6: Model accuracy analysis.

Evaluation index	$\pm 100$	$\pm 200$	$\pm 300$	$\pm 10\%$	$\pm 20\%$	$\pm 30\%$
Accuracy	0.9346	0.9706	0.9852	0.7582	0.8345	0.8822

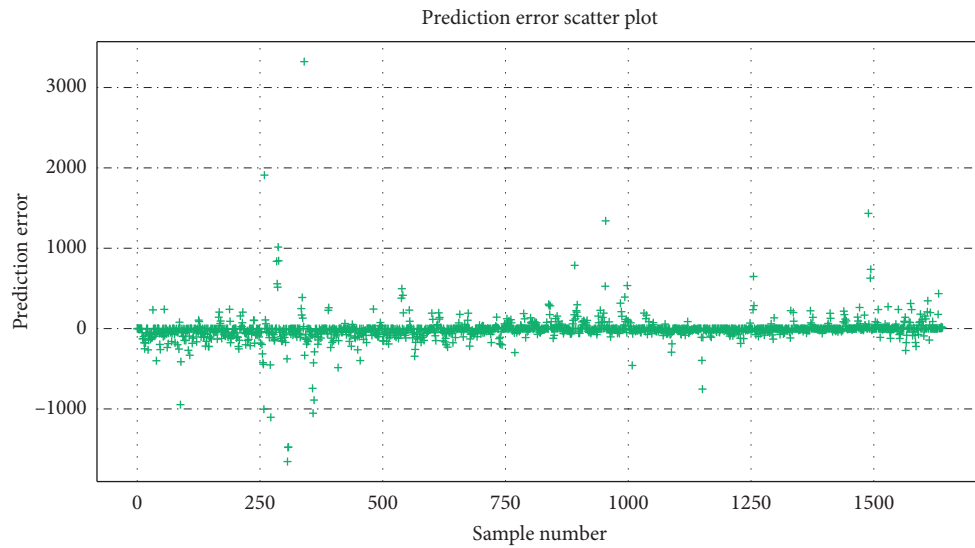


FIGURE 11: Scatter distribution of prediction error.

TABLE 7: Comparative analysis of six models.

Evaluation index	MAE	MSE	RMSE
No-model	0.436	0.215	0.464
LR	0.352	0.160	0.400
SVR	0.235	0.117	0.342
DTR	0.174	0.112	0.334
RF-global variables	0.150	0.061	0.247
RF-important variables	0.137	0.058	0.241

machine learning models and the No-model. Among them, the RF algorithm has the best effect, followed by DTR, SVR, LR, and the No-model. Compared with the No-model, MAE of the RF-global variable model decreased by 66%, MSE by 72%, and RMSE by 47% on average, which shows the effectiveness of the RF-global variable model trained in this paper. And, compared with the RF-global variable model, MAE of RF-important variable model (only eight variables are considered) was reduced by 8.8%, MSE by 18.4%, and RMSE by 2.7% on average, showing that the error based on the important variables is smaller than that based on the global variables. The main reason is that during the RF-

global variable modeling, more explanatory variables with strong correlation are introduced, leading to certain deviation of the trained prediction model.

To sum up, the prediction model of power outage quantity based on RF has a good effect. The errors of both RF-global variable model and RF-important variable model are lower than that of No-model, LR, SVR, and DTR. Meanwhile, the effect of RF-global variable model is close to that of RF-important variable model, and the prediction effect of RF-important variable model is better. Moreover, it takes less time to collect and sort out the original data of important variables. This improves the efficiency of



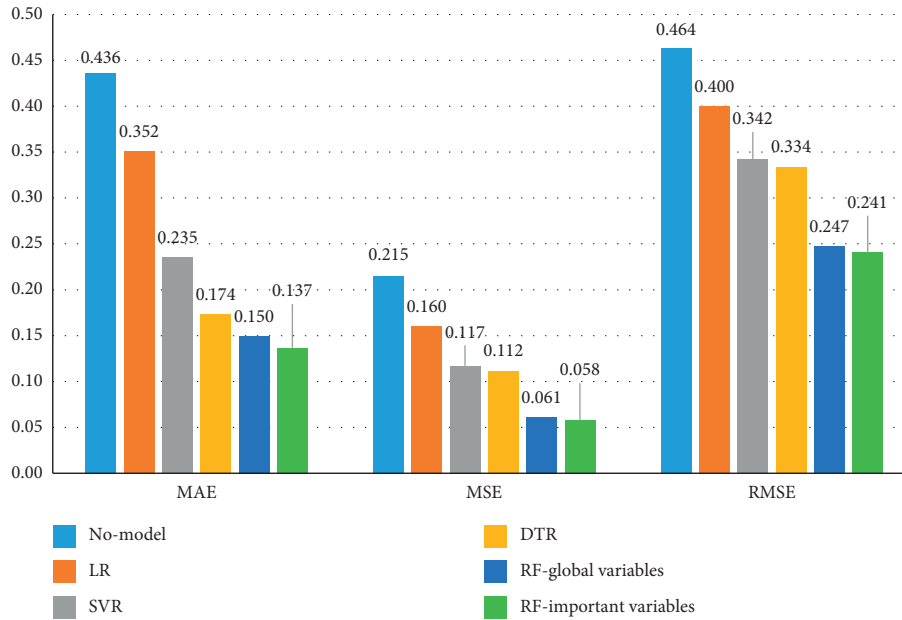


FIGURE 12: Error analysis of each model.

prediction and evaluation, and provides an effective basis for the early allocation of emergency repair resources, the reduction of power outage loss, and the improvement of distribution network user satisfaction.

## 7. Conclusion

In this paper, the prediction and evaluation method of power outage quantity of distribution network users under typhoon disaster is studied, and the prediction model of power outage quantity of distribution network users based on RF is proposed.

- (1) In order to make the evaluation process more convenient, this paper selects the eight most important explanatory variables for model training. The results show that the model errors do not increase seriously but decrease slightly, providing auxiliary guidance for rapid prediction.
- (2) The prediction and evaluation with the important variable model based on RF reduces the time spent collecting and processing other variables and improves the prediction efficiency of the power outage quantity of distribution network users.
- (3) Compared with the No-model, LR, SVR, and DTR, it is found that the RF-global variable model and RF-important variable model trained in this paper are better, and their MAE, MSE, and RMSE are significantly reduced. And the prediction effect of the RF-important variable model is slightly better than that of the RF-global variable model, which can provide an effective basis for disaster prevention and reduction of power grid.
- (4) In the actual application process, the predicted maximum gust wind speed of 72 hours, 48 hours,

and 24 hours before typhoon landing can be used as model inputs, respectively. The prediction results can provide some guidance for the formulation of pre disaster emergency dispatching strategy.

## Data Availability

The datasets used or analyzed during the current study are available from the authors upon reasonable request.

## Conflicts of Interest

The authors declare that they have no conflicts of interest.

## Acknowledgments

This research was funded by the University-Industry Collaborative Education Program of the Ministry of Education (grant no. 201902056044) and Guangdong Power GRID Co., Ltd., Electric Power Research Institute (grant no. GDKJXM20198382).

## References

- [1] H. Hui, G. Hao, X. Xiang et al., "Prediction and evaluation of outage area of distribution network users under Typhoon Disaster," *Power System Technology*, vol. 43, no. 06, pp. 1948–1954, 2019.
- [2] L. Xi, J. Wu, Y. Xu, and H. Sun, "Automatic generation control based on multiple neural networks with actor-critic strategy," *IEEE Transactions on Neural Networks and Learning Systems*, vol. 99, pp. 1–11, 2020.
- [3] L. Xi, L. Yu, Y. Xu, S. Wang, and X. Chen, "A novel multi-agent DDQN-AD method-based distributed strategy for automatic generation control of integrated energy systems," *IEEE Transactions on Sustainable Energy*, vol. 11, no. 4, pp. 2417–2426, 2020.



- [4] H. Liu, R. A. Davidson, and T. V. Apanasovich, "Spatial generalized linear mixed models of electric power outages due to hurricanes and ice storms," *Reliability Engineering & System Safety*, vol. 93, no. 6, pp. 897–912, 2008.
- [5] S. M. Quiring, L. Zhu, and S. D. Guikema, "Importance of soil and elevation characteristics for modeling hurricane-induced power outages," *Natural Hazards*, vol. 58, no. 1, pp. 365–390, 2011.
- [6] H. Liu, R. A. Davidson, and T. V. Apanasovich, "Statistical forecasting of electric power restoration times in hurricanes and ice storms," *IEEE Transactions on Power Systems*, vol. 22, no. 4, pp. 2270–2279, 2007.
- [7] H. Hui, Y. Shiwen, W. Hongbin et al., "Risk assessment and its visualization of power tower under typhoon disaster based on machine learning algorithms," *Energies*, vol. 12, no. 2, pp. 1–23, 2019.
- [8] T. B. Gutwin, "Application of BCTC standardized risk estimation model to assess risk due to ice storms," in *Proceedings of the 8th International Conference On Probabilistic Methods Applied To Power Systems*, pp. 970–974, Ames, Iowa, USA, September 2004.
- [9] S. D. Guikema, R. Nateghi, S. M. Quiring, A. Staid, A. C. Reilly, and M. Gao, "Predicting hurricane power outages to support storm response planning," *IEEE Access*, vol. 2, pp. 1364–1373, 2014.
- [10] S. D. Guikema and S. M. Quiring, "Hybrid data mining-regression for infrastructure risk assessment based on zero-inflated data," *Reliability Engineering & System Safety*, vol. 99, pp. 178–182, 2012.
- [11] D. T. Radmer, P. A. Kuntz, R. D. Christie, S. S. Venkata, and R. H. Fletcher, "Predicting vegetation-related failure rates for overhead distribution feeders," *IEEE Transactions on Power Delivery*, vol. 17, no. 4, pp. 1170–1175, 2002.
- [12] Z. Wen, S. Wanxing, L. Kexue et al., "Prediction method of distribution network fault risk level considering weather factors," *Power System Technology*, vol. 42, no. 08, pp. 2391–2398, 2018.
- [13] Z. Qingqing, Y. Zheng, J. Yanbing et al., "Reliability prediction of transmission line operation," *Automation of Electric Power Systems*, vol. 34, no. 24, pp. 18–22, 2010.
- [14] Z. Yongjun, C. Chao, and X. Liang, "Estimation of original parameters of power system reliability based on fuzzy clustering and similarity," *Power System Protection and Control*, vol. 39, no. 8, pp. 1–5, 2011.
- [15] C. Bin, S. Shengwen, H. Haikun et al., "Research progress on early warning technology of transmission and distribution lines against strong typhoon in coastal areas," *High Voltage Appliances*, vol. 54, no. 07, pp. 64–72, 2018.
- [16] X. Juqin, Z. Linyao, W. Guilian et al., "Multilevel grid division of urban distribution network based on hierarchical spatial reasoning," *Science and Technology Bulletin*, vol. 36, no. 02, pp. 55–58, 2020.
- [17] L. Haibin, R. A. Davidson, D. V. Rosowsky et al., "Negative binomial regression of electric power outages in hurricanes," *Journal of Infrastructure Systems*, vol. 11, no. 4, pp. 258–267, 2005.
- [18] D. W. Wanik, E. N. Anagnostou, B. M. Hartman, M. E. B. Frediani, and M. Astitha, "Storm outage modeling for an electric distribution network in Northeastern USA," *Natural Hazards*, vol. 79, no. 2, pp. 1359–1384, 2015.
- [19] Z. Linming, S. Shengwen, C. Bin et al., "Prediction method of 10 kV tower damage based on lattice and support vector machine in strong typhoon environment," *High Voltage Technology*, vol. 46, no. 01, pp. 42–51, 2020.
- [20] H. Hui, Y. Jufang, G. Hao et al., "Data-driven prediction for the number of distribution network users experiencing typhoon power outages," *IET Generation, Transmission & Distribution*, vol. 14, no. 24, pp. 5844–5850, 2020.
- [21] Electric Power Research Institute, *Analysis Report of 'Rammasun*, Guangdong Power Grid Co., Ltd., Guangdong, China, 2014.
- [22] Electric Power Research Institute, *Analysis Report of 'Kalmaegi*, Guangdong Power Grid Co., Ltd., Guangdong, China, 2014.
- [23] Electric Power Research Institute, *Analysis Report of 'Mujigae*, Guangdong Power Grid Co., Ltd., Guangdong, China, 2015.
- [24] Z. Hailong, Z. Dandan, H. song et al., "Analysis of the relationship between lightning flash density and lightning stroke fault in Hainan Province Based on Pearson correlation coefficient," *High Voltage Appliances*, vol. 55, no. 08, pp. 186–192, 2019.
- [25] C. Bihan, *Research on Variable Selection in Data Mining*, Huazhong University of science and technology, Wuhan, China, 2018.
- [26] A. Goldstein, A. Kapelner, J. Bleich, and E. Pitkin, "Peeking inside the black box: visualizing statistical learning with plots of individual conditional expectation," *Journal of Computational and Graphical Statistics*, vol. 24, no. 1, pp. 44–65, 2015.
- [27] R. Nateghi, S. D. Guikema, and S. M. Quiring, "Comparison and validation of statistical methods for predicting power outage durations in the event of hurricanes," *Risk Analysis*, vol. 31, no. 12, pp. 1897–1906, 2011.

## Research Article

# Probabilistic Chronological Production Simulation-Based Coordinated Dispatching for Cascaded Hydro-PV-PSH Combined Power Generation System

Shuai Zhang , Jingxian Yang , Hongjun Gao , Jichun Liu , and Junyong Liu 

College of Electrical Engineering, Sichuan University, Chengdu, China

Correspondence should be addressed to Jichun Liu; [jichunliu@scu.edu.cn](mailto:jichunliu@scu.edu.cn)

Received 15 November 2020; Revised 2 December 2020; Accepted 11 December 2020; Published 30 December 2020

Academic Editor: Xiao-Shun Zhang

Copyright © 2020 Shuai Zhang et al. This is an open access article distributed under the Creative Commons Attribution License, which permits unrestricted use, distribution, and reproduction in any medium, provided the original work is properly cited.

The comprehensive and effective utilization of multiple renewable sources involving water, solar, and other energies have been receiving more and more attention, and the coordinated dispatching considering multiple uncertainties has become one of the research focuses currently. To cope with the stochastic dispatching of cascaded hydro-PV-PSH (pumped storage hydropower, PSH) complementary power generation system, this paper has proposed a two-stage optimized dispatching method combining uncertainties simulation and complementary dispatching schemes optimization. Firstly, a modified PCPS (probabilistic chronological production simulation) method is proposed to simulate the uncertain power output of each energy type, and thus the complementary dispatching schemes and performance parameters are obtained. In the simulation process, a special treatment method combining overall uncertainties, overall dispatching measures, and interstage distribution for cascaded hydropower stations is given out. Secondly, a dual-objective optimized model considering reliability and economic performance and MOQPSO algorithm is introduced to calculate the optimal Pareto solution set of stochastic dispatching schemes. The results of the case study verified the feasibility and calculating performance of the proposed method in developing optimized dispatching schemes.

## 1. Introduction

Facing the global energy crisis, the comprehensive utilization of renewable energies involving solar, wind, hydropower, biomass, geothermal energy, and so forth [1] might be a feasible solution. The research of hybrid power generation of multiple renewable energies has achieved lots of remarkable progress reflected in the following aspects. The designing and planning of HREGS (hybrid renewable energy generation system, HREGS) is taken as a research focus, and it contains optimal overall sizing [2] and unit sizing [3] of the hybrid system, configurations [4–6] and placement [7] of each unit, and optimal planning and design [4]. Various analyses on HREGS such as cost [3, 8] and technoeconomic [9, 10] analysis, performance [11] and feasibility analysis, market evaluation, environmental and social benefits analysis, reliability [10, 12] and power quality assessment,

and so forth are another research interest. The business model [13] of HREGS is an emerging research hotspot recently. The stochastic and intermittent nature of renewables and the complex coupling of multiple uncertainties from the hybrid power system have become the largest barriers to the utilization of renewables [14, 15]. Therefore, aspects of modeling of the hybrid system [4, 15], uncertain output forecasting [16], multirenewable energies management [17], control [5, 6], dispatching [18, 19], and operation [20] strategies, which are different from general topics, should be taken seriously to research with more investment. PSH (pumped storage hydropower, PSH), one of the high-performance power generation sources, has excellent capabilities of rapid response and flexible regulation and is widely used in renewable power systems [21]. Its usage scenario of mitigating output variation of the hybrid power system and effect evaluation is displayed in [22]. Literature [5, 23] has also

presented the challenges, barriers, and future vision of the development and application of HREGS involving PSH. In conclusion, facing the multiple uncertainties and the complex coupling of HREGS, PSH might be a proper solution to the uncertainties. Therefore, how to realize the optimal operation and formulate dispatching strategies for HREGS is of great value to research.

Due to different random and intermittent natures of different renewables, the hybrid power generation system cannot be dispatched with the conventional manner applied on thermal power and diesel generators [24]. Moreover, operational problems such as frequency excursions and system stability cannot be addressed effectively only by conventional AGC [19, 25, 26]. Therefore, an optimal dispatching strategy is needed and implemented to address the problems. The general dispatching optimization techniques are divided into two major types including mathematical procedures and heuristic optimization [18] which are concerned with finding an optimal dispatching strategy considering the operation or system constraints. Almost each general technique only focuses on a specific objective task and has performed a bad generalization capability [27]. In current studies, the multiple uncertainties of renewables and their coupling cannot be taken into account and handled properly. Techniques of day-ahead and real-time optimal power flow are introduced to obtain the optimal dispatching strategy for power systems with considerable RERs (renewable energy resources) [28]. But the variabilities and uncertainties introduced by renewable energy are usually simply substituted with frozen static snapshot forecast values or nominal forecast values which leads to a result that the optimization model has turned into a deterministic model. Reference [29] has proposed a chance-constrained optimal power flow technique to account for the uncertainty of renewables to obtain the optimal load ensemble control strategy, but its application in the dispatching of HREGS still needs more exploration. Adaptive robust optimization for the economic dispatch of power systems with renewables highly penetrated is presented in [30], and the temporal and spatial correlation of uncertainty is modeled by using the idea of dynamic uncertainty sets. In [31], an idea of integrating the risk of renewable's uncertainty into profitability assessments for investors and regarding renewables as risky assets to be invested based on portfolio theory is proposed to obtain an optimal solution to the configuration and dispatching issues of HREGS. The idea is valuable, but the model is simply depicted, and extensive investigation is needed to be conducted on it. A method based on regression techniques and Chebyshev's inequality is introduced in [32] to calculate the dispatching or displacement ratio of the conventional generators under various contingencies from renewables. But its application in HEGES still needs much valuable research.

PPS (probabilistic production simulation) [33] is a powerful technique for power generation system, and the uncertainties are considered as random failure probability. Relevant data including power generation expectation, unit power generation cost, and generation reliability can be obtained by this technique. It is widely used in power

system cost analysis, planning and configuration, price setting, and reliability evaluation [34]. The basis of PPS is to transform the time-sequence load curve into ELDC (equivalent load duration curve), and the time-sequence related information and constraints are ignored. This will bring barriers to the dynamic operation constraints and the calculating accuracy cannot be guaranteed. Besides, a heavy computational burden will emerge due to a large number of convolution and deconvolution calculations [35]. Given the drawbacks of the PPS technique when applied to HREGS, a modified PPS technique considering the chronological characteristics of the system [36], named PCPS (probabilistic chronological production simulation) technique, is introduced to optimize the coordinated dispatch strategy for HREGS, and the uncertainties of multiple renewables are properly formulated by random failure probability. The PCPS technique could handle dynamic chronological constraints directly and obtain accurate reliability data efficiently. This technique provides an outstanding solution to the multiple uncertainties and complex coupling of HREGS.

In this paper, the joint complementary power generation system consisting of cascaded hydropower, PV, and PSH is taken as the research object to study the coordinated dispatching strategy of the complementary system composed of multiple renewables. Due to the different natures of each renewable type, different PCPS methods are proposed for cascaded hydropower, PV, and PSH respectively. Then, the comprehensive framework of PCPS for the hybrid system is obtained, and the dispatching strategy set is obtained through the coordinated PCPS technique. On this basis, a dual-objective optimal dispatching model considering reliability and economic performance is proposed, and the MOQPPO algorithm is introduced to calculate the optimal Pareto dispatching solution set.

The paper is organized as follows. Section 2 presents the coordinated PCPS method for the cascaded hydro-PV-PHS combined power generation system. Section 3 displays the dual-objective dispatching model and the solution method based on the MOQPPO algorithm. Section 4 introduces a case study to verify the effectiveness and calculating efficiency of the proposed method. Finally, Section 5 concludes the paper.

## 2. Coordinated PCPS Methods for the Complementary Power Generation System

Owing to the different natures of PV, cascaded hydropower, and PSH, the PCPS method suitable for each generation type has many differences. In this part, the PCPS method for each renewable will be presented respectively. On this basis, a comprehensive PCPS flow path of the complementary power generation system is given out.

*2.1. PCPS for PV.* PV output is divided into two parts: deterministic output and random output cuts, and the actual output is the difference between the deterministic output and random cuts. In the deterministic output, solar radiation

is the most influential factor, and a direct ratio exists between deterministic output and solar radiation intensity as expressed in formula (1). Other factors such as weather variation and temperature bring about random output cuts due to their strong uncertainties that reduce PV output by weakening deterministic output. Models of deterministic output and random output cuts are presented, respectively, as follows:

$$P_{c,t} = P_{st} \cdot \frac{I_t}{I_{st}}, \quad (1)$$

where  $P_{c,t}$  is the deterministic output;  $P_{st}$  is power output in standard conditions (solar radiation intensity  $I_{st}$  is  $1000 \text{ W/m}^2$ , and the temperature is  $25^\circ\text{C}$ );  $I_t$  is the maximum value of solar radiation intensity reaching the ground without occlusion;  $I_{st}$  is the solar radiation intensity in standard conditions.

**2.1.1. Modeling for Deterministic Output.** The radiation intensity from the sun directly radiated to the atmosphere  $I_0$  is only related to the relative position between the sun and the Earth [37], and the value can be calculated from formula (2). The solar radiation reaching the ground can be divided into direct radiation and diffuse radiation, and the transparency coefficient is introduced to describe the weakening effect of the atmosphere on solar radiation. The transparency of direct radiation can be obtained from formulas (3)–(6) [38], and the direct radiation intensity is shown in formula (7):

$$I_0 = S_0 \left( 1 + 0.033 \cos \left( \frac{2\pi(N+10)}{365} \right) \right), \quad (2)$$

$$\tau_{\text{dir}} = 0.56 \left( e^{-0.56M_h} + e^{-0.095M_h} \right), \quad (3)$$

$$M_h = \left( \sqrt{1229 + (614 \sin \alpha)^2} - 614 \sin \alpha \right) \cdot \left( \frac{288 - 0.0065h}{288} \right)^{5.256}, \quad (4)$$

$$\sin \alpha = \sin \delta \sin \phi + \cos \delta \cos \phi \cos \omega, \quad (5)$$

$$\delta = \frac{2\pi \cdot 23.45^\circ}{360^\circ} \cdot \sin \left( \frac{2\pi(284+N)}{365} \right), \quad (6)$$

$$I_{\text{dir}} = I_0 \tau_{\text{dir}} \sin \alpha, \quad (7)$$

where  $I_0$  is the radiation intensity directly radiated to the atmosphere from the sun;  $S_0$  is the solar constant which represents the total amount of solar radiation entering the Earth's atmosphere per unit area;  $N$  represents the daily sequence;  $\tau_{\text{dir}}$  is the transparency coefficient of direct radiation;  $M_h$  is air mass, a function of altitude and altitude angle

of the sun;  $h$  is the altitude of the specified location;  $\alpha$  is the altitude angle of the sun;  $\phi$  is the latitude of the specified location;  $\omega$  is the hour angle of the sun, related to the time of the specified day; and  $I_{\text{dir}}$  is the direct radiation intensity of the sun.

The diffuse radiation is related to multiple weather conditions, and existing experiments show that the transparency coefficient of direct radiation is approximated as a linear relationship with that of diffuse radiation [39] shown in formula (8), and the diffuse radiation intensity can be calculated by formula (9):

$$\tau_{\text{dif}} = 0.271 - 0.274\tau_{\text{dir}}, \quad (8)$$

$$I_{\text{dif}} = \frac{\sin \alpha}{2} \cdot \frac{1 - \tau_{\text{dif}}}{1 - 1.4 \ln(\tau_{\text{dif}}/M_h)} k, \quad (9)$$

where  $\tau_{\text{dif}}$  is the transparency coefficient of diffuse radiation;  $I_{\text{dif}}$  is diffuse radiation intensity of the sun; and  $k$  is a parameter related to  $M_h$ , and its value range is [0.60, 0.90].

In summary, ignoring other random factors, the total solar radiation intensity  $I_t$  at a certain position and at a certain time is obtained by formula (10), and the deterministic output of PV  $P_{c,t}$  can be achieved if  $I_t$  is brought into formula (1):

$$I_t = I_{\text{dir}} + I_{\text{dif}}. \quad (10)$$

**2.1.2. Modeling for Random Output Cuts.** The reduction factor  $\eta_t$ , the relative difference between the actual output and the deterministic output, is introduced to quantify the weakening effect of the randomness of shadows, cloud cover, weather variation, temperature, and so forth. According to the statistical research [40], it is believed that the probability density function of  $\eta_t$  conforms to beta distribution:

$$\eta_t \sim Be(\alpha, \beta). \quad (11)$$

Based on the probability density function of  $\eta_t$ , the uncertain PV output cuts can be expressed into several states; meanwhile,  $\eta_t$  and its probability  $p_t$  of each state is obtained. The PV output  $P_t^{\text{PV}}$  and its expectation  $EP_t^{\text{PV}}$  are given by the following formulas (12) and (13):

$$P_t^{\text{PV}} = (1 - \eta_t) P_{c,t}, \quad (12)$$

$$EP_t^{\text{PV}} = \left( 1 - \sum_{n=1}^N \eta_{t,n} p_{t,n} \right) P_{c,t}. \quad (13)$$

**2.1.3. Simulation Data of PV.** In the hybrid system, the total power load is  $L_t^0$ , and the power load of the PV station is set as  $L_t^{\text{PV}}$ . After receiving power supply service from PV, the remaining load in time sequence is described as formula (14), and the corresponding reliability indexes are obtained by formulas (15) and (16):

$$L'_t = \begin{cases} L_t^0 - \left(1 - \sum_{n=1}^N \eta_{t,n} P_{t,n}\right) P_{c,t}, & L_t^{\text{PV}} \geq P_{c,t}, \\ L_t^0 - \sum_{n=1}^{N_1} (1 - \eta_{t,n}) P_{t,n} P_{c,t} - \sum_{n=N_1+1}^N P_{t,n} L_t^{\text{PV}}, & L_t^{\text{PV}} < P_{c,t}, \end{cases} \quad (14)$$

$$\text{LOLP}_t^{\text{PV}} = \frac{\Delta t}{T} \sum_{n=1}^{N_1} P_{t,n}, \quad (15)$$

$$\text{EENS}_t^{\text{PV}} = \Delta t \cdot \left[ L_t^{\text{PV}} - \left(1 - \sum_{n=1}^{N_1} \eta_{t,n} P_{t,n}\right) P_{c,t} \right], \quad (16)$$

where  $L'_t$  is the remaining power load after receiving PV power;  $N$  is the number of PV output state;  $N_1$  is the number of the states that PV output is lower than  $L_t^{\text{PV}}$ , and if  $L_t^{\text{PV}} \geq P_{c,t}$ ,  $N_1$  is equal to  $N$ ;  $\text{LOLP}_t^{\text{PV}}$  is the loss of load probability;  $\text{EENS}_t^{\text{PV}}$  is the expectations of energy not served.

**2.2. PCPS for Cascaded Hydropower.** As the probabilistic output of cascaded hydropower at each stage is affected by many deterministic and uncertain factors such as installed capacity, net flow, reservoir capacity, water delay, interstage constraints, failure outage, evaporation, and leakage, direct modeling for cascaded hydropower is of great difficulty. Therefore, an indirect way is proposed to determine the equivalent available capacity of the entire cascaded system, and then a power capacity interstage distribution plan is developed. In this way, the PCPS for cascaded hydropower is accomplished.

**2.2.1. Equivalent Available Capacity of the Entire Cascaded System.** Take the greatest common divisor  $C_i$  of the installed capacities of the stations in the cascaded system as the capacity of the generation unit, and its randomness is described as a two-stage model expressed in formula (17). The moment  $M_i$  and cumulant  $\text{GC}_{i,r}$  are given by formulas (18) and (19), respectively. According to the properties of cumulant, the cumulant of equivalent available capacity EGC of the first  $k$  units can be expressed as the sum of cumulant of each unit shown in formula (20), and the probability distribution function  $F(z_1)$  and the probability density function of the first  $k$  units' equivalent available capacity based on Edgeworth series are obtained by formulas (21)–(27):

$$A_i = \begin{cases} C_i, & P_{t,i} = 1 - q_i, \\ 0, & P_{t,i} = q_i, \end{cases} \quad (17)$$

$$M_{i,r} = (1 - q_i) \cdot C_i^r, \quad (18)$$

$$\begin{cases} \text{GC}_{i,1} = M_{i,1}, \\ \text{GC}_{i,r+1} = M_{i,r+1} - \sum_{j=1}^r \frac{r!}{j!(r-j)!} M_{i,r} \cdot \text{GC}_{i,r-j+1}, \end{cases} \quad (19)$$

$$\text{EGC}_{k,r} = \sum_{i=1}^k \text{GC}_{i,r}, \quad (20)$$

$$F(z) = \int_{-\infty}^z N(z_1) dz_1 + \frac{\text{EGC}_{k,3}}{3!(\text{EGC}_{k,2})^{3/2}} \cdot \frac{d^2 N(z)}{dz} - \frac{\text{EGC}_{k,4}}{4!(\text{EGC}_{k,2})^2} \cdot \frac{d^3 N(z)}{dz} - \frac{10(\text{EGC}_{k,3})^2}{6!(\text{EGC}_{k,2})^3} \cdot \frac{d^5 N(z)}{dz}, \quad (21)$$

$$z = \frac{(x - \mu_k)}{\sigma_k} = \frac{(x - \text{EGC}_{k,1})}{\sqrt{\text{EGC}_{k,2}}}, \quad (22)$$

$$N(z) = \frac{e^{-(z^2/2)}}{\sqrt{2\pi}}, \quad (23)$$

$$\frac{d^2 N(z)}{dz} = (z^2 - 1)N(z), \quad (24)$$

$$\frac{d^3 N(z)}{dz} = (-z^3 + 3z)N(z), \quad (25)$$

$$\frac{d^5 N(z)}{dz} = (-z^5 + 10z^3 - 15z)N(z), \quad (26)$$

$$f(z) = \frac{dF(z)}{dz}, \quad (27)$$

where  $A_i$  and  $q_i$  are the available capacity and the outage rate of the  $i^{\text{th}}$  power unit;  $z$  is the standardized variable of the equivalent available capacity of the first  $k$  units; and  $N(z)$  is the probability density function of normal distribution.

**2.2.2. Simulation Data of the Cascaded System.** According to the probability density function  $f(z)$ , the equivalent available capacity  $P_t$  and its probability  $p_t$  can be obtained. The power load of the whole cascaded system is set as  $L_t^{\text{CH}}$ , and the expected power value of the cascaded system  $\text{EP}_t$  is given by formula (28). From the relationship between the probability distribution of random variable  $x$  and its probability density, formulas (29)–(31) can be obtained, and take them into formula (28), then formula (28) will be transformed in the form of formula (32):

$$EP_t^{\text{CH}} = \int_0^{L_t^{\text{CH}}} x \cdot f(x) dx + L_t^{\text{CH}} \cdot \int_{L_t^{\text{CH}}}^{\infty} f(x) dx, \quad (28)$$

$$F(x) = \int_{-\infty}^x f(x) dx = \int_0^x f(x) dx, \quad (29)$$

$$\int_0^{L_t^{\text{CH}}} x \cdot f(x) dx = L_t^{\text{CH}} F(L_t^{\text{CH}}) - \int_0^{L_t^{\text{CH}}} F(x) dx, \quad (30)$$

$$\int_{L_t^{\text{CH}}}^{\infty} f(x) dx = 1 - F(L_t^{\text{CH}}), \quad (31)$$

$$EP_t^{\text{CH}} = L_t^{\text{CH}} - \int_0^{L_t^{\text{CH}}} F(x) dx. \quad (32)$$

The remaining power load  $L_t^l$  after receiving the cascaded system power is given by formula (33), and the reliability indexes  $\text{LOLP}_t$ ,  $\text{EENS}_t$  are obtained by formulas (34) and (35):

$$\begin{aligned} L_t^l &= L_t^0 - \int_0^{L_t^{\text{CH}}} x \cdot f(x) dx - L_t^{\text{CH}} \cdot \int_{L_t^{\text{CH}}}^{\infty} f(x) dx \\ &= L_t^0 - L_t^{\text{CH}} + \int_0^{L_t^{\text{CH}}} F(x) dx, \end{aligned} \quad (33)$$

$$\text{LOLP}_t^{\text{CH}} = \frac{\Delta t}{T} \int_0^{L_t^{\text{CH}}} f(x) dx = \frac{\Delta t}{T} F(L_t^{\text{CH}}), \quad (34)$$

$$\text{EENS}_t^{\text{CH}} = \Delta t (L_t^{\text{CH}} - EP_t) = \Delta t \cdot \int_0^{L_t^{\text{CH}}} F(x) dx. \quad (35)$$

### 2.2.3. Power Capacity Interstage Distribution Method.

The target of power capacity distribution is to maximize energy storage and minimize the loss of energy. Set the total natural runoff power output of the cascaded system as  $P_t^{\text{runoff}}$ ; if  $P_t^{\text{runoff}} > L_t^{\text{CH}}$ , the cascaded system needs to store the extra energy, or the system needs to release more water to compensate for power output.

When  $P_t^{\text{runoff}} < L_t^{\text{CH}}$ , it needs the  $i$ -th reservoir to release water to compensate for the power output shortage, and the head loss  $\Delta H_i^{\text{loss}}$  in this course is given by formula (36). Take  $K = A_i \cdot \sum_{j=i}^M H_j$  as a discriminant coefficient, and it is clear that a large value of  $K$  indicates that the head loss caused by per unit power output is smaller. Therefore, the reservoir with a large discriminant coefficient should be given priority to release water for the power output supplement:

$$\Delta H_i^{\text{loss}} = \frac{(L_t^{\text{CH}} - P_t^{\text{runoff}}) \cdot \Delta t}{\eta \cdot A_i \cdot \sum_{j=i}^M H_j}, \quad (36)$$

$$\Delta H_i^{\text{increase}} = \frac{(P_t^{\text{runoff}} - L_t^{\text{CH}}) \cdot \Delta t}{A_i \cdot \sum_{j=i}^M H_j}, \quad (37)$$

where  $A_i$  is the cross-sectional area of the  $i^{\text{th}}$  reservoir;  $\sum_{j=i}^M H_j$  is the total head of the  $i^{\text{th}}$  reservoir and its downstream reservoirs.

Similarly, when  $P_t^{\text{runoff}} \geq L_t^{\text{CH}}$ , the extra energy should be stored in the  $i$ -th reservoir, and the head increase  $\Delta H_i^{\text{increase}}$  is given by formula (37).  $A_i \cdot \sum_{j=i}^M H_j$  in formula (37) is also regarded as a discriminant coefficient, and a small value of it will realize a large  $\Delta H_i^{\text{increase}}$  caused by per unit energy. Therefore, the reservoir with a small discriminant coefficient should be given priority to store extra energy.

The main steps of the interstage power capacity distribution based on the discriminant coefficient are listed as follows.

- (1) Calculate the total natural runoff power output  $P_t^{\text{runoff}}$ , and the discriminant coefficients of each reservoir in the cascaded system.
- (2) If  $P_t^{\text{runoff}} < L_t^{\text{CH}}$ , the hydropower station with the largest discriminant coefficient is ordered to generate electricity first, and the other stations generate electricity with its coming flow. If the load power demand cannot be met, the rest stations will release water in turn in order of the discriminant coefficient from large to small for power generation until the load demand balance is realized or the reservoirs are all in the lowest water storage level.
- (3) If  $P_t^{\text{runoff}} \geq L_t^{\text{CH}}$ , the hydropower station with the smallest discriminant coefficient is ordered to generate electricity with part of the coming flow, and the rest flow will be stored in the reservoir. The other stations generate electricity with its coming flow. If the water level of the working reservoir reaches the maximum and the extra energy still exists, reservoirs of the rest stations will be arranged in turn to store water in the order of discriminant coefficient from small to large until all the extra energy is stored or all the reservoirs reached the highest water storage level.

Due to the lack of regulating reservoirs of runoff hydropower stations, they do not possess water supplement and storage ability. This kind of power station is believed that its equivalent cross-sectional area is infinite, and the value of  $K$  is infinite. According to the distribution strategy aforementioned, when it needs to store energy, the runoff stations implement no action throughout the whole course; when it needs to compensate for power generation, the runoff stations will be arranged to generate electricity in priority.

2.3. PCPS for PSH. PSH is not affected by runoff flow, water delay, and other uncertain factors. It can realize the functions of peak regulation, frequency adjustment, emergency standby, and so forth under dispatching orders. The random forced outage rate of each unit of PSH is taken as the main uncertain factor here, and the probabilistic discrete available capacity of PSH is displayed by formula (38). Supposing that the  $n$  units of PSH have the same installed capacity  $c$  and the same forced outage rate  $q$ , the probabilistic available capacity  $c_i$  of PSH and its probability  $a_i$  is obtained from formulas (39) and (40):



$$\{c_1 a_1, c_2 a_2, \dots, c_m a_m\}, \quad (38)$$

$$c_i = ic, \quad i = 0 \sim n, \quad (39)$$

$$a_i = (1 - q)^i q^{n-i} \frac{n!}{i!(n-i)!}. \quad (40)$$

The simulation of the power generation process of PSH is the same as that of the conventional power generation unit. The load undertaken by PSH is set as  $L_t^{\text{PSG}}$ , and the expected power output  $EP_t^{\text{PSG}}$  at this moment is obtained by formula (41). The remaining load  $L'_t$  is calculated by formula (42), and the reliability indexes  $\text{LOLP}_t^{\text{PSG}}$ ,  $\text{EENS}_t^{\text{PSG}}$  are obtained by formulas (43) and (44):

$$EP_t^{\text{PSG}} = \sum_{i=1}^m a_i c_i + L_t^{\text{PS}} \sum_{i=m+1}^{n+1} a_i, \quad (41)$$

$$L'_t = L_t^0 - \sum_{i=1}^m a_i c_i - L_t^{\text{PS}} \sum_{i=m+1}^{n+1} a_i, \quad (42)$$

$$\text{LOLP}_t^{\text{PSG}} = \frac{\Delta t}{T} \sum_{i=1}^m a_i, \quad (43)$$

$$\text{EENS}_t^{\text{PSG}} = \Delta t \left( L_t^{\text{PS}} - \sum_{i=1}^m a_i c_i - L_t^{\text{PS}} \sum_{i=m+1}^{n+1} a_i \right), \quad (44)$$

where  $m$  is the number of the available generation capacity states and is determined by  $c_m < L_t^{\text{PS}} < c_{m+1}$ .

The pumping process of PSH is used for excess energy storage, and it occurs when the expected output of PV, the total natural runoff power of the cascaded system, or the sum of the two is greater than the total load demand. If the excess power used for pumping is set as  $P_t^{\text{pump}}$ , the expected pumping capacity  $EP_t^{\text{PSP}}$  of PSH is obtained by the following formula:

$$EP_t^{\text{PSP}} = \sum_{i=1}^k a_i c_i + P_t^{\text{pump}} \sum_{i=k+1}^{n+1} a_i, \quad (45)$$

where  $k$  is the number of the available pumping capacity states and is determined by  $c_k < P_t^{\text{pump}} < c_{k+1}$ .

**2.4. The Comprehensive PCPS Flow.** Without concerning power generation cost, the specified load demand can be burdened by anyone or any combination of PV, cascaded system, and PSH. If the load demand could not be met, another power source is arranged to generate until the load demand is minimized. If the load demand in a certain period is lower than each of or the sum of the expected PV output and the total natural runoff power of the cascaded system, the excess power should be stored in PSH system by pumping water. Reliability indexes such as LOLP, EENS of each generation unit can be obtained by the proposed method, and the total generation reliability indexes of this period are given by the following formulas:

$$\text{LOLP}_t = 1 - (1 - \text{LOLP}_t^{\text{PV}}) \cdot (1 - \text{LOLP}_t^{\text{CH}}) \cdot (1 - \text{LOLP}_t^{\text{PSG}}), \quad (46)$$

$$\text{EENS}_t = \Delta t \cdot \left[ L_t - \left( 1 - \sum_{n=1}^{N_1} \eta_{t,n} P_{t,n} \right) P_{c,t} - \int_0^{L_t^{\text{CH}}} F(x) dx - \left( \sum_{i=1}^m a_i c_i + L_t^{\text{PS}} \sum_{i=m+1}^{n+1} a_i \right) \right], \quad (47)$$

where  $\text{LOLP}_t^{\text{PV}}$ ,  $\text{LOLP}_t^{\text{CH}}$ , and  $\text{LOLP}_t^{\text{PSG}}$  are the loss of load probabilities of PV, cascaded hydropower system, and PSH, respectively.

The comprehensive probabilistic chronological production simulation flow is displayed in Figure 1.

### 3. Dual-Objective Optimized Dispatching Model

Based on the PCPS method, the generation dispatching scheme set that meets coordinated complementarity is obtained. Meanwhile, the reliability and economic indexes of each scheme are also obtained. In this section, a dual-objective dispatching model is proposed to seek the equilibrium scheme to balance the reliability and economic performance of the scheme. MOQPSO (Multiobjective Quantum-behaved Particle Swarm Optimization) algorithm is introduced to calculate the optimal Pareto solution set of the dispatching model.

In the dispatching model, the minimum probability of load loss and the minimum operating cost are taken as the dual objectives as follows:

$$\min \text{LOLP}_{i,t}, \quad (48)$$

$$\min C_{i,t}^{\text{ope}} = C_{i,t}^G + C_{i,t}^{\text{EN}} + C_{i,t}^{\text{cur}}, \quad (49)$$

$$C_{i,t}^G = C_{i,t}^{\text{CH}} + C_{i,t}^{\text{PV}} + C_{i,t}^{\text{PSG}} + C_{i,t}^{\text{PSP}}, \quad (50a)$$

$$\begin{cases} C_{i,t}^{\text{CH}} = EP_{i,t}^{\text{CH}} \cdot c_{i,t}^{\text{CH}}, \\ C_{i,t}^{\text{PV}} = EP_{i,t}^{\text{PV}} \cdot c_{i,t}^{\text{PV}}, \\ C_{i,t}^{\text{PSG}} = EP_{i,t}^{\text{PSG}} \cdot z_{i,t}^{\text{PSG}} \cdot c_{i,t}^{\text{PSG}}, \\ C_{i,t}^{\text{PSP}} = EP_{i,t}^{\text{PSP}} \cdot z_{i,t}^{\text{PSP}} \cdot c_{i,t}^{\text{PSP}}, \end{cases} \quad (50b)$$

$$C_{i,t}^{\text{EN}} = \text{EENS}_{i,t} \cdot c_{i,t}^{\text{EN}}, \quad (51)$$

$$C_{i,t}^{\text{cur}} = EP_{i,t}^{\text{cur}} \cdot c_{i,t}^{\text{cur}}, \quad (52)$$

where  $\text{LOLP}_{i,t}$  and  $C_{i,t}^{\text{ope}}$  are the loss of load probability and the operating cost of the  $i^{\text{th}}$  scheme.  $C_{i,t}^{\text{ope}}$  is composed of three parts: power generation cost  $C_{i,t}^G$ , penalty cost for energy not served  $C_{i,t}^{\text{EN}}$ , and penalty cost for energy curtailment  $C_{i,t}^{\text{cur}} \cdot C_{i,t}^{\text{CH}}$ ,  $C_{i,t}^{\text{PV}}$ ,  $C_{i,t}^{\text{PSG}}$ , and  $C_{i,t}^{\text{PSP}}$  are operating cost for cascaded hydropower, PV unit, power generation of PSH, and water pumping of PSH, respectively.  $c_{i,t}^{\text{CH}}$ ,  $c_{i,t}^{\text{PV}}$ ,  $c_{i,t}^{\text{PSG}}$ , and  $c_{i,t}^{\text{PSP}}$  are price

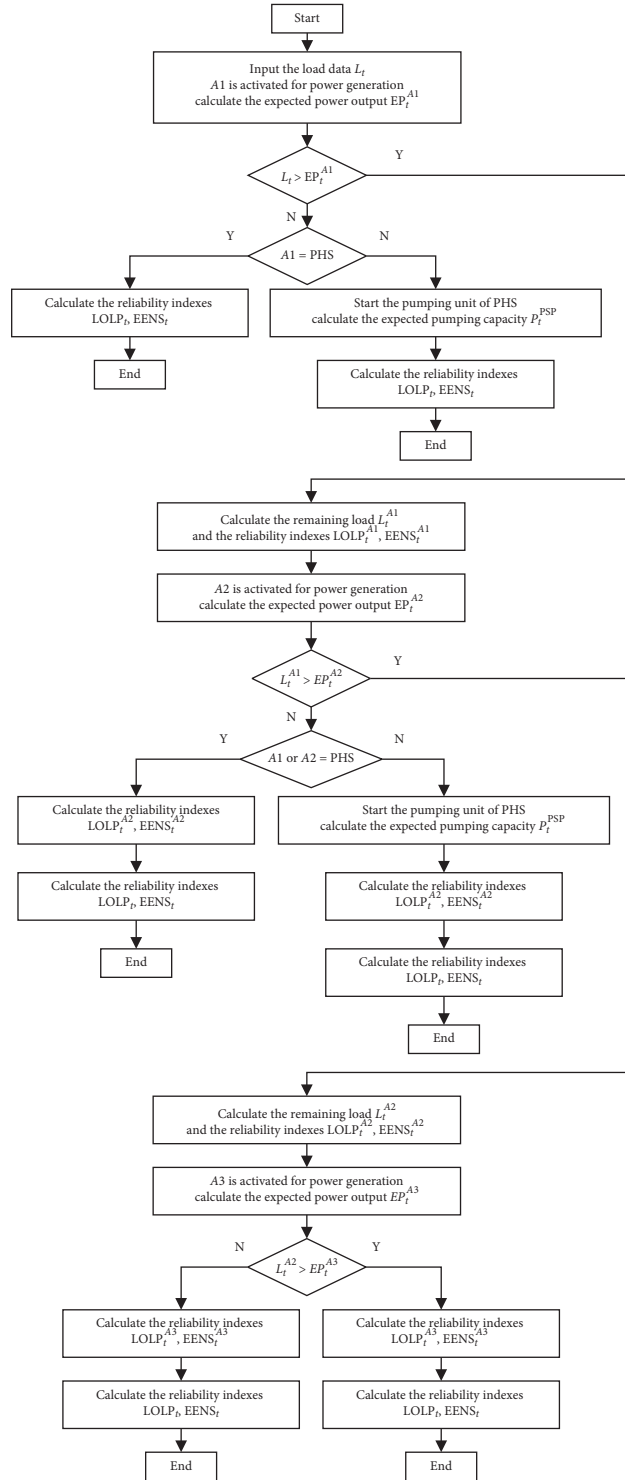


FIGURE 1: Probabilistic chronological production simulation flow.

coefficients of cascaded hydropower, PV unit, power generation of pumped storage, and water pumping of pumped storage, respectively.  $z_{i,t}^{PSG}$  and  $z_{i,t}^{PSP}$  are operation status variables of PSH. When  $z_{i,t}^{PSG}$  equals 1 or  $z_{i,t}^{PSP}$  equals 0, the system is in generation status or else in pumping status.

The operation constraints of the hybrid system are mainly listed as follows:

3.1. *Cascaded Hydropower Operation Constraints.* Operation constraints of cascaded hydropower mainly include reservoir capacity constraint (53), hydropower output constraint (54), discharged water flow constraint (55), water balance constraint (56), interstage hydraulic connection constraint (57), and ramp rate constraint (58):

$$V_k^{\min} \leq V_{k,t} \leq V_k^{\max}, \quad (53)$$

$$P_{k,t}^{\text{CH min}} \leq P_{k,t}^{\text{CH}} \leq P_{k,t}^{\text{CH max}}, \quad (54)$$

$$Q_k^{\text{CH min}} \leq Q_{k,t}^{\text{CH}} \leq Q_k^{\text{CH max}}, \quad (55)$$

$$\begin{aligned} V_{k,t+1} &= V_{k,t} + (Q_{k,t}^{\text{in}} - Q_{k,t}^{\text{out}}) \Delta t \\ &= V_{k,t} + (Q_{k,t}^{\text{in}} - Q_{k,t}^{\text{Gen}} - Q_{k,t}^{\text{Cur}}) \Delta t, \end{aligned} \quad (56)$$

$$Q_{k+1,t+\tau}^{\text{in}} = Q_{k,t}^{\text{out}} + Q_{k,t}^{\text{int}}, \quad (57)$$

$$\delta^L \Delta t \leq P_{k,t+1}^{\text{CH}} - P_{k,t}^{\text{CH}} \leq \delta^U \Delta t, \quad (58)$$

where  $V_{k,t}$ ,  $V_k^{\min}$ ,  $V_k^{\max}$  are the water storage of the  $k^{\text{th}}$  reservoir and its minimum and maximum value;  $P_{k,t}^{\text{CH}}$ ,  $P_{k,t}^{\text{CH min}}$ ,  $P_{k,t}^{\text{CH max}}$  are the power output and its minimum and maximum limitations of the  $k^{\text{th}}$  hydropower station in the cascaded system;  $Q_{k,t}^{\text{CH}}$ ,  $Q_{k,t}^{\text{CH min}}$ ,  $Q_{k,t}^{\text{CH max}}$  are the water flow and its minimum and maximum limitations of the  $k^{\text{th}}$  station; and  $Q_{k,t}^{\text{in}}$ ,  $Q_{k,t}^{\text{out}}$ ,  $Q_{k,t}^{\text{Gen}}$ ,  $Q_{k,t}^{\text{Cur}}$  are the input flow, output flow, generation flow, and curtailed water flow, respectively.  $\delta^L$ ,  $\delta^U$  are the minimum and maximum power variation limitations in a unit interval.

### 3.2. Pumped Storage System Operating Constraints.

Constraints of PSH include water storage changing constraints (59), generation and pumping power constraints (60), power balance constraint (61), ramp rate constraints (62), and operating status mutually exclusive constraint (63):

$$\begin{cases} V_{t+1}^U = V_t^U - \Delta t \frac{EP_t^{\text{PSG}}}{\eta_G}, \\ V_{t+1}^L = V_t^L + \Delta t \frac{EP_t^{\text{PSG}}}{\eta_G}, \\ V_{t+1}^U = V_t^U + \Delta t \eta_P EP_t^{\text{PSP}}, \\ V_{t+1}^L = V_t^L - \Delta t \eta_P EP_t^{\text{PSP}}, \\ V^{U \min} \leq V_{t+1}^U, V_t^U \leq V^{U \max}, \\ V^{L \min} \leq V_{t+1}^L, V_t^L \leq V^{L \max}, \end{cases} \quad (59)$$

$$\begin{cases} P^{\text{PSG min}} \leq EP_t^{\text{PSG}} \leq \min \left[ P^{\text{PSG max}}, \frac{V_t^U}{\Delta t} \eta_G \right] \text{ or } EP_t^{\text{PSG}} = 0, \\ P^{\text{PSP min}} \leq EP_t^{\text{PSP}} \leq \min \left[ P^{\text{PSP max}}, \frac{V_t^L}{\Delta t} \eta_P \right] \text{ or } EP_t^{\text{PSP}} = 0, \end{cases} \quad (60)$$

$$\sum_{t=1}^T EP_t^{\text{PSG}} \Delta t = \eta_P \cdot \eta_G \cdot \sum_{t=1}^T EP_t^{\text{PSP}} \Delta t, \quad (61)$$

$$\begin{cases} \delta_G^L \Delta t \leq EP_{t+1}^{\text{PSG}} - EP_t^{\text{PSG}} \leq \delta_G^U \Delta t, \\ \delta_P^L \Delta t \leq EP_{t+1}^{\text{PSP}} - EP_t^{\text{PSP}} \leq \delta_P^U \Delta t, \end{cases} \quad (62)$$

$$z_t^{\text{PSG}} \cdot z_t^{\text{PSP}} = 0, \quad (63)$$

where  $V_t^U$ ,  $V_t^L$ ,  $V^{U \min}$ ,  $V^{U \max}$ ,  $V^{L \min}$ , and  $V^{L \max}$  are water storage of the upper and lower reservoir, and their minimum and maximum limitations, respectively;  $\eta_G$ ,  $\eta_P$  are generating efficiency and pumping efficiency;  $P^{\text{PSG min}}$ ,  $P^{\text{PSG max}}$ ,  $P^{\text{PSP min}}$ ,  $P^{\text{PSP max}}$  are the minimum and maximum power limitations in generating and pumping status respectively; and  $\delta_G^L$ ,  $\delta_G^U$ ,  $\delta_P^L$ ,  $\delta_P^U$  are the minimum and maximum power variation limitations in generating and pumping status in a unit interval.

**3.3. DC Power Flow Constraint.** DC power flow constraint is taken into account in the dual-objective dispatching model:

$$\begin{cases} P_{\text{tline}} = B_{\text{diag}} L B^{-1} (EP_t^{\text{CH}} + EP_t^{\text{PV}} - EP_t^{\text{PSP}} z_t^{\text{PSP}} + EP_t^{\text{PSG}} z_t^{\text{PSG}} - P_t^L), \\ -\bar{P}_{\text{line}} \leq P_{\text{tline}} \leq \bar{P}_{\text{line}}, B_{\text{diag}} = \text{diag} \left( \frac{1}{x_1}, \frac{1}{x_2}, \dots, \frac{1}{x_N} \right), \end{cases} \quad (64)$$

where  $B$  is the admittance coefficient matrix;  $x_n$  is the reactance of the  $n^{\text{th}}$  branch;  $N$  is the number of branches in the system;  $\bar{P}_{\text{line}}$  is the upper limitation of branch power.

Based on the proposed dual-objective model, the MOQPSO algorithm [41] is introduced to calculate the model. This algorithm is derived from QPSO (Quantum-behaved Particle Swarm Optimization) algorithm, and improvements from three aspects—external file set, dominant individual selection, and chaotic mutation search—are implemented to meet the efficient calculation needs of multiobjective optimization problems. The overall calculating flow is shown in Figure 2.

From Figure 2, several steps are included in the flow and described as follows. Firstly, encode each output combination scheme obtained by the PCPS method, and each particle represents a possible dispatching scheme. Secondly, evaluate and calculate the corresponding objective function of each particle and update the external file set. Thirdly, update the optimal position of individuals in history, and perform the mutation search for the individuals. Fourthly, determine the global optimal position and update the position of each particle. Then, check the termination condition and determine whether the flow continues or terminates. Finally, output the Pareto optimal solution set and the dispatching data.

## 4. Case Study

The modified IEEE 24 bus test system [42] is introduced to examine the effectiveness of the proposed probabilistic dispatching approach for the cascaded hydro- PV-PSH joint complementary power system. The test system consists of 11 renewable power stations located on buses 1, 2, 7, 13, 14, 15, 16, 18, 21, 22, and 23, and their distribution is shown in

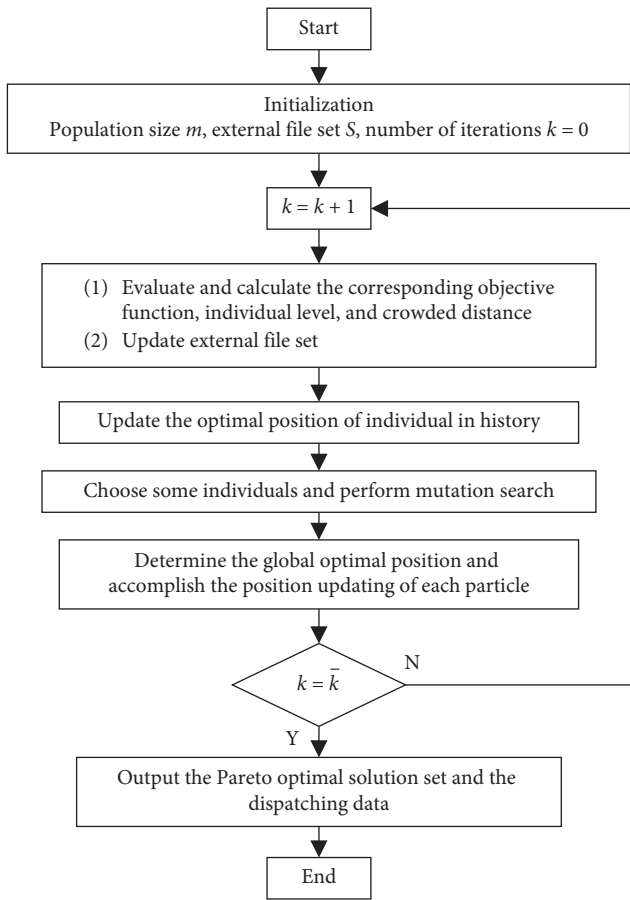


FIGURE 2: Calculating flow of MOQPSO algorithm.

Table 1. The corresponding data of each branch and loads of the test system is modified properly to accommodate the renewable generation. The details of each station are shown in Table 1. The station located at bus 7 is a runoff hydropower station, and the rest hydropower stations have the daily regulating capability. The profiles of PV output expectation in different weather conditions obtained by the PCPS approach are shown in Figure 3.

The cascade hydropower stations in the hybrid system are taken as an equivalent adjustable hydropower station, and its power output is divided into two parts: the uncertain natural runoff output and the adjustable water storage output. The former mainly depends on random runoff flow and the latter is related to the storage capacity of reservoirs. Based on historical hydraulic data of the cascade hydropower stations, the total runoff power output profiles in different seasons (wet season, normal season, and dry season) are displayed in Figure 4.

In the production simulation process, the probability distribution of the stochastic shielding factor of PV power output is considered to conform to the Beta distribution [40]. The corresponding parameters used in the production simulation process are listed in Table 2. The power generation distribution schemes of each station and the

corresponding reliability data and operating cost data can be obtained based on the proposed PCPS technique.

After obtaining the power generation distribution schemes that meet complementary requirements, the schemes are taken into the optimization process based on the MOQPSO algorithm to seek the Pareto optimal scheme. In the MOQPSO algorithm, population size  $m$  is set as 500, the number of individuals in the external file set  $S$  is 30, and the maximum number of iterations is set as 1000. Taking the sunny day/wet season scenario as an example, Figure 5 gives its Pareto optimal front set between reliability (LOLP) and cost factor. The cost factor is calculated by the ratio of power generation cost to the total operating cost of the hybrid system (including power generation cost, penalty cost, and power purchasing cost). It can be found from the scatterplot that the comprehensive LOLP decreases gradually with the increase of cost factor, and the speed of decrease is fast in the initial stage then becomes slow gradually. When the cost factor exceeds a certain value, the LOLP will not change significantly as the cost factor increases. If the reliability is still wished to further improvement at this moment, greater economic cost will be paid, and the economic performance of the dispatching schemes will deteriorate. The generation distribution scheme at this point is believed optimal.

Four representative power generation scenarios—sunny day/wet season, rainy day/wet season, sunny day/dry season, and rainy day/dry season—are chosen, and the optimal probabilistic chronological generation dispatching schemes for cascade hydro-PV-PSH complementary power system in each scenario are presented as follows.

Analyzing the optimal dispatching schemes in the case study displayed above, some beneficial discussions are carried out as follows:

- (1) The overall scale of hydropower output in the wet season has no great difference compared to that in the dry season. The influence of season variation is weakened. This is mainly attributed to the reservoir regulating capability of the cascaded hydropower system. Generally, the regulating performance of cascaded hydropower is better than that of single hydropower of the same scale [43].
- (2) Because of the policy of promoting the consumption of PV resources, its energy curtailment price is set to be higher than that of hydro resources in the case study. PV power stations take the priority to generate, and the hydropower stations support and cooperate with PV stations to meet the loads demand.
- (3) From Figures 6–9, it can be found that PSH is in pumping status in the wet season and generally occurs in the middle of the daytime. In contrast, PSH is in generating status in the dry season and occurs at night. To evaluate the economic performance of PSH in the hybrid system, four new operating scenarios without PSH are constructed and the average unit

TABLE 1: Parameters of each generator.

Bus ID	Power type	Installed capacity (MW)	Reservoir capacity ( $10^4 \text{ m}^3$ )	Water head (m)	Working flow ( $\text{m}^3/\text{s}$ )
1	PV-1	50	—	—	—
2	PV-2	50	—	—	—
7	CH-5	20	—	339.09	7.4
13	CH-3	36	37.2	91	33
14	—	—	—	—	—
15	CH-6	4.8	53	10.5	48.9
16	PSH	5	25.6/23.7	339.09	7.4
18	CH-2	60	20.9	127	53.4
21	CH-4	54	25.6	161	47.1
22	CH-1	45	16.1	123.65	43.32
23	CH-7	84	44.2	75	—

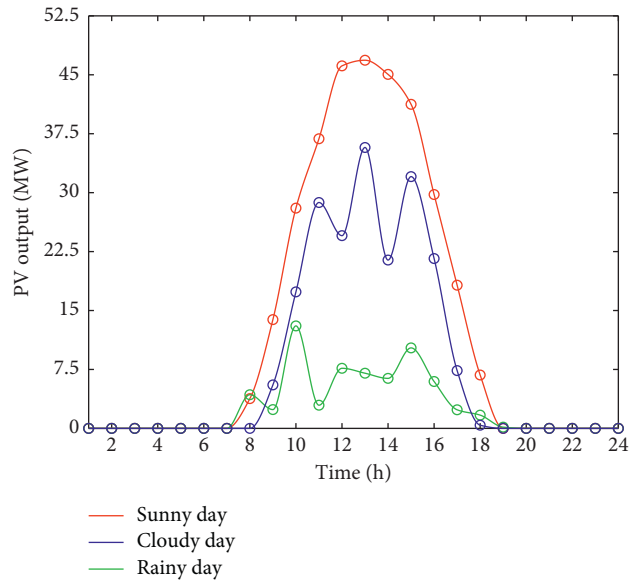


FIGURE 3: Profiles of PV output expectations.

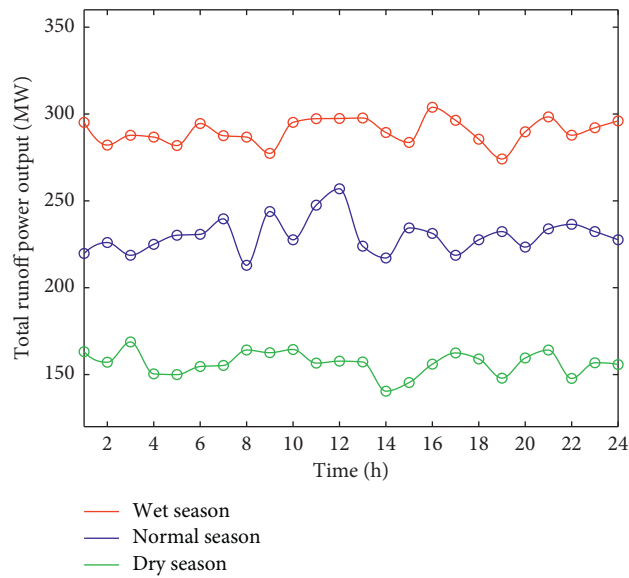


FIGURE 4: Total runoff power output profiles in different seasons.

TABLE 2: Parameters used in production simulation.

Power type	Unit capacity (MW)	Unit forced outage rate	Generation price (¥/MWh)	Shortage price (¥/MWh)	Curtailement price (¥/MWh)
Cascade hydro	1	0.089	150	185	185
Power type	Longitude (°)	Latitude (°)	Generation price (¥/MWh)	Shortage price (¥/MWh)	Curtailement price (¥/MWh)
PV	102.3644	30.99918	125	185	205
Power type	Unit capacity (MW)	Unit forced outage rate	Generation price (¥/MWh)	Shortage price (¥/MWh)	Pumping price (¥/MWh)
PSH	0.5	0.08	240	310	180

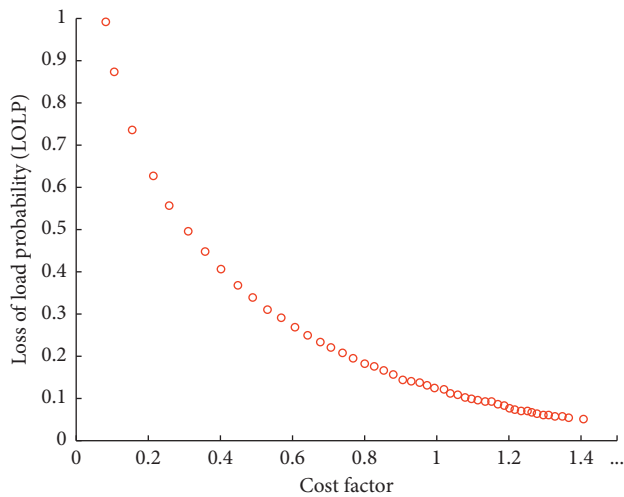


FIGURE 5: Pareto optimal front set of sunny day/wet season scenario.

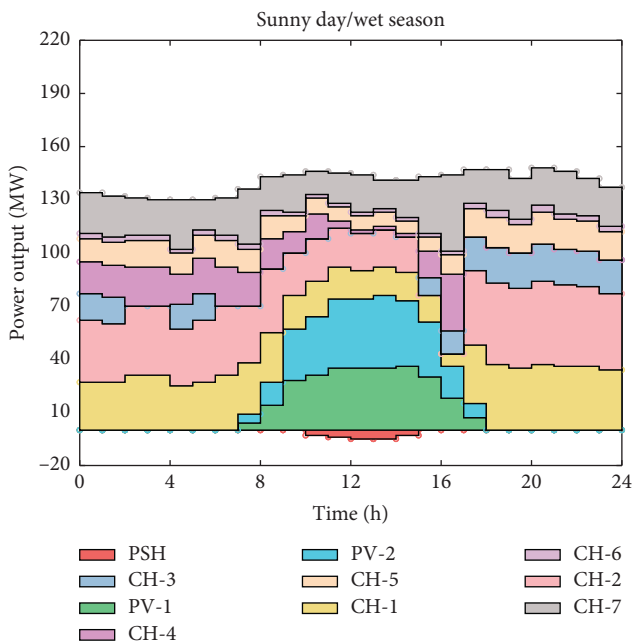


FIGURE 6: Optimized dispatching scheme in sunny day/wet season.

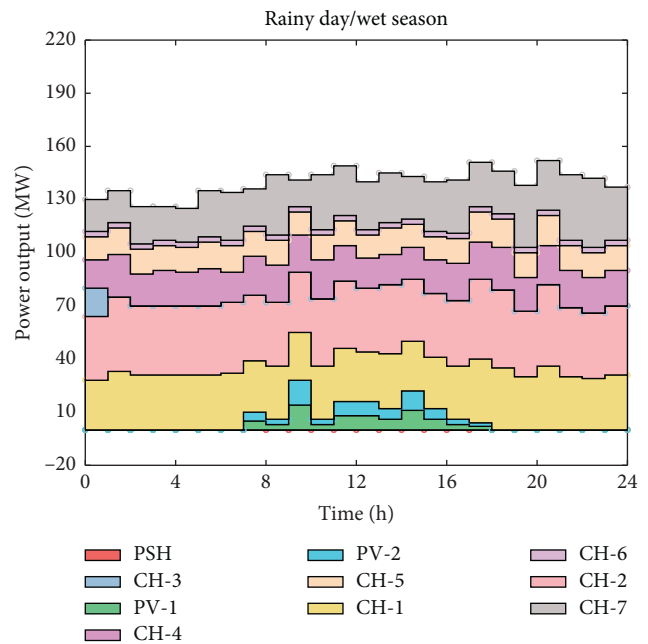


FIGURE 7: Optimized dispatching scheme in rainy day/wet season.

power generation cost of each scenario is calculated and shown in Table 3. The unit cost in the rainy day/dry scenario is the highest, and the cost in the sunny/wet scenario is the lowest. However, due to the application of PSH, the decline of unit cost in the rainy/dry scenario is much larger than the increases in other scenarios caused by the pumping operation. The effectiveness and value of PSH are testified from the comparison of the results.

- (4) Compared with the time data that it takes about 3.7 hours to complete the same scale calculation with DP (dynamic programming, DP) technique (discrete states number is 100) in [41], it only needs less than 10 seconds to complete the optimization process using the proposed method of this paper. It has verified the feasibility and efficiency of the proposed method through comparison with the benchmark data.



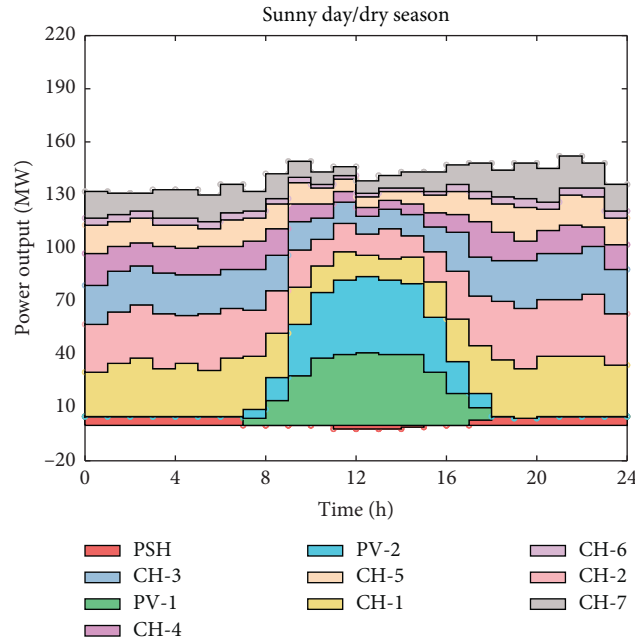


FIGURE 8: Optimized dispatching scheme in sunny day/dry season.

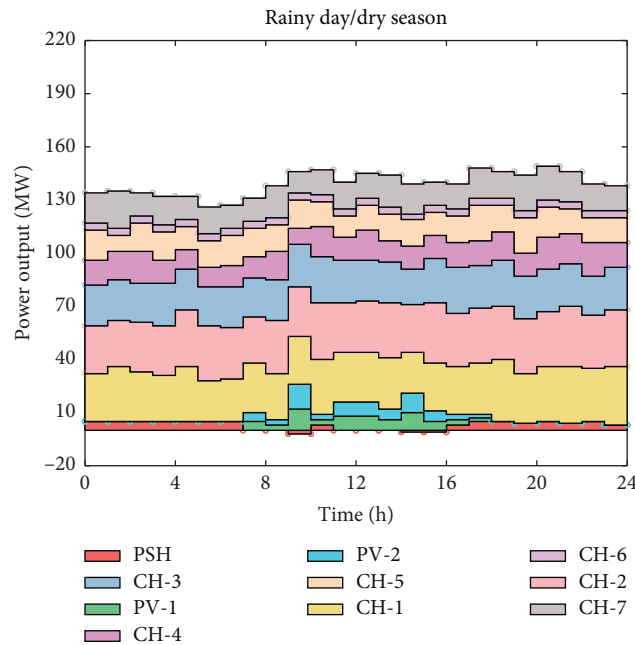


FIGURE 9: Optimized dispatching scheme in rainy day/dry season.

TABLE 3: Average unit power generation cost of different scenarios (¥/MWh).

Type	Sunny/wet	Rainy/wet	Sunny/dry	Rainy/dry
CH-PV	138.5945	147.0218	145.8147	152.3571
CH-PV-PSH	138.6383	147.0218	145.8322	151.9286

## 5. Conclusions

Focusing on the uncertainty and reliability problems in the power generation dispatching process of multiple renewables combined complementary system, a dual-stage probabilistic coordinated dispatching method is proposed in this paper. First, a modified probabilistic chronological production simulation method is proposed to simulate the uncertain power output characteristics of multiple renewables, such as cascaded hydropower, PV, and PSH, and to obtain the complementary dispatching schemes for the cascaded hydro-PV-PSH system and the reliability and economic indexes of each scheme. On this basis, a dual-objective optimization model of dispatching schemes considering the reliability and economic performance of power generation is introduced. Meanwhile, the MOQPSO algorithm is applied to calculate the optimal Pareto solution set. The results of the case study have verified the effectiveness and calculating efficiency of the proposed dispatching method. The main contributions of the paper are listed as follows:

- (1) A modified probabilistic chronological production simulation method for uncertain timing-output simulation of multiple renewables is proposed.
- (2) An efficient dual-objective optimization method for power generation dispatching schemes of renewable energy is obtained.
- (3) A dispatching method for cascaded hydropower system that the overall probabilistic chronological production simulation is performed first, then implementing the interstage distribution, is proposed to cope with the multiple uncertainties and coupling.
- (4) The feasibility and complementary capabilities of hydro-PV combined power generation have been further verified. The function of PSH to regulate the uncertain complementary output of renewables has been testified.

This paper mainly concerns the multiple uncertainties and coupling of multiple renewables combined power system and sheds less light on the benefits of each generation member. Therefore, how to maximize the benefits of each member to fully motivate them to participate in the complementary power generation and thus generate an optimized dispatching scheme for the cascaded hydro-PV-PSH complementary system will be the next research focus.

## Data Availability

The technical route, the model structure, and the parameters of case study are available from the corresponding author upon request.

## Conflicts of Interest

The authors have no conflicts of interest.

## Acknowledgments

This work was supported by the National Key R&D Program of China (2018YFB0905200)—Research and application

demonstration on complementary combined power generation technology for distributed PV and cascade hydropower.

## References

- [1] T. Niknam and B. B. Firouzi, "A practical algorithm for distribution state estimation including renewable energy sources," *Renewable Energy*, vol. 34, no. 11, pp. 2309–2316, 2009.
- [2] R. Hosseinalizadeh, H. Shakouri G, M. S. Amalnick, and P. Taghipour, "Economic sizing of a hybrid (PV-WT-FC) renewable energy system (HRES) for stand-alone usages by an optimization-simulation model: case study of Iran," *Renewable and Sustainable Energy Reviews*, vol. 54, pp. 139–150, 2016.
- [3] D. B. Nelson, M. H. Nehrir, and C. Wang, "Unit sizing and cost analysis of stand-alone hybrid wind/PV/fuel cell power generation systems," *Renewable Energy*, vol. 31, no. 10, pp. 1641–1656, 2006.
- [4] R. Siddaiah and R. P. Saini, "A review on planning, configurations, modeling and optimization techniques of hybrid renewable energy systems for off grid applications," *Renewable and Sustainable Energy Reviews*, vol. 58, pp. 376–396, 2016.
- [5] R. Siddaiah, "Resources, configurations, and soft computing techniques for power management and control of PV/wind hybrid system," *Renewable and Sustainable Energy Reviews*, vol. 69, pp. 129–143, 2017.
- [6] S. Upadhyay and M. P. Sharma, "A review on configurations, control and sizing methodologies of hybrid energy systems," *Renewable and Sustainable Energy Reviews*, vol. 38, pp. 47–63, 2014.
- [7] Z. Abdmouleh, A. Gastli, L. Ben-Brahim, M. Haouari, and N. A. Al-Emadi, "Review of optimization techniques applied for the integration of distributed generation from renewable energy sources," *Renewable Energy*, vol. 113, pp. 266–280, 2017.
- [8] W. D. Kellogg, M. H. Nehrir, G. Venkataramanan, and V. Gerez, "Generation unit sizing and cost analysis for stand-alone wind, photovoltaic, and hybrid wind/PV systems," *IEEE Transactions on Energy Conversion*, vol. 13, no. 1, pp. 70–75, 1998.
- [9] J. Samaniego, F. Alija, S. Sanz, C. Valmaseda, and F. Frechoso, "Economic and technical analysis of a hybrid wind fuel cell energy system," *Renewable Energy*, vol. 33, no. 5, pp. 839–845, 2008.
- [10] P. Zhou, R. Y. Jin, and L. W. Fan, "Reliability and economic evaluation of power system with renewables: a review," *Renewable and Sustainable Energy Reviews*, vol. 58, pp. 537–547, 2016.
- [11] S. Goel and R. Sharma, "Performance evaluation of stand alone, grid connected and hybrid renewable energy systems for rural application: a comparative review," *Renewable and Sustainable Energy Reviews*, vol. 78, pp. 1378–1389, 2017.
- [12] T. Tezer, R. Yaman, and G. Yaman, "Evaluation of approaches used for optimization of stand-alone hybrid renewable energy systems," *Renewable and Sustainable Energy Reviews*, vol. 73, pp. 840–853, 2017.
- [13] A. A. Eras-Almeida and M. A. Egado-Aguilera, "Hybrid renewable mini-grids on non-interconnected small islands: review of case studies," *Renewable and Sustainable Energy Reviews*, vol. 116, 2019.
- [14] M. Wu, L. Kou, X. Hou, Y. Ji, B. Xu, and H. Gao, "A bi-level robust planning model for active distribution networks

- considering uncertainties of renewable energies," *International Journal of Electrical Power & Energy Systems*, vol. 105, pp. 814–822, 2019.
- [15] A. Zakaria, F. B. Ismail, M. S. H. Lipu, and M. A. Hannan, "Uncertainty models for stochastic optimization in renewable energy applications," *Renewable Energy*, vol. 145, pp. 1543–1571, 2020.
- [16] C. Voyant, G. Notton, S. Kalogirou et al., "Machine learning methods for solar radiation forecasting: a review," *Renewable Energy*, vol. 105, pp. 569–582, 2017.
- [17] Z. Jun, L. Junfeng, W. Jie, and H. W. Ngan, "A multi-agent solution to energy management in hybrid renewable energy generation system," *Renewable Energy*, vol. 36, no. 5, pp. 1352–1363, 2011.
- [18] M. Nazari-Heris, B. Mohammadi-Ivatloo, and G. B. Ghahrepetian, "Short-term scheduling of hydro-based power plants considering application of heuristic algorithms: a comprehensive review," *Renewable and Sustainable Energy Reviews*, vol. 74, pp. 116–129, 2017.
- [19] K. Nghitevelekw and R. C. Bansal, "A review of generation dispatch with large-scale photovoltaic systems," *Renewable and Sustainable Energy Reviews*, vol. 81, pp. 615–624, 2018.
- [20] K. Sopian, A. Zaharim, Y. Ali, Z. M. Nopiah, J. A. Razak, and N. S. Muhammad, "Optimal operational strategy for hybrid renewable energy system using genetic algorithms," *WSEAS Transactions on Mathematics*, vol. 7, no. 4, pp. 130–140, 2008.
- [21] M. S. Javed, T. Ma, J. Jurasz, and M. Y. Amin, "Solar and wind power generation systems with pumped hydro storage: review and future perspectives," *Renewable Energy*, vol. 148, pp. 176–192, 2020.
- [22] T. Mahto and V. Mukherjee, "Energy storage systems for mitigating the variability of isolated hybrid power system," *Renewable and Sustainable Energy Reviews*, vol. 51, pp. 1564–1577, 2015.
- [23] J. Hu, R. Harmsen, W. Crijns-Graus, and E. Worrell, "Barriers to investment in utility-scale variable renewable electricity (VRE) generation projects," *Renewable Energy*, vol. 121, pp. 730–744, 2018.
- [24] M. K. C. Marwali, M. Haili, S. M. Shahidepour, and K. H. Abdul-Rahman, "Short term generation scheduling in photovoltaic-utility grid with battery storage," *IEEE Transactions on Power Systems*, vol. 13, no. 3, pp. 1057–1062, 1998.
- [25] X. S. Zhang, Z. Xu, T. Yu, B. Yang, and H. Z. Wang, "Optimal mileage based AGC dispatch of a GenCo," *Ieee Transactions on Power Systems*, vol. 35, no. 4, pp. 2516–2526, 2020.
- [26] X. S. Zhang, T. Tan, B. Zhou, T. Yu, B. Yang, and X. M. Huang, "Adaptive distributed auction-based algorithm for optimal mileage based AGC dispatch with high participation of renewable energy," *International Journal of Electrical Power & Energy Systems*, vol. 124, 2021.
- [27] M. Grami, M. Rekik, and L. Krichen, "Power dispatch strategy for interconnected microgrids based hybrid renewable energy system," *International Journal of Renewable Energy Research*, vol. 8, no. 2, pp. 838–850, 2018.
- [28] S. S. Reddy and P. R. Bijwe, "Day-ahead and real time optimal power flow considering renewable energy resources," *International Journal of Electrical Power & Energy Systems*, vol. 82, pp. 400–408, 2016.
- [29] A. Hassan, R. Mieth, M. Chertkov, D. Deka, and Y. Dvorkin, "Optimal load ensemble control in chance-constrained optimal power flow," *IEEE Transactions on Smart Grid*, vol. 10, no. 5, pp. 5186–5195, 2019.
- [30] A. Lorca and X. A. Sun, "Adaptive robust optimization with dynamic uncertainty sets for multi-period economic dispatch under significant wind," *IEEE Transactions on Power Systems*, vol. 30, no. 4, pp. 1702–1713, 2015.
- [31] Z. Hu, Z. Yan, and J. Wen, "Planning and dispatching of hybrid renewable power system based on portfolio theory," 2011.
- [32] S. Eftekharijad, G. T. Heydt, and V. Vittal, "Optimal generation dispatch with high penetration of photovoltaic generation," *IEEE Transactions on Sustainable Energy*, vol. 6, no. 3, pp. 1013–1020, 2015.
- [33] R. Booth, "Power system simulation model based on probability analysis," *IEEE Transactions on Power Apparatus and Systems*, vol. 91, no. 1, pp. 62–69, 1972.
- [34] M. Lin, A. Breipohl, and F. Lee, "Comparison of probabilistic production cost simulation methods," *IEEE Transactions on Power Systems*, vol. 4, no. 4, pp. 1326–1334, 1989.
- [35] X. Wang, "Equivalent energy function approach to power system probabilistic modeling," *IEEE Transactions on Power Systems*, vol. 3, no. 3, pp. 823–829, 1988.
- [36] Q. Xia, S. Wang, and N. Xiang, "The probabilistic power system production simulation based on chronological load curve," *Proceedings of the CSEE*, vol. 14, no. 3, pp. 21–28, 1994.
- [37] M. Alata, M. A. Al-Nimr, and Y. Qaroush, "Developing a multipurpose sun tracking system using fuzzy control," *Energy Conversion and Management*, vol. 46, no. 7–8, pp. 1229–1245, 2005.
- [38] F. S. Higgs, *Principles of Solar Engineering: By Frank Kreith and Jan F. Kreider*, McGraw-Hill Book Company, New York, NY, USA, 1978.
- [39] B. Y. H. Liu and R. C. Jordan, "The interrelationship and characteristic distribution of direct, diffuse and total solar radiation," *Solar Energy*, vol. 4, no. 3, pp. 1–19, 1960.
- [40] K. C. Zhang Xi, "Analysis of mid/long term random characteristic of photovoltaic power generation," *Automation of Electric Power Systems (In Chinese)*, vol. 38, pp. 6–12, 2014.
- [41] Z.-k. Feng, W.-j. Niu, and C.-t. Cheng, "Multi-objective quantum-behaved particle swarm optimization for economic environmental hydrothermal energy system scheduling," *Energy*, vol. 131, pp. 165–178, 2017.
- [42] C. Grigg, P. Wong, P. Albrecht et al., "Reliability test system task, "the IEEE reliability test system-1996," *IEEE Transactions on Power Systems*, vol. 14, no. 3, pp. 1010–1018, 1999.
- [43] C. Cheng, F. Chen, G. Li et al., "Reform and renewables in China: the architecture of Yunnan's hydropower dominated electricity market," *Renewable and Sustainable Energy Reviews*, vol. 94, pp. 682–693, 2018.

## Research Article

# Online Static Voltage Stability Monitoring for Power Systems Using PMU Data

Jianhong Pan, Aidi Dong, Jiashu Fan, and Yang Li 

State Grid Jilin Electric Power Company Limited, Changchun 130000, China

Correspondence should be addressed to Yang Li; liyang@neepu.edu.cn

Received 28 November 2020; Revised 11 December 2020; Accepted 16 December 2020; Published 29 December 2020

Academic Editor: Bo Yang

Copyright © 2020 Jianhong Pan et al. This is an open access article distributed under the Creative Commons Attribution License, which permits unrestricted use, distribution, and reproduction in any medium, provided the original work is properly cited.

A new online static voltage stability monitoring method for power systems is proposed by using phasor measurement unit (PMU) data in this paper. This approach uses the real-time power, voltage, and phase angle data collected by the PMU to estimate the power flow Jacobian matrix of the system, and then the static voltage stability is monitored via the minimum singular values (MSVs) of the power flow Jacobian matrix. The novelty of the approach lies in the fact that it only utilizes PMU data for implementing online monitoring of the power system static voltage stability, independent of the physical model and its parameters. The application results on the IEEE 57-bus test system verify the effectiveness of the proposed approach.

## 1. Introduction

Voltage stability assessment (VSA) has been recognized as an important task to ensure the secure and economical operation of power systems [1, 2]. Problems arising from the growing integration of intermittent renewable power generation in a variety of forms such as active distribution networks [3] and microgrids [4, 5] and integrated energy systems [6] are nudging power systems toward potential dynamic instability scenarios due to the inherent uncertainties of renewable generation [7]. As a new generation of DC transmission technique, voltage source converter-based high voltage direct current (VSC-HVDC) has become a popular opinion of power transmission due to its significant advantages such as independent adjustments of active and reactive powers [8], asynchronous interconnection between islands [9], and black-start capability [10]. In addition, the growing integration of energy storage [11], electric vehicles [12], cyber attacks [13–15], and increasingly diversified demands [16, 17] affect the stable operation of the system to a certain extent. All these shifts pose new challenges in maintaining the system working reliably and securely. In recent years, the wide-area measurement system (WAMS) using time-stamped phasor measurement units (PMUs) has

been receiving ever increasing attention from both academia and industry, which makes it possible to explore wide-area protection and control (WAPaC) schemes to avoid the system collapse [18–21]. Therefore, the voltage stability monitoring and assessment of power systems based on PMU data are of great significance in the new context [22–25].

Since the first  $dQ/dU$  criterion proposed by the Soviet scholar N.M in the 1940s, a large number of voltage stability analysis approaches of power systems have been developed, such as the sensitivity method [26], continuous power flow method [27], the singular value decomposition method [28], and so on. The sensitivity method is only suitable for simple power systems, and sometimes there are discriminant errors when it is used in multimachine systems. In theory, the feasible solution domain method can calculate the voltage stability margin of a given operation mode, but the calculation of critical injection vectors involves complex nonlinear problems, and the computation is heavy. The multivalued method of power flow needs to track and calculate the multivalued value of the injection quantity repeatedly, and the static stability margin of the system voltage is approximate. References [29–31] illustrate the feasibility of the singular value decomposition theory of the trend Jacobian matrix, but the above methods need to know the

topology and parameters of the system and cannot monitor the static voltage stability of the grid online. The widespread deployment and successful application of PMUs break through this bottleneck and shed new light on online monitoring of the static voltage stability of power systems [32–34].

In recent years, PMU data have been successfully used for real-time power system stability assessment due to its powerful data acquisition capabilities. In [35], an extreme learning machine- (ELM-) based transient stability assessment (TSA) model optimized by improved particle swarm optimization is proposed by using PMU data; to address the issue of lacking online learning ability in current methods, an online sequential ELM- (OS-ELM-) based TSA method is presented for power systems in [36]; a feature selection approach is presented for TSA based on improved maximal relevance and minimal redundancy criterion and PMU measurements in [37]; a new online learning mechanism based on an ensemble of OS-ELM (EOS-ELM) is developed for TSA in [38]; in [39], a rule extraction method is developed by using ELM and improved ant-miner algorithm for TSA; based on PMU data, reference [40] proposes a TSA method by using kernelized fuzzy rough sets and memetic algorithm for feature selection; in [41], a real-time TSA approach based on EOS-ELM coupled with binary-based feature selection is proposed. In [42], a short-term voltage stability assessment method is proposed by calculating the Lyapunov exponent using PMU data. However, research reports on online monitoring of power system static voltage stability using PMU data have still been relatively rare for a long time. Lim and DeMarco put forward a VSA approach with the use of singular value analysis of PMU data in [43, 44]. Inspired by these investigations and data-driven decision making [45, 46], this paper presents an online static voltage stability analysis method based on PMU data. This method is not limited by the network model and parameters. It only needs to use the active power, reactive power, and voltage amplitude and phase angle measurement collected from PMUs to monitor the static voltage stability of a power system. Finally, the effectiveness of the proposed method is verified by using the IEEE 57-bus system.

## 2. Establishment of the Jacobian Matrix Model for Power Flow

The power flow equation of the power system in polar form can be expressed as follows:

$$\begin{cases} P_i = V_i \sum_{j \in i} V_j (G_{ij} \cos \theta_{ij} + B_{ij} \sin \theta_{ij}), \\ Q_i = V_i \sum_{j \in i} V_j (G_{ij} \sin \theta_{ij} - B_{ij} \cos \theta_{ij}), \end{cases} \quad (1)$$

where  $j \in i$  denotes that buses  $i$  and  $j$  are connected;  $U_i$  and  $U_j$  represent the voltage amplitude of buses  $i$  and  $j$ , respectively;  $G_{ij}$  and  $B_{ij}$  represent the values of the real and imaginary parts of the admittance matrix between buses  $i$  and  $j$ , respectively;  $\theta_{ij}$  represents the phase angle difference

between buses  $i$  and  $j$ ; and  $P_i$  and  $Q_i$  represent the active and reactive power of bus  $i$ , respectively.

Excluding the equilibrium bus of the system, according to the Newton–Raphson method, formula (1) can establish the following linearization modified equations:

$$\begin{bmatrix} \Delta P \\ \Delta Q \end{bmatrix} = \begin{bmatrix} H_{ij} & N_{ij} \\ J_{ij} & L_{ij} \end{bmatrix} \begin{bmatrix} \Delta \theta \\ \Delta V \end{bmatrix}, \quad (2)$$

where  $\Delta P$  and  $\Delta Q$  represent the microincrement of active power and reactive power of the injection bus;  $\Delta \theta$  and  $\Delta V$  represent the microincrement of the voltage phase angle  $\theta$  and the voltage amplitude  $V$ , respectively;  $H_{ij}$  and  $N_{ij}$  represent the partial derivative of the active power  $P$  to the voltage phase angle  $\theta$  and the voltage amplitude  $V$ , respectively; and  $J_{ij}$  and  $L_{ij}$  represent the partial derivative of the reactive power  $Q$  to the voltage phase angle  $\theta$  and the voltage amplitude  $V$ , respectively. In equation (2),

$$J = \begin{bmatrix} H_{ij} & N_{ij} \\ J_{ij} & L_{ij} \end{bmatrix}, \quad (3)$$

where  $J$  is the Jacobian matrix of the linearized power flow equation.

## 3. Evaluation of Voltage Stability by Singular Value Decomposition

Suppose the system has  $n$  buses in addition to the slack bus, of which there are  $m$  PV buses, and the singular value decomposition (SVD) [47, 48] is performed on equation (3). Then, the following formula can be obtained:

$$J = E \delta U^T = \sum_{i=1}^{(2n-m)} e_i \delta_i u_i^T, \quad (4)$$

where  $e_i$  and  $u_i$  represent the  $i$ -th column elements of  $E$  and  $U$ , respectively, and  $\delta_i$  is the diagonal element of the diagonal matrix. If the Jacobian matrix is nonsingular, the effect of the increment  $\Delta P$  and  $\Delta Q$  of the injection powers  $P$  and  $Q$  on  $\theta$  and  $V$  can be obtained by equations (2) and (4):

$$\begin{bmatrix} \Delta \theta \\ \Delta V \end{bmatrix} = J^{-1} \begin{bmatrix} \Delta P \\ \Delta Q \end{bmatrix} = \sum_{i=1}^{2n-m} \delta_i^{-1} u_i e_i^T \begin{bmatrix} \Delta P \\ \Delta Q \end{bmatrix}. \quad (5)$$

It can be seen from equation (5) that when a singular value  $\delta_i$  is very small (close to zero), the small change of injection power  $P$  and  $Q$  will cause great fluctuation of  $\theta$  and  $V$ . The response of the system is completely determined by the minimum singular value (MSV)  $\delta_{\min}$  and its corresponding left and right singular vectors  $e_{\min}$  and  $u_{\min}$ , that is:

$$\begin{bmatrix} \Delta \theta \\ \Delta V \end{bmatrix} = \sum_{i=1}^{2n-m} \delta_i^{-1} u_{\min} e_{\min}^T \begin{bmatrix} \Delta P \\ \Delta Q \end{bmatrix}, \quad (6)$$

where  $u_{\min} = [\theta_1, \theta_2, \dots, \theta_n; v_1, v_2, \dots, v_{n-m}]^T$  and  $e_{\min} = [P_1, P_2, \dots, P_n; Q_1, Q_2, \dots, Q_{n-m}]^T$ .

Here,  $e_{\min}$  and  $u_{\min}$  are normalized to

$$\begin{cases} \sum_{i=1}^n \theta_i^2 + \sum_{i=1}^{n-m} v_i^2 = 1, \\ \sum_{i=1}^n P_i^2 + \sum_{i=1}^{n-m} Q_i^2 = 1, \end{cases} \quad (7)$$

and then

$$\begin{bmatrix} \Delta P \\ \Delta Q \end{bmatrix} = e_{\min}, \quad (8)$$

and thus

$$\begin{bmatrix} \Delta \theta \\ \Delta V \end{bmatrix} = \frac{u_{\min}}{\delta_{\min}}. \quad (9)$$

From equations (8) and (9), it can be concluded that since the MSV is sufficiently small, a small change in the injection power can cause a large change in voltage. The MSV of the Jacobian matrix can be used as a good indicator of static voltage stability [49, 50].

#### 4. Evaluation of Static Voltage Stability by PMU Data

The aforementioned static voltage stability method by using the MSV of Jacobian matrix can give the static voltage stability quantitatively, but it depends on the fixed physical model and cannot judge the static voltage stability online.

##### 4.1. Estimation of Power Flow Jacobian Matrix by PMU Data.

In polar coordinates, the terms of the Jacobian matrix of power flow can be represented by the partial derivative of  $\theta_j$  and  $V_j$  by  $P_i$  and  $Q_i$ , respectively, and then formula (3) can be expressed as

$$\begin{cases} H_{ij} = \frac{\partial P_i}{\partial \theta_j}, \\ N_{ij} = \frac{\partial P_i}{\partial V_j} V_j, \\ J_{ij} = \frac{\partial Q_i}{\partial \theta_j}, \\ L_{ij} = \frac{\partial Q_i}{\partial V_j} V_j. \end{cases} \quad (10)$$

Suppose both  $\theta_j$  and  $V_j$  have a very small change, represented by  $\Delta\theta_j$  and  $\Delta V_j$ , respectively. Then,  $P_i$  and  $Q_i$  will also change with the slight changes above, denoted by  $\Delta P_i^{\Delta\theta_j}$ ,  $\Delta P_i^{\Delta V_j}$  and  $\Delta Q_i^{\Delta\theta_j}$ ,  $\Delta Q_i^{\Delta V_j}$ , respectively; then, equation (10) can be expressed as [51]

$$\begin{cases} H_{ij} = \frac{\partial P_i}{\partial \theta_j} \approx \frac{\Delta P_i^{\Delta\theta_j}}{\Delta\theta_j}, \\ N_{ij} = \frac{\partial P_i}{\partial V_j} V_j \approx \frac{\Delta P_i^{\Delta V_j}}{\Delta V_j} V_j, \\ J_{ij} = \frac{\partial Q_i}{\partial \theta_j} \approx \frac{\Delta Q_i^{\Delta\theta_j}}{\Delta\theta_j}, \\ L_{ij} = \frac{\partial Q_i}{\partial V_j} V_j \approx \frac{\Delta Q_i^{\Delta V_j}}{\Delta V_j} V_j. \end{cases} \quad (11)$$

At time  $t$ :

$$\begin{cases} \Delta P_i(t) \approx \sum_{j \in N_g \cup N_l} \Delta P_i^{\Delta\theta_j}(t) + \sum_{j \in N_l} \Delta P_i^{\Delta V_j}(t), \\ \Delta Q_i(t) \approx \sum_{j \in N_g \cup N_l} \Delta Q_i^{\Delta\theta_j}(t) + \sum_{j \in N_l} \Delta Q_i^{\Delta V_j}(t), \end{cases} \quad (12)$$

where  $N_g$  represents the number of PV buses and  $N_l$  represents the number of PQ buses, and substituting equation (11) into (12) yields

$$\begin{cases} \Delta P_i(t) \approx \sum_{j \in N_g \cup N_l} \Delta\theta_j(t) H_{ij} + \sum_{j \in N_l} \Delta V_j(t) N_{ij}, \\ \Delta Q_i(t) \approx \sum_{j \in N_g \cup N_l} \Delta\theta_j(t) J_{ij} + \sum_{j \in N_l} \Delta V_j(t) L_{ij}. \end{cases} \quad (13)$$

Further consolidation of equation (13) is available:

$$\Delta P_i \approx \left[ (\Delta\theta_j)_{j \in N_g \cup N_l} (\Delta V_j)_{j \in N_l} \right] \begin{bmatrix} H_i \\ N_i \end{bmatrix}, \quad (14)$$

$$\Delta Q_i \approx \left[ (\Delta\theta_j)_{j \in N_g \cup N_l} (\Delta V_j)_{j \in N_l} \right] \begin{bmatrix} J_i \\ L_i \end{bmatrix}, \quad (15)$$

where  $H_i = [(H_{ij}), j \in N_g \cup N_l]$ ,  $N_i = [(N_{ij}), j \in N_l]$ ,  $J_i = [(J_{ij}), j \in N_g \cup N_l]$ ,  $L_i = [(L_{ij}), j \in N_l]$ .

**4.2. Model Solution.** In the assumption of equations (14) and (15), both the regression matrix and the measurement vector have measurement errors. For the convenience of expression, here we make  $A = [(\Delta\theta_j)_{j \in N_g \cup N_l} (\Delta V_j)_{j \in N_l}]$ ,  $b_i = P_i$ ; then, equation (14) can be expressed as

$$b_i \approx A \begin{bmatrix} H_i^T \\ N_i^T \end{bmatrix}^T. \quad (16)$$

Since equation (16) is an overdetermined equation, in this paper,  $[H_i \ N_i]^T$  is calculated by using the total least square (TLS) [52, 53]. This method is also suitable for equation (15).

In the ordinary least squares estimate (LSE), since the regression matrix is assumed to be error-free, the principle of this method is to correct  $b_i$  as little as possible under the



Euclidean norm [51], which forms the following optimization problem [54]:

$$\begin{cases} \min_{\hat{b}_i \in R^M} \|\Delta b_i\|_2, \\ \hat{b}_i = A [H_i^T \ N_i^T]^T, \end{cases} \quad (17)$$

where  $M$  represents sets of synchronized measurements,  $\Delta b_i = b_i - \hat{b}_i$  ( $\hat{b}_i$  is a very small value), and any  $[\widehat{H}_i \ \widehat{N}_i]^T$  that satisfies  $\widehat{b}_i = A [\widehat{H}_i \ \widehat{N}_i]^T$  is the solution of LSE of equation (16).

Assuming that  $A$  is full rank, the special solution of the closed form of equation (17) is

$$[\widehat{H}_i \ \widehat{N}_i]^T = (A^T A)^{-1} A^T b_i. \quad (18)$$

Unlike LSE, TLS also takes into account the measurement error in  $A$ ; similar to the Euclidean norm, the problem is to find a minimized F-norm, as follows:

$$\begin{cases} \min_{[\widehat{A} \ \widehat{b}_i] \in R^{M \times (N+1)}} \|[ \Delta A \ \Delta b_i ]\|_F, \\ \widehat{b}_i = \widehat{A} [H_i^T \ N_i^T]^T, \end{cases} \quad (19)$$

where  $\bar{N} = N_g + 2N_l$  and  $\Delta A = A - \widehat{A}$ ,  $\Delta b_i = b_i - \widehat{b}_i$ .

The TLS solution of equation (19) depends on the SVD. We describe this process and write equation (16) as follows:

$$[A \ b_i] [H_i^T \ N_i^T \ -1]^T \approx 0. \quad (20)$$

By using the SVD, the above formula can be rewritten as

$$[A \ b_i] = E \delta U^T, \quad (21)$$

where  $E = [e_1, e_2, \dots, e_m]$ ,  $U = [u_1, u_2, \dots, u_{N+1}]$  is a symmetric matrix whose diagonal element  $\delta_i$  is the singular value of  $[A \ b_i]$ . If  $\delta_{n+1} \neq 0$ ; then, the rank of  $[A \ b_i]$  is  $(N + 1)$ , and the only solution of equation (20) is zero vector. In order to obtain the nonzero solution of equation (20),  $[A \ b_i]$  must be reduced to the rank  $N$ . The matrix approximation theorem shows that

$$[\widehat{A} \ \widehat{b}_i] = E \widehat{\delta} U^T. \quad (22)$$

Since the rank of the approximate matrix  $[\widehat{A} \ \widehat{b}_i]$  is equal to  $N$ , equation (20) has a nonzero solution. According to the nature of the SVD,  $u_{N+1}$  is the unique vector belonging to the zero vector space  $[\widehat{A} \ \widehat{b}_i]$ , and the TLS solution is obtained by scaling the vector  $u_{N+1}$  until the last element is  $-1$ :

$$[\widehat{H}_i^T \ \widehat{N}_i^T \ -1]^T = -\frac{1}{u_{N+1}^{N+1}} u_{N+1}, \quad (23)$$

where  $u_{N+1}^{N+1}$  represents the  $(N + 1)$ th element of  $u_{N+1}$ ; then, the unique TLS solution of equation (16) is

$$[\widehat{H}_i^T \ \widehat{N}_i^T]^T = -\frac{1}{u_{N+1}^{N+1}} [u_{N+1}^1, u_{N+1}^2, \dots, u_{N+1}^{N+1}]. \quad (24)$$

## 5. Algorithm Flow and Basic Steps

The flowchart of the proposed method is shown in Figure 1. The specific steps are as follows:

- (1) Collect multiple sets of PMU data from different buses at the  $(t + \Delta t)$  time, and the number of collected groups is greater than the order of the Jacobian matrix.
- (2) Obtain  $\Delta P_i, \Delta Q_i, \Delta \theta_i, \Delta V_i$  by difference.
- (3) Taking the data obtained in step 2 into equation (14), the solution of the overdetermined equations is obtained by the TLS method, and the Jacobian matrix of power flow is obtained.
- (4) Calculate the MSV of the Jacobian matrix/obtained in step 3 and compare it with the threshold  $\tau$ , if the difference exceeds the margin  $\xi$ .
- (5) Repeat steps 1 to 4 to realize real-time monitoring of the power grid.

By collecting the electrical quantities of different buses at time  $(t + \Delta t)$ , including  $P_i, Q_i, \theta_i$ , and  $V_i$ , the power flow Jacobian matrix can be obtained according to equations (14) and (15). This process is shown in Figure 2.

Note that the number of samples is greater than the order of the Jacobian matrix. The results of the MSV of the power flow Jacobian matrix estimated by PMU data and calculated by the Newton–Raphson method are shown in Table 1.

Comparing the data in Table 1, it can be seen that the difference is small in terms of the MSV obtained by the Newton–Raphson method and the PMU data. This shows that the proposed method can be used to evaluate the static voltage stability of the system.

## 6. Case Study

In this study, it is assumed that all buses of the system are equipped with PMUs. In order to simulate the process of voltage collapse in the power system, the active power  $P$  is increased by 0.01 steps in the fifth node of the IEEE 57-bus system, and the MSV of the Jacobian matrix calculated by the proposed method is tracked in real time. The results are shown in Figure 3:

$P/V8 - \delta_{\min}$ ,  $P/V13 - \delta_{\min}$ ,  $P/V31 - \delta_{\min}$ , and  $P/V33 - \delta_{\min}$  above represent the process of the voltage  $V$  changing and the MSV  $\delta_{\min}$  of the buses 8, 13, 31, and 33 changing with the change of power  $P$ , respectively.  $P/\delta_{\min}$  represents the process in which the MSV of the system varies with power  $P$ .

It can be seen from the  $P/\delta_{\min}$  curve that as the power increases for the different buses, the MSV  $\delta_{\min}$  of the system decreases continuously. When  $\delta_{\min}$  is close to zero, the system collapses. Comparing the  $P/\delta_{\min}$  and  $P/V$  ( $pu$ ) curves,

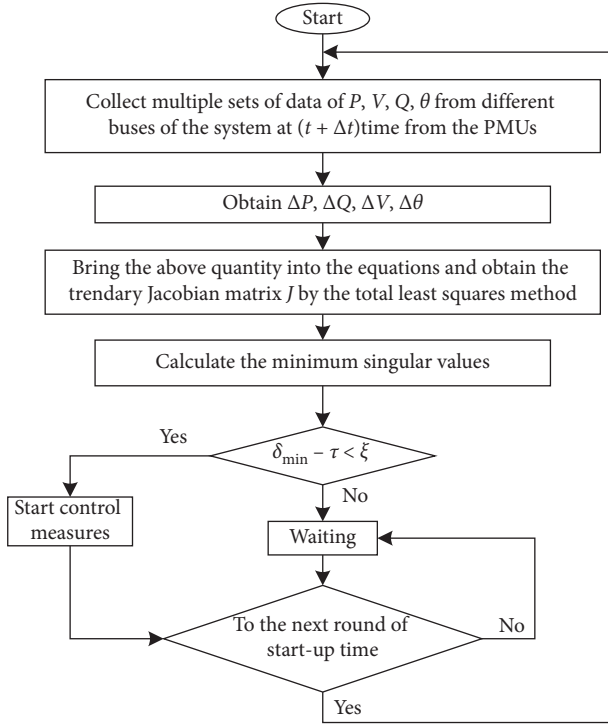


FIGURE 1: Flowchart of the proposed method.

$$\begin{aligned}
 & \dots P_{i(k)}, P_{i(k+1)}, \dots, P_{i(k+x)}, P_{i(k+x+y)} \dots \\
 & \dots Q_{i(k)}, Q_{i(k+1)}, \dots, Q_{i(k+x)}, Q_{i(k+x+y)} \dots \\
 & \dots \theta_{i(k)}, \theta_{i(k+1)}, \dots, \theta_{i(k+x)}, \theta_{i(k+x+y)} \dots \\
 & \dots V_{i(k)}, V_{i(k+1)}, \dots, V_{i(k+x)}, V_{i(k+x+y)} \dots
 \end{aligned}$$

FIGURE 2: Data collection of PMU.

TABLE 1: MSV based on Newton–Raphson method and PMU data.

Bus systems	Newton–Raphson method	PMU data
IEEE 9-bus system	0.8942	0.8928
IEEE 14-bus system	0.5464	0.5441
IEEE 30-bus system	0.2165	0.2068
IEEE 57-bus system	0.1745	0.1725
IEEE 118-bus system	0.1848	0.1836
IEEE 300-bus system	0.0397	0.0302

it can be seen that as  $\delta_{\min}$  decreases ( $P$  increases continuously), the voltage value also decreases and the rate of decrease is different. When  $\delta_{\min}$  is close to zero, a small change of  $P$  causes a large fluctuation in voltage, which is consistent with the context in equations (8) and (9).

During normal operation of the two systems, the sampling frequency of PMU is taken as 50 Hz/s, and the MSV values of the power flow Jacobian matrix are calculated every 4 seconds according to equations (14) and (15). In this way, the evolution curves of the MSV values are demonstrated in Figure 4.

$\delta_{1,\min}$  and  $\delta_{2,\min}$  represent the smallest singular value obtained by the Newton–Raphson method and PMU data, respectively. The mean square errors of the two methods are

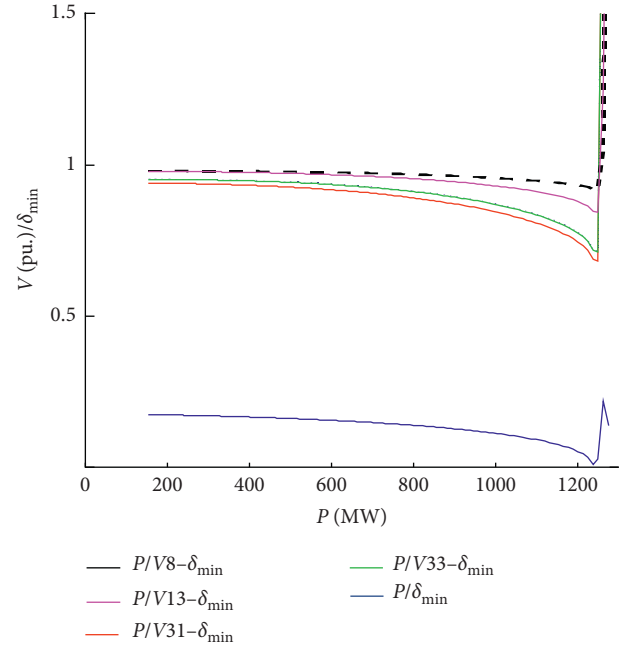
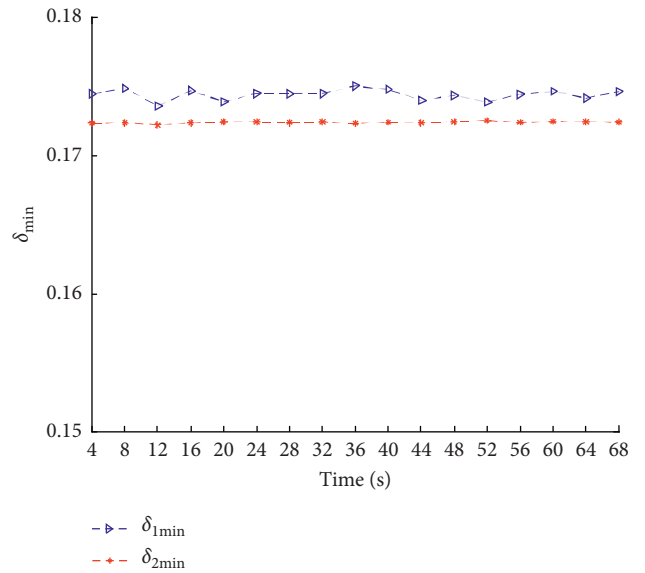

 FIGURE 3:  $P$ - $V/\delta_{\min}$  curves of the IEEE 57-bus system.


FIGURE 4: Evolution curves of the MSV values in the IEEE 57-bus system.

0.0023 and 0.0002, respectively. By comparing the matching degree of the curves of Figure 4, it can be seen that the curves obtained by the two methods are basically consistent, indicating that the method proposed in this paper can monitor the static voltage stability of the system online.

The active power  $P$  is increased by the step of 0.005 at bus 6 of the IEEE 57-bus system, and the static voltage stability of the power system is estimated from every 200 PMU measurements, as shown in Figure 5.

By comparing the matching degree of the curves in Figure 5, we can see that the curves obtained by the two

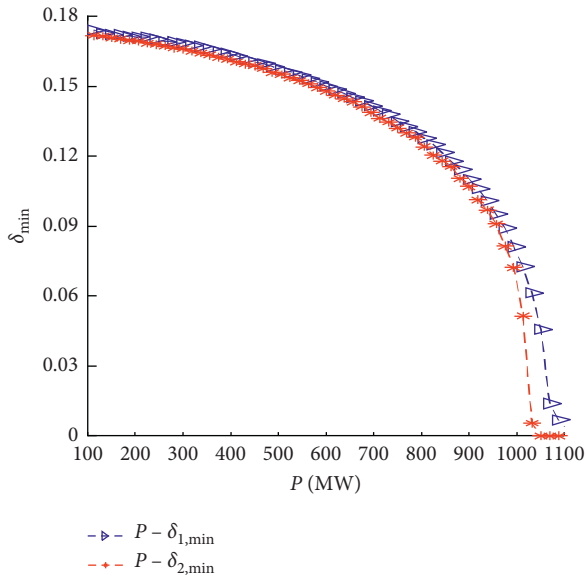


FIGURE 5: Curves of  $P$ - $\delta_{\min}$  of IEEE 57-bus system.

methods are basically consistent, which shows that the method proposed in this paper can realize online monitoring in the process of system instability.

## 7. Conclusion

A method for real-time evaluation of static voltage stability of a power system based on PUM data is proposed. The effectiveness of the proposed method is verified by the IEEE 57-bus system. The conclusions are as follows:

- (1) The proposed method is capable of realizing online monitoring of static voltage stability of power systems.
- (2) Compared with the traditional method, the proposed method does not need any model and parameter information of the power grid and only needs PMU data for the implementation.
- (3) The proposed method can be used in an online stability detection system of power systems for situational awareness improvement.

Our future work will focus on extending the proposed approach to estimate an accurate voltage stability boundary and address stability constraints in voltage stability-constrained optimal power flow [55–58]. It is interesting to investigate the voltage stability of power systems with new elements such as distributed generations [59–61] and combined heat and power plants [62]. Besides, the optimal placement of PMU will be further studied to realize the monitoring of the whole network with fewer PMUs. Another potential topic in future research is to develop voltage stability assessment model using new machine learning techniques such as the lasso algorithm [63], least squares support vector machines [64], and deep learning [65].

## Data Availability

The IEEE 57-bus system data used to support the findings of this study are included within the article.

## Conflicts of Interest

The authors declare that they have no conflicts of interest.

## References

- [1] P. M. Anderson and A. A. Fouad, *Power System Control and Stability*, IEEE, Piscataway, NJ, USA, 2nd edition, 2003.
- [2] P. Kundur, J. Paserba, V. Ajarapu et al., “Definition and classification of power system stability,” *IEEE Transactions on Industrial Electronics*, vol. 19, pp. 1387–1401, 2004.
- [3] Y. Li, B. Feng, G. Li, J. Qi, D. Zhao, and Y. Mu, “Optimal distributed generation planning in active distribution networks considering integration of energy storage,” *Applied Energy*, vol. 210, pp. 1073–1081, 2018.
- [4] Y. Li, Z. Yang, G. Li, D. Zhao, and W. Tian, “Optimal scheduling of an isolated microgrid with battery storage considering load and renewable generation uncertainties,” *IEEE Transactions on Industrial Electronics*, vol. 66, no. 2, pp. 1565–1575, 2019.
- [5] Y. Li, Z. Yang, G. Li et al., “Optimal scheduling of isolated microgrid with an electric vehicle battery swapping station in multi-stakeholder scenarios: a bi-level programming approach via real-time pricing,” *Applied Energy*, vol. 232, pp. 54–68, 2018.
- [6] Y. Li, C. Wang, G. Li, J. Wang, D. Zhao, and C. Chen, “Improving operational flexibility of integrated energy system with uncertain renewable generations considering thermal inertia of buildings,” *Energy Conversion and Management*, vol. 207, p. 112526, 2020.
- [7] P. Jin, Y. Li, G. Li, Z. Chen, and X. Zhai, “Optimized hierarchical power oscillations control for distributed generation under unbalanced conditions,” *Applied Energy*, vol. 194, pp. 343–352, 2017.
- [8] Y. Li, Y. Li, G. Li, D. Zhao, and C. Chen, “Two-stage multi-objective OPF for AC/DC grids with VSC-HVDC: incorporating decisions analysis into optimization process,” *Energy*, vol. 147, pp. 286–296, 2018.
- [9] Y. Li and S. Wu, “Controlled islanding for a hybrid AC/DC grid with VSC-HVDC using semi-supervised spectral clustering,” *IEEE Access*, vol. 7, pp. 10478–10490, 2019.
- [10] B. Feng, X. Zhai, Y. Li, and Z. Wang, “Experimental study on black-start capability of VSC-HVDC for passive networks,” in *Proceedings of the 2016 PES Asia-Pacific Power & Energy Engineering Conference (APPEEC)*, vol. 25–28, pp. 2560–2563, Xi’an, China, October 2016.
- [11] Y. Li, Z. Yang, D. Zhao, H. Lei, B. Cui, and S. Li, “Incorporating energy storage and user experience in isolated microgrid dispatch using a multi-objective model,” *IET Renewable Power Generation*, vol. 13, no. 6, pp. 973–981, 2019.
- [12] Y. Li and K. Li, “Incorporating demand response of electric vehicles in scheduling of isolated microgrids with renewables using a bi-level programming approach,” *IEEE Access*, vol. 7, pp. 116256–116266, 2019.
- [13] Y. Li, Z. Li, and L. Chen, “Dynamic state estimation of generators under cyber attacks,” *IEEE Access*, vol. 7, pp. 125253–125267, 2019.
- [14] Z. Qu, Y. Zhang, N. Qu, L. Wang, Y. Li, and Y. Dong, “Method for quantitative estimation of the risk propagation threshold

- in electric power CPS based on seepage probability," *IEEE Access*, vol. 6, pp. 68813–68823, 2018.
- [15] Z. Qu, Q. Xie, Y. Liu et al., "Power cyber-physical system risk area prediction using dependent Markov chain and improved grey wolf optimization," *IEEE Access*, vol. 8, pp. 82844–82854, 2020.
- [16] Y. Li, J. Wang, D. Zhao, G. Li, and C. Chen, "A two-stage approach for combined heat and power economic emission dispatch: combining multi-objective optimization with integrated decision making," *Energy*, vol. 162, pp. 237–254, 2018.
- [17] M. Zhang and Y. Li, "Multi-objective optimal reactive power dispatch of power systems by combining classification-based Multi-objective evolutionary algorithm and integrated decision making," *IEEE Access*, vol. 8, pp. 38198–38209, 2020.
- [18] V. Terzija, G. Valverde, C. Deyu Cai et al., "Wide-area monitoring, protection, and control of future electric power networks," *Proceedings of the IEEE*, vol. 99, no. 1, pp. 80–93, 2011.
- [19] X. Gu and Y. Li, "Transient stability assessment of power systems based on local learning machine and bacterial colony chemotaxis algorithm," *Transactions of China Electrotechnical Society*, vol. 28, pp. 271–279, 2013.
- [20] I. Kamwa, S. R. Samantaray, and G. Joos, "Compliance analysis of PMU algorithms and devices for wide-area stabilizing control of large power systems," *IEEE Transactions on Power Systems*, vol. 28, no. 2, pp. 1766–1778, 2013.
- [21] Y. Li, G. Li, Z. Wang, Z. Han, and X. Bai, "A multifeature fusion approach for power system transient stability assessment using PMU data," *Mathematical Problems in Engineering*, vol. 2015, p. 1, Article ID 786396, 2015.
- [22] M. Glavic and T. Van Cutsem, "Wide-area detection of voltage instability from synchronized phasor measurements. Part II: simulation Results," *IEEE Transactions on Power Systems*, vol. 24, no. 3, pp. 1417–1425, 2009.
- [23] C. D. Vournas, C. Lambrou, and P. Mandoulidis, "Voltage stability monitoring from a transmission bus PMU," *IEEE Transactions on Power Systems*, vol. 32, no. 4, pp. 3266–3274, 2017.
- [24] L. Zhu, C. Lu, and Y. Sun, "Time series shapelet classification based online short-term voltage stability assessment," *IEEE Transactions on Power Systems*, vol. 31, no. 2, pp. 1430–1439, 2016.
- [25] Y. Zhang, Y. Xu, Z. Y. Dong, and R. Zhang, "A hierarchical self-adaptive data-analytics method for real-time power system short-term voltage stability assessment," *IEEE Transactions on Industrial Informatics*, vol. 15, no. 1, pp. 74–84, 2019.
- [26] S. Li, Y. Tan, C. Li, Y. Cao, and L. Jiang, "A fast sensitivity-based preventive control selection method for online voltage stability assessment," *IEEE Transactions on Power Systems*, vol. 33, no. 4, pp. 4189–4196, 2018.
- [27] Z. H. Wang, Z. Y. You, Y. L. Huang et al., "Load margin analysis of hybrid AC/DC system with two terminal VSC-HVDC using continuous power flow method," *IEEE Transactions on Industrial Informatics*, vol. 46, no. 6, pp. 9–15, 2018.
- [28] A. O. Ekwue, H. B. Wan, D. T. Y. Cheng, and Y. H. Song, "Singular value decomposition method for voltage stability analysis on the National Grid system (NGC)," *International Journal of Electrical Power & Energy Systems*, vol. 21, no. 6, pp. 425–432, 1999.
- [29] I. Rahimi Pordanjani and W. Xu, "A singular value decomposition-based technique for decoupling and analyzing power networks," *International Journal of Electrical Power & Energy Systems*, vol. 74, pp. 265–273, 2016.
- [30] P.-A. Lof, G. Andersson, and D. J. Hill, "Voltage stability indices for stressed power systems," *IEEE Transactions on Power Systems*, vol. 8, no. 1, pp. 326–335, 1993.
- [31] Y. Zhang, Y. Zhang, B. Wu, and J. Zhou, "Power injection model of STATCOM with control and operating limit for power flow and voltage stability analysis," *Electric Power Systems Research*, vol. 76, no. 12, pp. 1003–1010, 2006.
- [32] D. Q. Zhou, U. D. Annakkage, and A. D. Rajapakse, "Online monitoring of voltage stability margin using an artificial neural network," *IEEE Transactions on Power Systems*, vol. 25, no. 3, pp. 1566–1574, 2010.
- [33] H.-Y. Su and C.-W. Liu, "Estimating the voltage stability margin using PMU measurements," *IEEE Transactions on Power Systems*, vol. 31, no. 4, pp. 3221–3229, 2016.
- [34] P. Zhang, F. Li, and N. Bhatt, "Next-generation monitoring, analysis, and control for the future smart control center," *IEEE Transactions on Smart Grid*, vol. 1, no. 2, pp. 186–192, 2010.
- [35] Y. Zhang, T. Li, G. Na, G. Li, and Y. Li, "Optimized extreme learning machine for power system transient stability prediction using synchrophasors," *Mathematical Problems in Engineering*, vol. 2015, p. 1, Article ID 529724, 2015.
- [36] Y. Li and X. Gu, "Power system transient stability assessment based on online sequential extreme learning machine," in *Proceedings of the 2013 PES Asia-Pacific Power & Energy Engineering Conference (APPEEC)*, vol. 2560–2563, pp. 1–4, Hong Kong, China, December 2013.
- [37] Y. Li and X. Gu, "Feature selection for transient stability assessment based on improved maximal relevance and minimal redundancy criterion," *Proceedings of the CSEE*, vol. 33, pp. 179–186, 2013.
- [38] Y. Li, G. Li, and X. Gu, "Transient stability assessment of power systems based on ensemble OS-ELM," *Transactions of China Electrotechnical Society*, vol. 30, pp. 412–418, 2015.
- [39] Y. Li, G. Li, and Z. Wang, "Rule extraction based on extreme learning machine and an improved ant-miner algorithm for transient stability assessment," *PLoS ONE*, vol. 10, no. 6, 2015.
- [40] X. Gu, Y. Li, and J. Jia, "Feature selection for transient stability assessment based on kernelized fuzzy rough sets and memetic algorithm," *International Journal of Electrical Power & Energy Systems*, vol. 64, pp. 664–670, 2015.
- [41] Y. Li and Z. Yang, "Application of EOS-ELM with binary Jaya-based feature selection to real-time transient stability assessment using PMU data," *IEEE Access*, vol. 5, pp. 23092–23101, 2017.
- [42] S. Dasgupta, M. Paramasivam, U. Vaidya, and V. Ajarapu, "Real-Time monitoring of short-term voltage stability using PMU data," *IEEE Transactions on Power Systems*, vol. 28, no. 4, pp. 3702–3711, 2013.
- [43] J. M. Lim and C. L. DeMarco, "Model-free voltage stability assessments via singular value analysis of PMU data," *Power Grid*, vol. 28, pp. 1–10, 2013.
- [44] J. M. Lim and C. L. Demarco, "SVD-based voltage stability assessment from phasor measurement unit data," *IEEE Transactions on Power Systems*, vol. 31, no. 4, pp. 2557–2565, 2016.
- [45] Z.-B. Shi, T. Yu, Q. Zhao, Y. Li, and Y.-B. Lan, "Comparison of algorithms for an electronic nose in identifying liquors," *Journal of Bionic Engineering*, vol. 5, no. 3, pp. 253–257, 2008.
- [46] H. Lan, T. Ai, and Y. Li, "Application of EMD on single-pole adaptive reclosure of transmission," *Power System Protection and Control*, vol. 38, no. 12, pp. 35–39, 2010.
- [47] K. Ben-Kilani and M. Elleuch, "Structural analysis of voltage stability in power systems integrating wind power," *IEEE*



- Transactions on Power Systems*, vol. 28, no. 4, pp. 3785–3794, 2013.
- [48] M. Dehghani, B. Shayanfard, and A. R. Khayatian, “PMU ranking based on singular value decomposition of dynamic stability matrix,” *IEEE Transactions on Power Systems*, vol. 28, no. 3, pp. 2263–2270, 2013.
- [49] A. Tiranuchit and R. J. Thomas, “A posturing strategy against voltage instabilities in electric power systems,” *IEEE Transactions on Power Systems*, vol. 3, no. 1, pp. 87–93, 1988.
- [50] O. A. Urquidez and L. Xie, “Singular value sensitivity based optimal control of embedded VSC-HVDC for steady-state voltage stability enhancement,” *IEEE Transactions on Power Systems*, vol. 31, no. 1, pp. 216–225, 2016.
- [51] Y. C. Chen, J. Wang, A. D. Domínguez-García, and P. W. Sauer, “Measurement-based estimation of the power flow Jacobian matrix,” *IEEE Transactions on Smart Grid*, vol. 7, no. 5, pp. 2507–2515, 2016.
- [52] H.-A. Diao, Y. Wei, and P. Xie, “Small sample statistical condition estimation for the total least squares problem,” *Numerical Algorithms*, vol. 75, no. 2, pp. 435–455, 2016.
- [53] A. M. Ibrahim, M. I. Marei, S. F. Mekhamer, and M. M. Mansour, “An artificial neural network based protection approach using total least square estimation of signal parameters via the rotational invariance technique for flexible AC transmission system compensated transmission lines,” *Electric Power Components and Systems*, vol. 39, no. 1, pp. 64–79, 2011.
- [54] L. Xu and F. Ding, “Recursive least squares and multi-innovation stochastic gradient parameter estimation methods for signal modeling,” *Circuits, Systems, and Signal Processing*, vol. 36, no. 4, pp. 1735–1753, 2017.
- [55] Y. Li and Y. Li, “Two-step many-objective optimal power flow based on knee point-driven evolutionary algorithm,” *Processes*, vol. 6, no. 12, p. 250, 2018.
- [56] Y. Li, Y. Li, and G. Li, “A multi-objective optimal power flow approach considering economy and environmental factors for hybrid AC/DC grids incorporating VSC-HVDC,” *Power System Technology*, vol. 40, pp. 2661–2667, 2016.
- [57] Y. Li, Y. Li, and G. Li, “A two-stage multi-objective optimal power flow algorithm for hybrid AC/DC grids with VSC-HVDC,” in *Proceedings of the 2017 IEEE Power & Energy Society General Meeting*, pp. 1–5, Chicago, IL, USA, July 2017.
- [58] Y. Li and Y. Li, “Security-constrained multi-objective optimal power flow for a hybrid AC/VSC-MTDC system with lasso-based contingency filtering,” *IEEE Access*, vol. 8, pp. 6801–6811, 2020.
- [59] K. Kawabe, Y. Ota, A. Yokoyama, and K. Tanaka, “Novel dynamic voltage support capability of photovoltaic systems for improvement of short-term voltage stability in power systems,” *IEEE Transactions on Power Systems*, vol. 32, no. 3, pp. 1796–1804, 2017.
- [60] U. Sultana, A. B. Khairuddin, M. M. Aman, A. S. Mokhtar, and N. Zareen, “A review of optimum DG placement based on minimization of power losses and voltage stability enhancement of distribution system,” *Renewable and Sustainable Energy Reviews*, vol. 63, pp. 363–378, 2016.
- [61] E. Vittal, M. O’Malley, and A. Keane, “A steady-state voltage stability analysis of power systems with high penetrations of wind,” *IEEE Transactions on Power Systems*, vol. 25, no. 1, pp. 433–442, 2010.
- [62] J. Sun and Y. Li, “Social cognitive optimization with tent map for combined heat and power economic dispatch,” *International Transactions on Electrical Energy Systems*, vol. 29, no. 1, p. e2660, 2018.
- [63] Y. Li, Y. Li, and Y. Sun, “Online static security assessment of power systems based on lasso algorithm,” *Applied Sciences*, vol. 8, no. 9, p. 1442, 2018.
- [64] Z. B. Shi, Y. Li, and T. Yu, “Short-term load forecasting based on LS-SVM optimized by bacterial colony chemotaxis algorithm,” in *Proceedings of the 2009 International Conference on Information and Multimedia Technology*, pp. 306–309, Jeju Island, South Korea, December 2009.
- [65] Y. LeCun, Y. Bengio, and G. Hinton, “Deep learning,” *Nature*, vol. 521, no. 7553, pp. 436–444, 2015.

## Research Article

# Dynamic Neighborhood-Based Particle Swarm Optimization for Multimodal Problems

Xu-Tao Zhang,<sup>1</sup> Biao Xu ,<sup>2,3</sup> Wei Zhang,<sup>1</sup> Jun Zhang,<sup>4</sup> and Xin-fang Ji<sup>5</sup>

<sup>1</sup>Department of Electrical Engineering, Jiangsu College of Safety Technology, Xuzhou 221100, China

<sup>2</sup>Department of Electronic Engineering, Shantou University, Shantou 515041, China

<sup>3</sup>Key Laboratory of Digital Signal and Image Processing of Guangdong Province, Shantou 515041, China

<sup>4</sup>Xuzhou Kuangyi Automation Technology Co., Ltd., Xuzhou 221100, China

<sup>5</sup>School of Information and Control Engineering, China University of Mining and Technology, Xuzhou 221100, China

Correspondence should be addressed to Biao Xu; xubiao@stu.edu.cn

Received 19 November 2020; Revised 4 December 2020; Accepted 8 December 2020; Published 21 December 2020

Academic Editor: Bo Yang

Copyright © 2020 Xu-Tao Zhang et al. This is an open access article distributed under the Creative Commons Attribution License, which permits unrestricted use, distribution, and reproduction in any medium, provided the original work is properly cited.

Various black-box optimization problems in real world can be classified as multimodal optimization problems. Neighborhood information plays an important role in improving the performance of an evolutionary algorithm when dealing with such problems. In view of this, we propose a particle swarm optimization algorithm based on dynamic neighborhood to solve the multimodal optimization problem. In this paper, a dynamic  $\epsilon$ -neighborhood selection mechanism is first defined to balance the exploration and exploitation of the algorithm. Then, based on the information provided by the neighborhoods, four different particle position updating strategies are designed to further support the algorithm's exploration and exploitation of the search space. Finally, the proposed algorithm is compared with 7 state-of-the-art multimodal algorithms on 8 benchmark instances. The experimental results reveal that the proposed algorithm is superior to the compared ones and is an effective method to tackle multimodal optimization problems.

## 1. Introduction

Various black-box problems to be tackled difficultly in the real world have the characteristic of multimodal problem [1]. Strictly speaking, a multimodal optimization problem (MMOP) refers to an optimization problem with multiple global or local optima. Typical instances include drug molecular design [2], truss structure optimization [3], and protein structure prediction [4]. When solving MMOPs, we expect to locate several optimal solutions simultaneously, for the following reasons [5, 6]: (1) finding multiple optimal solutions in different regions of the search space at the same time is conducive to maintaining the diversity of the population and offset the influence of genetic drift. (2) For many real-world engineering optimization problems, designers hope to freely choose solutions to meet different needs from several excellent solutions with great differences. (3) For the black-box problem, in the absence of prior knowledge, the

positions and the numbers of the global optima of the problem cannot be obtained. Locating multiple optimal solutions of the problem at the same time can improve the possibility of finding its global optimal solution and can also possibly provide multiple optimal solutions for decision makers. In view of this, the field of multimodal optimization has received more and more attention recently due to its scientific and technological significance.

Traditional population-based evolutionary algorithms (EAs), such as genetic algorithm (GA) [7, 8], differential evolutionary (DE) [9], and particle swarm optimization (PSO) [10], are natural candidates for solving MMOPs. However, it should be noted that, in the case of solving MMOPs without special treatment, these EAs can only converge to one optimal solution of the optimization problem at a single run. In order to find multiple optimal solutions of the problem, it is necessary to run them repeatedly and it is expected to find a different optimal solution each time.



In order to enable EAs to solve MMOPs effectively, researchers have proposed a series of techniques, most of which are aimed at enhancing the diversity of population and making it converge towards different search directions. These techniques are commonly referred to as niching [5]. Representative niche techniques include crowding [11], clustering [12–14], speciation [15], and stretching and shrinking method [16]. Recently, niching techniques are also embedded into PSO algorithm in a number of literatures. For example, MMOP is solved by changing the topology of PSO, such as niche PSO based on ring topology [13] and PSO based on star topology and ring topology [17]. In addition, the concept of speciation has also been introduced into the species-based PSO [18–20], where species can form adaptively in different optimal states. However, in order to define a species, a niching radius must be provided in advance. Accordingly, species can be merged or separated into new species in each iteration. Other methods, such as *nbest* PSO [21, 22] and multiswarms [23, 24], are also proposed.

To remedy the defect of requirement for providing the niching radius in advance, a parameter, which is easy to set or with little sensitivity to the performance of the algorithm, is employed to complete the clustering or grouping of individuals by replacing the niching radius. Schoeman and Engelbrecht proposed a vector-based PSO algorithm, which uses vector operations to demarcate the boundaries of niches and maintain subswarms without any prior knowledge of the problem domain [25]. A niche is determined by a radius value based on the distance between the optimal of group and the nearest particle. Qu et al. [26] proposed a distance-based locally informed PSO (LIPS), where the global best position is replaced by multiple local best positions to guide the update of particles for converging to different optimal subspaces. However, LIPS needs to specify the neighborhood size of the particles. Based on the locality sensitive hashing, Zhang et al. proposed a fast niching technique to find the neighborhood set of particles, which can keep a balance between the exploration and exploitation of the algorithm while reducing the computational complexity of EAs [27]. Nevertheless, the method depends on the constructed hash functions. Further, Zhang et al. proposed a concept of parameter-free Voronoi neighborhood; the information provided by the Voronoi neighbors is used to estimate the evolutionary state of an individual. And different types of individuals are assigned with different reproduction strategies to support the exploration and exploitation of the search space [28]. As the dimension of the problem increases, the computational complexity of Voronoi will increase dramatically.

In order to handle the above problems, a dynamic neighborhood-based multimodal PSO algorithm (DNPSO) is proposed in this paper. The aim is to design different evolutionary strategies based on neighborhood information to balance the exploration and exploitation of the algorithm without specifying an exact neighborhood size. The main contributions of DNPSO are provided as follows:

- (1) A dynamic  $\varepsilon$ -neighborhood selection mechanism is proposed. Compared with the existing neighborhood-

based method, the neighborhood size of a particle in this paper is dynamically changed, and it is different for different particles. In addition, the proposed mechanism may lead to a larger possibility of information interaction between distant particles, which is beneficial for generating an exploratory offspring and restoring the exploration ability of PSO.

- (2) Inspired by the successful application of neighborhood information to the design of the multimodal EAs, four different position updating strategies are presented according to the particle's position and performance in its neighborhoods. Consequently, the search performance of the algorithm can be improved.

The rest of this paper is arranged as follows. Section 2 gives the related work for PSO. The proposed DNPSO is presented in Section 3, including the dynamic  $\varepsilon$ -neighborhood selection mechanism, four different position updating strategies, and the framework of the proposed algorithm. In order to verify the effectiveness of the proposed DNPSO, comparison experiments are presented in Section 4. Section 5 highlights main findings and future research opportunities as a result of the survey.

## 2. Particle Swarm Optimization Algorithm

Consider the following maximization problem:

$$\begin{aligned} \max f(X), \\ \text{s.t. } X \in S \subseteq R^D. \end{aligned} \quad (1)$$

where  $X$  is a  $D$ -dimensional decision variable,  $S$  refers to the bound-constraint of the decision space,  $R^D$  means the  $D$ -dimensional space, and  $f(\cdot)$  is the objective function.

PSO is a heuristic search algorithm proposed by Kennedy et al. [29]. The searching principle of PSO comes from the imitation of bird foraging behavior. Due to its simple structure and efficient searching performance, PSO has been successfully applied to solving various optimization problems [30–32]. In PSO, the position of each particle in the search space represents the “potential feasible solution” of the problem to be optimized. The particles are initially random in the feasible search space with a random velocity, which aims to converge to the global optimal solution of the optimization problem. During the optimization process, each particle tracks two optimal positions simultaneously. One is the best position that it has achieved so far, also known as the individual guider (*Pbest*), and the other is the global best position detected so far in the neighborhood of the current particle or in the entire swarm, also known as the global guider (*Gbest*) [29]. Among them, the tracking of individual guider can be regarded as the component of self-cognition, and the learning of global optimal position can be seen as the component of social cognition. In the next iteration, both the ego and the social cognition components randomly influence the velocity of each particle.

Since the PSO was proposed, researchers have proposed numerous PSO variants. Two variants of PSO are presented here, i.e., PSO with inertia weight [29] and LIPS proposed by Qu et al. [26]. At each iteration, the velocity and position of a particle in the PSO with inertia weight are updated as follows:

$$v_{i,d}(t+1) = wv_{i,d}(t) + c_1r_1(Pbest_{i,d}(t) - x_{i,d}(t)) + c_2r_2(Gbest_d(t) - x_{i,d}(t)), \quad (2)$$

$$x_{i,d}(t+1) = x_{i,d}(t) + v_{i,d}(t+1),$$

where  $t$  is the number of iterations;  $X_i(t) = (x_{i,1}(t), x_{i,2}(t), \dots, x_{i,D}(t))$  and  $V_i(t) = (v_{i,1}(t), v_{i,2}(t), \dots, v_{i,D}(t))$  mean the position and velocity of the  $i$ -th particle at the  $t$ -th iteration, respectively.  $Pbest_i(t)$  represents the best position found by the  $i$ -th particle and refers to the best position of the swarm.  $w$  is the inertia weight;  $c_1$  and  $c_2$  are cognitive and social coefficients, respectively.  $r_1$  and  $r_2$  are two random values within  $[0, 1]$ . Figure 1 shows the flow chart of a conventional PSO.

The velocity of a particle in LIPS is determined by the information provided by its neighbors, and the velocity of each particle is updated as follows:

$$v_{i,d}(t+1) = w(v_{i,d}(t) + \varphi(P_{i,d}(t) - x_{i,d}(t))), \quad (3)$$

where

$$P_i(t) = \frac{\sum_{j=1}^{nsize} (\varphi_j nbest_j(t)) / nsize}{\varphi}, \quad (4)$$

where  $\varphi_j$  refers to a random value uniformly distributed in  $[0, 4.1/nsize]$  [26],  $\varphi = \sum_{j=1}^{nsize} \varphi_j$ ,  $nbest_j$  is the  $j$ -th nearest neighborhood to  $Pbest_i$ , and  $nsize$  means the neighborhood size.

### 3. Dynamic Neighborhood-Based PSO for Multimodal Problems

In this section, two key techniques are presented in the proposed DNPSO. One is the definition of dynamic  $\varepsilon$ -neighborhood; the other is the four tailored particle update strategies based on the neighborhood information of the current particle, and the framework of the proposed DNPSO is also provided.

**3.1. Dynamic  $\varepsilon$ -Neighborhood.** At present, a number of researchers try to solve the MMOPs by using distance-based neighborhood to form different species in the search space, and most of them show that neighborhood information is crucial to enhance the diversity of the population [26, 33–35]. However, with neighborhood information, the offspring produced by these methods tend to be attracted to the inner regions enclosed by the initial population. Therefore, the number of optimal solutions is likely to depend on the initial distribution of individuals. To address this issue, we expect that particles can exchange information not only from their nearby particles, but also from the

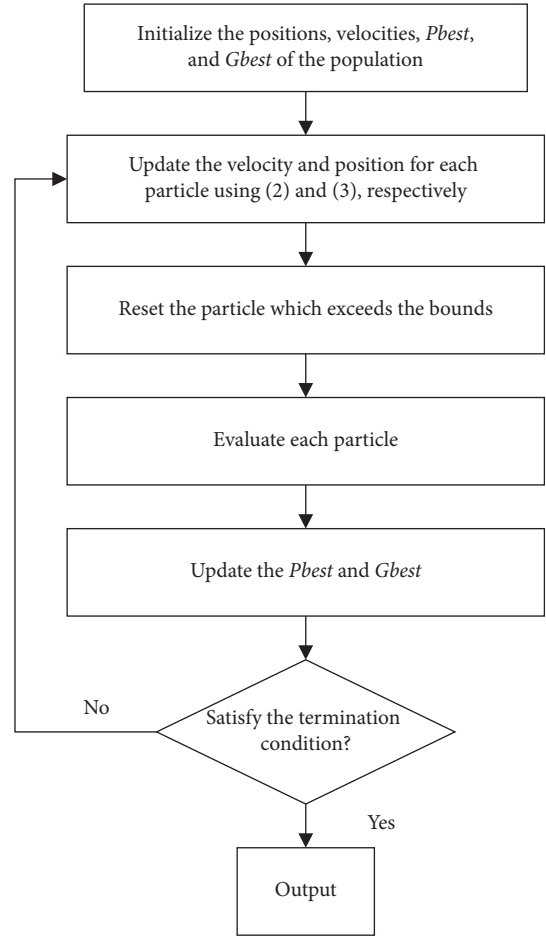


FIGURE 1: Flow chart of a conventional PSO.

distant particles. Thereby, a balance can be achieved between the exploration and exploitation of the algorithm.

In view of this, this section presents a dynamic  $\varepsilon$ -neighborhood approach, where  $\varepsilon$  refers to the neighborhood radius. This approach is inspired by the idea of density clustering, and readers interested in this can refer to [36]. Some definitions of dynamic  $\varepsilon$ -neighborhood are presented as follows.

**Definition 1.** (Core object).  $X_i$  is a core object if the  $\varepsilon$ -neighborhood of  $X_i$  contains at least  $MinPts$  samples.

**Definition 2.** (Directly neighborhood-reachable). If  $X_j$  is located in the  $\varepsilon$ -neighborhood of  $X_i$ , and  $X_i$  is the core object, then  $X_j$  is directly reachable by  $X_i$ .

**Definition 3.** (Neighborhood-reachable). For  $X_i$  and  $X_j$ , if there exists a point  $p$  that makes  $X_i$  and  $p$  directly neighborhood-reachable and  $p$  and  $X_j$  are also directly neighborhood-reachable, then  $X_j$  is reachable by neighborhood of  $X_i$ .

Figure 2 further illustrates the definitions of dynamic  $\varepsilon$ -neighborhood. From Figure 2, we can easily obtain that if  $X$  is a core object, then A, B, C, D, and E are directly

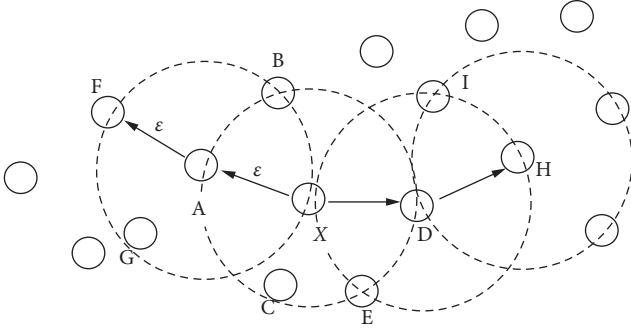


FIGURE 2: Diagram of dynamic  $\varepsilon$ -neighborhood.

neighborhood-reachable by X, and F, G, H, and I are neighborhood-reachable by X.

It should be noted that the purpose of dynamic  $\varepsilon$ -neighborhood selection mechanism is to obtain the neighbors of each particle in the population. Therefore, each particle in the population is regarded as the core object. According to Definition 1, the  $\varepsilon$ -neighborhood of a core object should include at least  $MinPts$  points. A fixed value for  $MinPts$  is first provided in this paper, as the value of  $\varepsilon$  is difficult to set without prior knowledge. Then, we set  $\varepsilon_i = dis_{max}$ , where  $dis_{max}$  refers to the maximum distance between  $X_i$  and the particles in the set of directly neighborhood-reachable. Based on this, the neighborhood-reachable particles of  $X_i$  are found, so as to form the dynamic neighborhood of particle  $X_i$ .

The proposed dynamic  $\varepsilon$ -neighborhood has three characteristics. (1) The neighborhood size of particle  $X_i$  varies dynamically in different evolutionary stage. (2) The neighborhood sizes of different particles in the same evolutionary stage may also be different. (3) Dynamic  $\varepsilon$ -neighborhood divides the neighborhood of the particle  $X_i$  into two levels. The particles in the group of directly neighborhood-reachable can be regarded as the close neighbors of  $X_i$ , while the particles in the group of neighborhood-reachable are regarded as the far neighbors of  $X_i$ . Algorithm 1 presents the pseudocode of dynamic  $\varepsilon$ -neighborhood selection mechanism.

**3.2. PSO Based on Neighborhood Information.** The neighborhood information of particles is employed to deal with the MMOPs in DNPSO. The detailed pseudocode of DNPSO is shown in Algorithm 2. At the beginning of DNPSO, Latin hypercube sampling (LHS) is utilized to generate the initial population with the size of  $N_{PSO}$  in the search space. Then, under  $MaxFEs$ , the particles are iteratively updated in the population. The detailed procedures are described as follows. Firstly, Algorithm 1 is employed to find the neighborhood of  $Pbest_i$  in  $Pbest$ , including the close neighbors in the group of directly neighborhood-reachable (Ndr) and far neighbors in the group of neighborhood-reachable (Nr). Then, comparing  $Pbest_i$  with the particles in Ndr and Nr, a position updating strategy is selected for  $X_i$ . After the new position of  $X_i$  is generated and evaluated, it will be compared with  $Pbest_i$ . If the performance of the updated  $X_i$  is better than

that of  $Pbest_i$ , update  $Pbest_i$ ; otherwise,  $Pbest_i$  remains unchanged.

The main idea of DNPSO is to assign the most appropriate position updating strategy to the particles, so that multiple optimal solutions of the optimization problem can be located simultaneously more effectively. Specifically, this paper adopts four updating strategies to generate offspring.

**Case 1.** When  $Pbest_i$  has the optimal performance in its directly neighborhood-reachable set, Ndr, and neighborhood-reachable set, Nr, it indicates that  $Pbest_i$  is likely to be close to a peak in the search space, as shown in Figure 3(a). Therefore,  $Pbest_i$  can be modified in a small scale by adding a Gaussian disturbance to it in the expectation that it will move in the direction of its nearest peak. The position update formula of  $X_i$  is given as follows:

$$x_{i,d}(t+1) = Pbest_{i,d}(t) + \text{Gaussian}(0, \sigma), \quad (5)$$

where  $\text{Gaussian}(0, \sigma)$  is the Gaussian distribution with mean zero and standard deviation  $\sigma$ .

**Case 2.** When  $P_{best_i}$  is optimal in its Ndr but is not the best in its Nr, it indicates that  $P_{best_i}$  may be on a valley or on an unimportant local optimal peak, as shown in Figure 3(b). Therefore, it is necessary to exchange information with the particles in its distant neighbors, i.e., the neighbors in Nr, to make it jump out of the unimportant local optimum. The velocity update strategy of  $X_i$  adopts formula (3), where nbest stores all the particles which is better than  $Pbest_i$  in Nr.

**Case 3.** When  $Pbest_i$  is not optimal in its Ndr and not worst in its Nr, it indicates that  $Pbest_i$  may be halfway up a hill in the search space, as shown in Figure 3(c). Therefore, the convergence speed can be improved and the exploitation of the algorithm can be improved by exchanging information with the superior particles in the nearest neighbors. Formula (3) is also used for the velocity update of  $X_i$ , where nbest is the nearest neighbor set, i.e., the particles which are better than  $P_{best_i}$  in Ndr.

**Case 4.** When  $Pbest_i$  has the worst performance in its Ndr and Nr, indicating that  $Pbest_i$  may be close to a valley, as shown in Figure 3(d), at this point, it can learn multiple directions, so as to improve the exploration of the algorithm. Then, the velocity update formula of  $X_i$  adopts the following formula:

$$v_{i,d}(t+1) = wv_{i,d}(t) + c_1r_1(Nbest_{Ndr,d}(t) - x_{i,d}(t)) + c_2r_2(Nbest_{Nr,d}(t) - x_{i,d}(t)), \quad (6)$$

where  $Nbest_{Ndr}(t)$  is the optimal particle in Ndr and  $Nbest_{Nr}(t)$  is the optimal particle in Nr of  $Pbest_i$ .

It should be noted that a neighborhood-reachable set, Nr, may be an empty set. In this case, two situations are discussed: (1) when  $Pbest_i$  is optimal in its Ndr, it will be processed in accordance with Case 1; (2) when  $Pbest_i$  is not the best in its Ndr, it will be processed in accordance with Case 3.

```

Input: Population size,  $N_{PSO}$ ,  $MinPts$ , the  $i$ -th particle in the population,  $X_i$ ;
Output: Ndr: Directly neighborhood-reachable group of  $X_i$ ; Nr: neighborhood-reachable group of  $X_i$ ;
(1) For  $j = 1: N_{PSO}$ ;
(2)   While  $X_i \sim X_j$  do;
(3)     Calculate the Euclidean distance between  $X_i$  and  $X_j$ ;
(4)   End;
(5) End;
(6) Take the nearest  $MinPts$  particles with  $X_i$ ,  $p_1, \dots, p_{MinPts}$ , and store them in Ndr;
(7) The maximum distance between  $X_i$  and the particles in Ndr is denoted as  $dismax$ , and set  $\epsilon_i = dismax$ ;
(8) For  $k = 1: MinPts$ ;
(9)   For  $j = 1: N_{PSO}$ ;
(10)    While  $p1-MinPts \sim X_j$  &  $X_i \sim X_j$  do;
(11)     Calculate the Euclidean distance between  $p_k$  and  $X_j$ . If the distance is less than  $\epsilon_i$ , then put it into Nr.
(12)    End;
(13)   End;
(14) End.

```

ALGORITHM 1: Dynamic  $\epsilon$ -neighborhood selection of particle  $X_i$ .

**3.3. Complexity Analysis.** The time complexity of multimodal EAs is governed by their niching components. Generally, it is estimated by the number of elementary operations performed at each generation. The computational complexity of the proposed DNPSO is composed of two parts: the construction of particle's neighborhood in Subsection 3.1 and the operation of PSO in Subsection 3.2. The complexity of constructing the neighborhood of a particle is  $O(D \cdot N_{PSO} + MinPts \cdot N_{PSO})$ . Then, the complexity of constructing all particle's neighborhood in the population is  $O((D + MinPts) \cdot N_{PSO}^2)$ , where  $D$  is the problem dimension and  $N_{PSO}$  is the population size. The time complexity of running PSO is  $O(DN_{PSO})$ . Hence, the total time complexity is  $O((D + MinPts) \cdot N_{PSO}^2 + D \cdot N_{PSO})$ . Since the value of  $N_{PSO}$  is large, the amortized cost of DNPSO for each generation is  $O((D + MinPts) \cdot N_{PSO}^2)$ .

## 4. Experiments and Analysis

In order to verify the effectiveness of the proposed DNPSO, the experiment is divided into the following two parts: (1) analyzing the sensitivity of the proposed algorithm to the value of  $MinPts$  and (2) comparing DNPSO with 7 state-of-the-art multimodal EAs to test its capability of tackling MMOPs. In this paper, eight widely used benchmark problems are selected to test the performance of the algorithm. These benchmark problems are derived from the IEEE CEC 2013 special section on multimodal optimization [37]. The characteristics of these instances are shown in Table 1, where the "Peak height" refers to the value of the global optimal solution. All the algorithms are implemented by MATLAB R2014b on a CPU with Intel Core i5 and 1.6 GHz, and the experimental results are the average of 30 independent runs.

**4.1. Parameter Settings.** In DNPSO, the population size,  $N_{PSO}$ , the maximum number of evaluations,  $MaxFEs$ , and the niching radius,  $r$  (which is used to distinguish the two

neighboring global optimal solutions) are all set according to [34], as shown in Table 2. The amplitude accuracy is set to  $1E-03$ .  $MinPts = 3$ ; in formula (4),  $w = 0.7298$ ; the standard deviation in formula (6) is 0.1; in formula (7),  $w = 0.7298$ ,  $c_1 = 2.05$ , and  $c_2 = 2.05$ . According to [26], the neighborhood size ( $nsize$ ) changes within  $\{2, 3, 4, 5\}$  as increase of generations.

**4.2. Performance Metrics.** In this paper, two commonly used performance indicators are used to evaluate the performance of an algorithm [28]:

- (1) Peak ratio (PR): the peak ratio is the average percentage of the global optima found in multiple independent runs. The PR is calculated using the following formula:

$$PR = \frac{\sum_{i=1}^R NPF_i}{NPF \times R}, \quad (7)$$

where  $NPF_i$  is the number of global optima found in the  $i$ -th run,  $NPF$  denotes the number of know global optima, and  $R$  is the number of runs.

- (2) Success rate (SR): success rate is the ratio between the number of successful runs (NSR) and the total number of runs ( $R$ ). A successful run of an algorithm is when all global peaks are found in a run. It is calculated as follows:

$$SR = \frac{NSR}{R}. \quad (8)$$

**4.3. Analysis on Key Parameters.** In this section, F2, F3, and F4 (when  $D = 2$  and 3) and F6 and F7 (when  $D = 5$ ) are selected as representatives to analyze the influence of the  $MinPts$  and  $\sigma$ , on the performance of DNPSO.



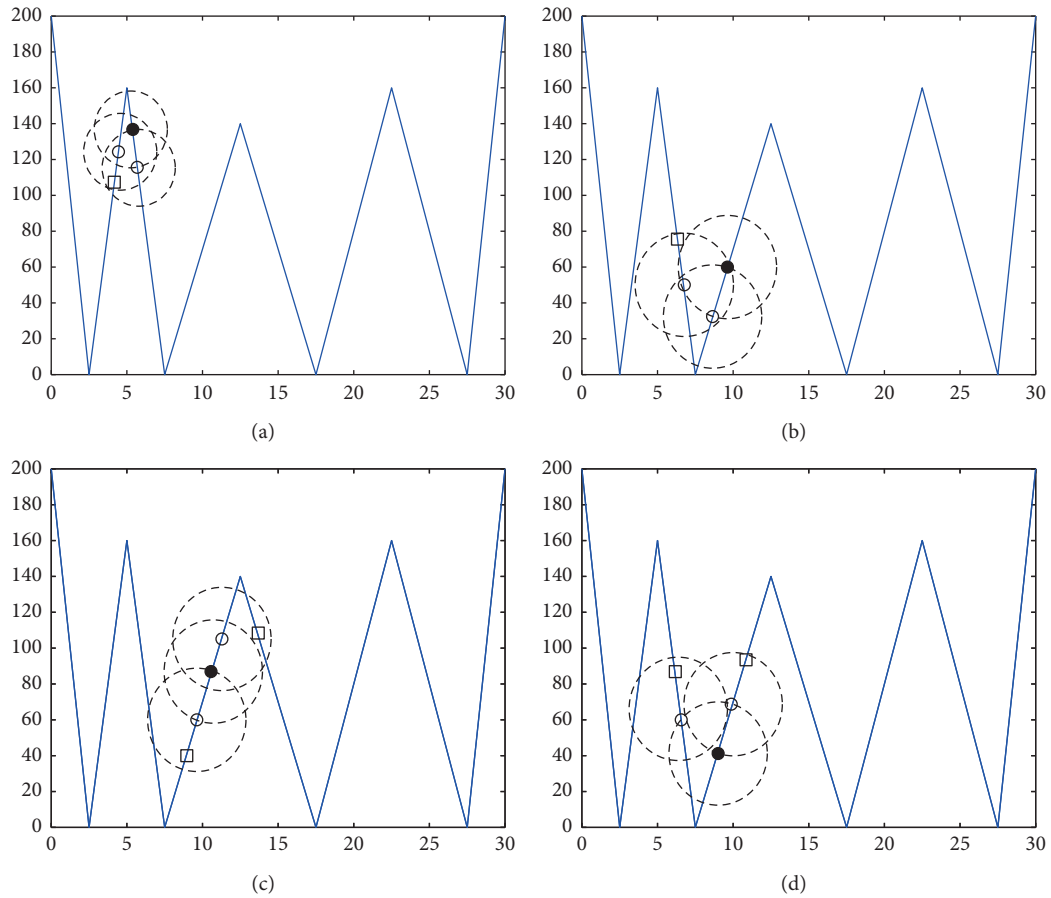


FIGURE 3: Illustration of the four cases of particles. The black solid circle is the core particle, the hollow circles are the direct neighborhood-reachable points of the core particle, and the squares are the neighborhood-reachable point of the core particle.

Input: The population size,  $N_{\text{PSO}}$ , the maximum number of evaluations,  $\text{MaxFEs}$ ;  
Output:  $P_{\text{best}}$ ;  
(1) Generate an initial population with the size of  $N_{\text{PSO}}$  with LHS, initialize  $P_{\text{best}}$ ;  
(2) Evaluate the fitness of the particles in the initial population;  
(3)  $\text{FEs} = N_{\text{PSO}}$ ;  
(4) While  $\text{FEs} < \text{MaxFEs}$  do;  
(5) For  $i = 1: N_{\text{PSO}}$ ;  
(6) Find the neighbors of  $P_{\text{best}_i}$  with Algorithm1, include  $N_{\text{dr}}$  and  $N_{\text{r}}$ ;  
(7) If the fitness of  $P_{\text{best}_i}$  is better than that of each individual in  $N_{\text{dr}}$  and  $N_{\text{r}}$ , then;  
(8) Update the position of  $X_i$  by strategy (6);  
(9) Elseif the fitness of  $P_{\text{best}_i}$  is the best in  $N_{\text{dr}}$  but is not the best in  $N_{\text{r}}$ , then;  
(10) Update the velocity and position of  $X_i$  using strategies (4) and (2), respectively;  
(11) Elseif the fitness of  $P_{\text{best}_i}$  is not the best in  $N_{\text{dr}}$  and is not the worst in  $N_{\text{r}}$ , then;  
(12) Update the velocity and position of  $X_i$  with strategies (4) and (2), respectively;  
(13) Elseif the fitness of  $P_{\text{best}_i}$  is worst in  $N_{\text{dr}}$  and  $N_{\text{r}}$ , then;  
(14) Update the velocity and position of  $X_i$  with strategies (7) and (2), respectively;  
(15) End;  
(16) Evaluate the fitness of  $X_i$ ;  
(17) Update  $P_{\text{best}_i}$ ;  
(18)  $\text{FEs} = \text{FEs} + 1$ ;  
(19) End;  
(20) End.

ALGORITHM 2: DNPSO.

TABLE 1: Benchmark instances.

	Function	$D$	Decision space	No. of global/ local optima	Peak height
F1	Equal maxima	1	$x \in [0, 1]$	5/0	1
F2	Uneven decreasing maxima	1	$x \in [0, 1]$	$\frac{1}{4}$	1
F3	Six-hump camel back	2	$x_1 \in [-1.9, 1.9]$ $x_2 \in [-1.1, 1.1]$	2/2	1.0316
F4	Shubert	2	$X \in [-10, 10]^2$	18/many	186.731
	Shubert	3	$X \in [-10, 10]^3$	81/many	2709.093
F5	Vincent	2	$X \in [0.25, 10]^2$	36	1
F6	Modified Rastrigin	2	$X \in [0, 1]^D$	12/0	-2
F7	Composition function 3	5/10	$X \in [-5, 5]^D$	6/many	0
F8	Composition function 4	5/10	$X \in [-5, 5]^D$	8/many	0

TABLE 2: Parameter settings.

	F1	F2	F3	F4(2D)	F4(3D)	F5	F6	F7	F8
$MaxFEs$	$5 \times 10^4$	$5 \times 10^4$	$5 \times 10^4$	$2 \times 10^5$	$4 \times 10^5$	$2 \times 10^5$	$2 \times 10^5$	$4 \times 10^5$	$4 \times 10^5$
$N_{pop}$	100	100	100	300	300	300	100	200	200
$R$	0.01	0.01	0.5	0.5	0.5	0.2	0.01	0.01	0.01

4.3.1. *Analysis of MinPts.* The value of  $MinPts$  determines the value of neighborhood radius,  $\epsilon$ , in Subsection 3.1, which indirectly affects the number of particles in the neighborhood-reachable set,  $N_r$ . Here, we analyze the influence of  $MinPts$  on the performance of DNPSO, when its values set is 2, 3, 4, and 5, respectively. Table 3 shows the PR and SR values obtained by DNPSO with different values of  $MinPts$ .

It can be concluded from Table 3 that (1) for problems F2, F3, and F6, the proposed DNPSO obtains the same PR and SR when  $MinPts = 2, 3, 4$ , and 5. (2) For other problems, the PR value achieved from DNPSO when  $MinPts = 3$  is the highest when  $MinPts = 2, 3, 4$ , and 5. (3) For F4 (2D), the SR value obtained from DNPSO when  $MinPts = 3$  is higher than those when  $MinPts = 2, 4$ , and 5; for F4(3D) and F7(5D), when  $MinPts = 2, 3, 4$ , and 5, the SR values obtained from DNPSO are equal to 0. Considering the performance of DNPSO with different values of  $MinPts$ , the value of  $MinPts$  is set as 3 in subsequent experiments.

4.3.2. *Analysis of  $\sigma$ .* The value of  $\sigma$  determines the size of Gaussian disturbance in formula (6), that is, the range of local search. This section analyzes the influence of  $\sigma$  on the performance of DNPSO, when  $\sigma$  set is 0.01, 0.05, 0.1, and 0.2. Table 4 shows the PR and SR values obtained by DNPSO under different  $\sigma$  values. It can be seen from Table 4 that (1) for F2, F3, and F6, the PR and SR values obtained by different values are similar. (2) For other problems, the PR value obtained when  $\sigma = 0.1$  is higher than those obtained when  $\sigma = 0.01, 0.05$ , and 0.2. Based on these results, the value  $\sigma$  is set as 0.1 in subsequent experiments.

4.4. *Comparison with Multimodal Evolutionary Algorithms.* In order to verify the effectiveness of DNPSO, this section compares it with seven state-of-the-art multimodal EAs. These comparison algorithms include three multimodal algorithms based on PSO (R2PSO, R3PSO [15], and LIPS [26]), three multimodal algorithms based on DE (NCDE,

TABLE 3: Results obtained by DNPSO with different  $MinPts$  values.

	2		3		4		5	
	PR	SR	PR	SR	PR	SR	PR	SR
F2	<b>1.00</b>	<b>1.00</b>	<b>1.00</b>	<b>1.00</b>	<b>1.00</b>	<b>1.00</b>	<b>1.00</b>	<b>1.00</b>
F3	<b>1.00</b>	<b>1.00</b>	<b>1.00</b>	<b>1.00</b>	<b>1.00</b>	<b>1.00</b>	<b>1.00</b>	<b>1.00</b>
F4(2D)	0.92	0.2	<b>1.00</b>	<b>1.00</b>	0.97	0.6	0.93	0.2
F4(3D)	0.15	0.00	<b>0.69</b>	0.00	0.55	0.00	0.41	0.00
F6	<b>1.00</b>	<b>1.00</b>	<b>1.00</b>	<b>1.00</b>	<b>1.00</b>	<b>1.00</b>	<b>1.00</b>	<b>1.00</b>
F7(5D)	0.13	0.00	<b>0.70</b>	0.00	0.68	0.00	0.68	0.00

NSDE [23], and VCNDE [28]), and one multiobjective EA (EMO-MMO [38–42]). In order to ensure the fairness of comparison, the population size,  $N_{PSO}$ , the maximum number of evaluations,  $MaxFEs$ , the niching radius,  $r$ , and amplitude accuracy of all comparison algorithms are consistent with the proposed DNPSO, and the remaining parameters are set according to their original literatures' suggestions.

Table 5 shows the mean value and standard deviation of  $PR$  obtained by DNPSO and 7 multimodal EAs when dealing with problems F1–F8, and the optimal results have been highlighted. In this paper, the Mann-Whitney test at a significance level of 5% is employed to evaluate significant difference between DNPSO and the compared algorithms, where “+” and “–” mean that DNPSO is significantly superior to and inferior to the compared one, respectively, and “=” indicates that there is no significant difference between them. In the table, “test” gives the results of the nonparametric test. In the penultimate row of Table 5, “win/tie/lose” is used to calculate the comparison result between DNPSO and each compared algorithm. Among them, “win” means the number of test problems that DNPSO dominates the compared one, “tie” indicates that the performance of DNPSO is similar to that of the compared one, and “lose” means the number of test problems that DNPSO is dominated by the compared one.



TABLE 4: Results obtained by DNPSO with different  $\sigma$  values.

	0.01		0.05		0.1		0.2	
	PR	SR	PR	SR	PR	SR	PR	SR
F2	1.00	1.00	1.00	1.00	1.00	1.00	1.00	1.00
F3	1.00	1.00	1.00	1.00	1.00	1.00	1.00	1.00
F4(2D)	0.98	0.80	1.00	1.00	0.98	0.80	1.00	1.00
F4(3D)	0.44	0.00	0.63	0.00	0.44	0.00	0.63	0.00
F6	1.00	1.00	1.00	1.00	1.00	1.00	1.00	1.00
F7(5D)	0.50	0.00	0.58	0.00	0.50	0.00	0.58	0.00

TABLE 5: Peak ratios (PRs) achieved from the compared algorithms.

	PR	DNPSO	LIPS	EMO-MMO	R2PSO	R3PSO	NCDE	NSDE	VNCDE
F1	Mean	<b>1.00</b>	<b>1.00</b>	<b>1.00</b>	<b>1.00</b>	<b>1.00</b>	<b>1.00</b>	0.99	<b>1.00</b>
	Std	0.00	0.00	0.00	0.00	0.00	0.00	0.00	0.00
	Test	\	=	=	=	=	=	=	=
F2	Mean	<b>1.00</b>	<b>1.00</b>	<b>1.00</b>	<b>1.00</b>	<b>1.00</b>	<b>1.00</b>	<b>1.00</b>	<b>1.00</b>
	Std	0.00	0.00	0.00	0.00	0.00	0.00	0.00	0.00
	Test	\	=	=	=	=	=	=	=
F3	Mean	<b>1.00</b>	<b>1.00</b>	<b>1.00</b>	<b>1.00</b>	<b>1.00</b>	<b>1.00</b>	<b>1.00</b>	<b>1.00</b>
	Std	0.00	0.00	0.00	0.00	0.00	0.00	0.00	0.00
	Test	\	=	=	=	=	=	=	=
F4 (2D)	Mean	<b>1.00</b>	0.75	<b>1.00</b>	0.53	0.69	0.14	0.27	0.96
	Std	0.00	0.22	0.00	0.11	0.05	0.01	0.02	0.01
	Test	\	+	=	+	+	+	+	=
F4 (3D)	Mean	0.69	0.49	<b>0.80</b>	0.32	0.28	0.68	0.13	0.74
	Std	0.14	0.03	0.23	0.10	0.02	0.04	0.01	0.13
	Test	\	+	=	+	+	=	+	=
F5	Mean	<b>1.00</b>	0.20	<b>1.00</b>	0.01	0.16	0.50	0.06	0.55
	Std	0.00	0.05	0.00	0.00	0.01	0.01	0.04	0.05
	Test	\	+	=	+	+	+	+	+
F6	Mean	<b>1.00</b>	0.84	<b>1.00</b>	0.88	0.87	1.00	0.40	<b>1.00</b>
	Std	0.00	0.13	0.00	0.01	0.11	0.00	0.01	0.00
	Test	\	+	=	=	=	=	+	=
F7 (5D)	Mean	<b>0.70</b>	0.41	0.60	0.14	0.13	0.26	0.35	<b>0.70</b>
	Std	0.01	0.01	0.10	0.01	0.01	0.02	0.02	0.02
	Test	\	+	=	+	+	+	+	=
F7 (10D)	Mean	0.54	0.20	<b>0.66</b>	0.06	0.37	0.63	0.52	<b>0.66</b>
	Std	0.00	0.00	0.01	0.09	0.00	0.01	0.02	0.00
	Test	\	+	-	+	-	=	=	-
F8 (5D)	Mean	<b>0.38</b>	0.09	0.19	0.00	0.02	0.10	0.11	0.37
	Std	0.01	0.09	0.04	0.00	0.00	0.02	0.12	0.11
	Test	\	+	+	+	+	+	+	=
F8 (10D)	Mean	0.16	0.06	0.12	0.00	0.05	0.24	0.12	<b>0.29</b>
	Std	0.10	0.02	0.08	0.00	0.10	0.21	0.15	0.33
	Test	\	+	=	+	+	=	=	-
Win/tie/lose	\	8/3/0	1/9/1	7/4/0	6/4/1	4/7/0	6/5/0	1/8/2	
Rank		2.81	5.18	2.86	6.27	5.90	4.32	5.95	<b>2.68</b>

TABLE 6: Post hoc analysis using DNPSO as control method.

DNPSO vs LIPS	LIPS	EMO-MMO	R2PSO	R3PSO	NCDE	NSDE	VNCDE
Statistic	2.26	0.04	3.30	2.95	1.43	3.00	0.13
Adjusted $p$ value	0.0409	0.9652	0.0065	0.0093	0.2047	0.0093	0.9287

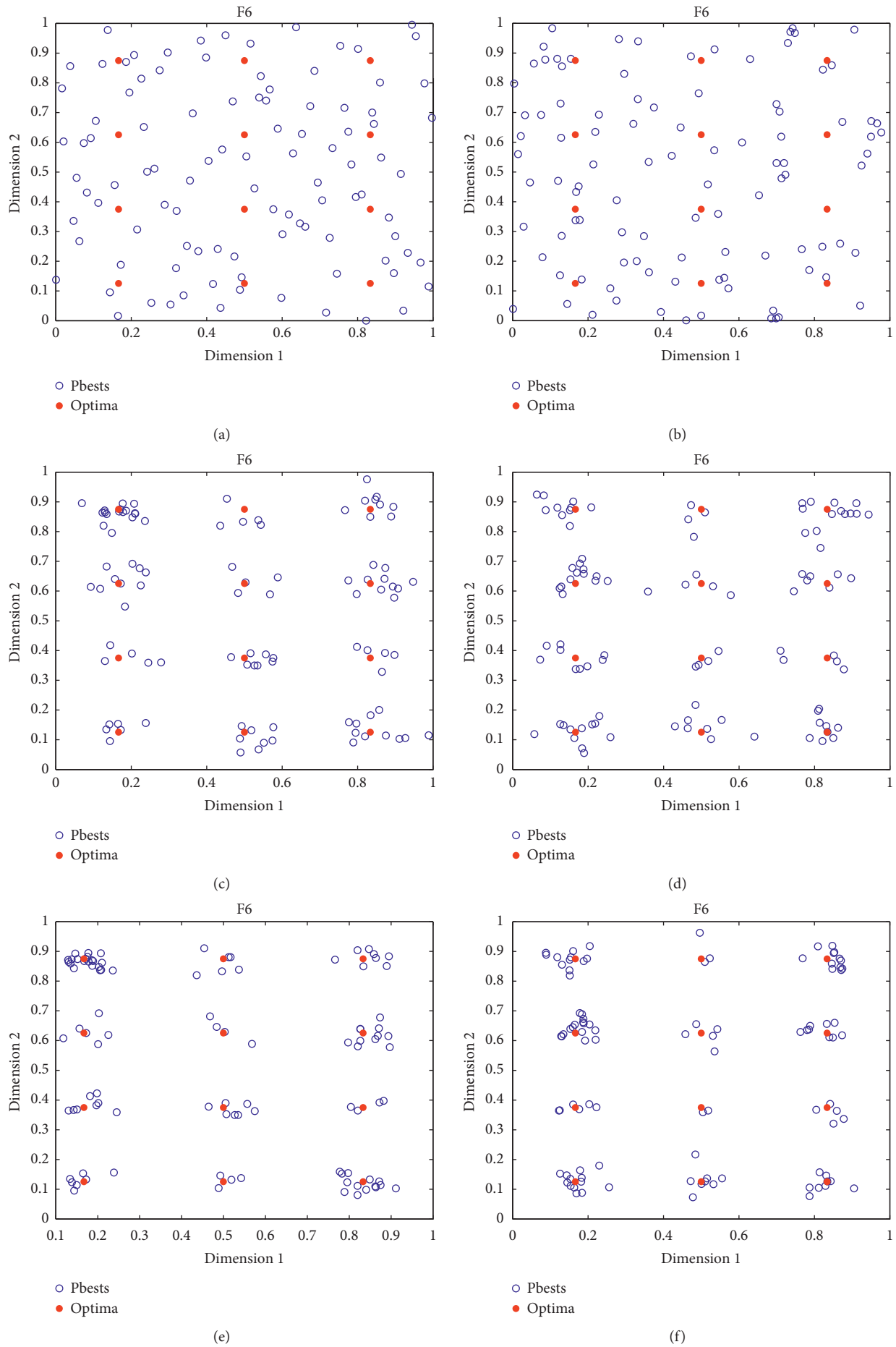


FIGURE 4: Continued.

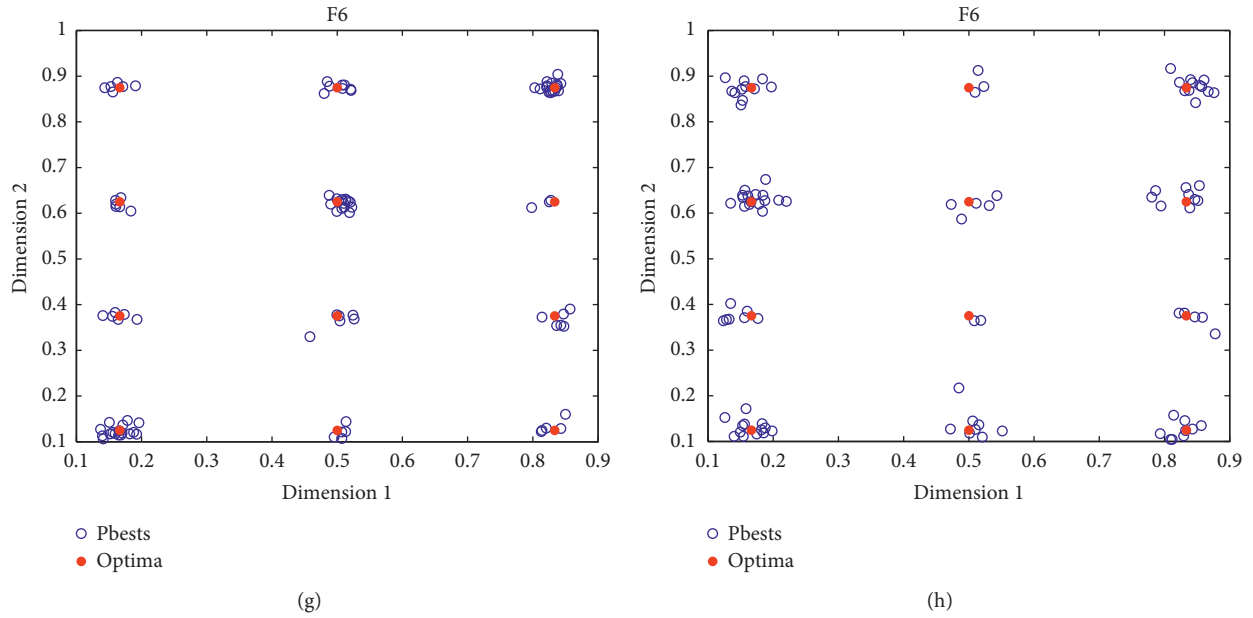


FIGURE 4: Distributions of Pbests of DNPSO and LIPS on different stages of F6. (a) Iteration 1 of DNPSO. (b) Iteration 1 of LIPS. (c) Iteration 5 of DNPSO. (d) Iteration 5 of LIPS. (e) Iteration 10 of DNPSO. (f) Iteration 10 of LIPS. (g) Iteration 15 of DNPSO. (h) Iteration 15 of LIPS.

It can be obtained from Table 5 that (1) for problems F1, F2, and F3 there is no significant difference between the PR obtained by DNPSO and all compared algorithms. (2) For F4 and F7(5D), except EMO-MMO and VNCDE, PRs obtained by the remaining five algorithms are significantly inferior to DNPSO. (3) For F5, there is no significant difference between DNPSO and EMO-MMO, but the PRs obtained by DNPSO are significantly better than those of the other six compared ones. (4) For F6, the PR obtained by DNPSO is significantly better than those of LIPS and NSDE, with no significant difference from the other 5 compared algorithms. (5) For F7 (10D), the PRs achieved by DNPSO are obviously better than those of LIPS and R2PSO, but worse than those of EMO-MMO, R3PSO, and VNCDE. (6) For F8 (5D), except VNCDE, PRs obtained by the remaining 6 algorithms are significantly inferior to DNPSO. (7) For F8 (10D), the PR achieved by DNPSO is obviously better than those of LIPS, R2PSO, and R3PSO, but worse than that of VNCDE. According to the overall statistical results, DNPSO dominated LIPS on at least 8 instances, superior than R2PSO on at least 7 instances, and outperformed R3PSO and NSDE on at least 6 instances, superior than NCDE on at least 4 instances.

In addition, STAC platform is used to test the difference between the proposed DNSPO and the compared algorithms, and Friedman test with significance level of 0.05 is used for analysis. The analysis results are shown in the last row of Table 5, and the comprehensive ranking values of all algorithms on PR are given. DNPSO is used as the control method, it can be seen that rank of DNPSO is slightly higher than that of VNCDE, but lower than those of the other 6 compared algorithms. Furthermore, we adjusted the  $p$  value of pairwise comparison by using Finner operation, and the results are listed in Table 6. As can be seen from Table 6, DNPSO is statistically superior to LIPS, R2PSO, R3PSO, and

NSDE and has similar performance with other three compared algorithms.

Figure 4 shows the distribution of  $Pbest$  of the proposed DNPSO and LIPS on different population iterations for F6, where F6 has 12 global optimal solutions, as shown by red solid circles in the figure. It can be achieved from the figure that (1) both of them can converge to the vicinity of 12 global optimal solutions within 15 iterations; (2) the blue circles in Figure 4(g) are closer to the red solid circles than those in Figure 4(h), which indicates that the convergence precision of DNPSO is higher than that of LIPS.

Table 7 lists the SR obtained by DNPSO and 7 multimodal EAs when dealing with problems F1–F8. The optimal results have been highlighted. The last row shows the comprehensive ranking values of SR of all algorithms. It can be seen from Table 7 that (1) for problems F1, F2, and F3 DNPSO and all the compared algorithms can find all the optimal solutions in each run. (2) For F4 (2D), the SR of DNPSO and EMO-MMO is equal to 1; the SR of VNCDE is equal to 0.54, while the SR obtained by the remaining 5 algorithms is 0. (3) For F5, the SRs of DNPSO and EMO-MMO are 1, and those of other algorithms are 0. (4) For F6, the SR values of DNPSO, EMO-MMO, NCDE, and VNCDE are all higher than those of the other three compared algorithms. (5) For F4 (3D), F7, and F8, the SR values obtained by all algorithms is 0; that is, no single run can find all the global optimal solutions. (6) From the perspective of rank value, DNPSO and EMO-MMO have similar performance, and the rank value is superior to the other compared algorithms.

Table 8 lists the running time of DNPSO and 7 multimodal EAs on the problems F1–F8. It can be seen from Table 8 that (1) R2PSO has the shortest running time and VNCDE has the longest running time. (2) The proposed

TABLE 7: Success rates (SRs) achieved from the compared algorithms.

	DNPSO	LIPS	EMO-MMO	R2PSO	R3PSO	NCDE	NSDE	VNCDE
F1	<b>1.00</b>	<b>1.00</b>	<b>1.00</b>	<b>1.00</b>	<b>1.00</b>	<b>1.00</b>	0.98	<b>1.00</b>
F2	<b>1.00</b>	<b>1.00</b>	<b>1.00</b>	<b>1.00</b>	<b>1.00</b>	<b>1.00</b>	<b>1.00</b>	<b>1.00</b>
F3	<b>1.00</b>	<b>1.00</b>	<b>1.00</b>	<b>1.00</b>	<b>1.00</b>	<b>1.00</b>	<b>1.00</b>	<b>1.00</b>
F4 (2D)	<b>1.00</b>	0.00	<b>1.00</b>	0.00	0.00	0.00	0.00	0.54
F4 (3D)	0.00	0.00	0.00	0.00	0.00	0.00	0.00	0.00
F5	<b>1.00</b>	0.00	<b>1.00</b>	0.00	0.00	0.00	0.00	0.00
F6	<b>1.00</b>	0.84	<b>1.00</b>	0.22	0.24	<b>1.00</b>	0.00	<b>1.00</b>
F7 (5D)	0.00	0.00	0.00	0.00	0.00	0.00	0.00	0.00
F7 (10D)	0.00	0.00	0.00	0.00	0.00	0.00	0.00	0.00
F8 (5D)	0.00	0.00	0.00	0.00	0.00	0.00	0.00	0.00
F8 (10D)	0.00	0.00	0.00	0.00	0.00	0.00	0.00	0.00
Rank	<b>3.72</b>	4.72	<b>3.72</b>	4.90	4.81	4.50	5.36	4.22

TABLE 8: Running time comparison of the multimodal algorithms.

	DNPSO	LIPS	EMO-MMO	R2PSO	R3PSO	NCDE	NSDE	VNCDE
F1	0.24	0.09	1.07	0.04	0.06	1.17	5.72	6.00
F2	0.24	0.09	1.08	0.03	0.08	1.12	6.48	5.90
F3	0.36	0.11	1.09	0.04	0.11	1.17	6.41	6.25
F4 (2D)	3.56	0.47	3.45	0.22	0.20	4.76	26.18	24.48
F4 (3D)	3.79	0.46	3.47	0.21	0.61	4.71	22.57	24.64
F5	6.91	1.25	8.90	0.60	0.93	10.01	51.42	46.88
F6	2.11	0.52	3.56	0.21	0.56	4.72	22.04	22.06
F7 (5D)	17.82	8.73	20.34	8.01	9.41	16.48	54.17	56.32
F7 (10D)	17.90	9.03	23.40	8.45	8.65	16.72	54.52	57.15
F8 (5D)	29.01	15.51	32.32	14.83	16.93	25.67	60.97	89.91
F8 (10D)	30.98	16.71	35.01	15.75	22.75	26.34	62.53	93.11

DNPSO has slightly longer running time than those of LIPS, R2PSO, and R3PSO, but less than those of the remaining four algorithms.

## 5. Conclusions

To tackle MMOPs, this paper presents a multimodal particle swarm optimization algorithm based on dynamic neighborhood, called DNPSO. The proposed DNPSO defines a dynamic neighborhood selection mechanism, which makes the neighborhood size of particles change dynamically in the process of evolution, and distinguishes the particles in the neighborhood between directly neighborhood-reachable and neighborhood-reachable at the same time, so as to balance the exploration and exploitation of the algorithm. Following that, based on the information provided by the neighbors, four different particle position updating strategies are designed to further support the algorithm's exploration and exploitation of the search space. The experimental results on eight test benchmark functions show that the proposed algorithm is competitive with several existing multimodal EAs and is an effective method to deal with MMOPs.

DNPSO, like other EAs, shows poor performance when dealing with high-dimensional MMOPs, which requires further study. It is also suggested to extend this dynamic neighborhood method to other EAs like DE in the future. In addition, it may be worthy to apply DNPSO to real-world problems such as feature selection.

## Data Availability

No data were used to support this study.

## Conflicts of Interest

The authors declare no conflicts of interest.

## Acknowledgments

This research was funded by the project of Jiangsu Provincial Department of Emergency Management (no. YJGL-YF-2020-15), the Scientific Research Staring Foundation of Shantou University (no. NTF20009), and the open project of Key Laboratory of Computational Intelligence and Signal Processing for Ministry of Education (no. 2019A002).

## References

- [1] C. Stoean, M. Preuss, R. Stoean, and D. Dumitrescu, "Multimodal optimization by means of a topological species conservation algorithm," *IEEE Transactions on Evolutionary Computation*, vol. 14, no. 6, pp. 842–864, 2011.
- [2] J. W. Krusselbrink, "Enhancing search space diversity in multi-objective evolutionary drug molecule design using niching," in *Proceedings of the 11th Annual Conference on Genetic Evolutionary Computation*, pp. 217–224, Montreal, QC, Canada, 2009.
- [3] G.-C. Luh and C.-Y. Lin, "Optimal design of truss-structures using particle swarm optimization," *Computers & Structures*, vol. 89, no. 23-24, pp. 2221–2232, 2011.

- [4] K. C. Wong, K. S. Leung, and M. H. Wong, "Protein structure prediction on a lattice model via multimodal optimization techniques," in *Proceedings of the Genetic and Evolutionary Computation Conference, GECCO 2010*, pp. 155–162, Portland, OR, USA, July 2010.
- [5] X. Li, M. G. Epitropakis, K. Deb, and A. Engelbrecht, "Seeking multiple solutions: an updated survey on niching methods and their applications," *IEEE Transactions on Evolutionary Computation*, vol. 21, no. 4, pp. 518–538, 2017.
- [6] X. Li, "Adaptively choosing neighbourhood bests using species in a particle swarm optimizer for multimodal function optimization," in *Proceedings of the Genetic and Evolutionary Computation - GECCO 2004*, pp. 105–116, Seattle, WA, USA, 2004.
- [7] D. E. Goldberg, *Genetic Algorithms in Search, Optimization, and Machine Learning*, Addison-Wesley, Boston, MA, USA, 1989.
- [8] Y. Tian, T. Zhang, J. Xiao, X. Zhang, and Y. Jin, "A coevolutionary framework for constrained multi-objective optimization problems," *IEEE Transactions on Evolutionary Computation*, p. 1, 2020.
- [9] L. Tang, Y. Dong, and J. Liu, "Differential evolution with an individual dependent mechanism," *IEEE Transactions on Evolutionary Computation*, vol. 19, no. 4, pp. 560–574, 2015.
- [10] H. Wu, C. Nie, F.-C. Kuo, H. Leung, and C. J. Colbourn, "A discrete particle swarm optimization for covering array generation," *IEEE Transactions on Evolutionary Computation*, vol. 19, no. 4, pp. 575–591, 2015.
- [11] S. W. Mahfoud, "Crowding and preselection revisited," in *Parallel Problem Solving from Nature 2*, R. Männer and B. Manderick, Eds., pp. 27–36, North-Holland, Amsterdam, The Netherlands, 1992.
- [12] X. Yin and N. Gernay, "A fast genetic algorithm with sharing scheme using cluster analysis methods in multimodal function optimization," in *Artificial Neural Nets and Genetic Algorithms*, R. F. Albrecht, C. R. Reeves, and N. C. Steele, Eds., pp. 450–457, Springer, Vienna, Austria, 1993.
- [13] X. Xiang, Y. Tian, J. Xiao, and X. Zhang, "A clustering-based surrogate-assisted multi-objective evolutionary algorithm for shelter location problem under uncertainty of road networks," *IEEE Transactions on Industrial Informatics*, vol. 16, no. 12, pp. 7544–7555. In press, 2020.
- [14] X. Zhang, Y. Tian, R. Cheng, and Y. Jin, "A decision variable clustering-based evolutionary algorithm for large-scale many-objective optimization," *IEEE Transactions on Evolutionary Computation*, vol. 22, no. 1, pp. 97–112, 2018.
- [15] X. Li, "Niching without niching parameters: particle swarm optimization using a ring topology," *IEEE Transactions on Evolutionary Computation*, vol. 14, no. 4, p. 665, 2010.
- [16] K. E. Parsopoulos, V. P. Plagianakos, G. D. Magoulas, and M. N. Vrahatis, "Objective function "stretching" to alleviate convergence to local minima," *Nonlinear Analysis: Theory, Methods & Applications*, vol. 47, no. 5, pp. 3419–3424, 2001.
- [17] B. Qu, L. Xie, and C. Li, "Particle swarm optimization algorithms based on multi-mode optimization problem," *Journal of Zhongyuan University of Technology* 2018, vol. 29, no. 4, pp. 70–76, 2018.
- [18] D. Parrott and X. Xiaodong Li, "Locating and tracking multiple dynamic optima by a particle swarm model using speciation," *IEEE Transactions on Evolutionary Computation*, vol. 10, no. 4, pp. 440–458, 2006.
- [19] Y. Zhang, D. W. Gong, and Z. H. Ding, "Handling multi-objective optimization problems with a multi-swarm cooperative particle swarm optimizer," *Expert Systems with Applications*, vol. 38, no. 11, pp. 3933–3941, 2011.
- [20] X. Zhang, X. Zheng, R. Cheng, J. Qiu, and Y. Jin, "A competitive mechanism based multi-objective particle swarm optimizer with fast convergence," *Information Sciences*, vol. 427, pp. 63–76, 2018.
- [21] R. Brits, A. P. Engelbrecht, and F. Van den Bergh, "Solving systems of unconstrained equations using particle swarm optimizers," in *Proceedings of the IEEE International Conference on Systems, Man and Cybernetics*, pp. 102–107, Hammamet, Tunisia, October 2002.
- [22] J. Qiu, J. Wan, L. Zhang, F. Cheng, and Y. Luo, "Community-grouping based particle swarm optimization algorithm for feature selection," in *Proceedings of the 2020 IEEE Congress on Evolutionary Computation (CEC)*, pp. 1–8, Glasgow, UK, July 2020.
- [23] T. Blackwell and J. Branke, "Multiswarms, exclusion, and anti-convergence in dynamic environments," *IEEE Transactions on Evolutionary Computation*, vol. 10, no. 4, pp. 459–472, 2006.
- [24] X. Zhang, T. Tan, B. Zhou, T. Yu, B. Yang, and X. Huang, "Adaptive distributed auction-based algorithm for optimal mileage based AGC dispatch with high participation of renewable energy," *International Journal of Electrical Power & Energy Systems*, vol. 124, 2020.
- [25] I. L. Schoeman and A. P. Engelbrecht, "Using vector operations to identify niches for particle swarm optimization," in *IEEE Conference on Cybernetics and Intelligent Systems*, pp. 361–366, Singapore, December 2004.
- [26] B. Y. Qu, P. N. Suganthan, and S. Das, "A distance-based locally informed particle swarm model for multimodal optimization," *IEEE Transactions on Evolutionary Computation*, vol. 17, no. 3, pp. 387–402, 2013.
- [27] Y. H. Zhang, Y. J. Gong, H. X. Zhang, T. L. Gu, and J. Zhang, "Toward fast niching evolutionary algorithms: a locality sensitive hashing-based approach," *IEEE Transactions on Evolutionary Computation*, vol. 21, no. 3, pp. 347–362, 2017.
- [28] Y.-H. Zhang, Y.-J. Gong, Y. Gao, H. Wang, and J. Zhang, "Parameter-free Voronoi neighborhood for evolutionary multimodal optimization," *IEEE Transactions on Evolutionary Computation*, vol. 24, no. 2, pp. 335–349, 2020.
- [29] J. Kennedy, R. C. Eberhart, and Y. Shi, *Swarm Intelligence*, Morgan Kaufmann, San Francisco, CA, USA, 2001.
- [30] I. Rodriguez-Fdez, A. Canosa, M. Mucientes, and A. Bugarin, "A web platform for the comparison of algorithms using statistical tests," in *IEEE International Conference on Fuzzy Systems*, Istanbul, Turkey, August 2015.
- [31] Y. Zhang, D.-w. Gong, and J. Cheng, "Multi-objective particle swarm optimization approach for cost-based feature selection in classification," *IEEE/ACM Transactions on Computational Biology and Bioinformatics*, vol. 14, no. 1, pp. 64–75, 2017.
- [32] Y. Hu, Y. Zhang, and D. Gong, "Multiobjective particle swarm optimization for feature selection with fuzzy cost," *IEEE Transactions on Cybernetics*, p. 1, 2020.
- [33] S. Biswas, S. Kundu, and S. Das, "Inducing niching behavior in differential evolution through local information sharing," *IEEE Transactions on Evolutionary Computation*, vol. 19, no. 2, pp. 246–263, 2015.
- [34] B. Y. Qu, P. N. Suganthan, and J. J. Liang, "Differential evolution with neighborhood mutation for multimodal optimization," *IEEE Transactions on Evolutionary Computation*, vol. 16, no. 5, pp. 601–614, 2012.
- [35] F. Cheng, Q. Zhang, Y. Tian, and X. Zhang, "Maximizing receiver operating characteristics convex hull via dynamic

- reference point-based multi-objective evolutionary algorithm,” *Applied Soft Computing*, vol. 86, 2020.
- [36] Z. Zhou, *Machine Learning*, Tsinghua University Press, Beijing, China, 2016.
- [37] X. Li, A. Engelbrecht, and M. G. Epitropakis, “Benchmark functions for CEC’2013 special session and competition on niching methods for multimodal function optimization,” *Evolutionary Computation Machine Learning Group*, Technical Report, RMIT University, Melbourne, VIC, Australia, 2013.
- [38] R. Cheng, M. Li, K. Li, and X. Yao, “Evolutionary multi-objective optimization-based multimodal optimization: fitness landscape approximation and peak detection,” *IEEE Transactions on Evolutionary Computation*, vol. 22, no. 5, pp. 692–706, 2018.
- [39] D. Gong, B. Xu, Y. Zhang, Y. Guo, and S. Yang, “A similarity-based cooperative co-evolutionary algorithm for dynamic interval multiobjective optimization problems,” *IEEE Transactions on Evolutionary Computation*, vol. 24, no. 1, pp. 142–156, 2020.
- [40] X. Zhang, Z. Xu, T. Yu, B. Yang, and H. Wang, “Optimal mileage based AGC dispatch of a GenCo,” *IEEE Transactions on Power Systems*, vol. 35, no. 4, pp. 2516–2526, 2020.
- [41] Y. Chen, X. Sun, D. Gong, Y. Zhang, J. Choi, and S. Klasky, “Personalized search inspired fast interactive estimation of distribution algorithm and its application,” *IEEE Transactions on Evolutionary Computation*, vol. 21, no. 4, pp. 588–600, 2017.
- [42] Y. Chen, X. Sun, D. Gong, and X. Yao, “DPM-IEDA: dual probabilistic model assisted interactive estimation of distribution algorithm for personalized search,” *IEEE Access*, vol. 7, pp. 41006–41016, 2019.



## Research Article

# Fast Atom Search Algorithm for Reactive Power Optimization of Power Grid with High-Penetration Wind and Solar Energies

Fang Zeng and Hongchun Shu 

*Faculty of Electric Power Engineering, Kunming University of Science and Technology, Kunming 650500, China*

Correspondence should be addressed to Hongchun Shu; fanger1119@kust.edu.cn

Received 21 November 2020; Revised 30 November 2020; Accepted 8 December 2020; Published 18 December 2020

Academic Editor: Xiao-Shun Zhang

Copyright © 2020 Fang Zeng and Hongchun Shu. This is an open access article distributed under the Creative Commons Attribution License, which permits unrestricted use, distribution, and reproduction in any medium, provided the original work is properly cited.

This paper constructs a reliable reactive power optimization (RPO) model of power grid with the controlled participation of high-penetration wind and solar energies and provides a novel fast atom search optimization (FASO) algorithm to reach a set of solutions to the RPO problem. The developed FASO algorithm owns prominent merits of high searching efficiency and premature convergence avoidance compared with the original atom search optimization (ASO) algorithm, which is applied to determine the optimal dispatch scheme including terminal voltage of generators, the capacity of static VAR compensator (SVC), reactive power output of wind and solar energies, and the tap ratio of transformers. There are two objective functions to be minimized for maintaining the safe and reliable operation of power grid, i.e., total power loss of transmission lines and total voltage deviation of nodes. Meanwhile, the regulation capacities of wind farms and photovoltaic (PV) stations are evaluated based on different weather conditions, i.e., wind speed and solar irradiation. Particularly, the reactive power outputs of wind and solar energies can be globally controlled to coordinate with other controllable units instead of a local self-control. Eventually, the extended IEEE 9-bus and IEEE 39-bus systems are introduced to test the performance of the FASO algorithm for RPO problem. It has been verified that FASO can not only meet the optimal regulation requirements of RPO but also obtain high-quality regulation schemes with the fastest convergence speed and highest convergence stability in contrast with else algorithms.

## 1. Introduction

Currently, the share of renewable energy sources (RESs) in the power grid is ever-increasing due to their relatively low-cost and sustainability features [1–3]. However, RESs such as wind energy [4–8] and solar energy [9–13] are intermittent and stochastic in their nature, of which the high-proportion integration into the power grid poses a great challenge on the stable operation of the whole power grid while brings new opportunities for reactive power optimization (RPO) [14–16]. Actually, RESs not only satisfy active power demand on the power grid but also have definite potential in reactive power regulation [17, 18]. In recent years, RPO has increasingly been a highlighted research focus in power system programming issues for practical engineering applications [19–21]. Generally, RPO is devoted to improve the voltage quality of nodes and reduce the total power loss of

transmission lines to enhance the safe and economic operation of the power grid [19–21]. In general, the objectives are reached by determining optimal control variables in the power system, including generator voltages, tap ratio of the transformers, and reactive power output of reactive power compensation device [22, 23]. For the sake of developing the full potential in reactive power regulation of RESs, the appropriate reactive power outputs of RESs should be globally controlled to coordinate with other control variables instead of local self-control [16, 24].

RPO is mathematically defined as a renowned nonlinear and nonconvex optimization problem involving discrete and continuous control variables, meanwhile, constrained by a series of equality and inequality constraints [25]. Note that all restrictions should be satisfied in the whole optimization process affirmatively. By far, remarkable research efforts have been done in RPO solution, among which the

overwhelming majority employ conservative optimization methods such as linear programming [26], Newton method [27], dynamic programming [28], interior point method [29], and quadratic programming [30]. However, these conventional techniques always suffer several serious drawbacks in handling nondifferentiable functions and inequality constraints, as well as discrete variables, which are computationally intractable and may lead to loss of accuracy [31].

Thus far, numerous amounts of metaheuristic algorithms and their variant have been developed to solve such obstacles. Such intelligence optimization algorithms display tremendous potential in power system optimization thanks to their prominent merits of high flexibility, relatively simple structure, and rapid response, as well as the ability of handling nonlinear, large-scale, and multivariable optimization problems [32]. In particular, some groups are more popular to solve the RPO problem such as genetic algorithm (GA) [33, 34], particle swarm optimization (PSO) algorithm [33, 35], and moth-flame optimization (MFO) algorithm [36]. Particularly, literature [34] presents an improved GA for RPO, in which real and binary codes are employed, respectively, to address continuous and discrete variables. However, the computation time is not substantially lower than that of the original GA. Besides, the optimal reactive power dispatch is achieved by grey wolf optimizer (GWO) [37], where the best combination of control variables is found such that total power loss and total voltage deviation issues can be effectively solved [38]. Moreover, work [39] proposes a discrete binary PSO algorithm to address the overriding risk of voltage caused by wind power fluctuation. In general, most of them really lack unified control and planning for the reactive power output of RESs such that the potential in reactive power regulation of RESs has not been maximized. Moreover, most of the metaheuristic algorithms suffer from low searching efficiency and premature convergence drawbacks [40].

To address the abovementioned problems, a reliable fast atom search optimization (FASO) algorithm that derives from the original atom search optimization (ASO) algorithm [41] is performed to solve the intractable RPO problem. Compared to the original ASO algorithm, the effective searching mechanism that Euclidian distance ratio is self-adaptively updated according to the optimization results is introduced by FASO algorithm to realize a better balance between local exploitation and global exploration [42] and most importantly can accelerate convergence to high-quality solutions.

The rest of this paper is organized as follows: Section 2 establishes the reactive power optimization model of power grid considering high-penetration wind and solar energies, in which the total power loss and total voltage deviation are, respectively, treated as the single objective function to be minimized; Section 3 elaborates the basic principle of FASO algorithm and detailed design for RPO, where the control variables to be optimized are determined; Section 4 undertakes two case studies to validate the superiority and efficiency of the proposed algorithm for solving the RPO

problem; eventually, several popular metaheuristic algorithms are executed along with the implementation of developed FASO algorithm to make a fair comparison; at last, conclusions are drawn in Section 5.

## 2. Reactive Power Optimization Model of Power Grid with High-Penetration Wind and Solar Energies

*2.1. Reactive Power Regulation of Wind Generators.* The configuration of doubly-fed induction generator (DFIG) connected to infinite power grid via two voltage source converters (VSCs) is illustrated in Figure 1, in which the mechanical power extracted from wind energy and active power injected into the power grid are directly related to wind speed [43].

Assume that the output of active power is accurately tracked by the maximum power point [44]. Based on the current wind speed, the active power can be calculated as follows [45]:

$$P_g = \begin{cases} 0, & \text{for } v_w < v_w^{\text{in}} \text{ and } v_w > v_w^{\text{out}}, \\ P_w^{\text{base}} \frac{v_w - v_w^{\text{in}}}{v_w^{\text{base}} - v_w^{\text{in}}}, & \text{for } v_w^{\text{in}} \leq v_w \leq v_w^{\text{base}}, \\ P_w^{\text{base}}, & \text{for } v_w^{\text{base}} \leq v_w \leq v_w^{\text{out}}, \end{cases} \quad (1)$$

where  $v_w$ ,  $v_w^{\text{in}}$ , and  $v_w^{\text{out}}$  denote current, cut-in, and cut-out wind speed, respectively;  $v_w^{\text{base}}$  means the rated wind speed; and  $P_w^{\text{base}}$  is the rated output power of wind turbine.

With the help of stator-side VSC and grid-side VSC, wind turbines can generate active power over a wide range of rotational speeds around the synchronous speed at constant voltage and frequency. And the magnitude and direction of the active power that flows between the rotor and the grid are controlled. Furthermore, the instantaneous reactive power of wind generators can be controlled independently by the reactive power output of stator-side VSC and grid-side VSC, as follows [46]:

$$\begin{cases} Q_{g,\text{max}} = Q_{s,\text{max}} + Q_{c,\text{max}}, \\ Q_{g,\text{min}} = Q_{s,\text{min}} + Q_{c,\text{min}}, \end{cases} \quad (2)$$

where  $Q_{g,\text{max}}$  and  $Q_{g,\text{min}}$  stand for the maximum and minimum reactive power regulation capacity for wind turbine that injected into power grid, respectively;  $Q_{s,\text{max}}$  and  $Q_{s,\text{min}}$  represent the maximum and minimum reactive power regulation capacity for stator-side VSC, respectively; and  $Q_{c,\text{max}}$  and  $Q_{c,\text{min}}$  are the maximum and minimum reactive power regulation capacity for grid-side VSC, respectively.

And then, the limits of the reactive power output of stator-side VSC are determined by the stator voltage, as well as maximum current specified on rotor-side and stator-side, as follows [47]:

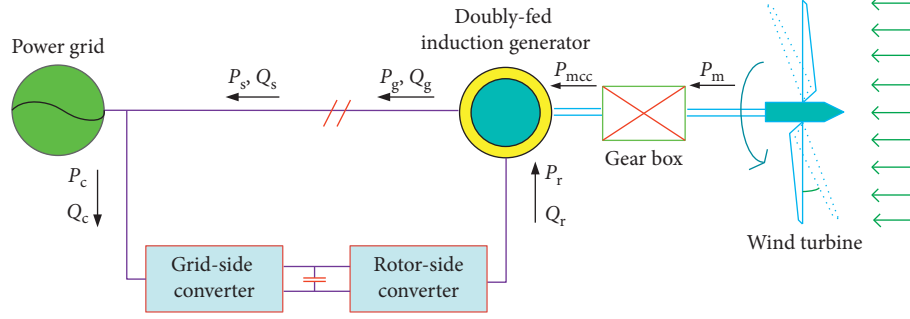


FIGURE 1: Energy conversion of doubly-fed induction generator.

$$\begin{cases} Q_{s,\max} = \min\{Q_{s1,\max}, Q_{s2,\max}\}, \\ Q_{s,\min} = \max\{Q_{s1,\min}, Q_{s2,\min}\}, \end{cases}$$

$$\begin{cases} Q_{s1,\max} = \frac{3U_s^2}{2\omega_1 L_s} + \sqrt{\left(\frac{3L_m U_s I_{r,\max}}{2L_s}\right)^2 - \left(\frac{P_m}{1-s}\right)^2}, \\ Q_{s1,\min} = -\frac{3U_s^2}{2\omega_1 L_s} - \sqrt{\left(\frac{3L_m U_s I_{r,\max}}{2L_s}\right)^2 - \left(\frac{P_m}{1-s}\right)^2}, \end{cases}$$

$$\begin{cases} Q_{s2,\max} = \sqrt{(U_s I_{s,\max})^2 - \left(\frac{P_m}{1-s}\right)^2}, \\ Q_{s2,\min} = -\sqrt{(U_s I_{s,\max})^2 - \left(\frac{P_m}{1-s}\right)^2}, \end{cases} \quad (3)$$

where  $Q_{s1,\max}$  and  $Q_{s1,\min}$  represent the lower and upper limits of reactive power regulation capacity for stator-side VSC under maximum current constraint on the rotor side, respectively;  $Q_{s2,\max}$  and  $Q_{s2,\min}$  mean the lower and upper of reactive power regulation capacity for stator-side VSC under maximum current constraint on the stator side, respectively;  $L_s$  and  $L_m$  stand for stator inductance and magnetizing inductance, respectively;  $I_{r,\max}$  and  $I_{s,\max}$  denote the maximum current specified on the rotor side and stator side, respectively;  $U_s$  refers to voltage virtual value of the stator;  $s$  is slip ratio; and  $\omega_1$  is the synchronous rotational speed.

Besides, the limits of reactive power output for grid-side VSC are mainly affected by the capacity of grid-side VSC, as follows [45]:

$$\begin{cases} Q_{c,\max} = \sqrt{S_{c,\max}^2 - \left(\frac{sP_m}{1-s}\right)^2}, \\ Q_{c,\min} = -\sqrt{S_{c,\max}^2 - \left(\frac{sP_m}{1-s}\right)^2}, \end{cases} \quad (4)$$

where  $S_{c,\max}$  represents the capacity of grid-side VSC.

Hence, the limits of reactive power regulation capacity of each wind turbine at a certain wind speed can be determined and then the whole wind farm [46].

**2.2. Reactive Power Regulation of PV Generators.** The active power output of photovoltaic (PV) stations depends mainly upon the solar irradiation and temperature. Assuming that the output power is regulated via the maximum power point tracking (MPPT) control; accordingly, the output of active power can be expressed as follows [47, 48]:

$$P_{pv} = P_{pv}^{\text{base}} (1 + \alpha_{pv} \cdot (T - T_{\text{ref}})) \cdot \frac{S_{pv}}{1000}, \quad (5)$$

where  $P_{pv}^{\text{base}}$  denotes the rated generated output of PV stations;  $\alpha_{pv}$  means temperature-power conversion factor;  $T$  and  $T_{\text{ref}}$  represent current ambient temperature and reference temperature, respectively; and  $S_{pv}$  refers to current solar irradiation.

Here, the limits of reactive power regulation capacity for PV stations largely rely on the current active power output and the capacity of PV inverter, as follows:

$$\begin{cases} Q_{pv,\max} = \sqrt{(S_{pv})^2 - (P_{pv})^2}, \\ Q_{pv,\min} = -\sqrt{(S_{pv})^2 - (P_{pv})^2}, \end{cases} \quad (6)$$

where  $Q_{pv,\max}$  and  $Q_{pv,\min}$  represent the lower and upper of reactive power regulation capacity for PV stations, respectively;  $S_{pv}$  stands for the capacity of PV inverter.

**2.3. Reactive Power Optimization Model.** The RPO model constructed in this paper aims to minimize the total power loss in all transmission lines and total voltage deviation of all nodes, as follows:

$$\begin{aligned} & \min f(x) \\ & \begin{cases} f(x) = P_{\text{loss}} = \sum_{i,j \in N_L} g_{ij} [V_i^2 + V_j^2 - 2V_i V_j \cos \theta_{ij}] \\ f(x) = V_d = \sum_{j \in N_i} (V_j - V_j^*)^2, \end{cases} \end{aligned} \quad (7)$$

where  $P_{\text{loss}}$  means total power loss of the power grid;  $V_d$  denotes total voltage deviation of all nodes, which refers to

per-unit value;  $V_i$ ,  $V_j$ , and  $\theta_{ij}$  represent the voltage amplitude of node  $i$  and node  $j$ , and the phase angle difference between them, respectively;  $g_{ij}$  refers to the admittance between node  $i$  and node  $j$ ;  $N_i$  and  $N_L$  stand for the set of all nodes and the set of all branches; and  $V_j^*$  is the rated voltage of node  $j$ .

In terms of the considered optimization problem, the objective functions are subjected to several equality and inequality constraints, in which all constraints to be considered are described as follows:

(1) Power flow constraints

$$\begin{cases} P_{Gi} - P_{Di} - V_i \sum_{j \in N_i} V_j (g_{ij} \cos \theta_{ij} + b_{ij} \sin \theta_{ij}) = 0, & i \in N_0, \\ Q_{Gi} - Q_{Di} - V_i \sum_{j \in N_i} V_j (g_{ij} \sin \theta_{ij} - b_{ij} \cos \theta_{ij}) = 0, & i \in N_{PQ}, \end{cases} \quad (8)$$

where  $P_{Gi}$  and  $Q_{Gi}$  are active and reactive power generation of node  $i$ , respectively;  $P_{Di}$  and  $Q_{Di}$  represent active and reactive power load, respectively;  $b_{ij}$  mean the susceptance between node  $i$  and node  $j$ ;  $N_0$  denotes the set of nodes except for slack bus; and  $N_{PQ}$  is the set of PQ buses.

(2) Generator constraints

$$\begin{cases} P_{Gb}^{\min} \leq P_{Gb} \leq P_{Gb}^{\max}, \\ Q_{Gi}^{\min} \leq Q_{Gi} \leq Q_{Gi}^{\max}, & i \in N_G, \\ V_{Gi}^{\min} \leq V_{Gi} \leq V_{Gi}^{\max}, & i \in N_G, \end{cases} \quad (9)$$

where  $P_{Gb}$  denotes active power generation of slack bus;  $P_{Gb}^{\min}$  and  $P_{Gb}^{\max}$  represent the maximum and minimum active power generation regulation at slack bus, respectively;  $Q_{Gi}^{\min}$  and  $Q_{Gi}^{\max}$  denote the maximum and minimum reactive power regulation of generator;  $V_{Gi}^{\min}$  and  $V_{Gi}^{\max}$  stand for the maximum and minimum output voltage of generators; and  $N_G$  is the number of all generators.

(3) Constraints of reactive power compensation device and transformer tap

$$\begin{cases} Q_{Ci}^{\min} \leq Q_{Ci} \leq Q_{Ci}^{\max}, & i \in N_C, \\ T_h^{\min} \leq T_h \leq T_h^{\max}, & h \in N_T, \end{cases} \quad (10)$$

where  $Q_{Ci}^{\min}$  and  $Q_{Ci}^{\max}$  stand for the maximum and minimum capacity of the  $i$ -th reactive power compensation device, respectively;  $T_h^{\min}$  and  $T_h^{\max}$  represent the lower and upper limits of the  $h$ -th transformer tap;  $N_C$  is the number of reactive power compensation devices; and  $N_T$  is the number of transformer taps.

(4) Security constraints

$$\begin{cases} V_i^{\min} \leq V_i \leq V_i^{\max}, & i \in N_{PQ}, \\ |S_l| \leq S_l^{\max}, & l \in N_L, \end{cases} \quad (11)$$

where  $V_i^{\min}$  and  $V_i^{\max}$  mean the lower and upper limits of voltage of node  $i$ , respectively;  $S_l$  and  $S_l^{\max}$  are apparent power and transmission power limit of line  $l$ , respectively; and  $N_L$  is the number of lines.

### 3. Design of Fast Atom Search Optimization Algorithm

The proposed FASO algorithm is developed from the original ASO algorithm, which is also inspired by the molecular dynamics in nature, where each atom in the populations will interact with others by means of the interaction forces resulting from Lennard–Jones (L-J) potential and the geometric constraints between them [40]. The interactions among atoms contain two options, i.e., repulsion and attraction. The farmer is used to avoid overcrowding of atoms while the latter is to bind atoms together. In particular, the repulsion brings a wider global exploration capability while the attraction ensures a deeper local exploitation ability. Note that the repulsion will gradually weaken and the attraction will increasingly strengthen for seeking the globally optimal solutions in the iteration process. Besides, geometric constraint also leads to a deeper local exploitation due to its ability to propel all atoms; especially, worse atoms approximate the current optimal solutions.

*3.1. Inspiration.* In FASO, the L-J potential essentially characterizes the potential energy between two interactive atoms, which is also seen as the power of atomic motion. The potential energy on the  $i$ th atom imposed by the  $j$ th atom can be rewritten as follows:

$$U(r_{ij}) = 4\epsilon \left[ \left( \frac{\sigma}{r_{ij}} \right)^{12} - \left( \frac{\sigma}{r_{ij}} \right)^6 \right], \quad (12)$$

where  $\epsilon$  and  $\sigma$  denote the depth of the potential well and the length scale, respectively, and  $r_{ij}$  denotes Euclidian distance between the  $j$ th and the  $i$ th atoms,  $r_{ij} = \|\mathbf{x}_j - \mathbf{x}_i\|$ .

Then, the interaction forces on the  $i$ th atom imposed by the  $j$ th atom can be expressed as follows [40]:

$$\begin{aligned} F_{ij} &= -\nabla U(r_{ij}) = \frac{24\epsilon}{\sigma^2} \left[ 2 \left( \frac{\sigma}{r_{ij}} \right)^{14} - \left( \frac{\sigma}{r_{ij}} \right)^8 \right] \mathbf{r}_{ij}, \\ F'_{ij} &= \frac{24\epsilon}{\sigma} \left[ 2 \left( \frac{\sigma}{r_{ij}} \right)^{13} - \left( \frac{\sigma}{r_{ij}} \right)^7 \right]. \end{aligned} \quad (13)$$

As demonstrated in Figure 2, the potential energy largely depends on the relative distance among atoms. It is easy to note that the whole potential energy area is fallen into repulsion region and attraction region, in which the equilibrium between two regions can be achieved when  $(\sigma/r) = 1.12$ . Note that the potential energy will dramatically decrease as the Euclidean distance between two atoms increases when two atoms repel each other. In addition, the potential energy will slowly decrease to be zero with the increase of Euclidian distance when two atoms attract each other. Crucially, more positive attraction and less negative repulsion are required to be assured as iterations increase.

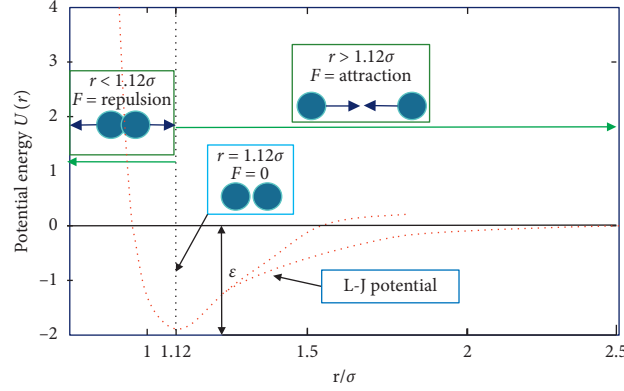


FIGURE 2: Potential energy of atoms under different input parameters.

Hence, the interaction forces can be calculated by a modified equation, as follows [41]:

$$F'_{ij}(k) = -\eta(k) \left[ 2(h_{ij}(k))^{13} - (h_{ij}(k))^7 \right], \quad (14)$$

where  $\eta(k)$  denotes the depth function at the  $k$ th iteration and  $h_{ij}(k)$  means distance ratio between the  $j$ th and the  $i$ th atoms, which can be updated by the following equation [41]:

$$\eta(k) = \alpha \left( 1 - \frac{k-1}{k_{\max}} \right)^3 e^{-(20k/k_{\max})},$$

$$h_{ij}(k) = \begin{cases} h_{\min}, & \text{if } \frac{r_{ij}(k)}{\sigma(k)} < h_{\min}, \\ \frac{r_{ij}(k)}{\sigma(k)}, & \text{if } h_{\min} \leq \frac{r_{ij}(k)}{\sigma(k)} \leq h_{\max}, \\ h_{\max}, & \text{if } \frac{r_{ij}(k)}{\sigma(k)} > h_{\max}, \end{cases} \quad (15)$$

$$\sigma(k) = \left\| \mathbf{r}_{ij}(k), \frac{\sum_{l \in \mathbf{X}_{\text{best}}} \mathbf{r}_{il}(k)}{L(k)} \right\|_2,$$

where  $\alpha$  denotes depth weight,  $h_{\max}$  and  $h_{\min}$  mean the upper and lower limits of distance ratios, and  $\mathbf{X}_{\text{best}}$  represents the subset of the best  $L$  atoms.

As illustrated in Figure 3,  $F'$  is directly related to the input variables  $\eta$  and  $h$ . Therefore, the interaction force could be also controlled by the limits of  $h$ , in which the upper limit of  $h$  is set to be 1.24 like the original ASO algorithm. Moreover, the lower limit of  $h$  is determined to be 1.1 or 1.2, which is one improvement of FASO. In FASO, atoms can perform a wider global exploration if a better solution that compared with the previous optimal solution cannot be found, and consequently, a smaller lower limit of  $h$  is required. On the contrary, a deeper local exploitation is needed if the best solution has been updated. The lower limit of  $h$  is expressed as follows:

$$h_{\min}(k) = \begin{cases} 1.1 + w(k), & \text{If } \text{Fit}(\mathbf{x}_{\text{best}}(k)) \leq \text{Fit}(\mathbf{x}_{\text{best}}^p), \\ 1.2, & \text{otherwise,} \end{cases}$$

$$w(k) = 0.1 \cdot \sin\left(\frac{\pi}{2} \cdot \frac{k}{k_{\max}}\right), \quad (16)$$

where  $\text{Fit}$  refers to the fitness function;  $\mathbf{x}_{\text{best}}(k)$  and  $\mathbf{x}_{\text{best}}^p$  mean the best solution obtained at the  $k$ th iteration and the previous best solution, respectively; and  $w(k)$  is a function that can drive the FASO algorithm drift from exploration to exploitation [43].

Moreover, variable  $L$  also has a great impact on the interaction force. In the ASO algorithm,  $L$  atoms with better fitness value are treated as the neighbors of a certain atom,



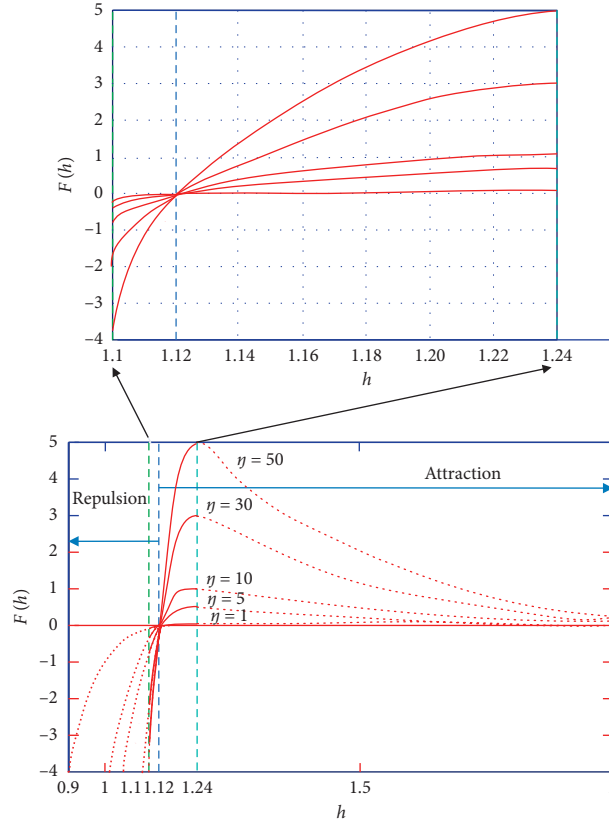


FIGURE 3: Function behaviours of  $F'$  under different input parameters.

and thus which variable  $L$  denotes the number of atoms that are selected to interact with such atom. In the first stage of iterations, larger  $L$ , i.e., as many atoms as possible, the  $L$  neighbors of such atom are needed to obtain the high exploration ability in the search space and thus can well avoid being trapped into the local optimal. On the contrary, each atom needs to interact with as few atoms with better fitness value as its  $L$  neighbors at the end of iterations are needed to rapidly obtain high-quality solution. In general, FASO should implement a wide global exploration when it cannot find a better solution compared with the previous best solution, while a deep local exploitation is required when it can find a better solution. Hence, as a function of time,  $L$  gradually decreases with the lapse of iterations. Besides, in this paper, the number of neighboring atoms is selected as 2 when it finds a better solution compared with the previous best solution. Hence, the FASO algorithm develops another improvement compared with the ASO algorithm [41], as follows:

$$L(k) = \begin{cases} n - (n - 2) \times \sqrt{\frac{k}{k_{\max}}}, & \text{If } \text{Fit}(\mathbf{x}_{\text{best}}(k)) \leq \text{Fit}(\mathbf{x}_{\text{best}}^p), \\ 2, & \text{otherwise,} \end{cases} \quad (17)$$

where  $n$  is the population size.

Hence, the total interaction force that acted on the  $i$ th atom from the  $j$ th atoms can be given by

$$F_i(k) = \sum_{j=1, j \neq i}^{L(k)} F_{ij}(k). \quad (18)$$

**3.2. Geometric Constraint.** The geometric constraint [49] plays a crucial role in atomic searching motion to keep the polyatomic molecule structure of FASO. Assume that each atom has a covalent bond with the best atom. Accordingly, the geometric constraint force of the  $i$ th atom from the best atom can be expressed as follows [37]:

$$\begin{aligned} \theta_i(k) &= \left[ |\mathbf{x}_i(k) - \mathbf{x}_{\text{best}}^p(k)|^2 - b_i^2 \right], \\ G_i(k) &= -\lambda(k) \nabla \theta_i(k) = -2\lambda(k) (\mathbf{x}_i(k) - \mathbf{x}_{\text{best}}^p(k)), \\ \lambda(k) &= \beta e^{-(20k/k_{\max})}, \end{aligned} \quad (19)$$

where  $\theta_i$  denotes the geometric constraint of the  $i$ th atom;  $G_i$  represents the constraint force of the  $i$ th atom; and  $\lambda$  and  $\beta$  mean the Lagrangian multiplier and multiplier weight, respectively.

**3.3. Atomic Searching Motion.** The interaction forces and geometric constraints have a joint influence on the atomic motion. Each atom moves to a new positive following



Newton's second law, in which the acceleration of each atom is given by [37]

$$M_i(k) = e^{((\text{Fit}(\mathbf{x}_{\text{best}}(k)) - \text{Fit}(\mathbf{x}_i(k))) / (\text{Fit}(\mathbf{x}_{\text{worst}}(k)) - \text{Fit}(\mathbf{x}_{\text{best}}(k))))},$$

$$m_i(k) = \frac{M_i(k)}{\sum_{j=1}^n M_j(k)},$$

$$\mathbf{a}_i(k) = \frac{F_i(k) + G_i(k)}{m_i(k)}, \quad i = 1, 2, \dots, n, \quad (20)$$

where  $\mathbf{x}_{\text{worst}}(k)$  is the worst solution required at the  $k$ th iteration.

It is similar to PSO algorithm [50], and the velocity and position of each atom can be updated as follows [37]:

$$\mathbf{v}_i(k+1) = \mathbf{c} \cdot \mathbf{v}_i(k) + \mathbf{a}_i(k), \quad (21)$$

$$\mathbf{x}_i(k+1) = \mathbf{x}_i(k) + \mathbf{v}_i(k+1),$$

where  $\mathbf{c}$  denotes a random vector with the same dimensions of  $\mathbf{x}_i$  in the range of  $[0, 1]$ .

### 3.4. The Implementation of FASO Algorithm

#### (1) Controllable variables

RPO of power grid with the participation of wind and solar energies is regarded as a multiconstrained nonlinear and nonconvex optimization problem, which contains both continuous variables and discrete variables, i.e., terminal voltage of generators, the capacity of static VAR compensator (SVC), reactive power output of wind and solar energies, and the tap ratio of transformers in the substations [14]. Continuous variables can converge to the optimal value in the iteration process while the optimal value of discrete variables is needed to be rounded in the continuous space [51].

#### (2) Fitness function

The fitness function of FASO depends largely on the objectives and constraints of the RPO model, which can be designed as follows:

$$\text{Fit}(\vec{C}) = \mu_1 \frac{P_{\text{loss}}}{P_{\text{base}}} + (1 - \mu_1) V_d + \eta q, \quad (22)$$

where  $\eta$  denotes penalty coefficient, which is generally set to be a biggish positive constant and  $q$  represents the number of constraints that are not satisfied.

#### (3) Overall optimizing process

In the end, the overall optimizing process of FASO-based RPO is elaborated in Figure 4.

## 4. Case Studies

The extended IEEE 9-bus and extended IEEE 39-bus test systems integrated with PV and wind generators are utilized in the simulation analysis of RPO for verifying the feasibility

of the proposed algorithm. Meanwhile, the effects of weather conditions on RPO results also are discussed. All simulations are programmed in the personal computer on the Matlab 2017b and Matpower 7.0b1. Optimization performance of FASO algorithm is compared to that of GA [34], PSO algorithm [39], GWO algorithm [37], and ASO [41]. Assume that the wind speed of wind farms and the solar irradiation of PV stations are maintained constant, respectively which are set to be 10 m/s and 800 W/m<sup>2</sup>. The control variables of RPO contain terminal voltages of conventional coal-fired units, SVC capacity, reactive power output of wind and solar energies, and the tap ratio of the transformers in the substations, of which the first three are continuous, while the last one is discrete. The ranges of these control variables are tabulated in Table 1. Meanwhile, the number of control variables applied in the extended IEEE 9 and IEEE 39-bus systems is given in Table 2.

**4.1. Simulation Analysis of IEEE 9-Bus Test System.** In the first case, the RPO is conducted in the extended IEEE 9-bus system, where the topology of the distribution network is demonstrated in Figure 5. Obviously, bus 1 represents the slack bus whose voltage magnitude is assumed to be constant, wind farm is connected to bus 7 and PV station is connected to bus 9, as well as SVC is connected to bus 4. As for the extended IEEE 9-bus test system, the base capacity of the system is 100 MW, the installed capacities of PV stations and wind farm are, respectively, 20 MW and 10 MW. For the sake of a relatively fair comparison, the population size of the proposed algorithm and other algorithms all are set to be 20, and the maximum iteration is set to be 100. Some specific parameters of all comparison algorithms are set to the default values. If the parameters are not chosen properly, the convergence time will be too long or the local optimum will be trapped. It is worth mentioning that the key parameters in the FASO algorithm, i.e., the depth weight  $\alpha$ , the multiplier weight  $\lambda$ , and the limits of distance ratios  $h$ , are determined to be 80, 1, and 1.1(1.2)/1.24 by four different benchmark functions, namely, the Sphere, Rosenbrock, Ackley, and Griewank functions, respectively [11, 41].

This paper performs the single objective optimization, in which total power loss of all transmission lines and total voltage deviation of all nodes are, respectively, regarded as the objective functions to determine the optimal scheme of RPO. Figures 6(a) and 6(b), respectively, provide the convergence curves of total power loss and total voltage deviation obtained by different algorithms in the extended IEEE 9-bus test system. Simulation results explicitly validate that FASO algorithm can acquire the high-quality solution most effectively and efficiently among all the algorithms. In contrast, PSO reveals the slowest convergence rate compared to that of other algorithms. Moreover, Figures 7(a) and 7(b), respectively, give the box-and-whisker diagrams of RPO results acquired by different algorithms, which indicate that FASO algorithm can distribute within the smallest range with minimal lower and upper bounds among all algorithms. It verifies that FASO algorithm owns the highest convergence stability and searching ability.

- 1: Initialize parameters, population, and maximum iteration  $k_{\max}$  for FASO algorithm;
- 2: Set  $k = 0$ ;
- 3: FOR1  $i = 1$  to  $n$
- 4: Implement the controllable variables of reactive power optimization for the  $i$ th atom to the IEEE test system;
- 5: Carry out the power flow calculation and gather the real-time grid data;
- 6: Calculate the fitness value of the  $i$ th atom;
- 7: END FOR1
- 8: Determine the best solution obtained by FASO at the  $k$ th iteration;
- 9: FOR2  $i = 1$  to  $n$
- 10: Calculate the total interaction force of the  $i$ th atom by Eqs. 18-25;
- 11: Calculate the constraint force of the  $i$ th atom by Eqs. 26-28;
- 12: Update the acceleration of the  $i$ th atom by Eqs. 29-31;
- 13: Update the position of the  $i$ th atom by Eqs. 32 and 33;
- 14: END FOR2
- 15: Update the current best solution;
- 16: Set  $k = k + 1$ ;
- 17: If  $k < k_{\max}$ , then output the best controllable variables of reactive power optimization model; otherwise, return to Step 4.

FIGURE 4: Overall optimizing process of FASO for RPO problem.

TABLE 1: The ranges of control variables applied in the extended IEEE 9 and IEEE 39-bus systems.

Test systems	Terminal voltage of generators (p.u.)	Capacity of SVC (Mvar)	Reactive power output of wind energy (Mvar)	Reactive power output of solar energy (Mvar)	Tap ratio of the transformers
IEEE 9-bus	[1, 1.05]	[1, 5]	[-7.62, 9.09]	[-7.55, 7.55]	—
IEEE 39-bus	[1, 1.07]	—	[-7.62, 9.09]	[-7.55, 7.55]	[0.96, 0.97, 0.98, ..., 1.07]

TABLE 2: The number of control variables applied in the extended IEEE 9 and IEEE 39-bus systems.

Test systems	Terminal voltage of generators	Capacity of SVC	Reactive power output of wind energy	Reactive power output of solar energy	Tap ratio of the transformers	Total
IEEE 9-bus	3	1	1	1	—	6
IEEE 39-bus	10	—	5	5	12	32

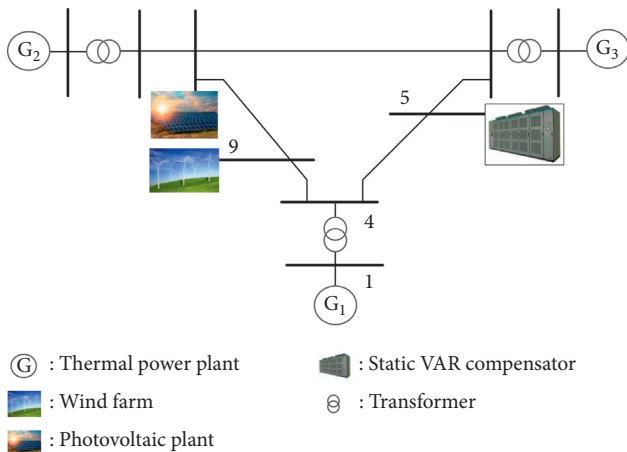


FIGURE 5: Network topology for IEEE 9-bus system.

For the sake of analyzing the impact of wind speed and solar irradiance on the RPO in the extended IEEE 9-bus system, the distributions of RPO results acquired by the

FASO algorithm under different weather conditions are shown in Figure 8. It can be easily found that power loss gradually increases with the increase of wind speed while gradually decreases as solar irradiance increases. Such results manifest that the increase of power loss does not entirely depend on the active power output of wind and solar energies, of which other effects include the locations of wind and PV generators installed and operating condition of power grid as well [31]. In addition, the total voltage deviation gradually decreases owing to the reduction of the active power output of wind and solar energies and accordingly the increase of reactive power regulation capacity when the wind speed or solar irradiance is significantly reduced.

**4.2. Simulation Analysis of IEEE 39-Bus Test System.** In the second case, the RPO is conducted in the extended IEEE 39-bus system, where the topology of the distribution network is demonstrated in Figure 9. Note that the slack bus is located in bus 1, five PV generators are, respectively, installed buses

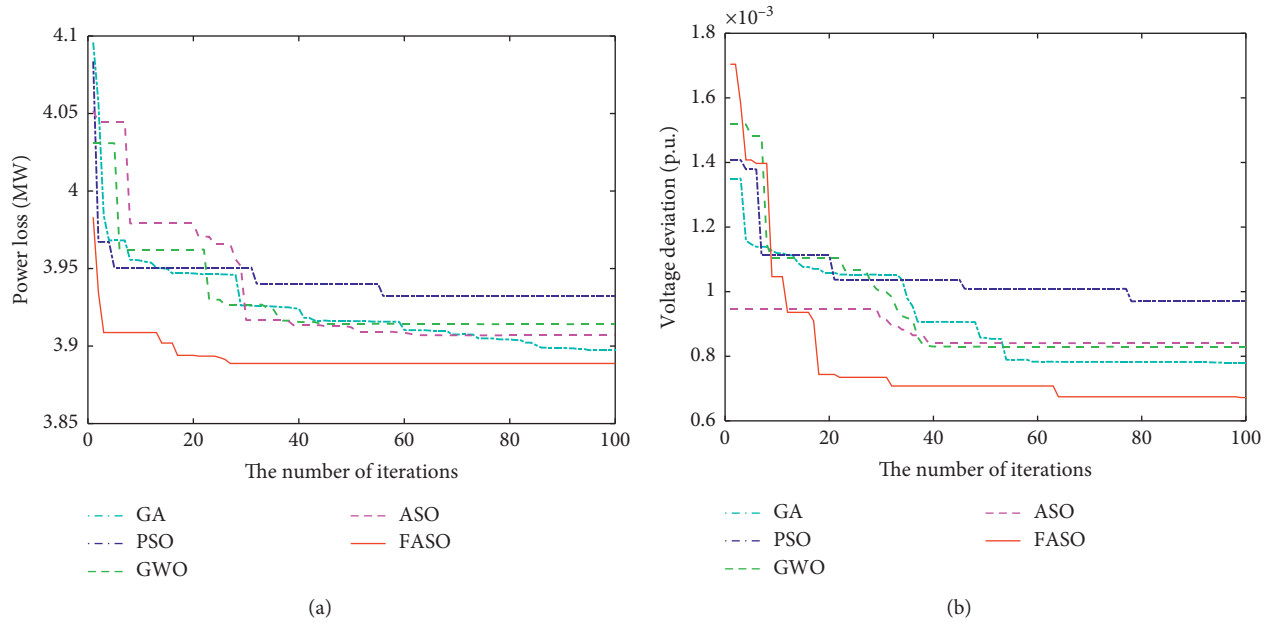


FIGURE 6: Convergence curves of RPO results obtained by different algorithms in the extended IEEE 9-bus system. (a) Power loss; (b) voltage deviation.

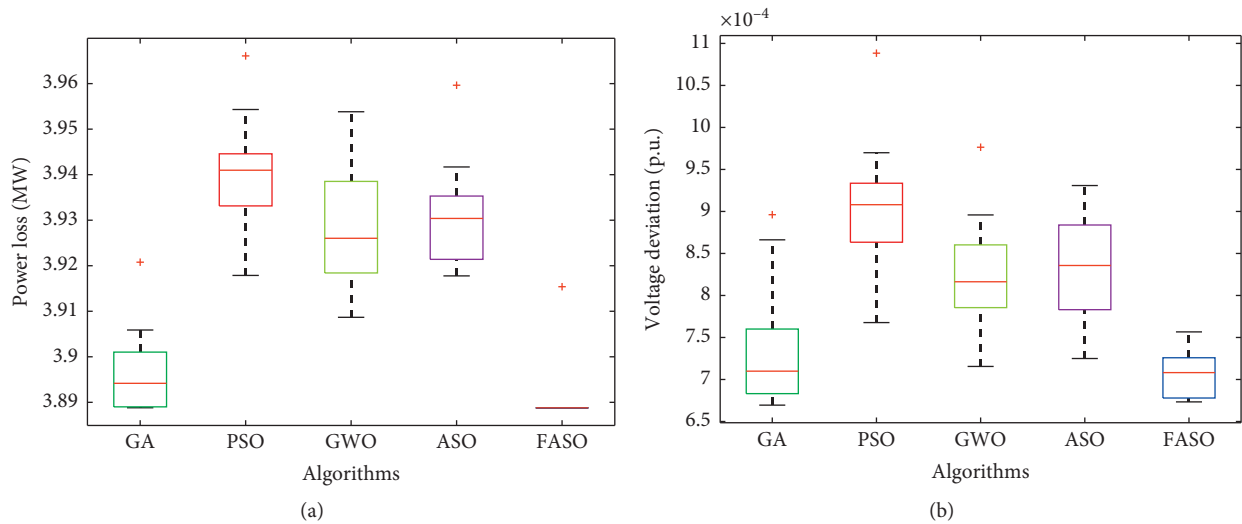


FIGURE 7: Box-and-whisker plots of RPO results obtained by different algorithms in 20 runs in the extended IEEE 9-bus system. (a) Power loss; (b) voltage deviation.

1, 4, 6, 7, and 20, and five wind generators are, respectively, installed buses 21, 23, 25, 27, and 28. The base capacity of the system is 100 MW, and the installed capacities of PV stations and wind farms are, respectively, 30 MW and 20 MW. In addition, the population size of all algorithms is set to be 40, and the maximum iteration is set to be 100.

In the extended IEEE 39-bus test system, the convergence curves and the box-and-whisker diagrams of RPO results produced by different algorithms are illustrated in Figures 10 and 11, respectively. Obviously, optimization performances of the FASO algorithm such as convergence

stability, convergence speed, and searching ability noticeably improve with the increase of system scale and the number of control variables. It indicates that FASO algorithm is also applicable to large-scale networks for RPO solution.

To investigate further, the distributions of total power loss and total voltage deviation under different weather conditions acquired by the FASO algorithm in the extended IEEE 39-bus system are illustrated in Figure 12. It can be concluded that power loss and voltage deviation are subject to some other factors rather than only the power output of renewable energies. For optimal operation in security and

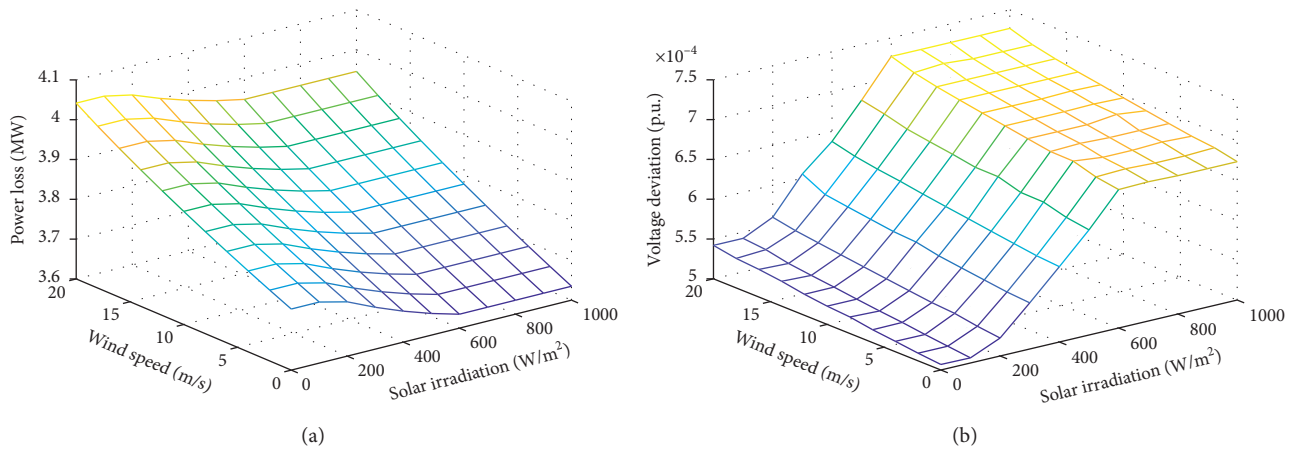


FIGURE 8: Distributions of RPO results obtained by FASO under different weather conditions of IEEE 9-bus system. (a) Power loss; (b) voltage deviation.

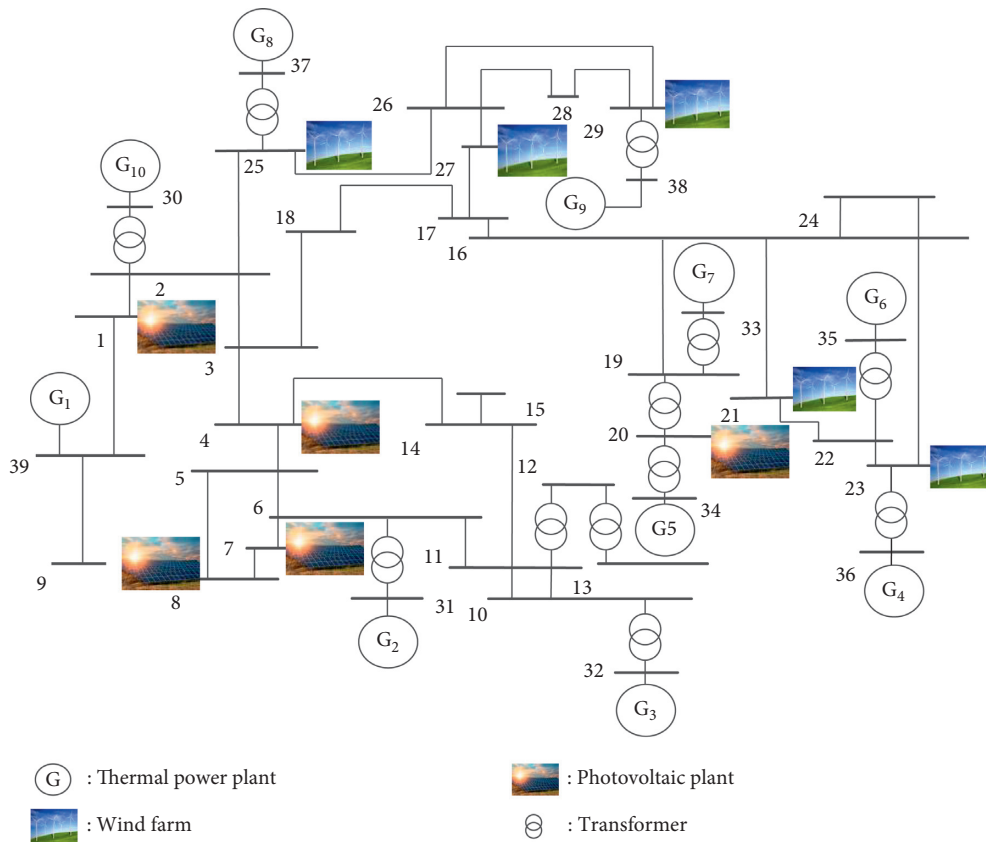


FIGURE 9: Network topology for IEEE 39-bus system.

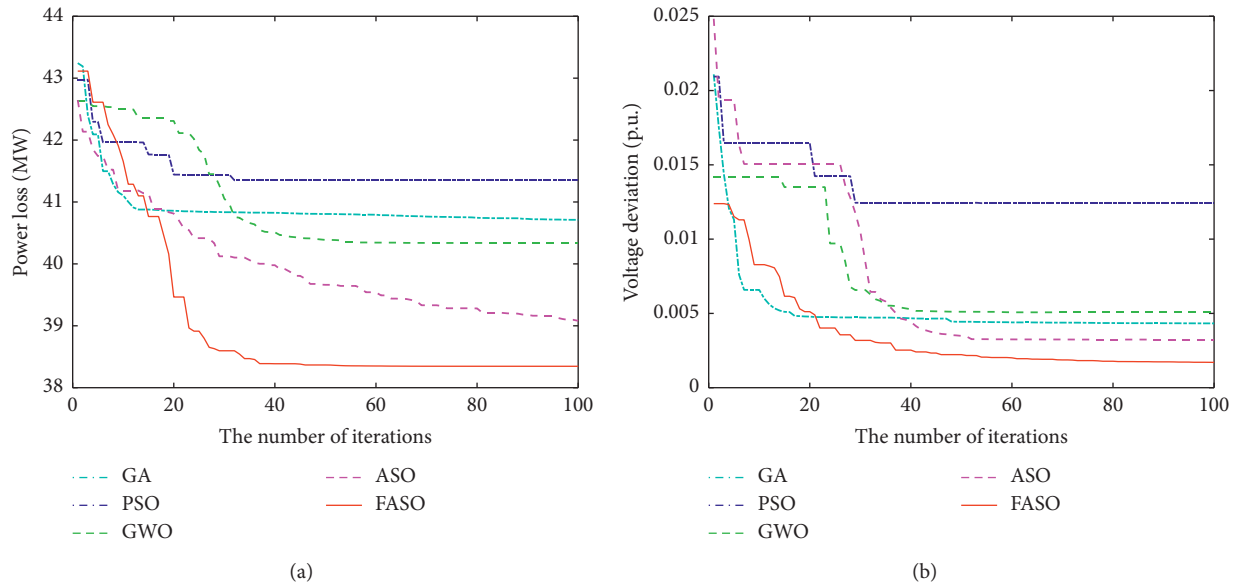


FIGURE 10: Convergence curves of RPO results obtained by different algorithms in the extended IEEE 39-bus system. (a) Power loss; (b) voltage deviation.

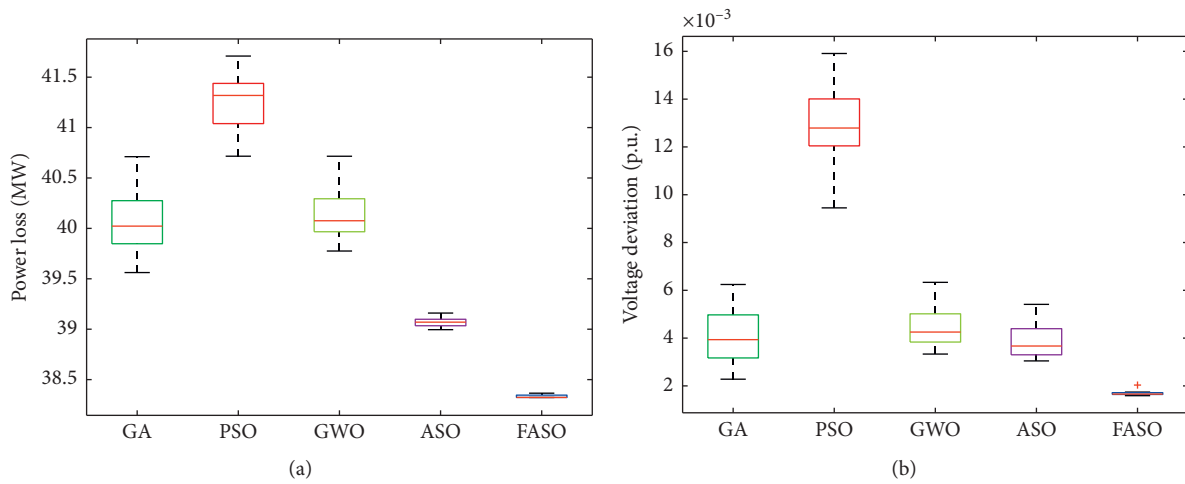


FIGURE 11: Box-and-whisker plots of RPO results obtained by different algorithms in 20 runs in the extended IEEE 39-bus system. (a) Power loss; (b) voltage deviation.

economy of the power grid with high-penetration wind and solar energies, the install locations of wind and PV generators are worth further investigating in the future.

**4.3. Comparative Analysis.** Table 3 provides the statistical results from five algorithms with regard to total power loss and total voltage deviation (bold indicates the best results). Note that all algorithms are executed in 20 independent runs to acquire statistical results and convergence graphs, where

the best solutions are used as the optimal RPO scheme. As a result, FASO algorithm effectively avoids local optimum trapping thanks to its dynamic searching mechanism, which can maintain an appropriate tradeoff between local exploitation global exploration. Moreover, the convergence speed of the FASO algorithm can be significantly improved. Particularly, voltage deviation of FASO algorithm is merely 51.16%, 24.44%, 59.45%, and 75.86% of that of GA, PSO, GWO, and ASO algorithms in the IEEE 39-bus test system, respectively.

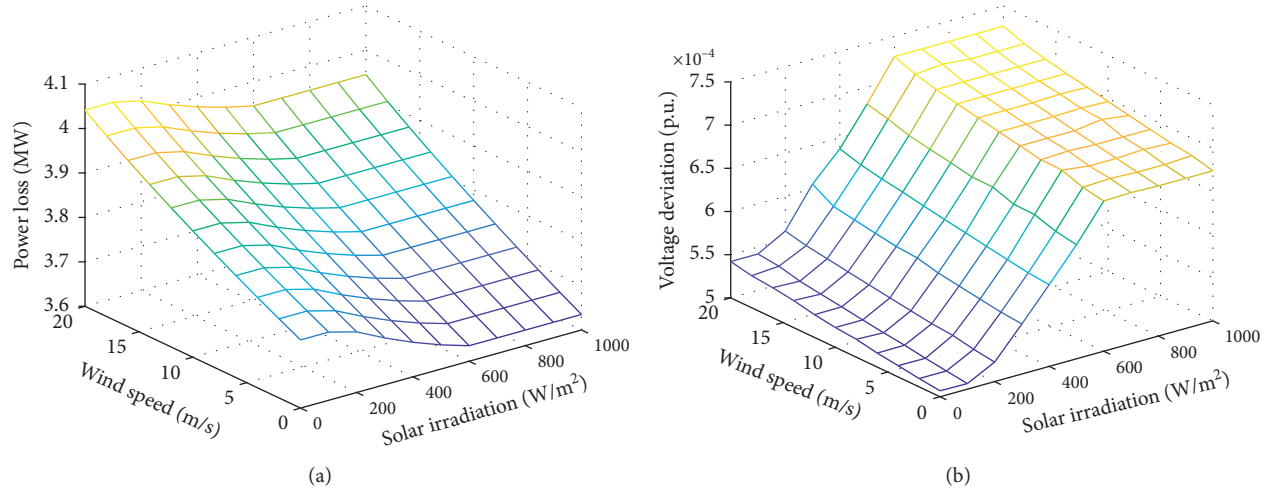


FIGURE 12: Distributions of RPO results obtained by FASO under different weather conditions of IEEE 39-bus system. (a) Power loss; (b) voltage deviation.

TABLE 3: Statistical results of convergence performance acquired by five algorithms in 20 runs.

Test systems	IEEE 9-bus		IEEE 39-bus	
Algorithms	Total power loss (MW)	Total voltage deviation (p.u.)	Total power loss (MW)	Total voltage deviation (p.u.)
GA	3.9092	$7.5853E-04$	39.8906	0.0043
PSO	3.9352	$8.8918E-04$	41.2976	0.0090
GWO	3.9248	$8.5823E-04$	40.0164	0.0037
ASO	3.8982	$6.7407E-04$	39.2954	0.0029
FASO	<b>3.8909</b>	<b><math>6.5070E-04</math></b>	<b>38.5866</b>	<b>0.0022</b>

## 5. Conclusions

This paper designs a FASO algorithm for RPO of power grid integrated with wind and solar energies, which owns the following three contributions/novelities:

- (1) A new RPO model considering high-penetration wind and solar energies is established, in which the reactive power regulation ability of PV and wind generators themselves is completely developed so as to compensate reactive power for the power grid.
- (2) In contrast with the original ASO algorithm, FASO can successfully realize better balance between local exploitation and global exploration via controlling the repulsion and attraction intensities among atoms based on current optimization results. Therefore, FASO can remarkably improve optimization efficiency and acquire high-quality optimum the fastest.
- (3) A series of case studies are undertaken to validate the competency of the FASO algorithm for RPO, such that the total power loss and voltage deviation can be minimized in two distribution networks. Particularly, statistical results clearly showcase that FASO algorithm can find the best quality solutions with the fastest convergence speed and highest convergence stability in contrast with else algorithms.

### Variables

$P_{\text{loss}}$ :	Total power loss of all transmission lines
$V_d$ :	Total voltage deviation of all nodes
$P_{Gi}$ , $Q_{Gi}$ :	Active and reactive power generation of node $i$
$P_{Di}$ , $Q_{Di}$ :	Active and reactive power load
$P_{Gb}$ :	Active power generation of slack bus
$Q_{Gi}^{\min}$ , $Q_{Gi}^{\max}$ :	The maximum and minimum reactive power regulation of generator
$V_{Gi}^{\min}$ , $V_{Gi}^{\max}$ :	The maximum and minimum output voltage of generator
$Q_{Ci}^{\min}$ , $Q_{Ci}^{\max}$ :	The maximum and minimum capacity of the $i$ -th reactive power compensation device
$T_h^{\min}$ , $T_h^{\max}$ :	The lower and upper limits of the $h$ -th transformer tap
$N_C$ , $N_T$ :	The number of reactive power compensation devices and transformer taps
$S_b$ , $S_l^{\max}$ :	Apparent power and transmission power limit of line
$T_h^{\min}$ , $T_h^{\max}$ :	The lower and upper limits of the $h$ -th transformer tap
$N_C$ , $N_T$ :	The number of reactive power compensation devices and transformer taps
$V_i^{\min}$ , $V_i^{\max}$ :	The lower and upper limits of voltage of node $i$
$S_b$ , $S_l^{\max}$ :	Apparent power and transmission power limit of line $l$



*FASO parameters*

$h_{\max}, h_{\min}$ :	Maximum and minimum distance ratios
$n$ :	Population size
$\beta$ :	Multiplier weight
$\lambda$ :	Lagrangian multiplier

*Wind generator parameters*

$L_s, L_m$ :	Stator inductance and magnetizing inductance
$\omega_1$ :	Synchronous rotational speed
$Q_{g,\max}$ :	The lower and upper limits of reactive power
$Q_{g,\min}$ :	regulation capacity for wind turbine
$S_{c,\max}$ :	Capacity of the grid-side VSC

*PV generator parameters*

$P_{pv}^{\text{base}}$ :	The rated generated output of PV stations
$\alpha_{pv}$ :	Temperature-power conversion factor
$S_{pv}$ :	Current solar irradiation
$Q_{pv,\max}$ :	The maximum and minimum reactive power
$Q_{pv,\min}$ :	regulation capacity for PV stations
$S_{pv}$ :	the capacity of PV inverter

**Abbreviations**

RESs:	Renewable energy sources
RPO:	Reactive power optimization
FASO:	Fast atom search optimization
SVC:	Static VAR compensator
L-J:	Lennard-Jones
GA:	Genetic algorithm
PSO:	Particle swarm optimization
MFO:	Moth-flame optimization
GWO:	Grey wolf optimizer.

**Data Availability**

The data that support the findings of this study are available on request from the corresponding author. The data are not publicly available due to privacy or ethical restrictions.

**Conflicts of Interest**

The authors declare that they have no conflicts of interest to report regarding the present study.

**Acknowledgments**

The authors gratefully acknowledge the support of key Project of National Natural Science Foundation of China (52037003) and Key Science and Technology Project of Yunnan Province (202002AF080001).

**References**

- [1] B. Yang, X. Zhang, T. Yu, H. Shu, and Z. Fang, "Grouped grey wolf optimizer for maximum power point tracking of doubly-fed induction generator based wind turbine," *Energy Conversion and Management*, vol. 133, pp. 427–443, 2017.
- [2] B. Yang, T. Yu, H. Shu et al., "Passivity-based sliding-mode control design for optimal power extraction of a PMSG based variable speed wind turbine," *Renewable Energy*, vol. 119, pp. 577–589, 2018.
- [3] D. R. Song, S. Y. Zheng, S. Yang et al., "Annual energy production estimation for variable-speed wind turbines at high-altitude sites," *Journal of Modern Power Systems and Clean Energy*, 2020.
- [4] B. Yang, T. Yu, H. Shu, J. Dong, and L. Jiang, "Robust sliding-mode control of wind energy conversion systems for optimal power extraction via nonlinear perturbation observers," *Applied Energy*, vol. 210, pp. 711–723, 2018.
- [5] B. Yang, T. Yu, H. Shu, X. Zhang, K. Qu, and L. Jiang, "Democratic joint operations algorithm for optimal power extraction of PMSG based wind energy conversion system," *Energy Conversion and Management*, vol. 159, pp. 312–326, 2018.
- [6] S. Mensou, A. Essadki, T. Nasser, and B. B. Idrissi, "A direct power control of a DFIG based WECS during symmetrical voltage dips," *Protection and Control of Modern Power Systems*, vol. 5, no. 5, pp. 36–47, 2020.
- [7] D. R. Song, Q. A. Li, Z. Cai et al., "Model predictive control using multi-step prediction model for electrical yaw system of horizontal-axis wind turbines," *IEEE Transactions on Sustainable Energy*, vol. 10, no. 4, pp. 2084–2093, 2019.
- [8] D. Song, X. Fan, J. Yang, A. Liu, S. Chen, and Y. H. Joo, "Power extraction efficiency optimization of horizontal-axis wind turbines through optimizing control parameters of yaw control systems using an intelligent method," *Applied Energy*, vol. 224, pp. 267–279, 2018.
- [9] Y. Chaibi, A. Allouhi, M. Salhi1, and A. El-jouni, "Annual performance analysis of different maximum power point tracking techniques used in photovoltaic systems," *Protection and Control of Modern Power Systems*, vol. 4, no. 4, pp. 171–180, 2019.
- [10] H. Hamdi, C. B. Regaya, and A. Zaafouri, "A sliding-neural network control of induction-motor-pump supplied by photovoltaic generator," *Protection and Control of Modern Power Systems*, vol. 4, no. 4, pp. 306–322, 2019.
- [11] B. Yang, L. Zhong, X. Zhang et al., "Novel bio-inspired memetic salp swarm algorithm and application to MPPT for PV systems considering partial shading condition," *Journal of Cleaner Production*, vol. 215, pp. 1203–1222, 2019.
- [12] B. Yang, T. Yu, X. Zhang et al., "Dynamic leader based collective intelligence for maximum power point tracking of PV systems affected by partial shading condition," *Energy Conversion and Management*, vol. 179, pp. 286–303, 2019.
- [13] X. Zhang, S. Li, T. He et al., "Memetic reinforcement learning based maximum power point tracking design for PV systems under partial shading condition," *Energy*, vol. 174, pp. 1079–1090, 2019.
- [14] P. K. Guchhait and A. Banerjee, "Stability enhancement of wind energy integrated hybrid system with the help of static synchronous compensator and symbiosis organisms search algorithm," *Protection and Control of Modern Power Systems*, vol. 5, no. 2, pp. 138–150, 2020.
- [15] B. Yang, L. Jiang, W. Yao, and Q. H. Wu, "Perturbation estimation based coordinated adaptive passive control for multimachine power systems," *Control Engineering Practice*, vol. 44, pp. 172–192, 2015.
- [16] M. Tan, C. J. Han, C. Han, X. Zhang, L. Guo, and T. Yu, "Hierarchically correlated equilibrium Q-learning for multi-area decentralized collaborative reactive power optimization,"

- CSEE *Journal of Power and Energy Systems*, vol. 2, no. 3, pp. 65–72, 2016.
- [17] X. Zhang, T. Tan, B. Zhou, T. Yu, B. Yang, and X. Huang, "Adaptive distributed auction-based algorithm for optimal mileage based AGC dispatch with high participation of renewable energy," *International Journal of Electrical Power & Energy Systems*, vol. 124, Article ID 106371, 2021.
  - [18] M. N. I. Sarkar, L. G. Meegahapola, and M. Datta, "Optimal reactive power dispatch considering reactive power support from renewable energy generators," in *Proceedings of the IEEE International Conference on Industrial Technology (ICIT)*, pp. 667–672, Melbourne, Australia, February 2019.
  - [19] M. N. I. Sarkar, L. G. Meegahapola, and M. Datta, "Reactive power management in renewable rich power grids: a review of grid-codes, renewable generators, support devices, control strategies and optimization algorithms," *IEEE Access*, vol. 6, pp. 41458–41489, 2018.
  - [20] Q. X. Chen, X. Y. Zhao, and D. H. Gan, "Active-reactive scheduling of active distribution system considering interactive load and battery storage," *Protection and Control of Modern Power Systems*, vol. 2, no. 2, pp. 320–330, 2017.
  - [21] D. Gutierrez Rojas, J. Lopez Lezama, and W. Villa, "Meta-heuristic techniques applied to the optimal reactive power dispatch: a review," *IEEE Latin America Transactions*, vol. 14, no. 5, pp. 2253–2263, 2016.
  - [22] M. Ettappan, V. Vimala, S. Ramesh, and V. T. Kesavan, "Optimal reactive power dispatch for real power loss minimization and voltage stability enhancement using artificial bee colony algorithm," *Microprocessors and Microsystems*, vol. 76, Article ID 103085, 2020.
  - [23] M. N. Gilvaei, H. Jafari, M. J. Ghadi, and L. Li, "A novel hybrid optimization approach for reactive power dispatch problem considering voltage stability index," *Engineering Applications of Artificial Intelligence*, vol. 96, Article ID 103963, 2020.
  - [24] H. B. Ruan, H. J. Gao, J. Y. Liu, and Y. B. Liu, "A distributionally robust reactive power optimization model for active distribution network considering reactive power support of DG and switch reconfiguration," *Energy Procedia*, vol. 158, pp. 6358–6365, 2019.
  - [25] J. Huang, Z. Li, and Q. H. Wu, "Fully decentralized multiarea reactive power optimization considering practical regulation constraints of devices," *International Journal of Electrical Power & Energy Systems*, vol. 105, pp. 351–364, 2019.
  - [26] M. K. Mangoli, K. Y. Lee, and Y. Moon Park, "Optimal real and reactive power control using linear programming," *Electric Power Systems Research*, vol. 26, no. 1, 1993.
  - [27] R. M. Jan and N. Chen, "Application of the fast Newton-Raphson economic dispatch and reactive power/voltage dispatch by sensitivity factors to optimal power flow," *IEEE Transactions on Energy Conversion*, vol. 10, no. 2, pp. 293–301, 1995.
  - [28] F.-C. Lu and Y. Y. Hsu, "Reactive power/voltage control in a distribution substation using dynamic programming," *IEEE Proceedings - Generation, Transmission and Distribution*, vol. 142, no. 6, pp. 639–645, 1995.
  - [29] J. Z. Zhu and X. F. Xiong, "Optimal reactive power control using modified interior point method," *Electric Power Systems Research*, vol. 66, no. 2, pp. 187–192, 2003.
  - [30] N. Grudin, "Reactive power optimization using successive quadratic programming method," *IEEE Transactions on Power Systems*, vol. 13, no. 4, pp. 1219–1225, 1998.
  - [31] S. M. Mohseni-Bonab and A. Rabiee, "Optimal reactive power dispatch: a review, and a new stochastic voltage stability constrained multi-objective model at the presence of uncertain wind power generation," *IET Generation, Transmission & Distribution*, vol. 11, no. 4, pp. 815–829, 2017.
  - [32] B. Yang, J. Wang, Y. Chen et al., "Optimal sizing and placement of energy storage system in power grids: a state-of-the-art one-stop handbook," *Journal of Energy Storage*, vol. 32, Article ID 101814, 2020.
  - [33] K. Iba, "Reactive power optimization by genetic algorithm," *IEEE Transactions on Power Systems*, vol. 9, no. 2, pp. 685–692, 1994.
  - [34] R. Bakhshi, J. Sadeh, and H.-R. Mosaddegh, "Optimal economic designing of grid-connected photovoltaic systems with multiple inverters using linear and nonlinear module models based on genetic algorithm," *Renewable Energy*, vol. 72, pp. 386–394, 2014.
  - [35] K. Ben Oualid Medani and S. Sayah, "Optimal reactive power dispatch using particle swarm optimization with time varying acceleration coefficients," in *Proceedings of the 2016 8th International Conference on Modelling, Identification and Control (ICMIC)*, pp. 780–785, IEEE, Algiers, Algeria, November 2016.
  - [36] N. S. M. Rebecca, M. H. Sulaiman, M. Zuriani, and D. Hamdan, "Optimal reactive power dispatch solution by loss minimization using moth-flame optimization technique," *Applied Soft Computing*, vol. 59, pp. 210–222, 2017.
  - [37] M. H. Sulaiman, Z. Mustaffa, M. R. Mohamed, and O. Aliman, "Using the gray wolf optimizer for solving optimal reactive power dispatch problem," *Applied Soft Computing*, vol. 32, pp. 286–292, 2015.
  - [38] A. Benslimane, J. Bouchnaif, M. Essoufi, B. Hajji, and L. Idrissi, "Comparative study of semiconductor power losses between CSI-based STATCOM and VSI-based STATCOM, both used for unbalance compensation," *Protection and Control of Modern Power Systems*, vol. 5, no. 1, pp. 56–69, 2020.
  - [39] J. Li, H. Huang, B. Lou, Y. Peng, Q. Huang, and K. Xia, "Wind farm reactive power and voltage control strategy based on adaptive discrete binary particle swarm optimization algorithm," in *Proceedings of the 2019 IEEE Asia Power and Energy Engineering Conference (APEEC)*, pp. 99–102, IEEE, Chengdu, China, March 2019.
  - [40] R. Sun, Y. Shu, Z. Lv, B. Chen, and Z. Wei, "Research on the multiple timescale reactive power optimization of receiving power grid based on model predictive control," in *Proceedings of the 2020 12th IEEE PES Asia-Pacific Power and Energy Engineering Conference (APPEEC)*, September 2020.
  - [41] W. Zhao, L. Wang, and Z. Zhang, "Atom search optimization and its application to solve a hydrogeologic parameter estimation problem," *Knowledge-Based Systems*, vol. 163, pp. 283–304, 2019.
  - [42] B. Yang, M. Zhang, X. Zhang et al., "Fast atom search optimization based MPPT design of centralized thermoelectric generation system under heterogeneous temperature difference," *Journal of Cleaner Production*, vol. 248, Article ID 119301, 2020.
  - [43] K. Sun, W. Yao, J. Fang, X. Ai, J. Wen, and S. Cheng, "Impedance modeling and stability analysis of grid-connected DFIG-based wind farm with a VSC-HVDC," *IEEE Journal of Emerging and Selected Topics in Power Electronics*, vol. 8, no. 2, pp. 1375–1390, 2020.
  - [44] B. Yang, L. Jiang, L. Wang, W. Yao, and Q. H. Wu, "Nonlinear maximum power point tracking control and modal analysis of DFIG based wind turbine," *International Journal of Electrical Power & Energy Systems*, vol. 74, pp. 429–436, 2016.

- [45] J. Hetzer, D. C. Yu, and K. Bhattarai, "An economic dispatch model incorporating wind power," *IEEE Transactions on Energy Conversion*, vol. 23, no. 2, pp. 603–611, 2008.
- [46] M. Edrah, K. L. Lo, and O. Anaya-Lara, "Reactive power control of DFIG wind turbines for power oscillation damping under a wide range of operating conditions," *IET Generation, Transmission & Distribution*, vol. 10, no. 15, pp. 3777–3785, 2016.
- [47] S. Brini, H. H. Abdallah, and A. Ouali, "Economic dispatch for power system included wind and solar thermal energy," *Leonardo Journal of Sciences*, vol. 14, pp. 204–220, 2009.
- [48] Q. Wang, W. Yao, J. Fang et al., "Dynamic modeling and small signal stability analysis of distributed photovoltaic grid-connected system with large scale of panel level DC optimizers," *Applied Energy*, vol. 259, Article ID 114132, 2020.
- [49] J.-P. Ryckaert, G. Ciccotti, and H. J. C. Berendsen, "Numerical integration of the cartesian equations of motion of a system with constraints: molecular dynamics of n-alkanes," *Journal of Computational Physics*, vol. 23, no. 3, pp. 327–341, 1977.
- [50] M. A. Abido, "Optimal power flow using particle swarm optimization," *International Journal of Electrical Power & Energy Systems*, vol. 24, no. 7, pp. 563–571, 2002.
- [51] X. Zhang, T. Yu, B. Yang, and L. Cheng, "Accelerating bio-inspired optimizer with transfer reinforcement learning for reactive power optimization," *Knowledge-Based Systems*, vol. 116, pp. 26–38, 2017.

## Research Article

# Memetic Salp Swarm Algorithm-Based Frequency Regulation for Power System with Renewable Energy Integration

Fang Zeng and Hongchun Shu 

*Faculty of Electric Power Engineering, Kunming University of Science and Technology, Kunming 650500, China*

Correspondence should be addressed to Hongchun Shu; fanger1119@kust.edu.cn

Received 12 November 2020; Revised 25 November 2020; Accepted 29 November 2020; Published 14 December 2020

Academic Editor: Xiao-Shun Zhang

Copyright © 2020 Fang Zeng and Hongchun Shu. This is an open access article distributed under the Creative Commons Attribution License, which permits unrestricted use, distribution, and reproduction in any medium, provided the original work is properly cited.

As the penetration of renewable energy to power grid increases gradually, to ensure the safety and stable operation of power system, it is necessary for renewable energy to participate in the secondary frequency regulation of power system. Therefore, this paper proposes an optimal control model of renewable energy participating in the secondary frequency regulation to solve the dynamic power distribution problem. Besides, memetic salp swarm algorithm (MSSA) is used to solve this complex nonlinear optimization problem, so as to quickly obtain high-quality power distribution schemes under different power perturbations and maximize the dynamic response regulation performance of the entire regional power grid. Finally, based on the improved IEEE standard two-area model, the established model is verified and the performance of the applied algorithm is tested by comparing the traditional engineering allocation method and other intelligent optimization algorithms.

## 1. Introduction

In recent years, to cope with climate change and sustainable energy development, the penetration of renewable energy connected to power grid has increased rapidly [1–3]. Different from traditional hydrothermal power, wind power and photovoltaic (PV) power with relatively mature technologies are greatly affected by meteorological conditions, so their power fluctuations are highly random [4–6]. As the regional power grid usually cannot fully absorb renewable energy such as wind or solar energy, it is easy to disconnect the wind farm or PV station from the power grid, which also greatly increases the pressure of frequency regulation of the system [7–10]. In this situation, the traditional configuration of hydropower plant and thermal power station as the main frequency regulation resources has been difficult to meet the high quality of the system's dynamic frequency regulation needs [11–13].

Therefore, the development of new high-quality frequency regulation resources has become one of the main means to relieve the pressure of regional power grid [14–16].

Compared with traditional hydropower plant and thermal power station, wind farm and PV station have faster response speed as well as climbing speed and rapid power fluctuations can be balanced more quickly [17–19]. Therefore, for regional power grids with high renewable energy penetration, especially in low-load areas, and wind farm, PV station can be used on power point control method to control it in below the operation condition of maximum power point, with a certain reserve capacity to participate in the secondary frequency regulation [6, 20, 21], called automatic generation control (AGC) [22–24].

In general, AGC mainly consists of two parts [25–27]: (1) based on the real-time acquisition of frequency and power deviation of the tie line, a centralized controller, such as proportional-integral (PI) controller, is used to acquire the approximate actual power fluctuation of the system, and then the total power instruction of the regional power network is issued; (2) according to the power allocation algorithms, the total power instruction is assigned to each unit participating in the frequency regulation [28–30]. Literature [31] proposes a sliding mode controller for



multisource AGC system using teaching and learning-based optimization algorithm. Literature [32] proposes a lifelong learning-based complementary generation control of power grids with renewable energy sources. Literature [33] proposes AGC of a multiarea multisource hydrothermal power system. However, although the abovementioned literature realizes the control of multisource participating in AGC, the modeling is relatively simple, considering only the climbing response characteristics of the units and not other dynamic response characteristics of different frequency regulation resources, which will affect the overall control effect of the system and easily make the system deviate greatly from the optimal operating point. Therefore, this paper proposes a multisource optimal collaborative control method for wind and solar renewable energy based on its dynamic response characteristics to participate in secondary frequency regulation.

In essence, AGC optimal control is a complex nonlinear optimization problem [34–36]. In practice, power distribution is often not optimized but arranged according to adjustable capacity ratio and climbing speed, which cannot meet the optimal control requirements of the system [37–40]. On the other hand, traditional mathematical optimization methods (such as interior point method [41]), although fast in solving problems, have poor global searching ability and are prone to fall into local optimal solutions. In comparison, genetic algorithm (GA) [42–44] and other metaheuristic algorithms [45–47] have higher application flexibility and better global search capability, but their solving speed is slow and cannot meet the needs of AGC online control for large-scale regional power grids [48–50]. Therefore, MSSA with a faster convergence speed is used to solve the problem. Compared with the original salp swarm algorithm (SSA), memetic salp swarm algorithm (MSSA) employs multiple independent slap chains to simultaneously implement the exploration and exploitation [51]. Besides, MSSA also has low dependence on the mathematical model. To verify the validity of the proposed method, this paper used the improved IEEE standard two-area model for simulation test and analysis.

The remaining of this paper is organized as follows: Section 2 develops the optimal control model for automatic generation control. In Section 3, MSSA is described. Comprehensive case studies are undertaken in Section 4. Section 5 summarizes the main contributions of the paper.

## 2. Optimal Control Model for Automatic Generation Control

**2.1. Control Framework.** Generally, AGC has the following three control modes: (a) flat frequency control, (b) flat tie-line control, and (c) tie-line bias control. Also, tie-line bias control was used in this paper. The two-region interconnection power network is depicted in Figure 1, in which the AGC control process of each region includes two parts: controller control and optimal power distribution. A PI controller is adopted to convert the power deviation and frequency deviation of the real-time

receiving tie line into regional control deviation as input and output to the real-time adjusting power of the regional power grid  $\Delta P$ . Then,  $\Delta P$  is assigned to each AGC unit through the power allocation algorithm. Different from the traditional power system with hydropower plant and thermal power station as the main reserve capacity, wind farm and PV station no longer need to be disconnected from the grid but participate in the power AGC regulation of the system.

**2.2. Dynamic Response Model of Units.** The establishment of dynamic response model of the units is mainly in order to more accurately describe the units after the received power adjusts instruction power dynamic response process. For different types of units, the dynamic response model not only regulates the upper and lower limits of capacity, climbing rate, frequency regulation delay, and other common parts [52] but also includes transmission links with their own energy conversion characteristics. Besides, AGC often uses the frequency domain model to describe the dynamic response process of the units, as shown in Figure 2.  $T_d$  represents the secondary frequency regulation delay of the units;  $G(s)$  represents the power response transfer function of the units, as shown in Table 1.  $T_1 \sim T_9$  are the known parameters of the transfer function, respectively [53]. Therefore, according to the inverse Laplace transform of the frequency domain transfer function, the real-time output of the regulated power can be calculated through the input power, as follows:

$$\Delta P_i^{\text{out}}(t) = L^{-1} \left\{ \frac{G_i(s)}{s(1 + T_d^i s)} \cdot \sum_{k=1}^N \left[ e^{-\Delta T \cdot (k-1)s} \cdot D_i^{\text{in}}(k) \right] \right\}, \quad (1)$$

$$D_i^{\text{in}}(k) = \Delta P_i^{\text{in}}(k) - \Delta P_i^{\text{in}}(k-1), \quad (2)$$

$$\Delta P_i^{\text{out}}(k) = \Delta P_i^{\text{out}}(t = k \cdot \Delta T), \quad (3)$$

where  $i$  represents the  $i^{\text{th}}$  AGC unit;  $K$  represents the  $k^{\text{th}}$  discrete control period;  $\Delta P_i^{\text{in}}$  and  $\Delta P_i^{\text{out}}$  represent the input regulation power command and real-time output of regulated power of the  $i^{\text{th}}$  AGC unit, respectively; and  $\Delta T$  represents the control period of AGC, with a value of 1 to 16 seconds.

**2.3. Optimization Mathematical Model.** A performance index is assigned to quantify the total power response deviation, which is defined as the sum of the absolute deviation value of the regulating power command value and the power output value of all units, as follows:

$$\min f = \sum_{j=k}^N \sum_{i=1}^n \left| \Delta P_i^{\text{in}}(j) - \Delta P_i^{\text{out}}(j) \right|, \quad (4)$$

where  $N$  represents the number of control periods and  $n$  represents the number of AGC units.

In addition to considering the dynamic response transfer process of the units, some constraint conditions, such as power balance constraint, units capacity constraint, and

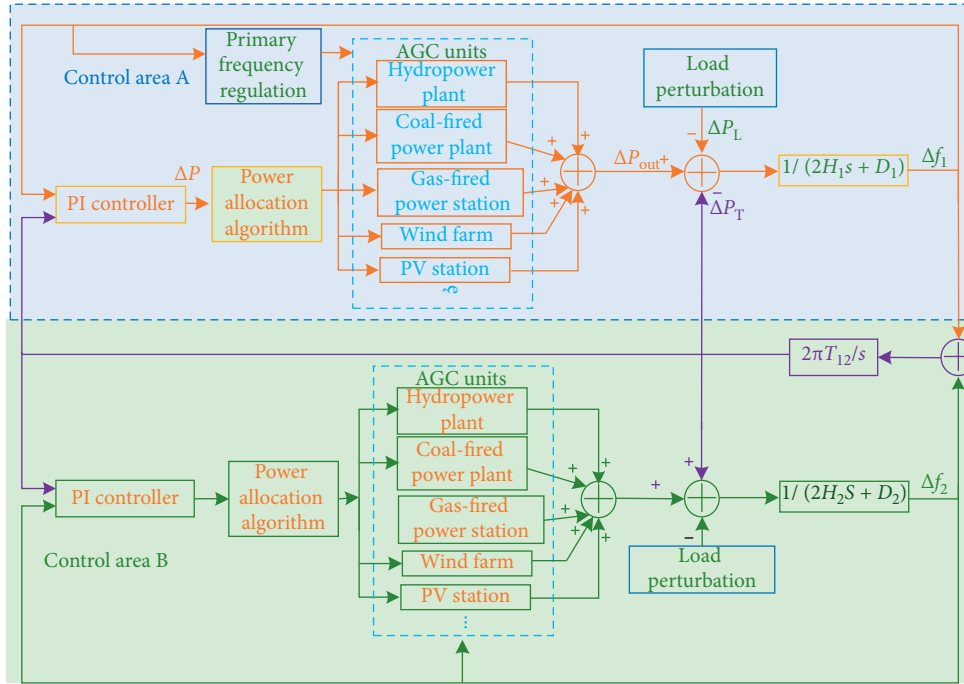


FIGURE 1: Illustration of coordinated control of multisource for AGC under two-area framework.

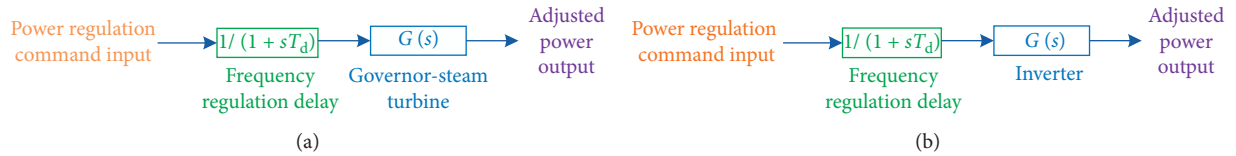


FIGURE 2: Dynamic response models of different types of AGC units. (a) Traditional hydropower plant and thermal power station. (b) Wind farm and PV station.

climbing constraint, should also be considered in the power distribution process, as follows:

$$\Delta P^{\text{in}}(k) = \sum_{i=1}^n \Delta P_i^{\text{in}}(k), \quad (5)$$

$$\Delta P_i^{\text{in}}(k) \cdot \Delta P_i^{\text{in}}(k) \geq 0, \quad i = 1, 2, \dots, n, \quad (6)$$

$$\Delta P_i^{\text{min}} \leq \Delta P_i^{\text{in}}(k) \leq \Delta P_i^{\text{max}}, \quad i = 1, 2, \dots, n, \quad (7)$$

$$\left| \Delta P_i^{\text{in}}(k) - \Delta P_i^{\text{in}}(k-1) \right| \leq \Delta P_i^{\text{rate}}, \quad i = 1, 2, \dots, n, \quad (8)$$

where  $\Delta P^{\text{in}}$  represents total power regulation command and  $\Delta P_i^{\text{rate}}$  represents the maximum climbing speed of the  $i^{\text{th}}$  AGC units.

### 3. Memetic Salp Swarm Algorithm

**3.1. Inspiration.** Salps are marine creatures that resemble jellyfish in body structure and movement. They are usually joined end to end to form a chain, also known as a salp chain. The leader is located at the first end of the chain and has the best judgment of environment and food source. The remaining salps are followers, who follow the previous one

in turn. This movement mode is conducive to the rapid coordinated movement and feeding of the salps group. Literature [54] established a mathematical model of salps chain in 2017 and proposed SSA to solve a series of optimization problems.

**3.2. Optimization Framework.** This paper is combined with cultural genetic algorithm, aiming at the shortcomings of SSA algorithm to improve, and defined as MSSA. The optimization process is as follows: the culture of each salp is defined as a solution to the optimization problem. All salps in the community are divided into different populations in the unit of salp chain, and each salp chain has its own culture and independently searches for food sources. At the same time, the culture of each salp affects and is influenced by other individuals and evolves with the evolution of the population. When the population evolution reaches a certain stage, the whole community will exchange information to realize the mixed evolution of the population until the convergence condition of the optimization problem is satisfied.

The optimization framework of MSSA is shown in Figure 3, which mainly includes the following two operations, as follows [54]:



TABLE 1: Dynamic response transfer functions of different AGC units.

Type	Transfer function
Nonreheat turbine	$1/1 + T_1s$
Reheat turbine	$(1 + T_2s)/(1 + T_3s)(1 + T_4s)(1 + T_5s)$
Hydropower	$((1 - T_6s)(1 + T_7s)/(1 + 0.5T_6s)(1 + T_8s))$
Wind and solar renewable energy	$1/1 + T_9s$

- (a) Local search in each chain: each salp chain will implement a local search to improve the ability of global exploration and local exploitation;
- (b) Global coordination in virtual population: each salp is taken as a virtual population, and the population will be regrouped into multiple new salp chains. Hence, a global coordination can be achieved.

**3.3. Local Search in Each Chain.** The salp chain can be divided into two roles, i.e., the leader and the follower. It is worth noting that the leader is responsible for directing the entire salp chain to the food source, following each other. For the  $m^{\text{th}}$  salp chain, the position of the leader can be updated, as follows [55]:

$$x_{m1}^j = \begin{cases} F_m^j + c_1(c_2(ub^j - lb^j) + lb^j), & c_3 \geq 0, \\ F_m^j - c_1(c_2(ub^j - lb^j) + lb^j), & c_3 < 0, \end{cases} \quad (9)$$

$$Y^m = [x_{mi}, f_{mi} | x_{mi} = X(m + M(i - 1)), f_{mi} = F(m + M(i - 1)), \quad i = 1, 2, \dots, n], \quad m = 1, 2, \dots, M, \quad (11)$$

where  $x_{mi}^j$  is the position vector of the  $i^{\text{th}}$  salp in the  $m^{\text{th}}$  chain;  $f_{mi}$  is the fitness value of the  $i^{\text{th}}$  salp in the  $m^{\text{th}}$  chain;  $F$  is the fitness value set of all the salps following the descending order; and  $X$  is the corresponding position vector set of all the salps, i.e., a position matrix, as follows:

$$X = \begin{bmatrix} x_1^1 & x_1^2 & \dots & x_1^d \\ x_2^1 & x_2^2 & \dots & x_2^d \\ \vdots & \vdots & \ddots & \vdots \\ x_{n \times M}^1 & x_{n \times M}^2 & \dots & x_{n \times M}^d \end{bmatrix}, \quad (12)$$

where  $d$  is the number of dimensions, and each row vector represents the position vector of each salp.

In addition, the overall flowchart of MSSA is given in Figure 5.

**3.5. MSSA Design for AGC System.** In order to ensure that the initial solution is a feasible solution, this paper forms the initial solution according to an engineering method called PROP method. In other words, the initial solution is obtained by the same adjustable capacities' ratio.

where the superscript  $j$  represents the  $j^{\text{th}}$  dimension of the searching space;  $x_{mi}^j$  is the position of the leader in the  $m^{\text{th}}$  salp chain;  $F_m^j$  denotes the position of the food source, i.e., the current best solution obtained by the  $m^{\text{th}}$  salp chain; and  $ub^j$  and  $lb^j$  are the upper and lower bounds of the  $j^{\text{th}}$  dimension, respectively;  $c_1 = 2e^{-(4k/k_{\max})^2}$ , where  $k$  is the current iteration number and  $k_{\max}$  is the maximum iteration number, respectively. Besides,  $c_2$  and  $c_3$  are the random numbers, respectively, and  $c_2, c_3 \in [0, 1]$  [56].

In addition, the position of the followers can be updated, as follows [55]:

$$x_{mi}^j = \frac{1}{2} (x_{mi}^j + x_{m,i-1}^j), \quad i = 2, 3, \dots, n, m = 1, 2, \dots, M, \quad (10)$$

where  $x_{mi}^j$  is the position of the  $i^{\text{th}}$  salp in the  $m^{\text{th}}$  salp chain;  $n$  is the population size of each salp chain; and  $M$  is the number of salp chains, respectively.

**3.4. Global Coordination in Virtual Population.** To achieve a global coordination, the virtual population will be regrouped into different salp chains according to the salps' fitness values, as shown in Figure 4. Specifically, all salps are sorted according to the order of fitness from large to small. Finally, the salps will be divided into  $M^{\text{th}}$  salp chains, and the distribution rules are as follows: the first salp regroups into the first chain, the  $M^{\text{th}}$  salps into the  $M^{\text{th}}$  chain, the  $M + 1^{\text{th}}$  into the first chain, and so on. The update rules of the  $M^{\text{th}}$  salp chain are described as follows [57]:

On the other hand, this paper applies the penalty function method to the fitness function  $\text{Fit}(x)$  to satisfy the constraint conditions (5)–(8), as follows:

$$\text{Fit}(x) = \begin{cases} f(x), & \text{if constraints are satisfied,} \\ f(x) + M(Z_u - Z_u^{\text{lim}})^2, & \text{otherwise,} \end{cases} \quad (13)$$

where  $M$  is the penalty function factor, and its value is usually a relatively large positive number;  $Z_u$  is the  $u^{\text{th}}$  constraint; and  $Z_u^{\text{lim}}$  is the limit of the  $u^{\text{th}}$  constraint.

## 4. Case Studies

The proposed methodology is tested on the IEEE load frequency control model. It is worth noting that 1 AGC unit in region A is increased to 5 units, as shown in Figure 1. Besides, Tables 2 and 3 show the main parameters of response transfer and power regulation of the units, respectively, and the control period of AGC is set to 4 seconds. Also, the response performance is compared to that of PROP, GA, and SSA. To achieve a fair comparison, the population size is set to 10 and the maximum number of

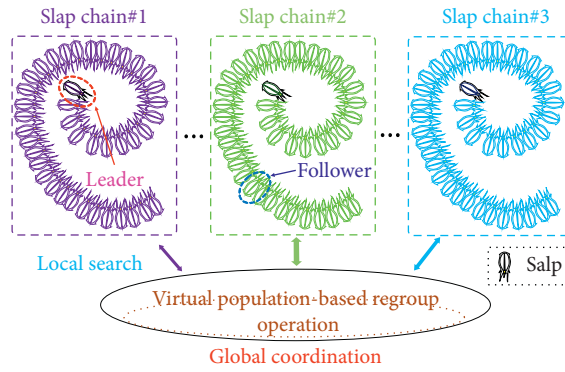


FIGURE 3: Optimization framework of MSSA.

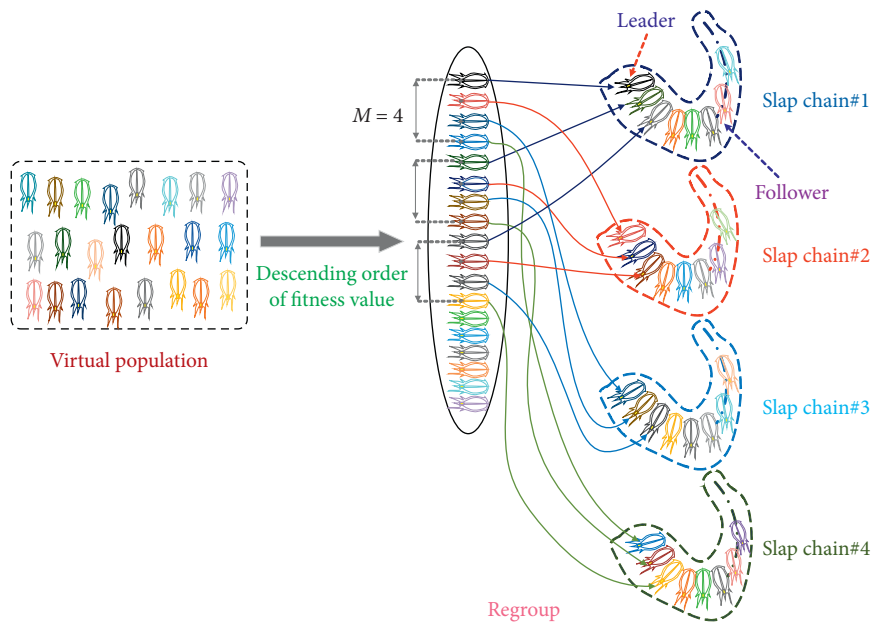


FIGURE 4: Regroup operation of virtual population.

iterations is set to 100. It is worth noting that if the parameters are not chosen properly, the convergence time will be too long or the local optimum will be trapped. Besides, ode23 was selected as the solver, and the sampling rate was set to 0.001 s.

**4.1. Convergence Research.** Figure 6 shows the convergence curves of MSSA under different power distribution instructions. It can be found that MSSA can solve the optimal solution with high quality after 30 steps of iteration, and the subsequent iteration only makes slight reduction adjustment, which also indicated the fast convergence of the algorithm. In order to better evaluate the quality of the optimal solution of different methods, Table 4 shows the comparison of the convergence results of different methods, in which each indicator unit is MW. It shows that PROP performs power allocation according to the ratio of the adjustable capacity of the unit, so the power output of thermal power units with larger regulating capacity is relatively high, and it will lead to a large power deviation. On the other hand, GA,

SSA, and MSSA can significantly reduce power deviation after their respective optimization operation, and MSSA has the best performance.

**4.2. Online Optimization.** In order to evaluate the online optimization performance of MSSA, in the area of A, a step power perturbation  $\Delta P_L = 80$  MW has occurred. The online optimization results of MSSA and PROP are compared as shown in Figure 7. Compared with previous optimization, the power deviation obtained by MSSA is smaller, and the overshoot of the total power instruction can be avoided. In addition, wind farm and PV station can recover the power system disturbed by high power quickly in the initial stage of power disturbance because of their fast response speed.

To further test the optimization performance of different algorithms, Table 5 presents the online optimization results of different algorithms (the optimal value is marked in bold), in which area control error (ACE),  $|\Delta f_1|$ , and CPS1 are the average values in the simulation. Besides, the power deviation is the total deviation in the simulation

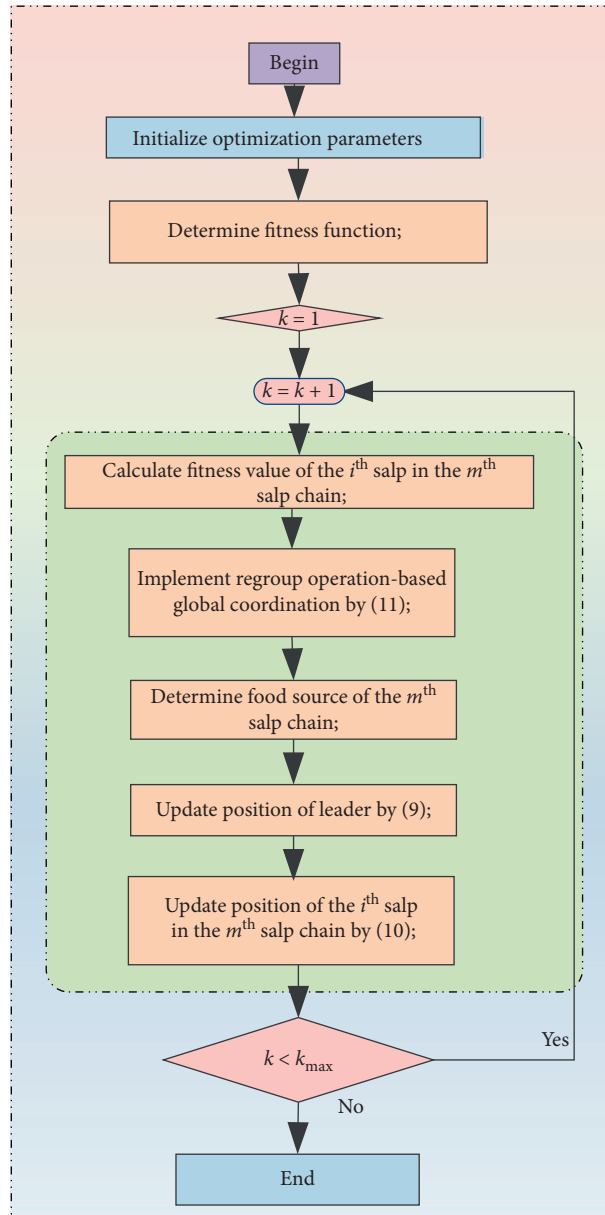


FIGURE 5: The general procedure of MSSA.

TABLE 2: Parameters of dynamic response transfer functions of AGC units.

Units	Type	Parameters of transfer function
$G_1$	Thermal power station	$T_2 = 5, T_3 = 0.08, T_4 = 10, T_5 = 0.3$
$G_2$	LNG units	$T_2 = 2, T_3 = 0.05, T_4 = 5, T_5 = 0.2$
$G_3$	Hydropower plant	$T_6 = 1, T_7 = 5, T_8 = 0.513$
$G_4$	Wind farm	$T_1 = 0.01$
$G_5$	PV station	$T_1 = 0.01$

time. Accuracy is used to measure the fitting degree of the actual adjustment output and the adjustment instruction curve in the simulation time. It can be found that, compared with PROP, the other three methods can significantly reduce power deviation, thus significantly improving the

system's dynamic response performance. Compared with GA and SSA, the online optimization results of MSSA are better, which is because memetic computing framework can observably improve the ability of exploration and exploitation.

TABLE 3: Main parameters of power regulation of AGC units.

Units	$T_d$ (s)	$\Delta P^{rate}$ (MW/min)	$\Delta P^{max}$ (MW)	$\Delta P^{min}$ (MW)
$G_1$	60	30	50	-50
$G_2$	20	18	30	-30
$G_3$	5	150	20	-10
$G_4$	1	—	15	-5
$G_5$	1	—	10	-10

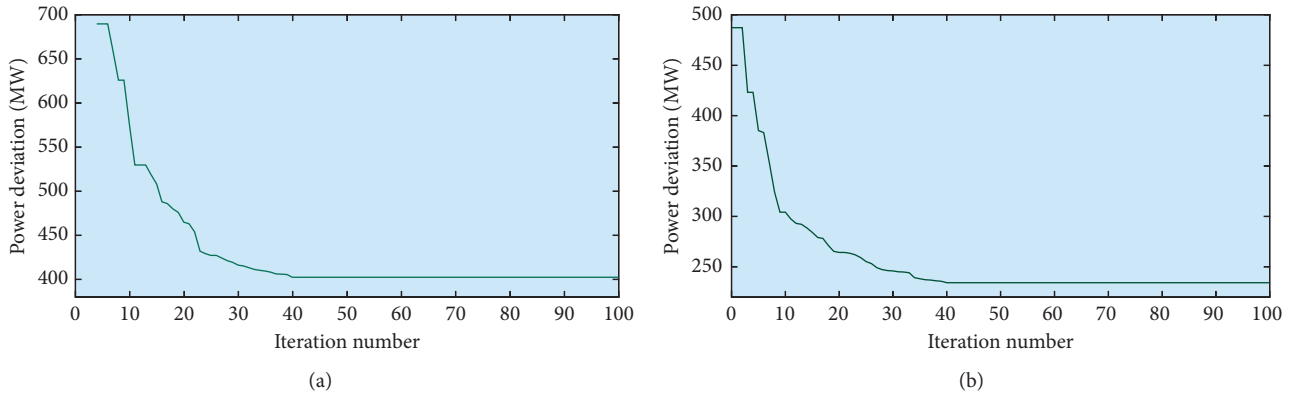


FIGURE 6: Convergence curves of MSSA. (a)  $\Delta P_{in} = 80$  MW. (b)  $\Delta P_{in} = -50$  MW.

TABLE 4: Comparison on convergence results obtained by different methods.

$\Delta P^{in}$	Method	$\Delta P_1^{in}$	$\Delta P_2^{in}$	$\Delta P_3^{in}$	$\Delta P_4^{in}$	$\Delta P_5^{in}$	Power deviation
80	PROP	32.00	19.20	12.80	9.60	6.40	676.95
	GA	15.52	23.18	17.92	12.7	10.68	529.86
	SSA	10.61	25.74	17.26	14.67	11.72	471.48
	MSSA	14.26	20.84	19.52	15.12	10.26	402.451
-50	PROP	-23.81	-14.29	-4.76	-2.38	-4.76	479.83
	GA	-4.26	-23.24	-10.02	-3.86	-8.62	274.26
	SSA	-8.65	-20.62	-9.85	-4.29	-6.59	307.48
	MSSA	-4.48	-20.69	-9.14	-5.58	-10.11	234.254

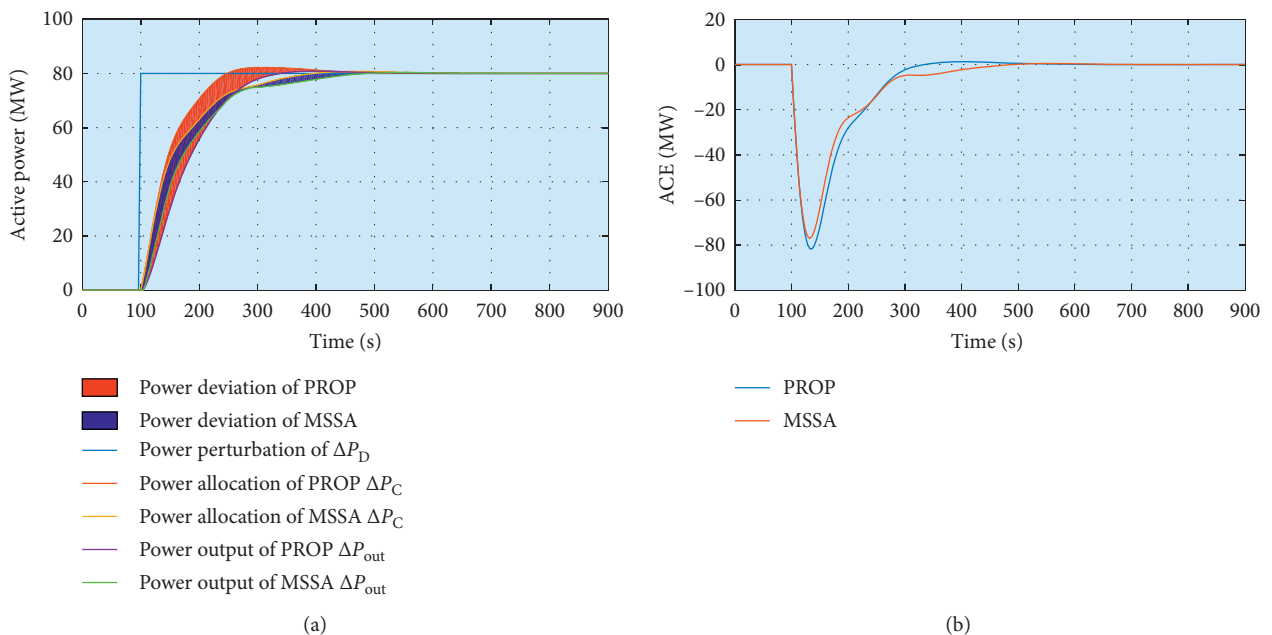


FIGURE 7: Continued.

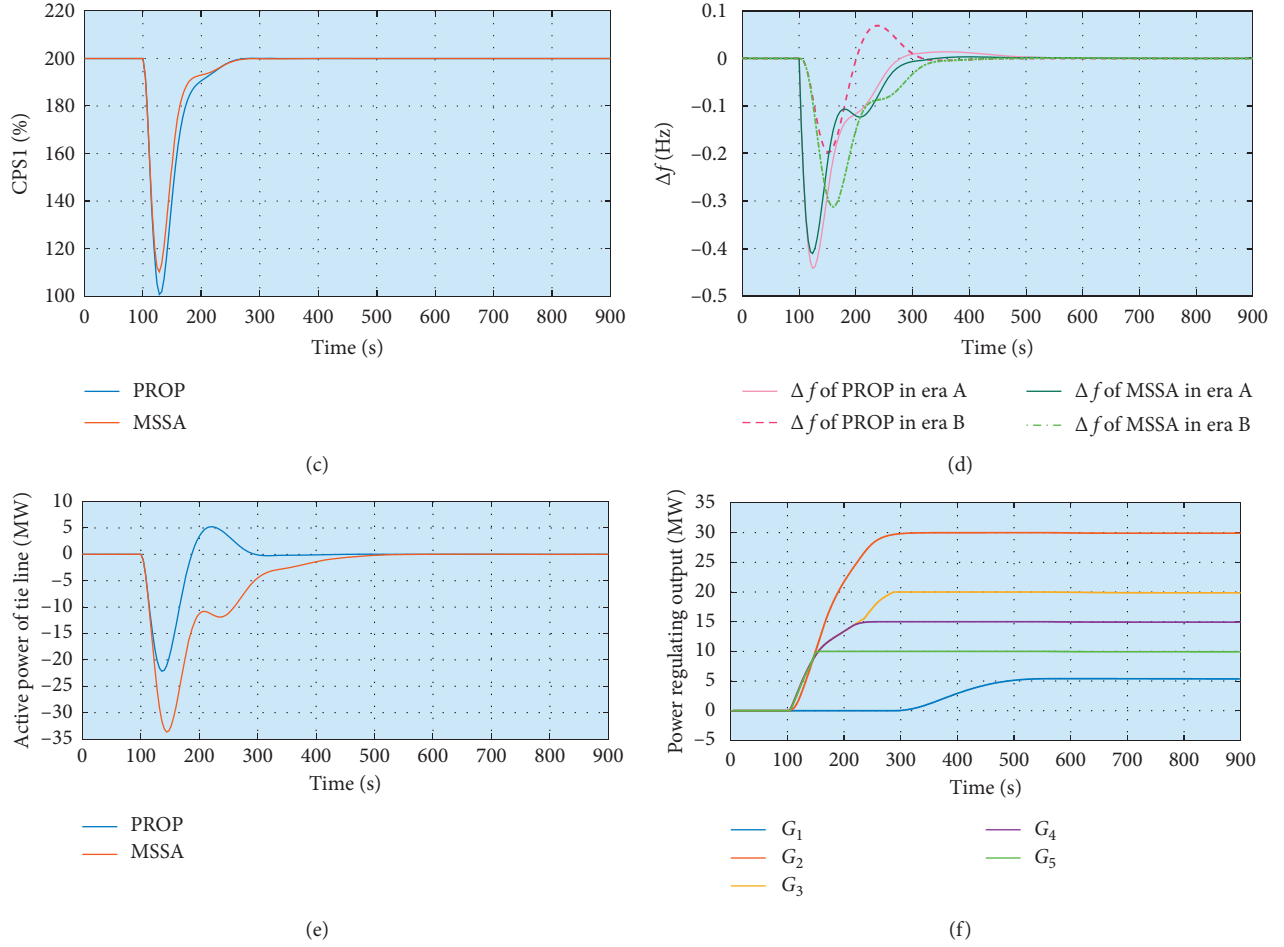


FIGURE 7: Result comparison of online optimization by MSSA and without optimization when  $\Delta P_L = 80$  MW. (a) Total power regulation curve. (b) Curve of ACE. (c) Curve of CPS1. (d) Frequency deviation  $\Delta f$ . (e) Active power of tie line (MW). (f) Power output curve of the units.

TABLE 5: Result comparison of online optimization obtained by different methods.

$\Delta P_L$	Algorithms	ACE  (MW)	$\Delta f_1$ (Hz)	CPS1 (%)	Accuracy (%)	Power deviation (MW)
80	PROP	7.7678	0.0356	194.69	95.84	630.05
	GA	7.4209	0.0323	195.86	98.25	261.32
	SSA	7.5095	0.0321	195.84	98.17	267.52
	MSSA	7.3995	0.0316	195.57	98.84	254.21
-50	PROP	5.0541	0.0235	197.78	94.99	477.46
	GA	4.6046	0.0203	198.25	98.21	164.26
	SSA	4.6044	0.0202	198.29	98.23	161.48
	MSSA	4.6040	0.0196	198.36	98.41	149.96

## 5. Conclusions

In this paper, a multisource optimal collaborative control method for power system with renewable energy participation in secondary frequency regulation is proposed. The main contributions can be summarized as follows:

- (i) A novel AGC control model is established for the power system with high renewable energy penetration

to improve the dynamic response performance of the system;

- (ii) The study verified the effectiveness of MSSA for AGC. It can not only meet the online regulation requirements of AGC but also quickly obtain high-quality regulation schemes with high convergence stability, and the dynamic response performance of the entire regional power grid is significantly improved.

Besides, electric vehicles will be considered to participate in AGC in future studies.

## Abbreviations

$\Delta P_i^{\text{in}}$ : Input regulation power command of the  $i^{\text{th}}$  AGC unit  
 $\Delta P_i^{\text{out}}$ : Real-time output of regulated power of the  $i^{\text{th}}$  AGC unit  
 $\Delta T$ : Control period of AGC  
 $N$ : Number of control periods  
 $n$ : Number of AGC units  
 $\Delta P_i^{\text{rate}}$ : Maximum climbing speed of the  $i^{\text{th}}$  AGC units  
 $x_{mi}^j$ : Position of the leader in the  $m^{\text{th}}$  salp chain  
 $F_m^j$ : Position of the food source  
 $x_{mi}^j$ : Position vector of the  $i^{\text{th}}$  salp in the  $m^{\text{th}}$  chain  
 $f_{mi}$ : Fitness value of the  $i^{\text{th}}$  salp in the  $m^{\text{th}}$  chain  
 $F$ : Fitness value set of all the salps following the descending order  
 $X$ : Corresponding position vector set of all the salps  
 $PV$ : Photovoltaic  
 $AGC$ : Automatic generation control  
 $GA$ : Genetic algorithm  
 $SSA$ : Salp swarm algorithm  
 $MSSA$ : Memetic salp swarm algorithm.

## Data Availability

The data that support the findings of this study are available upon request from the corresponding author. The data are not publicly available due to privacy or ethical restrictions.

## Conflicts of Interest

The authors declare no conflicts of interest.

## Acknowledgments

The authors gratefully acknowledge the support of the National Natural Fund of China (52037003) and Key Science and Technology Project of Yunnan Province (202002AF080001).

## References

- [1] B. Yang, L. Jiang, L. Wang, W. Yao, and Q. H. Wu, "Nonlinear maximum power point tracking control and modal analysis of DFIG based wind turbine," *International Journal of Electrical Power & Energy Systems*, vol. 74, pp. 429–436, 2016.
- [2] B. Yang, T. Yu, X. Zhang et al., "Dynamic leader based collective intelligence for maximum power point tracking of PV systems affected by partial shading condition," *Energy Conversion and Management*, vol. 179, pp. 286–303, 2019.
- [3] B. Yang, T. Yu, H. Shu et al., "Passivity-based sliding-mode control design for optimal power extraction of a PMSG based variable speed wind turbine," *Renewable Energy*, vol. 119, pp. 577–589, 2018.
- [4] X. Zhang, T. Yu, B. Yang, and L. Li, "Virtual generation tribe based robust collaborative consensus algorithm for dynamic generation command dispatch optimization of smart grid," *Energy*, vol. 101, pp. 34–51, 2016.
- [5] Z. Wang, J. Zhong, and J. Li, "Design of performance-based frequency regulation market and its implementations in real-time operation," *International Journal of Electrical Power & Energy Systems*, vol. 87, pp. 187–197, 2017.
- [6] L. R. Chang-Chien, C. C. Sun, and Y. J. Yeh, "Modeling of wind farm participation in AGC," *IEEE Transactions on Power Systems*, vol. 29, no. 3, pp. 1204–1211, 2013.
- [7] J. M. Morales, L. Baringo, A. J. Conejo, and R. Mínguez, "Probabilistic power flow with correlated wind sources," *IET Generation, Transmission & Distribution*, vol. 4, no. 5, pp. 641–651, 2010.
- [8] M. Sun, H. Wu, Y. Qiu, and Y. Song, "Probability load flow for wind power integrated system based on generalized polynomial chaos method," *Automation of Electric Power Systems*, vol. 41, no. 7, pp. 54–60, 2017.
- [9] B. R. Prusty and D. Jena, "A critical review on probabilistic load flow studies in uncertainty constrained power systems with photovoltaic generation and a new approach," *Renewable and Sustainable Energy Reviews*, vol. 69, pp. 1286–1302, 2017.
- [10] V. Lakshmanan, M. Marinelli, J. Hu, and H. W. Bindner, "Provision of secondary frequency control via demand response activation on thermostatically controlled loads: solutions and experiences from Denmark," *Applied Energy*, vol. 173, pp. 470–480, 2016.
- [11] R. Fantino, J. Solsona, and C. Busada, "Nonlinear observer-based control for PMSG wind turbine," *Energy*, vol. 113, pp. 248–257, 2016.
- [12] L. Dong, W. Cheng, and Y. Yang, "Probabilistic load flow calculation for power grid containing wind farms," *Power System Technology*, vol. 16, pp. 87–91, 2009.
- [13] B. Yang, L. Jiang, W. Yao, and Q. H. Wu, "Perturbation estimation based coordinated adaptive passive control for multimachine power systems," *Control Engineering Practice*, vol. 44, pp. 172–192, 2015.
- [14] B. Yang, J. Wang, X. Zhang et al., "Comprehensive overview of meta-heuristic algorithm applications on PV cell parameter identification," *Energy Conversion and Management*, vol. 208, Article ID 112595, 2020.
- [15] M. S. Čalović, "Advanced automatic generation control with automatic compensation of tie-line losses," *Electric Power Components and Systems*, vol. 40, no. 7, pp. 807–828, 2012.
- [16] X. Zhao, Z. Lin, B. Fu, L. He, and N. Fang, "Research on automatic generation control with wind power participation based on predictive optimal 2-degree-of-freedom PID strategy for multi-area interconnected power system," *Energies*, vol. 11, no. 12, p. 3325, 2018.
- [17] B. Yang, X. Zhang, T. Yu, H. Shu, and Z. Fang, "Grouped grey wolf optimizer for maximum power point tracking of doubly-fed induction generator based wind turbine," *Energy Conversion and Management*, vol. 133, pp. 427–443, 2017.
- [18] G. Rashid and M. H. Ali, "Nonlinear control-based modified BFCL for LVRT capacity enhancement of DFIG-based wind farm," *IEEE Transactions on Energy Conversion*, vol. 32, no. 1, pp. 284–295, 2016.
- [19] N. H. Saad, A. A. Sattar, and A. E.-A. M. Mansour, "Low voltage ride through of doubly-fed induction generator connected to the grid using sliding mode control strategy," *Renewable Energy*, vol. 80, pp. 583–594, 2015.
- [20] B. Yang, T. Yu, H. Shu, J. Dong, and L. Jiang, "Robust sliding-mode control of wind energy conversion systems for optimal power extraction via nonlinear perturbation observers," *Applied Energy*, vol. 210, pp. 711–723, 2018.
- [21] P. P. Zarina, S. Mishra, and P. C. Sekhar, "Exploring frequency control capability of a PV system in a hybrid PV-rotating



- machine-without storage system,” *International Journal of Electrical Power & Energy Systems*, vol. 60, pp. 258–267, 2014.
- [22] G. Sharma, I. Nasiruddin, and K. R. Niazi, “Optimal automatic generation control of asynchronous power systems using output feedback control strategy with dynamic participation of wind turbines,” *Electric Power Components and Systems*, vol. 43, no. 4, pp. 384–398, 2015.
- [23] X. Zhang, T. Yu, B. Yang, L. Zheng, and L. Huang, “Approximate ideal multi-objective solution  $Q(\lambda)$  learning for optimal carbon-energy combined-flow in multi-energy power systems,” *Energy Conversion and Management*, vol. 106, pp. 543–556, 2015.
- [24] C. Zhang, J. Chen, M. Liu et al., “Regulation mechanism of biomolecule interaction behaviors on the superlubricity of hydrophilic polymer coatings,” *Protection and Control of Modern Power Systems*, 2020.
- [25] A. G. Pillai, E. R. Samuel, and A. Unnikrishnan, “Minimal realized power systems for load frequency control using optimal theory based PID controller,” *IETE Journal of Research*, vol. 5, no. 1, pp. 1–13, 2020.
- [26] J. Liu, W. Yao, J. Wen et al., “Impact of power grid strength and PLL parameters on stability of grid-connected DFIG wind farm,” *IEEE Transactions on Sustainable Energy*, vol. 11, no. 1, pp. 545–557, 2020.
- [27] D. Song, X. Fan, J. Yang, A. Liu, S. Chen, and Y. H. Joo, “Power extraction efficiency optimization of horizontal-axis wind turbines through optimizing control parameters of yaw control systems using an intelligent method,” *Applied Energy*, vol. 224, pp. 267–279, 2018.
- [28] X. Zhang, Z. Xu, T. Yu, B. Yang, and H. Wang, “Optimal mileage based AGC dispatch of a GenCo,” *IEEE Transactions on Power Systems*, vol. 35, no. 4, pp. 2516–2526, 2020.
- [29] X. S. Zhang, T. Tan, B. Zhou, T. Yu, B. Yang, and X. M. Huang, “Adaptive distributed auction-based algorithm for optimal mileage based AGC dispatch with high participation of renewable energy,” *International Journal of Electrical Power & Energy Systems*, vol. 124, Article ID 106371, 2020.
- [30] Y. Shen, W. Yao, J. Wen, H. He, and L. Jiang, “Resilient wide-area damping control using GrHDP to tolerate communication failures,” *IEEE Transactions on Smart Grid*, vol. 10, no. 3, pp. 2547–2557, 2019.
- [31] B. Mohanty, “TLBO optimized sliding mode controller for multi-area multi-source nonlinear interconnected AGC system,” *International Journal of Electrical Power & Energy Systems*, vol. 73, pp. 872–881, 2015.
- [32] X. S. Zhang, T. Yu, Z. N. Pan, B. Yang, and T. Bao, “Lifelong learning for complementary generation control of interconnected power grids with high-penetration renewables and EVs,” *IEEE Transactions on Power Systems*, vol. 33, no. 4, pp. 4097–4110, 2018.
- [33] X. S. Zhang, Q. Li, T. Yu, and B. Yang, “Consensus transfer Q-learning for decentralized generation command dispatch based on virtual generation tribe,” *IEEE Transactions on Smart Grid*, vol. 9, no. 3, pp. 2152–2165, 2018.
- [34] M. Tan, C. J. Han, C. Han, X. Zhang, L. Guo, and T. Yu, “Hierarchically correlated equilibrium Q-learning for multi-area decentralized collaborative reactive power Optimization,” *CSEE Journal of Power and Energy Systems*, vol. 2, no. 3, pp. 65–72, 2016.
- [35] D. R. Song, S. Y. Zheng, S. Yang et al., “Annual energy production estimation for variable-speed wind turbine at high-altitude site,” *Journal of Modern Power Systems and Clean Energy*, 2020.
- [36] X. Peng, W. Yao, C. Yan, J. Wen, and S. Cheng, “Two-stage variable proportion coefficient based frequency support of grid-connected DFIG-WTs,” *IEEE Transactions on Power Systems*, vol. 35, no. 2, pp. 962–974, 2020.
- [37] X. He, L. Chu, R. C. Qiu, Q. Ai, Z. Ling, and J. Zhang, “Invisible units detection and estimation based on random matrix theory,” *IEEE Transactions on Power Systems*, vol. 35, no. 3, pp. 1846–1855, 2019.
- [38] X. Zhang, T. Yu, B. Yang, and L. Cheng, “Accelerating bio-inspired optimizer with transfer reinforcement learning for reactive power optimization,” *Knowledge-Based Systems*, vol. 116, pp. 26–38, 2017.
- [39] Y. Arya and N. Kumar, “AGC of a multi-area multi-source hydrothermal power system interconnected via AC/DC parallel links under deregulated environment,” *International Journal of Electrical Power & Energy Systems*, vol. 75, pp. 127–138, 2016.
- [40] A. S. El-Bakry, R. A. Tapia, T. Tsuchiya, and Y. Zhang, “On the formulation and theory of the Newton interior-point method for nonlinear programming,” *Journal of Optimization Theory and Applications*, vol. 89, no. 3, pp. 507–541, 1996.
- [41] S. P. Ghoshal, “Application of GA/GA-SA based fuzzy automatic generation control of a multi-area thermal generating system,” *Electric Power Systems Research*, vol. 70, no. 2, pp. 115–127, 2004.
- [42] A. Demiroren and H. L. Zeynelgil, “GA application to optimization of AGC in three-area power system after deregulation,” *International Journal of Electrical Power & Energy Systems*, vol. 29, no. 3, pp. 230–240, 2007.
- [43] T. Yu, X. S. Zhang, B. Zhou, and K. W. Chan, “Hierarchical correlated Q-learning for multi-layer optimal generation command dispatch,” *International Journal of Electrical Power & Energy Systems*, vol. 78, pp. 1–12, 2016.
- [44] X. Zhang, B. Yang, T. Yu, and L. Jiang, “Dynamic Surrogate Model based optimization for MPPT of centralized thermo-electric generation systems under heterogeneous temperature difference,” *IEEE Transactions on Energy Conversion*, vol. 35, no. 2, pp. 966–976, 2020.
- [45] X. Zhang, S. Li, T. He et al., “Memetic reinforcement learning based maximum power point tracking design for PV systems under partial shading condition,” *Energy*, vol. 174, pp. 1079–1090, 2019.
- [46] H. Golpîra, H. Bevrani, and H. Golpîra, “Application of GA optimization for automatic generation control design in an interconnected power system,” *Energy Conversion and Management*, vol. 52, no. 5, pp. 2247–2255, 2011.
- [47] R. K. Sahu, S. Panda, and G. T. Chandra Sekhar, “A novel hybrid PSO-PS optimized fuzzy PI controller for AGC in multi area interconnected power systems,” *International Journal of Electrical Power & Energy Systems*, vol. 64, pp. 880–893, 2015.
- [48] S. Panda, B. Mohanty, and P. K. Hota, “Hybrid BFOA-PSO algorithm for automatic generation control of linear and nonlinear interconnected power systems,” *Applied Soft Computing*, vol. 13, no. 12, pp. 4718–4730, 2013.
- [49] A. K. Barisal and S. Mishra, “Improved PSO based automatic generation control of multi-source nonlinear power systems interconnected by AC/DC links,” *Cogent Engineering*, vol. 5, no. 1, Article ID 1422228, 2018.
- [50] X. He, Q. Ai, R. C. Qiu, W. Huang, L. Piao, and H. Liu, “A big data architecture design for smart grids based on random matrix theory,” *IEEE Transactions on Smart Grid*, vol. 8, no. 2, pp. 674–686, 2015.

- [51] B. Yang, L. Zhong, X. Zhang et al., "Novel bio-inspired memetic salp swarm algorithm and application to MPPT for PV systems considering partial shading condition," *Journal of Cleaner Production*, vol. 215, pp. 1203–1222, 2019.
- [52] T. Yu, Y. M. Wang, W. J. Ye, B. Zhou, and K. W. Chan, "Stochastic optimal generation command dispatch based on improved hierarchical reinforcement learning approach," *IET Generation, Transmission & Distribution*, vol. 5, no. 8, pp. 789–797, 2011.
- [53] M. Datta and T. Senjyu, "Fuzzy control of distributed PV inverters/energy storage systems/electric vehicles for frequency regulation in a large power system," *IEEE Transactions on Smart Grid*, vol. 4, no. 1, pp. 479–488, 2013.
- [54] S. Mirjalili, A. H. Gandomi, S. Z. Mirjalili, S. Saremi, H. Faris, and S. M. Mirjalili, "Salp Swarm algorithm: a bio-inspired optimizer for engineering design problems," *Advances in Engineering Software*, vol. 114, no. 6, pp. 163–191, 2017.
- [55] M. Eusuff, K. Lansey, and F. Pasha, "Shuffled frog-leaping algorithm: a memetic meta-heuristic for discrete optimization," *Engineering Optimization*, vol. 38, no. 2, pp. 129–154, 2006.
- [56] S. Daraban, D. Petreus, and C. Morel, "A novel MPPT (maximum power point tracking) algorithm based on a modified genetic algorithm specialized on tracking the global maximum power point in photovoltaic systems affected by partial shading," *Energy*, vol. 74, no. 5, pp. 374–388, 2014.
- [57] M. M. Eusuff and K. E. Lansey, "Optimization of water distribution network design using the shuffled frog leaping algorithm," *Journal of Water Resources Planning and Management*, vol. 129, no. 3, pp. 210–225, 2003.